SLAC – 336
CONF – 880747
UC-34d
(T/E)

PROCEEDINGS

OF

SUMMER INSTITUTE ON PARTICLE PHYSICS

July 18-29, 1988

PROBING THE WEAK INTERACTION: CP VIOLATION AND RARE DECAYS

Program Directors

Gary J. Feldman

Frederick J. Gilman

David W. G. S. Leith

Ed. by Eileen C. Brennan

Sponsored by Stanford University and Stanford Linear Accelerator Center under contract with the U.S. Department of Energy. Contract DE-AC03-76SF00515.

January 1989

Printed in the United States of America. Available from National Technical Information Service, U.S. Department of Commerce, 5285 Port Royal Road, Springfield, VA 22161.

SUMMER SCHOOL LECTURES

PREFACE

The sixteenth annual SLAC Summer Institute on Particle Physics was held from July 18-29, 1988. The subject of "Probing the Weak Interaction: CP Violation and Rare Decays" was studied in both its experimental and theoretical aspects by a total of 342 participants from thirteen countries. The school portion of the Institute featured excellent lectures on this subject by K. Berkelman, I. Bigi, B. Cabrera, L. Hall, H. Harari, J. Sandweiss, A.J.S. Smith, M. Witherell, and L. Wolfenstein. The afternoon discussion were very much enhanced and enlivened by C. Ahn, R. Aleksan, M. Davier, C. Dibb, R. Ezmaizaldeh, R. Frey, J. Frieman, M. Karliner, R. Kauffman, I. Klebanov, A. Lankford, B. Lockman, C. Munger, J. Ritchie, D. Shroeder, N. Wang, A. Weinstein, and M. Woods who acted as "provocateurs." As is traditional, the last three days of the Institute were taken up by a Topical Conference, with invited talks from ongoing experiments and the associated theory.

We thank Eileen Brennan for organizing and running the meeting, and with great persistence, editing these Proceedings. She and her staff contributed much to the success of the meeting both through their hard work and their good humor.

Gary Feldman
Frederick J. Gilman
David W. G. S. Leith
Program Directors

TABLE OF CONTENTS

Part II. TOPICAL CONFERENCE **page**

APPENDIX

RESULTS ON b-DECAY IN e^+e^- COLLISIONS, WITH EMPHASIS ON CP VIOLATION

Lectures given at the SLAC Summer Institute, 18-29 July 88

Karl Berkelman, Laboratory of Nuclear Studies, Cornell University

1. STANDARD MODEL BASICS

Decays of the b-quark take place through the flavor changing weak interaction. In the standard electroweak model the GIM mechanism[1] requires that there be no flavor changing neutral current interactions (which is confirmed by the absence of $B \to \ell^+\ell^- X$ decays[2]). The flavor changing weak interaction is a gauge interaction carried by the charged W intermediate vector boson, of mass 81.8 GeV. The $W^{\pm}$ couples to doublets of left-handed leptons or quarks (Fig. 1.1). There are at least three lepton doublets, $(\ell^-,\nu) = (e^-,\nu_e)$, (μ,ν_μ), or (τ,ν_τ), and three quark doublets, $(D,U) = (d,u)$, (s,c), or (b,t). The color-weighted sum of charges for each of the three families should be zero ($q_e + q_\nu + 3q_d + 3q_u = 0$, for instance), or the triangle anomaly contribution to processes such as Compton scattering (Fig. 1.2) will violate unitarity. Therefore, in the standard model the number of lepton families has to equal the number of quark families. There are good reasons to believe that the number of families cannot be much greater than the three we know, but as far as I know, there is no proof yet that there cannot be a fourth family.

Two familiar examples (Fig. 1.3) of flavor changing weak interactions are muon decay,

$$\Gamma = \frac{1}{3\cdot 2^{11}\pi^3}\frac{g^4}{M_W^4} m_\mu^5 f(m_e/m_\mu),$$

and pion decay,

$$\Gamma = \frac{1}{2^8\pi}\frac{g^4}{M_W^8} |V_{ud}|^2 f_\pi^2 m_\mu^2 m F(m_\mu/m_\pi).$$

The formulas illustrate several important dependences of the weak interaction rates: (a) family mixing, (b) phase space, (c) helicity, and (d) hadron binding.

0050888-014

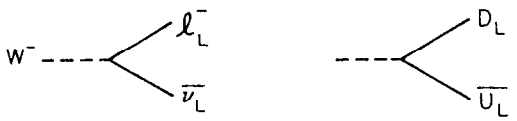

Fig. 1.1 Charged current weak couplings, leptonic and hadronic.

0050888-015

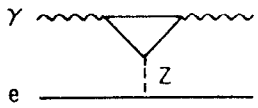

Fig. 1.2 The triangle anomaly graph for Compton scattering.

0050888-016

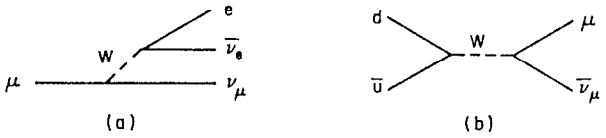

Fig. 1.3 (a) Muon decay $\mu^- \to \nu_\mu e^- \bar{\nu}_e$; (b) pion decay $\pi^- \to \mu^- \bar{\nu}_\mu$.

(a) Weak coupling

Reactions involving only leptons are characterized by a single universal coupling constant g, which can be related to the electromagnetic coupling and the Weinberg angle parametrizing the electroweak symmetry breaking: $g = e/\sin\theta_w = 0.637$. Since the interactions we are considering involve a virtual four-momentum $q_w \ll M_w$, the coupling and propagator factor $g^2/(q_w^2 - M_w^2)$ always reduces to $g^2/M_w^2 = (8/\sqrt{2})G_F = 6.60\times10^{-5}$ GeV^{-2}.

(b) Phase space

The rate for any final state in a weak decay is suppressed by a relative phase space factor that depends on the final state particle masses and the total available energy. In the case of the muon decay the factor is

$$f(x) = 1 - 8x + 8x^3 - x^4 - 12x^2 \ln(x),$$

which is very close to one for $x = (m_e/m_\mu)^2$. If we apply the same rate formula to the $\tau^- \to \nu_\tau \mu^- \bar{\nu}_\tau$ decay the phase space factor is $f = 0.973$ for $x = (m_\mu/m_\tau)^2$.

In the case of a decay of a particle of mass m_1 to two particles of mass m_2 and one massless particle, the appropriate phase space factor is

$$g(x) = (1 - \frac{7x}{2} - \frac{x^2}{8} - \frac{3x^3}{16})\sqrt{1-x} + 3x^2(1 - \frac{x^2}{16})\ln\frac{1-\sqrt{1-x}}{\sqrt{x}}$$

with $x = (2m_2/m_1)^2$.

The phase space factor for π or K decay to $\ell+\nu$ is

$$F(x) = (1 - x)^2,$$

which is $F = 0.182$ for $x = (m_\mu/m_\pi)^2$ and $F = 0.910$ for $x = (m_\mu/m_K)^2$.

(c) Helicity suppression

In the decay $\pi^- \to \ell\bar{\nu}$ the two final state fermions are emitted in opposite directions in the pion rest frame and must have the same helicity in order to have angular momentum components that sum to zero, the spin of the pion. The V-A nature of the weak interaction requires that the virtual W^- couple to a left-handed ℓ^- and a right-handed $\bar{\nu}$. Since the massless neutrino travels at velocity c, its

helicity cannot be changed by a choice of frame. Angular momentum conservation then forces the ℓ^- to have the wrong helicity, which is not impossible if it is nonrelativistic. The decay rate however is then suppressed by the factor $1 - \beta_\ell = 2m_\ell{}^2/(m_\pi{}^2 + m_\ell{}^2)$. This explains the factor $m_\mu{}^2$ in the $\pi \to \mu \bar{\nu}_\mu$ decay rate formula and accounts for the fact that the $\pi \to e \bar{\nu}_e$ branching ratio is only 1.23×10^{-4}, in spite of the more favorable phase space factor.

(d) Hadronic binding

When a meson decays leptonically the bound quark and antiquark annihilate into the W that produces the $\ell+\nu$ final state. In a non-relativistic model of quark-antiquark binding, the amplitude would be proportional to $\psi(0)$, the $q\bar{q}$ wave function at zero separation. More generally, this is contained in the "decay constant" f of the meson, which can in principle be calculated from QCD with lattice gauge theory methods. The observed charged pion and kaon leptonic decay rates imply that $f_\pi = 0.94m_\pi$, and $f_K = 0.34m_K$.

(e) Family mixing

The effective couplings in reactions involving quarks are reduced, especially in cases where the W couples two quarks from different families, as for example in the $K \to \mu\nu$ decay. First parametrized in terms of the Cabibbo angle, the effect is now described in terms of a 3-by-3 unitary family-mixing matrix (Kobayashi-Maskawa[3]). That is, the D (charge -1/3) members of the weak interaction doublets, d' s' b', are related to the pure quark states, d s b (eigenstates of the strong interaction) by a unitary matrix V. The effective coupling for any WUD vertex is given by gV_{UD}.

The nine matrix elements are not independent, but depend on the three angles specifying the rotation from the d s b basis to the d's'b' basis, plus a complex phase. They can be chosen in various ways; rather than the original Kobayashi-Maskawa convention, I prefer the choice which defines the angles to correspond to the three most easily measurable off-diagonal family transitions, θ_{12} for $s \to u$, θ_{23} for $b \to c$, θ_{13} for $b \to u$, and concentrates the phase dependence in the corners farthest from the diagonal:

$$V = \begin{pmatrix} V_{ud} & V_{us} & V_{ub} \\ V_{cd} & V_{cs} & V_{cb} \\ V_{td} & V_{ts} & V_{tb} \end{pmatrix}$$

$$= \begin{pmatrix} c_{12}c_{13} & s_{12}c_{13} & s_{13}e^{-i\delta} \\ -s_{12}c_{23}-c_{12}s_{23}s_{13}e^{i\delta} & c_{12}c_{23}-s_{12}s_{23}s_{13}e^{i\delta} & s_{23}c_{13} \\ s_{12}s_{23}-c_{12}c_{23}s_{13}e^{i\delta} & -c_{12}s_{23}-s_{12}c_{23}s_{13}e^{i\delta} & c_{23}c_{13} \end{pmatrix},$$

where $c_{ij} = \cos\theta_{ij}$ and $s_{ij} = \sin\theta_{ij}$. It is easier to understand the matrix in the limit in which the three angles are small, so that $c_{ij} = 1$:

$$V = \begin{pmatrix} 1 & s_{12} & s_{13}e^{-i\delta} \\ -s_{12}-s_{23}s_{13}e^{i\delta} & 1 & s_{23} \\ s_{12}s_{23}-s_{13}e^{i\delta} & -s_{23} & 1 \end{pmatrix}.$$

An equivalent form, due to Wolfenstein,[4] substitutes λ for $\sin\theta_{12}$, $A\lambda^2$ for $\sin\theta_{23}$, and $A\lambda^3(\rho+i\eta)$ for $\sin\theta_{13}e^{-i\delta}$. In the $\lambda<<1$ limit it reduces to

$$V = \begin{pmatrix} 1 & \lambda & A\lambda^3(\rho+i\eta) \\ -\lambda & 1 & A\lambda^2 \\ A\lambda^3(1-\rho-i\eta) & -A\lambda^2 & 1 \end{pmatrix}.$$

The angles and phases (θ_{12}, θ_{23}, θ_{13}, and δ or alternatively λ, A, ρ, and η) are assumed parameters in the Standard Model on the same footing as lepton and quark masses, coupling constants, etc. In order to come up with a more general theory which predicts all the assumed parameters, it is important that we know their values. In measuring them we are also testing the Standard Model and the

assumption that there are only three families. With four families the 4×4 matrix can be parametrized by nine independent constants. If the neutrinos have mass, there will in general be a mixing matrix for leptons also. From now on we will assume three quark families and no lepton mixing.

Provided that the KM angles, θ_{23} and θ_{13}, involving the third quark family are small enough, the matrix elements in the upper-left 2×2 quadrant depend only on θ_{12}, essentially the Cabibbo angle. Measurements of decay rates for the first two families give the following matrix elements:[5]

$$\begin{pmatrix} |V_{ud}| & |V_{us}| \\ |V_{cd}| & |V_{cs}| \end{pmatrix} \approx \begin{pmatrix} 0.9744\pm0.0009 & 0.2196\pm0.0023 \\ 0.19 \pm0.03 & 0.96 \pm0.08 \end{pmatrix}.$$

The measurements are all consistent with $\theta_{12} = 0.226$. If we assume three quark families and unitarity of the matrix, they also imply that $|V_{ub}| < 0.084$ and $|V_{cb}| < 0.46$ (90% confidence).

To find out anything about the remaining two mixing angles, we have to involve the third quark family. If these angles are small (they are), the model predicts that the dominant flavor changing decay of the t quark is to the b quark, so that even if we could readily observe the decays of hadrons containing the top quark, there would not be much sensitivity to the off-diagonal matrix elements containing θ_{23} and θ_{13}. That is, we have to depend on measurements of the decay of the b quark, which has to decay through family mixing.

2. B MESON DECAY MECHANISMS

(a) Idealized spectator decays

Ideally, one could get the KM matrix elements $|V_{cb}|$ and $|V_{ub}|$ by measuring, for example, the rates for $b \to ce^-\bar{\nu}_e$ and $b \to ue^-\bar{\nu}_e$, then using the formula given above for muon decay (with the appropriate factor of $|V|^2$) to extract the matrix elements. Since we don't have free quarks, we look instead at $B \to X_c e^-\bar{\nu}_e$ and $B \to X_u e^-\bar{\nu}_e$, where X_c and X_u represent all charmed meson and all uncharmed meson final states inclusively. The hope is that the b quark would decay according to the muon decay diagram, while its partner antiquark in the B would continue without affecting the weak interaction (Fig. 2.1) and combine with some unpaired quark in the inclusive hadron final state. In this ideal model the existence of the "spectator" antiquark and its strong interactions with the b quark and the final c or u quark would not affect the weak decay rate. In fact, however, we should expect corrections which may be difficult to calculate and/or decay amplitude contributions from other decay mechanisms. We have to measure in some detail the decays of mesons containing heavy quarks before we can have confidence in extracting experimental information about the basic parameters of the quark decay.

Whether a meson containing a heavy quark is charged or neutral is determined by the partner light antiquark: $\bar{K}^o = s\bar{d}$, $K^- = s\bar{u}$; $D^+ = c\bar{d}$, $D^o = c\bar{u}$; $\bar{B}^o = b\bar{d}$, $B^- = b\bar{u}$. If it is only a spectator in the weak decay, then the lifetimes of the charged and neutral heavy mesons should be identical. The measured ratio of lifetimes τ_{ch}/τ_{neut} for K and D mesons show important nonspectator effects; the data for B's are inconclusive:

K^+/K_S, K^+/K_L:	139, 0.239	(PDG[6])
D^+/D^o:	2.4	(E691[7])
B^+/B^o:	between 0.5 and 2.3	(CLEO[8])

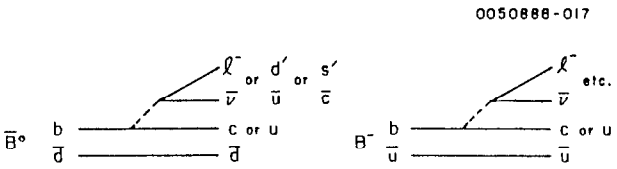

Fig. 2.1 Spectator graphs for B decay.

In the spectator picture the branching ratios at the lepton and quark level are predictable using the muon decay rate formula. We substitute the approximate masses ($m_u = m_d = 0.34$, $m_s = 0.50$, $m_c = 1.66$, $m_b = 5.04$ GeV) and KM matrix elements along with a factor of three for quark colors to arrive at the following predicted branching ratios, as compared to experiment:

Quark Decay	Prediction	Data(±)	Data(o)	Data Ref.
$c \to s e^+ \nu_e$	0.21	0.18	0.07	Mark III[9]
$s \mu^+ \nu_\mu$	0.21	0.18	0.07	assume μ=e
$s u \bar{d}$	0.57	0.61	0.85	closure
$s u \bar{s}$	0.01	0.028	0.014	Mark III[10,11]
$b \to c e^- \bar{\nu}_e$	0.16	0.11		CLEO[12]
$c \mu^- \bar{\nu}_\mu$	0.16	0.11		"
$c \tau^- \bar{\nu}_\tau$	0.04			
$c \bar{u} d$	0.47			
$c \bar{u} s$	0.02			
$c \bar{c} s$	0.13	0.12		CLEO, ARGUS[13,14]
$c \bar{c} d$	0.01			

The predicted branching ratios involving the dominant $c \to s$ and $b \to c$ transitions are not very sensitive to the assumed values of the KM matrix elements, but for the numerical values I have assumed that $|V_{cd}/V_{cs}|^2 = \tan^2\theta_{12} = 0.052$ and that $|V_{ub}/V_{cb}|^2$ is negligible. The conclusion from the comparison of predictions and data is that D decays deviate significantly from spectator dominance, and B decays less so.

Although neither the lifetimes[7] τ nor the semileptonic branching ratios[9] B_s are the same for charged and neutral D's, the corresponding semileptonic decay rates ($\Gamma_s = B_s/\tau$) are equal, as one would expect if the spectator mechanism were dominant just for the semileptonic decays:

$$\Gamma(D^+ \to X e^+ \nu_e) = 0.17 \pm 0.02 \text{ psec}^{-1}$$
$$\Gamma(D^o \to X e^+ \nu_e) = 0.16 \pm 0.03 \text{ psec}^{-1}.$$

In a simple spectator decay the initial light quark or antiquark continue through the decay to the final state. One example of an observed decay for which this is not true is $D^0 \to \bar{K}^0\phi$, which has a branching ratio = 0.95 ± 0.21%.[15] This can be compared with the Mark III result[11] for the corresponding nonresonant mode

$D^0 \to \bar{K}^0K^+K^-$ Branching ratio = 0.8 ± 0.3 ± 0.2%,

which could go through the simple spectator mechanism. The comparison suggests that other mechanisms are present in D decays.

Even if the light antiquark in the initial heavy meson is present in the hadronic final state, it is not an <u>ideal</u> spectator decay unless the final hadrons can be divided into two groups, one charged combination that could be the product of the W (W^+ for D or B decay, W^- for $\bar{D}$ or $\bar{B}$ decay), and one combination that could be the product of the spectator and the direct daughter of the original heavy quark. We can write down some low multiplicity modes that are allowed by all the conservation laws but do not fit this criterion (assuming that c quarks are not produced in hadronization). Their branching ratios (below left) can be compared with those for similar final states (below right) that can be reached by ideal spectator decays.[16,11]

$D^0 \to \bar{K}^0\pi^0$	1.9±0.4±0.2%	$D^0 \to K^-\pi^+$	4.2±0.4±0.4%
		$D^+ \to \bar{K}^0\pi^+$	3.2±0.5±0.2%
$D^0 \to \bar{K}^0\rho^0$	0.8±0.1±0.5%	$D^0 \to K^-\rho^+$	10.8±0.4±1.7%
$D^+ \to \bar{K}^{*0}\pi^0$	2.6±0.3±0.7%	$D^+ \to \bar{K}^{*0}\pi^+$	5.9±1.9±2.5%

A subset of this class of nonideal decays consists of the modes in which the c quark from the $b \to cW^-$ transition pairs with the $\bar{c}$ from the $W^- \to s\bar{c}$ to form a bound charmonium state, ψ, ψ', χ, or η_c (Fig. 2.2). The inclusive branching ratio for $B \to \psi X$ is measured to be 1.2 ± 0.3%.[14]

Obviously, the simplest spectator picture is a poor description of hadronic D decays, and is not strictly true for B decays. Can we understand the nonspectator effects?

0050888-018

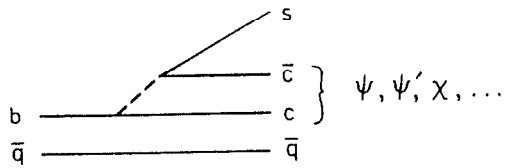

Fig. 2.2 Charmonium formation in B decay.

(b) Annihilation and exchange contributions

The diagram for pion decay (Fig. 1.3b) is an example of a nonspectator mechanism. In a charged heavy meson (negatively, say) the heavy quark and its antiquark partner can annihilate into a W^-, which can form either a $\ell^- + \bar{\nu}$ leptonic final state or a hadronic final state evolved from a $D + \bar{U}$ quark combination (Fig. 2.3a). If annihilation is the dominant amplitude, the decay rate is given by the same formula as in the pion decay, except for the substitution of the appropriate masses, decay constant, and KM element. Note that the annihilation mechanism is more likely to be important when the initial quark and antiquark are in the same weak doublet (e.g., $D_S = c\bar{s}$), so that $|V|^2$ is large. For a quark-antiquark $D + \bar{U}$ final state there will be an extra $|V_{UD}|^2$ factor in the rate for the final $WD\bar{U}$ coupling and a factor of three to account for the color degree of freedom.

Although annihilation into a W^- is forbidden for a neutral meson, there is an analogous exchange mechanism (Fig. 2.3b). The heavy quark (b for instance) exchanges a W^- with its partner antiquark (say a $\bar{d}$), changing the b to a c or u and changing the $\bar{d}$ to a $\bar{u}$ (or $\bar{c}$). Since the W mass is large compared to the other masses, the distinction between s-channel and t-channel propagator factors for the virtual W in the annihilation and exchange diagrams is immaterial. Both are effectively four-fermion interactions, with the same factor M_W^{-2} in the amplitude.

The KM matrix affects the annihilation and exchange decays of the D^+, D^0, and D_s differently. The $c\bar{u} \to W^+$ vertex in D^+ decay costs a factor of λ^2 in the rate, while in the D^0 and D_s decays all vertices can be with diagonal KM elements (a factor of 1). So even if annihilation and exchange decays are important contributors to hadronic D^0 and D_s decays, they are unlikely to have an effect on the D^+ decay rate. One would expect $\tau_+ > \tau_0 \sim \tau_s$, and indeed that is roughly what is observed[7]:

$$\tau_+ = 1.06 \pm 0.05 \pm 0.03 \text{ psec}$$
$$\tau_0 = 0.44 \pm 0.02 \pm 0.01 \text{ psec}$$
$$\tau_s = 0.48 \pm 0.06 \pm 0.02 \text{ psec}.$$

0050888-019

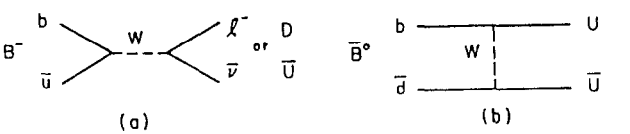

Fig. 2.3 (a) Annihilation and (b) exchange graphs in B decay.

We should note that the muon decay rate formula implies that the decay through the spectator mechanism of a meson containing a heavy quark has a rate proportional to the fifth power of the mass of the decaying quark, while the pion decay rate formula indicates a more gradual dependence on the mass of the decaying meson for the annihilation or exchange case. Obviously, the higher the mass of the heavy quark, the greater the chance that the spectator picture will dominate.

In first order, the annihilation or exchange mechanism cannot lead to a semileptonic decay like $B \rightarrow X\ell\bar{\nu}$, but one could imagine the b and $\bar{u}$ in a charged B annihilating into $\ell\bar{\nu}$, with extra hadrons X emerging from one of the initial quarks via a gluon line (Fig. 2.4). The emission of a hard gluon would modify the decay rate formula; although the decay would be inhibited by a factor of α_s, it could avoid the helicity suppression. Such a mechanism could contribute to semileptonic charged B decay and not to the corresponding neutral B decay, although the fact that the semileptonic rates are the same for charged and neutral D's suggests that it is not a significant contributor. It does not follow that we can neglect the annihilation or exchange mechanism in nonleptonic decays.

(c) Penguin Decays

The standard model forbids flavor changing neutral current decays in lowest order. That is, couplings like $b \rightarrow sZ^0$ cannot occur. One can construct however a higher order graph (Fig. 2.5) which accomplishes the same effect. The heavy quark decays to a lighter quark of the same charge through a virtual loop containing a W and a quark of the other charge (KM factors favor c or t). Energy-momentum conservation is preserved by emitting gluons and/or photons that may or may not couple to the spectator antiquark. This is called a "penguin" diagram.

The possibility of such a decay contribution first arose in connection with the $\Delta I=1/2$ rule in K decay. The spectator, annihilation, and exchange graph for hadronic K decay each has two weak vertices, one involving $s \rightarrow uW^-$ or $s\bar{u} \rightarrow W^-$ (with isospin

0050888-020

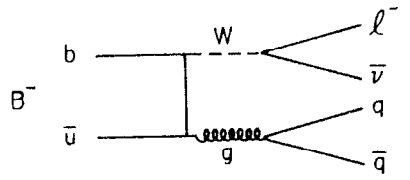

Fig. 2.4 Semileptonic B decay by weak annihilation.

0050888-021

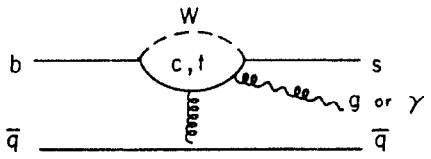

Fig. 2.5 Penguin graph in B decay.

change $|\Delta I|=1/2$), the other involving $W^- \to d\bar{u}$ or $\bar{d}W^- \to \bar{u}$ (with $|\Delta I|=1$). The net effect can be $|\Delta I|=1/2$ or 3/2. Observed charge ratios, such as $(K_S^o \to \pi^+\pi^-)/(K_S^o \to \pi^o\pi^o) = 2$ and $(K^+ \to \pi^+\pi^-)/(K_S^o \to \text{all } \pi\pi) \ll 1$, imply the dominance of $|\Delta I|=1/2$ in hadronic K decays. It could happen naturally if K decays were dominated instead by the penguin graph, giving an effective single-step $s \to d$ decay with $|\Delta I|=1/2$. The penguin graph, which contains a KM-suppressed vertex, has a chance of competing because the conventional decay graphs are suppressed by essentially the same KM factor.

Such a mechanism could contribute to the decay of the b quark. The signature would be the decay of a B meson into a noncharm, but strange, final state. Several modes have been searched for (see Fig. 2.6), so far unsuccessfully.[17] The experimental upper limits are getting close to the predictions.

MODE	measured %Br		predicted %Br
$B^- \to \bar{K}^o\pi^-$	0.068	CLEO	0.006[18]
$\bar{K}^{*o}\pi^-$	0.013	"	0.005[18]
$K^-\rho^o$	0.007	"	0.001[18]
$K^-\phi$	0.008	"	0.004,[18] 0.005[19]
$K^{*-}\gamma$	0.10	ARGUS	
$K^-e^+e^-$	0.005	CLEO	0.0001-0.0003[18,20]
$K^-\mu^+\mu^-$	0.012	"	"
$B^{\bar{o}} \to K^-\pi^+$	0.009	CLEO	0.01,[18] 0.007[21]
$K^{*-}\pi^+$	0.07	"	0.01[18]
$\bar{K}^o\rho^o$	0.08	"	0.0004[18]
$\bar{K}^o\phi$	0.13	"	0.004,[18] 0.005[21]
$\bar{K}^{*o}\rho^o$	0.12	"	
$\bar{K}^{*o}\phi$	0.047	"	0.005[18]
$\bar{K}^{*o}\gamma$	0.04	ARGUS	0.001-0.03[20]
$\bar{K}^{*o}e^+e^-$	0.065	CLEO	0.0001-0.0003[20]
$\bar{K}^{*o}\mu^+\mu^-$	0.045	"	"

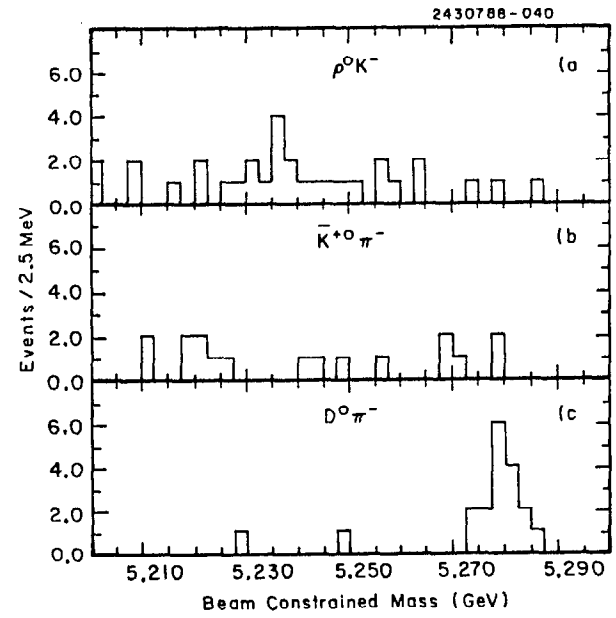

Fig. 2.6 CLEO candidates (Ref. 17) for $B^- \to K^-\pi^+\pi^-$ with (a) $\pi^+\pi^- = \rho^o$, (b) $K^-\pi^+ = \bar{K}^{*o}$, and (c) $K^-\pi^+ = D^o$.

(d) QCD Effects

Once the final quarks are produced by the weak interaction, the hadronization process takes over to produce the various modes of hadron final states. We have tacitly assumed that the decay rate is not modified by the second stage, which involves poorly understood soft hadronic interactions. There are several ways in which this assumption can be wrong.

(1) Even if the overall hadronic decay rate were not affected by strong interactions, we would still need to understand them in order to calculate the branching ratios for the various exclusive decay modes. The distribution of multiplicities of the final state hadrons in D or B decay depends on the detailed dynamics of the hadronization process, as do the branching ratios for the low multiplicity final states that are the most convenient experimental signatures for charm or bottom production.

(2) Hadronic interactions can remix the quarks and turn a simple spectator configuration into a first-order forbidden final state. For instance, in the "spectator" decay $b\bar{q} \rightarrow (c\bar{q})W^- \rightarrow (c\bar{q})(d\bar{c})$ one expects that a hadronization interaction in which the c and $\bar{c}$ quarks combine to form a ψ (Fig. 2.2) would have a rate that is suppressed by a factor $(1/3)^2$ because of the 1/3 chance that the two combining quarks would have the right color-anticolor combination. Decay modes which suggest weak annihilation or exchange diagrams (Fig. 2.3) can be the product of spectator decays with strong final state interactions; for example, the $D^o \rightarrow \phi \bar{K}^o$ decay can be explained either by an exchange graph (with an $s\bar{s}$ popped in the final state), or for example as a spectator-dominated $D^o \rightarrow \rho^+K^-$ weak decay followed by a strong, Zweig violating rescattering $\rho^+K^- \rightarrow \phi \bar{K}^o$.

(3) Interferences between different diagrams can be influenced by the identity of the spectator quark; that is, they can cause the decay rates of the charged and neutral heavy mesons to be different, even when the basic weak decay is predominantly through the spectator graph. For example, in the spectator decay of the D^+, $c\bar{d} \rightarrow (s\bar{d})+(u\bar{d})$ leading to final states like $\bar{K}^o\pi^+$, the two ways of pairing the $\bar{d}$ quarks in the hadronization process can interfere, while in the corresponding decay of the D^o, $(c\bar{u}) \rightarrow (s\bar{u})+(u\bar{d})$ leading to $K^-\pi^+$, or of the D_s, $(c\bar{s}) \rightarrow (s\bar{s})+(u\bar{d})$ leading to $\phi\pi^+$, there is no such possibility. This could be part of the explanation why the D^+ lifetime is significantly longer than that of the D^o or D_s.

(4) Particle-antiparticle oscillations, which can occur in the $B^o\bar{B}^o$ system as in the $K^o\bar{K}^o$ system, are intrinsically non-spectator. I will consider this in more detail later.

There have been a number of attempts to understand exclusive branching ratios for two-body D and B decays. I will discuss here briefly the calculations of Bauer, Stech, and Wirbel,[22] based on a factorization hypothesis, that is, that the short range effects of perturbative gluon exchange and long range quark binding can be dealt with separately. This model has been quite successful in explaining D decay branching ratios, with the exception of $D^o \rightarrow \bar{K}^o\phi$ (perhaps because the model neglects final state rescattering). All amplitudes for two-body B $(=b\bar{q})$ decays are expressed as linear combinations of only two amplitudes on the basis of "flavor flow", one amplitude a_1 corresponding to the case in which the initial partner $\bar{q}$ is paired in a final state hadron with the daughter quark of the initial heavy quark (the c or u from the b), and the other amplitude a_2 in which the initial $\bar{q}$ and the heavy quark daughter are not in the same hadron.

There are only three two-body B decay modes to final states containing charm for which CLEO[23] and ARGUS[24] have measured the branching fractions well enough to make a meaningful comparison with the theory. Of the three, one depends on a_1, one depends on a_2, and one involves both amplitudes.

Mode	% B.R., expt	Predicted decay rate, $psec^{-1}$
$\bar{B}^o \to D^{*+}\pi^-$	0.34±0.14	$1.3\|V_{cb}V_{ud}\|^2 a_1^2$
$\bar{B}^o \to \psi \bar{K}^{*o}$	0.37±0.13	$290\|V_{cb}V_{cs}\|^2 a_2^2$
$B^- \to D^o\pi^-$	0.47±0.17	$1.7\|V_{cb}V_{ud}\|^2 (a_1+0.75a_2)^2$

The numerical factors in the predicted rates are calculated assuming a simple model for the effect of quark binding. From the factorization hypothesis one expects $a_1 = C_1 + \xi C_2$ and $a_2 = \xi C_1 + C_2$, where the coefficients $C_1 = 1.1$ and $C_2 = -0.24$ are calculated from perturbative QCD at the b mass scale. Note that in the approximation $C_2 << C_1$, the ψK^* mode (which requires color-matched c and $\bar{c}$) would have an amplitude proportional to the color factor ξ, which naively should be 1/3. If we use the experimental branching ratios and the PEP-PETRA average value for the b lifetime,[25] the data imply $|a_1| = 1.0 \pm 0.2$, $|a_2| = 0.09 \pm 0.02$, and $|a_1+0.75a_2| = 1.0 \pm 0.2$. The three measurements are consistent with each other and with the QCD factorization prediction, implying $\xi = 0.31 \pm 0.05$ (if a_1 and a_2 have the same sign) or $\xi = 0.13 \pm 0.03$ (if they have opposite signs).

The measured two-body B branching ratios are therefore well reproduced by the factorization model, and the value of the color factor ξ is probably close to the expected value of 1/3, although there is evidence from other experiments (the inclusive $B \to \psi X$ rate, for example) that ξ may be near zero. In the following we will use this model to predict branching ratios for other two-body modes.

3. MEASUREMENTS OF V_{cb} AND V_{ub}

(a) The B meson semileptonic decay rate

While we cannot assume that the spectator diagram dominates all B decays, it may be more nearly true for the B semileptonic decays. We have noted above (Sec. 2a) that the measured D^+ and D^o semileptonic decay rates are independent of the spectator quark type. Because of the m_q^5 factor in the spectator decay rate, it is even more likely that it will dominate in the B case.

The average lifetime of b hadrons has been measured in several experiments at PEP and PETRA.[25] It is not possible to separate unambiguously the 1/11 of the e^+e^- annihilation events that are $b\bar{b}$; one selects an enriched sample either by requiring a lepton with a high p_T with respect to the jet axis or by making a cut related to sphericity. The measurement averages over B^-, B^o, B_s, Λ_b, and so on, weighted by the unknown relative abundances in high energy hadron jets and weighted by the relative efficiencies of the selection cuts for the various kinds of b hadrons.

The effective average decay distance for the selected event sample is measured either by determining the mean impact parameter of the lepton tracks or by actually locating a secondary vertex event by event. To extract an average b lifetime one has to model the contamination of non-b events in the sample, the momentum spectrum and angular distribution of the b-hadrons, the tracking resolution, and other systematic effects. In spite of the rather indirect nature of the measurements, different detectors using different techniques give compatible results (Fig. 3.1), all consistent with the world average,[25] $\tau = 1.18 \pm 0.14$ psec.

To get the semileptonic decay rate we also need the branching ratio for the average b-hadron to decay into electron or muon. Although this has been measured in the same PEP and PETRA experiments for presumably the same mixture of b-hadrons as in the lifetime measurement, the most accurate measurements come from experiments at the $\Upsilon(4S)$ resonance, where only B^+B^- and $B^o\bar{B}^o$ are produced. In the PEP and PETRA experiments one models the effect of

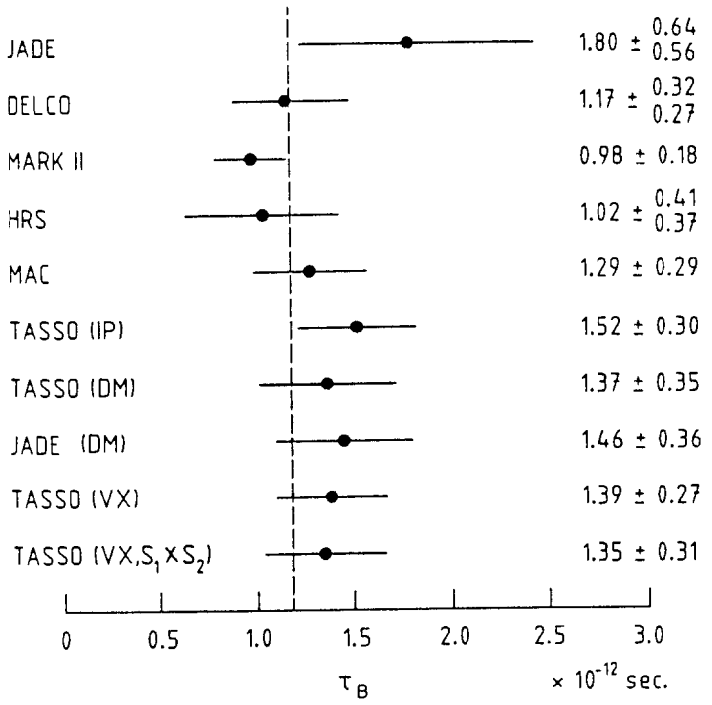

Fig. 3.1 b lifetime measurements (from Ref. 25).

contaminations in the enriched b-jet sample and assumes that the rate for $e^+e^- \to b\bar{b}$ is 1/11 of the total. At the $\Upsilon(4S)$ resonance the data rates are much greater, and the non-$B\bar{B}$ backgrounds, both in the total $B\bar{B}$ rate and in the lepton sample, are easily subtracted using data taken below $B\bar{B}$ threshold. The branching ratio results (see Fig. 3.2), averaged for electrons and muons are[26]

B_s = 12.4 ± 0.8% (PEP, PETRA)

11.1 ± 0.5% (CESR, DORIS)

11.5 ± 0.4% (world average).

The consistency of the threshold and high energy measurements is evidence that the difference in the mix of b-hadrons is not too important. We will therefore use the weighted average branching ratio, combine it with the world average lifetime measurement, and assume that the spectator quark is irrelevant, to arrive at the following semileptonic b-decay rate

$$\Gamma[b \to (c \text{ or } u) + \ell\bar{\nu}] = 0.094 \pm 0.012 \text{ psec}^{-1}.$$

The theoretical expression for the rate (essentially the muon decay rate formula given in Section 1) has to be summed over the c and u quark final states, each with its KM factor and phase space factor:

$$\Gamma(B \to \ell\bar{\nu}X) = \frac{G_F^2 m_b^5}{193\pi^3}\,\eta\,(f_c|V_{cb}|^2 + f_u|V_{ub}|^2).$$

The QCD correction factor η is estimated to be 0.87 ± 0.05. The phase space factor is 0.97 for the light u quark; and assuming m_c = 1.65 GeV, it is about 0.46 for the charmed quark, although one can get different estimates using meson masses. The largest uncertainty, however, comes from the b-quark mass, which is raised to the fifth power. Taking m_b = 5.00 ± 0.15 GeV we have

$$\Gamma(B \to \ell\bar{\nu}X) = (94 \pm 14 \text{ psec}^{-1})[0.46|V_{cb}|^2 + 0.97|V_{ub}|^2].$$

The measurement therefore implies

$$|V_{cb}|^2 + |V_{ub}|^2/.048 = 0.0022 \pm 0.0004.$$

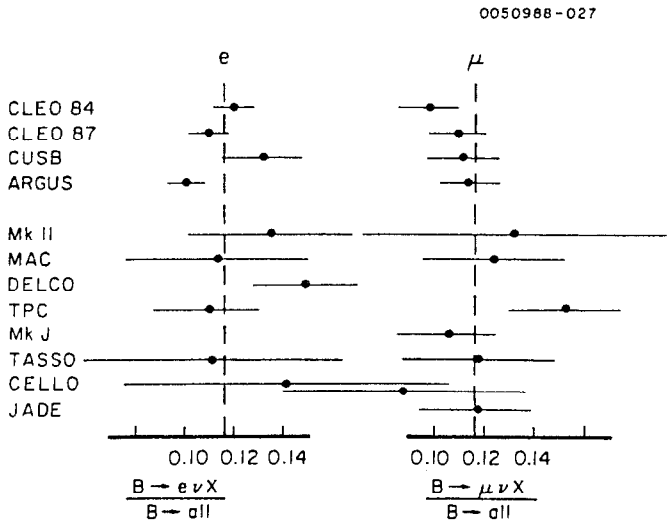

Fig. 3.2 B semileptonic branching ratio measurements (from Ref. 26).

(b) Charmless B Decays

It was clear from the earliest CLEO observations of the $\Upsilon(4S)$ decays that the decay of the B meson is predominantly through the V_{cb} coupling rather than via V_{ub}. The inclusive kaon rate[27] is large (from $b \to c \to s$), and the total inclusive rate for D^+, D^0,[28] D_s,[13] Λ_c,[29] and ψ[14] is not far from one per B. This makes getting a measurement or even an interesting upper limit on V_{ub} rather difficult. There are two techniques that may be sensitive enough: (1) observing the shape of the end point of the lepton momentum spectrum in semileptonic B decays, and (2) searching for exclusive charmless B decay modes.

The first technique relies on the fact that the minimum final state hadronic effective mass M_X in charmed $B \to X_c \ell\bar{\nu}$ decays is at least m_D, while in the charmless $B \to X_u \ell\bar{\nu}$ decays it can be as low as m_π. This should be reflected in the end point of the lepton momentum spectrum:

$$p_{\ell,max} = \frac{M_B^2 - M_X^2}{2M_B},$$

which in the rest frame of the decaying B is $p_{\ell,max} = 2.31$ GeV/c for $M_X = m_D$ and 2.64 GeV/c for $M_X = m_\pi$. Figure 3.3 shows the CLEO[30] observed p_e and p_μ spectra for B mesons produced almost at rest in $\Upsilon(4S)$ decays. The contribution from non-$B\bar{B}$ sources is subtracted using data taken below $B\bar{B}$ threshold. There is no evidence for any contribution beyond p = 2.4 GeV/c; that is, no contribution from the $b \to uW^-$ coupling.

In order to turn the observed upper limit on the rate for $B \to X_u \ell\bar{\nu}$ with $p_\ell > 2.4$ GeV/c into an upper limit on $|V_{ub}|$ we need a theoretical model for $\Gamma(B \to X_u \ell\bar{\nu};\ p_\ell > 2.4)/|V_{ub}|^2$. There are two kinds of models (see Fig. 3.4); the "inclusive" starts at the quark level and predicts the full lepton momentum spectrum, and the "exclusive" starts with a few low multiplicity channels ($\pi\ell\bar{\nu}$, $\rho\ell\bar{\nu}$, etc.) and predicts only the high momentum end of the spectrum where they dominate. In the inclusive model the overall $B \to X_u \ell\bar{\nu}$ rate is given by the free quark decay rate ($b \to u\ell\bar{\nu}$), but one has to guess the initial quark momentum distribution and the hadronization

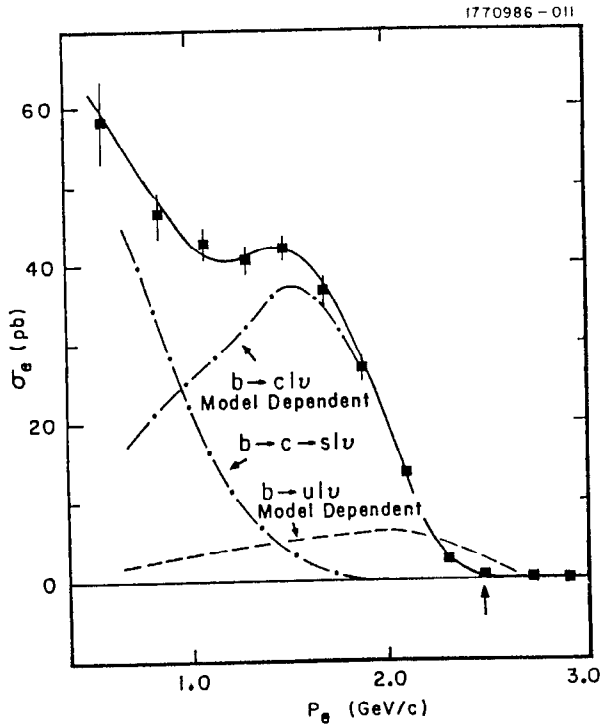

Fig. 3.3 Electron momentum spectrum in semileptonic B decays (CLEO data 30).

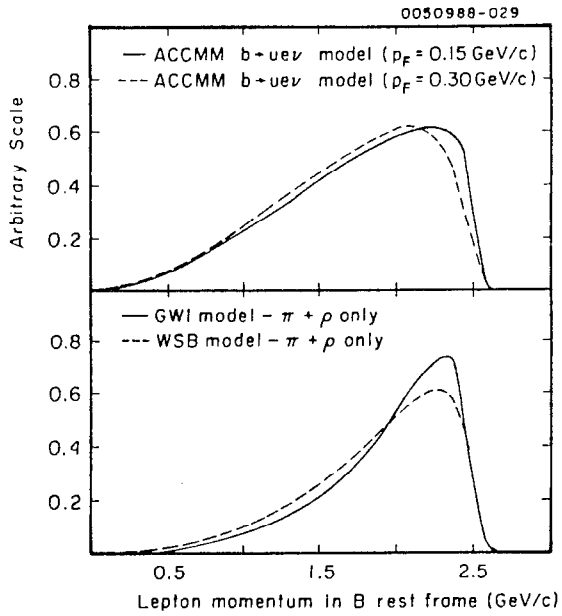

Fig. 3.4 Model predictions for lepton momentum spectrum in charmless (b → u) semileptonic B decays (Ref. 31-ACCMM, 33-GWI, 34-WSB.

spectrum in M_x in order to predict the high momentum end of the lepton spectrum where the measurements are made. On the other hand, the exclusive models can predict only the high momentum end of the spectrum. They are sensitive to assumptions about form factors, and different calculations vary widely. Based on CLEO data and several models, here are the 90% confidence upper limits for $|V_{ub}/V_{cb}|$:

$|V_{ub}/V_{cb}| < 0.10$ inclusive[31]

0.13 inclusive[32]

0.17 exclusive[33]

0.14 exclusive.[34]

Without clear guidance on what calculation to believe, we have to take the one that gives the highest upper limit.

In a variation on this technique we can try to decrease the statistical effect of the non-$B\bar{B}$ background subtraction by looking for the exclusive charmless semileptonic modes $B \to \rho \ell \bar{\nu}$ and $\pi \ell \bar{\nu}$. Because of the unseen neutrino, one cannot make an overconstrained kinematic reconstruction of the decay, but one can at least check each candidate event with $p_\ell > 2.4$ GeV/c for the possible presence of a kinematically consistent ρ or π. Because of efficiency losses the limits one derives on $|V_{ub}|$ turn out to be no better than the ones derived inclusively.

In the other technique we try to reconstruct exclusive B decays to modes which do not contain a charmed (or strange) particle in the final state. In order to keep the combinatoric background of spurious reconstructions low, we have to restrict ourselves to low multiplicity modes. We also suppress background from two-jet non-$B\bar{B}$ continuum by requiring a minimum sphericity for the "other B". The efficiency for reconstructing these charmless modes is fortunately much higher than for the charmed modes, because one does not have to use a low-branching-ratio D mode as a signature. Figure 3.5 shows a CLEO search[17] for $B \to \pi^+\pi^-$ in the dipion invariant mass spectrum on the $\Upsilon(4S)$ resonance. The charmless branching ratios reported by CLEO[17] and ARGUS[35] are given in the table below, along with the

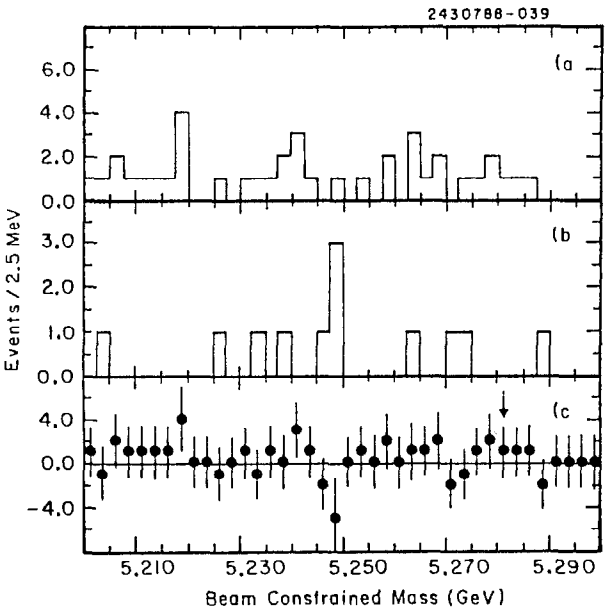

Fig. 3.5 CLEO candidates (Ref. 17) for $B^o \to \pi^+\pi^-$: (a) on the $\Upsilon(4S)$ resonance, (b) below $B\bar{B}$ threshold, (c) net $B\bar{B}$ contribution.

Bauer, Stech, and Wirbel predictions[22] for the mesonic modes normalized to $|V_{ub}/V_{cb}| = 1$.

MODE	CLEO %Br	%Br for $\lvert V_{ub}/V_{cb}\rvert$=1
$B^- \to \pi^0\pi^-$	0.23	0.062
$\rho^0\pi^-$	0.015	0.022
$\rho^0 a_1(1270)^-$	0.32	0.33
$\rho^0 a_2(1320)^-$	0.23	
$\Delta^0 \bar{p}$	0.033	
$p \bar{\Delta}^{--}$	0.01	
$p \bar{p}\pi^-$	0.03	
$\bar{B}^0 \to \pi^+\pi^-$	0.009	0.20
$\rho^+\pi^-$ & $\rho^-\pi^+$ (sum)	0.61	0.68
$\rho^0\rho^0$	0.05	0.011
$\pi^+ a_1(1270)^-$ & -+	0.12	0.60
$\pi^+ a_2(1320)^-$ & -+	0.16	
$p \bar{p}$	0.004	
$\Delta^0 \bar{\Delta}^0$	0.18	
$\Delta^{++} \bar{\Delta}^{--}$	0.013	
$p \bar{p}\pi^+\pi^-$	0.12	

Since the theory used to predict the charmless branching ratios gives reasonable values for the measured charmed branching ratios (Section 5c, above), we may be justified in using it to derive conclusions about the value of $|V_{ub}|$ implied by the data. The most stringent limit (90%) from the mesonic modes comes from the $\bar{B}^0 \to \pi^+\pi^-$ decay:

$$|V_{ub}/V_{cb}| < 0.21,$$

which is not as good as the limit from the lepton spectra.

ARGUS[36] has reported signals in two baryonic modes, $B^- \to p \bar{p}\pi^-$ and $\bar{B}^0 \to p \bar{p}\pi^+\pi^-$. CLEO[37] sees no evidence for these decays and sets branching ratio upper limits that are considerably lower than the ARGUS numbers. Until this is resolved we have no experimental lower limit on V_{ub}.

(c) Results

Figure 3.6 shows the 90% confidence limits in the $|V_{ub}|$, $|V_{cb}|$ plane. Note however that the upper limit on $|V_{ub}|$ is quite model dependent and may turn out to be wrong. Taking the limits at face value and assuming only three families, we can write

$$|V_{cb}| = \theta_{23} = A\lambda^2 = 0.047 \pm 0.004$$

$$|V_{ub}| = \theta_{13} = A\lambda^3\sqrt{(\rho^2+\eta^2)} < 0.008.$$

Recalling that $\theta_{12} = \lambda = 0.226$, we then have the Wolfenstein parameters:

$$A = 0.92 \pm 0.08$$

$$\sqrt{(\rho^2 + \eta^2)} < 0.8.$$

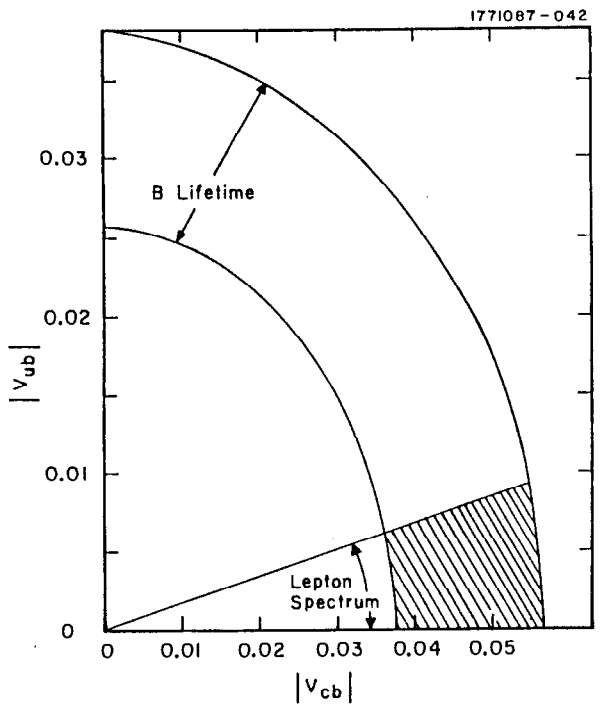

Fig. 3.6 90% confidence limits in V_{ub} versus V_{cb}.

4. PARTICLE-ANTIPARTICLE OSCILLATIONS

a) Mixing Phenomenology

The B^0 and $\bar{B}^0$ (or the B_s^0 and $\bar{B}_s^0$) differ only in the sign of the quantum number ("beauty") carried by the b quark. Since this is not a conserved quantity in weak decays, the eigenstates for which the lifetimes and masses are defined are not the b-eigenstates created in the production reaction. A pure b-eigenstate, which is a superposition of the two mass eigenstates propagating with different frequencies given by m_1 and m_2, will then develop an admixture of the anti-b-eigenstate with a beat frequency $\Delta m = m_1 - m_2$. If the ratio x_d (or x_s in the B_s case) of the beat rate Δm and the decay rate Γ is near one or greater, there is a chance that a produced B^0 will decay as a $\bar{B}^0$, or vice versa. Or if $B^0\bar{B}^0$ pairs are produced, as in $\Upsilon(4S)$ decay, one can observe B^0B^0 and $\bar{B}^0\bar{B}^0$ decays, as indicated by like-sign semileptonic final states, for instance.

For both the B and the K the particle-antiparticle oscillation has a chance to take place because the decay of the heavy quark (b or s) is suppressed by a small KM angle. One important difference between the B and K cases, however, is the fact that most of the B decay modes are common to both mass eigenstates, so that the two lifetimes should be the same and a single decay rate Γ can be assumed.

In general the mass eigenstates are orthogonal superpositions of the B^0 and $\bar{B}^0$ states:

$$|B_1\rangle = p|B\rangle + q|\bar{B}\rangle, \qquad |B_2\rangle = p|B\rangle - q|\bar{B}\rangle.$$

For now, we will assume that CP is conserved in B decay (probably only approximately true), so that the mass eigenstates are just the CP-even and CP-odd combinations and $p = q = 1/\sqrt{2}$. The time evolution of a decay eigenstate, $|B_1\rangle$ or $|B_2\rangle$, is given by

$$|B_j(t)\rangle = |B_j(0)\rangle\, e^{-\Gamma t/2} \exp(-im_j t).$$

Expressing $|B\rangle$ and $|\bar{B}\rangle$ as superpositions of $|B_1\rangle$ and $|B_2\rangle$ and substituting the above time dependence, one gets

$$|B(t)\rangle = a_+(t)|B(0)\rangle + a_-(t)|\bar{B}(0)\rangle$$

$$|\bar{B}(t)\rangle = a_-(t)|B(0)\rangle + a_+(t)|\bar{B}(0)\rangle,$$

where $|a_\pm(t)|^2$ is the fraction of an original B or $\bar{B}$ present at time t as a B or $\bar{B}$ (or vice versa):

$$|a_\pm(t)|^2 = e^{-\Gamma t}(1 \pm \cos\Delta m t)/2 \qquad (\Delta m = m_2 - m_1),$$

shown in Fig. 4.1.

Although the oscillation is easily observable in neutral K decays, over meters of flight path, the much shorter lifetime of B mesons requires one to measure decay lengths in the tens of microns in order to observe the oscillation directly. It is therefore useful to integrate over time:

$$\text{Prob}(B \to \bar{B}) = \text{Prob}(\bar{B} \to B) = \int |a_-(t)|^2 dt = \frac{1}{2\Gamma}\,\frac{x^2}{1+x^2}$$

$$\text{Prob}(B \to B) = \text{Prob}(\bar{B} \to \bar{B}) = \int |a_+(t)|^2 dt = \frac{1}{2\Gamma}\,\frac{2+x^2}{1+x^2},$$

where $x = \Delta m/\Gamma$. The ratio of probabilities for an initial isolated B to decay as a $\bar{B}$ or to decay as a B is therefore $x^2/(2+x^2)$.

The above formulas can be used to calculate the probability that an originally produced $B\bar{B}$ pair will decay as BB or $\bar{B}\bar{B}$:

$$y = \frac{\text{Prob}(B\bar{B} \to BB) + \text{Prob}(B\bar{B} \to \bar{B}\bar{B})}{\text{Prob}(B\bar{B} \to B\bar{B}) + \text{Prob}(B\bar{B} \to \bar{B}\bar{B})} = \frac{(2+x^2)x^2}{2+2x^2+x^4}.$$

This formula is relevant only if the two initial B states are uncorrelated. In $\Upsilon(4S)$ decays however the two B's are in a p-wave state, which is odd under exchange, so that because of Bose statistics we can never get a B_1B_1 or B_2B_2 pair. We have to write the $|B\bar{B}(t)\rangle$ two-particle state as a superposition of $|B_1B_2(t)\rangle$ and $|B_2B_1(t)\rangle$ decay eigenstates, before calculating the probabilities. The result is that as far as mixing is concerned the $B\bar{B}$ state from the $\Upsilon(4S)$ acts just like a single B, and the mixing ratio is

$$y = \frac{\text{Prob}(B\bar{B} \to BB) + \text{Prob}(B\bar{B} \to \bar{B}\bar{B})}{\text{Prob}(B\bar{B} \to B\bar{B}) + \text{Prob}(B\bar{B} \to \bar{B}\bar{B})} = \frac{x^2}{2+x^2},$$

which is about half of the corresponding ratio for uncorrelated $B\bar{B}$. If on the other hand we start out with the $B\bar{B}$ in an even C state, for example in the case of $e^+e^- \to B\bar{B}^* \to B\bar{B}\gamma$, then the corresponding mixing ratio is enhanced (see Fig. 4.2):

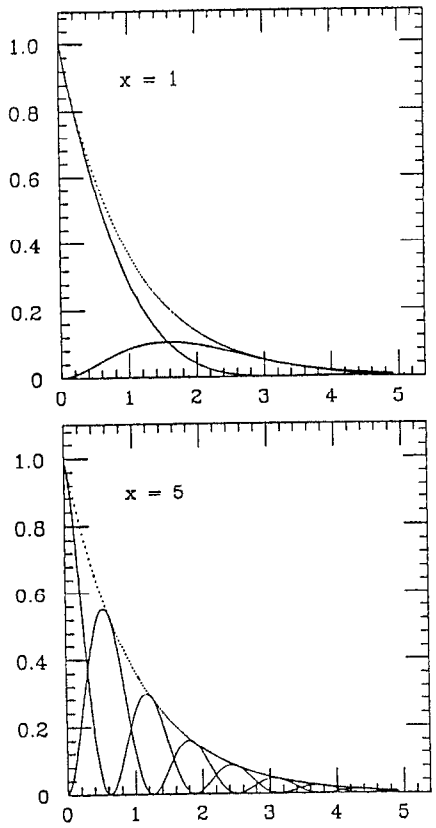

Fig. 4.1 Time dependence (in units of mean lifetimes) of the of the probabilities for an initially pure B^0 to decay as a B^0 (the curve starting at 1.0) or as a $\bar{B}^0$ (the curve starting at 0), for two values of $x = \Delta m/\Gamma$. The dotted curve is a plot of $\exp(-\Gamma t)$.

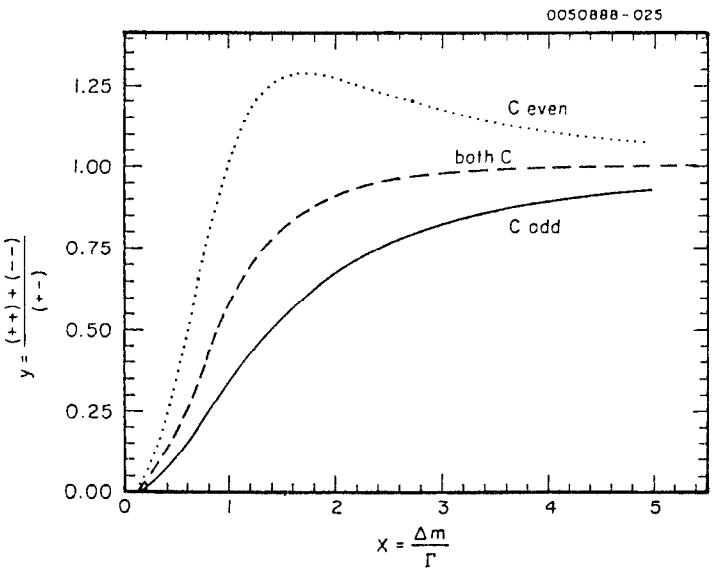

Fig. 4.2 The ratio y of like-sign to opposite-sign dilepton decays of initial $B^0\bar{B}^0$ pairs, versus $x = \Delta m/\Gamma$.

$$y = \frac{\text{Prob}(B\bar{B} \to BB) + \text{Prob}(B\bar{B} \to \bar{B}\bar{B})}{\text{Prob}(B\bar{B} \to B\bar{B}) + \text{Prob}(B\bar{B} \to \bar{B}\bar{B})} = \frac{3x^2 + x^4}{2 + x^2 + x^4} .$$

(b) The Box Diagram

In the Standard Model the B^o - $\bar{B}^o$ transition takes place through the box diagrams (Fig. 4.3). Note that the process is inherently "non-spectator"; the heavy quark and the light antiquark have to interact, and the amplitude will therefore depend on the details of the bound state wavefunction. Although the intermediate state involves all the charge 2/3 quarks and hence most of the KM matrix elements, the effect of the virtual t quark dominates over the contribution of the c and u quarks. From the box diagram the ratio x_d of B^o-$\bar{B}^o$ oscillation rate to decay rate is

$$x_d = \frac{\Delta m}{\Gamma} \frac{G_F^2}{6\pi^2} m_t^2 \tau_B f_B^2 B_B |V_{tb}V_{td}^*|^2 g(m_t/M_w) \eta_{QCD} .$$

The factor g is one for $m_t \ll M_w$, and gradually decreases to about 1/2 at $m_t = 2M_w$.[38] The QCD correction factor η_{QCD} is about 0.85.[39]

The same formula holds for x_s with V_{td} replaced by V_{ts}, and with B parameters replaced by the corresponding values for B_s. In principle, the measurement of x_d and x_s are our only source of information on V_{td} and V_{ts} until we are able to observe KM-suppressed t quark decays; V_{tb} will be close to one, if there are only three families. In practice, however, there are serious theoretical obstacles to extracting V_{td} and V_{ts}. The mass of the t quark is probably between 44 GeV[40] and 200 GeV,[41] but is otherwise unknown. The bound state dependence may eventually be calculated reliably by lattice gauge theory, but for now one can take $f_B\sqrt{B_B} = 140 \pm 40$ MeV.[42]

Note that the ratio x_s/x_d should be greater than or approximately equal to $|V_{ts}/V_{td}|^2$. In the Wolfenstein parametrization this is $\lambda^{-2}[(1-\rho)^2 + \eta^2]^{-1}$, which is likely to be at least 5, based on what we know about V_{cb} and V_{ub}.

0050888-022

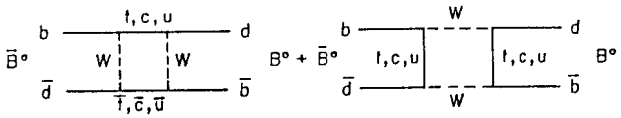

Fig. 4.3 Box diagrams for neutral B oscillations.

(c) Measurement

Observations of $B\bar{B}$ oscillations have so far been made by starting with the presumed production of a $B\bar{B}$ pair and looking for both mesons to decay into final states that indicate whether the decaying meson was B or $\bar{B}$. Such final state modes include $B^0 \to \ell^+ X$ and $\bar{B}^0 \to \ell^- X$, which have a reasonably large branching ratio (22% for ℓ = e or μ), and $B^0 \to \bar{D}X$ and $\bar{B}^0 \to DX$, which although the branching ratio is almost 100%, involves a small branching ratio to a low multiplicity final state in order to identify the D or $\bar{D}$. Using the semileptonic decay as an indicator, the mixing ratio y is equal to $[N(\ell^+\ell^+) + N(\ell^-\ell^-)]/N(\ell^+\ell^-)$.

The first indication of a positive signal for $B\bar{B}$ mixing was reported by UA1.[43] They saw an excess of like-sign muon pairs above the Monte Carlo calculation of the rate from mundane sources, such as pion, kaon, and charm decays and misidentification of other particles. They had to model the production of hadrons containing b quarks in order to interpret the signal in terms of x_d and x_s. The observed rate of $\mu^+\mu^+$ and $\mu^-\mu^-$ then defines the allowed region in the x_d versus x_s plane shown in Fig. 4.4. There are also JADE, Mark II, and MAC measurements[44] of like-sign muon pairs in high energy $b\bar{b}$ jets produced by e^+e^-. Here again the interpretation is model dependent, but perhaps one can have more confidence in the assumed rate for $e^+e^- \to b\bar{b}$ than for $p\bar{p} \to b\bar{b}X$.

Measurements made by ARGUS[45] and CLEO[46] at the $\Upsilon(4S)$ resonance are sensitive to mixing only in $B^0\bar{B}^0$; semileptonic decays from B^+B^- dilute the observed effect. The branching fractions for $\Upsilon(4S) \to B^0\bar{B}^0$ and $\Upsilon(4S) \to B^+B^-$ have to be assumed: 45 ± 5% is a good guess for $B^0\bar{B}^0$. One also has to make an assumption about the relative semileptonic branching ratios for charged and neutral B's: experimentally,[2] they could be as much as a factor of two apart although one expects them to be nearly equal. To minimize background from misidentified leptons and especially from D

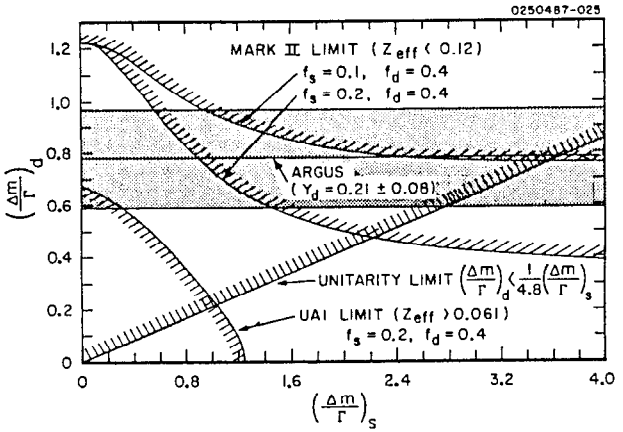

Fig. 4.4 Experimental limits in x_s versus x_d.

semileptonic decays one sets a minimum lepton momentum cut, typically about 1.5 GeV/c. The measured results for the fraction of like-sign dileptons, uncorrected for the B^+B^- contributions, are

	CLEO '86[47]	ARGUS[45]	CLEO '88[46]
$N(\ell^+\ell^+) + N(\ell^-\ell^-)$	5 ± 5	25 ± 8 ± 4	32 ± 8 ± 9
$N(\ell^+\ell^-)$	117 ± 12	270 ± 19 ± 5	436 ± 24
y, corr'd for B^+B^-	0.11 ± 0.11	0.21 ± 0.08	0.18 ± 0.08
average y		0.18 ± 0.05	
x_d		0.66 ± 0.12	

Fig. 4.4 shows the limits on x_s implied by this result for x_d and the UA1[43] and Mark II[44] data.

(d) Constraints on the KM Matrix

Through the box diagram formula the present experimental value of x_d implies

$$m_t\sqrt{g}|V_{td}| = m_t\sqrt{g}A\lambda^3[(1-\rho)^2 + \eta^2] = 0.5 \pm 0.1 \text{ GeV},$$

$$m_t\sqrt{g}[(1-\rho)^2 + \eta^2] = 50 \pm 8 \text{ GeV},$$

where the errors include the contribution of the theoretical uncertainty in $f_B^2B_B$. As we have seen in Section 5, the experimental limits on charmless b decays imply $\sqrt{(\rho^2 + \eta^2)} < 0.8$. The allowed region in the η vs. ρ plane is shown in Fig. 4.5 for several assumed values of m_t. Note that there is no solution for $m_t < 50$ GeV (taking account of the uncertainty in x_d). For m_t up to about 150 GeV the mixing result favors negative ρ values.

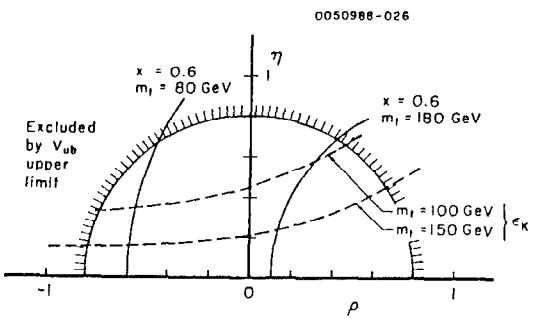

Fig. 4.5 Experimental limits on the Wolfenstein parameters η vs. ρ.

5. CP VIOLATION PHENOMENOLOGY

Since 1964 we have known that CP is not conserved in kaon decays. The mass (i.e. decay) eigenstates of the neutral kaon, K_L and K_S, are not the CP eigenstates, but contain a small admixture of the "wrong" CP. In 1973 Kobayashi and Maskawa[3] discovered that the most general quark family mixing matrix for three families contains a phase parameter that can give rise naturally to CP violation at the level observed in kaon decay. In principle, the effect should be observable also in B decays. As in the case of kaon decay, CP can be violated in B decay either through the possibility that the mass eigenstates are not CP eigenstates or directly in the decay amplitudes.

(a) Case I: Mass Eigenstates Are Not CP Eigenstates

We will start with the case most familiar from kaon decay. If the mass eigenstates are not the CP eigenstates, the factors $p = q = 1/\sqrt{2}$ in the Section 6 expressions for $|B_1\rangle$ and $|B_2\rangle$ in terms of $|B\rangle$ and $|\bar{B}\rangle$ are replaced by generalized factors $p = (1 + \varepsilon_B)/\sqrt{2}(1+\varepsilon_B^2)$ and $q = (1 - \varepsilon_B)/\sqrt{2}(1+\varepsilon_B^2)$. CP is not conserved if $|q/p| \neq 1$ (that is, $\varepsilon_B \neq 0$). The mass eigenstates are then

$$|B_1(t)\rangle = p|B(t)\rangle + q|\bar{B}(t)\rangle = \exp(-\Gamma_1 t/2)\exp(im_1 t)|B_1(0)\rangle$$
$$|B_2(t)\rangle = p|B(t)\rangle - q|\bar{B}(t)\rangle = \exp(-\Gamma_2 t/2)\exp(im_2 t)|B_2(0)\rangle.$$

We therefore have

$$|B(t)\rangle = e^{-\Gamma t/2}e^{imt}[\cos(\Delta mt/2)|B(0)\rangle + i(q/p)\sin(\Delta mt/2)|\bar{B}(0)\rangle]$$
$$|\bar{B}(t)\rangle = e^{-\Gamma t/2}e^{imt}[i(p/q)\sin(\Delta mt/2)|B(0)\rangle + \cos(\Delta mt/2)]|\bar{B}(0)\rangle],$$

where $m = (m_1 + m_2)/2$, $\Delta m = m_1 - m_2$, and $\Gamma = \Gamma_1 \sim \Gamma_2$. The probabilities for an initial B_i to be observed at time t as a B_j are given by squaring the coefficients in the above equations:

$$\text{Prob}(B \to B) = e^{-\Gamma t}\cos^2(\Delta mt/2)$$
$$\text{Prob}(B \to \bar{B}) = |p/q|^2 e^{-\Gamma t}\sin^2(\Delta mt/2)$$
$$\text{Prob}(\bar{B} \to \bar{B}) = e^{-\Gamma t}\cos^2(\Delta mt/2)$$
$$\text{Prob}(\bar{B} \to B) = |q/p|^2 e^{-\Gamma t}\sin^2(\Delta mt/2).$$

The asymmetry between $B \to \bar{B}$ and $\bar{B} \to B$ is a measure of CP violation:

$$A = \frac{\text{Prob}(B \to \bar{B}) - \text{Prob}(\bar{B} \to B)}{\text{Prob}(B \to \bar{B}) + \text{Prob}(\bar{B} \to B)} = \frac{|p|^4 - |q|^4}{|p|^4 + |q|^4}$$
$$\sim 4\,\text{Re}\varepsilon_B \quad (\text{for } \text{Re}\varepsilon_B \ll 1).$$

It is time independent and is therefore equal to the asymmetry in the corresponding time integrated decay rates for any mode, provided there is no significant direct CP violation (cases II and III) in that mode.

This expression holds for B mesons regardless of how they are produced. However, since the effect depends on mixing, its observability in the decay of a $B\bar{B}$ pair depends on the quantum state of the pair. To get the difference in BB and $\bar{B}\bar{B}$ rates relative to the <u>overall</u> $B\bar{B}$ rate, we have to multiply the CP asymmetry A by the appropriate mixing ratio y, which we discussed in the previous section.

An inequality in the neutral B oscillation rates $B^0 \to \bar{B}^0$ and $\bar{B}^0 \to B^0$ is what gives rise to the fact that the CP eigenstates B_1 and B_2 (equal proportions of B^0 and $\bar{B}^0$) will not remain pure as they propagate and decay. Such an inequality can arise from the box diagram amplitudes if there is an imaginary part in one or several KM matrix elements. In the Wolfenstein parametrization the dominant term in the amplitude contains

$$V_{tb}V_{td}^* = A\lambda^3(1 - \rho + i\eta).$$

The resulting interference terms contribute with opposite sign to the $B \to \bar{B}$ and $\bar{B} \to B$ rates to give $\varepsilon_B \neq 0$. As Kobayashi and Maskawa discovered, CP violation effects involve all three quark families; any CP violating rate contribution is proportional to $s_{12}s_{23}s_{13}s\delta$. For the ε parameter in kaon decay this has to be divided by the kaon decay rate, so that one might expect $\varepsilon \sim \lambda \cdot A\lambda^2 \cdot A\lambda^3\eta/\lambda^2 \sim 0.002$, which is actually the measured value. The same reasoning applied to B decays gives $\varepsilon(B^0) \sim \varepsilon(B_s) \sim \lambda \cdot A\lambda^2 \cdot A\lambda^3\eta/(A\lambda^2)^2 \sim 0.05$.

However, a more detailed calculation[48] gives much lower asymmetry values:

$$A(B^0) \sim 4\mathrm{Re}\varepsilon(B^0) \leq 10^{-3}$$

$$A(B_s) \sim 4\mathrm{Re}\varepsilon(B_s) \leq 10^{-4}.$$

Since we are looking for the effect of a "wrong CP" admixture in the mass eigenstate, it doesn't matter which mode we pick to look at, provided it is flavor specific and is not expected to exhibit CP violation directly in the decay amplitude. The semileptonic decay $\bar{B}^0 \to \ell^- X$ has the highest branching ratio and detection efficiency, although other modes are also suitable. That is, we wish to measure

$$A = \frac{N(\ell^+\ell^+) - N(\ell^-\ell^-)}{N(\ell^+\ell^+) + N(\ell^-\ell^-)} .$$

The statistical error in the measurement of an asymmetry $A = \Delta N/N$ is $1/\sqrt{N}$, so establishing a nonzero effect to s standard deviations requires a sample size $N = s^2/A^2$. For like-sign semileptonic decay pairs this is $N = N(B\bar{B})b^2\varepsilon^2 y/2$. The factor of 1/2 is for B neutral/total; b is the semileptonic branching ratio; ε is the lepton detection efficiency (including the effect of lepton charge separation impurity); and y is the mixing ratio (see Section 4a). The total number of $B\bar{B}$ events required to get an s standard deviation effect is therefore $N(B\bar{B}) = 2s^2/(b^2A^2\varepsilon^2 y)$. If we assume $s=\sqrt{10}$, $A=10^{-3}$, $b=0.2$, $\varepsilon=0.7$, and $y=0.2$, we require $N(B\bar{B}) = 5\times10^9$ produced $B\bar{B}$ events to establish CP violation. If this is true, it will be practically impossible in the foreseeable future to see CP violation in this way.

(b) Case II: Interference in Decay to Flavor-Specific Final States

For a phase to be measurable in a direct decay rate we have to have an interference between two amplitudes. Two diagrams for the same direct decay process $B \to f$ can have an interference term containing η that contributes oppositely for the corresponding $\bar{B} \to \bar{f}$ decay, thus giving rise to a CP violating asymmetry. To avoid the effects of B-$\bar{B}$ oscillations, which we will consider in case III, we require that the decays be "flavor specific," that is, the b or $\bar{b}$ content of the decaying meson be implied by the final state. This is always true for charged B decays, but for neutral modes, such as $\bar{B}^0 \to K^-\pi^+$, one needs some other final state quantum number such as strangeness to indicate whether it was a B^0 or $\bar{B}^0$ decay. Starting with a sample of equal numbers of B and $\bar{B}$, one looks for an asymmetry in the occurrence of f and $\bar{f}$ final states. The asymmetry will be largest if the two interfering amplitudes (a) are comparable in magnitude, (b) have different strong interaction phases, and (c) involve several small KM matrix elements.

An example is the decay $B^- \to K^-\rho^0$ (versus $B^+ \to K^+\rho^0$), which goes through either a spectator $b \to u+s\bar{u}$ graph or a penguin $b \to s+u\bar{u}$ graph (Fig. 5.1). The predicted asymmetry[48] is

$$A = \frac{\Gamma(K^-\rho^0) - \Gamma(K^+\rho^0)}{\Gamma(K^-\rho^0) + \Gamma(K^+\rho^0)} = 1 \text{ to } 10\%.$$

Although the asymmetry is large compared to the CP violation asymmetry in kaon decay, the branching ratio is below 10^{-4}. It is typical for large asymmetries to be associated with small branching ratios, because the only way to make a CP violation effect (proportional to $s_{12}s_{23}s_{13}s\delta$) give a large asymmetry is to find a rare mode involving several small KM angles that can cancel those in the CP violation factor.

Other examples involve a spectator diagram interfering with annihilation, for instance, $B^- \to \pi^-\rho^0$ or $B^- \to D^{0*}D^-$ (Fig. 5.2). The interference can even involve different intermediate decay paths, for example, $B^- \to (D^0K^-$ or $\bar{D}^0K^-) \to K_s{}^0\pi^0K^-$. Figure 5.3 shows a plot of asymmetry versus branching ratio on which are located estimates for a number of decay modes of interest. For all asymmetries in this category, the predictions depend on a detailed understanding of the hadron dynamics in the decay. Once the asymmetry is known experimentally it will be difficult to extract reliably the value of the CP violating phase (δ or η) from the measurement.

Starting with equal numbers of B and $\bar{B}$ produced, the experiment consists in measuring the asymmetry in the occurrence of charge

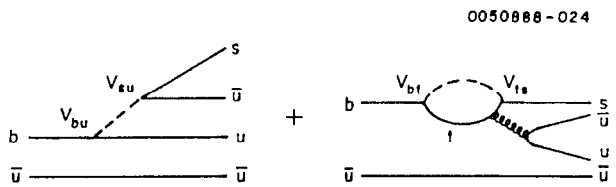

Fig. 5.1 Spectator and penguin graphs for $B^- \to K^-\rho^0$.

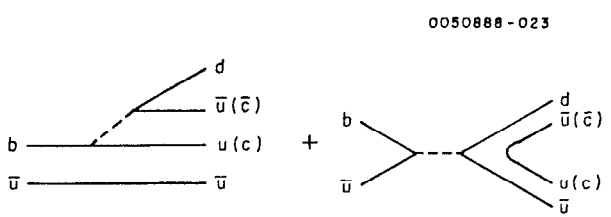

Fig. 5.2 Spectator and annihilation graphs for $B^- \to \pi^-\rho^0$ (D^-D^{*0}).

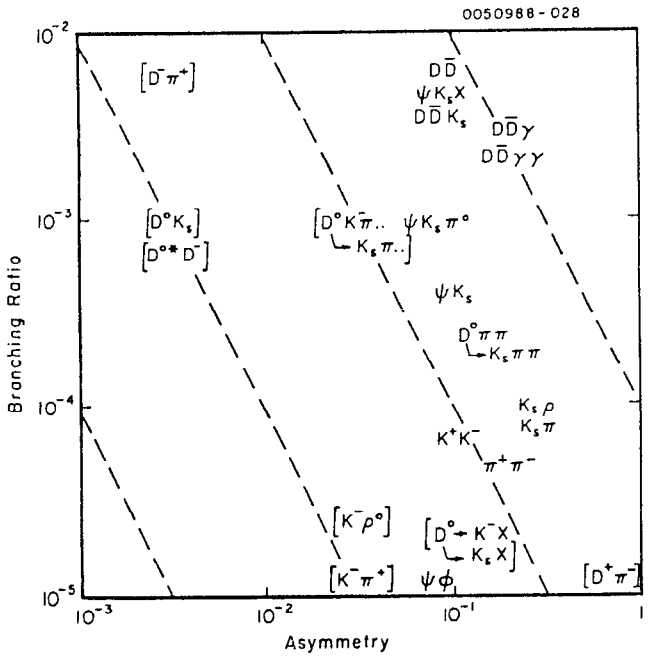

Fig. 5.3 Estimates of branching ratios and CP violating asymmetries for several interesting B decays modes (Ref. 48). Modes in brackets do not require tagging (case II); the others do (case III). Dashed lines are loci of fixed sensitivity to CP violation (fixed ba^2).

conjugate $B \to f$ and $\bar{B} \to \bar{f}$ decays. The sample size for any particular mode is $N = N(B\bar{B})b\varepsilon$ (note that the factor of 2 for B and $\bar{B}$ cancels the factor of 1/2 for B charged/total). The total number of $B\bar{B}$ events required to get a s standard deviation effect in the this mode alone is $s^2/ba^2\varepsilon$, and therefore $N(B\bar{B}) = s^2/ba^2\varepsilon$. Experimentally, one of the more favorable modes seems to be $K^-\rho^0$, for which we estimate (using Fig. 5.3) $b = 10^{-4}$, $a = 0.03$, $\varepsilon = 0.5$. We would then need $N(B\bar{B}) = 2\times10^8$ produced events in order to establish CP violation in this mode alone. If there were, in effect, four modes with this sensitivity, we could combine the data and establish an effect with 5×10^7 events.

Note that many of the favorable modes are charmless modes. Although they have small branching ratios, they do not suffer from the low detection efficiencies typical of charmed final states. There is no advantage in seeing separated B decay vertices and measuring decay times unless it helps to reduce the combinatorial background. The search can be carried out in any experiment in which B and $\bar{B}$ are produced in equal numbers, either at an e^+e^- collider, where the rate favors running at the $\Upsilon(4S)$ resonance, or at a $\bar{p}p$ collider, where the production rate is much higher but the backgrounds may be prohibitive.

(c) Case III: Interference Between Mixed and Unmixed Decays to Non-Flavor-Specific Final States

To avoid the small KM angles that make it so difficult to see CP violation in case II, we can let the rather large $B\bar{B}$ oscillation amplitude do the job of providing the alternate decay route needed for interference. By definition, a non-flavor-specific final state f^0 can be reached by either B^0 or $\bar{B}^0$ decay. The interference between $B^0 \to f^0$ and $B^0 \to \bar{B}^0 \to f^0$ can be of opposite sign from the inteference between $\bar{B}^0 \to \bar{f}^0$ and $\bar{B}^0 \to B^0 \to \bar{f}^0$. The time dependent differential decay rates for an initial B^0 and for an initial $\bar{B}^0$ are then

$$\gamma(B \to f;t) = e^{-\Gamma t}\,[2\cos^2\frac{\Delta mt}{2}\,|A|^2 + 2\sin^2\frac{\Delta mt}{2}\,\frac{q}{p}|\bar{A}|^2 - 2\sin(\Delta mt)\,\mathrm{Im}(A\bar{A}^*\,\frac{p}{q})]\,,$$

$$\gamma(\bar{B} \to \bar{f};t) = e^{-\Gamma t}\,[2\cos^2\frac{\Delta mt}{2}\,|A|^2 + 2\sin^2\frac{\Delta mt}{2}\,\frac{p}{q}|\bar{A}|^2 + 2\sin(\Delta mt)\,\mathrm{Im}(A\bar{A}^*\,\frac{p}{q})]\,,$$

where A is the decay amplitude for $B \to f$ and $\bar{A}$ is the one for $\bar{B} \to f$. For the example $f = \psi K_s$ Figure 5.4 shows the expected time evolution for $B^0 \to f$ and $\bar{B}^0$ for three values of $x = \Delta m/\Gamma$.

To observe the CP violating asymmetry in the decay rates we have to know for each decay whether the produced meson was a B or $\bar{B}$, but we cannot tell from the final states, since f and $\bar{f}$ are common to both. We therefore have to rely on the fact that b-hadrons are produced in pairs of opposite flavor. In order to "tag" the flavor of the first b-hadron decaying into a non-flavor-specific final state, we observe the second b-hadron decaying into a flavor-specific final state. If the tagging b-hadron is a neutral B, it can also oscillate to its antiparticle, and we have to consider the joint decay rate of the $B^0\,\bar{B}^0$ pair, which depends on its C state. In general for $C = \pm1$ we have

$$\gamma[B\bar{B} \to f(t)f'(t')] = e^{-\Gamma(t+t')}\,[2\cos^2\frac{\Delta m(t\pm t')}{2}\,|A\bar{A}'\pm A'\bar{A}|^2 + 2\sin^2\frac{\Delta m(t\pm t')}{2}\,|\frac{p}{q}AA' \pm \frac{q}{p}\bar{A}\bar{A}'|^2 + 2\sin\Delta m(t\pm t')\,\mathrm{Im}(\frac{p}{q}AA' \pm \frac{q}{p}\bar{A}\bar{A}')(A\bar{A}' \pm A'\bar{A})^*]\,.$$

We will assume for now that the semileptonic mode is used to tag the flavor of the second B, although other channels could be used. The tagged asymmetry with the decay to final state f or $\bar{f}$ at time t and the lepton tag ℓ^+ or ℓ^- at time t' is

$$A(t,t') = \frac{\gamma(f\ell^+) - \gamma(\bar{f}\ell^-)}{\gamma(f\ell^+) + \gamma(\bar{f}\ell^-)} = 2\sin\Delta m(t\pm t')\,\mathrm{Im}\,\frac{p}{q}\,\frac{A\bar{A}^*}{|A|^2 + |\bar{A}|^2}\,.$$

It contains the factor $\sin\Delta mT$, where T depends on the C of the $B\bar{B}$ state:

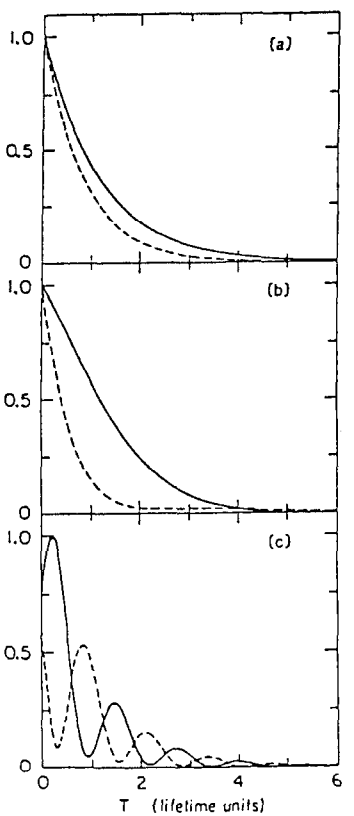

Fig. 5.4 Predicted time evolution for the decays $B^0 \to \psi K_s$ (solid) and $\bar{B}^0 \to \psi K_s$ (dashed) for (a) $x = 0.2$, (b) $x = 0.79$, (c) $x = 5.0$.

(i) $C = -1$ (such as at the $\Upsilon(4S)$) for which $T = t - t'$,

(ii) $C = +1$ (like $e^+e^- \to B\bar{B}^* \to B\bar{B}\gamma$) for which $T = t + t'$,

(iii) a $B^0 X_b$ combination without a definite C, for which $T = t$.

Measuring the asymmetry without observing the decay lengths is equivalent to integrating $e^{-\Gamma(t+t')}\sin\Delta mT$ over all t and t'. For the three cases we get

(i) identically zero,

(ii) a factor $4x/(1+x^2)^2$,

(iii) a factor $x/(1+x^2)$.

In the $C = -1$ case (i) the oscillations in the semileptonic tagging decay and in the $B \to f$ decay occur in unison in such a way that the time integrated asymmetry vanishes. In the other two cases the asymmetry for $x >> 1$ (in B_s decays, for instance) is reduced by the near cancellation of the contributions to the integral from alternate half cycles of $\sin\Delta mT$. For $x < 1$ only the first half cycle survives the exponential decay factor, so that although the CP violating asymmetry vanishes in the $x = 0$ limit, no sensitivity is lost by integrating over decay times. The cancellations can be avoided by observing decay times and binning the data in T. In effect, one can then integrate over the rectified oscillation, $e^{-\Gamma(t+t')}|\sin\Delta mT|$. At low x the result is not significantly different from the simple time integral (except that it is not zero for source (i)), but at large x alternate half cycles do not cancel and the x-dependent factor gets replaced by a constant of order one.

Figure 5.3 shows a plot of asymmetry versus branching ratio on which are located estimates (with the x-dependent factor set equal to one) for a number of decay modes of interest. There are two categories: (i) final states for which f and $\bar{f}$ are distinct (ex., $D^0\rho^0$, $D^-\pi^+$, D^0K_s, $\pi^+\rho^-$), and (ii) CP eigenstates $f = \bar{f}$ (ex., ψK_s, $\psi\phi$, $\pi^+\pi^-$, K^+K^-, D^+D^-). Theorists favor the latter because in that case $\rho_f = |\bar{A}/A| = 1$ and the calculation of the CP asymmetry is more reliable. With $|p/q| \sim 1$ too, the only dependence on the dynamics of the particular mode, that is the $\mathrm{Im}(\rho_f p/q)$ factor, is just the sine of a complex phase depending only on the KM matrix elements.

To establish a nonzero CP violation asymmetry to s standard deviations in a mode with branching ratio b, effective asymmetry a, and efficiency ε, the number of $B\bar{B}$ events required will be $N(B\bar{B}) = s^2/(b_s\,\varepsilon_s\,ba^2\varepsilon)$. One of the experimentally more favorable modes seems to be ψK_S, with $b \sim 5\times10^{-4}$, $a \sim 0.03$, and $\varepsilon \sim 0.1$ (at CESR, say). Assuming for the tagging that $b_s = 0.2$ and $\varepsilon_s = 0.7$, we therefore need about $N(B\bar{B}) = 2\times10^8$ events in this mode in order to see CP violation at the level of three standard deviations. Just to get an idea of the order of magnitude, I assume that we can sum over about four similarly favorable modes so that $N(B\bar{B}) \sim 5\times10^7$ events. The optimum search strategy depends critically on the kind of B factory one has available.

- o At a symmetric e^+e^- collider in the threshold energy region (like CESR or the PSI proposal) the produced B's are traveling too slowly to make observable decay lengths. We will therefore not be able to observe a time-binned asymmetry at the $\Upsilon(4S)$, but could run 50 to 100 MeV higher where the $B^0\bar{B}^0$ production cross section is probably dominated by $e^+e^- \rightarrow B\bar{B}^*$ (and charge conjugate) $\rightarrow B^0\bar{B}^0\gamma$, with the final $B^0\bar{B}^0$ in a C=+1 state. We sacrifice about a factor of four in production cross section relative to the $\Upsilon(4S)$. With a pure $B\bar{B}$ or $B\bar{B}^*$ final state one uses the known incident beam energy to achieve very narrow mass resolution (2.5 MeV r.m.s. at CESR) in B reconstruction and suppress the combinatoric background.

- o With an asymmetric e^+e^- collider one could measure tagged neutral B decay times t-t', since the collision frame is boosted in the lab. One would therefore run at the $\Upsilon(4S)$ resonance to look for CP violation in the B^0, and perhaps at the $\Upsilon(5S)$ in the case of B_s.

- o A high energy e^+e^- collider (like CESR running at 14 GeV c.m., PEP, TRISTAN, SLC, or LEP) could in principle observe CP asymmetries with tagged decay time measurements, but very high luminosities would be needed to offset the low production cross sections between the $\Upsilon(4S)$ and Z^0 resonances. The high multiplicities and low $b\bar{b}$/total production fractions will make it difficult to get good reconstruction efficiencies. Lepton tagging at PEP suffers from charm background, but at the Z^0 the electroweak interference causes a forward-backward asymmetry in $B^0\bar{B}^0$ production (especially if the beams are polarized), so that one may be able to dispense with tagging and thereby gain as much as an order of magnitude in sensitivity.

- o The $b\bar{b}$ production rate at a $\bar{p}p$ collider or in a high energy fixed target experiment can be very high. The problem in measuring time dependent CP asymmetries will be to get acceptable reconstruction efficiencies in the face of severe backgrounds. Fixed target experiments typically have better access close to the production vertex and may be able to pick out the decay vertices more easily.

(d) Case IV: CP Violation in Single Events

Since $B\bar{B}$ pairs are produced in e^+e^- collisions near threshold in states of definite CP, we can look for a violation in individual events, instead of measuring a rate asymmetry. To establish that CP is not conserved it would be sufficient to observe the decay of a $B^0\bar{B}^0$ state of known CP into a pair of eigenstate modes ff' for which the combined CP is different. Since the CP of the virtual photon in the e^+e^- annihilation is even (odd C, odd P), an example would be $e^+e^- \rightarrow B^0\bar{B}^0 \rightarrow ff'$ with f and f' being either both even or both odd under CP (f and f' have to be in a relative p-state which contributes a factor of -1 to the CP).

The rate for the CP violating decay of an initial state of $B\bar{B}$ with C = -1 into a pair of final states ff′ is

$$\Gamma(B\bar{B} \to ff') = \Gamma(B \to f)\,\Gamma(\bar{B} \to f') = \frac{1}{1+x^2}\,4\,\mathrm{Im}(\rho_f \frac{q}{p})\,\mathrm{Im}(\rho_{f'} \frac{q}{p}).$$

The effective rate for $e^+e^- \to B^0\bar{B}^0 \to ff'$ is

$$N(\ell\ell)/N(B\bar{B}) = [(\Sigma_+ b_i a_i \varepsilon_i)^2 + (\Sigma_- b_j a_j \varepsilon_j)^2]/2,$$

where b_i, a_i, and ε_i are the branching ratio, asymmetry, and reconstruction efficiency for the ith mode, and the sums are over the even (+) and odd (-) CP eigenstate modes. Typical $b_i a_i$ products are around 10^{-4} (Fig. 5.4); ε_i may average about 10^{-1}; and there may be about 10 usable modes. The estimated rate per $B\bar{B}$ would therefore be of the order of 10^{-9}, which is not very encouraging.

There is no advantage in seeing separated B decay vertices and measuring decay times except insofar as it may help reduce the combinatorial reconstruction backgrounds. The search is best done at the $\Upsilon(4S)$ resonance.

(e) General Comments

The above rate estimates seem to favor either (II) the measurement of untagged flavor-specific B decay asymmetries or (III) the measurement of tagged B^0 non-flavor-specific decay asymmetries. A search for the former can be done at the $\Upsilon(4S)$ with a symmetrical e^+e^- machine, and since all our present experimental information on B mesons has come this way, I bet that our first evidence of CP violation in B decay will too. Note that to measure such an asymmetry, neither tagging nor time measurements are required. Also, since the detection efficiency is high for the interesting modes ($K^-\rho^0$, $K^-\pi^+$, etc.), there may be little or no advantage in boosting the $B\bar{B}$ frame. About 5×10^7 produced $\Upsilon(4S)$ will be required for a first indication. At the present CESR luminosity level of 25 pb^{-1}/week, that would take 40 years of 40 weeks each. We need to come up with at least an order of magnitude increase in luminosity. Such an increase in CESR luminosity is not out of the question.

Eventually it will be useful to see also the time evolution of the asymmetry in tagged neutral B decays, coming from the interplay of CP violation with mixing (case III). Also the asymmetry for tagged decay into a CP eigenstate is more directly interpretable in terms of the CP violating phase in the KM matrix. If an asymmetric e^+e^- collider at the $\Upsilon(4S)$ can be built with high enough luminosity, it might provide the best conditions for observing such an asymmetry.

Since we do not know the value of the KM phase that is supposed to be responsible for CP violation, the asymmetry estimates are wild guesses. The calculation of rare branching ratios and interference amplitudes presumes that we understand the hadronic physics of heavy quark decay better than we do. Reconstruction efficiencies of course are strongly dependent on detector technology and background discrimination. So the estimates for the required number of produced $B\bar{B}$ events can easily be off by orders of magnitude.

The prediction that some modes can have CP asymmetries which are much larger than in kaon decay is an almost inescapable consequence of the Kobayashi-Maskawa three-family Standard Model. If CP violation is not there, there must be New Physics. On the other hand, if the dilepton charge asymmetry turns out to be larger than 1%, it probably means that there are more than three quark families. So there is good reason to keep an eye on the potential CP violating asymmetries even before we have produced 5×10^7 $\Upsilon(4S)$ events. And of course the first priorities are (1) to measure $B^0\bar{B}^0$ and $B_s\bar{B}_s$ mixing and (2) measure the branching ratios of the rare decay modes of interest: charmless, penguin, and CP eigenstate modes.

1. S.L. Glashow, J. Iliopoulos, and L. Maiani, Phys. Rev. D 2, 1285 (1970).

2. A. Bean et al. (CLEO) Phys. Rev. D 35, 3533 (1987).

3. M. Kobayashi and T. Maskawa, Prog. Theor. Phys. 35, 252 (1077).

4. L. Wolfenstein, Phys. Rev. Lett. 51, 1945 (1984).

5. Sheldon Stone, in CP Violation, ed. C. Jarlskog, World Scientific, Singapore, 1988.

6. Particle Data Group, Phys. Lett. 170B, 1 (1986).

7. J.R. Raab et al. (E691), Phys. Rev. D 37, 2391 (1988).

8. A. Bean et al. (CLEO), Phys. Rev. Lett. 58, 183 (1987).

9. R.M. Baltrusaitis et al. (Mark III), Phys. Rev. Lett. 54, 1976 (1985).

10. R.M. Baltrusaitis et al. (Mark III), Phys. Rev. Lett. 55,150 (1985).

11. J. Adler et al. (Mark III), Phys. Rev. Lett. 60, 89 (1988).

12. S. Behrends et al. (CLEO), Phys. Rev. Lett. 59, 407 (1987).

13. P. Haas et al. (CLEO), Phys. Rev. Lett. 56, 2781 (1986); H. Albrecht et al. (ARGUS), Phys. Lett. 187B, 425 (1987).

14. H. Albrecht et al. (ARGUS), Phys. Lett. 162B, 395 (1985); M.S. Alam et al. (CLEO), Phys. Rev. D 34, 3279 (1986).

15. H. Albrecht et al. (ARGUS), Phys. Lett. 158B, 525 (1985); C. Bebek et al. (CLEO), Phys. Rev. Lett. 56, 1893 (1986); R.M. Baltrusaitis et al. (Mark III), Phys. Rev. Lett. 56, 2136 (1986).

16. J. Adler et al. (Mark III), Phys. Lett. 196B, 107 (1987).

17. P. Avery et al. (CLEO), Phys. Lett. 183B, 429 (1987); P. Baringer et al. (CLEO), preprint CBX-88-26 submitted to XXIV International Conference on High Energy PHysics (Munich, 1988); H. Albrecht et al. (ARGUS), XXIV International Conference on High Energy Physics (Munich, 1988).

18. L.L. Chau and H.Y. Cheng, Phys. Rev. Lett. 53, 1037 (1984) and Phys. Lett. 165B, 429 (1986).

19. N.G. Deshpande, Proceedings of the UCLA Workshop on SSC Physics; N.G. Despande, G. Eilam, and A. Soni, Phys. Rev. Lett. 57, 1106 (1986).

20. P.J. O'Donnell, Phys. Lett. 175B, 369 (1986).

21. M.B. Gavela et al., Phys. Lett. 154B, 425 (1985).

22. M. Bauer, B. Stech, and M. Wirbel, Z. Phys. C 34, 103 (1987).

23. C. Bebek et al. (CLEO), Phys. Rev. D 36, 1289 (1987).

24. H. Albrecht et al. (ARGUS), Phys. Lett. 185B, 218 (1987).

25. S.L. Wu, 1987 International Symposium on Lepton and Photon Interactions at High Energies, ed. W. Bartel and R. Ruckl (North-Holland, Amsterdam, 1988).

26. E.H. Thorndike and R. Poling, Annual Reviews of Nuclear and Particle Science (U. of Rochester preprint UR-1022); H. Schroeder (ARGUS), International School of Subnuclear Physics (Erice, 1988).

27. A. Brody et al. (CLEO), Phys. Rev. Lett. 48, 1070 (1982); M.S. Alam et al. (CLEO), Phys. Rev. Lett. 58, 1814 (1987).

28. D. Bortoletto et al. (CLEO), Phys. Rev. D 35, 19 (1987).

29. M.S. Alam et al. (CLEO), Phys. Rev. Lett. 59, 22 (1987).

30. S. Behrends et al. (CLEO), Phys. Rev. Lett. 59, 407 (1987).

31. G. Altarelli et al., Nucl. Phys. B208, 365 (1982).

32. L. Angelini et al., Universita di Bari preprint BA-CT/85-16 (1985).

33. B. Grinstein, M. Wise, and N. Isgur, Phys. Rev. Lett. 56, 298 (1986).

34. M. Wirbel, B. Stech, and M. Bauer, Z. Phys. C29, 637 (1985).

35. W. Schmidt-Parzefall (ARGUS), 1987 International Symposium on Lepton and Photon Interactions at High Energies (Hamburg, 1987).

36. H. Albrecht et al. (ARGUS), Phys. Lett. 209B, 119 (1988).

37. C. Bebek et al. (CLEO), preprint CBX-88-34 submitted to the XXIV International Conference on High Energy Physics (Munich, 1988).

38. T. Inami and C.S. Lim, Progr. Theor. Phys. 65, 297 (1981).

39. A.J. Buras , W. Slominski and H. Steger, Nucl. Phys. B238, 529 (1984); B245, 369 (1984).

40. C. Albajar et al. (UA1), preprint CERN-EP/87-190(1987) submitted to Z. Phys. C.

41. W.J. Marciano and A. Sirlin, Phys. Rev. D 22, 2695 (1980); A. Sirlin, 1987 International Symposium on Lepton and Photon Interactions at High Energies (Hamburg, 1987).

42. G. Altarelli and P.J. Franzini, preprint CERN-TH.4745/87.

43. C. Albajar et al. (UA1), Phys. Lett. 186B, 247 (1987).

44. W. Bartl et al. (JADE), Phys. Lett. 146B, 437 (1984); T. Schaad et al. (Mark II), Phys. Lett. 160B, 188 (1985); H.R. Band et al. (MAC), Phys. Lett. 200B, 221 (1988).

45. H. Albrecht et al. (ARGUS), Phys. Lett. 192B, 245 (1987).

46. R. Fulton et al. (CLEO), preprint CBX-88-13 submitted to the XXIV International Conference on High Energy Physics (Munich, 1988).

47. A. Bean et al. (CLEO), Phys. Rev. Lett. 58, 183 (1987).

48. I. Bigi, V.A. Khoze, N.G. Uraltsev, and A. Sanda in CP Violation, ed. C. Jarlskog, World Scientific, Singapore, 1988, and preprint SLAC-PUB-4476, 1987; including references to earlier work.

Precious Rarities -

On Rare Decays of K, D and B Mesons

I. I. Bigi

Department of Physics
University of Notre Dame
Notre Dame, IN 46556

Abstract:

A detailed analysis of K decays has been quite instrumental, if not even crucial for developing the present Standard Model of particle physics. There is no reason to believe that such a line of research has already exhausted its discovery potential. Quite on the contrary we can suspect that further dedicated studies of the rare decays of K, B and maybe even D mesons will reveal "New Physics." At the very least they will provide highly sensitive tests of the Standard Model. A crucial element in any such analysis is the reliability of the theoretical tools that are employed. I attempt to give a comprehensive and detailed evaluation of the scope and the limitations of the various theoretical technologies that are presently available.

Invited lectures given at the 1988 SLAC Summer Institute, Stanford, CA, July 18-29, 1988.

I. INTRODUCTION

An event is called rare if it occurs with a probability much smaller than unity. This, however, does not make it automatically an interesting object for study. The case of elephant-antielephant fluctuations is sometimes used to illustrate this point. While there exists no first principle forbidding them to contribute to, say, (g-2) for muons it is utterly obvious that those contributions can safely be ignored. In the following I will call a rare event precious only if there exists a realistic chance for it to be ever observed - even if it takes many years.

Since I am the first lecturer at this Summer Institute, I can be forgiven for making a few general remarks although later speakers will address these issues in more detail and with presumably more eloquence as well.

The theoretical landscape presents itself today as a combination of strong and electroweak forces which are described in terms of a gauge theory based on the group $SU(3)_c \times SU(2)_L \times U(1)$. (For these lectures I ignore the existence of gravity and I do so without feelings of guilt.) Tomorrow's theoretical landscape will still contain QCD as the theory of strong interactions; yet the question on the underlying electroweak theory remains quite unsettled. This is to say that QCD is the "only thing" whereas the $SU(2)_L \times U(1)$ gauge theory is only the "best thing"; for the latter merely incorporates many of the fundamental mysteries of particle physics without offering any explanations: what is the origin of the various flavour degrees of freedom, why do they exhibit a family structure and family replication, etc. etc.?

Enlightenment can be sought via two alternative routes:

A) One can adopt the approach pioneered by the "Eastern Monks" --- These sages living typically by themselves or in very small groups sought enlightenment by pure thinking and meditating. Their contacts with the rest of society were rather limited: pious people from the surrounding villages and towns would come out to see these venerable monks and would do so in the hope of being addressed by them (though with scant hope to understand such teachings).

B) One can follow the example set by the "Western Monk Orders" --- Large collaborations that set out to cut down forests, take virgin land under the plow, baptize the heathens (with occasional, unfortunate losses) and do all of this under the motto of "ora et labora"!

I believe that "praying" for inspiration coupled with "working" hard to make measurements and to calculate rates represents the appropriate method for our field; therefore, I will use this approach as guidance in the subsequent discussion. May I add in passing that any similarity between the approach sketched under A) and an existing theoretical school is purely accidental.

The question we want to address then is:

"Flavours: Whence do they come - where do they go?"

Yet it has to be understood that even a detailed study of flavour decays ("where do they go") *will not reveal directly and immediately the reason behind* the existence of different flavours ("whence do they come"). What can be achieved or learnt is the following:

(α) There has to be a dynamical distinction between the different flavours; the existence of such new forces - i.e., "New Physics", hereafter referred to as NP - would in general lead to decay processes

$$M \longrightarrow \ell_1^+ \ell_2^- \tag{1.1}$$

$$M \longrightarrow m \ell_1^+ \ell_2^- \tag{1.2}$$

where M and m denote mesons and ℓ_1 and ℓ_2 different charged leptons. Examples are

$$K_L \longrightarrow e^\pm \mu^\mp$$

$$K^+ \longrightarrow \pi^+ e^\pm \mu^\mp \ .$$

These processes are strictly forbidden in the Standard Model since they would violate the individual lepton number.

Processes of the type

$$M \longrightarrow \ell^+ \ell^- \tag{1.3}$$

$$M \longrightarrow m \ell \bar{\ell} \tag{1.4}$$

on the other hand can be generated in the Standard Model as a 1-loop quantum effect; yet NP can boost their transition rates very significantly, modify the kinematical distributions of the decay products or it could even produce CP asymmetries!

I had already stated the obvious: discovery of this kind of New Physics per se would not resolve the flavour mystery. However it would teach us lessons that

I had already stated the obvious: discovery of this kind of New Physics per se would not resolve the flavour mystery. However it would teach us lessons that are of crucial importance for any such resolution, namely (i) that a dynamical distinction does indeed exist and (ii) by which mass scale it is characterised.

(β) Measuring the rates of those transitions that - within the Standard Model - can proceed only via 1-loop effects will allow us to probe fundamental parameters like m(top) and the KM parameters V(td), V(ts).

(γ) At the very least we will learn important or even crucial lessons on QCD - lessons that are rather unique due to the interplay of weak forces and strong forces that occurs in flavour decays.

The last item points also to a central problem in this line of research: when one finds a difference between an expected and a measured decay rate one would like to claim that such a discrepancy indirectly establishes the existence of New Physics! Yet one has to be concerned that this merely signals the need for "New, i.e., better Physicists or Theorists" meaning that our theoretical computations contained hidden uncertainties. Therefore we have to subject our tools to a very careful evaluation and re-evaluation.

There exists a naive folklore about the available theoretical technologies, namely that our calculations become necessarily more reliable for heavier flavours, i.e., when going from K decays to D decays and then B decays. One usually cites as supporting evidence for this folklore that the heavier a flavour hadron is, the more short-distance dominated its dynamics become. This is reflected also in the emergence of a more and more universal lifetime for flavour hadrons when their mass increases: $\tau(K^{\pm}) \sim 600\ \tau(K_S)$ vs. $\tau(D^{\pm}) \sim 2.5\ \tau(D^0)$ vs. $\tau(B^{\pm}) < 2\ \tau(B_d)$.

However I want to urge you not to accept this folklore at face value. For it is based on rather simplistic considerations read off from quark diagrams. There are other theoretical technologies that enjoy a much less tenuous relationship with QCD and that yield quite a different pattern of reliability for their predictions . This is sketched in Table I, where the symbol " $\varnothing$ " means "not applicable", " $\surd\surd$ " "quite reliable application" and "$\surd$" "order of magnitude estimates." Thus we see that the trustworthiness of a theoretical computation has to be evaluated almost on a case-by-case level - a central point of these lectures.

These lectures are organized as follows: in Sect. II, I discuss K, D and B decays that are strictly forbidden in the Standard Model; in Sect. III and IV, I treat K decays that occur due to quantum corrections; in Sect. III it is the process $K^+ \to \pi^+ +$ "unseen" whereas in Sect. IV, I analyse radiative K decays in the framework of Chiral Perturbation Theory; rare D decays are treated in Sect. V and rare B decays in Sect. VI; the conclusions are presented in Sect. VII.

tools / flavour	quark diagrams	ChPT	1/N	QCD SR
K	$\varnothing$	$\surd\surd$	$\surd$	$\surd$
D	$\surd$??	$\varnothing$	$\surd\surd$	$\surd\surd$
B	$\surd$	$\varnothing$	$\surd$	$\surd$

Table I

Pattern of reliability that different theoretical tools offer for heavy flavour decays

II. "A FARMER AND HIS SON VISIT VIENNA" OR "BREAKING THE FLAVOUR CODE"

Our understanding of the flavour puzzle - why are there families, why are they so much alike? - can be illustrated by the following story: A farmer from a little town had to visit the great city of Vienna to take care of some business. He decided to bring his little son along who had never seen Vienna. While they walked through the streets the little boy was all eyes and looked left and right. He then pointed at a big building and asked: "Hey, Daddy, what is this?" His father looked at it, scratched his head, looked at it again, shook his head and said: "I don't know, my son." This sequence - the son asking a question and his father being unable to answer it - repeated itself a few times. Then the son said: "Daddy, are you getting mad at me for asking all these questions?" whereupon his father replied: "Of course not, my son, how can you learn something if you don't ask questions!" The fact that we have not received yet a satisfactory answer to the flavour puzzle does not imply that no such answer can ever be secured; it only means that we have to be more persistent and maybe have to rephrase our questions.

In all likelihood there has to be a dynamical distinction between the different families, i.e. one that goes beyond the mere difference in mass; in particular there could be a neutral boson Y which connects members of different families

$$Y \longrightarrow \ell_1 \bar{\ell}_2, \ell_1 \neq \ell_2 \ .$$

Exchanges of such bosons would produce processes like

$$e^+e^- \rightarrow e\mu,\ e\tau,\ \mu\tau$$

or

$$ep \rightarrow \mu X,\ \tau X$$

which can be searched for. At low energies they will produce decay processes

$$\begin{aligned} M &\longrightarrow \ell_1 \bar{\ell}_2 \\ M &\longrightarrow m\ \ell_1 \bar{\ell}_2 \ . \end{aligned} \qquad (2.1)$$

It is those that we are going to analyze.

A. Zoology

A very convenient classification of the effective couplings that generate these reactions has been provided by Buchmüller and Wyler.[1] Only "low energy" fields appear explicitly, namely

matter fields	f	(either leptons or quarks)
photons	γ	
weak bosons	W, Z	and
light Higgs fields	ϕ	

All other fields are "integrated out" in the same fashion as W boson fields are "integrated out" in the effective weak Lagrangian. There this procedure introduced the non-renormalizable Fermi interaction of dimension six; here more generally it will generate non-renormalizable interactions of dimension $d \geq 5$:

$$\mathfrak{L}_{eff} = \mathfrak{L}_{GSW}^{(d=4)} + \frac{1}{\Lambda_{NP}^{(5)}}\,\mathfrak{L}_{NP}^{(d=5)} + \frac{1}{\left(\Lambda_{NP}^{(6)}\right)^2}\,\mathfrak{L}_{NP}^{(d=6)} + \ldots \qquad (2.2)$$

L_{GSW} denotes the Lagrangian of the Standard Model and $\Lambda_{NP}^{(i)}$ characterize the mass scale of the new interactions - again in analogy to the Fermi constant $G_F \propto 1/M_W^2$. Anticipating that $\Lambda_{NP} >> \sqrt{G_F}$ - otherwise we would have seen already these processes - we conclude that $\mathfrak{L}_{NP}$ better be invariant under $SU(3)_C \times S(2)_L \times U(1)$ rotations.

$L_{NP}^{(5)}$ describes the coupling of two scalar fields - ϕ or ϕ^* - to two fermion fields f_1 and f_2 as shown in Fig. 1. Since the two fermion fields have to form a scalar (or pseudoscalar), one of them has to be left-handed and the other one right-handed. Accordingly they carry the same electroweak quantum numbers as the left-handed field alone, namely a weak isospin of half a unit and a non-vanishing hypercharge. If the two scalars that couple to these fermions are the Higgs field ϕ and its conjugate ϕ^* then they carry zero hypercharge; such a coupling cannot be $SU(2)_L \times U(1)$ invariant and, following our prescription stated above, is therefore ruled out. If on the other hand the two scalars are $\phi\phi$ or $\phi^*\phi^*$ then they carry weak isospin one. The two fermions would have to carry isospin one as well which - as mentioned above - is not possible. There is one tiny loophole in this last argument: the right-handed fermion field could be the charge conjugate of a left-handed field and a weak isospin of one unit is thus attainable. However such a coupling violates fermion number by two units and is thus allowed at

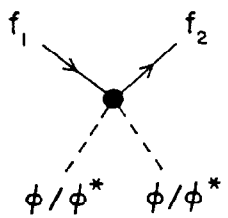

Fig. 1

Fig. 1: A dimension five coupling of two scalar fields to two fermion fields.

best for neutral fermion fields, namely neutrinos, where such couplings produce Majorana mass terms. Yet the corresponding scale $\Lambda_{NP}^{(5)}$ has to be huge and a term $\frac{1}{\Lambda_{NP}^{(5)}}\ \mathcal{L}_{NP}^{(5)}$ is quite academic in the present context.

Thus one arrives at a result that one would have guessed immediately and quite naively, namely that the New Physics can be described by a dimension six term:

$$\mathcal{L}_{eff} \simeq \mathcal{L}_{GSW}^{(d=4)} + \frac{1}{\left(\Lambda_{NP}^{(6)}\right)^2}\ \mathcal{L}_{NP}^{(d=6)} \qquad (2.3)$$

$$\mathcal{L}_{NP}^{(d=6)} = \sum_i c_i \bullet \text{ current x current} \qquad (2.4)$$

The c number coefficients c_i are determined by the specific dynamical model one has in mind.

There is no shortage of such dynamical models: there are many GUTs on the market that contain "horizontal" interactions, i.e., flavour changing neutral currents (= FCNC) mediated via spin one or spin zero bosons; extended technicolour models can be accused of many vices, but not of forbidding FCNC; the same holds for composite models. Such new forces can in particular be mediated by so-called "lepto-quarks" (= LQ), i.e., bosons that carry both lepton and quark quantum numbers. They emerged first in Pati-Salam models based on a gauge group SU(4) where lepton number is treated as a fourth colour. Yet they appear in many other models as well and represent a rather generic feature of models that are inspired by a superstring ansatz. Even "ordinary" Supersymmetry enters this arena if sneutrinos develop a non-vanishing vacuum expectation value. In summary, there are many models that will produce non-vanishing values for the coefficients c_i in (2.4); however nothing definite can be said or predicted concerning their actual values. In addition, the couplings of FCNC to up-type quarks - u, c, t - could a priori be completely different from those to down-type quarks - d, s, b. In that sense one gains independent pieces of information when searching for $K \to e\mu$ and $D \to e\mu$ decays.

B. The Down Side

So far we have looked at the optimistic side of things; now let us review the more depressing aspects.

(i) *No decay that violates lepton flavour conservation* like $K \to e\mu$, $\pi\ e\mu$, $D \to e\mu$, $e\mu\pi$, or $B \to e\mu$, $e\mu K$ has been observed yet. The bounds on Λ_{NP} that can be derived from that will be given below .

(ii) Exactly because the New Physics contributions are new they cannot interfere with the Standard Model contributions. Therefore one finds for the branching ratios

$$BR \propto \left(\frac{c_i}{\Lambda^2_{NP}} \right)^2 \propto \frac{g^2_{Yq} g^2_{Y\ell}}{M^4_Y} \qquad (2.5)$$

where M_Y denotes the mass of the "new" boson Y and $g_{Yq}[g_{Y\ell}]$ its couplings to quarks [leptons]. An increase in experimental sensitivity, as far as branching ratios are concerned, by a highly impressive factor of 10^4 translates itself into a much more modest increase by a factor of 10 in sensitivity for the mass M_Y! This is not encouraging when one keeps in mind that no theoretical upper limit on M_Y has been suggested so far that is reasonably reliable. A non-observation of these decays will therefore not lead to a breakdown of any meaningful theoretical benchmark. Such searches are therefore not for the faint-hearted!

(iii) However they are not for the reckless either! The decay of a pseudoscalar meson $PS = (Q\bar{q}) \to \ell_1 \ell_2$ is represented in Fig. 2 for an s-channel exchange of the Y boson. Its transition rate is subject to two concurrent suppression mechanisms:

(α) If Y carries spin one then the rate is helicity suppressed, i.e., it vanishes for $m(\ell_1), m(\ell_2) \to 0$. More specifically

$$BR(PS \xrightarrow[J=1]{} \ell_1 \bar{\ell}_2) \propto \frac{m^2_1 \text{ or } m^2_2}{M^2_{PS}} \qquad (2.6)$$

If Y is spinless there is no such "kinematical" suppression. Yet scalar couplings violate chiral invariance; since this symmetry is apparently the only principle that can keep fermion masses light one (as a theorist) is very reluctant to give it up. Accordingly, one suspects that all such scalar or pseudoscalar couplings depend on the mass of the field they couple to - exactly like Higgs bosons. Thus

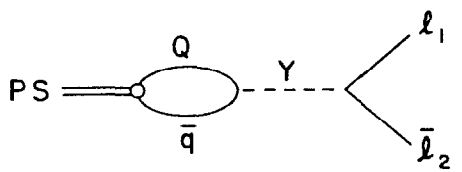

Fig. 2

Fig. 2: Diagram for the decay of a pseudoscalar meson into a lepton pair.

$$\text{BR (PS} \xrightarrow[J=0]{} \ell_1 \bar{\ell}_2) \propto \frac{m_1^2 \text{ or } m_2^2}{M_{PS}^2} \qquad (2.7)$$

as before, but this time due to genuine dynamical considerations - as perceived by theorists.

(β) The exchange of these massive Y bosons produces pointlike interactions, i.e., forces of zero range. The transition amplitude then depends on the wave function of the decaying meson at zero separation or the decay constant:

$$\text{BR (PS} \to \ell_1 \bar{\ell}_2) \propto \left(\frac{f_{PS}}{M_{PS}} \right)^2. \qquad (2.8)$$

For $K \to e\mu$ we have

$m_\mu \sim \frac{1}{5} M_K$

$f_K \sim \frac{1}{3} M_K$

and these suppression factors are not huge.

For $D \to e\mu$, $B \to e\mu$ on the other hand, we encounter huge suppression factors since $m_\mu << m_D < m_B$, $f_D << m_D$ and $f_B << m_B$. Let me list just one telling example: the mode $D^o \to e^\pm \mu^\mp$ has been searched for unsuccessfully leading to[2]

$$\text{BR } (D^o \to e^\pm \mu^\mp) \leq 0.41 \times 10^{-4} \qquad \text{E 691} \qquad (2.9)$$

Yet this apparently impressive bound loses its luster if compared to the upper limit on the quite ordinary mode $D^+ \to \mu^+ \nu_\mu$:[3]

$$\text{BR } (D^+ \to \mu^+ \nu_\mu) \leq 6 \times 10^{-4} \quad \text{MARK III} \qquad (2.10)$$

From this number one extracts $f_D \leq 290$ MeV; theoretically one estimates $f_D \sim$ 150-200 MeV and therefore

$$\text{BR } (D^+ \to \mu^+ \nu_\mu) \simeq 1.5 \times 10^{-4} \left(\frac{f_D}{150 \text{ MeV}} \right)^2 \qquad (2.11)$$

Compare (2.9) with (2.11), and I can rest my case.

When extracting bounds on mass scales that characterize New Physics one should therefore quote numbers for two quantities, namely Λ_{NP} as it appears in (2.3) with $c_i = 1$ (see 2.4) and $\tilde{\Lambda}_{NP}^2 = \Lambda_{NP}^2 \times \frac{M_\ell}{M_{PS}}$, i.e., $c_i = \frac{M_\ell}{M_{PS}}$. As explained above, I believe that $\tilde{\Lambda}_{NP}$ is the appropriate quantity for $M \to \ell_1 \bar{\ell}_2$ transitions whereas $M \to m\, \ell_1 \bar{\ell}_2$ decays offer a much better chance to probe Λ_{NP} without mass suppression factors.

The existing bounds are summarized in Table II, where I have underlined the "most likely" bounds as explained above.

Process	BR	Λ_{NP}	$\tilde{\Lambda}_{NP}$
$K_L \to e\mu$	$< 10^{-8}$	< 35 TeV	<u>≤ 16 TeV</u>
$K^+ \to \pi^+ e\mu$	$< 4.8 \times 10^{-9}$	<u>≤ 20 TeV</u>	< 9 TeV
$D^o \to e\mu$	$< 4.1 \times 10^{-5}$	< 1 TeV	<u>≤ 0.24 TeV</u>
$B \to e\mu$	$< 3 \times 10^{-5}$	< 3.4 TeV	<u>≤ 0.5 TeV</u>

Table II

For details on the experimental numbers see the lectures by K. Berkelman and A. J. S. Smith.[4, 5]

C. <u>Resume on the forbidden decays $M \to (m)\, \ell_1 \ell_2$</u>

(i) There is an obligation to continue careful and dedicated searches for these striking decay modes.

(ii) Improved experimental upper bounds just raise the bounds on Λ_{NP}, the mass scale characterizing the New Physics that distinguishes between the different families, and they do it very slowly

$$\Lambda_{NP,\,min} \sim \frac{1}{\sqrt[4]{\text{BR (max)}}}$$

Unfortunately, no sound theoretical upper bounds on Λ_{NP} have been established so far, but this might change in the future.

(iii) Searches for $D \to e\mu$ or $B \to e\mu$ are classical examples of "lamp post searches": one looks for something where it can be seen most easily, not where one has the best chance of finding it. Nevertheless it would be imprudent to discontinue them.

(iv) In any case one must search for $D \to \pi/\rho\, e\mu$ and $B \to K/K^* e\mu$ decays as well, or even better for the inclusive modes $D \to e\mu + X$, $B \to e\mu + X$. They are not affected by helicity suppression and the inclusive rates are also not reduced by $(f_D/m_D)^2$ or $(f_B/m_B)^2$ respectively.

(v) Furthermore the different decays are governed by different hadronic matrix elements; e.g.,

$$D \to e\mu \quad \Leftrightarrow \quad <0 \mid A_\mu/P \mid D>$$
$$D \to \pi e\mu \quad \Leftrightarrow \quad <\pi \mid V_\mu/S \mid D>$$
$$D \to \rho e\mu \quad \Leftrightarrow \quad <\rho \mid A_\mu/P \mid D>$$

where S, P, V_μ, A_μ denote scalar, pseudoscalar, vector and axialvector currents respectively.

(vi) The mixing angles that are contained in the couplings of these FCNC could in principle be "dialed" in such a way as to greatly suppress, say, $K \to \pi e\mu$, while not reducing $D \to \pi e\mu$. In that sense studies of rare K and rare D decays are complementary, not competitive. It is however a different question whether this can make up for the much smaller branching ratios that can be reached in K decays vs. D decays.

III. $K^\pm \to \pi^\pm$ + "nothing seen" - THE PRECIOUS RARITY PAR EXCELLENCE

The transition

$$K^+ \to \pi^+ \nu \bar{\nu} \tag{3.1}$$

requires a FCNC; in the Standard Model it has therefore to proceed via a one-loop process as shown in Fig. 3. Computing the contributions of these diagrams -- which amounts to integrating out the heavy fields W, Z, t, c -- one obtains the effective interaction $\mathcal{H}_{\rm eff}(\Delta S = 1)$.[6] To calculate a rate one has to form the appropriate matrix element

$$<\pi^+ \nu \bar{\nu} \mid \mathcal{H}_{\rm eff}\,(\Delta S = 1) \mid K^+> \simeq \text{coeff.}\ j_\mu^{(\ell)} <\pi^+ \mid J_\mu^{(q)} \mid K^+> \tag{3.2}$$

With this perturbative treatment one can compute the c number coeff., the leptonic current $j_\mu^{(\ell)}$ and one can identify the general transformation properties of the hadronic current $J_\mu^{(q)}$. Yet one cannot obtain the magnitude of the on-shell matrix element $<\pi^+ \mid J_\mu^{(q)} \mid K^+>$ this way since the latter depends on long-distance dynamics. Fortunately the well-measured decay $K \to \pi\, e\nu$ depends on a matrix element $<\pi^0 \mid J_\mu^{(q)} \mid K^+>$ that can be related to $<\pi^+ \mid J_\mu^{(q)} \mid K^+>$ via an isospin rotation of the hadronic current and that is probed at almost the identical momentum transfer.

There is a small loophole in this line of reasoning which is analyzed in the Appendix A and then discarded. BR $(K^+ \to \pi^+ \nu\nu)$ can thus be expressed mainly in terms of quark and lepton parameters - masses, KM angles; the impact of long-distance dynamics is isolated into one hadronic matrix element whose size can be obtained from the measured decay $K \to \pi e\nu$:

$$BR(K^+ \to \pi^+ \nu \bar{\nu}) \simeq 1.43 \times 10^{-5} \sum_\ell \left| \sum_q V^*(qs)\, V(qd)\, D(x_q, y_\ell) \right|^2 \tag{3.3}$$

$$\ell = e, \mu, \tau\,; \quad q = u, c, t$$

$$y_\ell = \frac{m_\ell^2}{M_W^2}\,; \quad x_q = \frac{m_q^2}{M_W^2}$$

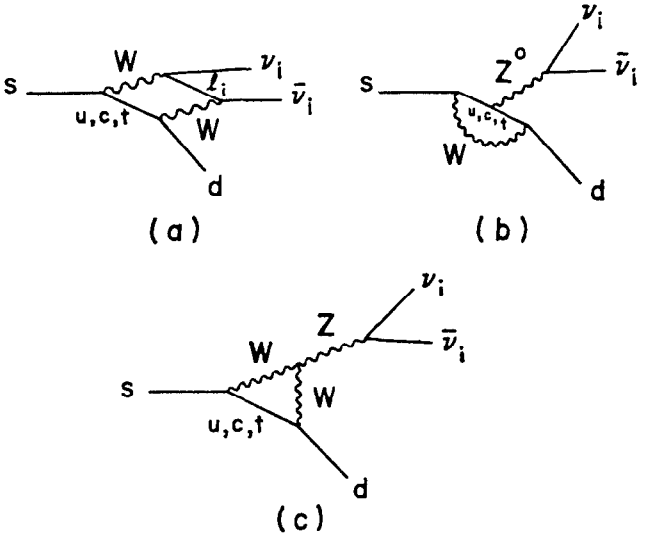

Fig. 3

Fig. 3a, b, c: Quark diagrams that generate the transition operator $s \to d\,\bar{\nu}\,\bar{\nu}$.

V(ij) denote the corresponding KM matrix elements and the function $D(x_q, y_\ell)$ enter when one integrates out the internal loop in the diagrams of Fig. 3. They were first calculated by Inami and Lin[6] and for $y_\ell \simeq 0$ they read

$$D(x,0) = \frac{1}{8}\left(1 + \frac{3}{(1-x)^2} - \left(\frac{4-x}{1-x}\right)^2\right) x \log x + \frac{x}{4} - \frac{3x}{4(1-x)} . \qquad (3.4)$$

With three families there are thus three unknown parameters - m_t, V(td) and V(ts) - that determine the rate:

$$BR(K^+ \to \pi^+ \nu_e \bar{\nu}_e) \simeq 1.43 \times 10^{-5} \left| V^*(cs)\, V(cd)\, D(x_c, 0) \right|^2 \times$$
$$\times \left| 1 + \frac{V^*(ts)\, V(td)}{V^*(cs)\, V(cd)} \frac{D(x_t, 0)}{D(x_c, 0)} \right|^2 \qquad (3.5)$$
$$\simeq BR(K^+ \to \pi^+ \nu_\mu \bar{\nu}_\mu)$$

$BR(K^+ \to \pi^+ \nu_\tau \bar{\nu}_\tau)$ is slightly smaller (at most 20%) since the τ mass that enters in the loop cannot be completely ignored.

Using the unitarity of the 3 x 3 KM matrix one obtains

$$V(ts) \simeq -V(cb) \simeq A\lambda^2 \qquad (3.6)$$

where the last equality refers to the Wolfenstein representation [21]

$$\lambda = \sin\theta_c$$
$$A \simeq 1.1 \pm 0.2 \qquad (3.7)$$

For V(td) no such definite statement can be made:

$$V(td) \simeq A\lambda^3 (1 - \rho - i\eta) \qquad (3.8)$$
$$V(ub) \sim A\lambda^3 (\rho - i\eta)$$

Bounds on $|V(ub)|$ yield information on $\sqrt{\rho^2+\eta^2}$ only, but not on the sign of ρ which is quite relevant for $|V(td)| \simeq A\lambda^3 \sqrt{(1-\rho)^2+\eta^2}$. Using $|\rho| \leq 0.8$ as inferred from semi-leptonic B decays one finds

$$\begin{Bmatrix} 0.32 \\ 0.37 \\ 0.42 \end{Bmatrix} \leq BR(K^+ \to \pi^+ \nu \bar{\nu}) \times 10^{10} \leq \begin{Bmatrix} 1.0 \\ 3.4 \\ 7.4 \end{Bmatrix} \text{ for } m_t = \begin{Bmatrix} 40 \\ 100 \\ 160 \end{Bmatrix} \text{ GeV} \qquad (3.9)$$

where the upper [lower] bound holds for ρ = -0.8 [+0.8]. If one ignores the top contribution completely one gets $BR(K^+ \to \pi^+ \nu \bar{\nu}) \simeq 3 \times 10^{-11}$.

The strength of $B_d - \overline{B}_d$ mixing is directly and crucially affected by $|V(td)|$ and m_t. The signals observed by ARGUS and by CLEO strongly favour $\rho < 0$ and tend to push ρ towards -0.8 unless top quarks are very massive. For the range $50\ \text{GeV} \leq m_t \leq 200\ \text{GeV}$ one can use the approximate scaling laws

$$\Delta m_B \propto (m_t)^{1.75}$$

$$D(x_t, 0) \propto m_t$$

The predictions in (3.9) have to be taken with a certain grain of salt: they were obtained using

$$m_c = 1.5\ \text{GeV}. \qquad (3.10)$$

While this represents a reasonable choice, it is not a uniquely determined one. A range

$$m_c \simeq 1.2 - 1.8\ \text{GeV}$$

has to be allowed for; this in turn leads to a non-negligible variation in $BR(K^+ \to \pi^+ \nu \bar{\nu})$ in particular for moderate top masses. Using "reasonable" and "typical" values for the KM parameters, namely

$$A = 1.1,\ \rho = -0.7,\ \eta = 0.25$$

one finds for example a roughly 50%[35%] variation in the branching ratio for a top mass of 40[100] GeV.

With these caveats in mind we conclude that the present findings on $B_d - \overline{B}_d$ mixing imply

$$BR(K^+ \to \pi^+ \nu \bar{\nu}) \sim 10^{-10} - 10^{-9} \qquad (3.11)$$

More accurate information on m_t, $B_d - \overline{B}_d$ mixing, etc. when it becomes available will enable us to restate (3.11) in a more precise way. To say it differently: there is an upper limit on $BR(K^+ \to \pi^+ \nu \bar{\nu})$ that the Standard Model with three families can accommodate; its present value is given in (3.11):

$$BR(K^+ \to \pi^+ \nu\bar{\nu})\Big|_{\text{St - M, 3 fam.}} \leq L \qquad (3.12)$$

$$L(\text{"now"}) \sim 10^{-9}$$

If data were to show a branching ratio in excess of such a limit we would have to conclude that New Physics were at work. There is a whole host of candidates for New Physics of which I will sketch just a few typical examples that can produce sizeable rates for

$$K^+ \to \pi^+ + \text{"unseen"}$$

1. The least radical extension: a fourth family

There could exist a fourth family with two new quarks t' and b' and two new leptons Δ and ν_Δ. The new parameters that are most significant for the process under study are the mass m(t') and the KM parameters V (t's) and V (t'd). (For the quark contributions act coherently whereas the lepton terms are incoherent due to the absence of lepton flavour mixing. This is explicitly expressed in (3.3).)

Making V(t'd) and V(t's) as large as still allowed by the unitarity constraints on a 4 x 4 KM matrix would allow to push $BR(K^+ \to \pi^+ \nu \bar{\nu})$ up to the present experimental upper limits. On the other hand generalizing a Wolfenstein ansatz to four families or inferring the t' and b' parameters from fixed point solutions to the renormalization group equations leads typically to

$$Br(K^+ \to \pi^+ \nu\bar{\nu}) \leq \text{few x } 10^{-9}, 10^{-8} \qquad (3.13)$$

2. The most elegant extension: SUSY

Supersymmetry introduces new neutrino-like states, namely photinos $\tilde{\gamma}$ (which can contain some admixtures of other neutralinos). The process $K^+ \to \pi^+ +$ "nothing seen" can then be realized by

$$K^+ \to \pi^+ \tilde{\gamma}\tilde{\gamma} \qquad (3.14)$$

if the photinos are sufficiently light - a possible, though not very likely scenario.

Flavour mixing among the different down-type squarks $\tilde{D} = (\tilde{d}, \tilde{s}, \tilde{b})$ can generate $K^+ \to \pi^+ \tilde{\gamma}\tilde{\gamma}$ already on the tree level as shown in Fig. 4 where the dots point out the odd R-parity of the field involved. One finds that[7]

$$BR(K^+ \to \pi^+ \tilde{\gamma}\tilde{\gamma}) \geq 10^{-10}, 10^{-9} \qquad (3.15)$$

represent conceivable cases.

Without such flavour mixing in the squark mass matrix, one has to invoke one-loop reactions as sketched in Fig. 5. They typically yield rather small numbers,

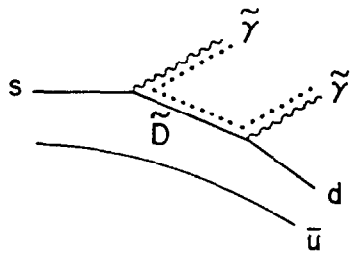

Fig. 4: Tree level diagram for $K^- \to \pi^- \gamma\tilde{\gamma}$.

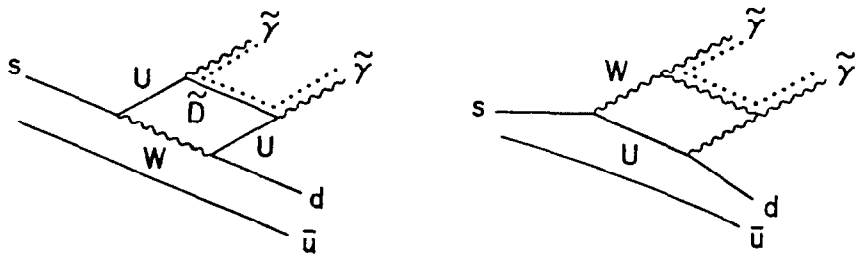

Fig. 5: One-loop diagrams for $K^- \to \pi^- \gamma\tilde{\gamma}$.

namely

$$BR\,(K^+ \to \pi^+ \gamma\gamma) \sim 10^{-11} - 10^{-10} \qquad (3.16)$$

3. The most stirring extension: direct FCNC via ETC, LQ, ...

With direct FCNC mediated by the exchange of a new boson of mass M_X one finds

$$BR\,(K^+ \to \pi^+ \nu_e\bar{\nu}_\mu \; + \pi^+\nu_\mu\bar{\nu}_e) \sim 10^{-10}\left(\frac{25\ \mathrm{TeV}}{M_X}\right)^4 \qquad (3.17)$$

where I have ignored any helicity suppression.

4. The odd-ball extensions

Adopting a phrase coined by M. K. Gaillard one includes here

$$K^+ \to \pi^+ + \text{"funnies"}$$

where "funnies" stand for axion, familon, majoron, Higgs and all the other even more fascinating objects that have not been invented yet. I will list just two examples which are - relatively speaking - the ones with the most specific phenomenology.

(α) Higgs:

The Standard Model contains just one flavour diagonal neutral Higgs field; its mass m_φ is - strictly speaking - undetermined. Theoretical constraints like the Weinberg-Linde bound can be evaded if there is a sufficiently heavy quark field Q, i.e.

$$M_Q \geq 80\ \mathrm{GeV} \qquad (3.18)$$

This has actually become a more likely scenario in the absence of a direct observation of top quarks. A very light Higgs becomes then conceivable and the process

$$K^+ \to \pi^+ \varphi, \quad \varphi \to \mu^+\mu^-, e^+e^-, \text{"unseen"} \qquad (3.19)$$

could occur due to higher order processes.[8]

No decay of this type has been observed; unless some delicate cancellations between different contributions occur one has to conclude that $K^+ \to \pi^+ \varphi$ is forbidden kinematically, i.e.

$$m_\varphi \geq 360\ \mathrm{MeV} \qquad (3.20)$$

Going beyond the Standard Model and extending the Higgs sector will lead to more flavour diagonal neutral Higgs fields φ_i. Their Yukawa couplings are not

uniquely fixed anymore by the requirement that they give mass to the gauge bosons and fermions.

Thus

$$m(\varphi_i) < 360\,\text{MeV} \qquad (3.21)$$

is still allowed if the Yukawa coupling of this light Higgs boson is roughly an order of magnitude smaller than prescribed by the Standard Model.

(β) Majoron:

Neutrinos can obtain a Majorana mass only if lepton number is violated. If this global symmetry is broken spontaneously then a Goldstone boson will emerge - the (generic) Majoron. It can be accomplished by a scalar partner, and both are typically rather light objects. Then the decay[9]

$$K^+ \to \pi^+ + 2 \text{ light scalars}$$

would be allowed kinematically. Unfortunately it is unlikely that its branching ratio would exceed that for $K^+ \to \pi^+ \bar{\nu}\nu$ (with three families).

This tour d' horizon of Old and New Physics can lead to one conclusion only: Dedicated searches for $K^+ \to \pi^+ +$ "unseen" are a definite must for serious research!

IV. OTHER PRECIOUS RARE K DECAYS -- A FIELD DAY FOR CHIRAL PERTURBATION THEORY

There is a rich class of rare K decays that involve photons both on-and off-shell:

$$K_L, K_S \to \gamma\gamma, \gamma\gamma^* \to \ell^+\ell^- \qquad (4.1)$$

$$K \to \pi\gamma^* \to \ell^+\ell^- \qquad (4.2)$$

$$K \to \pi\gamma\gamma \qquad (4.3)$$

[$K \to \pi\gamma$ is forbidden by gauge invariance (or alternatively, by angular momentum conservation).]

Unfortunately there exists a certain complication that we have to address at this juncture - a complication that is sometimes referred to as the "Problem of the Two Worlds."

(i) On the one hand there is the world in which theorists work; it is characterized by distances $d \leq 10^{-15}$ cm; it is populated by quarks and gluons (and... and ...) and it is this world where theorists indulge themselves in building models and computing transition rates .

(ii) On the other hand there is the "Real World" where everybody else works and everybody (theorists included) lives; it is characterized by much larger distances $d \geq 10^{-13}$ cm and is inhabited by hadrons: pions, ρ mesons, protons etc. It is in this world that detectors are built and transition rates measured.

Obviously one has to establish communication between these two worlds which allows to translate results that have been obtained in the Theorists' World into those that are testable in the Real World and vice versa. This task is, we all believe, performed by QCD - in principle. In practice however we have so far fallen short of realizing this noble goal in a comprehensive way.

To cite but one (relevant) example. The decay $K_L \to \gamma\gamma$ is viewed to proceed via the diagram in Fig. 6a (and related ones) in the Theorists' World, whereas it is represented by Fig.6b in the Real World.

A. Fundamentals

Fortunately there are some favourable circumstances that can come to our rescue

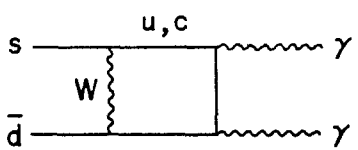

Fig. 6a

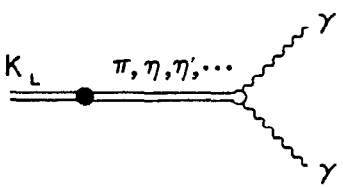

Fig. 6b

Fig. 6: The decay $K_L \to \gamma\gamma$ viewed in the Theorist's World (6a) and in the Real World (6b).

if properly exploited:

- the only hadrons that appear in K decays are pions and kaons; they double as $\bar{q}q$ bound states and as chiral Goldstone bosons, i.e., bosons that emerge due to the spontaneous realization of the chiral (and global) $SU(3)_{FL}$ group:

$$SU(3)_L \otimes SU(3)_R \to SU(3)_{L+R} + \pi\text{'s, K's, } \eta_8 \tag{4.4}$$

- the masses and momenta that appear are "soft":

$$|p|^2 \leq m_K^2 << (\text{"normal hadronic scale"} \sim 1\ \text{GeV})^2 \tag{4.5}$$

This vague statement will be made more precise later on.

Chiral perturbation theory (hereafter referred to as ChPT) describes the theoretical framework that exploits these two facts: it starts from the fundamental dogma already mentioned, namely that (approximate) chiral symmetry is realized spontaneously in nature. This dogma consists actually of two parts:

(i) For massless u, d and s quarks, i.e.

$$m_u = m_d = m_s = 0 \tag{4.6}$$

there are eight massless Goldstone bosons

$$\begin{matrix} \pi^{\pm}, \pi^{\circ} \\ K^{\pm}, K^{\circ}, \overline{K}^{\circ} \\ \eta \end{matrix} \tag{4.7}$$

and one mass scale

$$4\pi\ \bar{f}_\pi \simeq 1.2\ \text{GeV} \tag{4.8}$$

where

$$\bar{f}_\pi = \frac{f_\pi}{\sqrt{2}} \simeq 93.3\ \text{MeV} \tag{4.9}$$

denotes the pion decay constant. The Goldstone nature of these mesons puts severe constraints on how they couple to each other and to electromagnetic and weak currents.

(ii) When u, d and s quarks obtain non-vanishing masses, chiral symmetry is broken

explicitly and the eight pseudoscalar mesons cease to be massless .
Yet

$$m_u^2,\ m_d^2 << m_s^2 << (4\pi\,\bar{f}_\pi)^2$$
$$m_\pi^2 << m_K^2 << (4\pi\,\bar{f}_\pi)^2 \qquad (4.10)$$

still holds; thus the real world where pions and kaons do have a mass is not expected to be so different form one where they are massless. More specifically, the real world can be described as a perturbation around a world where chiral invariance is realized spontaneously. The small quantity which serves as an expansion parameter in this treatment is given by

$$\left(\frac{m_q}{4\pi\,\bar{f}_\pi}\right)^2,\ \left(\frac{m_a}{4\pi\,\bar{f}_\pi}\right)^2 << 1 \qquad (4.11)$$

(where q = u, d, s; a = π, K, η).

ChPT thus generates an effective Lagrangian for the strong interactions among pseudoscalar mesons

$$\mathfrak{L}_{str}^{ChPT} = \sum_{i=1}^{\infty} \tilde{c}_i\, O_i^{GB} \ . \qquad (4.12)$$

The O_i^{GB} denote operators that describe the couplings of Goldstone bosons; $\tilde{c}_i$ are numerical coefficients that contain the small expansion parameters given in (4.11)

$$\tilde{c}_i = \left(\frac{p^2}{(4\pi\,\bar{f}_\pi)^2}\right)^i c_i \qquad (4.13)$$

where $\sqrt{p^2}$ denotes quark masses, meson masses or the momenta carried by the mesons; in K decays we have for on-shell fields $p^2 \le m_K^2$.

It is instructive to compare the expression (4.12) with the one that is usually written down to describe the effective weak interactions of u, d and s quarks:

$$\mathfrak{L}_{eff}\ (\Delta S = 1) \propto \sum_{i=1}^{6} c_i^{(H)} O_i^{(u,d,s)} \qquad (4.14)$$

with the six operators $O_i^{(u,d,s)}$ expressed as a product of two currents.[10]

There are structural similarities between (4.12) and (4.14):

- The operators $O_i^{(u,d,s)}$ are expressed solely in terms of the u, d and s quarks, i.e., the light fields. The operators O_i^{GB} also contain only the light fields, namely the Goldstone bosons π, K and η.
- The coefficients $c_i^{(H)}$ represent the effects due to the existence of the heavy fields - the c, b and t quarks and the W bosons - that have been "integrated out" and do not appear explicitly in the low-energy Lagrangian. Similarly the heavy fields - the ρ and A_1 mesons etc. - do not appear explicitly in (4.12); however they determine the magnitude of the coefficients c_i in (4.12, 13).

Yet there are essential differences as well between the expressions (4.12) and (4.14):

- There is a finite number of operators appearing in (4.14), namely six, and their coefficients $c_i^{(H)}$ are calculable through an analysis of renormalization group equations, at least at sufficiently high momentum scales. In (4.12) on the other hand an infinite string of operators O_i^{GB} appears; furthermore the coefficients c_i are, as a matter of principle, completely undetermined by ChPT.

These findings should not come as a surprise: for the chiral Lagrangian describes a non-renormalizable interaction as is explained in more detail in Appendix B. Quantum corrections do therefore force upon us new effective operators at each loop level and their coefficients are undetermined as a matter of principle. These coefficients will in general be scale dependent since the higher loop contributions will typically contain divergent momentum integrals.

Details can be found in the literature.[11] What we should keep in mind for our subsequent discussion is the following:

(i) ChPT is more than just another cute model; it is not based on any assumption concerning the smallness of the strong coupling α_s -- instead ChPT is QCD at (sufficiently) low energies!

(ii) Not surprisingly, a certain price has to be paid up-front for this panacea: when we go to higher orders in the expansion parameter $\frac{p^2}{(4\pi\bar{f}_\pi)^2}$ we are forced to include new operators with undetermined coefficients c_i (though with a well-defined chiral structure). Their values can either be extracted from one set of data and then applied to another; or one can attempt to estimate their magnitude by employing

additional theoretical technologies: phenomenological models like ρ exchange dominance, 1/N expansions, QCD sum rules and - blessed be the day! - lattice QCD.

This leads typically to a very involved and lengthy analysis and it costs us in predictive power, but there is nothing ad-hoc about it! And there is still lots of predictive power left as can be studied in the literature.

Here we concentrate on the radiative K decays listed in (4.1 - 4.3) where strong, electromagnetic and weak forces are intertwined

$$\mathfrak{L}_{eff}^{ChPT}\ (\Delta S = 1) = \mathfrak{L}_{str}^{ChPt} + \mathfrak{L}_{em}^{ChPT} + \mathfrak{L}_{weak}^{ChPT} \qquad (4.15)$$

The reader that is interested in results rather than how to obtain them can skip the next section and go to section C.

B. Construction of the effective Lagrangian

(a) $\mathfrak{L}_{str}^{ChPT}$

The strong Lagrangian can be expressed by three terms:

$$\mathfrak{L}_{eff}^{ChPT} = \frac{\bar{f}_\pi^2}{4}\ tr\,(\partial_\mu \underline{U} \partial_\mu \underline{U}^+) + v\ tr\,(\underline{M}\,\underline{U} + \underline{U}^+ \underline{M}) + \text{+ higher order terms} \qquad (4.16)$$

with

$$\underline{U} = \exp\left(\frac{i\sqrt{2}}{\bar{f}_\pi}\,\underline{\Phi}\right) \qquad (4.17)$$

where the matrix $\underline{\Phi}$ contains the eight Goldstone boson fields

$$\underline{\Phi} = \begin{pmatrix} \frac{\pi^\circ}{\sqrt{12}} + \frac{\eta}{\sqrt{6}} & \pi^+ & K^+ \\ \pi^- & -\frac{\pi^\circ}{\sqrt{2}} + \frac{\eta}{\sqrt{6}} & K^\circ \\ K^- & \overline{K}^\circ & -\frac{2\eta}{\sqrt{6}} \end{pmatrix} \qquad (4.18)$$

and $\underline{M}$ denotes the quark mass matrix

$$\underline{M} = \begin{pmatrix} m_u & & 0 \\ & m_d & \\ 0 & & m_s \end{pmatrix} \qquad (4.19)$$

The meaning of the first term in (4.16) becomes clearer when one expands (4.17) in the pion fields

$$\frac{\bar{f}_\pi^2}{4}\ tr\,(\partial_\mu \underline{U} \partial_\mu \underline{U}^+) \propto \partial_\mu \pi\, \partial_\mu \pi + \frac{1}{\bar{f}_\pi^2}\,\partial_\mu \pi^2\, \partial_\mu \pi^2 + \ldots \qquad (4.20)$$

i.e., it contains the kinetic terms for massless meson fields and their (derivative) interactions.

The second term which contains the quark mass matrix represents the explicit breaking of chiral invariance that yields non-vanishing meson masses

$$v = \frac{\bar{f}_\pi^2 M_{\pi^+}^2}{2\,(m_u + m_d)} = \frac{\bar{f}_\pi^2 M_{K^+}^2}{2\,(m_u + m_s)} = \frac{\bar{f}_\pi^2 M_{K^\circ}^2}{2\,(m_d + m_s)} \qquad (4.21)$$

Finally the last term in (4.16) is produced by loop corrections that generate couplings of the meson fields that contain four, six etc. derivatives (or momenta) each of which is scaled by $\bar{f}_\pi$.

(b) $\mathfrak{L}_{em}^{ChPT}$

(i) As usual the electromagnetic couplings are obtained by replacing the normal derivatives with covariant ones:

$$\partial_\mu \underline{U} \rightarrow D_\mu \underline{U} \equiv \partial_\mu \underline{U} - i\,e\,A_\mu\,[\underline{Q}\,,\,\underline{U}\,] \qquad (4.22)$$

where A_μ denotes the electromagnetic field and $\underline{Q}$ the quark charge matrix

$$Q = \begin{pmatrix} \frac{2}{3} & & 0 \\ & -\frac{1}{3} & \\ 0 & & -\frac{1}{3} \end{pmatrix} \qquad (4.23)$$

There are now additional higher order terms, two of which are of relevance for radiative K decays[12]

$$\mathfrak{L}^{(4)}_{em} = -i e L_9 F_{\mu\nu} \mathrm{tr}\,(Q D_\mu U D_\nu U^+ + Q D_\mu U^+ D_\nu U) + e^2 L_{10} F_{\mu\nu} F_{\mu\nu} \mathrm{tr}\,(U Q U^+ Q) \qquad (4.24)$$

$$F_{\mu\nu} = \partial_\mu A_\nu - \partial_\nu A_\mu$$

The two quantities L_9, L_{10} are undetermined parameters of the type discussed before.

(ii) With the couplings written down so far

$$\pi^\circ, \eta \rightarrow \gamma\gamma$$

cannot proceed; to implement it one has to include the Wess-Zumino-Witten term

$$\mathfrak{L}_{WZW} = \frac{\alpha}{8\pi \tilde{f}_\pi} \varepsilon_{\mu\nu\rho\sigma} F_{\mu\nu} F_{\rho\sigma} (\pi^\circ + \frac{1}{\sqrt{3}} \eta) \qquad (4.25)$$

(c) An intermediate resume

$\mathfrak{L}^{ChPT}_{STR} + \mathfrak{L}^{ChPT}_{em}$ describes the strong and electromagnetic interactions of π's, K's and η's

- to <u>all</u> orders in the strong coupling
- for "<u>soft</u>" momenta $|p| < 1$ GeV
- in terms of a priori <u>undetermined</u> parameters:

$\tilde{f}_\pi$, L_9, L_{10} ...

It has yielded a successful phenomenology with two possible exceptions, namely an underestimate of $\Gamma(\eta \rightarrow \pi^+ \pi^- \pi^\circ)$ and $\Gamma(\eta \rightarrow \pi^\circ \gamma\gamma)$. One can actually give some rather natural arguments why terms that are of higher order in ChPT are nevertheless of great numerical importance in those <u>particular</u> cases.[13]

Otherwise if those discrepancies turned into failures or new ones emerged one would face a very awkward situation: keeping in mind that ChPT is QCD at low energies one would have to adapt a dictum by B. Brecht: "I suggest", says Mr. K., "that QCD dissolves Nature and elects a new one."

(d) $\mathfrak{L}^{ChPT}_{weak}$

Ecker, Pich and de Rafael (hereafter referred to as EPR) using the pioneering work of Donaghue *et al.*[16] have shown in a beautiful series of papers [14] how to implement the weak interactions in a chiral Lagrangian. One starts from the same quark level Lagrangian that was already discussed:

$$\mathfrak{L}^{(q)}(\Delta S = 1) = \frac{G_F}{\sqrt{2}} V(ud) V^*(us) \sum_{i=1}^{6} c_i^{(H)} O_i^{(u,d,s)} + \text{h.c.}$$

The operators $O_i^{(u,d,s)}$ which are products of two currents can belong to an <u>8</u> or a <u>27</u> of $SU(3)_{FL}$. According to the $\Delta I = 1/2$ rule the <u>8</u> piece is by far the dominant one. In the following we will mostly ignore the <u>27</u>-plet. It is this algebraic structure that one has to mimick in ChPT:

$$\mathfrak{L}^{ChPT}_{weak}(\Delta S = 1) = G_8 (\underline{L}_\mu \underline{L}_\mu)_{23} + \text{h.c.} + \text{non-octet terms} + \text{higher orders} \qquad (4.26)$$

$$G_8 = \frac{G_F}{\sqrt{2}} V(ud) V^*(us) g_8 \qquad (4.27)$$

where $\underline{L}_\mu$ denotes the matrix that represents the Noether current for the V-A chiral rotation:

$$\underline{L}_\mu = i\tilde{f}_\pi^2 \underline{U} \partial_\mu \underline{U}^+ \qquad (4.28)$$

The appropriate numerical size of the parameter g_8 is obtained from the observed width for $K_S \rightarrow \pi\pi$:

$$|g_8| \simeq 5.1 \qquad (4.29)$$

For radiative K decays we still need electromagnetic corrections to these weak

couplings; as before they are implemented by introducing covariant derivatives, see (4.22). They also induce terms of higher order in ChPT:

$$\mathcal{L}^{(4)}(\Delta S = 1, \text{em}) = -\frac{ie\,G_8}{2\bar{f}_\pi^2} F_{\mu\nu} \{ w_1\, tr(Q\,\lambda_{6-i7}\tilde{L}_\mu\tilde{L}_\nu) + $$

$$+ w_2\, tr(Q\,\tilde{L}_\mu\,\lambda_{6-i7}\tilde{L}_\nu) + w_3\,\varepsilon_{\mu\nu\rho\sigma}\, tr(Q\,\tilde{L}_\rho)\, tr(\lambda_{6-i7}\tilde{L}_\sigma) \} \quad (4.30)$$

$$+ \text{h.c.}$$

$$\mathcal{L}^{(4)}(\Delta S = 1, (\text{em})^2) = \frac{e^2\bar{f}_\pi^2 G_8}{2}\, w_4\, F_{\mu\nu}F_{\mu\nu}\, tr(\lambda_{6-i7}\,Q\,U\,Q\,U^+) + \text{h.c.} \quad (4.31)$$

where

$$\tilde{L}_\mu = i\bar{f}_\pi^2\, U\, D_\mu\, U^+$$

and λ_{6-i7} denote the appropriate Gell-Mann matrices acting in $SU(3)_{FL}$ space; w_1, w_2, w_3 and w_4 are new a priori unspecified parameters.

(e) Summary on the theoretical tools

ChPT describes the strong and electroweak interactions of pseudoscalar mesons by an effective Lagrangian that contains Goldstone boson fields GB, their (covariant) derivatives, electroweak currents and c number coefficients:

$$\mathcal{L}_{\text{eff}} = \mathcal{L}^{\text{ChPT}}(\text{GB}, D_\mu\,\text{GB}, j_\mu^{(\text{em})+(\text{weak})}, \text{coeff.}) \quad (4.32)$$

It describes the dynamics to all orders in the strong coupling and to the appropriate perturbative order in the electro-weak couplings.

Feynman diagrams can be written down which contain as building blocks

- propagators of Goldstone bosons
- vertices that describe their couplings among themselves
- vertices that in addition contain couplings to electro-weak currents.

The expansion parameter is given by

$$\frac{p^2}{(4\pi\,\bar{f}_\pi)^2} \sim \frac{p^2}{(1.3\,\text{GeV})^2} \quad (4.33)$$

making ChPT applicable if only soft momenta are present.

There is a price to be paid for including the strong interactions to all orders in their coupling strength: a priori undetermined parameters are introduced as the coefficients of the chiral operators. There are three such parameters to the quadratic order in ChPT

$$\mathcal{L}^{(2)}: \bar{f}_\pi, g_8 [, g_{27}] \quad (4.34)$$

and six additional ones to the quartic order:

$$\mathcal{L}^{(4)}: L_9, L_{10};\ w_1, w_2, w_3, w_4 \quad (4.35)$$

These parameters can be momentum scale dependent, i.e.,

$$w_i = w_i\,(q^2/\Lambda^2) \quad (4.36)$$

and this happens when the loop integrals that are generated by quantum corrections diverge.

The numerical value of these parameters can be inferred from data: e.g., $\bar{f}_\pi$ from $\pi \to \ell\nu$ and g_8 from $K_S \to \pi\pi$. This, by the way, does not mean that we have finally understood the dynamical origin of $\Delta I = 1/2$ rule and its range of validity. However once the $\Delta I = 1/2$ rule has been postulated in one reaction, then ChPT allows us to implement it in a theoretically consistent way and apply it to other processes.

C. Applications

There are two simple, yet important theorems that apply to radiative K decays:

Theorem I

$$\text{Ampl}(K \to \pi\gamma) = 0 \quad (4.37)$$

The conflicting requirements of gauge invariance and conservation of orbital angular momentum enforce the vanishing of this amplitude.

Theorem II

$$\text{Ampl}(K \to (\pi) + \gamma\text{'s} + \ell\text{'s}) = \mathcal{O}\left(\frac{p^4}{(4\pi\bar{f}_\pi)^4}\right) \quad (4.38)$$

where the final state contains any number of photons and charged lepton pairs and at most one pion. It is again the conflict between two requirements, this time between those of gauge invariance and chiral invariance, that leads to a vanishing amplitude to second, i.e., lowest order in ChPT.

There is a two-fold motivation for studying these decays in a dedicated fashion:

(i) They provide stringent tests of our understanding of chiral invariance - a concept

that is deeply rooted in QCD (remember "B. Brecht").

(ii) Direct CP violation represents itself as a minute (though highly important) phenomenon in $K_L \to \pi\pi$ decays. This is partly due to the dominance of the $\Delta I = 1/2$ over the $\Delta I = 3/2$ amplitude in these non-leptonic decays. In radiative K decays on the other hand one finds, as stated above in Theorem II that the large $\Delta I = 1/2$ enhancement is at least partly off-set by the chiral suppression $\sim p^2 / (4\pi \bar{f}_\pi)^2$. This can make $\Delta I = 3/2$ and 5/2 amplitudes more significant thus allowing direct CP violation to manifest itself in a less suppressed manner.

(a) $K^\circ, \bar{K}^\circ \to \gamma\gamma$

CP invariance is assumed for this discussion. The mass eigenstates K_S and K_L have - in this approximation - to be identified with even and odd CP eigenstates respectively.

Fig. 7a (7b) contains the diagrams of lowest order in ChPT that generate $K_S \to \gamma\gamma$ ($K_L \to \gamma\gamma$). They are not shown to establish bragging rights, but to illustrate two points of general interest for the serious student of ChPT:

- some vertices have a decidedly hedgehog-like appearance which will actually intensify in higher orders. This should not surprise us - after all ChPT is produced from a non-renormalizable dynamical description.
- The reactions $K_S \to \gamma\gamma$ and $K_L \to \gamma\gamma$ that look so (deceptively) similar on the quark level are described by very different diagrams in ChPT.

The diagrams of Fig. 7a yield

$$BR(K_S \to \gamma\gamma) \simeq 2.0 \times 10^{-6} \left| \frac{g_8}{5.1} \right|^2 \qquad (4.39)$$

where we have calibrated g_8 according to (4.29). There exists a preliminary experimental number from NA 32 on it

$$BR(K_S \to \gamma\gamma) = (2.4 \pm 1.2) \times 10^{-6} \qquad (4.40)$$

which agrees with this prediction although the statistical significance is not overwhelming.

So far no reliable number on $BR(K_L \to \gamma\gamma)$ has been derived within ChPT. For

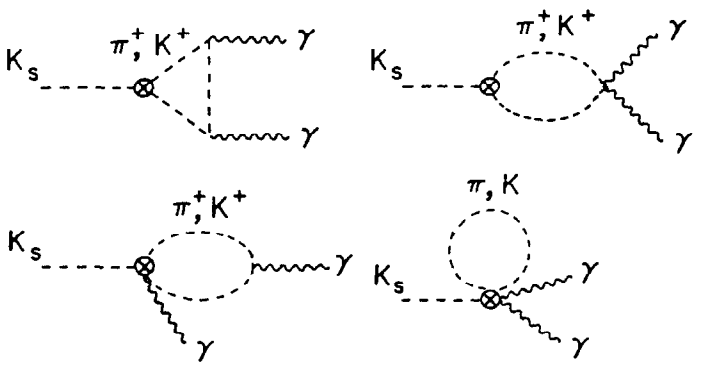

Fig. 7a: Diagrams of lowest non-trivial order in ChPT for $K_S \to \gamma\gamma$.

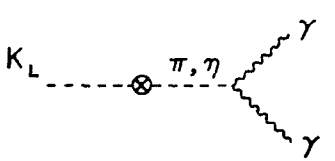

Fig. 7b: Same as Fig. 7a, but for $K_L \to \gamma\gamma$.

- The theoretical predictions on $\Gamma(K_S \to \gamma \mu^+\mu^-)$ differ by 10% to at most 20%. The experimental sensitivity level therefore has to reach the few percent level before the different predictions can be distinguished.

The ratio $\Gamma(K_L \to \gamma \ell^+\ell^-)/\Gamma(K_L \to \gamma\gamma)$ is not sensitive to $SU(3)_{FL}$ breaking and can thus be predicted:

$$\frac{\Gamma(K_L \to \gamma \ell^+ \ell^-)}{\Gamma(K_L \to \gamma\gamma)} \simeq \begin{cases} 1.59 \times 10^{-2} & \text{for } \ell = e \\ 4.09 \times 10^{-4} & \ell = \mu \end{cases} \qquad (4.41)$$

The spectrum $\frac{1}{\Gamma}\frac{d}{dz}\Gamma(K_S \to \gamma\mu^+\mu^-)$ with $z = m^2(\mu^+\mu^-)/M_K^2$ is predicted to peak just above z=0.2 and to drop off rapidly for larger z both in ChPT and in a phase space description. Yet in ChPT the peak is even more pronounced and the drop-off is even steeper than in the phase space ansatz. These differences occur roughly on the 20% level. Details can be found in Ref. 14.

(c) $K^\circ, \bar{K}^\circ \to \pi^\circ\gamma\gamma$

ChPT allows to relate $K_L \to \pi^\circ\gamma\gamma$ to $K_S \to \gamma\gamma$ independently of the value of g_8:

$$\frac{\Gamma(K_L \to \pi^\circ\gamma\gamma)}{\Gamma(K_S \to \gamma\gamma)} = 5.9 \times 10^{-4} \qquad (4.42)$$

which translate into [see (4.39)]:

$$BR(K_L \to \pi^\circ\gamma\gamma) \simeq 6.9 \times 10^{-7} \left|\frac{g_8}{5.1}\right|^2 \qquad (4.43)$$

In describing $K_S \to \pi^\circ\gamma\gamma$ one introduces a cut-off in $m(\gamma\gamma)$ to avoid the physical π° pole since here one is not interested in studying $K_L \to \pi^\circ\pi^\circ$, $\pi^\circ \to \gamma\gamma$ where both pions are on-shell. One then finds

$$BR(K_S \to \pi^\circ\gamma\gamma)\Big|_{z \geq 0.2} = 4 \times 10^{-8} \qquad (4.44)$$

with $z = m^2(\gamma\gamma)/M_K^2$.

Again ChPT leads to a different distribution in z than, say, a phase space ansatz. As shown in Fig. 8 this difference is really striking for $\frac{d}{dz}\Gamma(K_L \to \pi^\circ\gamma\gamma)$: chiral symmetry produces a dramatic suppression at low values of z.

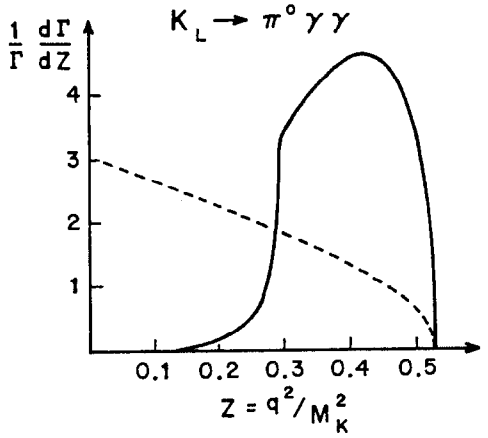

Fig. 8: The di-photon mass distribution in $K_L \to \pi^\circ\gamma\gamma$, both for ChPT (solid line) and a pure phase space ansatz (broken line); from Ref. 14.

(d) $K^{\pm} \to \pi^{\pm} \gamma\gamma$

The transition rates for the decays considered so far depended on g_8 and $\tilde{f}_\pi$, but on no other hadronic coupling parameters. This is not true for $K^{\pm} \to \pi^{\pm} \gamma\gamma$: higher order terms $\mathfrak{L}^{(4)}$ that are produced by quantum corrections contribute here; they actually enter via the following combination of their coefficients

$$\hat{c} = 32\pi^2 \left[4 (L_9 + L_{10}) - \frac{1}{3} (w_1 + 2w_2 + 2w_4) \right]. \qquad (4.45)$$

The parameters $L_9 + L_{10}$ can be extracted from the observed width of $\pi \to e \nu \gamma$; no such reliable information has so far been obtained on the parameters w_1, w_2 and w_4. However we can state a lower limit

$$BR (K^+ \to \pi^+ \gamma\gamma) \geq 4 \times 10^{-7} \qquad (4.46)$$

and a "most likely" value

$$BR (K^+ \to \pi^+ \gamma\gamma) \sim 10^{-6} \qquad (4.47)$$

since a QCD treatment suggests $\hat{c} \simeq \mathcal{O}(1)$.

(e) $K^{\pm} \to \pi^{\pm} \ell^+\ell^-$

At last there exists a measurement of one of these decay modes:

$$\frac{\Gamma (K^+ \to \pi^+ e^+ e^-)}{\Gamma (K^+ \to \pi^0 e^+ \nu)} = (5.6 \pm 1.1) \times 10^{-6} \qquad (4.48)$$

The ratio in (4.48) appears surprisingly tiny since naively one might give a different guestimate:

$$\frac{\Gamma (K^+ \to \pi^+ e^+ e^-)}{\Gamma (K^+ \to \pi^0 e^+ \nu)} \sim \mathcal{O}(e^4) \sim \text{few} \times 10^{-3}. \qquad (4.49)$$

Of course one can do better than this overly naive ansatz: one can describe $K^+ \to \pi^+ e^+ e^-$ as an electromagnetic correction to the non-leptonic (pole) transition $K \to \pi$ with its non-leptonic enhancement factor g_{NL}:

$$\frac{\Gamma (K^+ \to \pi^+ e^+ e^-)}{\Gamma (K^+ \to \pi^0 e^+ \nu)} \sim \left(\frac{e^2 \tilde{f}_\pi^2 \, g_{NL}}{m_K^2} \right)^2 \sim 10^{-5} \, g_{NL}^2 \qquad (4.50)$$

which overshoots the observed ratio (4.48) even in the absence of a non-leptonic enhancement.

Yet what we have ignored so far is Theorem II, (4.38), which states that we have to go to the quartic order in ChPT. Accordingly, one estimates roughly

$$\frac{\Gamma (K^+ \to \pi^+ e^+ e^-)}{\Gamma (K^+ \to \pi^0 e^+ \nu)} \sim \left(\frac{e^2 \tilde{f}_\pi^2 \, g_{NL}}{m_K^2} \right)^2 \left(\frac{m_K^2}{(4\pi \tilde{f}_\pi)^2} \right)^2 \sim 3 \times 10^{-7} \, g_{NL}^2 \qquad (4.51)$$

That shows that even the tiny ratio (4.48) allows for a sizeable non-leptonic enhancement in $K^+ \to \pi^+ \ell^+\ell^-$ if one takes into account the chiral suppression expressed in (4.38).

To turn this qualitative "success" of ChPT into a quantitative one is, however, quite a different matter: for the counter terms that are produced by the 1-loop quantum corrections contribute to $K^+ \to \pi^+ \ell^+ \ell^-$. Their impact is represented by the coefficients L_9, L_{10}, w_1, w_2, w_3, w_4; since the one-loop integrations now yield divergent results one has to deal with the scale dependent part of these coefficients. This represents an additional complication relative to the case of $K^+ \to \pi^+\gamma\gamma$ where only the scale independent part of these coefficients entered. EPR chose the following procedure to deal with this complication:

- fix, within reason, the parameters such that the absolute width $\Gamma (K^+ \to \pi^+ e^+ e^-)$ is reproduced.
- Then predict $\Gamma (K^+ \to \pi^+ \mu^+ \mu^-)$ and the distributions $\frac{1}{\Gamma} \frac{d}{dz} \Gamma (K^+ \to \pi^+ \ell^+ \ell^+)$, $z = m^2 (\ell^+ \ell^-) / M_K^2$.

This program can be fulfilled up to a two-fold ambiguity; for details consult Ref. 14.

(f) $K^\circ, \bar{K}^\circ \to \pi^\circ \ell^+ \ell^-$

The discussion of $K_S \to \pi^\circ \ell^+\ell^-$ proceeds in complete analogy to $K^{\pm} \to \pi^{\pm} \ell^+\ell^-$. A completely new element - and one of fundamental importance - however enters when one analyzes

$$K_L \to \pi^\circ \ell^+\ell^- \qquad (4.52)$$

For the final state in

$$K_L \to \pi^\circ \gamma^* \\ \qquad\quad \hookrightarrow \ell^+ \ell^- \qquad (4.53)$$

represents an <u>even</u> eigenstate of CP

$$CP\left[(\pi^\circ \gamma^*)_{\ell=1} \right] = CP[\pi^\circ]\, CP[\gamma^*]\, (-1)^{\ell} = (-1)(+1)(-1) = +1 \qquad (4.54)$$

Yet the initial K_L is CP odd in the (almost realized) limit of CP invariance; since therefore

$$CP[\text{initial}] \neq CP[\text{final}] \qquad (4.55)$$

one realizes that the reaction (4.53) can proceed only via a violation of CP invariance! Accordingly one obtains as an order of magnitude estimate

$$BR(K_L \to \pi^\circ \gamma^* \to \pi^\circ e^+ e^-) \sim |\varepsilon_K|^2\, BR(K^+ \to \pi^+ e^+ e^-) \sim 10^{-12} - 10^{-11} \qquad (4.56)$$

Yet before an observation of $K_L \to \pi^\circ \ell^+\ell^-$ can be listed as another manifestation of CP violation in K_L decays one has to guard against two other possibilities:

(α) The $\ell^+\ell^-$ pair is produced not from a (virtual) photon, like in (4.53); instead it comes from a Higgs scalar (that can be on-shell or off-shell for that matter). The observation of $K_L \to \pi^\circ \ell^+\ell^-$ --- with presumably $BR(K_L \to \pi^\circ \mu^+\mu^-) >> BR(K_L \to \pi^\circ e^+e^-)$ --- would in this scenario not represent a CP violation, but instead the presence of New Physics. This would obviously constitute a highly desirable interpretation.

(β) Unfortunately there exists a much more mundane process leading to $K_L \to \pi^\circ \ell^+\ell^-$, namely

$$K_L \to \pi^\circ \gamma^* \gamma^* \qquad \hookrightarrow \ell^+\ell^- \qquad (4.57)$$

i.e., a process of higher order in QED, yet without CP violation.

There is no simple way to estimate the relative weight between the two reactions, namely the CP violating one-photon processes (4.53) and the CP conserving two-photon process (4.57) since they are characterized by parameters of comparable size:

$$|\varepsilon_K|^2 \sim \mathcal{O}\left(\left(\frac{\alpha}{2\pi}\right)^2\right) \qquad (4.58)$$

A more detailed dynamical treatment is therefore called for. Sehgal has applied an analysis that is based on vector meson dominance and found [15]

$$\left| A(K_L \to \pi^\circ \gamma^* \to \pi^\circ \ell^+\ell^-) \right| \sim \left| A(K_L \to \pi^\circ \gamma^* \gamma^* \to \pi^\circ \ell^+\ell^-) \right| \qquad (4.59)$$

The ChPT loyalists of EPR and previously the authors of Ref.16 as well have arrived at quite different conclusions:

- $K_L \to \pi^\circ e^+e^-$ is dominated by the CP violating one-photon process

$$BR(K_L \to \pi^\circ \gamma^* \gamma^* \to \pi^\circ e^+e^-) \sim \mathcal{O}(10^{-14}) \qquad (4.61)$$

$$BR(K_L \to \pi^\circ \gamma^* \to \pi^\circ e^+e^-) \simeq \begin{cases} 1.5 \times 10^{-12} \\ 1.5 \times 10^{-11} \end{cases} \qquad (4.62)$$

where the two values listed in (4.62) reflect the two-fold ambiguity in the size of the higher order parameters w_i that was mentioned in our discussion of $K^+ \to \pi^+\ell^+\ell^-$. No direct CP violation has actually been included in obtaining (4.62).

- Acordingly very little manifest CP violation is expected in the lepton distributions etc.
- The two-photon contribution to $K_L \to \pi^\circ \mu^+\mu^-$ is not suppressed leading to a relatively sizeable branching ratio

$$BR(K_L \to \pi^\circ \mu^+\mu^-) \sim \frac{1}{5} BR(K_L \to \pi^\circ e^+e^-) \qquad (4.63)$$

- CP violation can then manifest itself in a transverse polarizationof the muons in $K_L \to \pi^\circ \mu^+\mu^-$. Rough estimates for the degree of transverse polarization yield

$$Pol_\perp(\mu) \sim 0.05 - 0.5 \qquad (4.64)$$

I want to address the conflict between (4.59) and (4.61) with the following two preconceived notions:

(i) ChPT when applied carefully and properly cannot be wrong.

(ii) It is highly unlikely that this conflict is due to algebraic mistakes.

EPR have examined the most general effective chiral Lagrangian where vector and axial vector fields appear explicitly. (In the usual approach these fields are integrated out and enter only indirectly via the coefficients of the Goldstone boson operators). They find that the vector coupling employed in Ref. 15 cannot appear directly due to the constraints imposed by chiral invariance. Although they can be induced indirectly by higher order contributions their coefficients in ChPT are so tiny as to render them totally insignificant. To say it differently: it would constitute an extremely heavy blow to ChPT if the dynamical description of Ref.15 were borne out by experiment!

Let me add two more notes on CP violation in radiative K decays before

concluding this section:

- $$\frac{\Gamma(K^+ \to \pi^+ e^+ e^-) - \Gamma(K^- \to \pi^- e^+ e^-)}{\Gamma(K^+ \to \pi^+ e^+ e^-) + \Gamma(K^- \to \pi^- e^+ e^-)} \sim 10^{-5} \qquad (4.65)$$

a depressing result and

- $$\frac{\Gamma(K^+ \to \pi^+ \gamma\gamma) - \Gamma(K^- \to \pi^- \gamma\gamma)}{\Gamma(K^+ \to \pi^+ \gamma\gamma) + \Gamma(K^- \to \pi^- \gamma\gamma)} \lesssim 10^{-3} \qquad (4.66)$$

which does not appear to be beyond our experimental capabilities.

Interlude: Resume on Rare K Decays

(1) A study of radiative K decays will teach us significant and quite important lessons on QCD; in particular it will provide us with crucial tests of our understanding of chiral symmetry and its breaking.

(2) A well developed theoretical technology has emerged that provides us with a quantitative treatment of these K decays: Chiral Perturbation Theory.

(3) As always there is a prize to be paid: ChPT introduces - as a matter of principle - a priori unspecified parameters: g_8, g_{27}, L_9, L_{10}, w_1, ... w_4. Yet ChPT produces many highly non-trivial relations between different transition rates: Therefore one has to measure many decay rates and distributions to fully exploit the opportunities that are offered by K decays. This makes a K factory a highly desirable undertaking.

Item (1) - (3) concerned our understanding of QCD. Yet also our understanding of the weak forces and of New Physics can be extended by further experimentation in this field.

(4) A dedicated search for
$$K^+ \to \pi^+ + \text{"unseen"}$$
is an unequivocal must - as stated before.

(5) Helicity suppression etc. presumably do not affect $K \to e\mu$, $\pi e\mu$ in a crucial way.

(6) CP violation:
It has been stated with increasing vigour (though not necessarily rigour as well) that dedicated searches for CP violation in B decays present an almost irresistible temptation, at least for a theorist:

- The theoretical prediction that can be made there are typically more reliable than for K decays;
- Finding them or not finding them has very obvious implications for or against the KM implementation of CP violation;
- A very rich structure exists in their phenomenology.

I subscribe quite strongly to these statements. Nevertheless I would consider it quite foolish to suspend further searches for CP violation in K decays:

- After all, nobody has really demonstrated yet that sufficient experimental sensitivity can be acquired in B decay studies.
- It should not be forgotten that theoretical predictions could be contradicted by the experimental findings. If that happened as far as CP violation in B decays is concerned we would have made progress in a negative way: we would have learnt that the KM ansatz does not represent the leading source of the observed CP violation in K_L decays. Yet we would not know which force it is that generates this fundamentally important phenomenon.

Dedicated searches for CP asymmetries in K decays and in B decays should therefore not be viewed as competitors, but as complementing each other.

V. "Waiting for a Miracle" -- Rare D Decays

According to the Standard Model D decays represent a decidedly dull affair: the relevant KM parameters -- V(cs) and V(cd) -- are "known" since they can be inferred from V(ud), V(us) and V(cb); at most tiny D^0-$\bar{D}^0$ mixing, no observable CP violation or other flavour changing neutral currents are expected. This apparent vice can however be turned into a twofold virtue:

(i) Our alleged understanding of the electroweak forces in the charm sector allows us to use charm decays as a unique laboratory for studying the strong forces in a novel environment.

(ii) If -- contrary to our jaded expectation -- an interesting weak phenomenon like flavour changing neutral currents were observed we would have found unequivocal evidence for "New Physics" beyond the Standard Model. Of course, it would still be ambiguous as to the precise nature of this New Physics.

In the following discussion of one-loop D decays and doubly Cabibbo suppressed decays (hereafter referred to as DCSD) I will expand on these general statements and make them more specific. But first I want to mention briefly two technical complications that arise in treatments of D decays.

(i) The one-loop $\Delta C=1,2$ operators are non-local: the internal quarks that appear in the diagrams of Figs.9 are lighter than the external charm quark

$$m_s < m_c. \qquad (5.1)$$

The strange quark can therefore not be integrated out to obtain a local effective $\Delta C=1,2$ operator. The opposite situation arises for $\Delta S=2$ etc. transitions.

(ii) There cannot be a trustworthy application of ChPT. For the hadrons that appear in these reactions, e.g.

$$D \to \rho + X \qquad (5.2)$$

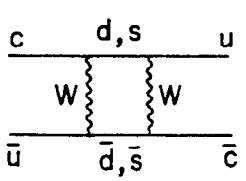

Fig.9a

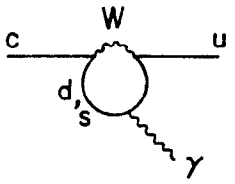

Fig.9b

Fig. 9a, b: Quark level transition operators with $\Delta C = 2$ and $\Delta C = 1$, respectively.

cannot be described as Goldstone bosons and "hard" momentum transfers appear

$$m_D^2,\ p^2 >> (4\pi \bar{f}_\pi)^2 \tag{5.3}$$

A. One-loop Decays

There are quite a few processes that come to one's mind here

$$D^\circ \to \ell^+ \ell^- \tag{5.4}$$

$$D^\circ \to \gamma\gamma \tag{5.5}$$

$$D^\circ \to \pi/\rho + \text{"nothing seen"} \tag{5.6}$$

$$D^\circ \to \gamma + \text{"nothing seen"} \tag{5.7}$$

Unfortunately, one has to expect truly tiny branching ratios for these modes since more than one suppression factor will typically intervene -- like helicity suppression in (5.4), wavefunction suppression in (5.4,5,7) and GIM suppression in all four of them. And in addition, the normal D decays are not -- unlike K decays -- Cabibbo suppressed.

A few semi-quantitative comments can be added:

(i) $D^\circ \to \gamma\gamma$

In analogy to $K_L \to \gamma\gamma$ one can describe this reaction as a two-step process

$$D^\circ \to \text{"}\pi,\ \eta,\ \pi\pi,\ K\overline{K},\ 3\pi,\text{..."} \to \gamma\gamma \tag{5.8}$$

Since the first step represents a Cabibbo suppressed non-leptonic transition and the second one a second order electromagnetic process one guestimates

$$BR(D^\circ \to \gamma\gamma) \leq \mathcal{O}\,(tg^2\theta_c\ \alpha^2) \sim 2.7 \times 10^{-6} \tag{5.9}$$

This is probably a very generous number if not even a considerable overestimate (which is why I used the "<" sign in (5.9)). For on general grounds one has to allow for -- if not even expect -- sizeable cancellations to occur between the contributions from different intermediate states in (5.8). Describing $D^\circ \to \gamma\gamma$ on the other hand by a quark diagram that is analogous to the one in Fig.6a would presumably lead to a gross underestimate of the rate.

(ii) $D \to \pi/\rho$ + "nothing seen"

Supersymmetry introduces the decay channel

$$D \to \pi/\rho + \bar{\gamma}\bar{\gamma} \tag{5.10}$$

if the photinos $\bar{\gamma}$ are sufficiently light. The relevant tree-level diagram is analogous to the one shown in Fig. 4; the corresponding amplitude is subject to GIM suppression that enters through the couplings of the internal squarks $\bar{U} = (\tilde{u}, \tilde{c}, \tilde{t})$. Unfortunately -- for the present analysis -- almost all SUSY models that are imbedded in a supergravity environment exhibit the following property for the squark mass splittings:

$$\Delta m^2\,(\tilde{u}) \sim m_s^2,\ m_b^2 \tag{5.11}$$

$$\Delta m^2\,(\tilde{D}) \sim m_c^2,\ m_t^2 \tag{5.12}$$

The GIM suppression that results from (5.11) makes considering $D \to \pi/\rho + \bar{\gamma}\bar{\gamma}$ a completely academic affair.

(iii) $D^\circ \to \gamma$ + "nothing seen"

SUSY again allows for a realization of such a mode, namely

$$D^\circ \to \gamma + \bar{\nu}\bar{\nu} \tag{5.13}$$

if the sneutrinos are sufficiently light. GIM suppression enters via the couplings of an internal $\tilde{D}$ squark where the more favourable scenario (5.12) holds. Yet even so it is hard to see how a measurable branching ratio could result.

B. Doubly Cabibbo Suppressed D Decays -- DCSD

These are necessarily non-leptonic decays. Thus one has to tackle the "Problem of the Two Worlds" as described in Sec. IV, although it appears in a less virulent form here. Starting from the observation that almost everything is of order one in the strong interactions -- the relative weight of higher order corrections, Clebsch-Gordan coefficients etc. -- two thinkers arrived quite independently at the Ma-Ik Theorem: To be off in one's predictions by an order of magnitude or more one has to be

α) quite unlucky or

β) rather dense or,

γ) most likely, both of these two requirements are fulfilled simultaneously.

The $\Delta I=1/2$ rule is the classical example for case (α); everybody will know examples of cases (β) and (γ) from his or her own experience.

One consequence of this theorem is that one cannot claim reliability for a model just because it predicted a handful of decay rates more or less correctly. For a proper evaluation one has to keep the wider theoretical and phenomenological landscape in mind.

An expansion in 1/N, N being the number of colours, provides a very compact and rather successful phenomenology of Cabibbo allowed and once Cabibbo suppressed D decays (a detailed description can be found in the literature [17]). It is quite natural then to apply it to DCSD as well.[18]

Before I do that I would like to recall to your attention the four-fold motivation for a detailed and dedicated study of DCSD:

- As is well known by now a good understanding of DCSD is relevant in searches for D°-$\bar{D}^\circ$ mixing.
- As explained below interesting lessons can be obtained on QCD.
- Such lessons are of obvious significance for attempts to extract the values of the KM parameter V(ub) from non-leptonic B decays.
- There exists a certain (though by no means large) potential for New Physics to show up. For example, New Physics could be realized by the existence of charged Higgs fields H the exchange of which leads to $c \to s(u\bar{d})$ as well as $c \to d(u\bar{s})$ transitions. In the first case the Higgs exchange produces a coupling proportional to $m_c \cdot m_d$ (or $m_c \cdot m_u/m_H^2$, in the latter one to $m_c \cdot m_s/m_H^2$. The highly forbidden DCSD can thus have a much higher sensitivity to New Physics than Cabibbo allowed D decays [19]:

$$\frac{\text{rate ("NP")/rate ("Old Physics") } [c\to d(u\bar{s})]}{\text{rate ("NP")/rate ("Old Physics") } [c\to s(u\bar{d})]} \sim \left(\frac{m_s}{m_d}\right)^2 \frac{1}{tg^4\theta_c} \sim 4 \times 10^4 \ !$$

(a) DCSD of D°:

Invoking the 1/N ansatz as rationale for including factorizable contributions only, ignoring W exchange and putting the Bauer-Stech parameter ξ to zero one finds

$$\frac{BR(D^\circ \to K^+\pi^-)}{BR(D^\circ \to K^-\pi^+)} \sim 2\, tg^4\Theta_c \qquad (5.14)$$

$$\frac{BR(D^\circ \to K^+\rho^-)}{BR(D^\circ \to K^-\rho^+)} \sim 0.5\, tg^4\,\Theta_c \qquad (5.15)$$

$$\frac{BR(D^\circ \to K^{+*}\pi^-)}{BR(D^\circ \to K^{-*}\pi^+)} \sim 3\, tg^4\,\Theta_c \qquad (5.16)$$

It is of course the Cabibbo angle θ_c that sets the overall order of magnitude for DCSD. The coefficient of $tg^4\theta_c$ which reflects hadronization effects is of order one -- in accordance with the Ma-Ik Theorem; for example the enhancement in (5.14) can be traced back largely to $|f_K/f_\pi|^2 \sim 1.6$ etc. Furthermore

$$\frac{BR(D^\circ \to K^+\pi^-,\ K^+\rho^-,\ K^{+*}\pi^-)}{BR(D^\circ \to K^-\pi^+,\ K^-\rho^+,\ K^{-*}\pi^+)} \sim 1.2 - 1.5 \qquad (5.17)$$

i.e. summing over these channels yields an amusing (semi-quantitative) realization of quark-hadron duality.

(b) DCSD of D^+

A rather intriguing scenario emerges here:

$$\frac{BR(D^+ \to K^+\pi^\circ)}{BR(D^+ \to \bar{K}^\circ\pi^+)} \sim 3\ tg^4\,\Theta_c \qquad (5.18)$$

$$\frac{BR(D^+ \to K^{\circ *}\pi^+)}{BR(D^+ \to \bar{K}^{\circ *}\pi^+)} \sim (5\text{-}11)\ tg^4\Theta_c \qquad (5.19)$$

$$\frac{BR(D^+ \to K^{+*}\pi^\circ)}{BR(D^+ \to \bar{K}^{\circ *}\pi^+)} \sim (12\text{-}25)\ tg^4\,\Theta_c \qquad (5.20)$$

$$\frac{BR(D^+ \to K^+\rho^\circ)}{BR(D^+ \to \bar{K}^\circ\rho^+)} \sim 0.35\ tg^4\Theta_c \qquad (5.21)$$

The apparently dramatic enhancement factors in (5.18-20) reflect actually the destructive interference that occurs in the Cabibbo allowed D^+ decays which in turn is the main motor for the D^+-D° lifetime difference [19]. Such a destructive interference does not occur in DCSD and their relative weight is thus enhanced. This can be seen most easily by considering the isospin of the final states rather than drawing cute diagrams.

- The final states in $D^+ \to$ (S=-1) transitions carry a unique isospin, namely $(I,I_3) = (\frac{3}{2}, +\frac{3}{2})$; these decays are therefore described by a single amplitude in isospin space, namely $(\Delta I, \Delta I_3) = (1, +1)$. Interference can thus occur.

- $D^+ \to$ (S=+1) transitions on the other hand are described by the combination of two amplitudes that differ in isospin, namely $(\Delta I, \Delta I_3) = (0, 0)$ and $(1, 0)$. This curtails the possibility of interference.

The coefficient in (5.18) can then be understood as basically due to

$$\left(\frac{f_K}{f_\pi}\right)^2\left(\frac{c_+ + c_-}{2c_+}\right)^2\left(\frac{1}{\sqrt{2}}\right)^2 \sim 2.7 \qquad (5.22)$$

The first factor -- f_K/f_π -- reflects $SU(3)_{FL}$ breaking in the K and π w
the last one -- $1/\sqrt{2}$ -- the Clebsch-Gordan coefficient that e
wavefunction. The coefficients c_+, c_- finally denote the renormalizatio
weak quark couplings by QCD radiative corrections: $c_+ \sim 0.7$, $c_- \sim 2$;
term does not contribute to $D^+ \to$ (S=-1) modes due to the destruct
mentioned above [19].

Analogous effects occur in (5.19, 20). The expected enhance
much larger, but also numerically more uncertain there: the destructiv
quite considerable in $D^+ \to \bar{K}^{\circ *}\pi^+$ and at the same time very sensitiv
changes in the model parameters. Comparing $\Gamma(D^+ \to \bar{K}^{\circ *}\pi^+)_{theo}$
suggest that the lower end in (5.19, 20) should be favoured.

Therefore I have to stress a general caveat concerning this ana
final state interactions have been completely ignored in the true spirit of
While matters of practicality favour this procedure there is good rea
universal wisdom. A detailed analysis of DCSD that is based on QC
quite desirable, but is not yet available at this time [19].

C. Resume on Rare D Decays

(i) The prospects of ever observing 1-loop decays of D mesons
gloomy since quite typically several concurrent suppression factor
mechanism, helicity arguments, small wavefunction overlaps, small
etc.

(ii) D°-$\bar{D}^\circ$ mixing could be as "large" as to produce [18]

$$\frac{\Delta m,\ \Delta\Gamma}{\Gamma} \sim 0.04$$

New Physics could lead to

$$\frac{\Delta m}{\Gamma} \sim 0.1$$

(iii) A detailed study of DCSD of D mesons appears to be
experimentally as well as theoretically. An intriguing and instructive patt

to emerge teaching us unique lessons on the strong interactions at the interface between the perturbative and non-perturbative regime.

(iv) Miracles can occur. Do not let them slip away by not watching!

VI. "GUARANTEED DISCOVERIES" - RARE B DECAYS

The B decays are simply "exciting" - even within the confines of the Standard Model:

- A priori unknown KM parameters - V (cb), V (ub), V (td), V (ts) - enter.
- B° - $\overline{B}^\circ$ mixing had been predicted and - even better - it was observed (actually on a higher level than anticipated).
- B decays present the best odds to observe CP violation outside K decays.
- Charmless decays like $B \to K^* \gamma$ will occur.

Since one is dealing here with reactions that typically require the presence of loop processes, i.e., that represent genuine quantum effects, one encounters a rather high sensitivity to New Physics in these transitions. The three generic scenarios for New Physics that I am going to invoke are

- a *fourth family*;
- an extended Higgs sector;
- Supersymmetry (= SUSY).

Unfortunately there are a few technical complications we have to face here:

- ChPT is clearly not applicable in decays like $B \to D \rho$, $B \to K^* \gamma$ etc.
- The two-body modes $B \to PP, PV, VV$ where P [V] denotes a pseudoscalar [vector] meson are not the dominant decay channels anymore (although they are not insignificant either) . QCD sum rules that have been developed for these exclusive modes are therefore of restricted use in B decays.
- It seems that rare inclusive decays like $B \to (C=0, S = 1)$ are hard to measure. This is quite unfortunate since theoretically they can be treated more directly.

A. KM suppressed tree level B decays

There are charmless B decays that occur already on the level of tree diagrams via the KM coupling V (ub). Among these there is a certain subset of modes with a particularly clean experimental signature: two-prong, two-body decays of beauty of which there are six channels

$$B \to \pi^+\pi^- , K^+K^- \qquad (6.1)$$

$$B \to K^{\pm} \pi^{\mp} \qquad (6.2)$$

$$B \to p \bar{p} \qquad (6.3)$$

$$\Lambda_b \to p\pi^-, pK^- \qquad (6.4)$$

(a) Following the same procedure as in Sect. V.B - i.e. including factorizable contributions only, setting $\xi \simeq 0$ and ignoring final state interactions (hereafter referred to as FSI)- we find [20]

$$BR(\bar{B}_d \to \pi^+\pi^-) \simeq BR(\bar{B}_s \to K^+\pi^-) \simeq 2 \times 10^{-3} \left| \frac{V(ub)}{V(cb)} \right|^2 \qquad (6.5)$$

$$BR(\bar{B}_d \to K^-\pi^+) \simeq BR(\bar{B}_s \to K^+K^-) \simeq \left(\frac{f_K}{f_\pi} \right)^2 tg^2\theta_c \, BR(\bar{B}_d \to \pi^+\pi^-) \simeq 1.6 \times 10^{-4} \left| \frac{V(ub)}{V(cb)} \right|^2 \qquad (6.6)$$

$$BR(\Lambda_b \to p\pi^-) \sim 3 \times 10^{-3} \left| \frac{V(ub)}{V(cb)} \right|^2 \qquad (6.7)$$

$$BR(\Lambda_b \to pK^-) \simeq \left(\frac{f_K}{f_\pi} \right)^2 tg^2\theta_c \, BR(\Lambda_b \to p\pi^-) \sim 2.3 \times 10^{-4} \left| \frac{V(ub)}{V(cb)} \right|^2 \qquad (6.8)$$

$$BR(\bar{B}_d \to p\bar{p}) \leq \text{few} \times 10^{-4} \left| \frac{V(ub)}{V(cb)} \right|^2 \qquad (6.9)$$

$$\left| \frac{V(ub)}{V(cb)} \right|^2 \leq 0.05$$

These processes, in particular $\bar{B}_d \to K^-\pi^+$ and $B_s \to K^+K^-$ can receive contributions from Penguin graphs which we have ignored here; this point will be re-addressed later on. Altogether we estimate the uncertainties due to the hadronization process to amount to factors of 2 - 3 roughly.

None of these rare decays have been observed yet -- which is not surprising in view of the predicted tiny branching ratios. The present 90 % C.L. upper limits read as follows (for a more detailed discussion see Ref. 4):

$$BR(\bar{B}_d \to \pi^+\pi^-) \leq 9 \times 10^{-5} \quad \text{CLEO} \qquad (6.5a)$$

$$BR(\bar{B}_d \to K^-\pi^+) \leq 9 \times 10^{-5} \quad \text{CLEO} \qquad (6.6a)$$

$$BR(\bar{B}_d \to p\bar{p}) \leq 4 \times 10^{-5} \quad \text{CLEO} \qquad (6.9a)$$

The bounds (6.5a) and (6.9a) have already reached theoretically interesting territory as expressed by (6.5) and (6.9). The bound of (6.6a) appears to be still an order of magnitude above it -- yet, as already indicated -- this is a point to which we will return.

(b) There are three more of these decay modes, but they should be further suppressed, i.e.

$$BR(\bar{B}_d \to K^+K^-) << BR(\bar{B}_d \to \pi^+\pi^-) \qquad (6.10)$$

$$BR(\bar{B}_s \to \pi^+\pi^-) << BR(\bar{B}_s \to K^+K^-) \qquad (6.11)$$

$$BR(\bar{B}_s \to p\bar{p}) <<< BR(\bar{B}_d \to p\bar{p}) \qquad (6.12)$$

The reason for that is the following: the decays $\bar{B}_d \to K^+K^-$, $\bar{B}_s \to \pi^+\pi^-$ and $\bar{B}_s \to p\bar{p}$ cannot proceed via simple tree diagrams; instead they require the intervention of FSI (i.e., rescattering and channel mixing), of annihilation or of KM suppressed penguin contributions - circumstances which are expected to reduce the rate (maybe I should add that it is somewhat academic on this level to distinguish those three mechanisms). A violation of the relations (6.10-12) might not necessarily amount to a disaster for theory - after all we have included factorizable contributions only - yet it would at least represent an acute embarassment for our theoretical description of heavy flavour decays.

(c) The three modes

$$\bar{B}_d \to K^-\pi^+, \bar{B}_s \to K^+K^-, \Lambda_b \to pK^-$$

on the other hand could be significantly enhanced over the rates given in (6.5-6.8) due to the intervention of FSI, annihilation and/or KM favoured penguins. Let me sketch just one scenario involving a two-step process

$$\bar{B}_d \to " \bar{D}_s^{(*)} D^{(*)} " \Rightarrow K^- \pi^+ \qquad (6.13)$$

The first transition has a huge enhancement factor over the direct process $\bar{B}_d \to K^- \pi^+$:

$$EF \sim \frac{|V(cb)|^2}{|V(ub)|^2} \cdot \frac{1}{tg^2\theta_c} \sim 500 \qquad (6.14)$$

The re-scattering efficiency for the second transition in (6.13) will certainly be quite small; yet we do not know how tiny it is. A re-scattering efficiency of 1% might not represent an inflated number - after all the process takes place less than 1.5 GeV above the $\bar{D}_s^* D^*$ threshold; even then this two-step process would dominate the $\bar{B}_d \to K^- \pi^+$ mode in view of (6.14).

Clearly more theoretical work is needed here. A refined analysis based on QCD sum rules appears quite promising, be it only to give a theoretical underpinning to some of the rather ad hoc phenomenological assumptions made so far.

In any case, dedicated experimental searches for these decay modes should receive a high priority. Determining their branching ratios will yield new and unique informations on the hadronization process and thus on QCD. For that purpose it is not essential to obtain these branching ratios with high precision - I would consider a 30% measurement as quite adequate: on the other hand it is highly desirable to obtain data on several of these decay channels.

These informations on hadronization can then serve as essential input for even more ambitious searches in these rare B decays, namely for B^0- $\bar{B}^0$ mixing and - ultimately - CP violation. (32)

B. One-loop $\Delta B = 1$ Processes in the Standard Model

(a) Generalities

The generic diagram for $Q \to q + \gamma$ or Z or g is shown in Fig. 10 where the loops with a charm and a (virtual) top quark have been singled out; the u quark contribution acts mainly as a GIM subtraction. It is understood that the photon or the gluon can be on- or off-shell (a somewhat murky distinction for the gluon). The dependence on the KM parameters for such a transition with an internal t quark is then given by

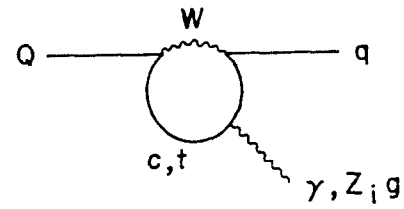

Fig. 10: Quark level diagram for induced FCNC.

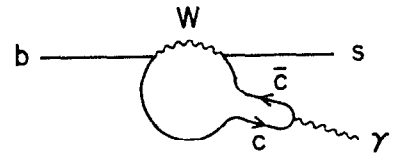

Fig. 11: Quark diagram for $b \to "\psi" s \to \gamma s$.

$$\text{rate}\,(b \to s + \gamma/Z/g) \propto |V(tb)\,V(ts)|^2 \simeq A^2\lambda^4 \qquad (6.15)$$

$$\text{rate}\,(s \to d + \gamma/Z/g) \propto |V(ts)\,V(td)|^2 \simeq A^4\lambda^{10}\left[(1-\rho)^2 + \eta^2\right] \qquad (6.16)$$

where I have used the Wolfenstein representation [21] of the KM matrix. Therefore we find for the branching ratios

$$BR\,(b \to s + \gamma/Z/g) \propto \frac{|V(tb)\,V(ts)|^2}{|V(cb)|^2} \simeq 1 \qquad (6.17)$$

$$BR\,(s \to d + \gamma/Z/g) \propto \frac{|V(ts)\,V(td)|^2}{|V(us)|^2} \simeq A^4\lambda^8\left[(1-\rho)^2 + \eta^2\right]$$

$$\sim (1-2) \times 5.5 \times 10^{-6} \qquad (6.18)$$

i.e., these rare decays of beauty have a much higher sensitivity to the presence of heavy quarks - the top quark in particular - than rare decays of stangeness. This makes them such an exciting field of study ! [22]

(b) $B \to \gamma + (S = -1)$

(i) Quark-level results.

From the diagram in Fig. 10 we obtain [23] the effective coupling for the quark-level transition $b \to s\gamma$

$$\mathcal{L}_{\text{eff}}(b \to s\gamma) = \frac{G_F}{\sqrt{2}}\, m_b\, \bar{b}_L\, \sigma_{\mu\nu}\, q_\mu\, A_\nu\, s\, F_2^\circ(q^2; m_c, m_t; \text{KM param.}) \qquad (6.19)$$

where A_ν denotes the photon field and q_μ its momentum. Gauge invariance tells us that for $q^2 = 0$, i.e., real photons, there can be only one form factor, namely F_2°. It depends, due to the GIM mechanism, approximately on the square of the internal quark mass, i.e.

$$F_2^\circ(\text{top}) \propto \frac{m_t^2}{M_W^2} \quad , \quad F_2^\circ(\text{charm}) \propto \frac{m_c^2}{M_W^2} \qquad (6.20)$$

This makes the charm contribution numerically quite insignificant and at the same time introduces a strong sensitivity of $\Gamma(b \to s\gamma)$ to the top mass. The dependence of this width on the KM parameters can be eliminated by considering the ratio $\Gamma(b \to s\gamma) / \Gamma(b \to c\,\ell\,\bar{\nu})$ since $|V(tb)| \simeq 1$, $|V(ts)| \simeq |V(cb)|$. One then finds [23]

$$\frac{\Gamma(b \to s\gamma)}{\Gamma(b \to c\,\ell\,\bar{\nu})} \simeq \begin{cases} 2 \times 10^{-4} & \text{for } m_t \simeq 65\ \text{GeV} \\ 10^{-3} & \text{for } m_t \simeq 150\ \text{GeV} \end{cases} \qquad (6.21)$$

Equating $\Gamma(b \to c\ell\nu)$ with the measured width $\Gamma(B \to \ell\nu\ X)$ one obtains for the branching ratio

$$BR\,(b \to s\gamma) \simeq \begin{cases} 2 \times 10^{-5} & \text{for } m_t \simeq 65\ \text{GeV} \\ 1 \times 10^{-4} & \text{for } m_t \simeq 150\ \text{GeV} \end{cases} \qquad (6.22)$$

Yet - as discussed before - what is measured are (exclusive) transitions involving hadrons rather than free quarks.

Gauge invariance again implies

$$\Gamma(B \to K\gamma) = 0 \qquad (6.23)$$

The mode $B \to K^*\gamma$ can proceed; since $BR(B \to K^*\gamma)$ can neither be 100% nor 0% one "infers" as an application of the Ma-Ik Theorem

$$\frac{BR\,(B \to K^*\gamma)}{BR\,(b \to s\gamma)} \sim 5 - 10\% \qquad (6.24)$$

a guestimate that is "confirmed" by computations [24] employing specific models for the hadronic wave functions. The final estimate then reads

$$BR\,(B \to K^*\gamma) \sim \begin{cases} 2 \times 10^{-6} & \text{for } m_t \simeq 65\ \text{GeV} \\ 1 \times 10^{-5} & \text{for } m_t \simeq 150\ \text{GeV} \end{cases} \qquad (6.25)$$

This steep dependence on m_t does not allow us to make a reliable prediction on the branching ratio. Yet such an apparent vice can swiftly be turned into a virtue by noting that a measurement of BR $(B \to K^*\gamma)$ would in turn give us a good handle on Nature's value of m_t! Before however jumping to this conclusion it behooves us to pause and think whether such a strong dependence indeed makes sense or not. After all, we have considered mainly quark level diagrams so far, i.e., short-distance dynamics.

(ii) On the impact of long-range dynamics - Duality lost?

The authors of Ref.25 addressed the question whether there is another mechanism leading to the same final state; in particular they considered a two-step process a la Vector Meson Dominance

$$B \to "\psi" K^* \to \gamma K^* \qquad (6.26)$$

One can make a very crude estimate for its branching ratio

$$BR(B \to \gamma K^*) \sim BR(B \to "\psi' K^*) \times Prob("\psi" \to \gamma)$$
$$\sim (5 \times 10^{-3}) \times \frac{\alpha}{\pi} \sim 10^{-5} \qquad (6.27)$$

The point of this exercise is not to produce a reliable prediction, but to point out that there could be a contribution to $B \to \gamma K^*$ that is independent of m_t, yet of comparable magnitude to the numbers listed in (6.25). Furthermore these two contributions are coherent; therefore their amplitudes could add or subtract thus influencing the overall result quite dramatically. Such an observation -- namely that there is a numerically significant contribution to $B \to K^*\gamma$ that is not produced by the diagram in Fig. 10 -- would spell trouble for the applicability of quark-hadron duality in B decays if it were true.

(iii) QCD radiative corrections - Duality regained!

The suggestion made above that there is no quark-level diagram corresponding to (6.26) has to be examined more carefully. The diagram shown in Fig. 11 would fit the bill and it merely represents a permissible distortion of the charm loop in Fig. 10. However we had argued before that the GIM mechanism relegates this diagram to numerical insignificance!

A more careful analysis of the GIM mechanism will help here: If two quarks Q and q with masses m_Q and m_q respectively appear in a loop diagram together with W bosons then such a diagram has to yield a vanishing contribution in the limit $m_Q = m_q$. However this can happen in two different ways:

- $$\text{Ampl.} \propto \frac{m_Q^2 - m_q^2}{M_W^2} \qquad (6.28)$$

this is usually called "hard" GIM suppression (at least for $m_q^2, m_Q^2 < M_W^2$).

- $$\text{Ampl.} \propto \log \frac{m_Q^2}{m_q^2} \qquad (6.29)$$

which is commonly referred to as "soft GIM suppression" although it actually amounts to an enhancement for $m_q^2 \ll m_Q^2$.

Returning to the case under study here: as already stated, the diagram in Fig. 10 reproduces hard GIM suppression, (6.28). However QCD radiative corrections change the situation very significantly:

- Diagrams like the one in Fig. 12 produce "soft GIM suppression", i.e., actually an enhancement $\sim \log (M_t/m_c)^2$ which is particularly effective for $m_t \leq M_W$. (For $m_t > M_W$ also the expression in (6.28) yields an enhancement. This at first sight paradoxical result is due to the coupling of longitudinal W bosons).
- New and more leading log terms emerge for $m_t \sim O(M_W)$ since

$$\frac{\alpha_s(m_b^2)}{\pi} \log \frac{m_t^2}{m_b^2} \leq 1$$

in that case.

Putting everything together and including leading log terms only the authors of Ref. 26 found the results shown in Fig. 13. From it we draw the following conclusions:

- The QCD radiative corrections are very large indeed.
- They decrease somewhat in relative importance as m_t increases: e.g., for $m_t \simeq$ 50 GeV they produce an enhancement by a factor 17 whereas for $m_t = 125$ GeV this factor has shrunk to 4.3. As discussed above such a trend was to be expected since the biggest difference between soft and hard GIM suppression occurs for small values of m_t.
- The dependence on m_t therefore becomes less steep.
- This makes it doubtful that the decay $B \to K^* \gamma$ could reveal information on the presence of a fourth family.
- The lowered sensitivity to m_t implies that the charm-loop contribution becomes numerically much more significant.
- This means that the concept of quark-hadron duality escapes the disaster it was facing before QCD radiative corrections were included.
- These radiative corrections obviously contain sizeable numerical uncertainties; for example, the appropriate normalization scales have not been uniquely determined so far. Yet the fact that they are large or even dominant per se does not make them completely untrustworthy. For - as discussed before - we do understand on fairly general grounds why in this particular case these correction terms are so large: it is firstly the conversion of hard GIM suppression into soft GIM suppression; secondly the appearance of large logarithms $\log m_t^2$ which have been summed to all orders on the leading log level. Higher order terms which have been ignored so far cannot benefit from additional enhancements over the terms already included. The situation here has something in common with the one encountered in e^+e^- annihilation: the two-photon process

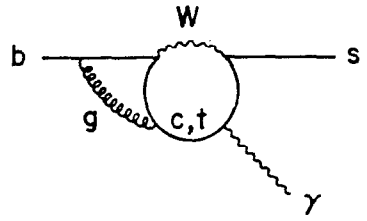

Fig. 12: QCD radiative corrections that produce "soft GIM suppression".

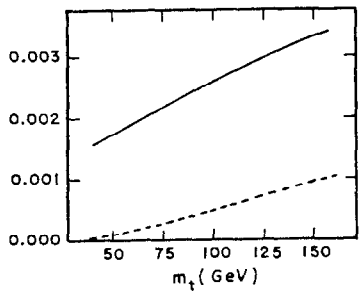

Fig. 13: The ratio $\Gamma(b \to s\gamma) / \Gamma(b \to c\ell\nu)$ with (solid line) and without (broken line)QCD radiative corrections; from ref. 26.

dominates the one-photon reaction at the highest presently available energies; yet nobody claims a breakdown of perturbative QED since we understand the structural reasons behind the prominence of the two-photon process.

As an (optimistic) reference point we can then state:

$$BR(B \to K^* \gamma) \sim 3.3 \times 10^{-5} \quad \text{for} \quad m_t \simeq 150\ \text{GeV}$$

This is to be compared to the upper bounds [4]

$$BR(B_d \to K^* \gamma) \sim \begin{cases} 2.9 \times 10^{-4} & \text{ARGUS} \\ 2.8 \times 10^{-4} & \text{CLEO} \end{cases}$$

(c) $B \to \ell^+\ell^- + (S = -1)$

Some new features emerge in a treatment of the transition $b \to s\ \ell^+\ell^-$:

- It can proceed due to the exchange of a photon in $b \to s\ "\gamma" \to s\ \ell^+\ell^-$. Since this photon is off-shell a new form factor that is not present in $b \to s\gamma$ appears here; it is usually referred to as F_1.
- The lepton pair $\ell^+\ell^-$ can be produced from an intermediate Z° or W^+W^- pair as well. This introduces new terms for which there is no analogue in $b \to s\gamma$; for heavy top quarks, say $m_t > M_W$, they actually yield the dominant contribution (which is due to the coupling of the longitudinal Z or W bosons to the top quarks that appear in the loop).

Putting these ingredients together one obtains [27]

$$BR_o(b \to s\, e^+e^-) \simeq \begin{cases} 3.5 \times 10^{-6} \\ 6.4 \times 10^{-6} \\ 1.0 \times 10^{-5} \end{cases} \quad \text{for } m_t = \begin{cases} 50 \\ 100 \\ 150 \end{cases} \text{GeV} \qquad (6.30)$$

QCD radiative corrections treated in a leading log framework[28] enhance these numbers considerably, in particular for moderate values of m_t:

$$BR_{QCD}(b \to s\, e^+e^-) \simeq \begin{cases} 7.3 \times 10^{-6} \\ 1.1 \times 10^{-5} \\ 1.4 \times 10^{-5} \end{cases} \quad \text{for } m_t = \begin{cases} 50 \\ 100 \\ 150 \end{cases} \text{GeV} \qquad (6.31)$$

A few observations should be added here:

(i) The QCD corrections while considerable are not nearly as huge as the case of $b \to s\gamma$. That is not surprising: it was pointed out before that the transition $b \to s\gamma$ depends on a single form factor in a very restricted way and does represent the exception rather than the rule. In $b \to s\ell^+\ell^-$ on the other hand several short-distance contributions appear, as discussed before.

(ii) Information on the underlying dynamics is contained not just in the branching ratio, but in the di-lepton mass distribution as well; details can be found in Ref. 29.

(iii) The virtual photon has a definite preference to materialize in an e^+e^- rather than a $\mu^+\mu^-$ pair. The rate for $b \to s\,\mu^+\mu^-$ is thus suppresssed relative to $b \to s\,e^+e^-$ beyond the mere phase space reduction; for details see Ref. 29.

Exclusive decay modes exhibit a cleaner experimental signature, while introducing further theoretical uncertainties in the treatment of hadronization. Two channels have been studied in particular, namely $B \to K\,e^+e^-$ and $B \to K^*\,e^+e^-$, for which the following estimates have been given [29]

$$\frac{BR\,(B \to K^* e^+e^-)}{BR\,(b \to s\,e^+e^-)} \sim 0.2 \tag{6.32}$$

$$\frac{BR\,(B \to K\,e^+e^-)}{BR\,(b \to s\,e^+e^-)} \sim 0.05 \tag{6.33}$$

combining these numbers with (6.31) we arrive finally at

$$BR\,(B \to K^* e^+e^-) \sim [1.5,\ 2.2,\ 2.8] \times 10^{-6}$$
$$BR\,(B \to K\,e^+e^-) \sim [0.3,\ 0.6,\ 0.84] \times 10^{-6} \tag{6.34}$$

for $m_t = [\,50,\ 100,\ 150]$ GeV.

These are tiny numbers indeed, but not zero. And they could be enhanced quite considerably if there is a fourth family.

CLEO has obtained the following upper bound:

$$BR\,(B^+ \to K^+ e^+e^-) \leq 5 \times 10^{-5}$$

(d) $B \to \nu\bar{\nu} + (S = -1)$

Theoretically this represents a truly lovely mode whose branching ratio increases very strongly with m_t (the virtual photon contribution is of course absent here). For $m_t \simeq 100$ GeV one finds [30]

$$BR\,(b \to s\,\nu\bar{\nu}) \simeq 2 \times 10^{-5} \tag{6.35}$$

which is twice the value of BR $(b \to se^+e^-)$ for this m_t. This should not come as a surprise since one sums over the three neutrino species (and the Z^0 couples more strongly to neutrinos than charged leptons). Unfortunately it appears that the experimental signature for such decays, even for exclusive channels like $B \to K^*\nu\bar{\nu}$ is not sufficiently clean.

(e) $B \to (S = 1) + \text{glue}$

On the one-loop level there are four types of quark processes in this category, namely $b \to sg$, $b\bar{q} \to s\bar{q}$, $b \to sq\bar{q}$ and $b \to s\,gg$. It is actually the latter two that dominate and altogether one obtains [31]

$$BR\,(b \to s + \text{glue},\ q\bar{q}) \sim 1 - 2\% \tag{6.36}$$

for $m_t \simeq 30 - 200$ GeV, i.e. the branching ratio exhibits fairly little sensitivity to the top mass.

There exists a second source for charm-less final states with strangeness, namely the KM and Cabibbo suppressed transition $b \to u\bar{u}s$. A crude estimate yields

$$BR\,(b \to u\,\bar{u}s) \sim 2\mathrm{tg}^2\theta_c \left|\frac{V(ub)}{V(cb)}\right|^2 \leq 1\,\% \tag{6.37}$$

where the factor two reflects the phase space advantage of $b \to u$ over $b \to c$.

The rates for these two reactions, namely the one-loop process $b \to s$ + glue and the tree-level process $b \to u\bar{u}s$, are therefore of a magnitude that is not very dissimilar. Not only is this interesting by itself, but it also creates very favourable conditions for the emergence of CP asymmetries in this class of B decays. [32]

Alas, we have to face up to the usual unpleasant business of hadronization. Gluon fragmentation

$$g \to gg,\ q\bar{q}$$

is "soft" thus transforming the original (virtual) masses of up to a few GeV into high hadronic multiplicities. It is therefore a multitude of exclusive channels that builds up the not-so-small inclusive branching ratio given in (6.36). To make this

statement more quantitative we have at present to rely on phenomenological models. They tend to yield numbers like [33]

$$BR(\overline{B}_d \to K^- \pi^+) \sim \text{few} \times 10^{-5} \qquad (6.38a)$$

$$BR(\overline{B}_d \to \overline{K}^0 \phi) \sim \text{few} \times 10^{-5} \qquad (6.38b)$$

A comparison of (6.38a) with (6.6) shows the considerable impact Penguin-like contributions can have even on the branching ratios. In particular the number quoted in (6.38a) is relatively close to the present experimental upper bound.We do not have a reliable method for gauging the theoretical uncertainties in these predictions, but we have to suspect they are large, say a factor of three or so.

For the same reason we have to conclude that the sensitivity to the presence of a fourth family is submerged in this "theoretical noise", at least as far as exclusive decay modes are concerned.

C. One-loop $\Delta B = 1$ Processes with New Physics

The predictions given so far for these one-loop B decays contain two types of uncertainties:

- The "embarrassing" uncertainties that enter into our estimates of branching ratios for exclusive modes in particular; they are due to our less than satisfactory mastery of hadronization.
- The "good" uncertainties concerning parameters of the quark world, in particular the top mass. The unknown value of m_t severely restricts the numerical precision of our predictions; yet a measurement of the relevant branching ratios would produce a lower and an upper bound on m_t.

We have reason to entertain even bolder hopes, namely to search for the presence of New Physics in these B decays which represent classically forbidden processes. In the preceding discussion of subsection B I had already included one such scenario, namely the Standard Model with one additional, the fourth family. There we had encountered the one general impediment for such an analysis: due to the "embarrassing" uncertainties we can hope to perform a successful hunt only, if some big game is waiting for us out there, i.e., if the measured rate is considerably larger than the expected rate.

I will briefly review the situation with two other realizations of New Physics, namely a non-minimal Higgs sector and supersymmetry (= SUSY); I will also add a short remark on light Higgs scenarios although they could be realized in the Standard Model as well.

(a) Non-minimal Higgs sector with Natural Flavour Conservation

The Standard Model contains one complex SU(2) doublet Higgs field. Three of its four degrees of freedom are transmogrified into the longitudinal components of the weak bosons while the fourth one emerges as the physical Higgs field, which is neutral.

Since flavour changing neutral currents are highly suppressed in nature one does not want to enlargen the Higgs sector in a reckless manner. Instead one introduces new Higgs doublets in such a way that they couple either to the up- or to the down-type quarks .[36] For two doublets we are left with five physical Higgs fields, two of which are charged and three neutral. (CP invariance is still maintained; it is broken spontaneously if three Higgs doublets are introduced.)

Even with this imposition of natural flavour conservation we are dealing with a high-dimensional space of new parameters. To identify an interesting corner in this parameter space one can turn to B_d - $\overline{B}_d$ mixing.

The ARGUS and CLEO findings do not establish a need yet for New Physics in the $\Delta B = 2$ channel; on the other hand it cannot be ruled out that New Physics does provide the dominant motor of B^0- $\overline{B}^0$ mixing. It is thus legitimate to consider that part of the parameter space where Higgs exchanges dominate $\Delta B = 2$ dynamics and then search for sizeable enhancements in $\Delta B = 1$ reactions.

Such an analysis has been undertaken in Ref. 37 . The authors' conclusions for two quite different models with two Higgs doublets are summarized in Table IV. One should add here that model II serves as an imagination stretcher rather than a realistic dynamical scenario.

transition	BR[in %] Model I	Model II	Enhancement Factor I	II
$b \to s\gamma$	few x 0.1	≤ 2	$O(10)$	$O(100)$
$b \to s\ell^+\ell^-$	$\leq$ few x 10^{-3}	$\leq$ few x 10^{-2}	$O(10)$	$O(100)$
$b \to s\, g^{(*)}$	≤ 4	≤ 100 (!)	2 - 4	$O(10)$

Table IV

These numbers have to be taken with a grain of salt since radiative QCD corrections have not been included here. Yet even so they show how large a discovery potential there is in these transitions.

(b) Supersymmetry

There is one feature of particular relevance here [38]: gluino exchanges mediate flavour changing neutral currents with a strength of order α_s, i.e. the strong rather than the electroweak coupling. This enhances the rates for $b \to s\gamma$ and $b \to sg^{(*)}$ by an order of magnitude for moderately heavy Susyons, i.e. if M (gluino, squarks) ~ M_W [39]! Again, QCD radiative corrections have not been fully included.

(c) Light Higgs scenario

It was already mentioned in Sect. III that an arbitrarily light Higgs boson can emerge in the presence of heavy quark fields Q, i.e. if $M_Q > 80$ GeV. The decay $b \to sH$ is dominated by the loop diagram containing the top quark and is roughly proportional to m_t^2: one factor of m_t enters through the Yukawa coupling of the Higgs, the other is produced by the chiral structure. Therefore [40]

$$BR(b \to sH) \propto m_t^4 \qquad (6.39)$$

Assuming

$$m_t \gtrsim 80 \text{ GeV} \qquad (6.40)$$

as the raison d'être for a light Higgs one infers from the available limits on such B decays [41]

$$m_H > 3.7 \text{ GeV} \qquad (6.41)$$

There is still another window open, namely

$$0.3 \text{ GeV} < m_H < 2 \text{ GeV};$$

it can be closed only by making more detailed theoretical assumptions on the relevant Higgs decay channels. Those can be checked (or challenged) by further experimentation.

D. Resume on Rare B Decays

B physics is "full of promise"; there is tantalizing "poetry in beauty"! All of this is of course a euphemism for saying that B physics has not reached the maturity level yet, neither experimentally nor theoretically.

- Experimentally: as a theorist one cannot help but complain that measurements of inclusive B decay rates have so far produced rough numbers only.
- Theoretically:
  - As far as inclusive decay rates are concerned there is still some homework to be done: QCD radiative corrections have to be included properly and comprehensively [42]; more detailed thinking should be applied to the question of whether one can trust quark-hadron duality in B decays on the 10% or only on the 50% level.
  - More formidable tasks await our dedicated attention in exclusive B decays: most hadronization prescriptions -- like potential models - are of untested reliability; trustworthy results from lattice Monte Carlo computations are still a few years away; it appears that an application and refinement of QCD sum rules a la the Blok-Shifman treatment of D decays is the best available technology.
  - As far as numbers are concerned one should keep in mind that the exclusive branching ratios for these rare B decays are typically of order 10^{-6}-10^{-5}; the inclusive transitions on the other hand command branching ratios that are higher by a factor 10-100!

In summary: if we apply the principles on which the Napoleonic campaigns were built - i.e. employ large numbers, i.e. $\geq 10^7$ B's, spend a small fortune (but get others to pay for it) and, very importantly, rely on "fortune" in the French sense - then we are faced with the prospect of guaranteed discoveries!

VII - OUTLOOK

We should keep in mind how much New Physics has been unearthed in K decays: parity violation, suppression of flavour changing neutral currents, CP violation and the existence of the internal quantum numbers strangeness and charm (and even top quarks). There is no reason to believe that the potential for indirect discoveries of New Physics has been exhausted in any way. Yet there are two important lessons we should draw from the past:

(1) A careful and continuous evaluation of our theoretical tools has to take place: lattice Monte Carlo computations will answer all these questions sometime in the future; for now (and for some time to come) we have to rely on a judicious and detailed application of different theoretical technologies: ChPT for K mesons, QCD sum rules etc., for D and B mesons.

(2) We have to pursue a comprehensive experimental program: for example the relevant quark mixing angles could be completely different for down-type quarks --like s and b -- than for up-type quarks -- like charm. Therefore one has to study also rare D decays in a dedicated fashion to obtain a complete picture even though one needs a gambler's luck to find New Physics there.

Dedicated searches for and studies of rare B decays are "assured" to yield a rich harvest. Yet even so one should view studies of rare K and rare B decays as perfectly complementary, not as competing.

Acknowledgements

I have benefitted from enjoyable discussions with G. Ecker, H. Galic, A. Pich, E. de Rafael, B. Stech and R. Willey. Thanks are also due to the organizers for their customary success in creating a very pleasant environment.

Appendix A: Long-distance dynamics in $K \to \pi\nu\nu$

The diagrams in Fig. 3 generate a local $\Delta S = 1$ operator which - as stated in the text - can then be related to the operator that underlies $K \to \pi e \nu$ decays. However there exists another mechanism which is of relevance, at least in principle, namely the two-step process

$$K^+ \to "R^+" \to \pi^+ \nu\bar{\nu} \qquad (A.1)$$

R^+ represents an intermediate state with $S = 0$: $R = \pi, \rho, A_1, \pi\pi, 3\pi, \ldots$ Since such states are not necessarily far off-shell, they can propagate over typical hadronic distances; the process (A.1) therefore represents long-distance dynamics and it is not included in the reference reaction $K \to \pi e \nu$ to the same degree[34] (it appears there as a radiative correction only). An analogous situation is encountered when one attempts[35] to compute the long-distance contribution to K° - $\bar{K}^\circ$ mixing. Using similar arguments one estimates that the process (A.1) could be numerically significant if top quarks are only moderately heavy, i.e., $m_t < M_W$.

Appendix B: Some technical remarks on the basics of ChPT

Let g_L [q_R] generate the transformation of the fields under the action of the group $SU(3)_L$ [$SU(3)_R$]. The unitary matrix $\underline{U}$ as defined in (4.17) then obeys a simple transformation law:

$$\underline{U} \rightarrow g_L \underline{U} g_R^+ \qquad (B.1)$$

under $SU(3)_L \times SU3)_R$.

(B.1) is so remarkable because it shows that the matrices $\underline{U}$ and $\underline{U}^+$ are the appropriate building blocks for constructing chirally invariant Lagrangians. There is then a simple prescription: form pairs $\partial\underline{U}\,\partial\underline{U}^+$ (the derivative operator commutes with chiral transformations since those are global) and take the trace; the simplest non-trivial expression one can write down reads

$$\mathcal{L}^{(2)} \propto tr\, \partial_\mu \underline{U}\, \partial_\mu \underline{U}^+ \qquad (B.2)$$

The matrix $\underline{U}$ can be expressed by an expansion in powers of the Goldstone boson fields ϕ, see (4.17); the expansion parameter contains $1/f_\pi$, i.e. has dimension of an inverse mass. Thus we are dealing with a non-renormalizable interaction. It is then completely obvious that loop, i.e. quantum corrections will necessarily introduce new coupling terms like

$$\mathcal{L}^{(4)} \propto tr\, \partial_\mu \underline{U} \partial_\nu \underline{U}^+ \partial_\mu \underline{U} \partial_\nu \underline{U}^+ \qquad (B.3)$$

with a relative weight that is completely undetermined by chiral invariance. Going to higher loops will enforce couplings $\mathcal{L}^{(6)}$, $\mathcal{L}^{(8)}$ etc. where the superscript denotes the number of derivatives.

References

1) W.Buchmüller and D.Wyler, Nucl.Phys.B268 (1986) 621.
2) J.C.Anjos et al., "A Search for Flavour Changing Neutral Current Processes in Decays of Charmed Mesons", XXIVth International Conference on High Energy Physics, Munich (1988).
3) J.Adler et al., Phys.Rev.Lett. 60 (1988) 1375.
4) See the lectures by K.Berkelman, these Proceedings.
5) See the lectures by A.J.S.Smith, these Proceedings.
6) T.Inami and C.S.Lim, Prog. Theor. Phys. 49 (1973) 652.
7) S.Bertolini and A.Masiero, Phys.Lett. 174B (1986) 343.
8) R.S.Chivukula and A.V.Manohar, preprint CTP#1580, BUHEP-88-7 (1988).
9) S.Bertolini and A.Santamaria, preprint CMU-HEP88-2 (1988).
10) For a recent review, see: F.Gilman, lectures at the SLAC Summer Institute 1986.
11) See for example: H.Georgi, Weak Interactions and Modern Particle Theory, Benjamin/Cummings Pub. Co., 1984.
12) J.Gasser and H.Leutwyler, Nucl.Phys. B250 (1985) 465.
13) G.Ecker, A.Pich and E.deRafael, in preparation (private communication).
14) G.Ecker, A.Pich and E.deRafael, Nucl.Phys. B291 (1987) 692; Phys.Lett. 189B (1987) 363; preprint CERN-TH.4853/87 (1987).
15) L.Sehgal, preprint PITHA-88/2 (1988).
16) J.F.Donoghue, B.R.Holstein and G.Valencia, Phys.Rev. D35 (1987) 2769.
17) A.J.Buras, "The 1/N Approach to Non-leptonic Weak Interactions", in: " CP Violation", C.Jarlskog (ed.), World Scientific, 1989, with references to earlier work.
18) I.I.Bigi and A.I.Sanda, Phys.Lett. 171B (1986) 320.
19) For a recent review on D decays, see: I.I.Bigi, preprint UND-HEP-88-BIG01, to appear in the Proceedings of the Ringberg Workshop "Hadronic Matrix Elements and Weak Decays", 1988;
M.Wirbel, preprint DO-TH 88/2 (1988), to appear in Progress in Particle and Nuclear Physics.
20) I.I.Bigi and B.Stech, preprint SLAC-PUB-4495 (1987), in: Proceedings of the Workshop on High Sensitivity Beauty Physics at Fermilab, 1987;
M.B.Gavela et al., Phys.Lett. 154B (1985) 425.
21) L.Wolfenstein, Comm. Nucl.Part.Phys. 14 (1985) 135.
22) For e recent discussion, see: A.Soni, "Aspects of Rare B Decays", in: Proceedings .

of the B-Meson Factory Workshop, SLAC, 1988, SLAC-Report 324.
23) W.-S.Hou, A.Soni and H.Steger, Phys.Lett. 192B(1987) 441;
N.Deshpande et al., Phys.Rev.Lett. 59 (1987) 184.
24) N.Deshpande and J.Trampetic, in : Proceed. of the International Symposium on Production and Decay of Heavy Flavours, Stanford, 1987, E.Bloom and A.Fridman (ed.), Ann.N.Y.Acad.Sci., Vol. 535.
25) E.Golowich and S.Pakvasa, preprint UMHEP-293 (1988).
26) B.Grinstein, R.Springer and M.Wise, Phys.Lett. 202B (1988) 138.
27) N.Deshpande et al., Phys.Rev.Lett. 57 (1986) 1106;
J.O'Donnell, Phys.Lett. 175B (1986) 369;
W.-S.Hou, A.Soni and R.Willey, Phys.Rev.Lett. 58 (1987) 1608.
N.Deshpande and J.Trampetic, preprint OITS 379, 1988.
28) B.Grinstein, M.Savage and M.Wise, preprint LBL-25014, 1988.
29) Ref. 28; N.Deshpande and J.Trampetic, preprint OITS 379, 1988.
30) W.-S.Hou, A.Soni and R.Willey, Phys.Rev.Lett. 58 (1987) 1608.
31) For a recent discussion, see: W.-S. Hou, preprint MPI-PAE/PTh 7/88, 1987.
32) M.Bander, D.Silverman and A.Soni, Phys.Rev.Lett. 43 (1979) 242;
I.I.Bigi et al., "The Question of CP Noninvariance -- as seen through the Eyes of Neutral Beauty", preprint SLAC-PUB-4476, 1987, in: "CP Violation", C.Jarlskog (ed.), World Scientific, 1989.
33) M.Bauer, B.Stech and M.Wirbel, Z.Phys. C34 (1987) 103;
M.B.Gavela et al., Phys.Lett. 154B (1985) 425.
34) This emerged from an interesting discussion with R.Willey.
35) I.I.Bigi and A.I.Sanda, Phys.Lett. 148B (1984) 205.
36) S.L.Glashow and S.Weinberg, Phys.Rev. D15 (1977) 1958
37) W.-S. Hou and R.Willey, Phys.Lett. 202B (1988) 591.
38) M.J.Duncan, Nucl.Phys.B221 (1983) 285;
J.F.Donoghue et al., Phys.Lett. 128B (1983) 55.
39) S.Bertolini, F.Borzumati and A.Masiero, preprint CMU-HEP88-08, 1988.
40) R.Willey and H.L.Yu, Phys.Rev.D26 (1982) 3086;
R.M.Godbole et al., Phys.Lett. 194B (1987) 302.
41) B.Grinstein, L.Hall and L.Randall, preprint LBL-25095, 1988.
42) The results of Ref.26 have been criticized by R.Grigjanis et al., preprint UTPT-88-11.

SUPERCONDUCTING DETECTORS FOR MONOPOLES AND WEAKLY INTERACTING PARTICLES

B. Cabrera

Physics Department, Stanford University
Stanford, California 94305

In our laboratories at Stanford, we have undertaken several research programs to search for dark matter candidates in our galaxy with laboratory based detectors. The first effort is a search for magnetic monopoles in the cosmic rays. These would be supermassive (10^{16}-10^{19} GeV/c^2) and a density of only one per 10-10,000 km^3 would be sufficient to account for the local dark matter around our galaxy. We have been operating a 1.3 m^2 times 4π sr detector utilizing eight SQUIDs. It is the largest superconductive monopole detector. The second effort involves the development of large mass (~1 kg) elementary particle detectors capable of sensing weakly interacting particles. These utilize silicon crystals at temperatures below 1 K, have spatial resolution in three dimensions and would measure the total energy deposition. Such detectors will be used for direct dark matter searches and for neutrino experiments capable of setting better limits on the neutrino mass.

PART A:
SEARCH FOR MAGNETIC MONOPOLES IN THE COSMIC RAYS

Introduction

In 1931, P.A.M. Dirac proposed the existence of magnetically charged particles to explain the observed quantization of electric charge. He showed that only integer multiples of a fundamental magnetic charge g (Dirac charge) = $hc/4\pi e$ are consistent with quantum mechanics. Many years of experimental searches produced no convincing candidates. In 1974 't Hooft and independently Polyakov showed that in all true unification theories (those based on simple or semi-simple compact groups) magnetically charged particles are necessarily present. The modern theory predicts the same long-range field and thus the same charge g as the Dirac solution; now, however, the near field is also specified leading to a calculable mass. The standard SU(5) model predicts a monopole mass of 10^{16} GeV/c^2, much heavier than had been considered in previous searches. More recent unification theories based on supersymmetry or Kaluza-Klein models yield even higher mass values up to the Planck mass of 10^{19} GeV/c^2.

Such supermassive magnetically charged particles would possess qualitatively different properties from those assumed in earlier searches. These include necessarily nonrelativistic velocities from which follow weak ionization and extreme penetration through matter. Thus such particles may very well have escaped detection in earlier searches based on heavy ionization of relativistic monopoles.

Although GUTs theories are very clear in their prediction of the existence of monopoles, cosmological theories based on GUTs lead to impossibly high or unobservably low predictions for monopole particle flux limits with the latter results being exponentially model dependent. Thus, only astrophysical arguments provide guidance for the relevant detector sensing areas for experiments. An upper bound of 10^{-15} cm^{-2} sr^{-1} s^{-1} is obtained assuming an isotropic flux from arguments based on the existence of the 3 microgauss galactic magnetic field (Parker bound). The Parker bound becomes less severe linearly with monopole mass for masses above 10^{17} GeV/c^2. In addition, several authors have demonstrated that models incorporating monopole plasma oscillations would allow a much larger particle flux, approaching in some cases the local galactic dark mass limit. All of these bounds assume particle velocities in gravitational virial equilibrium, i.e., very near 10^{-3} c.

Much more severe astrophysical limits can be obtained based on proton decay catalysis. It has been shown theoretically that the supermassive monopoles arising from many grand unification theories would catalyze nucleon decay processes. If the cross section for such events is of order the hadron cross section, as has been suggested, then all attempts at direct detection of the monopoles from such theories may be doomed to failure. Arguments based on x-ray flux limits from galactic neutron stars, which assume a strong interaction cross section for proton decay catalysis, lead to an upper bound for magnetic particle flux of about 10^{-21} cm^{-2} sr^{-1} s^{-1}. There remain unanswered questions concerning the detailed theoretical understanding of the catalysis cross section and concerning the astrophysical arguments based on our incomplete understanding of neutron stars. In addition, proton decay has not yet been observed. Thus, from an experimental point of view more weight should be given to the less model dependent astrophysical limits.

Superconductive technologies, many developed at Stanford University over the last decade, have led naturally to very sensitive detectors for magnetically charged particles. These superconductive detectors directly measure the magnetic charge independently of particle velocity, mass, electric charge and magnetic dipole moment [1]. In addition, the detector response is based on simple and fundamental theoretical arguments which are extremely convincing. Because of their velocity-independent response, these detectors are a natural choice in searches for a particle flux of supermassive (and therefore slow) magnetically charged particles. By far, the most definitive positive identification of a magnetic charge would be made with a superconductive detector. Other detectors, though larger, are less satisfactory for positive identification of monopoles since the interaction of monopoles with matter through ionization processes is less well understood [2].

Detailed reviews of the theoretical, the experimental and the astrophysical work can be found in **Magnetic Monopoles** [R.A. Carrigan and W.P. Trower, eds., Plenum 1983] and **Monopole '83** [J. Stone, ed., Plenum 1984].

Operation of Three Loop Detector

Between February, 1983 and March, 1986, we operated a three loop coincident superconducting magnetic monopole detector [3]. The rms current noise levels in an effective noise bandwidth of ≈ 0.16 Hz were 0.02 ϕ_o/L in all three loops, less than 1% of the signal expected from the passage of a Dirac magnetic charge through one of the two turn loops (4 ϕ_o/L). The sensing area based on this low noise operation was 476 cm^2 (71 cm^2 loop area and 405 cm^2 near miss area) for events greater than 0.1 ϕ_o/L in

at least two of the three loops. The data were extremely clean and no candidate events were seen. Based on the 1008 days of accumulated active running time, these data set an upper limit of 4.4×10^{-12} cm^{-2} sr^{-1} s^{-1} (90% C.L.) on any uniform flux of magnetic monopoles passing through the earth's surface at any velocity [3].

New Large Area Octagonal Detector

Our group at Stanford, consisting of B. Cabrera, M. Huber, M. Taber and R. Gardner, has designed, constructed, and brought into continuous operation an eight loop detector [4] with a cross section averaged over 4π sr of 1.3 m^2 for double coincident events and a signal-to-noise ratio of 30 for the passage of a single Dirac charge. This detector shown schematically in Fig. 1, is composed of eight planar superconducting detection coils arranged around a cylinder with an octagonal cross section. Each coil is a gradiometer 16 cm wide and 6 m long and is connected to a high sensitivity rf SQUID current sensor. The entire assembly is surrounded by a superconducting lead shield and housed in a dewar which is enclosed in a μ-metal shield. This detector has a sensing area 30 times larger than that of the three loop detector.

A very important design feature for the large scale use of superconducting coils as monopole detectors is the use of a gradiometer winding pattern [5,6]. The sensitivity of a gradiometer to external magnetic field changes is substantially reduced over that from a simple coil whereas the sensitivity to the passage of a magnetic charge remains high since the particle passes through only one element of the gradiometer pattern. We have utilized computer calculations to optimize our coil design under constraints from dewar size and minimum acceptable signal to noise ratio. The optimum pattern which we have used for our design is shown in Fig. 2. The conducting elements are NbTi ribbon, 2mm wide and 50 μm thick. It is a repeating rectangular pattern with an aspect ratio of 0.6 to 1.0. A further improvement was achieved by breaking the loop up into a number of parallel elements which are connected together to one SQUID. This technique reduces the coupling losses to the SQUID from a 1/L proportionality to $1/\sqrt{L}$, where L is the inductance of the single series loop [7].

The new 1.3 m^2 monopole detector requires eight low-noise SQUID systems, one for each panel of the detector array. We have chosen to use rf SQUIDs manufactured by Biomagnetic Technologies Inc. [B.T.i.], (formerly S.H.E. Corp.) together with rf electronics from Quantum Design. A shield of high magnetic permeability metal (μ-metal) has been designed and constructed to shield the detector

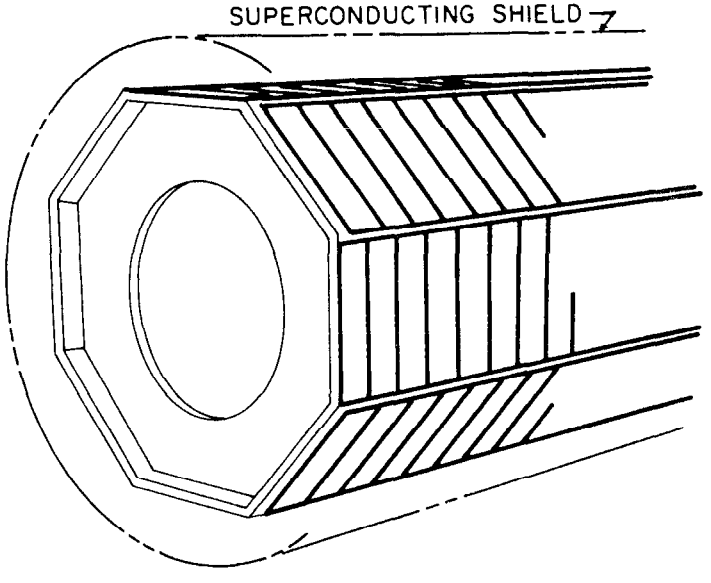

Fig. 1. Schematic diagram of octagonal detector.

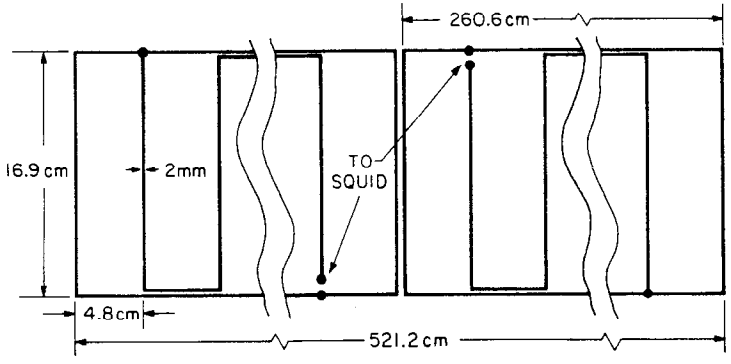

Fig. 2. Loop parameters for octagonal detector.

from the earth's magnetic field during the initial cooldown, as the inner superconducting lead shield goes through its transition temperature. The external shield consists of 0.038 inch-thick sheets of μ-metal mounted on an aluminum frame. The shield provides an absolute field below 10 milligauss throughout most of its interior. We are utilizing a Model 1200 closed-cycle liquid helium refrigeration system from Koch with the new octagonal detector. We have modified the operation of the helium liquifier to maintain a constant dewar pressure relative to atmosphere. This modification eliminates SQUID signals resulting from the pressure variations of the original cooling-capacity control system. A very slow drift remains, caused by atmospheric pressure changes, but it is well below the bandwidth of our detection system and poses no degradation of our signal to noise ratio for monopoles. There are two significant advantages derived from using this system: lower long-term operating costs, and the virtual elimination of disturbances that are produced by liquid cryogen transfers. Now that the new system is cooled down and stabilized, we achieve essentially 100% live time.

The geometry of our detector provides greater confidence in coincidence correlations for true monopole events than our earlier detectors. A monopole can intersect no more than two loops, and the only trajectories intersecting one loop are those passing through the detector ends (which are not covered by detector loops) or through small gaps between the panels. We thus exclude from consideration all signals appearing in one loop only or in three or more loops. The response of the detector is calculated from a numerical simulation of a uniform flux of cosmic ray monopoles. This response is shown in Fig. 3 for positive signals in both loops; it is symmetric in the other quadrants and includes trajectories which intersect one or two wires.

A computer and strip-chart recorder collect data at 10 Hz and 0.1 Hz, respectively, from the SQUIDs, strain gauge, and other anti-coincidence instrumentation. The strain gauge senses mechanical disturbances which sometimes induce spurious offsets. Also recorded are a line voltage monitor, ultrasonic motion detector, and flux-gate magnetometer in the anti-coincidence instrumentation. We also have added a wide-band radio frequency voltmeter for EMI anti-coincidence.

We began obtaining low noise data on May 5, 1987 [8]. Figure 4 shows typical filtered data (one point every 10 sec) from the computer data acquisition system. Included is a calibration signal showing the signal to noise for a Dirac size magnetic charge. Figure 5 shows the high bandwidth data available around any events. This particular event was caused by a bump of the dewar system clearly seen in the strain

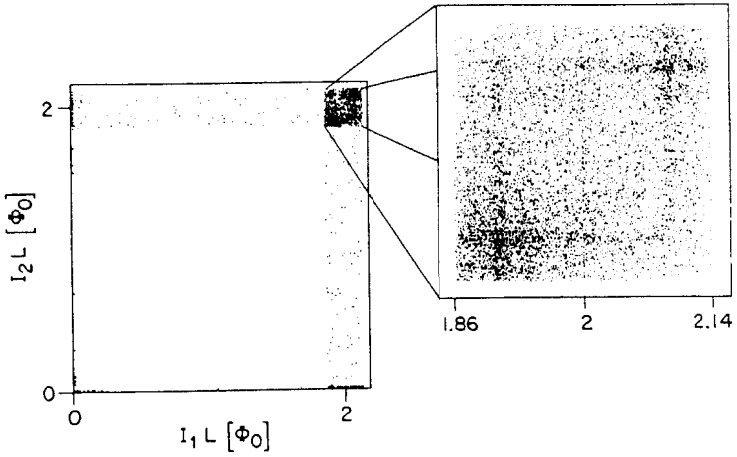

Fig. 3. Calculated response of the detector to a uniform flux of cosmic ray monopoles. The signal sizes for the two loops intersected by the monopole trajectory are plotted for each Monte Carlo event.

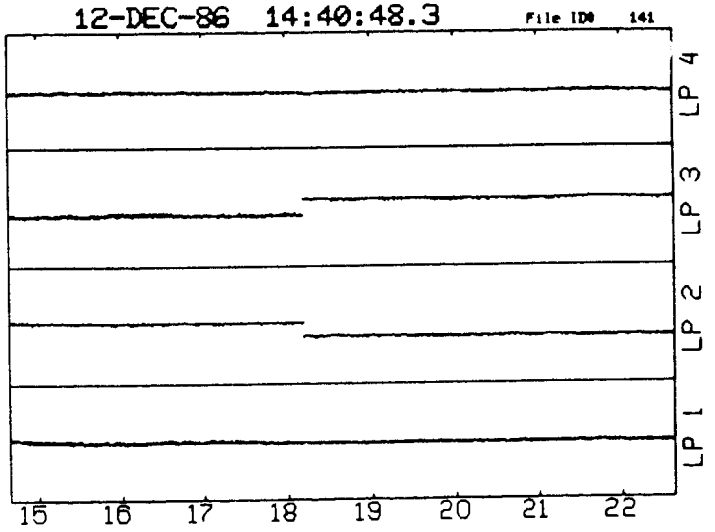

Fig. 4. Digitally filtered data (one point every 10 sec) from octagonal detector showing the first four SQUID channel readouts. The data include a Dirac sized calibration signal through two adjacent coils.

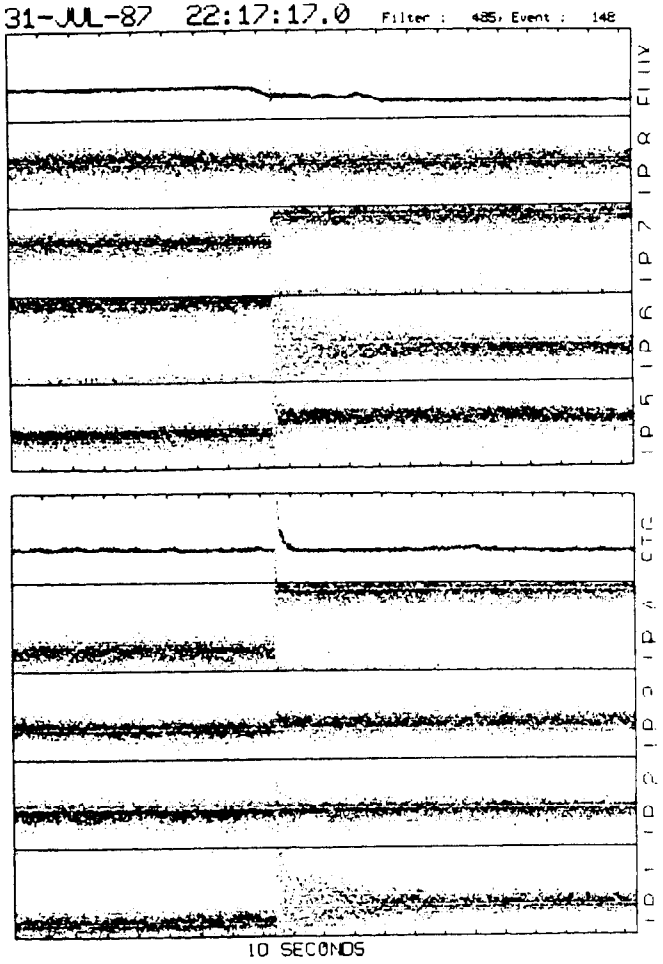

Fig. 5. High bandwidth data (twenty points per sec) from trigger showing the eight SQUID channels, the strain gauge channel and the external flux-gate magnetometer channel. This disturbance was caused by a bump to the dewar.

gauge and external flux-gate magnetometer channels. As of July 14, 1988, we have accumulated 6,000 hours of live time. A preliminary analysis of these data [8] contain no candidate events and set a limit of 7.8×10^{-13} cm^{-2} sr^{-1} s^{-1} (90% C.L.) for any particle flux of magnetically charged particles passing through the surface of the earth. We intend to run the detector continuously for at least three years.

Particle Flux Limits From Our Detector Exposures

In Fig. 6 we summarize the current status of our research efforts with respect to astrophysical bounds. The Parker bound as modified to include supermassive monopoles has a mass independent floor at ~10^{-15} cm^{-2} sr^{-1} s^{-1} and rises linearly with mass above ~10^{17} GeV/c^2 until it intersects the local dark matter bound around the Planck mass (10^{19} GeV/c^2). Since more recent unification theories suggest a monopole mass approaching the Planck mass, searches at a flux level of ~10^{-13} cm^{-2} sr^{-1} s^{-1} are particularly important. Also shown in Fig. 6 are possible monopole particle flux levels 2 to 3 orders of magnitude above the Parker bound. These models are based upon monopole plasma oscillations within the galaxy. Detailed computer simulations performed by the Cornell group confirm the stability of such solutions and to my knowledge they are not ruled out by any galactic observations.

The particle flux limit obtained from our three loop superconductive detector was 4.4×10^{-12} cm^{-2} sr^{-1} s^{-1} at 90% C. L. Four other groups (Chicago-FermiLab-Michigan; IBM, Yorktown Heights; Imperial College; and NBS, Boulder) had obtained similar limits, for a combined world limit of 1.4×10^{-12} cm^{-2} sr^{-1} s^{-1} at 90% C. L. In a preliminary analysis of 15 months of data from our new octagonal detector, we find no candidate events for the passage of a monopole through the detector and set an upper limit on such a particle flux of 7.8×10^{-13} cm^{-2} sr^{-1} s^{-1} (90% C.L.). In addition, the IBM, Yorktown Heights group is operating a 1 m$^2 \times 4\pi$ sr sensing area detector and has reported a similar preliminary result in slightly more run time. The combined world limit for velocity independent detectors is now ~ 3×10^{-13} cm^{-2} sr^{-1} s^{-1} (90% C.L.) and is shown in Fig. 6. Also shown is the limit our detector will achieve after three years of operation.

These data effectively rule out the plasma oscillation models and approach the mass-dependent Parker bound near the Planck mass.

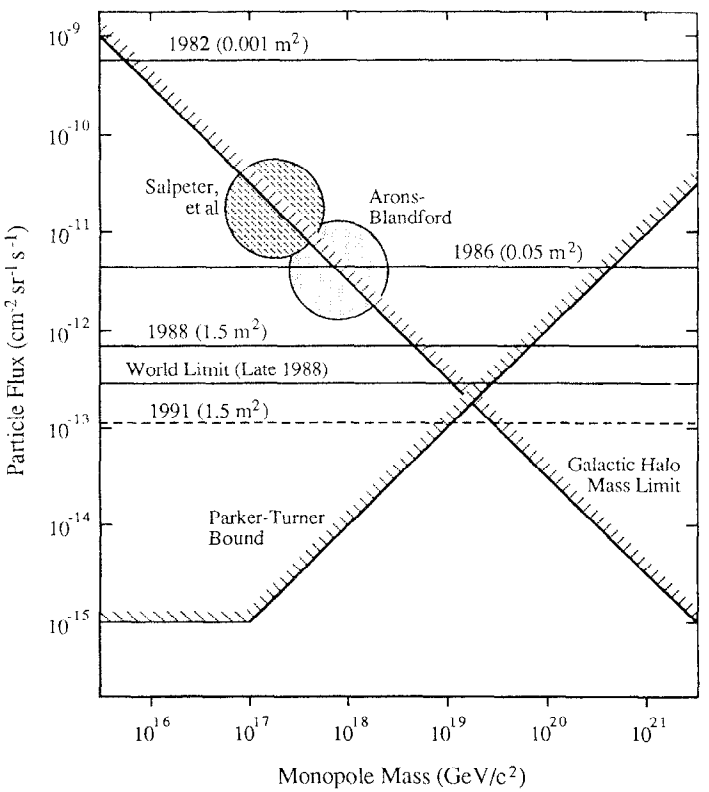

Fig. 6. Cosmic ray particle flux limits from our superconductive detectors compared with various astrophysical limits.

Acknowledgements

Our group at Stanford has included B. Cabrera, M. Huber, M. Taber and R. Gardner and J. Bourg. This research is funded in part by DOE Contract DE-AM03-76-SF00-326.

PART II:
SILICON CRYSTAL ACOUSTIC DETECTORS FOR NEUTRINOS

Introduction

Semiconductor diode particle detectors now provide the highest energy resolution (~ 3 keV FWHM for 1 kg) and the lowest thresholds available (~ 5 keV) for large mass detectors. In this energy range less than 30% of the deposition energy is converted directly into electron-hole pairs which produce the observed signal in the semiconductors, the rest forming phonons. The characteristic energies of these phonons is ~ 1 meV, 10^3 less than the excitation energy for an electron-hole pair in a semiconductor (~ 1 eV). Thus in principle, energy resolutions over an order of magnitude better are possible if the phonon signal is used. Recent work on bolometers, which sense the thermal phonons, has demonstrated an improvement in energy resolution (most recently 17 eV, FWHM, by Moseley, McCammon, et al [9]) by measuring the temperature rise in a small ultra-low heat capacity sensor (~ 10^{-5} g of silicon). B. Cabrera, L. Krauss and F. Wilczek [10] suggested scaling such bolometers up to a mass ~ 1 kg.

Motivated by this suggestion, our group, now composed of B. Cabrera, B. Young and A. Lee at Stanford and B. Neuhauser at San Francisco State University, has proposed direct sensing of the ballistic phonons produced by an event in a large insulating single crystal [11]. Since this wavefront carries information on the event total energy and location within these silicon crystal acoustic detectors (SiCADs), substantial improvements in background rejection are possible over detection schemes which measure total energy deposition only. A threshold of 1 keV or better is important for our primary interest in using SiCADs as neutrino detectors. For example, at power reactors all nuclear recoil signals from elastic neutrino scattering are below 10 keV with 60% above 1 keV, and a 1 kg SiCAD with a 1 keV threshold would register an event rate of ~ 100 events/day.

Ballistic Phonons from Point Events in Crystal Cubes

For a deposition of energy in a well localized volume within a single crystal of silicon, a thermal-like spectral phonon distribution is generated with a characteristic temperature of 10-20 K. This spectral distribution arises from the rapid decay of electron-hole excitations to the band edge, first generating very short wavelength phonons, which quickly relax to longer wavelength phonons within less than ~10 nsec. The decay rates are very strongly dependent on phonon energy ($\propto \nu^5$) and for wavelengths of several hundred lattice spacings further decays are entirely negligible. These longer wavelength phonons propagate throughout the crystal with little scattering and no dispersion. This mode has come to be called the the ballistic phonon mode [12].

An interesting and important aspect of ballistic phonon propagation is that strong focussing effects occur within the crystal, although the propagation is dispersionless. These focussing patterns, which have been well verified experimentally, permit three dimensional reconstruction of event locations within the crystal and can resolve tracks or multiple scattering events. We have performed Monte Carlo calculations on these effects [11]. Figure 7a shows the result of such a calculation for a point energy deposition within a silicon cube with all faces cut along [100] axes. The number of phonons used in the calculation is for a 1 keV energy deposition at a point within the crystal. It is clear that information on the event location as well as tracking information is available. We call such a detector a SiCAD (silicon crystal acoustic detector).

We have considered several phonon sensor configurations for the surface readout. The most promising to date consists of parallel strips on each face and provides spatial resolution based on the intensity and arrival time profiles across the sensors on each face (Fig. 7b). The sensors on the front and back faces perpendicular to the x (y and z) axis have their sensors parallel to the z (x and y) axis and thus can be used to determine the y (z and x) coordinate of the event location. As an example, the phonon energy flux intensities incident on each of the 384 strips for the event location in Fig. 7a is shown in Fig. 8. As can be seen, sharp peaks in each of the face intensity profiles locate the event to better than the width of a sensor and there is always at least one sensor with an intensity greater than ~ 2 % of the total energy in the event. To obtain a 1 keV energy threshold for event detection within a 1 kg SiCAD cube (for example to detect neutrino-nucleus elastic scattering at a reactor) then each parallel strip sensor must have an energy sensitivity of ~ 20 eV.

Superconducting Phonon Sensors

During this past year we have worked on two phonon sensor designs which utilize superconductivity. The first, called a transition edge sensor, is a simple single layer thin-film patterned into a series superconducting circuit and biased with a constant current. A phonon flux incident on the film will drive those portions normal where the phonon energy density has exceeded a critical phonon energy density. Then a voltage

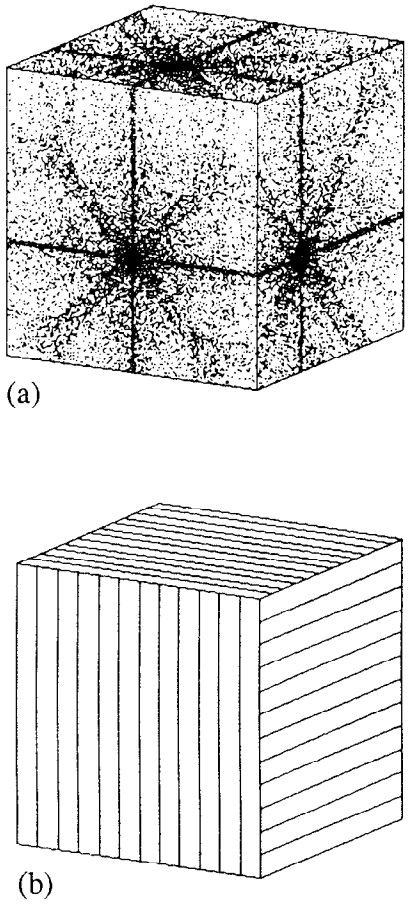

Fig. 7. (a) Calculated phonon energy density incident on silicon cube with [100] faces from point source within the crystal. (b) Arrangement of parallel senors on crystal faces.

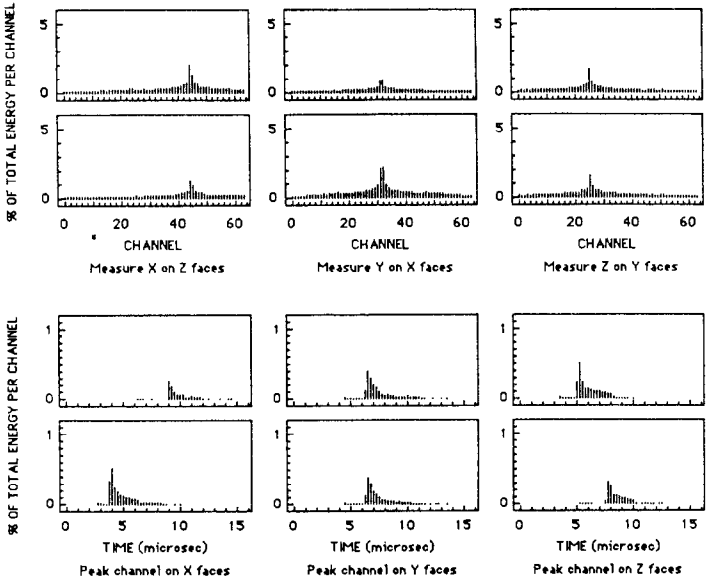

Fig. 8. Simulated signals from 64 channels per face. Lower two rows correspond to time evolution of peak channel on each face.

is seen across the circuit providing a signal which is proportional to the length of the circuit driven normal. If the current is below a latching critical current, then self-extinguishing pulses are seen, otherwise the resistive heating of the normal state is sufficient to expand the normal region across the whole circuit. Such a system is straightforward to manufacture using photolithographic techniques, but the physics governing the response is non-linear and complicated. Below we discuss this point in more detail.

A second device, the superconducting tunnel junction, possess the opposite properties. These are more difficult to manufacture, but the physics is more linear and simple. Such a device consists of two superconducting films separated by a thin oxide barrier (typically 1-2 nm). This device is biased with a constant voltage given by Δ/e, where Δ is the superconducting energy gap. Phonons from an event within the crystal reach the surface and enter the superconducting film. Once inside the superconducting, those phonons with energies greater than 2Δ (most) are strongly absorbed by breaking Cooper pairs and forming electron-like excitations called quasiparticles. In fact for phonon energies well above threshold, several Cooper pairs will be broken. These quasiparticles will tunnel across the oxide barrier providing a signal if the tunneling times are short compared to the quasiparticle recombination time. This condition is satisfied for $T < T_c/10$, where quasiparticle recombination with thermal quasiparticles is negligible. For these devices the tunneling current is proportional to the energy absorbed by the film as long as the quasiparticle density produced by the phonon flux remains dilute so that little self-recombination of the quasiparticles occurs prior to tunneling.

Given the results of our experiments during this past year and calculated improvements, we now believe that transition edge detectors can be used successfully to construct SiCAD detectors capable of a 1 keV energy threshold. Such devices will become our central focus during this next year for our first generation detectors. However, we also believe that better ultimate resolution and thresholds will be obtained with tunnel junctions, and we will maintain a parallel effort to develop this more difficult technology over a longer time scale. As available, we will substitute the tunnel junction technology into future generations of the SiCADs.

Experiments with Titanium Transition Edge Sensors on Silicon Wafers

Our first generation of SiCADs will utilize superconducting transition edge devices as phonon senors. These devices consist of thin superconducting lines deposited on the surfaces of the silicon crystals and biased with a constant current. For currents below a latching critical current, self-terminating voltage pulses are observed. These pulses are caused by the heating of line segments above the superconducting transition temperature. Last year, we demonstrated this technique using aluminum films with alpha particle sources [13], and most recently we have obtained a factor of one hundred improvement in energy resolution and threshold using titanium films in x-ray experiments [14]. These most recent sensors are made by depositing 40 nm of titanium on crystalline silicon wafers which are 1 mm thick. The polished wafer faces are perpendicular to the [100] axis. The meander pattern, shown schematically in Fig. 9, was produced using conventional photolithographic techniques and consist of 299 parallel lines each 2 μm wide with 3 μm space between lines. The pattern is aligned parallel to the [110] crystalline axis of the wafer. The active area of the pattern is 4.5 mm long and 1.5 mm wide. The normal resistance just above their superconducting transition temperature ($T_c \approx 312$ mK) is ~ 18 kW per line. These films have sharp transition widths of ≤ 5 mK (from 10% to 90% of the resistive transition), indicating homogeneous properties across the film. A typical superconducting to normal resistive transition for one of these patterns is shown in Fig. 10.

Here we describe two recent x-ray experiments. These were performed by Betty Young with a 24 μC source of ^{241}Am. The decay spectrum of ^{241}Am is dominated by two alpha particle energies at ≈ 5.5 MeV. In addition to these two alphas are a nuclear gamma at 60 keV and two atomic x-rays at 14 and 18 keV. An appropriate absorber placed in front of the source readily stops all of the alphas and essentially all of the 14 and 18 keV x-rays before they reach the sensor; however the 60 keV gamma rays, being much more penetrating, pass through the absorber attenuated in number by ~ 0.5. We used .005" (125 μm) thick foils of Sn and Pb as absorbers.

Using a cryopumped ^{3}He refrigerator at 0.3 K (described below) we biased the titanium/silicon devices at the foot of the resistive transition in temperature and below the latching critical current in bias current, and we observe self-terminating voltage pulses when the film is bombarded by phonons produced by the interaction of an incident x-ray (or gamma ray) within the Si substrate. These pulses occur because enough phonon energy from the photoelectron in the silicon reaches the Ti film to drive portions of the film normal. To estimate the threshold energy density E_ρ necessary for this superconducting to normal state transition, we integrate the heat capacity of the superconductor from the bias temperature to T_c:

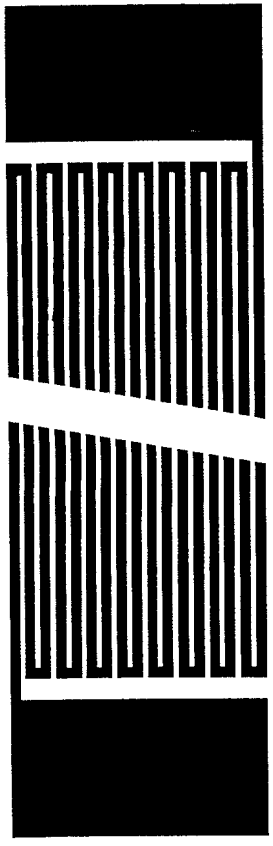

Fig. 9. Phototithographic patterning for titanium sensors.

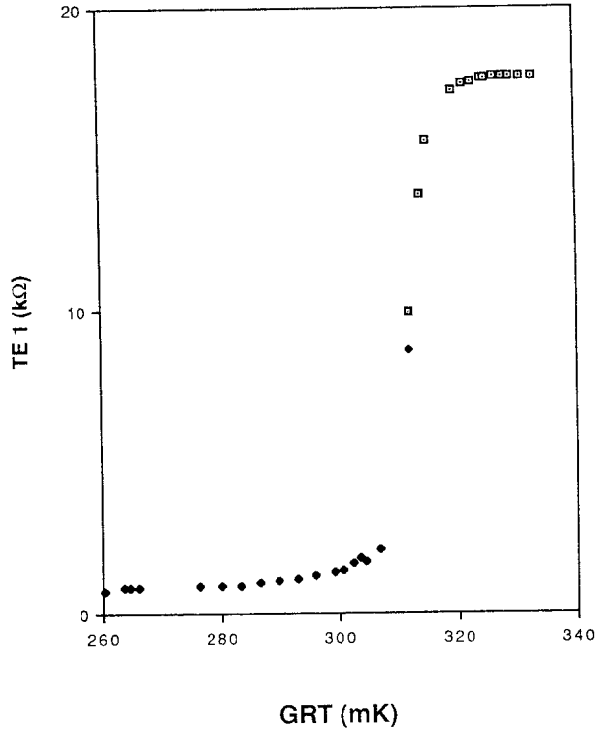

Fig. 10. Resistive transition as a function of temperature.

$$E_\rho = \int_T^{Tc} C_{es}(T)dT ,$$

where C_{es} is the electronic heat capacity below T_c as given by the BCS theory. We assume that the time constants are sufficiently long to allow quasi-thermal equilibrium. The asymptotic form near T_c is:

$$E_\rho \approx 5N(0)\,\Delta_0^2\,(1-T/T_c) ,$$

where Δ_0 is the gap at T = 0 and N(0) is the density of states at the Fermi surface in the normal metal.

For our Ti films, $N(0) \approx 4 \times 10^{22}$ cm^{-3} eV^{-1} and $\Delta_0 \approx 47$ μeV, yielding $E_\rho \approx 22$ eV/μm^3 at $T/T_c = 0.95$. In terms of the energy density per unit area of film, E_σ, we get $E_\sigma \approx$ (22 eV/μm^3) × (40nm) = 0.88 eV/μm^2. We may also estimate the minimum detectable energy for a Ti sensor as follows. In our current experimental setup we use a cryogenic GaAs MESFET voltage-sensitive amplifier (described below) which introduces an amplifier noise level of $\Delta V_{rms} \approx 1$ nV/$\sqrt{\text{Hz}}$ at 1 MHz. At $T/T_c \approx 0.95$ and a bias current (I_b) of 60 nA we can detect a minimum sensor resistance of $\Delta R_{rms} = \Delta V_{rms}/I_b = 17\ \Omega$. At $T \geq T_c$ the resistance of our sensor is ~ 18 kΩ per 2 μm wide line 5 mm long, or 8.5 Ω per 2 μm × 2 μm square of the Ti film. Therefore the area of film which corresponds to a normal area resistance of $\Delta R_{rms} = 17\ \Omega$ is (17 Ω/8.5 Ω) × (2 μm x 2 μm) = 8 μm^2. The minimum detectable energy deposited in the Ti sensor is then $\Delta E_{rms} < E_\sigma \times \text{Area}_{rms}$ = (0.88 eV/μm^2) × (8 μm^2) = 7 eV. The inequality holds because Joule heating contributes to the actual area driven normal.

Figure 11a shows (for I_b = 120 nA and T ≈ 286 mK) some typical single pulses, of ~ 10-15 μsec duration, resulting from the interaction of 60 keV gamma rays (from ^{241}Am) in the Si substrate of a TE sensor. In Fig. 11b (for I_b = 60 nA and T ≈ 299 mK), we have expanded the time scale to show the leading edge of each pulse with electronics-limited risetimes of ~ 140 nsec.

We mounted the ^{241}Am source such that its active area faced the backside of the 299-line sensor, and investigated the effect on detector response when various absorbers were placed between the source and sensor. We chose two convenient absorber materials (Pb and Sn) and used appropriate thicknesses such that we could study the TE response primarily due to 60 keV gamma ray radiation with zero incident alpha-particle flux, and essentially zero 14 and 18 keV x-ray flux. The measured count rates for all spectra obtained, for various operating temperatures, bias currents and

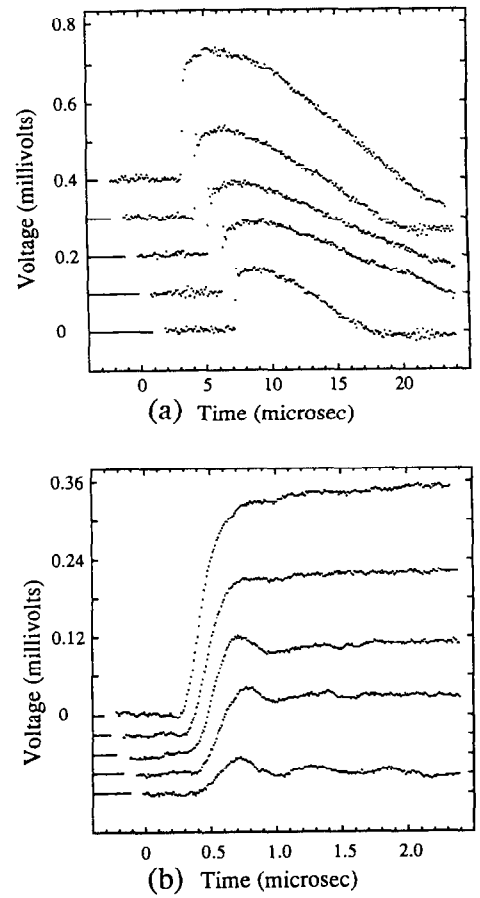

Fig. 11. (a) Individual pulses from 60 and 25 keV x-rays. (b) Leading edges of pulses with 140 ns rise time.

absorbers, were consistent with the calculated values.

Figure 12a is a pulse height spectrum obtained for the case of a .005" (125 μm) thick Pb absorber. The prominent peak towards the center of the spectrum is the photopeak due to interaction of 60 keV gamma rays in the Si substrate of the detector. The sharp feature at 11 keV is consistent with the position of the Compton edge for 60 keV gamma rays in silicon. In Fig. 12b, we show a pulse height spectrum under similar running conditions, but with a .005" Sn absorber. We note that the prominent features due to the 11 keV and 60 keV interactions appear, as expected, in the same positions as they did with the Pb absorber. Furthermore, in the Sn absorber spectrum, we observe an additional peak around 25 keV. This peak is readily recognized as that due to secondary emission of K_α x-rays from the Sn.

We can qualitatively reproduce typical pulse height spectra (such as those shown in Figs.12a and b) by applying Monte Carlo methods to a simple model of the detector response. We assume that an incident photon, if it interacts at all, interacts in the silicon substrate only once, and that this interaction is point-like. We imagine that, to first order, the phonon energy generated by such a scattering event spreads spherically outward through the crystal, producing heat spots on the surfaces. The energy density (per unit area) of such a heat spot is then given by

$$E_\sigma(\rho,z) = z\,E_0/[4\pi(z^2+\rho^2)^{3/2}]$$

where ρ is the radius of the heat spot, z is the perpendicular distance from the Si surface to the location of the scattering event, and E_0 is the total energy of the heat spot. Defining E_{sc} as the (minimum) critical energy density required to drive the detector film normal, we find that the area driven normal is given by

$$A(z) = \pi\rho^2 = \pi\,[(zE_0/4\pi E_{sc})^{2/3} - z^2] = \pi\, z_0^2\,[(z/z_0)^{2/3} - (z/z_0)^2]$$

where $z_0^2 \equiv E_0/(4\,\pi\,E_{sc})$.

The amplitude of the voltage pulse resulting from an interaction in the crystal is simply proportional to the amount of line driven normal, and the number of interactions producing pulses is proportional to (dA/dz)-1 for events uniformly distributed in z. For incident particles of given energies, we can then plot a theoretical pulse height spectrum for the Ti transition edge response -- as shown in Fig. 13a for the case of incident 30 and 60 keV photons.

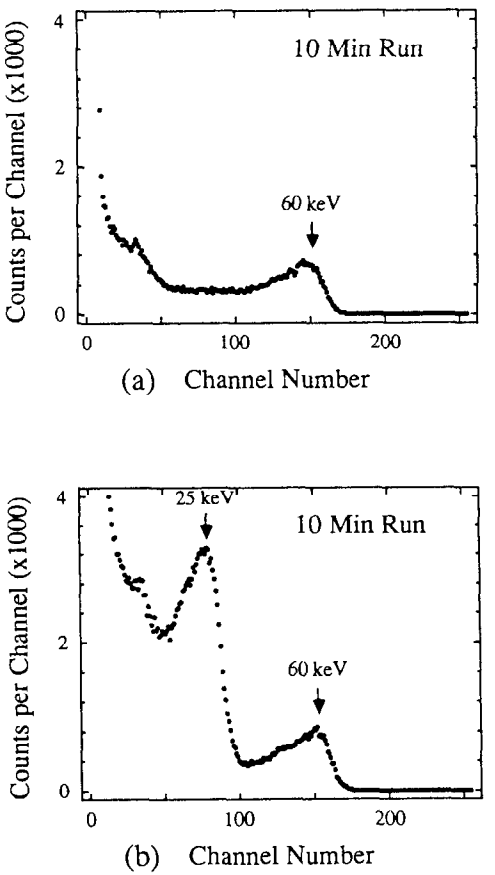

Fig. 12. (a) Pulse height spectrum for ^{241}Am source using Pb absorber. (b) Pulse height spectrum for same source and geometry using Sn absorber.

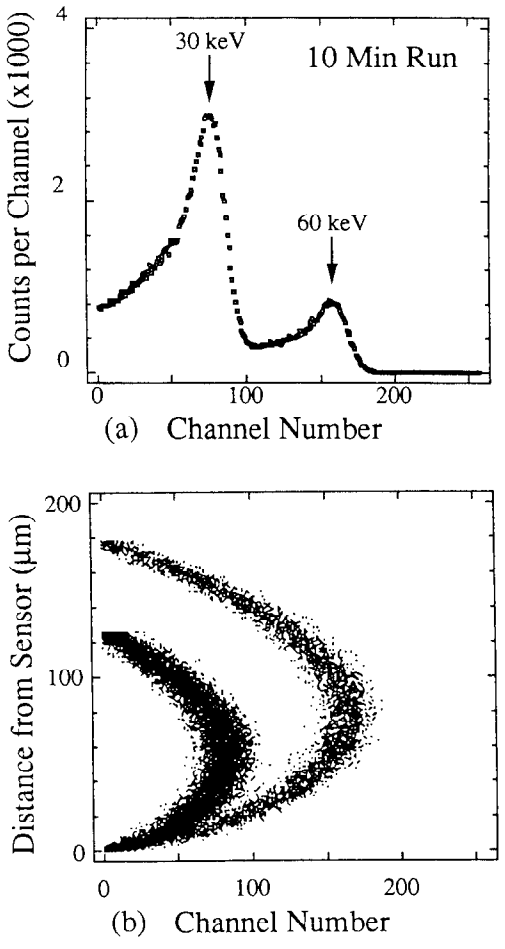

Fig. 13. (a) Monte Carlo generated pulse height spectrum from simple model. (b) Pulse height versus distance from titanium sensor function used in Monte Carlo.

Another interesting and very useful plot is generated by graphing the calculated normal area A as a function of interaction depth z for incident particles of a given energy. By considering various initial particle energies, one obtains a family of curves as shown in Fig. 13b. Assuming this simple heat spot model is valid to first order (i.e. neglecting focussing effects), we can extract important spatial information about events by comparing such curves with those obtained experimentally. We are in the process of carrying out the more computer intensive calculations which fully include phonon focussing effects.

We are currently working to fabricate 1 and 2 mm thick, double-sided (Ti meander patterns on both sides of the Si wafer) transition edge devices. These devices will enable us to do timing experiments and to obtain spatial information about each event occurring in the detector. We shall also be able to experimentally measure Fig. 13b and obtain an energy for each event. These improvements will take us one step closer towards our goal of developing a ≈ 1 kg scale SiCAD.

Cryopump ^{3}He Test Probe

We have performed these experiments using our laboratory-built fast-turn-around probe for device testing down to 250 mK and we are delighted with its performance. The probe was designed by Barbara Neuhauser, and we cannot overemphasize the importance of quick and inexpensive access to ultra-low temperatures for the successful development of both transition edge and tunnel junction devices. Until a well characterized design is available, many devices are either defective or do not perform as designed. We are now able to rapidly test a range of different devices and we have significantly increased our rate of progress.

This refrigerator is based on a sealed ^{3}He and charcoal cryopump design. In a typical run we begin precooling in the morning and by early afternoon we can begin taking data at ~ 270 mK. The initial liquid ^{4}He transfer (~ 5 liquid liters) lasts twenty-four hours allowing more than twenty hours of data below 300 mK.

Low Noise JFET Preamplifiers Operated Cryogenically

Another important component for our recent progress has been the use of cryogenic preamplifiers in the titanium sensor SiCAD experiments [15]. These were designed and constructed by Adrian Lee. The peak resistance of the titanium line, typically ~ 3 kΩ for 60 keV x-rays, would produce a large "RC" time constant if the first stage of amplification were at room temperature. This time-constant can have two

adverse effects. First if the rise-time is long compared to the signal duration, the signal will be truncated since the input pulse will start to decay before the output can reach its full pulse height. Second, a long time constant will make it harder to resolve the leading edge of the pulse. The spatial resolution of the detector will, in the future, depend on being able to resolve timing differences between different channels, which makes a long time constant undesirable. Mounting the first stage of amplification down in the cryostat reduces the capacitance seen by the amplifier dramatically. The GaAs MESFET (Plessy P35-1101), which we use, has the advantage of operation at 1.5 K and has very good noise above 100 kHz.

The total power dissipation of this amplifier is about 14 mW. The bandwidth of the amplifier is 10 MHz, but the rise-time is dominated by the RC time at the input. The gain of this device is very low, about 1.5 into 50 Ω, which necessitates a low noise room-temperature stage. We use a Trontech W50ATC instrumentation amplifier with a noise voltage of ~ 1.2 $nV/\sqrt{Hz}$ and a bandwidth from 10 kHz to 50 MHz.

Superconducting Tunnel Junctions as Phonon Detectors

On a longer time scale, we believe that the most promising sensors for high sensitivity phonon detection are superconducting tunnel junctions. For our proposed application as a SiCAD readout, we are beginning the development of aluminum junctions. These are formed by a ~ 200 nm thick aluminum film deposited directly onto the surface of the silicon crystal, followed by the formation of a thin oxide tunnel barrier (~ 1-2 nm thick) and then deposition of a second aluminum upper film. Phonons from an event within the crystal reach the surface and enter the aluminum, which has an excellent acoustic match with silicon. Once inside the superconducting aluminum, most phonons have energies greater than 2Δ (where Δ is the superconducting energy gap) and are strongly absorbed by breaking Cooper pairs and forming electron-like excitations called quasiparticles. In fact for phonon energies well above threshold, several Cooper pairs will be dissociated. We have performed junction tests down to a temperature of 250 mK utilizing the sealed ^{3}He system with a charcoal cryopump. Ultimately we intend to operate at $T < T_c/10$ (~100 mK for aluminum), where quasiparticle recombination with thermal quasiparticles is negligible.

Recently several European groups [16,17] have reported excellent energy sensitivities and resolutions for X-rays. The S.I.N. group [16] in Zurich, Switzerland has reported ~ 48 eV FWHM for the detection of low energy x-rays (~ 6 keV) using a 100 μm × 100 μm area Sn - Sn oxide - Sn junction at ~ 0.38 K. Pulse rise times of ~ 15 μsec were observed.

In fact, this sensitivity is already sufficient for our detection threshold requirement of 1 keV in a 1 kg SiCAD. However, the area of each parallel strip sensor needs to be ~ 1 cm^2, a factor of ~ 10^4 greater than used by the S.I.N. group. We are pursuing several techniques for obtaining comparable energy sensitivity in these much larger area tunnel junctions.

Conclusions

Ballistic phonon focussing effects greatly enhance the spatial resolution in silicon crystal acoustic detectors (SiCADs). Utilizing titanium superconducting transition edge devices as phonon sensors on the crystal surfaces, we believe that an energy threshold of ~ 1 keV can be achieved for a 1 kg SiCAD. Such a detector would be of great interest for a number of experiments including dark matter searches for weakly interacting neutral particle candidates and low energy neutrino experiments to set better limits on the neutrino mass.

Acknowledgements

The work at Stanford has been performed by B. Cabrera, C. J. Martoff, A. T. Lee, and B. A. Young. Also, B. Neuhauser now at San Francisco State University has participated extensively. This work has been funded in part by a Research Corporation Grant, a Lockheed Research Grant and DOE Contract DE-AM03-76-SF00-326.

References

[1] B. Cabrera, *Phys. Rev. Lett.* **48**, 1378 (1982).

[2] See the review article by D. E. Groom, *Phys. Rep.* **140**, 323 (1986).

[3] B. Cabrera, M. Taber, R. Gardner and J. Bourg, *Phys Rev Lett.* **51**, 1933 (1983); and R. Gardner, B. Cabrera, M. Taber and M. Huber, to be submitted to *Phys. Rev.* **D**.

[4] R. D. Gardner, Ph. D. Thesis, Stanford University (1987); and M. E. Huber, Ph. D. Thesis, Stanford University (1988).

[5] S. Bermon, P. Chaudhari, C. C. Chi, C. D. Tesche, and C. C. Tsuei, *Phys. Rev. Lett.* **55**, 1850 (1985).

[6] J. Incandela, M. Campbell, H. Frisch, S. Somalwar, M. Kuchnir, and H. R. Gustafson, *Phys. Rev. Lett.* **53**, 2067 (1984).

[7] S. Somalwar, H. Frisch, J. Incandela, and M. Kuchnir, *Nucl. Inst.* **A226**, 341 (1984).

[8] M.E. Huber, B. Cabrera, M.A. Taber and R.D. Gardner, *Jap. J. of Appl. Phys.* **26**, 1687 (1987); and M.E. Huber, B. Cabrera, M.A. Taber and R.D. Gardner, Proceedings of Applied Superconductivity Conference, San Francisco, Aug., 1988, in press.

[9] S.H. Moseley, J.C. Mather and D. McCammon, J. Appl. Phys. **56**, 1257 (1984); D. McCammon, S.H. Moseley, J.C. Mather and R.F. Mushotzky, J.Appl. Phys. **56**, 1263 (1984).

[10] B. Cabrera, L. Krauss and F. Wilzcek, Phys. Rev. Lett. **55**, 25 (1985).

[11] B. Cabrera, J. Martoff and B. Neuhauser, Stanford Preprint No. BC44-86.

[12] See for example: **Nonequilibrium Phonon Dynamics**, ed. W.E. Bron, NATO ASI Series **B124**, Plenum Press, N.Y., 1985. An excellent review of recent developments in phonon physics.

[13] B. Neuhauser, B. Cabrera, C.J. Martoff and B.A. Young, *Jap. J. of Appl. Phys.* **26**, 1671 (1987).

[14] B. A. Young, B. Cabrera, A. T. Lee and C. J. Martoff, Proceedings of Applied Superconductivity Conference, San Francisco, Aug., 1988, in press.

[15] A. T. Lee, Stanford Preprint No. BC73-88.

[16] D. Twerenbold, Europhys. Lett. **1**, 209 (1986).

[17] H. Krauss, T. Peterreins, F. Probst, F.v. Feilitzsch, R.L. Mossbauer and E. Umlauf, Europhys. Lett. **1**, 161 (1986).

Cosmic Relics From The Big Bang *

Lawrence J. Hall

Department of Physics
University of California
and
Theoretical Physics Group
Physics Division
Lawrence Berkeley Laboratory
1 Cyclotron Road
Berkeley, California 94720

Abstract

A brief introduction to the big bang picture of the early universe is given. Dark matter is discussed; particularly its implications for elementary particle physics. A classification scheme for dark matter relics is given.

*This work was supported in part by the Director, Office of Energy Research, Office of High Energy and Nuclear Physics, Division of High Energy Physics of the U.S. Department of Energy under Contract DE-AC03-76SF00098 and in part by the National Science Foundation under grant PHY85-15857.

Table of Contents

(I) The Importance Of Cosmic Relics

It is probable that the next leap forward in our understanding of particle physics will come from accelerator experiments. There are many possibilities: unexpected decay modes of K, D, B, μ, τ, Z particles and the discovery of new particles at high energies are two clear examples. Accelerator physics is crucial in unravelling the origin of electroweak symmetry breakdown. It will also shed light on flavor physics: at the very least we can learn how fermion masses are described at the TeV scale.

It is also quite possible that the next major advance in particle physics will come from astrophysics and cosmology. Most astrophysics and cosmology is done for other reasons: the questions being addressed have their own intrinsic worth. What is the nature of such objects as supernova and quasars? How did the observed mass distribution of the universe come about? What triggered clustering into galaxies, why are there so many varieties of galaxies, why do they have the size they do, and why do they themselves form clusters of galaxies? For a particle physicist perhaps the most exciting thing about astrophysics and cosmology is that there seems to be an endless succession of interesting unanswered questions. However, in these lectures I want to take a more limited viewpoint; what can we hope to learn about particle physics from astrophysics?

In fact this still leaves a wealth of possibilities open. We can certainly use our understanding of various astrophysical objects to place limits on new particles. For example, scalar particles with a mass of less than a keV and long mean free paths could be emitted from the entire volume of a star, and not just form its surface, so the existence of these particles is severely constrained. Perhaps the best example is the supernova which went off in a nearby galaxy last year, SN1987A[1]. Although the mass limit or ν_e from this event turned out to be remarkably close to that from laboratory experiments, we did learn a great deal about particle physics from SN1987A. We learnt about other properties of ν_e: its lifetime, electric charge, magnetic moment, mixing and right-handed currents. Perhaps we even learnt more about ν_τ than we did about ν_e. Since we are now sure of the size of ν emission from a supernova we now know that a supernova per century in our galaxy is populating the galaxy with ν_τ. If ν_τ is heavy it could decay giving γ or $e^\pm$; in either case very stringent lifetime limits can be placed from observational limits on X and γ-ray backgrounds. We now have great confidence in these decade old limits [2].

I will reduce my scope again, and concentrate on the question of dark matter and its implications for particle physics. There is a great deal of evidence that there is much more to the universe than meets the eye. I will not discuss this evidence; there are now several books on the subject [3,4]. It is worth looking at the evidence and thinking it over for yourself. A new experimental field is opening, that of searching for dark matter [5], and we should be sure of its foundation. A typical piece of evidence has the following form: a system will be observationally analyzed to determine the mass and velocities of its constituents. One then asks whether this is a gravitationally stable system or whether more, unobserved mass is needed to stabilize it. For a great many systems; for example, stars in the local neighborhood of our galaxy, hydrogen clouds in our and other spiral galaxies, hot gas in elliptic galaxies and even for galaxies in the whole universe, it does seem that a great deal of extra mass is required. Since we have not detected this matter by means other than this gravitational dynamics, we call it dark matter.

You might guess that there is virtually no constraint on the nature of dark matter: "if we cannot see it, surely it could be anything." As with most statements containing the word "surely" it is completely false. We have three very powerful constraints which restrict the nature of dark matter:

1. We know the location of the dark matter. (Of course there could also be dark matter in locations other than those we have studied.)

2. We know that it is dark. This is especially important for the dark matter in the local neighborhood. If the dark matter is composed of particles of mass m it is raining down on us with a flux of $\simeq 10^7/(m/GeV)cm^{-2}s^{-1}$ and we just cannot see it.

3. Dark matter should result from a reasonable big bang cosmology. If you start the big bang off with a given set of particles with given interactions they typically annihilate and do not survive until today. Requiring survival with the observed abundance is a very powerful constraint on any relic object.

To implement the third constraint, it is necessary to have an understanding of the hot big bang model of the early universe. In the next section we discuss this picture, which emerges uniquely from three cornerstones: the isotropy of the 3^0K microwave background radiation, the general theory of relativity and the $SU(3) \times SU(2) \times U(1)$ gauge interactions of the elementary particles. In Section III I discuss three general points which have to do with dark matter. I give a few remarks on the experimental results, I discuss whether the dark matter could be baryonic or whether it requires an extension of particle physics to include exotic stable objects, and finally I consider inflation and its implications for dark matter. In Section IV I introduce a classification scheme for dark matter candidates and give examples and experimental signatures.

Why have I chosen to orient these lecture at the question of cosmic relics? Cosmic relics, both visible baryonic and dark non-baryonic, are the best evidence that we have for particle physics beyond the standard model.

(II) A Brief Introduction To The Big Bang

The purpose of this section is to present the framework of the big bang cosmology in a simple and brief way. Many important details will be omitted and can be found together with references, elsewhere [6,7,8]. Emphasis will be on ideas rather than formalism.

A simple interpretation of the Hubble red-shift law for distant galaxy recessional velocities and of the isotropy of the 3^0K microwave radiation is that the present universe is expanding and has evolved from an early era of a hot expanding homogeneous and isotropic plasma. This system can be described at any era by the plasma temperature $T(t)$, its pressure $p = p(\rho)$, and the chemical potentials for species i $\mu_i(T)$. These are determined from a knowledge of the constituents of the plasma and their interactions. The expansion itself is described in terms of the Robertson-Walker scale factor $R(t)$ which appears in the metric:

$$d\tau^2 = dt^2 - R(t)^2 \left(\frac{dr^2}{1 - kr^2} + d\Omega^2 \right) \tag{2.1}$$

$d\Omega$ is the usual element of solid angle, t the proper time at any location of fixed r, and r is a dimensionless coordinate. The proper distance between fluid elements at r_A and r_B at time t is given by

$$d(t) = \int_{r_A}^{r_B} \frac{R(t)dr}{\sqrt{1 - kr^2}}. \tag{2.2}$$

Hubble's law, $\dot{d} = Hd$, follows directly from this, with $H = \dot{R}/R$ being the spatially constant but time dependent Hubble parameter. I will scale the coordinate r so that the dimensionless constant k either vanishes or has unit magnitude. If $k = +1$ the universe is closed, if $k = -1$ it is open, while if $k = 0$ it is critical. Although k is crucial for the future behavior of the universe it is frequently unimportant during early times and can be set to zero.

The present value of the Hubble parameter has been measured to be

$$H_0 = 100h \ km \ s^{-1} Mpc^{-1} \tag{2.3}$$

with $1/2 \lesssim h \lesssim 1$. In many cosmologies H_0^{-1} sets the scale for the age of the universe. For example suppose the expansion of the universe is given by some power law $R = R_0(t/t_0)^n$, then $H = n/t$ and $t_0 = nH_0^{-1} \simeq nh^{-1}10^{10}$yr.

The simple picture of the expanding universe as the surface of an inflating balloon is helpful. Commoving coordinates are fixed to the surface of the balloon. A photon at time t_A with wavelength λ_A will have a stretched wavelength at some later time t_B given by $\lambda_B/\lambda_A = R(t_B)/R(t_A)$. The red-shift of a photon emitted at t_A and received at t_B is defined to be $(\lambda_B - \lambda_A)/\lambda_A$ and for $t_B >> t_A$ this just becomes $R(t_B)/R(t_A)$.

The dynamics of the expansion is given by Einstein's field equations for general relativity applied to the metric of equation (2.1)

$$\left(\frac{\dot{R}}{R} \right)^2 = \frac{8\pi G}{3}\rho - \frac{k}{R^2} \tag{2.4}$$

where G is the Newtonian gravitational constant, and ρ is the total energy density at any point in the homogeneous fluid at time t. A useful mnemonic for this equation is inspired by Newtonian ideas as depicted in Figure 1. Imagine the expansion of a small spherical commoving region with a unit test mass at coordinate radius $r << 1$. The sum of its kinetic and potential energies $\dot{R}^2/2 - GM/R$, where M is the mass enclosed in the unit sphere, is just $-k/2$. Thus if $k = -1$

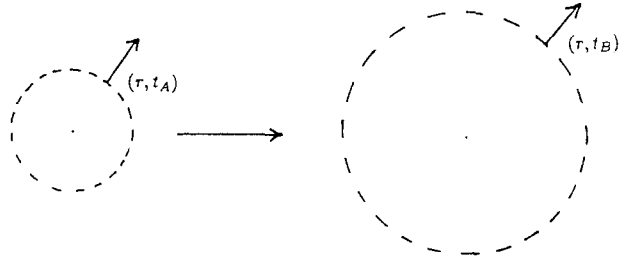

Figure 1

Newtonian mnemonic for interpretation of $\dot{R}/R$.

the total energy is positive and the universe is open. The Newtonian picture is not correct for the whole system. However, equations (2.4) is correct as it follows from general relativity. It is about the most important equation of big bang cosmology since it tells you how fast the universe is expanding at any time. If the universe is flat, $k = 0$, equation (2.4) can be solved to give $\rho \propto H^2$. This critical density today is

$$\rho_c = \frac{3}{8\pi G} H_0^2 \simeq 10^{-5} GeV cm^{-3}. \tag{2.5}$$

I like to interpret the right–hand side of equation (2.4) as the terms which drive the expansion. At early times we know that $G\rho >> R^{-2}$ so the expansion of the universe is driven by energy density rather than curvature. We do not know what dominates the driving today; it could be the curvature term. If $G\rho_0$ dominates in driving the expansion today it is probably only through the invisible or dark components of ρ_0. The energy density today has various components: $\rho_0 = \rho_{VB} + \rho_{EM} + \rho_\nu + \rho_{DM} + \rho_V$ (VB is visible baryons, EM i.e. the electromagnetic content of the universe dominated by the 3^0K microwave radiation, ν refer to massless neutrinos, DM to dark matter and V to vacuum energy ie. a cosmological constant). Defining Ω_i to be the ratio of density in any component i relative to the critical density

$$\Omega_i = \frac{\rho_i}{\rho_c} \tag{2.6}$$

we know that $\Omega_{EM} \simeq 0(10^{-5}), \Omega_{VB} = 0(10^{-2})$ and for very light neutrinos $\Omega_\nu = 0(10^{-5})$. When we observe distant galaxies we see them as and where they were during a previous era: that when the detected photons left them. This leads to a violation of Hubble's law which is dependent on the deceleration parameter $q_0 = -\ddot{R}R/\dot{R}^2|_{t_0} = \Omega_0/2$. Experimental measurements of q_0 lead to $\Omega_0 \lesssim 2$. Hence we know from very direct observations that

$$10^{-2} \lesssim \Omega_0 \lesssim 2. \tag{2.7}$$

If Ω_0 is larger than Ω_{VB} the difference is predominately due to the presence of dark matter.

At early times during the big bang the temperature was high so that particle number densities in the plasma were large enough to give reaction rates sufficient to maintain thermal equilibrium between many species of particle. For a reaction rate to be fast enough to maintain thermal equilibrium it should basically be faster than the expansion rate of the universe, that is the mean free time for interactions

should be less than the age of the universe at the era under consideration. For example, for a reaction $AB \to X$ to keep particle A in thermal equilibrium at time t requires the reaction rate

$$\Gamma_{AB\to X} = n_B \langle \sigma_{AB\to X} v_{AB} \rangle \; > \Gamma_{exp}(t) = H(t) = \frac{\dot{R}}{R} \tag{2.8}$$

where $R_{A,B}(t)$ are particle member densities at time t and $\langle \sigma_{AB\to X} v_{AB} \rangle$ is the thermally averaged cross section times relative speed for this process at temperature $T(t)$. In thermal equilibrium the particle number densities are given by

$$n_i^{(e)}(T) = \frac{g_i}{8\pi^2} \int \frac{d^3\vec{p}}{e^{\frac{E-\mu_i}{kT}} \pm 1} \tag{2.9}$$

where g_i is the number of spin states of particle i, $\mu_i(T)$ is the chemical potential and ± 1 refers to fermions and bosons. The particle mass m_i enters via $E^2 = \vec{p}^2 + m_i^2$. Useful order of magnitude approximations are

$$n_i^{(e)}(T >> m_i) \; \sim T^3 \tag{2.10a}$$

$$n_i^{(e)}(T << m_i) \; \sim (m_i T)^{3/2} e^{(\mu_i - m_i)/T}. \tag{2.10b}$$

In the standard hot big bang model ρ is dominated by contributions from relativistic species (with $T >> m_i$, so $n_i \sim T^3$) for virtually all times for which there is a plasma which is thermally coupled; that is for all temperatures above about 1 eV. Although this is not the case for non–standard cosmologies with heavy long–lived exotic particles or with periods of inflation, the radiation dominated era is a very important one. During this era, since $n \sim T^3$ and $< E_i > \sim T$, we have $\rho \sim T^4$, so that Einstein's equation has the form

$$\dot{R}/R \sim (G\rho)^{1/2} \sim T^2/M_p. \tag{2.11}$$

When the universe expands it does work and hence cools; there must be a relationship between $T(t)$ and $R(t)$. During the radiation dominated era the relationship is that RT is constant. This is equivalent to the entropy in a commoving volume (one which grows as R^3) being constant. The gas is expanding adiabatically under most circumstances, so that RT = constant holds more generally, and is violated only when there is a mechanism which creates entropy. Using $\dot{R}/R = -\dot{T}/T$ together with (2.11) allows for a solution for $\dot{T}(t)$ during the radiation dominated era: $t \sim M_p/T^2$. The constant of proportionality does have a weak dependence on T. Near an MeV:

$$\frac{t}{sec} \simeq \left(\frac{MeV}{T}\right)^2. \tag{2.12}$$

How does this hot plasma at $T > eV$ evolve into the universe we see today? At first sight they seem very different: apart from local hot–spots, we see a very cold universe with few particle interactions, also it is grossly inhomogeneous on all scales up to at least 50 Mpc. However, we have come to realize that it is perfectly reasonable that the plasma of the hot big bang should evolve into a cold, non–interacting, inhomogeneous universe. As the temperature of the plasma drops all the particle reaction rates $\Gamma_R(T) \sim n < \sigma v >$ fall much more rapidly than does the expansion rate $\Gamma_{exp}(T)$, so that for each reaction there is some critical temperature beneath which it is "frozen out". Furthermore, once the electromagnetic scattering processes freeze out, there is no longer any pressure to prevent mass perturbations in the plasma from undergoing gravitational growth. Although we are far from a complete picture of the resulting clustering, it can only stop once gravitationally stable systems, such as galaxies and stars, are formed.

There is a very basic question about the evolution from the hot plasma to the observed cold, inhomogeneous universe that we must address. What determines the abundance of all the stable fundamental particles in the universe today? Is it reasonable that the universe we see should contain p, e, γ in the observed ratios? If we introduce exotic stable particles into theories of particle physics can we calculate their present abundance in the universe?

The calculation of these abundances is very simple [9]. Consider a stable particle species i. As long as a process which changes the number of i particles is in thermal equilibrium, $n_i(T)$ will be given by equation (2.9). Suppose T_{if} is the freezeout temperature of the last such reaction to be in thermal equilibrium. At lower temperatures since the i particles do not decay and assuming they are not produced (for example by the decay of some other species) we have $n_i(t) \simeq (R(t)/R(t_f))^3 n_i^{(e)}(t_f)$ where t_f is the time corresponding to the temperature T_{if}. After freezeout the remaining i particles are just diluted by the volume expansion. Since $R \sim T^{-1}$ it is convenient to consider "reduced" number densities $f_i(t) = n_i/T^3$ which become independent of t after freezeout. Note that for a particle which is still relativistic at freezeout ($m_i < T_{if}$), $n_i^{(e)}(T_f)$ is given by (2.10a) so

that the relic abundance $f_i \simeq 1$. However, if the particle was non-relativistic at freezeout $n_i^{(e)}(T_f)$ is given by (2.10b) so that $f_i \simeq \left(\frac{m_i}{T}\right)^{3/2} \exp\left((\mu_i - m_i)/T_{if}\right)$ which can reflect an enormous Boltzman suppression at freezeout for small μ_i and $m_i >> T_{if}$.

The above relic abundances are approximate since freezeout is treated as a sudden process, which it is not. The physical ideas are correct however as can be seen by numerical integration of the rate equation. For example, consider a particle x for which the last x number changing process to freeze out is $x\overline{x} \rightarrow \cdots$ Ignoring a possible chemical potential the rate equation is

$$\frac{dn}{dt} = -\frac{3\dot{R}}{R}n - < \sigma_A v >_{x\overline{x}\rightarrow\cdots} (n^2 - n^{(e)2}) \tag{2.13}$$

where $n_x = n_{\overline{x}} = n$. This has been numerically integrated and the freezeout behavior is shown in Figure 2. A useful analytic approximation for the freezeout abundance is

$$f_{xf} = \frac{n_{xf}}{T^3} \simeq \frac{\ln Z}{Z} \tag{2.14}$$

where $Z = m_x M_p \langle \sigma_A v \rangle$, the freezeout temperature $T_f \simeq m_X / \ln Z$ and the result is valid for large Z.

For very large $Z, f_{xf} \simeq Z^{-1}$, so that $\Omega_x \simeq (m_x f_{xf}/T_0 f_{\gamma f})\Omega_\gamma$ or

$$\Omega_x \sim \left(\frac{1}{10^3 TeV}\right)^2 \frac{1}{< \sigma_A v >}. \tag{2.15}$$

This result has one astounding consequence which is rarely mentioned. Even if $x\overline{x}$ annihilation proceeds via strong interactions it will be bounded by $< \sigma_A v > \lesssim \frac{1}{m_x^2}$ on dimensional grounds. Hence $\Omega_x \lesssim 2$ implies $m_x \lesssim 10^3 TeV$. It is not possible to have a stable fundamental particle with mass larger than $10^3 TeV$. This is encouraging, if the dark matter is composed of fundamental particles it is not possible to push their mass arbitrarily high, and consequently their number density and flux at the earth cannot be made arbitrarily small. This bound could only be avoided by having a phase transition give a mass to x after it has already frozen out at a low abundance.

What are the relic abundances of the four known particles (ν, γ, e, p) which we believe to be stable? The photons are massless and have relativistic freezeout $f_\gamma = 0(1)$. Photons are the only relics which were relativistic at freezeout which we have observed. They play a crucial role in determining the age of the universe.

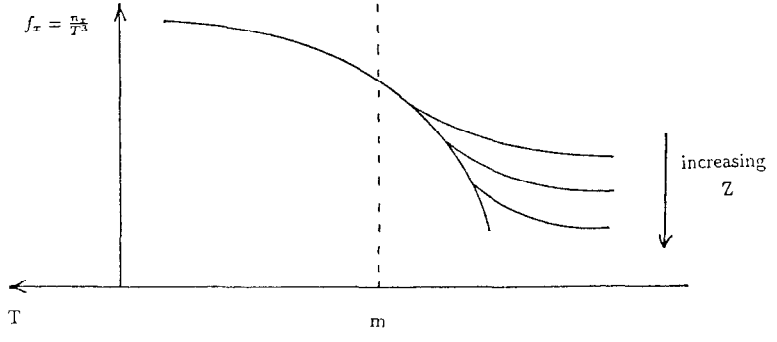

Figure 2

Schematic illustration of particle abundance freezeout behavior

We believe the observed 3^0K microwave background radiation is the photon relic of the hot big bang. These photons are no longer coupled to any plasma, but they maintain a thermal distribution with wavelength being stretched by the universal expansion: $\lambda \propto R$, so the effective temperature which describes the distribution $T \propto R^{-1}$. Knowing $T(t)$ from Einstein's equation then gives the age of the universe t_0 from the observation of $T_0 = 3^0K$. Of the neutrinos of the standard model, ν_e and ν_μ are known to be sufficiently light that they also were relativistic at decoupling: $f_\nu \sim 1$. If they are stable and massless they contribute roughly the same to ρ_0 as do photons: $\Omega_\nu(m_\nu = 0) \simeq 0(10^{-5})$. If their mass were $10^5 T_0 \simeq 30eV$ they would give $\Omega_\nu(m_\nu = 30eV) = 0(1)$. This could also be true for a light tau neutrino.

If m_{ν_τ} is above 1 MeV, ν_τ would freezeout non-relativistically. For the non-relativistic freezeout of a heavy neutrino $< \sigma_A v > \sim G_F^2 m_\nu^2$ and equation (2.15) gives

$$\Omega_\nu(m_\nu) \sim \left(\frac{m_\nu}{10GeV}\right)^2. \tag{2.16}$$

(Since we have dropped factors of 4π equations (2.15) and (2.16) are not numerically accurate). This is excluded for a stable heavy ν_τ. If 1 MeV $< m_{\nu_\tau} <$ 35 MeV, then ν_τ must be unstable. In this case the decay products typically lead to other astrophysical or cosmological problems: I expect m_{ν_τ} to be less than about 30eV. Evidence to the contrary would have very exciting cosmological implications. Equation (2.16) applies to any neutral fermion whose dominant annihilation occurs via W and Z exchange. Such a particle with mass in the range 1-10 GeV is a good candidate for the dark matter.

At temperatures above the QCD phase transition u, d and s quarks are in thermal equilibrium with the eight gluons, and these strongly interacting particles are all relativistic. For simplicity assume that by $T = 50$ MeV the phase transition is completed and the baryon number is carried predominantly by p and n. (The picture could be much more complicated; supercooling could take place or baryon number could get trapped into quark nuggets for example.) Reactions such as $p\overline{p} \rightarrow n(\pi)$ rapidly thermalize the baryon distributions. If the chemical potential for baryon number vanishes, $\mu_B = 0$, then the freezeout abundance of p and $\overline{p}$ is given by equations (2.14), and Ω_B is given by (2.15). Since $< \sigma_A v > \sim m_p^{-2}$ this gives $\Omega_B \sim 10^{-12}$. We conclude that the standard big bang scenario requires $\mu_B \neq 0$, i.e. it requires a cosmological baryon excess to be present by $T = 50$ MeV. This conclusion is not altered by more complicated assumptions about the nature of the QCD phase transition. You might argue that it was obvious that we would need this: we do not see any evidence of primordial anti-matter anywhere in the solar system or indeed anywhere in the cluster of galaxies of which our Milky Way is a member. The only way that the entire universe could be baryon symmetric is if there are enormous domains, some baryonic and some anti-baryonic. This domain structure must have existed at $T \sim 50$ MeV to prevent over-annihilation of p with $\overline{p}$. Although an era of inflation could produce such enormous domains it has not been possible to write down a complete cosmology incorporating such a scheme.

Charge neutrality of the universe implies that the cosmic asymmetry in electrons is equal to that in protons, at least for a closed universe. This does not necessarily mean that the chemical potential for lepton number $\mu_L = \mu_B$, since there could be additional lepton asymmetries carried by neutrinos.

To obtain $\Omega_B = 0(10^{-2})$ it is necessary, just before the QCD phase transition, to have a quark asymmetry $(n_q - n_{\bar{q}})/n_q = 0(10^{-9})$. The absence of antimatter today would lead us to expect a non-zero cosmic baryon asymmetry. The importance of the standard big bang framework is that it allows us to calculate how big such an asymmetry should be. The asymmetry today is enormous and obvious because essentially all anti-protons come across a proton to annihilate. However early on in the big bang it would not have been very obvious, it was a one part in a billion effect. Although small it is of crucial importance: it is non-zero and it must have come from somewhere. Assuming that it is not just a randomly adjusted initial condition to the universe, it must have been generated during an era of the universe when CP and B violating processes occurred in a non-thermal equilibrium environment. This is fascinating because it implies particle physics beyond the standard model. It also implies additional phase transitions at some early era, although the nature of the phase transition (inflation, gauge symmetry breaking ..) is pure speculation at the moment.

I will end this section with a brief summary of the main events in the hot big bang cosmology as inspired by the $SU(3) \times SU(2) \times U(1)$ model of particle gauge interactions. These events are shown in Figure 3. This model should be good up to a few hundred GeV so this is where we begin. It is likely, but not necessary, that the cosmic baryon asymmetry exists even at this high temperature. At a

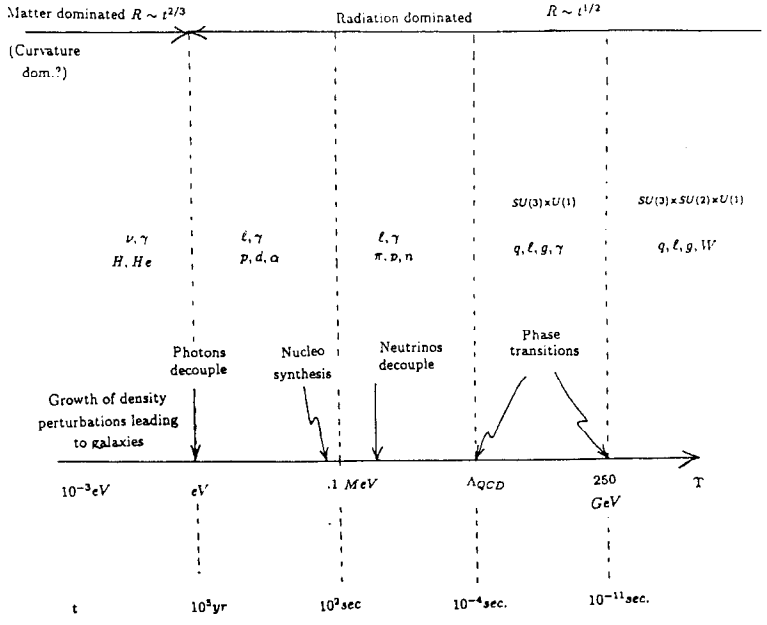

Figure 3

Important events in the hot big bang cosmology for $T < 1$ TeV.

temperature near 250 GeV there is a phase transition at which the W, Z bosons acquire a mass as well as all the quarks and charged leptons. If the Higgs boson is light considerable supercooling (but insignificant inflation) is possible at this phase transition. I know of no feature or attribute of this phase transition which leads to observable cosmological consequences today. As the temperature drops below M_Z, M_W, m_b, m_τ, and m_c these particles are depleted by annihilation until they freezeout. Any relic abundance rapidly decays, again leaving no observable footprints. After the QCD phase transition essentially every anti-baryon annihilates with a baryon so the baryon excess now becomes an important component to the plasma rather than a miniscule asymmetry. The QCD phase transition if it is first order may lead to density inhomogeneities which could effect primordial abundance of the light elements.

At the MeV era many important events take place. This era, like the previous ones, has the expansion rate $\dot{R}/R$ driven by relativistic radiation energy density, so that the time–temperature relation is as given in equation (2.12). Since $m_n - m_p = O(MeV)$ neutron decay becomes important beneath an MeV in reducing the neutron to proton number density ratio. Since nuclear binding energies are $O(MeV)$ it also becomes possible to form nuclei which are not immediately photo–disassociated by the plasma. Most of the neutrons which escape decay are processed into ^4He nuclei, with trace quantities ending up in $^2H, ^3He$, and ^7Li. The abundance of these nuclei predicted by nucleosynthesis in the standard hot big bang are in good agreement with primordial abundance inferred from a variety of observations. This is a very important success; there is direct experimental support for the big bang model back to times of $O(1\,\mathrm{sec})$. The success has important consequences for deviations from the standard big bang and is especially important to the issue of whether dark matter could be baryonic, as we will discuss in the next section. At $O(MeV)$ the light neutrinos decouple and $e^+e^- \to \gamma\gamma$ depletes the charged leptons down to essentially just the electron excess. Hence the interacting plasma now contains electrons, protons and photons in the ration $1:1:O(10^9)$, and also contains the heavy nuclei. This dilute plasma continues to cool until $T = O(eV)$. At this point $ep \to H\gamma$ takes place as the reverse photodisintegration process freezes out. Once neutral hydrogen is formed the plasma ceases to be interacting, the photons now free–stream and are red–shifted by a factor of $\simeq 3000$ until the present era.

At all temperatures smaller than $O(10MeV)$ we have $\rho_B = n_B m_B \sim 10^{-9} T^3 m_B$

and $\rho_\gamma = n_\gamma < E_\gamma > \sim T^4$. At $T = 1MeV, \rho_\gamma >> \rho_B$, however $\rho_\gamma/\rho_B \propto T$ and drops until $\rho_\gamma = \rho_B$ when $T \sim 10^{-9} m_B = 1eV$. Beneath $1eV$ the universe enters an era when $\dot{R}/R$ is driven by the hydrogen rest mass. Since $\sqrt{G\rho} \sim T^{3/2}$ and RT = constant, Einstein's equation, (2.4), gives $R \sim t^{2/3}$ in this matter dominated era. If $k = 0$ this behavior continues until today. However if $\Omega < 1$ then a curvature dominated era with $R \sim t$ is reached.

The plasma at $1eV$ was homogeneous to a very high degree. We know this because we see the 3^0K microwave background to be isotropic once the peculiar motion of the earth has been accounted for. The photons of this background radiation have their last scatter at the era when $T = O(eV)$. Hence the inhomogeneities in the baryon distribution seen today, galaxy clusters, galaxies and stars must have evolved during this last factor of 3000 in redshift of the universe. The seeds for this inhomogeneity could be small density perturbations in baryons or dark matter present at $T = O(eV)$ or large density fluctuations produced by a late phase transitions at $T < 1eV$. Understanding the origin of this large scale structure which we see the universe to have is one of the most active areas of cosmological research. It is a field with many aspects: the clustering depends critically on the nature of the dominant energy density of the universe, and since this energy density is dark there are only speculations as to its nature. From the viewpoint of clustering only a few properties of the dark matter need be known, so it is sensible to group together those dark matter candidates which give essentially identical behavior. Elementary particle candidates can be divided into three such groups: hot, warm and cold. In the next section I introduce an alternative classification scheme for dark matter; one which is motivated more by the underlying particle physics.

(III) Dark Matter

Any form of energy density whose existence is inferred solely from its gravitational effects is called dark matter. There is direct evidence for dark matter on all scales from the solar neighborhood to groups of galaxies, and indirect evidence that one component of dark matter may be fairly smoothly distributed over the entire universe [3,4,5]. The form of this dark matter is not known. It could be a gas of elementary particles, chunks of solid material, vacuum energy, topological defects such as monopoles, etc. and each of these classes has many particular examples.

There is evidence that dark matter is associated with galaxies of quite different types: dwarf, elliptic, and spirals, for example. I will make a few comments on the case of spiral galaxies [10], which is of particular interest as our own galaxy is spiral and from the viewpoint of direct detection of dark matter it is the local dark matter density which is of most importance. There are many different visible components to a spiral galaxy such as our own. There is the disk containing the spiral arms of stars; the sun is in such an arm about 15 kpc from the galactic center. There is also a spheroid component near the galactic center and hydrogen clouds, which extend beyond the visible limit of the spiral arms. These are sketched in Figure 4. Together they yield masses in the range of $10^{11} - 10^{12}$ times the solar mass for a typical spiral galaxy. The H clouds distant from the galactic center rotate about the symmetry axis. Since the galaxy should be in a stable gravitational configuration, and since these distant clouds provide only a small contribution to the total visible mass of the galaxy, the rotation speed should be given by $v^2/r = GM/r^2$ where M is the galactic mass. Thus one expects $v(r) \propto r^{-1/2}$. This has not been seen. In fact constant values of $v(r)$ have been observed for many spiral galaxies out to very large r (up to 100 kpc). This suggests that there is an additional component to a spiral galaxy, that of the dark halo. It should have $M(r)$ increasing as r out to very large distances, and it is frequently estimated that the halo mass is an order of magnitude larger than the visible mass.

From the viewpoint of particle physics the first important question to ask about dark matter is: is it baryonic? Examples of baryonic dark matter would be cool stars with low luminosities or perhaps planetary sided lumps of cold solid material. If this were the dark matter it would be interesting for particle physics, but certainly not revolutionary. It would simply mean that the baryonic freezeout abundance,which is related to the cosmic baryon asymmetry, is larger than previously thought. To ignore the baryonic option simply because we do not have an understanding of how such objects are formed is a mistake: formation of all types of stars and galaxies are, to varying degrees, not understood.

One constraint on Ω_B comes from big bang nucleosynthesis [11]. As the baryonic density at the MeV era is increased so the nucleosynthesis reaction rates are increased. This depletes the low mass nuclei (^2H,^3He) since they are more fully burnt to the higher mass nuclei (^4He,^7Li) whose abundances consequently increase. The preferred range of Ω_B from a comparison of big bang nucleosynthesis

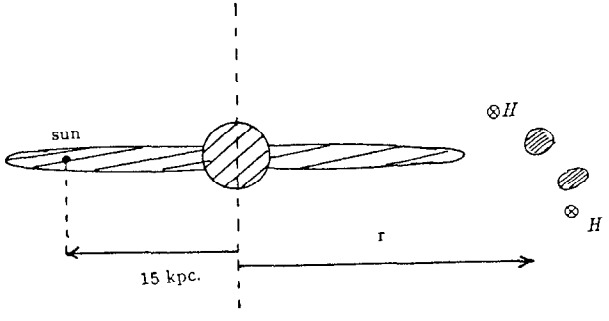

Figure 4

Schematic view of spiral galaxy.

with the observationally inferred abundances is a few percent. However, there are many uncertainties to do with the interpretation of the various observations, and consequently one cannot use this alone to rule out the possibility that all the known dark matter ($\Omega_{Dark} \simeq .1$) is in fact baryonic.

It is widely believed that at some temperature, presumably larger than the weak scale, the universe began an era when the Robertson–Walker scale factor $R(t)$ underwent a very rapid increase [12, 13]. This inflationary era would also produce very rapid cooling ($RT = const.$). This era is ended by some very non–adiabatic process which releases a stupendous amount of entropy and reheats the universe. There are several theoretical reasons as to why this quite bizarre history is attractive to many cosmologists. I will describe the way in which inflation solves the "flatness" problem.

Recall Einstein's equation for the rate of expansion of the universe; it has the form $(\dot{R}/R)^2 \sim G\rho - 1/R^2$. Direct observations today tell us that the curvature term cannot be larger than about ten times the energy density term: $1/R^2 \lesssim 10 G\rho$. As we go to earlier times ρ increases first as T^3 (matter dominated era) then as T^4 (radiation dominated era) while R^{-2} increases only as T^2. Thus at very early times $G\rho$ dominates by an enormous amount. In fact at the Planck scale the initial condition required for evolution to reach the present universe is

$$\left.\frac{1/R^2}{G\rho}\right|_{T=M_p} \lesssim 10^{-60}. \tag{3.1}$$

A much more natural initial condition would be for this ratio to be unity. In that case the universe will rapidly become curvature dominated: $\dot{R}/R = 1/R$ or $R = t$. Furthermore with $RT =$ constant, the initial condition implies $T \simeq t^{-1}$. Since $\rho \sim T^4$ and $\rho_c \sim H^2/G \sim M_p^2 T^2$ we find that in this universe $\Omega(T) \sim T^2/M_p^2$. Thus when $T = T_0 = 3^0 K$, $\Omega_0 \sim 10^{-60}$. This temperature of the universe is reached at a time $t_0 \simeq T_0^{-1} \sim 10^{-12}$ sec. Naturalness implies that open universes become cold very quickly, certainly this is not our universe. You might argue that to avoid this problem just set $k = 0$ (I took $k = -1$ in the above). This is avoiding the issue: putting $k = 0$ is the same fine tune as making the $1/R^2$ term negligible compared with $G\rho$.

The inflationary solution to this problem is sketched in Figure 5. There is a natural initial condition $G\rho \sim 1/R^2$ at $T \sim M_p$. A curvature dominated era then takes place, but long before the present era, the $1/R^2$ curvature term is made very

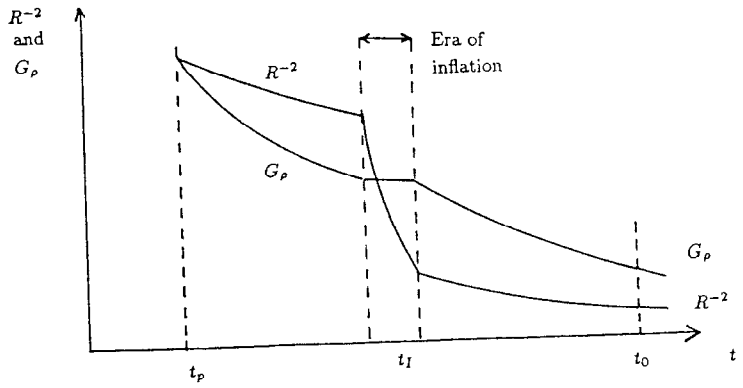

Figure 5

Inflation solves the flatness problem.

small by inflation: recall that inflation rapidly increases R. You might think that since T drops rapidly ρ would also decrease catastrophically. That is not correct; during inflation ρ is dominated by vacuum energy density ρ_V which is constant. It is true that the radiation energy density $\rho_r \sim T^4$ does drop, however at the end of inflation it is replenished because ρ_V is converted to radiation energy density. After inflation $G\rho$ is much larger than R^{-2}. While $G\rho$ subsequently drops faster than R^{-2} there is no reason to expect that we are now in the era when they are comparable, indeed this would itself constitute a fine tune. Hence inflation gives $G\rho >> R^{-2}$ today, *i.e.* it gives $\Omega = 1$.

The visible contributions to Ω are a few percent. Known dark matter contributions give an Ω of ten to twenty percent. In view of the theoretical motivation from inflation, it seems to be a small step to assume that further dark matter is out there and that Ω is really very close to unity. However, from the viewpoint of particle physics this is the crucial step: standard nucleosynthesis allows $\Omega_B = .1$, but $\Omega_B = 1$ really is excluded since the deuterium abundance is then three orders of magnitude too small. Inflation is tremendously exciting: it not only solves cosmological problems such as the flatness problem but it dictates considerable new particle physics beyond the standard model. There should be new exotic stable objects which contribute perhaps 90% to Ω and are not clustered on galactic scales (I'll call this the diffuse dark matter component). There must also be the particle physics which is responsible for the vacuum energy which drives the inflation.

It is also clear that we should tread very carefully: suppose somebody invents a new idea which plays the role of inflation but which does not require $\Omega = 1$. In this case there is no need for the diffuse component of dark matter. In this case there is still the issue of the clustered dark matter. It could be baryonic or exotic, and both forms are worth searching for. It is also worth stressing that the case for exotic dark matter also relies on our understanding of nucleosynthesis. Both theory and interpretation of observation have many interesting unresolved issues. An important theoretical question currently under study is whether inhomogeneities created at the QCD phase transition could have persisted to the nucleosynthesis era with sufficient size to radically alter the conventional abundances which are predicted assuming homogeneity [14]. This is not yet resolved; it seems that in a small region of parameter space $\Omega_B = 1$ might yet be consistent with the standard model.

A more radical question is whether we have identified the main era of light element abundance in the big bang. It is possible to reproduce acceptable abundances for ^2H,^3He,^4He and ^7Li with $\Omega_B = 1$ in schemes which have an exotic particle decaying during the keV era to produce showers in which nucleosynthesis is rekindled [15]. From the viewpoint of particle physics, it is not clear that a stable exotic particle should be preferred over an unstable one. Form the viewpoint of observation it is important to know whether or not the dark matter is baryonic or exotic. Such late decaying schemes predict a higher primordial abundance of ^6Li than the standard model, and this can be searched for [16].

It is possible that the dark matter has several components. This certainly complicates issues such as galaxy formation, but it is not unreasonable: we know of many objects which arise quite naturally in gauge theories which could survive the big bang and would be dark today. I will divide these components into two classes, those which clump and those which do not.

The clumped components contribute about .1 to Ω. They are clumped on galactic scales and hence are non–relativistic. If these components are elementary particles their typical speeds will be $O(10^{-3})$c, this is the typical infall velocity into a galaxy. Faster speeds would lead to the particles escaping from the galaxy. The clumped components could be baryonic or exotic. The components which are not clumped on galactic scales could contribute up to $\Omega = 1$. Such a large, smooth contribution to Ω is certainly not baryonic. To avoid clumping it should be something like relativistic particles or vacuum energy.

If there is a dark matter halo in our galaxy composed of exotic particles, why do we not see these particles in the earth? To understand this it is useful to remember how stars form in a galaxy. A condensation of a pre–stellar gas cloud occurs only because the components (H_2 molecules for example) can sink in the gravitational potential of the cloud by dissipating their energy. For example molecular collisions excite rotational modes which give photons on de–excitation: kinetic energy is radiated away from the cloud. This dissipation is crucial for any gravitational collapse to form a stable dense object. Presumably the reason why the earth and sun do not contain enormous quantities of dark matter is that the halo dark matter particles are sufficiently weakly interacting that they are unable to dissipate this kinetic energy, they have no option but to move on bound orbits around the galaxy. This is quite reasonable. Since they are dark, these particles cannot have strong or electromagnetic interactions. Presumably their interaction strength is that of the weak interactions; they are often called WIMPS: weakly interacting massive particles.

It is a mistake to think that the scattering cross sections for these particles is really $O(G_F^2)$. A sufficient requirement for a halo stable against dissipation is simply that the mean free time for collisions of a dark matter particle in the halo, Γ^{-1}, should be longer than the age of the galaxy, τ_G. This allows a cross section $< \sigma\beta >$ for dark matter particles scattering from baryons as large as a millibarn, hardly a weak cross section.

I will finish this section with a few simple estimates of event rates which could be expected if the dark matter of our halo is composed of particles of mass m_D. From rotation curves of our galaxy and other observations, the best estimate for the local density of halo dark matter is .3 GeV cm^{-3}. Thus with speeds of 10^{-3}c the flux expected at the earth is $\sim 10^7 cm^{-2}s^{-1}(GeV/m_D)$. Suppose that we build a detector to try and observe this enormous flux. If the dark matter particles scatter from the nuclei of the detector, of mass m_N, with some cross section $\sigma_{S,N}$, then the event rate per kilogram of detector is

$$\left(\frac{Events}{kg\ Day}\right) \simeq \left(\frac{\sigma_{S,N}}{2.10^{-39}cm^2}\right)\left(\frac{GeV}{m_D}\right)\left(\frac{GeV}{m_N}\right). \tag{3.2}$$

For large enough cross sections the rates could be enormous. However, detecting the events is a considerable experimental challenge. Since the dark matter particles are non–relativistic with $\beta = 10^{-3}$, their kinetic energies are

$$T_D \simeq \left(\frac{m_D}{GeV}\right) keV \tag{3.3}$$

and only a fraction of this will appear as nuclear recoil. The challenge is to build detectors which can measure energy depositions of O(keV). Searches have already been performed with low background Ge detectors which have masses of $O(1Kg)$ and which were originally designed to search for double beta decay. The approximate excluded region in the $m_D, \sigma_{S,Ge}$ plane is shown in Figure 6.

Most interesting is the region $1 < m_D < 10$ GeV, which has not yet been excluded. The reason that this region is so interesting is straightforward. The necessary annihilation cross section σ_A for a cosmic relic to survive the big bang and contribute $\Omega \simeq .1$ today can be read from equation (2.15). For several interesting candidates, such as a Dirac neutrino, σ_A is a known function of m_D

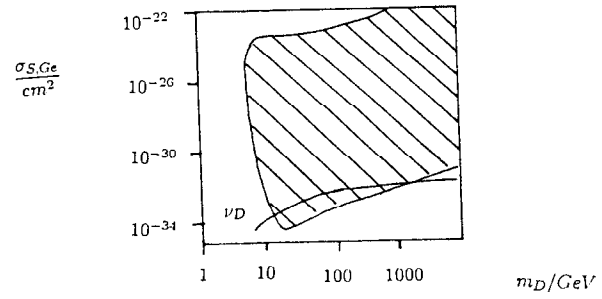

Figure 6

Excluded region in the $m_D/\sigma_{S,Ge}$ plane assuming the particle is responsible for the local dark mass. The upper edge of the shaded region corresponds to the cross section for scattering from the rock overburden. The plot is taken from Ref. 22 and results from use of a double beta decay Ge spectrometer. The curve labelled ν_D is for a Dirac neutrino with conventional weak interactions.

and hence one can predict m_D and it turns out to lie in this region of a few GeV. Furthermore, if the annihilation process is to ordinary matter, eg $D\overline{D} \to q\bar{q}$, then by a crossing relation it is possible to calculate the scattering cross section from nucleus N : $\sigma_{S,N}$. Putting these values of m_D and $\sigma_{S,N}$ into (3.2) one finds that the event rates are quite large. The problem with seeing these events can be seen from equation (3.3). The lower value of m_D decreases the kinetic energy of the dark matter particle. Future detectors will be sensitive to such low energy depositions and will explore this crucial region.

Our failure to directly detect dark matter on the earth can have a variety of explanations. Typically it is either that $\sigma_{S,N}$ is too small, m_D is so large that the event rate is too low, or m_D is so small that the signal is too feeble.

(IV) A Classification Scheme For Cosmic Relics

Cosmic relics can be classified according to the way in which they are produced in the big bang and the way in which they survive until today. All relics of which I am aware fall into one of six classes. For three of these classes the relics were once in thermal equilibrium and they underwent a freezeout process. Relics of the remaining three classes were produced in catastrophic events such as phase transitions and were never in thermal equilibrium. We discuss each class in turn and the classification scheme is summarized in the table at the end.

(IV.1) Plasma Relics

Plasma relics are elementary particles which are relativistic when they decouple. That is at decoupling their number density is $n_D \sim T_D^3$, and today $n_0 \sim T_0^3$. If their mass is less than T_0 then $\rho_0 \sim T_0^4$ so $\Omega_0 \sim 10^{-5}$. The three degree microwave photon background is the best illustration of a plasma relic which is still relativistic today. If the masses for ν_i are less than T_0 they are also plasma relics which are relativistic today. Such plasma relics are not important for dark matter, unless there were $O(10^4)$ such species. This bizarre possibility is excluded since they would greatly increase ρ and therefore $\dot{R}/R$ at the time of nucleosynthesis, thus destroying the successful predictions of primordial nucleosynthesis. Hence although plasma relics which are still relativistic today will not be clustered, they cannot contribute much to Ω.

Plasma relics which have masses larger than T_0 would be non-relativistic today and would clump. Any of the three neutrinos could have such masses and could therefore make an important contributions to Ω.

(IV.2) Freezeout Relic

This important case was discussed in the previous sections. Freezeout relics are particles which were once in thermal equilibrium and are non-relativistic when the reactions which change their comoving number densities freeze out. Their contribution to Ω is given by equation (2.15) for any such species x. Although the mass does not appear explicitly in Ω_x, their is almost always implicit dependence via the annihilation cross section. Since $< \sigma_A v > \lesssim 1/m_x^2$ even for a strongly interacting particle, a freezeout relic is expected to be lighter than 10^3 TeV. For a particle with a weak annihilation cross section $< \sigma_A v > \simeq G_F^2 m_x^2$ so that $\Omega_x \simeq .1$ for halo dark matter results with $m_x \simeq O(GeV)$. Although these candidates, such as Dirac neutrinos or supersymmetric photinos are quite plausible, they are not the only possible freezeout relic.

Consider a new version of QCD, shadow QCD, which has an asymptotically free gauge coupling which gets strong at Λ' causing confinement of shadow quarks q' into shadow baryons B' which acquire mass $O(\Lambda')$. These baryons can annihilate into $\pi' : B'\overline{B}' \to \pi' \cdots$ with $< \sigma_A v > \sim 1/\Lambda'^2$. If $\Lambda' \simeq 300$ TeV these shadow baryons would give $\Omega \simeq .1$ even if there were no cosmic B' asymmetry.

Similarly one could imagine a world with a new unbroken $U(1)$ gauge group: shadow QED. If m_e' is the mass of the shadow electron, the lightest particle carrying shadow charge, then $e'\overline{e}' \to \gamma'\gamma'$ has $< \sigma_A v > \simeq \alpha'^2/m_{e'}^2$ so that $\Omega_{e'} \simeq .1$ arises with $m_{e'} \simeq \alpha' 300$ TeV, again taking zero shadow lepton asymmetry.

(IV.3) Asymmetric Relic

Asymmetric relics are freezeout relics whose survival abundance has been greatly enhanced because of a cosmic particle anti-particle asymmetry. Protons and electrons are the best examples. It is very plausible that the dark matter is an asymmetric relic: we know native produced a cosmic asymmetry in baryon number B, so it is reasonable that it has done the same for some other quantum number. Dark matter would have survived until today for precisely the same reason that the visible matter did.

It is fun to redo the Lee-Weinberg [9] freezeout calculation including a chemical potential. In particular, while the chemical potential directly determines the abundance of the surviving major component, the minor component is annihilated way below what would have survived with zero chemical potential. None of the antiprotons seen in cosmic rays survived directly from the big bang, they were made recently in high energy collisions.

A very intriguing possibility arises if the halo dark matter is an asymmetric relic. The sun can gravitationally bind dark matter particles by scattering them into a bound orbit as they pass through the sun. Over the age of the sun significant concentrations of dark matter particles could have built up in the sun, providing they are asymmetric relics so that $x\overline{x} \to \cdots$ does not deplete the concentration. It has been found that for certain masses such bound relics could contribute to the thermal opacity of the sun, decreasing the central temperature of the sun and decreasing the reaction rate which produces the high energy solar neutrinos thus solving the solar neutrino problem [17]. While a freezeout relic (no asymmetry) can also be trapped by the sun, $x\overline{x} \to \cdots$ will prevent buildup of a sufficient concentration to be important in changing the solar opacity. However, $x\overline{x} \to \cdots$ may itself result in high energy neutrinos (now much higher in energy than usual solar neutrinos) which would be an interesting signature for some freezeout relic candidates.

(IV.4) Oscillaton Relic

Consider a scalar field $\phi(\overline{x}, t)$. If the zero temperature potential for this field is as sketched in Fig. 7. then at some critical temperature T_0 a phase transition will occur: initially $\phi = 0$ everywhere, while at the phase transition it rolls to the minimum of the potential $\phi = \sigma$ everywhere. If ϕ has strong couplings it can radiate the energy density V_0 easily, so the equation governing the evolution of ϕ has a solution which is strongly damped. On the other hand, if ϕ has only very weak interactions the equation of motion will have small damping and the solution will be oscillatory. In the limit that the damping can be neglected

$$\phi(\overline{x}, t) = \sigma + \phi_0 e^{imt} \tag{4.1}$$

where m is the mass of the quanta which the field ϕ creates. These oscillatons which are initiated by the phase transition would survive until today. What does this oscillaton represent physically? Because the oscillatons are the same at all spatial locations it is a mode of the field which carries no momentum. The energy density in the oscillaton represents a uniform distribution of ϕ quanta at rest; $\rho_0 = nm$. Of course, equation (4.1) is not quite correct: as the universe expands the number density of these particles gets diluted $n \sim 1/R^3$, so ϕ_0 also has a time dependence due to the expansion. However, even if these non-relativistic particles had only a small contribution to ρ at the phase transition

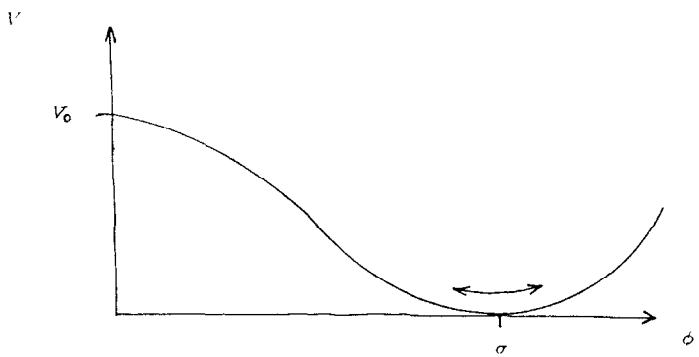

Figure 7

Typical potential for an oscillaton relic

$\rho_0(T_c) << \rho(T_c)$ they could easily dominate by today if T_c falls in the radiation dominated era. This is illustrated in Figure 8. The most well know example of an oscillaton is the axion. In the absence of QCD the axion is in fact a massless Goldstone boson which results from the breaking of a global $U(1)$ symmetry, the Peccei–Quinn symmetry, at some scale f. The QCD interactions produce the potential of Fig. 7, $V_0 \sim \Lambda^4$ where Λ is the QCD parameter, and the order parameter for the symmetry breaking, σ, is f. However, oscillatons occur very frequently; they result from symmetry breaking with a weakly coupled scalar, and are much more general than the axion.

(IV.5) Secondary Relics

So far we have assumed that relics are stable, or at least that their lifetimes are longer than the age of the universe. However, any of the relics considered so far could have lifetimes less than the age the universe. Their cosmologically stable decay products I will call secondary relics. They are of particular interest for obtaining $\Omega = 1$ in a smooth distribution without galactic size clumping. None of the first few classes of relic lead to dark matter today which is both relativistic, unclumped and gives $\Omega = 1$. However, a secondary relic could be relativistic today even if it came from a non–relativistic primary.

There are many examples of secondaries. The inflaton is an oscillaton. However equation (4.1) is insufficient to describe its oscillation because it is unstable so the oscillaton gets suppressed by $\exp(-\Gamma t)$. In this sense, everything is a secondary relic, we owe our existence to the decays of inflatons which reheated the universe after inflation.

As another example, consider supersymmetric theories where the lightest superpartner, which we take to be the photino, although long lived does decay via small R parity violating interactions. One example, $\tilde{\gamma} \rightarrow e^+e^-\nu$, is illustrated in Fig. 9. This gives $e^{\pm}, \nu$ as secondary relics. In this case we can follow the evolution of the relativistic $e^{\pm}$ and demonstrate that they cannot contribute significantly to Ω. The $e^{\pm}$ lose energy rapidly by inverse Compton scattering from the background plasma photons $e\gamma \rightarrow e\gamma$. Once the $e^{\pm}$ are non-relativistic they clump. However, the majority of the photino rest mass has ended up in electromagnetic radiation which today would be X and γ rays. We know from background X and γ rays observations that Ω in these components are very small ($< 10^{-8}$). As usual, one finds that the big bang is a tightly constrained frame-

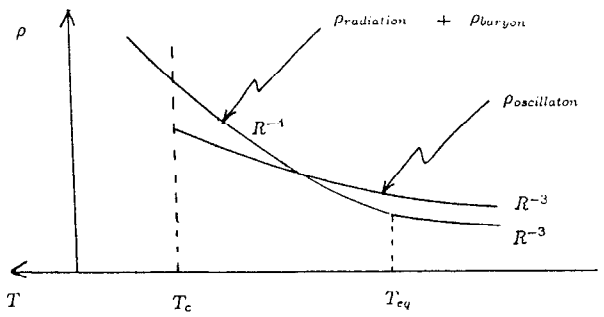

Figure 8

Temperature evolution of ρ in oscillatons and ρ in radiation and baryons. The oscillatons are produced at T_c. At T_{eq}, $\rho_{radiation}$ and ρ_{baryon} are equal.

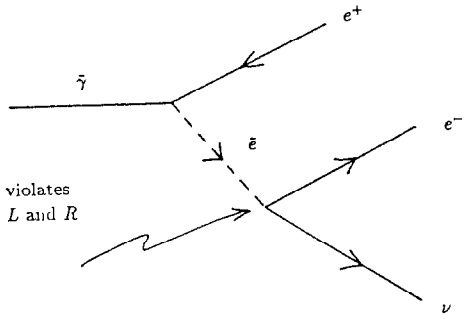

Figure 9

Photino decay via lepton and R parity violation.

work. The majority of new particle physics ideas for creating cosmic relics simply do not work. They lead to universes quite unlike our own.

(IV.6) Soliton Relics

By "soliton" I mean energy which is spatially localized and which is produced at a phase transition. This is not the same as other uses of the term. Some soliton relics are topologically stable defects: domain walls, strings and monopoles [18, 19]. For example consider a theory which contains a real scalar field $\phi(\overline{x},t)$ which has a potential $V(\phi) = \lambda(\phi^2 - \sigma^2)$. This potential has two discrete degenerate minima. As shown in Fig. 10(a), if a phase transition takes place such that the field ϕ takes on a vacuum value $+\sigma$ near region A and $-\sigma$ near region B, then these regions will be separated by a domain wall at which ϕ is not at either of the minima. This domain wall contains localized field energy. If the ϕ is now made complex and the theory processes a $U(1)$ phase invariance then $V(\phi) = \lambda(\phi^*\phi - \sigma^2)^2$. In this case a pattern of vacuum field configurations result in a topological string as shown in Fig. 8(b). In fact for the energy of this field configuration to be localized on the line defect the $U(1)$ should be gauged. A monopole arises in gauge theories when a non-Abelian internal symmetry group is broken, in the monopole case the defect occurs at a point as shown in Fig. 8(c). A simple example is a theory of three real scalar fields $(\phi_1\varphi_2\varphi_3)$ which has a potential which has an $SO(3)$ invariance: $V(\phi) = \lambda(\phi_i^2 - \sigma^2)$.

The calculation of production rates for vacuum defects is not straightforward in particle collisions or in the big bang. Simple estimates for a phase transition in the big bang can be made. Suppose that at $T > T_c, \phi = 0$ in each of the above examples, while at T_c ϕ makes a transition to $|\phi| = \sigma$ everywhere except near the defects where it vanishes. The direction of ϕ is random on scales of the correlation length ζ of the phase transition. Hence, as an order of magnitude estimate the defect number density is $n_D(T_c) \simeq \zeta^{-3}$. Since ζ is certainly less than the horizon there will typically be many defects per horizon volume at T_c.

The subsequent evolution of the collection of defects can be very intricate. However, under certain simplified conditions $\rho_{DW} \sim R^{-1}$, $\rho_s \sim R^{-2}$ and $\rho_M \sim R^{-3}$ for domain walls, strings and monopoles. I know of no complete cosmologies where ρ today is dominated by domain walls or cosmic strings. Domain walls rapidly overwhelm other contributions to ρ and lead to universes quite unlike our own, unless they can be made to disappear. Cosmic strings which self-intersect

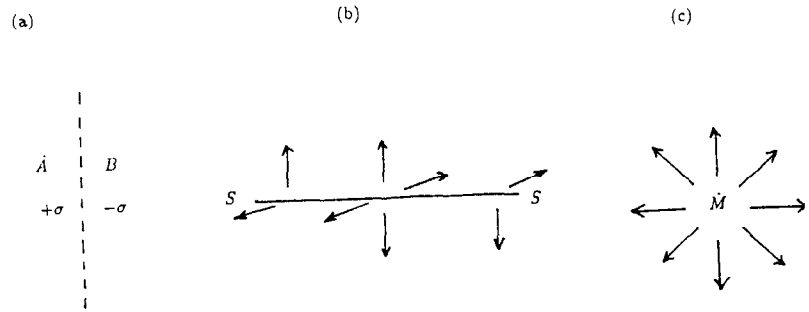

Figure 10

Topologically stable defects (a) a two-dimensional domain wall (b) a one-dimensional string S (c) a point monopole M. In cases (b) and (c) the arrows represent the direction of the scalar field in internal space.

and produce loops which can then disappear by gravitational radiation may not be problematic. At any era ρ_s then scales the same way with R as ρ_{TOTAL}. Today one finds $\Omega_s \lesssim \sigma/M_p$. For σ of 10^{16} GeV it is possible that the string network may provide the inhomogenities about which galaxy clustering first occurs.

If monopoles are made at a very early phase transition their number density must be depleted by a subsequent era of inflation otherwise the universe will not evolve to the one we see. It is not possible that a monopole with magnetic charge and mass near the grand unification scale is depleted just enough to be the dark matter today. This would produce a flux of monopoles at the earth which has been experimentally excluded. It is possible that the dark matter could be a monopole which carries some other charge.

There is a second class of soliton relics. There are regions of false vacuum which have become stabilized by the presence of matter or charge. These non topological solitions I will call false vacuum nuggets. The most well known example is that of quark nuggets which could arise during the QCD phase transitions and which I describe below [20].

In Fig. 11 I sketch how the QCD phase transition would proceed cosmologically assuming that it is first order, as indicate by lattice calculations. At first small bubbles of hadronic phase are nucleated in the previously homogenous quark gluon plasma. Since the vacuum energy of these hadronic bubbles is lower than in the quark phase the bubbles expand as shown in Fig. 11(a). The bubbles will collide and coalesce until half of space is filled by the hadronic phase. Subsequently, the picture is that regions of quark phase which are collapsing within the hadronic medium as shown in Fig. 11(b). The original quark plasma had nearly equal numbers of quarks and antiquarks, although there was a quark excess of one part per billion. However, if the critical temperature is say 100 MeV the many quarks and antiquarks must annihilate because in the hadron phase at $T_c, n_B \simeq n_{\overline{B}} \simeq (T_c, m_B)^{3/2} e^{-m_B/T_c} << T_c^3$ (see 2.10). The $q\bar{q}$ annihilation can occur to $\nu\bar{\nu}$ via the Z, and since neutrinos transport energy over large distances thermal equilibrium at T_c is maintained. Now imagine following the quark excess. When the phase boundary moves into the quark fluid the quark excess tends to be swept along with the boundary. This is because for baryon number to go across the boundary energy must be found to create the baryon mass. To some degree it is therefore energetically favorable for the quark excess to remain in the

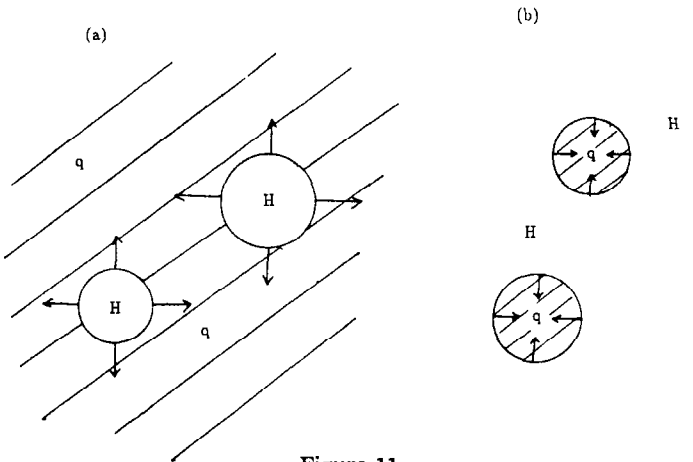

Figure 11

The cosmological QCD phase transition (a) nucleated bubbles of hadron phase expand into the quark plasma (b) shrinking bubbles of quark phase.

quark plasma. If this effect is quite powerful then the collapse of a quark bubble shown in Fig. 11(b) will eventually be prevented by the stabilizing effect of the pressure of the quark excess inside the bubble. A quark nugget has been formed at temperature T_c.

We do not know whether such nuggets would be stable at zero temperature, they might just decay to ordinary baryons. However, it has been argued that even if quark nuggets were formed at T_c and even if they were stable at $T = 0$, they do not survive the cosmological evolution from T_c to $T = 0$, rather they evaporate [21]. While it seems that quark nuggets are not the dark matter, it is possible that some false vacuum nugget of another phase transition contributes to the dark matter.

Summary

The hot big bang model of the early universe provides a simple and elegant framework in which to study the effects of various gauge models of particle physics on cosmological issues. The standard gauge theory apparently does not lead to the universe which we observe. There is the need for baryogenesis and there is the need for a cosmic relic to be the dark matter. The cosmological description would also be more acceptable if particle physics gave rise to an era of inflation, when $R(t)$ grew very rapidly.

Most additions to the standard model which give cosmic relics do not give them with the correct abundance. The requirement of $0.1 \simeq \Omega \simeq 2$ places considerable restrictions on the interactions which generate the relics. Nevertheless an enormous number of candidate relics have been proposed. I have introduced a classification scheme to describe these cosmic relics, and it is summarized in the Table. Plasma and freezeout (including asymmetric) relics are particles which were once in thermal equilibrium with the plasma of the hot big bang. Secondary relics are particles which arise from the decay of any of these three types of primary particle relics. Oscillatons and solitons are directly associated with phase transitions in the quantum field theory, and occur in a surprising variety of forms.

As indicated in the Table, there are many ways to search for the various relics. Several searches have been done for many years and new ones with novel techniques are planned for the future. The discovery of any of these relics would be a major turning point in cosmology. It would also give us solid guidance in understanding particle physics beyond the standard model.

Category	Characteristics	Examples	Possible Implications	Detection
Plasma	$m < T_0$ Decoupled	γ ν_e, ν_μ?	New light Particles eg Goldstone Bosons	Difficult as low energy
Freezeout	$m > T_0$ Froze out while non-relativistic	$\nu_{M,D}$ $\tilde{\gamma}$	New physics at weak scale	Direct detection Detection of products from annihilation in sun or halo.
Asymmetric	$m > T_0$ Abundance determined by cosmological asymmetry	p, e ν_D	CP violation New quantum number	Direct detection
Oscillation	Very weakly coupled scalar	axion	New phase transition.	Difficult as weakly coupled. Axion to γ conversion
Secondary	$X_1 \rightarrow X_2 \ldots$ $\tau(X_1) \lesssim t_0$	$\nu_H \rightarrow \nu_L \gamma$	An approximate symmetry	Other decay products of X_1 may give γ, X ray signals.
Soliton	Defects from phase transitions with localized energy.	Domain walls Strings Monopoles Nuggets	New phase transition	Direct searches Gravitational lensing Gravitational radiation

TABLE

A classification scheme for cosmological relics.

References

1. L. Okun, Proceedings of Neutrino '88 Conference, Boston MA, MIT–CTP–1606 (1988).

2. S. Falk and D. Schramm, *Phys. Lett.* **79B**, 511 (1978).

3. J. Kormendy and J. Knapp, Dark Matter In The Universe, IAU Symposium 117 (1987); J. Bahcall, T. Piran and S. Weinberg, Dark Matter In The Universe, Jerusalem Winter School Volume 4 (1987). World Scientific.

4. J. Binney and S. Tremaine, Galachi Dynamics, Ch. 10, Princeton University Press, 1987.

5. Proceedings fo the Workshop on Particle–Astrophysics, Berkeley, Dec. 1988, Ed. E. Norman, World Scientific.

6. S. Weinberg, Gravitation and Cosmology, Wiley (1972).

7. M. Turner, Proceedings of Les Houches Summer School, 1985, Ed. P. Ramond and R. Stora, North Holland.

8. E.W. Kolb, Proceedings of the TASI in Elementary Particle Physics, Santa Cruz, 1986. Ed. H. Haber, World Scientific.

9. B. Lee and S. Weinberg, *Phys. Rev. Lett.* **39**, 169 (1977).

10. V. Rubin, Science **220**, 1339 (1983).

11. R.V. Wagoner, W.A. Fowler and F. Hoyle, *Astrophys. J.* **148**, 3 (1967); J. Yang, M.S. Turner, G. Steigman, D.N. Schramm and K. Olive, Asrophys. J. **281**, 493 (1984).

12. A. Guth, *Phys. Rev.* **D23**, 347 (1981).

13. L. Abbott and S. -Y. Pi, Inflationary Cosmology, World Scientific, 1986.

14. J. Applegate and C. Hogan, *Phys. Rev.*, **D31**, 3037 (1985).

15. S. Dimopoulos, R. Esmailzadeh, L. Hall and G. Starkman, *Phys. Rev. Lett.* **60**, 7 (1988).

16. L. Brown and D. N. Schramm, Fermilab–Pub–88/20–A.

17. W. Press and D. Spergel, Astrophys. J. **296**, 679 (1985).

18. T. Kibble, *J. Phys.* **A9**, 1387 (1976).

19. J. Preskill, *Phys. Rev. Lett.* **43**, 1365 (1979).

20. E. Witten, *Phys. Rev.* **D30**, 272 (1984).

21. C. Alcock and E. Farhi, *Phys. Rev.* **D32**, 1273 (1985).

22. D. Caldwell et al., *Phys. Rev. Lett.* **61**, 510 (1988).

DOUBLE BETA DECAY

M. S. Witherell

Department of Physics
University of California
Santa Barbara, CA. 93106

ABSTRACT:

In these two lectures I give a review of double beta decay. I begin with an introduction to the physics of massive Majorana neutrinos and lepton number violation. Following that is a review of two-neutrino double beta decay. There is a detailed discussion of neutrinoless double beta decay experiments, their results, and the interpretation of these results. I also list options for future experiments. Finally, there is a description of the application of a double beta decay experiment to a dark matter search.

Lectures given at the SLAC Summer Institute on Particle Physics, Stanford, CA., July 18–29, 1988.

PHYSICS MOTIVATION

What is double beta decay and why is it interesting to particle physicists? In 1935, Maria Goeppert-Mayer[1] first calculated the decay rate for the nuclear decay

$$(A, Z) \rightarrow (A, Z+2) + 2e^- + 2\overline{\nu_e} \qquad (\beta\beta_{2\nu}).$$

There are a number of even-even nuclei which are more stable than odd-odd neighbors but can decay by this second-order weak interaction. In 1937, Majorana[2] and Racah[3] introduced the concept of self-conjugate neutrinos, and two years later Furry[4] suggested that such a particle could lead to neutrinoless double beta decay,

$$(A, Z) \rightarrow (A, Z+2) + 2e^- \qquad (\beta\beta_{0\nu}).$$

More recently,[5] a possible third type of double beta decay has been suggested,

$$(A, Z) \rightarrow (A, Z+2) + \chi \qquad (\beta\beta_{\chi})$$

where χ is the majoron,[6] a hypothetical massless scalar which could arise from the breaking of B-L symmetry.

The important physics issues in neutrinoless double beta decay are lepton number conservation, neutrino masses and mixing, and right-handed currents. There are two requirements for $\beta\beta_{0\nu}$ to occur. Lepton number must not be conserved, since two leptons are emitted with no associated antileptons, which is possible if neutrinos are Majorana particles. In addition, the helicity of the neutrino cannot be exactly -1. This requirement can be satisfied by a number of mechanisms, most notably if the neutrino has mass. Both requirements could be satisfied only by physics beyond the standard model.

The original evidence for conservation of lepton number came from the experiment of Davis,[7] which showed that the process $\overline{\nu_e} + (A, Z) \rightarrow (A, Z+1) + e^-$ does not occur at the rate expected for ν_e. The conventional explanation for this difference is that the neutrino and antineutrino are distinct particles, and there is a conserved quantum number L_e. An alternative explanation became apparent with the discovery of maximal parity violation. It could be that ν_e and $\overline{\nu_e}$ are left-handed and right-handed helicity states of the same Majorana neutrino ν^M. The only sensitive test of the Majorana nature of neutrinos is double beta decay. It is similar to the Davis experiment, but with virtual neutrinos. The antineutrino emitted at the first weak interaction is reabsorbed at the second as a neutrino.

There have been extensive studies of the physics of Majorana versus Dirac neutrinos.[8,9] For the case of Dirac neutrinos there are four states: ν_L, ν_R, $\overline{\nu_L}$, and $\overline{\nu_R}$. The CPT operator acting on the ν_L produces $\overline{\nu_R}$. If the neutrino mass is not zero, a Lorentz boost can transform ν_L into ν_R, which is distinct from $\overline{\nu_R}$. Under this scheme, it is possible for the neutrino to possess a magnetic dipole moment, $\vec{\mu}$. If $\vec{\mu} \neq 0$, a magnetic field can cause a precession of ν_L into ν_R.

If the neutrino is a Majorana particle, there are only two states, ν_L and ν_R. If the neutrino is massive, a Lorentz boost and the CPT operation both transform ν_L into ν_R. There can be no magnetic dipole moment, because by CPT, $\vec{\mu}(\overline{\nu}) = -\vec{\mu}(\nu)$. If $m_\nu = 0$, it is impossible to distinguish between the two neutrino types.

If $m_\nu \neq 0$, it should then be possible to distinguish Dirac from Majorana neutrinos by magnetic moment. As Lincoln Wolfenstein points out in his lectures,[10] the magnetic dipole moment for a massive Dirac neutrino is

$$\mu_\nu = 3 \cdot 10^{-19} \mu_B \times \left[\frac{m_\nu}{1\ \mathrm{eV/c^2}}\right].$$

It is therefore unobservably small. This is an example of a general problem. If $m_\nu = 0$, it is impossible to flip helicity and the Majorana–Dirac distinction disappears. Moreover, the approach to this limit is a smooth one. As m_ν/E_ν goes to zero, any quantity sensitive to the neutrino type goes to zero, too. At first glance it seemed that $\beta\beta_{0\nu}$ required two independent violations of the standard model. We now see that they are inextricably connected. The smallness of m_ν effectively conceals the possible Majorana nature of the neutrino.

Why should we expect that neutrinos have nonzero rest masses? We know that neutrinos are members of doublets with leptons. In Grand Unified Theories, quarks join the family. It is more natural if all members have mass. The problem then becomes why are the neutrino masses so small? The most popular explanation is that the neutrinos have one property the charged fermions cannot, their Majorana nature.

The most attractive realization of this general picture is the see-saw mechanism,[11] which is discussed in some detail in Wolfenstein's lectures. The mass matrix looks like

$$\begin{pmatrix} 0 & M_{\rm D} \\ M_{\rm D} & M_{\rm R} \end{pmatrix}$$

where $M_{\rm D}$ is the Dirac mass and should be comparable to the mass of a charged fermion, either lepton or quark, in the same family; $M_{\rm R}$ is the mass of a right-handed neutrino, which can be quite large because it is a singlet. Diagonalization of this matrix gives mass eigenstates with masses $M_{\rm N} = M_{\rm R}$ and $M_\nu = M_{\rm D}^2/M_{\rm R}$. Thus the two neutrino masses satisfy the see-saw rule $M_\nu M_{\rm N} = M_{\rm D}^2$. For example, if $M_{\nu_e} = 1$ eV and $M_{\rm D} = 0.5$ MeV, the electron mass, then $M_{\rm N} \simeq 10^3$ GeV. If $M_{\rm D} = 300$ MeV, like a quark mass, then $M_{\rm N} \simeq 10^8$ GeV. Thus in this scheme, limiting the electron neutrino mass to 1 eV is probing masses for the right-handed neutrino which are quite large.

Majorana neutrinos also have unusual CP properties, as pointed out by Boris Kayser.[12] If CP is conserved, then each Majorana neutrino has an intrinsic CP parity $\tilde{\eta} = \pm i$ (not ± 1). The effective mass that enters in double beta decay is

$$\langle m_\nu \rangle = \left| \sum_m \tilde{\eta}_m \left| U_{em} \right|^2 M_m \right| = \sum_m \lambda_m |U_{em}|^2 M_m$$

where $\lambda_m = \pm 1$. The sum is over all Majorana neutrinos coupled to the electron. Opposite CP-parity neutrinos can destructively interfere, although in most models this is not an important effect. As an interesting result of these properties, unrelated to double beta decay, there are more CP-violating phases in the lepton sector than in the quark sector if neutrinos are Majorana. In that case, there is a CP-violating phase possible even with two generations.

DOUBLE BETA DECAY

It is worthwhile recalling the description of single beta decay. If the two nuclei have the same parity and the change in spin is $|\Delta J| \leq 1$, it is an allowed decay. The energy spectrum is given by the expression

$$\frac{dN}{dE} = \frac{G_F^2 M_e^5 c^4 \cos^2\theta_c}{2\pi^3 \hbar^7} \; |M|^2 \; F(Z,E) p E \, (E_0 - E)^2$$

where M is the nuclear matrix element, F(Z,E) is a Coulomb correction, and E_0 is the endpoint energy. The nuclear structure does not effect the shape of the energy spectrum, only the total rate. In double beta decay, a similar calculation is possible, but one must study a two-step transition, summing over the virtual intermediate states. This complicates the calculation significantly.

The typical candidate nucleus for double beta decay is an even-even nucleus which has proton number two less than the most stable nucleus for a given nucleon number. The odd-odd nucleus between these two even-even nuclei has lower binding energy by about 4 MeV, and is not an allowed daughter for single beta decay. Not only the ground state of the intermediate nucleus must be considered as an intermediate state, but many of the excited states as well. A typical momentum of the virtual neutrino exchanged in neutrinoless double beta decay is 10 MeV. Thus, the range of the virtual neutrino is much larger than the nuclear size for light neutrinos.

Why is $\beta\beta_{0\nu}$ such a sensitive test of small Majorana neutrino mass? First, the decay rate for the calculable two-neutrino process is

$$[T_{1/2}^{2\nu}]^{-1} \simeq 10^{-21} \, (E_0/2 \text{ MeV})^{11} \text{ y}^{-1}.$$

The four-body phase space causes a very steep dependence on the endpoint energy, and a suppressed rate. In the case of neutrinoless decay,

$$[T_{1/2}^{0\nu}]^{-1} \simeq 10^{-13} \, (E_0/2 \text{ MeV})^5 (\langle m_\nu \rangle / m_e)^2 \text{ y}^{-1}.$$

If the neutrino mass were comparable to the electron mass, and therefore there were no helicity suppression, the rate could be eight orders of magnitude greater than that for $\beta\beta_{2\nu}$. One is now sensitive to $\beta\beta_{0\nu}$ rates 10^3 lower than the two-neutrino rate, which corresponds to a ratio of $\langle m_\nu \rangle / m_e \simeq 10^{-5} - 10^{-6}$.

Figure 1(a) shows the quark-level diagram for $\beta\beta_{0\nu}$ induced by massive Majorana neutrinos. The neutrino is emitted as a right-handed particle, but at the absorption vertex the left-handed component is needed. The amplitude for the neutrino to be emitted (or absorbed) in a wrong-sign helicity state is similar to that for $\pi \to e\nu$ decay. There the decay rate is proportional to $(1 - v_e/c) = (m_e^2/2\, p_e^2)$. A similar term for the virtual neutrino in $\beta\beta_{0\nu}$ means that the rate is proportional to (m_ν^2/q^2). In more detail, the amplitude is proportional to

$$(1+\gamma_5) \left[\frac{-i\gamma^\sigma q_\sigma + m_\nu}{q^2 + m_\nu^2} \right] \gamma_\mu \, (1-\gamma_5)$$

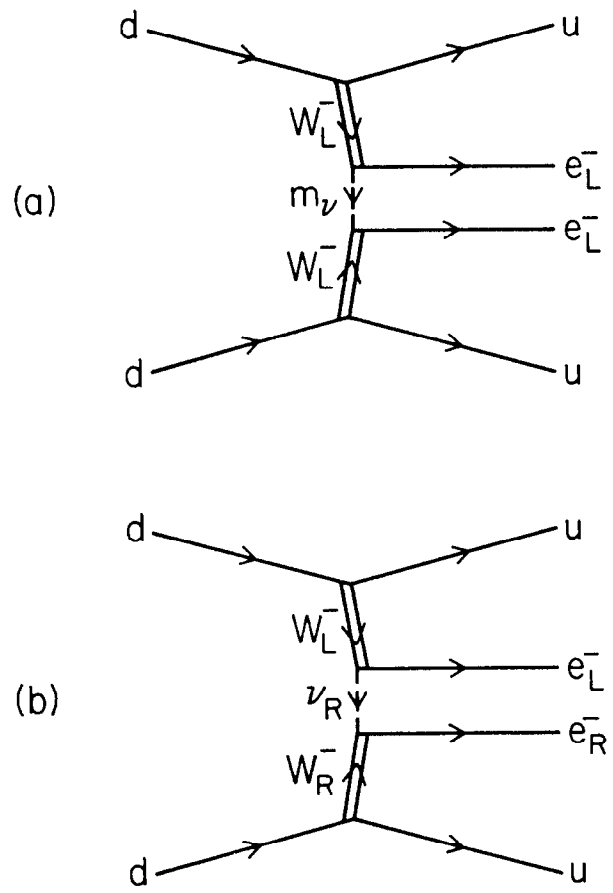

Fig. 1. Two of the processes that could lead to neutrinoless double beta decay: (a) a massive Majorana neutrino coupling to the usual W, and (b) a right-handed W.

including the fermion propagator. Because of the commutation properties of the γ-matrices one is left with the term $m_\nu/(q^2 + m_\nu^2) \simeq m_\nu/q^2$.

Figure 1(b) shows the same type of diagram for the neutrinoless double beta decay caused by right-handed currents (R.H.C.). In this case the amplitude is proportional to

$$(1+\gamma_5)\ \left[\frac{-i\gamma^\sigma q_\sigma + m_\nu}{q^2+m_\nu^2}\right]\gamma_\mu\ (1+\gamma_5).$$

This means that only the $[\gamma^\sigma q_\sigma/(q^2 + m_\nu^2)]$ term survives, and there is no suppression due to m_ν. It is easy to see why it was thought that neutrinoless double beta decay should occur if neutrinos are Majorana and RHC exist, even if $m_\nu = 0$. This is wrong, however, as was pointed out by Kayser, Petcov, and Rosen.

The problem with the above argument is that it assumes the exchanged neutrino couples to both the right-handed and left-handed weak current with full strength. In fact, this is not the case in any gauge theory. Recall the process $\nu + \bar{\nu} \rightarrow W^+ + W^-$. This was thought to proceed only by electron exchange, which caused the cross section to violate unitarity at high energy. This leads to the need of the Z^0 to provide an s-channel diagram that provides the needed cancellation.

A similar effect occurs in the reaction $e^- + e^- \rightarrow W_L^- + W_R^-$, for which Majorana neutrino exchange is the only diagram.[9] Once again, the fermion propagator causes the cross section to rise without limit at high energy, and no neutral gauge boson can help. What saves the high energy behavior is the fact that $\sum_m U_{em}^L\ U_{em}^R = 0$, where U_{em}^L is the matrix connecting the mth Majorana neutrino with the electron and W_L, and the sum is over all Majorana neutrinos. The same effect in Fig. 1(b) means that the linear combination of neutrinos that couples at one vertex does not couple at the other. The exception to this is if the neutrinos have different masses, and at least one mass is high enough that the associated neutrino has a range which can be probed by $\beta\beta_{0\nu}$. Thus even if RHC exist, $\beta\beta_{0\nu}$ requires at least one massive Majorana neutrino.

There are other possible causes for helicity reversal. A heavy neutrino with left-handed couplings has no helicity suppression. The term $m/(q^2 + m^2)$ then becomes approximately $1/m$, assuming that m is larger than about 10 MeV. In addition, there is an allowed decay if there is a particle which couples to

$\nu_L\nu_L$ (rather than $\nu_L\nu_R$, as the Z^0 does.) An example of such a particle is the majoron,[5] and the corresponding decay is $\beta\beta_\chi$, as described earlier.

TWO-NEUTRINO DOUBLE BETA DECAY EXPERIMENTS

The first double beta decay experiments were designed to test the possibility of a large neutrinoless rate. These were done with beta spectrometers in which the signal would be two electrons emanating from the same point. This required thin source foils ($\lesssim$ 5 mg/cm^2) to preserve angles and energies of the 1 MeV electrons and to suppress two-step processes which initiate double beta decay. With present limits, it is unfeasible to search for $\beta\beta_{0\nu}$ with sufficient sensitivity using this technique. The sources would have to be unrealistically large, or the running time unrealistically long.

Due to this limitation, there developed a split in technique. Figure 2 shows the energy spectra, using energy normalized to the endpoint energy E_0, for the three types of double beta decay. The process $\beta\beta_{0\nu}$ produces a sharp peak at E_0 which is limited only by energy resolution. (The natural width of the transition would be in the range of 10^{-45} MeV!) Thus a detector with good energy resolution can be used to suppress background by a large factor. On the other hand, the other two decays give continua, for which resolution is not important. One technique used for these cases is to use the two-electron signature to suppress the background. The other is to use long integration times and measure the decay daughter, which is the basis of the geochemical technique.

In geochemical experiments, the daughter nucleus is a noble gas. The source is a rock of known age (10^9 years) that includes a substantial amount of the parent nucleus, such as ^{130}Te, which can decay to ^{130}Xe. One looks for the daughter isotope occluded in the rock, after subtraction using the other isotopes of the noble gas. Such a technique does not distinguish between $\beta\beta_{0\nu}$ and $\beta\beta_{2\nu}$. Because it is known that $T^{0\nu}_{1/2}$ is very long, however, it is assumed that the two-neutrino rate is being measured. Table 1 shows the results of geochemical results on $\beta\beta_{2\nu}$. It is clear that discrepancies exist between the measured and predicted rates. Such discrepancies led to the desire to measure one of these decays in the laboratory.

In the laboratory $\beta\beta_{2\nu}$ experiments, one must see both electrons. The crucial

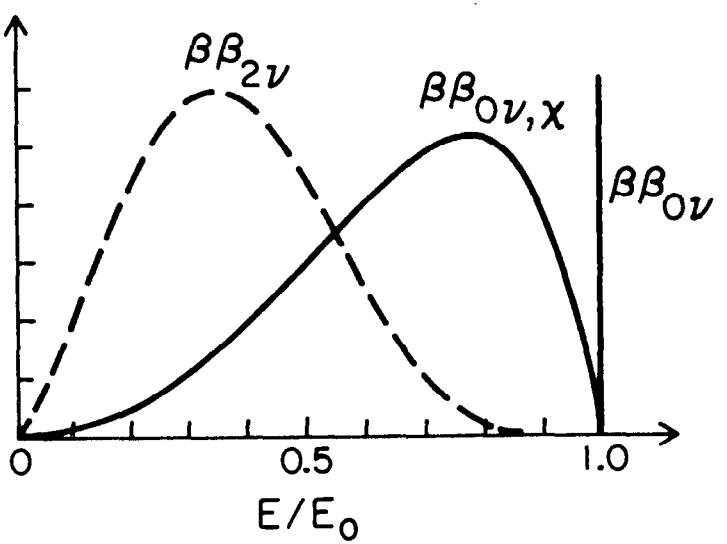

Fig. 2. The energy spectra for the three types of double beta decay. E_0 is the endpoint energy.

problem is radioactivity from the uranium and thorium decay chains. I will discuss in some detail the experiments at UC Irvine of M. Moe *et al.* which led to the first laboratory observation of $\beta\beta_{2\nu}$. One large background for such experiments was ^{214}Bi, whose β decay is occasionally accompanied by a second electron from internal conversion. There is an alpha decay 164 μs later from ^{214}Po. The Irvine group first built a cloud chamber experiment[17] to see the delayed alpha. Unfortunately, there were problems due to radon and there was also a problem of scanning many pictures.

Table 1: Two-Neutrino $\beta\beta$ Lifetimes

Nucleus	Geochemical (10^{20}y)		Theoretical[16]
^{82}Se	1.30 ± 0.05 [13]	1.2 ± 0.1 [14]	$.05 - .40$
^{128}Te	$> 5 \times 10^4$ [13]	$(1.8 \pm 0.7) \times 10^4$ [15]	10^3
^{130}Te	21 ± 6 [13]	7.5 ± 0.3 [14]	0.2

The next generation device at Irvine was a time projection chamber (TPC).[18,19] Figure 3 shows one view of the TPC. It consists of octagonal planes for the cathode, anode, and source foil. The dimensions are 54 cm for the source, and $\pm$10 cm from the source to the two detector planes. Each of the two electrons follows a spiral trajectory around the magnetic field. The ionization electrons drift to the anode, and they are detected on anode wires and nearby cathode wires. The resolution is measured to be about 20% FWHM at 1 MeV, using internal conversion electrons. The resolution is somewhat worse for electrons at small angles to the magnetic field. All construction materials were chosen to be low in radioactivity, and the detector sits inside a lead shielding wall and a cosmic ray veto system. Helmholtz coils are used to provide the magnetic field. One of the main backgrounds in the TPC are gamma rays which are probably from (n, γ) reactions caused by cosmic rays. Such a gamma can produce a Compton electron which is turn produces a Moeller scattering. This gives the two electron signature which can fake double beta decay. This background has a characteristic angular distribution, with many events having $\cos\theta > 0$.

A second major background is the beta decay of ^{208}Tl, followed by an internal conversion which produces the second electron. This produces a characteristic singles energy spectrum in which one of the two electrons is quite soft. The rate of these is known from the large number of beta decays without internal conversion.

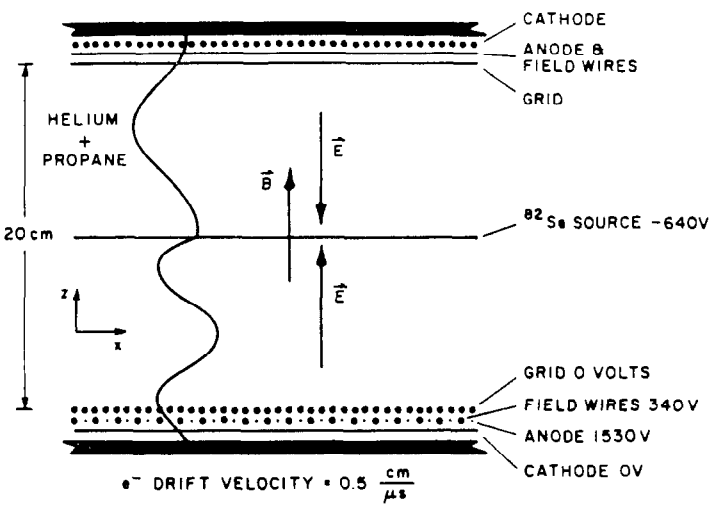

Fig. 3. Schematic drawing of the TPC used by the UC Irvine group to observe two-neutrino double beta of ^{82}Se.

Figure 4 shows the observed sum-energy spectrum for two electron events. The curve is the theoretical $\beta\beta_{2\nu}$ spectrum normalized to $1.1 \cdot 10^{20}$y. It is at least plausible that the energy spectrum is dominated by the signal from 1.3–2.0 MeV. In this range, with a cut on minimum singles energy of 150 keV, they expect 2.8 ± 0.7 events from ^{208}Tl and 9.3 ± 2.6 events from Moeller scattering of Compton electrons. They see 46 events satisfying these criteria. For further assurance that the signal is understood, the Irvine group looks at the singles energy spectrum and the distribution of angles between the two electron. Figure 5 shows these spectra. The curves are for the three major sources, $\beta\beta_{2\nu}$, ^{208}Tl, and Moeller, but assuming that each contributes the total number of events. The singles energy spectrum from ^{208}Tl and the angle spectrum from Moeller scattering are inconsistent with the data, giving additional confidence that $\beta\beta_{2\nu}$ is the dominant source. A global fit gives the result

$$T^{2\nu}_{1/2} = (1.1^{+0.8}_{-0.3}) \cdot 10^{20}\text{y for } ^{82}\text{Se}.$$

Thus the Irvine result confirms the geochemical measurements. The nuclear theory overestimates the decay rates for $\beta\beta_{2\nu}$. The Irvine group has rebuilt the detector, which is now called TPC2, with lower backgrounds. Figure 4 shows the spectrum from this detector, which confirms the original result.

There has been continuing work by nuclear theorists to understand the long lifetimes for two-neutrino decay. Haxton[16] and colleagues used a shell model calculation with a large number of intermediate states in their original calculation. They included only allowed transitions ($J^P = 0^+, 1^+$) to the intermediate odd-odd state. More recently, he has included a $J^P = 0^-$ operator,[20] which is not negligible. This has the effect of increasing the lifetimes by about 30%, reducing the discrepancy.

Three other groups, Vogel and Zirnbauer,[21] Muto and Klapdor,[22] and Civitarese, Faessler and Tomoda[23] have used the quasiparticle random phase approximation (QRPA). They introduce a particle-particle spin-isospin force, as a new adjustable parameter. In principle, this should be included in the shell model approach of Haxton, but with fixed amplitude. The result is that the rate can be reduced by the proper amount. The crucial question is whether the effect changes the neutrinoless rate by a large factor. At this time, the Caltech group[24] says yes, the others say no.[25] Until this issue is resolved, one needs

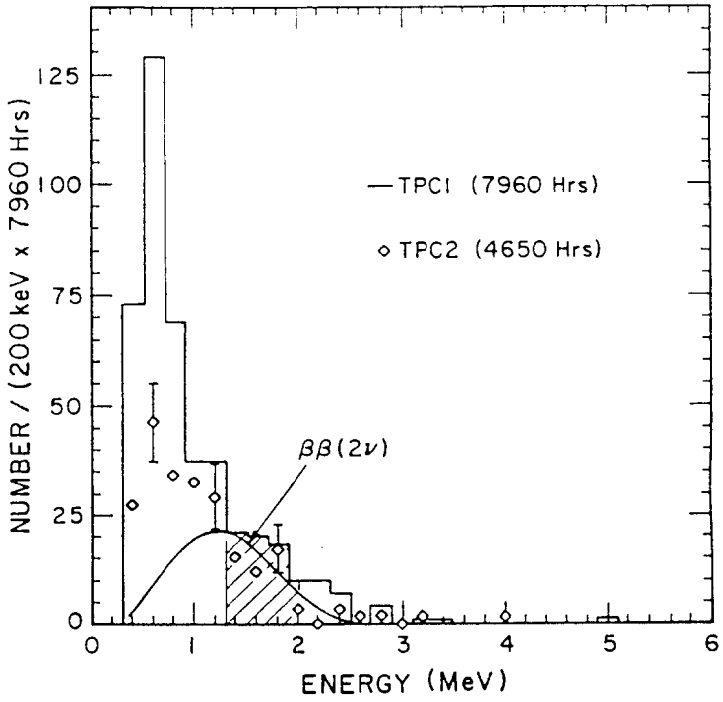

Fig. 4. The spectrum of the total energy for the two electrons in the Irvine experiment. The histogram shows the original data[19] from TPC1. The TPC2 points come from a rebuilt detector with lower backgrounds. The curve shows the expected spectrum for the signal.

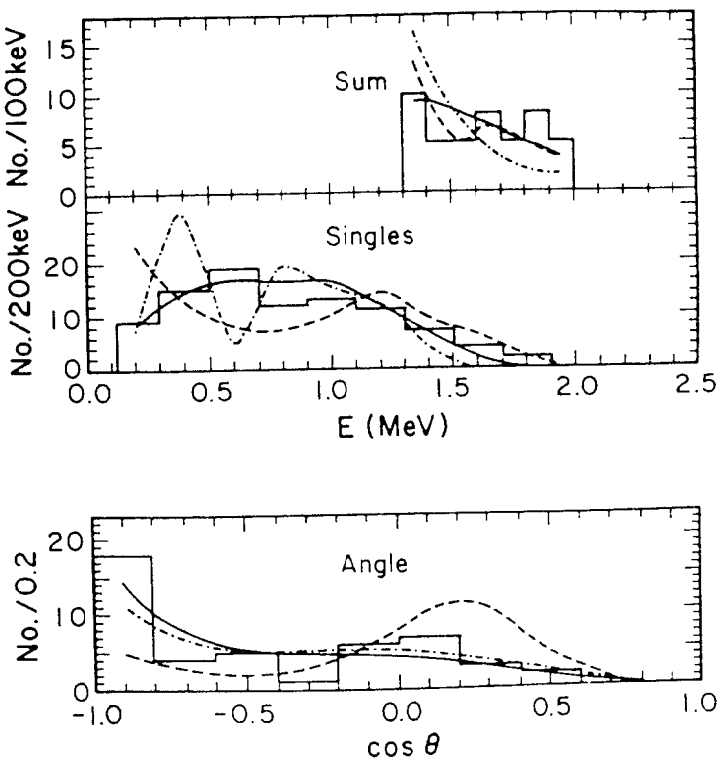

Fig. 5. The spectra for the two-electron events with energy sum between 1.3 and 2.0 MeV. The singles spectrum shows the energy spectrum for the individual electrons. The angle is the angle between the two electrons. The curves show the shapes of the three assumed contributions, but normalizing to the total number of events: $\beta\beta_{2\nu}$ (solid curve), Moeller scattering (dashed curve), and ^{208}Tl (dot-dashed curve).

to keep a factor of about 3 uncertainty in the scale factor for neutrino masses coming from $\beta\beta_{0\nu}$ limits. It would be very useful to have a series of nuclei for which the two-neutrino rate is measured. Very recently, a ITEP-Yerevan group,[26] has given a preliminary report that they see $\beta\beta_{2\nu}$ in ^{76}Ge. A LBL-Mt. Holyoke-Univ. of New Mexico group[27] is making substantial progress in trying to measure ^{100}Mo. I will discuss both of these experiments below.

NEUTRINOLESS DOUBLE BETA DECAY EXPERIMENTS

As I discussed at the beginning, the experiment which is most sensitive to Majorana neutrinos is neutrinoless double beta decay. The great deal of activity in recent years has been in search of the decay $^{76}\mathrm{Ge} \rightarrow {}^{76}\mathrm{Se} + 2e^-$. There are a number of reasons why the most sensitive experiments use this isotope. Most importantly, ^{76}Ge is an 8% component of natural germanium, which is used to make solid state ionization detectors with excellent energy resolution (0.15% FWHM at 2 MeV). Since the source is distributed throughout the detector, it is possible to use a large source without degradation of the signal due to thick source foils. The very pure germanium in such detectors contains very little radioactive contamination. Finally, the endpoint energy of 2.04 MeV is high enough that the sensitivity to a neutrino mass is quite good. One simply looks for a peak at 2.04 MeV in the energy spectrum. The experimental goal is to suppress the background continuum as much as possible.

The experiment which sets the best limits on neutrinoless double beta decay is that of the UCSB/LBL collaboration.[28] The group members are D.O. Caldwell, R.M. Eisberg, D.M. Grumm, and myself from UCSB and F.S. Goulding, and A.R. Smith from LBL. The experiment is designed to have a large volume of active germanium, with shared active and passive shields to reduce background.

One major source of background is cosmic radiation. Although direct cosmic rays are easily vetoed, muon-induced neutrons are a serious problem. They can be reduced to a reasonable level by putting the experiment in a shallow underground site. The UCSB/LBL experiment is situated in the powerhouse of the Oroville Dam in California, with an overburden of 600 m.w.e. Among the worst remaining backgrounds is activity induced in the detector by cosmic rays when the materials were above ground. The chief background of this type is from the process ^{70}Ge (n, 3n)^{68}Ge, with the ^{68}Ge decaying by electron capture

to ^{68}Ga with a 280 day halflife. After 68 minutes the ^{68}Ga emits a 1.89 MeV β^+, which can produce up to 2.91 MeV in the detector if the two annihilation photons are both absorbed.

The other type of background is from natural radioactivity. Most activity in the surrounding matter is absorbed in the passive shield surrounding the experiment. Radon is removed by purging the enclosure with nitrogen. With these steps taken, the dominant source of natural radioactivity is the experiment. Impurities in the cryostat produce gamma rays which Compton scatter in the germanium, depositing a continuous energy spectrum. The goal of the experiment is to reduce the background level of 2000 counts/year·kg·keV at 2 MeV, which is seen above ground in a standard detector, to a level of 1–2 counts/year·kg·keV.

The detector is shown in Figure 6. There are eight detectors, each about 160 cm^3 in volume with a shared shield. The detectors have been remounted in a homemade, low-activity cryostat. The vacuum box was made from electroformed copper, and the cold finger is a piece of single-crystal silicon. There is no separate can for infrared shielding, but the outer surface of the Ge detectors are metallized.

The Ge detectors are surrounded by a NaI Compton veto. The purpose is to detect the gamma ray escaping from a Compton scatter in which 2 MeV is deposited. The NaI counters are 15 cm thick and are packaged in a copper jacket with low radioactivity. The outside of the experiment is a lead enclosure 8" thick. There is 2" of borated polyethylene inside this for neutrons.

Figure 7 shows the energy spectrum from some early running of the experiment. There are many gamma ray peaks, mostly from the uranium and thorium chains, except for the very prominent ^{40}K peak at 1.5 MeV. Much of the continuum is from the sum of the Compton scattering associated with all of these peaks. Figure 8 shows the region of interest for neutrinoless double beta decay, in 1 keV bins. The signal of $\beta\beta_{0\nu}$ would be a peak at 2.041 MeV, with a width of 3 keV FWHM. There is in fact a dip at this energy, and thus no evidence for $\beta\beta_{0\nu}$.

A maximum likelihood fit to this spectrum yields a limit of 1.4×10^{24}y at 68% C.L., which is the standard used for such experiments. On the other hand,

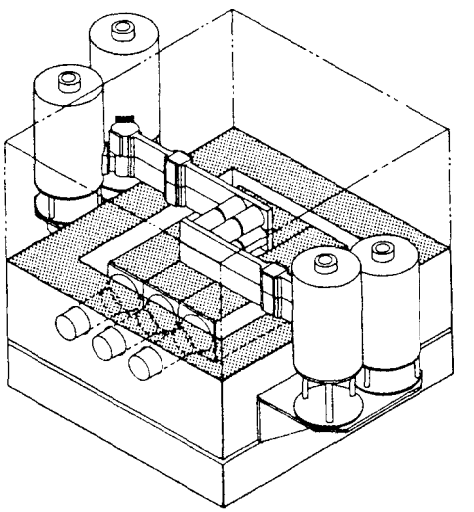

Fig. 6. The UCSB/LBL experiment designed to look for neutrinoless double beta decay in ^{76}Ge. The inner cylinders are the germanium detectors.

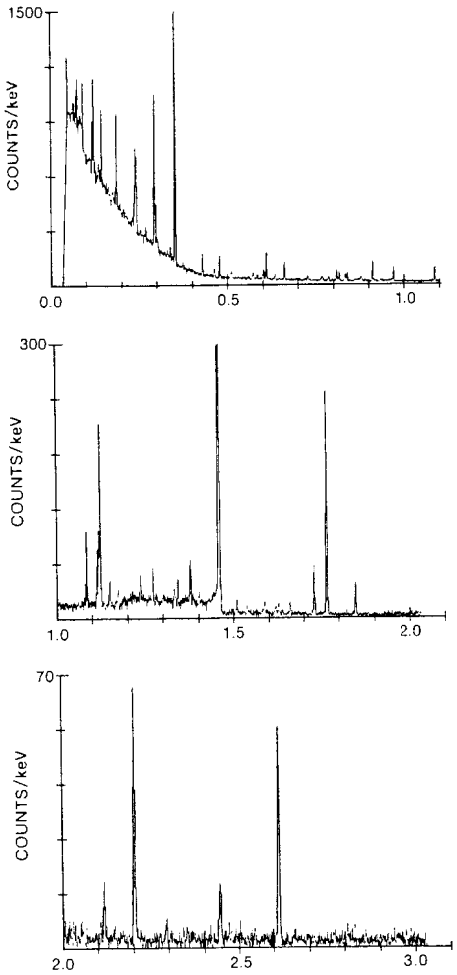

Fig. 7. The energy spectrum from 0–3 MeV from a short run with the ^{76}Ge experiment.

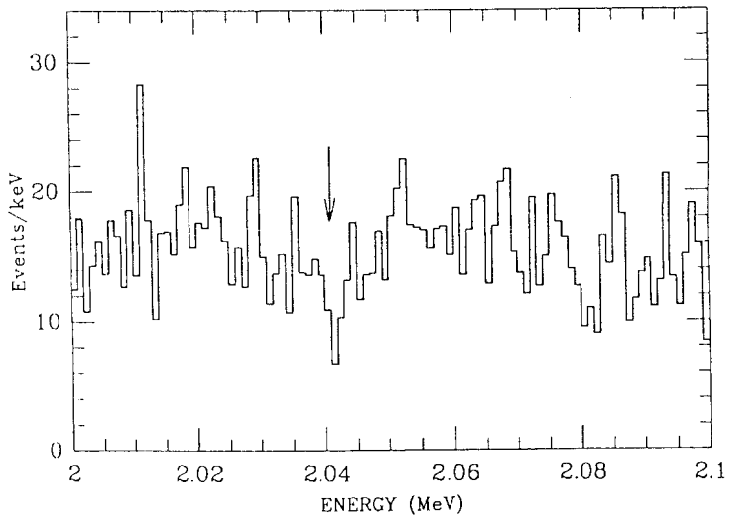

Fig. 8. The energy spectrum in the vicinity of 2.041 MeV. The signal of $\beta\beta_{0\nu}$ would be a peak at 2.041 MeV with a width of 3 keV FWHM.

one is uncomfortable at that confidence level with the dip at 2.041, so I will use the 90% C.L. limit of 8×10^{23}y. Table 2 shows the limits on $\beta\beta_{0\nu}$ for all of the ^{76}Ge experiments.

Table 2: Neutrinoless $\beta\beta$ Results for Ge

Group	Background c/keV·kg·y	kg·y	$T_{1/2}$ Limits (10^{23}y) $0^+ \to 0^+$	$0^+ \to 2^+$
Zar./Bord./Stras.[29]	2.3 ($0^+ \to 2^+$)	1.6	—	0.6
Osaka[30]	6	0.87	0.7	0.6
Guelph/Apt./Que.[31]	2.2	1.9	1.6	—
PNL/USC[32]	1.5	2	3	0.8
Milan[33]	22, 5*	2.8	1.7–3.3	0.3
CIT/PSI/Neuchatel[34]	3.0	2.5	3	0.7
ITEP/Yerevan[26]	3	†	4	—
UCSB/LBL[28]	1.4	12.1	8–14	2–3

* Two detectors were used with quite different backgrounds, but the rest of the information combines their results.
† This 0.5 kg detector was made from 85% enriched ^{76}Ge.

I will use the limit of 8×10^{23}y from the UCSB/LBL group to calculate limits on the quantities of physical interest. The limit on Majorana mass for the electron neutrino is above 1 eV/c^2, with some spread among various nuclear models.[35–37] In the one case[24] where the matrix element changes considerably because of the two-neutrino result, the limit is closer to 6 eV/c^2. It is hoped that more $\beta\beta_{2\nu}$ measurements and work on the theoretical models will resolve this discrepancy. In any case, the limits are much smaller than the value of about 20 eV/c^2 for Dirac neutrinos from tritium beta decay or SN 1987A.

As mentioned earlier, if there is a mixture of neutrinos the limit is on the combination

$$\langle m_\nu \rangle = \sum_m \lambda_m \, |U_{em}|^2 \; M_m$$

where λ_m is a relative CP phase factor, ± 1. There can be a cancellation which makes $\langle m_\nu \rangle$ less than any single mass. It now appears unlikely[38] that this is a problem.

If one neutrino dominates, then $\langle m_\nu \rangle = |U_{ej}|^2 \, M_j \lesssim 1$eV/c^2. Over a wide range of neutrino mixing parameters, this sets the best limit. For example, in the mass range 100 keV/c^2 – 1 MeV/c^2, the best limits for Dirac neutrinos come from searches for kinks in single beta decay, with limits of $|U_{ej}|^2 \lesssim 10^{-3}$. This can be compared with the limits from $\beta\beta_{0\nu}$ of $|U_{ej}|^2 \lesssim 10^{-5} - 10^{-6}$.

For heavy Majorana neutrinos, the limits are expressed differently depending on whether they couple to left- or right-handed W-bosons. For neutrinos which couple to L.H.C., such as those for a fourth generation, there is no helicity suppression for $M_j \gtrsim 100$ MeV/c^2. On the other hand, the range of the virtual neutrinos is very short, and the rate depends on the overlap of two nucleons in the nuclear wave function. For a heavy neutrino, the limit in this case corresponds to

$$|U_{ej}|^2 \leq 10^{-7} M_j \; (\mathrm{GeV/c^2}).$$

Figure 9 shows a figure adapted from a paper by Fred Gilman[39] which reports the limits on fourth-generation neutrinos. I have added a line corresponding to the $\beta\beta_{0\nu}$ limit.

The other type of Majorana neutrinos are those which couple to right-handed W-bosons. These arise in left-right symmetric models, such as those which lead to the see-saw mechanism. In this case the limits depend on both the neutrino mass and the right-handed W mass. Figure 10 is taken from work by Mohapatra[40] updated to recent results. The limits are very good, requiring $M(W_R) \gtrsim 1$ TeV/c^2 for neutrino masses in the range of 100s of GeV.

MAJORON-INDUCED DOUBLE BETA DECAY

The majoron[5,6] is a hypothetical massless scalar boson which could arise from the breaking of B–L symmetry. The important characteristics of the particle are that it is massless and that it couples to $\nu\nu$ (as opposed to the Z^0, which couples to $\nu\bar{\nu}$). By far the most stringent limit on the coupling of such a particle comes from looking for double beta decay with majoron emissions. In this case the two virtual neutrinos emitted annihilate into the majoron. Since two of the three particles are seen in the detector, the energy spectrum is peaked much higher than for $\beta\beta_{2\nu}$, as shown in Figure 2.

This decay mode attracted a great deal of interest around January of 1987, when the group from Pacific Northwest Laboratory and University of South Carolina (PNL/USC) announced evidence for its observation.[41] The energy spectrum on which this announcement was based is shown in Figure 11. There is

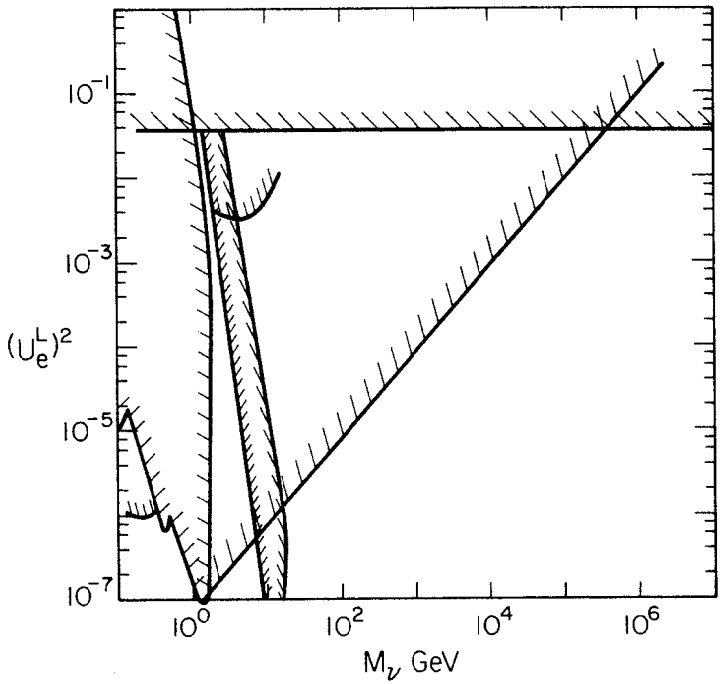

Fig. 9. Limits on $|U_{eL}|^2$ versus M_ν, for a fourth-generation neutrino, adopted from Gilman.[39] The diagonal line is the limit for Majorana neutrinos set by the $\beta\beta_{0\nu}$ limit.

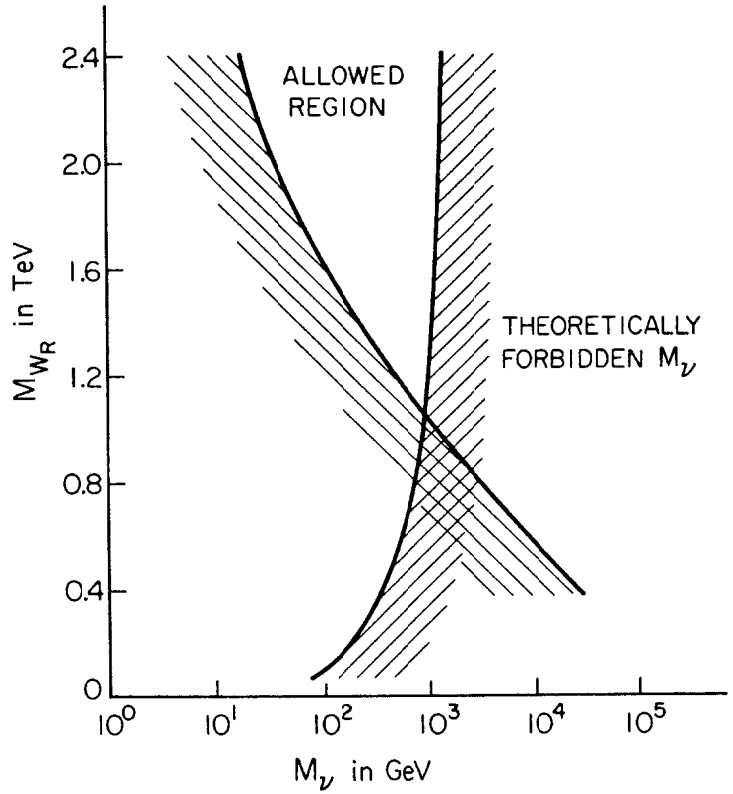

Fig. 10. The limits set on mass for a right-handed W-boson versus mass of the electron neutrino coupling to that W. This is adopted from Mohapatra[40] to take into account the present $\beta\beta_{0\nu}$ limit.

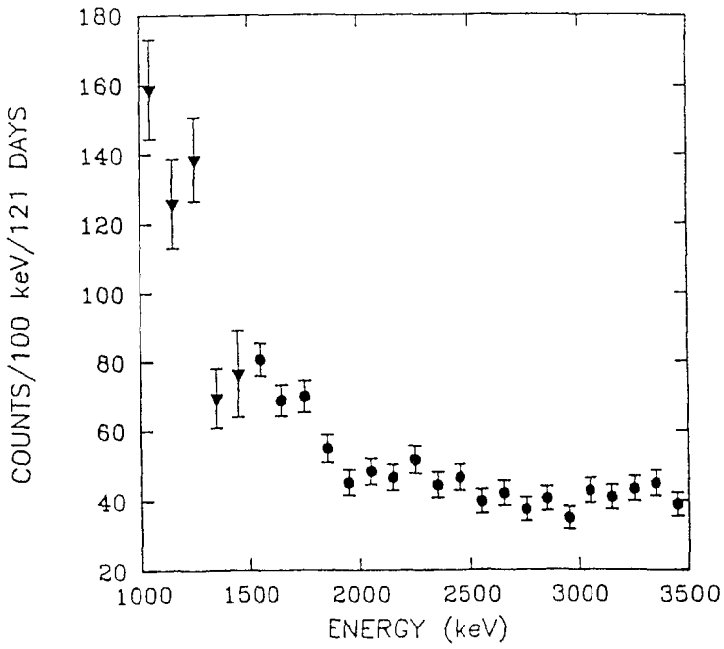

Fig. 11. The energy spectrum from the ^{76}Ge experiment of the PNL/USC group,[41] with peaks removed.

an almost flat spectrum from 3.5 MeV down to about 1.9 MeV, with increased activity below that. The PNL/USC group could not explain that step with any known background, and thought that it could be explained most easily as $\beta\beta_\chi$. The lifetime corresponding to the excess seen is $(6 \pm 1) \times 10^{20}$y. Of course if this is the observation of double beta decay with majoron emission, it establishes not only the existence of the Goldstone boson, but also that the electron neutrino is a Majorana particle.

The UCSB/LBL group analyzed existing data more carefully to increase its sensitivity to this mode.[42] The energy spectrum is shown in Figure 12. There is a good fit to the data using only Compton shapes for known peaks, the positron spectrum from ^{68}Ga, and a small constant term. There is no evidence of an additional $\beta\beta_\chi$ shape, and the limits that can be set on that mode is $T_{1/2} > 1.4 \times 10^{21}$y at 90% C.L. The CIT/SIN/Neuchatel group achieved similar results.[43]

Table 3: No-Neutrino $\beta\beta$ Decay with Majoron Emission

Nuclide	Group	Halflife (10^{20}y)	$\lvert\langle g_\chi\rangle\rvert \cdot 10^4$
^{76}Ge	PNL/USC	6 ± 1	7.4
	CIT/SIN/Neuch.	> 12	<5.3
	UCSB/LBL	> 14	<4.8
^{82}Se	Irvine	> 16	<1.9
^{100}Mo	LBL/Mt. Hol./NM	> 3.3	<2.0

More recently, the best limits on the majoron decay mode come from the Irvine ^{82}Se experiment[44] and the LBL/Mt. Holyoke/New Mexico experiment using ^{100}Mo.[45] The latter group uses 17g of 98% enriched ^{100}Mo foils inserted between planar Si(Li) detectors, so that the two electrons would make coincidence counts. Table 3 shows the results from groups with the most sensitive results on $\beta\beta_\chi$. Comparisons can be made by noting the limits on $|\langle g_\chi\rangle|^2$, the coupling of the Majoron to the electron neutrino ($T_{1/2} \propto |\langle g_\chi\rangle|^2$). While the limits from ^{82}Se and ^{100}Mo correspond to effective rate limits about an order of magnitude beyond that indicated by the PNL/USC experiment. The evidence is now overwhelming that the interesting double beta decay with majoron emission has not yet been observed.

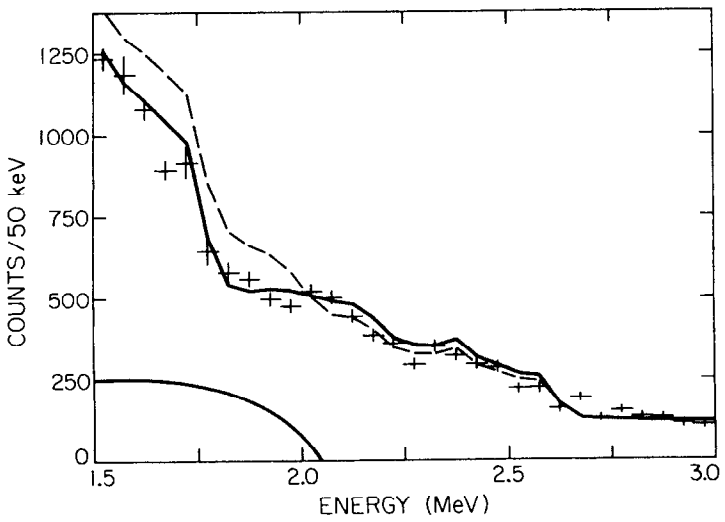

Fig. 12. The energy spectrum from the UCSB/LBL experiment, with peaks removed.[42] The solid line is the fit with no double beta decay with majoron emission. The dashed line is the lower limit possible if the $\beta\beta_\chi$ spectrum is added.

FUTURE PROSPECTS FOR NEUTRINOLESS DOUBLE BETA DECAY

There has been an enormous improvement in the sensitivity of the neutrinoless double beta decay experiments over the last few years. Although these experiments are continuing, the gain in the limit of the halflife is now quite slow. There are a number of ideas for large improvements in the future, and they all involve the use of enriched isotopes.

The ITEP-Yerevan group has three 85% enriched ^{76}Ge detectors, the total mass of which corresponds to 2.4 times as much of the active isotope as for the UCSB/LBL experiment. After taking into account the fact that there is somewhat more background per kg of Ge, but less per kg of ^{76}Ge, this experiment can set limits 4 times longer for the same running period. A Moscow-Leningrad group is reported to have 15 kg of enriched ^{76}Ge, but this has not been made into detectors yet. The cost of the enriched isotope is prohibitively expensive in the West.

The ^{82}Se experiment and ^{100}Mo experiments will do well at setting better limits on $\beta\beta_\chi$, but since the energy resolution is much worse than for germanium detectors, they may not become competitive for $\beta\beta_{0\nu}$. Another isotope which is an interesting source/detector is ^{136}Xe. The operating experiments includes a proportional counter[46] and an ionization chamber,[47] both with high pressure and good resolution, and both in the Baksan laboratory. The Milan group[48] has a 10 atmosphere MWPC operating in the Gran Sasso Laboratory. The resolution is 5% FWHM and the detector can use up to 3.6 kg of 60% enriched ^{136}Xe. The Caltech/PSI/Neuchatel group has a 355-liter TPC capable of operating with five atmospheres of 60% enriched ^{136}Xe, with an energy resolution of 5% and excellent spatial resolution. An even larger TPC (13 m^3) which can use 10 kg of 93% enriched ^{136}Xe is being constructed by an INR/ITEP group in Moscow. The hope is that the background will be low enough in these detectors so that the 5% energy resolution is sufficient.

DARK MATTER SEARCH

There is an extensive discussion of the theory behind our understanding of dark matter in the universe in Hall's lectures.[49] The best limits on weakly interacting massive particles are set by the ^{76}Ge double beta decay experiments. Such

experiments represent the lowest background levels, and therefore the greatest sensitivity to the elastic scattering of dark matter.

For this discussion I assume that dark matter exists, and that it accounts for the critical density ($\Omega = 1$). I also assume that it is not baryonic. The primary classes of dark matter are hot and cold dark matter. Models using cold dark matter gives the best description of galaxy formation. Of the cold dark matter candidates, the major types are axions and weakly interacting massive particles (WIMPs), which is what these experiments look for. I will use the symbol δ to denote the dark matter particle.

The present density fixes the annihilation cross section and by crossing the elastic scattering cross section on a nucleus. This cross section, the Lee-Weinberg[50] cross section, is equal to the weak interaction cross section for δ mass of about 4 GeV/c^2, and is lower for higher masses. For a somewhat larger cross section, such a particle also cools the sun enough to lower the solar neutrino flux.[51–54] Such particles are often called cosmions. In cosmion models, there must have been an initial asymmetry, as with baryons, to explain the present density. The Lee-Weinberg cross section is $\sigma \simeq 4 \cdot 10^{-38}\text{cm}^2 \times \text{CF}$, where CF is the coherence factor for nuclei.

There are tight constraints on the quantities which determine the rate of elastic scattering. Absence of evidence for the δ in e^+e^- interactions sets limits $M_\delta \gtrsim 3$ GeV/c^2. The r.m.s. velocity is about 270 km/s, and the halo density is $\rho \simeq 0.3$ GeV/cm^3. The only major uncertainty is the coherence factor.

Bernard Sadoulet has calculated rates for three archetypes of dark matter, shown in Figure 13. The first is for the Lee-Weinberg cross section and a particle, like the photino, that couples to spin. For this case, spinless nuclei are of little use, and for a nucleus such as boson the rate is a few events/day for a kilogram of material.

The favorable cases for a germanium detector are the other two. If the cross section is coherent over the nucleus, and proportional to the square of the number of nucleus, A^2, then the rate is about 40 events/kg·day. If the coupling of the particle is similar to that of massive Dirac neutrinos, the rate is over 100 events/kg·day. A particle-antiparticle would be necessary if these particles are responsible for all of dark matter.

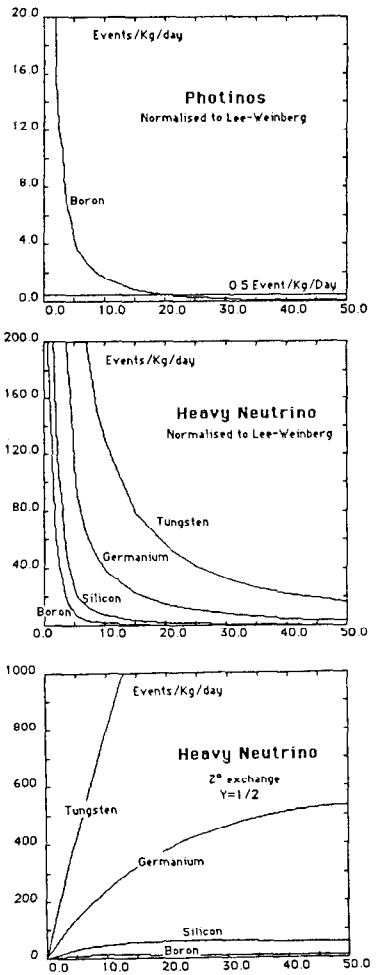

Fig. 13. Interaction rates on various nuclear targets for three examples of possible dark matter particles: photinos, which couple to spin; heavy neutrinos, but with the Lee-Weinberg cross section; heavy neutrinos with the usual Z^0 exchange, which would require initial asymmetry.

For such a particle of mass m scattering from a Ge nucleus of mass M, the average energy deposition at low energy is

$$\langle E_d \rangle = m^2 M \langle v^2 \rangle / (m+M)^2$$

where $\langle v^2 \rangle$ is the mean square speed of m. For $m \simeq 10$ GeV/c^2 this corresponds to about $\langle E_d \rangle \simeq 10$ keV $(\frac{m}{10 \text{ GeV/c}^2})^2$. These are already small energy deposits, but there is an additional factor to take into account the small fraction of the energy deposited as ionization. The recoiling nucleus gives an ionization signal about 20% of that caused by an electron of the same kinetic energy. Thus the energy deposit in the detector is about 2 keV or less, with a tail above that.

The energy spectrum in the UCSB/LBL double beta decay experiment (Fig. 7) showed a marked rise below 400 keV, with a relatively high counting rate in the 100 keV energy range. This background was due to the presence of half a gram of In, which has a 486 keV β^- with a halflife of $4 \cdot 10^4$ years! When the In was replaced with gold, the background for that detector became flat down to about 15 keV at a level of $\frac{1}{2}$ count/keV·kg day, except for some X-ray peaks. Figure 14 shows the most recent energy spectrum in the 2–20 keV region. There are X-ray peaks at 10.4 keV and 9.7 keV, for Ga and Zn respectively, due to the ^{68}Ge decay chain. The counting rate below 3 keV rises dramatically because of the tail of the amplifier noise spectrum. Between 3 keV and 15 keV, there is a significant continuum, with an integrated intensity of about 20 counts/kg·day, which is due to tritium. This tritium is probably produced as a cosmic ray spallation product when the detector was above ground.

One can set very useful limits on mass and cross section of the dark matter from this spectrum.[55] Limits are set by fitting the data to the background shape plus the expected spectrum for a massive Dirac neutrino. If such a spectrum is added to the known background shape, we can rule out masses of 12 GeV/c^2 to 1.4 TeV/c^2. Since there are many models which predict weakly interacting particles in this mass range, it is important to display the results of this experiment in a way which does not depend on the model used. Figure 15 shows an exclusion plot in dark particle mass vs. interaction cross section, primarily of that particle with Ge. In the region of large masses the upper limit on cross section corresponds to the case in which the energy deposition in the NaI is sufficient to veto the event. At lower masses, particles with a large enough cross section with

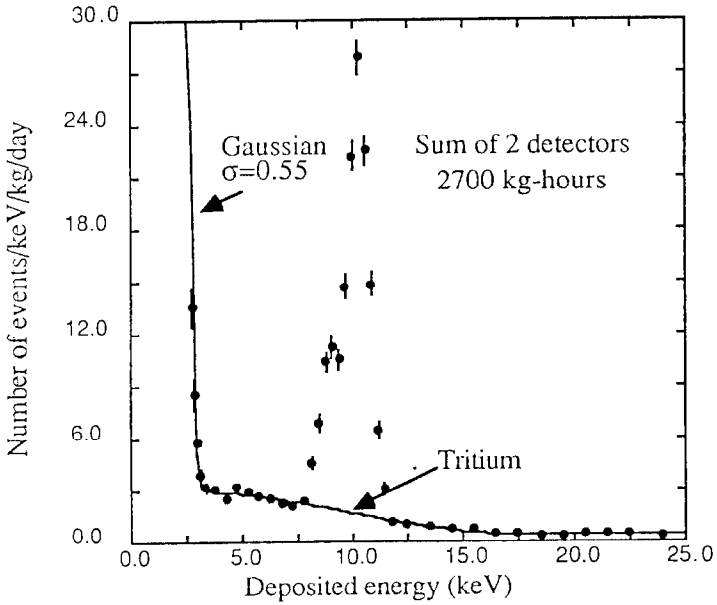

Fig. 14. Ionization energy spectrum for two germanium detectors operated for a total exposure of 2700 kg-hours. The curve shows the background shape, described by a flat background above 16 keV, a tritium spectrum below that, and a sharp rise due to electronic noise around 3 keV. There are two peaks due to Ga and Zn X-ray peaks near 10 keV.

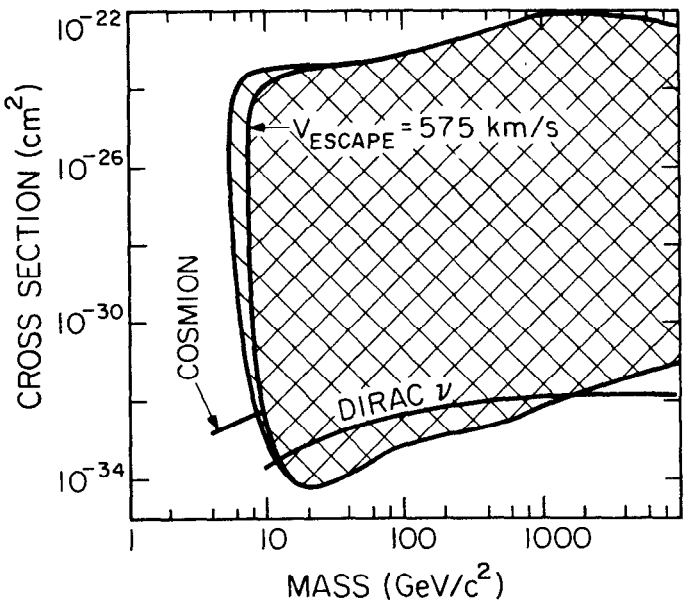

Fig. 15. Mass exclusion plot for particular cross section for the interaction with Ge (or for the upper boundary, with the earth). The shaded area is excluded at the 2σ level. Expected cross section lines are shown for cosmions and Dirac neutrinos.

the earth are slowed before they reach the apparatus enough that they produce insufficient recoil energy to be observed. The left edge of the exclusion region is determined by the data near threshold. All limits are at the two standard deviation level. Earlier limits from a similar experiment are somewhat weaker.[56]

There is an interesting possibility for improving on these limits.[57] Silicon detectors provide better sensitivity for three reasons. Lower energy is attainable, which is important for the mass limit. The silicon nucleus is lighter, so the average energy deposit is greater. In addition, the ionization efficiency is higher in silicon than in germanium. About 100 grams of silicon detectors will be installed this year into the experiment, to get a first look at the improvement. Eventually we hope to cover the full range (down to 4 GeV/c^2) of interest for cosmions, which have cross section of about 10^{-36}cm^2.

CONCLUSIONS

For a wide range of models which extend the standard model of particle physics, the tightest constraint comes from neutrinoless double beta decay. In particular, the limit of $T_{1/2} > 8 \times 10^{23}$y corresponds to a limit of $\sim$ 1 eV/c^2 on the Majorana mass of the electron neutrino. There is no evidence for double beta decay with majoron emission. Many experiments rule out the earlier signal. To go beyond the present limits new technologies are needed, probably with separated isotopes.

The low radioactive backgrounds achieved for the UCSB/LBL ^{76}Ge experiment have been important for conducting a sensitive dark matter search. Best limits on cold dark matter in the GeV/c^2 mass range come from this experiment. Silicon detectors should improve the sensitivity, and will be installed soon.

ACKNOWLEDGEMENTS

I am especially indebted to Boris Kayser, who was at Snowmass and therefore was forced to answer all of my questions on the finer points of double beta decay theory. In addition, I have drawn on the expertise of my colleagues, especially David Caldwell, Fred Goulding, Al Smith, and Bernard Sadoulet.

REFERENCES

1. M. Goeppert-Mayer, *Phys. Rev.* **48**, 512 (1935).
2. E. Majorana, *Nuovo Cimento* **14**, 171 (1937).
3. G. Racah, *Nuovo Cimento* **14**, 322 (1937).
4. W.H. Furry, *Phys. Rev.* **56**, 1184 (1939).
5. G. Gelmini and M. Roncadelli, *Phys. Lett.* **99B**, 411 (1981); H.M. Georgi, S.L. Glashow, and S. Nussinov, *Nucl. Phys.* **B193**, 297 (1981).
6. Y. Chikashige, R.N. Mohapatra, and R.D. Peccei, *Phys. Lett.* **98B**, 265 (1981).
7. R. Davis, *Phys. Rev.* **97**, 766 (1955).
8. There is an extensive discussion with many references in "Physics of Massive Neutrinos", by Felix Boehm and Petr Vogel, Cambridge University Press (Cambridge, 1987).
9. B. Kayser, "The Physics of Massive Neutrinos", Saclay preprint DPhPE87–21 (to be published as a book).
10. L. Wolfenstein, these Proceedings.
11. M. Gell-Mann, P. Ramond, and R. Slansky, in "Supergravity," North Holland (Amsterdam, 1979).
12. See Reference 9.
13. T. Kirsten *et al.*, in "Nuclear Beta Decays and Neutrinos," editors T. Kotani, H. Ejiri, and E. Takasugi (World Scientific, Singapore, 1986) p. 81 and references therein.
14. W.J. Lin *et al.*, *Nucl. Phys.* **A481**, 477 (1988).
15. W.J. Lin *et al.*, *Nucl. Phys.* **A481**, 484 (1988).
16. W.C. Haxton and G.J. Stephenson, Jr., *Progress in Particle and Nuclear Physics* **12**, 409 (1984).
17. M.K. Moe and D.D. Lowenthal, *Phys. Rev. C* **22**, 2186 (1980).
18. S.R. Elliott, A.A. Hahn, and M.K. Moe, *Phys. Rev. Lett.* **59**, 2020 (1987).
19. S.R. Elliott, Ph.D. dissertation, University of California, Irvine, (1987, unpublished).
20. A.G. Williams and W.C. Haxton, Univ. of Washington preprint, (1988, unpublished).
21. P. Vogel and M.R. Zirnbauer, *Phys. Rev. Lett.* **52**, 3148 (1986).
22. K. Muto and H.V. Klapdor, *Phys. Lett.* **B201**, 420 (1988).
23. O. Civitarese, A. Faessler, and T. Tomoda, *Phys. Lett.* **B194**, 11 (1987).
24. J. Engel, P. Vogel, and M.R. Zirnbauer, *Phys. Rev. C* **37**, 731 (1988).
25. T. Tomoda and A. Faessler, *Phys. Lett.* **B199**, 475 (1987). This was also reported as private communication from H.V. Klapdor of Ref. 22 to D.O. Caldwell.
26. A.A Vasenko *et al.*, paper submitted to the 13th Int. Conf. on Neutrino Physics and Astrophysics, Boston, MA (1988), and private communication.
27. M. Alston-Garnjost *et al.*, *Phys. Rev. Lett.* **60**, 1928 (1988).
28. D.O. Caldwell *et al.*, *Phys. Rev. Lett.* **59**, 419 (1987). More recent results are published in this text.
29. A. Morales, Proc. of the Ninth Workshop on Grand Unification, Aix-les-Bains, France (1988); and F. Leccia *et al.*, *Nuovo Cimento* **78A**, 50 (1983), and **85A**, 19, (1985).
30. H. Ejiri *et al.*, *J. Phys. G.: Nucl. Phys.* **13**, 839 (1987).
31. P. Jagam *et al.*, *Nucl. Instr. Meth.* **A267**, 486 (1988).
32. F.T. Avignone *et al.*, *Phys. Rev. C* **34**, 666 (1986).
33. E. Bellotti *et al.*, *Nuovo Cimento* **95A**, 1 (1986).
34. P. Fisher *et al.*, in Proc. of the 13th Int. Conf. on Neutrino Physics and Astrophysics, Boston, MA (1988).
35. W.C. Haxton and G.J. Stephenson, Jr., *Progress in Particle and Nuclear Physics* **12**, 409 (1984); modified by M. Doi *et al.*, *Prog. Theor. Phys. Supplement* **83**, 1 (1985).
36. See Ref. 25 and T. Tomoda *et al.*, *Nucl. Phys.* **A452**, 591 (1986).
37. K. Grotz and H.V. Klapdor, *Phys. Lett.* **153B**, 1 (1985) and **157B**, 242, (1985); also *Nucl. Phys.* **A460**, 395 (1986).
38. P. Langacker, B. Sathiapalan, and G. Steigman, *Nucl. Phys.* **B266**, 669 (1986).
39. F. Gilman, *Comments Nucl. Part. Phys.* **16**, 231 (1986).
40. R.N. Mohapatra, *Phys. Rev. D* **34**, 909 (1986).
41. F.T. Avignone *et al.*, Proc. APS Div. of Particles and Fields, Salt Lake City, ed. C. Detar and J. Ball (World Scientific, Singapore, 1987), p. 359.
42. See Ref. 28.
43. P. Fisher *et al.*, *Phys. Lett.* **B192**, 460 (1987).
44. S.R. Elliott *et al.*, *Phys. Rev. Lett.* **59**, 1649 (1987).
45. See Ref. 27.
46. V.V. Kuzminov *et al.*, *Nucl. Instr. Meth.* **B17**, 452 (1986).

47. A.S. Barabash *et al.*, *Nucl. Instr. Meth.* **B17**, 450 (1986).

48. E. Bellotti *et al.*, in Proc. Telemark IV, ed. V. Barger *et al.* (World Scientific, 1987), p. 307.

49. L. Hall, these Proceedings.

50. B.W. Lee and S. Weinberg, *Phys. Rev. Lett.* **39**, 165 (1977).

51. R.L. Gilliland, J. Faulkner, W.H. Press, and D.N. Spergel, *Ap. J.* **306**, 703 (1986).

52. G.B. Gelmini, L.J. Hall, and M.J. Lin, *Nucl. Phys.* **B281**, 726 (1987).

53. G.G. Ross and G.C. Segré, *Phys. Lett.* **B197**, 45 (1987).

54. S. Raby and G.B. West, *Phys. Lett.* **B202**, 47 (1988).

55. D.O. Caldwell *et al.*, *Phys. Rev. Lett.* **61**, 510 (1988).

56. S.P. Ahlen *et al.*, *Phys. Lett.* **B195**, 603 (1987).

57. B. Sadoulet *et al.*, Ap. J. **324**, L75 (1988).

NEUTRINO MASSES AND MIXINGS

Lincoln Wolfenstein
Carnegie Mellon University
Physics Department
Pittsburgh, PA 15213

Lectures given at the 1988 SLAC Summer Institute - July 18-29, 1988

1. *Introduction*

The neutrino is distinguished from other elementary fermions in that it has only weak interactions. It is produced in the laboratory as a result of weak decays. Like other fermions neutrinos are believed to exist in three "flavors" ν_e, ν_μ, and ν_τ associated with the charged leptons e, μ, and τ respectively. Each type of neutrino is known to be much less massive than its charged partner. We are concerned in these lectures with theoretical ideas and experimental evidence concerning neutrino mass.

I must start by making it clear that there is no definitive experimental evidence and no compelling theoretical argument in favor of a non-zero neutrino mass. It may well be that all neutrinos are massless. However, we will try to show that it is quite natural as one introduces physics beyond the minimal standard electroweak model that neutrinos acquire a small mass. Thus neutrino mass is of interest in particle physics as a possible window on new physics. In addition massive neutrinos could be of great importance in cosmology, conceivably providing the dark matter discussed in the lectures by Prof. Hall. Also effects of neutrino mass could seriously change the detected flux of neutrinos from astrophysical sources, in particular, the neutrinos from the sun.

In the first lecture I will concentrate on theoretical ideas and then I will turn to available and prospective evidence concerning neutrino mass.

2. *Mass Terms in Gauge Theories*

The framework of our theoretical discussion will be gauge theory; in particular, the standard SU(2) x U(1) electroweak gauge theory. A crucial feature of the gauge theory is that all fermions are introduced as massless chiral (Weyl) fields. The reason for this, of course, is that left-handed fermions have the standard weak SU(2) interactions and so must transform as doublets. Right-handed fermions do not interact and so must transform as singlets. The usual mass term which links the left-handed fermions to the right-handed fermions is forbidden by SU(2) invariance. Conversely the mass of all the usual fermions is proportional to the SU(2)-breaking, or weak, scale.

The free left-handed chiral fields may be expanded as

$$\psi_L(x) = \Sigma[b_{Lp}u_{Lp}e^{-ip\cdot x} + d^+_{Rp}v_{Rp}e^{ip\cdot x}] \tag{1}$$

where the sum is over momentum $\vec{p}$. Here b_L annihilates left-handed particles and d^+_R creates right-handed antiparticles. The existence of left-handed particles implies the existence of right-handed particles by fundamental principles of relativistic quantum field theory embodied in the CPT theorem. One can similarly write the right-handed fields $\psi_R(x)$. The usual Dirac field $\psi(x)$ is related by

$$\psi_L(x) = \frac{1}{2}(1+\gamma_5)\psi(x)$$

$$\psi_R(x) = \frac{1}{2}(1-\gamma_5)\psi(x) \tag{2}$$

$$\psi(x) = \psi_L(x) + \psi_R(x).$$

A technical point of importance is that one can define a right-handed field from the charge-conjugate of ψ_L

$$\psi^c_R(x) = C(\bar{\psi}_L(x))^T. \tag{3a}$$

This is the field which, when expanded, annihilates right-handed anti-particles and creates left-handed particles. (Here C is the Dirac charge conjugation matrix and T is transpose; the particular way this is written guarantees that ψ^c_R has the correct Lorentz transformation property.) Note I use the subscript R to emphasize that right-handed fermions are annihilated, but in fact ψ^c_R is just an alternative way of writing ψ^*_L. In the same way an alternative to ψ^*_R is

$$\psi^c_L = C(\bar{\psi}_R)^T. \tag{3b}$$

It is usual to introduce a set of fields $\psi_{Li}(x)$ and another set $\psi_{Rj}(x)$. Before we introduce interactions, however, we don't know the difference between particle and anti-particles so we could (and sometimes do) start only with a set ψ_{Li} and no ψ_{Rj} without loss of generality.

Let me first review how the other fermions, quarks and charged leptons, acquire their mass. The fermion fields are the left-handed doublets and right-handed singlets

$$\begin{pmatrix} N_{iL} \\ L_{iL} \end{pmatrix} \quad , \quad \begin{pmatrix} U_{iL} \\ D_{iL} \end{pmatrix} \quad , \quad L_{iR}, U_{iR}, D_{iR} \tag{4}$$

where $i = 1, 2, 3$ is the generation index, N_i and L_i represent neutrino and charged lepton, and U_i, D_i are the quarks. (We ignore throughout color and the associated SU(3) of QCD.) The question of whether to introduce the fields N_{iR} will be discussed in detail later.

The interactions of the fermions with the four gauge bosons of SU(2) x U(1) are dictated by the gauge principle and lead to the usual electromagnetic and weak interactions. In particular the charged current interactions have the form

$$\sum_i \; g \; W^\lambda \; \bar{U}_{iL} \; \gamma_\lambda \; D_{iL} \; + h.c. \tag{5}$$

$$\sum_i \; g \; W^\lambda \; \bar{N}_{iL} \; \gamma_\lambda \; L_{iL} \; + h.c.$$

The fields of Eq. (4) define the weak eigenstates, which as we shall see may not be the mass eigenstates. The right-handed fields have only U(1) interactions leading to the standard assignment of electric charge.

To make a sensible theory it is necessary to introduce the Higgs bosons. In the standard version of the standard model a single complex doublets of Higgs bosons is introduced

$$\Phi = \begin{pmatrix} \Phi^+ \\ \Phi^o \end{pmatrix}. \tag{6a}$$

The antiparticles also form a doublet

$$\tilde{\Phi} = i\tau_2 \Phi^* = \begin{pmatrix} \Phi^{o*} \\ -\Phi^- \end{pmatrix}. \tag{6b}$$

When the neutral Higgs boson Φ^o acquires a vacuum expectation value (VEV)

$$< \Phi^o > = v \tag{7}$$

the SU(2) x U(1) symmetry breaks down to the electromagnetic U(1) with W and Z becoming massive. One also introduces a Yukawa interaction between the fermions and the Higgs bosons as a means of converting the original chiral massless fields into massive Dirac fields. The Yukawa interaction is SU(2) invariant

$$Y = (Doublet\ \Phi) x (Doublet\ F_L) x (Singlet\ F_R). \tag{8}$$

Considering only the coupling involving the neutral Φ^o we have

$$Y(\Phi^o) = [f_{ij} \bar{D}_{Li} D_{Rj} \Phi^o + g_{ij} \bar{U}_{Li} U_{Rj} \Phi^{o*}] + [h_{ij} \bar{L}_{Li} L_{Rj} \Phi^o] + h.c. \tag{9}$$

where the sum over repeated indices is implied. Using Eq. (7) and setting

$$\Phi^o = \varphi + v \tag{10}$$

we have

$$Y(\Phi^o) \rightarrow M_d + M_u + M_e + Y(\varphi) \tag{11}$$

$$M_d = f_{ij} v \bar{D}_i D_j \tag{12a}$$

$$M_u = g_{ij} v \bar{U}_i U_j \tag{12b}$$

$$M_e = h_{ij} v \bar{L}_i L_j. \tag{12c}$$

Here φ represents the physical Higgs boson field and $Y(\varphi)$ the fermion interaction with φ. The M_a are now the mass terms for the quarks and the charged leptons.

Comment: In Eq. (12) the fermion fields are actually Dirac fields rather than Weyl fields. Considering the leptons, for example, one obtains directly from Eq. (9) with the aid of Eq. (2)

$$v(h_{ij} \bar{L}_{Li} L_{Rj} + h^*_{ij} \bar{L}_{Rj} L_{Li}) = \frac{1}{2} v(h_{ij} \bar{L}_i (1 - \gamma_5) L_j + h^*_{ji} \bar{L}_i (1 + \gamma_5) L_j) = v h_{ij} \bar{L}_i L_j \tag{13}$$

provided the matrix h is hermitean. In fact one can always choose h_{ij} hermitean without loss of generality by redefining the basis for the right-handed fields.

When we diagonalize the mass matrices (12) we obtain the mass eigenvalues and a mixing matrix. Considering the quarks first

$$D_j = (V_d)_{ji} d_i \tag{14a}$$

$$U_j = (V_u)_{ji} u_i \tag{14b}$$

where $d_i = (d, s, b)$ and $u_i = (u, c, t)$ are the usual "mass eigenstates." When we substitute Eqs. (14) into Eq. (5) we find

$$W^\lambda \bar{u}_{Lj} \gamma_\lambda U_{ji} d_{Li} \tag{15}$$

$$U = V_u^+ V_d \tag{16}$$

where U is the famous 3x3 Cabibbo-Kobayashi-Maskawa (KM) quark mixing matrix. Note that the Lagrangian contains two arbitrary 3x3 matrices (chosen here as hermitean), thus 18 arbitrary parameters for the quarks, but only 10 of these end up as observables: the six quark masses and the four KM parameters (three angles and one phase). The standard model which is so economical and elegant in its gauge sector (only two coupling constants) becomes extravagant and ugly in its Yukawa sector. For the charged leptons we have similarly

$$L_j = (V_e)_{ji} \ell_i \tag{17}$$

where the ℓ_i are the usual e, μ, τ. Because the neutrinos remain massless in the standard model we can redefine them by operating on the original N_{iL} with V_e so that the lepton analogue of U is just the unit matrix. Therefore, with massless (or degenerate massive) neutrinos the lepton mixing matrix V_e is unobservable.

Let me return now to the neutrino. In the usual presentation of the standard model we never introduce the fields N_{iR} since we have no essential need for them. On the other hand the symmetry between leptons and quarks as seen in the doublets of Eq. (4) may suggest that there really should be N_{iR} and indeed they are required in many extensions of the standard model. It is then possible to give neutrinos a mass term completely equivalent to those for charged leptons and quarks (Eq. (12))

$$M_D = m_{ij} \bar{N}_{Li} N_{Rj} + h.c. \tag{18}$$

This is referred to as a Dirac mass term since, as discussed above, N_L and N_R can be combined to form the four-component Dirac field. There is another way to construct a mass term in the case of neutrinos called the Majorana mass term. We can construct a mass term using only N_L

$$M_L = \mu_{ij} \bar{N}_{Li} N^c_{Rj} + h.c. \tag{19}$$

Notice that this is really proportional $N_L^* N_L^* + N_L N_L$ and therefore changes the "particle number" by two. Such a term would be forbidden by charge conservation for the other fermions but is conceivable for neutrinos. This term does violate the total "lepton number" $(N(N) + N(L^-) - N(\bar{N}) - N(L^+))$. However, lepton number L is not sacrosanct like electric charge since it is not associated with a gauged symmetry. In most theories of neutrino mass the fundamental new physics introduced is related to lepton number violation. The term M_L also violates weak isospin by one unit (since it annihilates or creates two N_L with $I_3 = \frac{1}{2}$) in contrast to M_D which violates weak isospin by $\frac{1}{2}$ unit. It is also possible to construct a Majorana mass term from N_R

$$M_R = \mu'_{ij} \bar{N}_{Ri} N^c_{Lj} + h.c. \tag{20}$$

Characteristics of those three types of mass terms are summarized in Table 1.

Table 1

	M_D	M_L	M_R
$\Delta \vec{I}$	$\frac{1}{2}$	1	0
ΔL	0	± 2	± 2

If we have only the Majorana mass term, say M_L, then the final particles will be massive but still have only two components. These are called Majorana particles. In their rest frame these particles have the usual two spin states and the anti-particles are identical to the particles. It is possible to have both Dirac and Majorana mass terms. In this case in general the final solution will be a set of two-component Majorana particles. The Dirac term in this case may be viewed simply as mixing the Majorana neutrinos obtained from M_L with those obtained from M_R. More details on the general formulation of neutrino mass terms can be found in Reference 1.

While conceptually a four-component Dirac neutrino is very different from a two-component Majorana, experimentally they are practically indistinguishable. The reason is that neutrinos are produced almost completely with left-handed helicity and at high energies ($E >> m$). In order to distinguish Dirac from Majorana neutrinos one needs to determine the character of the right-handed part (whether it is the new particle ψ_R or just the anti-particle ψ_R^c) and this in general requires observations suppressed by a factor $(m/E)^2$. An important distinction is that the Dirac neutrino can have a magnetic moment μ_ν but in all models we can imagine μ_ν is proportional to m_ν and so very small. In the "standard model" with a neutrino mass solely due to M_D one finds[2]

$$\mu_\nu = 3 \cdot 10^{-19} m_\nu(ev) \ Bohr \ magnetons \tag{21}$$

which is much too small to be detected.

An indirect, but very sensitive, indication of a Majorana mass for ν_e could come from the observation of neutrinoless double beta-decay, a process involving a change of lepton number by two units. As discussed in the lectures of Prof. Witherell the virtual exchange of a Majorana neutrino could induce this process. The amplitude is proportional to the diagonal element μ_{ee} of the Majorana mass matrix rather than to a mass eigenvalue.

3. *Models of Neutrino Mass*

In the standard SU(2) x U(1) gauge theory the neutrinos are massless provided (1) there is no N_R, (2) there are no Higgs bosons other than the doublet, and (3) there is no physics beyond the standard model. The ways to get a non-zero m_ν are:

1. Include the N_{Rj} so as to get the Dirac mass term of Eq. (18). While this provides the simplest way to get a non-zero neutrino mass, it is usually not considered as the sole origin of neutrino mass because it provides no insight into the smallness of neutrino mass.

2. Do not include N_{Rj} but add a Higgs triplet that has a Yukawa coupling to leptons. This provides a Higgs mechanism for producing the Majorana mass term of Eq. (19). The most interesting version is the Gelmini-Roncadelli model[3] discussed below.

3. Consider effects of new physics at a large mass scale M, in particular the violation of lepton number which results in Majorana mass terms. It is this idea which we will pursue in most detail.

The basic idea of the Gelmini-Roncadelli (GR) model is the addition of the triplet with the charge states

$$T = (T^o, T^+, T^{++}) \ .$$

The gauge invariant coupling of T to the product of two lepton doublets is

$$Y_T = \frac{1}{\sqrt{2}} k_{ij} \bar{\psi}_{Ri}^c \vec{\tau} \cdot \vec{T} \psi_{Lj} + h.c.$$

where ψ_L is the lepton doublet from Eq. (4). Looking just at neutrinos

$$Y_T \sim k_{ij} \bar{N}_{Ri}^c N_{Lj} T^o + h.c. \tag{22}$$

When T^o acquires a vacuum expectation value V_T Eq. (22) yields the mass term M_L of Eq. (19) with

$$\mu_{ij} = k_{ij} v_T .$$

Note that given its charge structure (corresponding to the choice of the U(1) quantum number of T) the triplet does not couple to the quarks. The smallness

of neutrino mass is "explained" by or related to the smallness of v_T/v, which is constrained by astrophysical arguments[4] to be less than 10^{-7} in the GR model.

The Yukawa interaction Y_T conserves lepton number provided T has a lepton number of two. In the GR model the Higgs potential $V(\Phi, T)$ also conserves lepton number L (there is no term of the form $\Phi\Phi T$). As a consequence when T^o acquires its vacuum expectation value, L is spontaneously broken. By Goldstone's theorem there results a massless spin-zero boson (essentially ImT^o); unlike the usual Higgs boson this boson remains as a true physical particle because lepton number is not a gauge symmetry. This particle is called the *Majoron*. There are many interesting phenomenological consequences of having such a massless particle. One of these is the possibility of neutrinoless double beta-decay with emission of a majoron discussed in Prof. Witherell's lectures. Indeed the major advantage of the GR model is that majorons are so much fun.[5] The main disadvantage is that it has little motivation and it is necessary to fine tune $V(T, \Phi)$ in order to create the necessary small value of (v_T/v).

Let me now turn to the idea that neutrino mass arises from new physics at a large scale M. At the SU(2) x U(1) scale the consequences of new physics are effective interactions that are inversely proportional to some power of M. Such interactions typically arise out of diagrams involving virtual particles with masses of the order M but external particles of the normal SU(2) x U(1) variety. (At a lower mass scale the weak interaction can be described as an effective four-fermion interaction proportional to $[m(W)]^{-2}$.) Such effective interactions are not renormalizable and are to be used only in lowest-order perturbation theory. Of interest to us here is the effective interaction of the form[6]

$$\frac{f_{ij}}{M}\{\bar{N}_{Li}N^c_{Rj}\Phi^o\Phi^o + h.c.\}, \tag{23}$$

Note this is part of a gauge invariant term made of two fermion doublets combined to form a triplet together with two Higgs doublets also combined to form a triplet. When Φ^o acquires a vacuum expectation value (Eqs. (7) and (10)) we obtain the Majorana mass term M_L of Eq. (19) with

$$\mu_{ij} = \frac{f_{ij}v^2}{M}\,. \tag{24}$$

This is the famous Gell-Mann-Ramond-Slansky-Yanagida see-saw formula.[7] The proportionality to v^2 necessarily arises because, as shown in Table 1, M_L requires $\Delta\vec{I} = 1$ whereas $<\Phi^o> = v$ provides only $\Delta\vec{I} = \frac{1}{2}$. Equation (23) violates lepton number by two units and it is presumed that this is due to the new physics at mass scale M. This is called a see-saw formula because the larger M the smaller the neutrino mass.

The simplest realization of the see-saw formula comes in theories with right-handed neutrinos N_{Ri}. One assumes that these neutrinos acquire a very large Majorana mass given by Eq. (20) with the μ'_{ij} of order $M >> v$. Because M_R is an SU(2) singlet there is no reason for the μ'_{ij} to be of order v and we assume that the magnitude of M_R defines the scale M at which lepton number is broken. We now assume that in addition there is a Dirac mass term M_D of normal magnitude (similar to quarks and charged leptons) but keep $M_L = 0$. Then the form of the mass matrix is

	N_L	N^c_L
N^c_R	0	M_D
N_R	M_D	M_R

Diagonalizing this we find for $M_D << M_R$ that there are heavy Majorana particles characterized by M_R and light neutrinos with a mass matrix given by

$$M_\nu = D^T M_R^{-1} D. \tag{26}$$

Neglecting mixing this means the neutrino mass is

$$m_\nu = m_D^2/M \tag{27}$$

where m_D is the Dirac mass, that is, the mass the neutrino would have had if M_R were zero. Since m_D comes from expressions like Eq. (12), it follows that

Eq. (27) has the general form of Eq. (24). Assuming m_D is of the same order as the mass of a quark or a lepton we see that the neutrino mass is reduced by the factor (m_D/M).

The motivation for this approach is the symmetry between leptons and quarks which suggests there should be N_R and that there should be a Dirac mass term similar to that of other fermions. Note that mass generation in the standard model is a weak phenomenon, associated with the breaking of SU(2), so that the mass of quarks does not appear to be related to their strong interactions and the mass of the charged leptons is unrelated to their electromagnetic interaction. There is, of course, a difference between the N_R and all other fermions; the N_R are completely neutral with respect to SU(2) x U(1). As a consequence it becomes possible for N_R to acquire a Majorana mass much larger than the SU(2) breaking scale that determines m_D. A disadvantage of this approach is that the large ratio between M and v is technically unnatural; however, such a large ratio is needed in any theory that introduces new physics at a large mass scale.

The original idea for the see-saw formula and for the form of mass matrix of (25) comes from the SO(10) grand unified theory (GUT). GUTs are models[8] in which at a high mass scale M_{GUT} one starts with a single gauge group that breaks down to SU(3) x SU(2) x U(1) just as SU(2) x U(1) eventually breaks down to U(1). The weak, electromagnetic, and strong interactions are just different parts of the original gauge interactions. Similarly quarks and leptons are different components of a grand fermion field.

The simplest GUT in which all the fermions of a single generation are united in a single representation is based on the group SO(10). (A simpler GUT based on SU(5) has the fermions divided into two different representations, which seems unnatural. In SU(5) there are no N_R.) The fermions in SO(10) form a 16-dimensional representation

$$\psi_{16} = \begin{pmatrix} u_{\alpha L} & d_{\alpha L} & N_L & e_L \\ u^c_{\alpha L} & d^c_{\alpha L} & N^c_L & e^c_L \end{pmatrix} \tag{28}$$

where α is the color index. We show only left-handed fields, but as shown in Eq. (3b) the fields e^c_L, etc., are really the charge conjugates of e_R, etc. Of importance to the present discussion the 16 of SO(10) contains both N_L and N_R, the latter showing up in the form N^c_L. The conjugate fields $\bar{\psi}_{16}$ transform under SO(10) as the representation $\bar{16}$, which is not equivalent to 16 (just as 3 and $\bar{3}$ are not equivalent in SU(3)).

The Yukawa interaction involves

$$\bar{\psi}^c_{16}\psi_{16}$$

which transforms as 16 x 16 which breaks down to irreducible representations

$$16 \times 16 = 10 + 120 + 126.$$

Higgs bosons that can couple to fermions are thus ϕ_{10}, ϕ_{120}, and ϕ_{126} so that we can write the Yukawa interaction of SO(10) in the form

$$\begin{aligned} Y = {} & F_{10}[\bar{\psi}^c_{16}\psi_{16}]_{10}\phi_{10} \\ & + F_{120}[\bar{\psi}^c_{16}\psi_{16}]_{120}\phi_{120} \\ & + F_{126}[\bar{\psi}^c_{16}\psi_{16}]_{126}\phi_{126}. \end{aligned} \tag{29}$$

By substituting Eq. (28) into Eq. (29) one can see that Majorana mass terms as well as Dirac terms can arise when the Higgs bosons acquire vacuum expectation values. The Dirac mass terms arise when the top row of Eq. (28) couples to the bottom; the Majorana mass terms when N_L couples to itself or N^L_c to itself. The Higgs field ϕ_{10} contains two SU(2) doublets Φ_i that can play the role of the normal Higgs while ϕ_{126} contains an SU(2) triplet T and a singlet S. Thus the mass matrix schematically take the form

$$Mass\ matrix\ \sim \begin{pmatrix} F_{126} < T > & F_{10} < \Phi > \\ F_{10} < \Phi > & F_{126} < S > \end{pmatrix} \tag{30}$$

which reduces to the form (25) if we, somewhat arbitrarily, set $< T >= 0$. The value of $< S >$ and thus of M can be equal to the GUT scale ($\geq 10^{15}$ Gev) but

could be smaller. In fact the SO(10) model with only two mass scales M_{GUT} and v tends to have the failures of SU(5) in predicting too fast a rate for proton decay and too low a value of $\sin^2\theta_w$. Thus there may be an argument for choosing M at a value more like 10^{11} Gev.

Because the SO(10) model has such a large number of parameters in its Yukawa interaction and its Higgs potential there are no definitive predictions. However, most analyses[9] that fit the quark and charged lepton masses yield the following qualitative conclusions concerning neutrinos:

1. The neutrinos have a mass hierarchy analogous to those of the other fermions

$$m(\nu_e) \ : \ m(\nu_\mu) \ : \ m(\nu_\tau) = m^n(u) : m^n(c) : m^n(t) \tag{31}$$

with n=1 or 2.

2. The neutrino flavor eigenstates are mixtures of the mass eigenstates in analogy with the quark mixing described by Eqs. (14). As a result the weak interactions expressed in mass eigenstates have the form

$$W^\lambda \bar{\nu}_j \gamma_\lambda U^\ell_{ji} \ell_{Li} \tag{32}$$

where $\nu_j = (\nu_e, \nu_\mu, \nu_\tau)$ and U^ℓ is the lepton analogue of the KM matrix, representing mixing of the neutrinos relative to that of the charged leptons. The mixing angles in U^ℓ are all small of the order of the Cabibbo mixing angle ($\theta_c \sim 0.2$) with particularly small mixing between the first and third generation.

4. *Limits on Neutrino Masses*

The most direct way to study neutrino masses is by the determination of the missing mass from the kinematics of decays involving neutrinos. Present limits are shown in Table 2. In the case of ^3H decay one experiment has persistently indicated a non-zero mass of ν_e around 30 ev, but this result has not been confirmed by other experiments. It is unlikely that any of these limits can be reduced by more than a factor of three in the foreseeable future. Detailed reviews of neutrino mass experiments are found in Ref. 10.

Table 2 - Limits on Neutrino Mass

	Decay	Mass Limit
ν_e	$^3H \rightarrow {}^3He + e^- + \bar{\nu}^3$	$< 18ev$
ν_μ	$\pi \rightarrow \mu + \nu_\mu$	$< 3 \cdot 10^5 ev$
ν_τ	$\tau \rightarrow \nu_\tau + 5\pi$	$< 35Mev$

A limit on the mass of ν_e can be obtained[11] from the observation of neutrinos of different energies arriving in a short time interval from the supernova SN 1987a. Because of the small number of neutrinos (19 in Kamiokande and IMB together) the limit obtained depends on the particular statistical analysis and assumptions used. I believe a reasonable conclusion is $m(\nu_e) \leq 15ev$, similar to the limit obtained from ^3H decay. For a future supernova with more neutrinos detected it is possible that a study of the neutronization burst (a pulse of ν_e preceding the main thermal emission which produces all flavors of neutrinos) could provide limits down to 2 ev or less. Furthermore it is possible that analysis of neutrinos from a future supernova could detect a large range of ν_μ or ν_τ masses between 100 ev and 100 kev.

Limits on neutrino masses can also be obtained from cosmological arguments. In the standard cosmology the observed microwave background is a relic from an earlier time when the universe was hotter and denser. The same theory says there should also be relic neutrinos filling all space with a density of 110 cm^{-3} for each generation. This number is about 10^9 times the number of baryons in the universe. Thus if the neutrinos have a mass of several ev they dominate the energy density of the universe and thus determine the rate at which the universal expansion is slowing down. It is then possible to calculate lifetime t_o of the universe as a function of the neutrino mass and the present rate of expansion specified by the Hubble constant H_o. If the neutrino mass is too large the value t_o will turn out too small to be consistent with times determined from radiochemical and other evidence. Assuming

$$H_o > 50 \ km \ sec^{-1} \ Mpc^{-1}$$

$$t_o > 10 \cdot 10^9 \ yrs$$

one finds[12]

$$m(\nu_e) + m(\nu_\mu) + m(\nu_\tau) < 80ev. \tag{33}$$

This limit does not hold if neutrinos decay rapidly enough and so disappear at an earlier time in the history of the universe. It is hard to find a theoretical decay mechanism that satisfies cosmological, astrophysical, and experimental constraints. In the GR model the limit (33) can be evaded because the neutrinos will annihilate into massless majorons when the temperature of the universe is of the order of the neutrino mass provided the k_{ij} are not too small.

If we accept the cosmology result (33) we have a constraint on $m(\nu_\mu)$ and $m(\nu_\tau)$ which is many orders of magnitude more stringent than the direct limits in Table 2. If we further accept the hierarchy of Eq. (31) then $m(\nu_\tau) < 80$ ev, $m(\nu_\mu) \leq 1$ ev, and $m(\nu_e) << 1$ ev. The only way to explore such small masses requires neutrino oscillation studies.

We note in passing that a neutrino mass between 25 and 50 ev could provide the critical energy density of the universe; that is, provide the dark matter needed to satisfy $\Omega = 1$.

5. *Neutrino Oscillations : Formulation*

It is possible to probe small neutrino masses using neutrino oscillations provided there is a significant mass difference and the mixing is not too small. These conditions are met in most theories of neutrino masses.

The basic idea of neutrino oscillations can be illustrated using just two generations; the extension to three is straightforward. The flavor eigenstates ν_e and ν_μ may be written as mixtures of the mass eigenstates ν_1 and ν_2

$$\mid \nu_e > = \cos\theta \mid \nu_1 > + \sin\theta \mid \nu_2 >$$

$$\mid \nu_\mu > = -\sin\theta \mid \nu_1 > + \cos\theta \mid \nu_2 > . \tag{34}$$

A beam that is originally ν_e becomes as a function of time

$$\mid \nu(t) > = e^{-iE_1 t}\cos\theta \mid \nu_1 > + e^{-iE_2 t}\sin\theta \mid \nu_2 > \tag{35}$$

where

$$E_2 - E_1 \approx (m_2^2 - m_1^2)/2p \tag{36}$$

assuming

$$\Delta m^2 \equiv (m_2^2 - m_1^2) << p^2. \tag{37}$$

The state (35) is no longer purely ν_e because of the change in the relative phase of its two components and has a non-zero projection on the state ν_μ given by

$$< \nu_\mu \mid \nu(t) > = -\sin\theta\cos\theta e^{-iE_1 t} + \cos\theta\sin\theta e^{-iE_2 t}. \tag{38}$$

The probability of an oscillation into ν_μ is then given by

$$P_{\mu e} = |< \nu_\mu \mid \nu(t) >|^2 = 2\sin^2\theta\cos^2\theta \times [1 - \cos^2(\frac{m_2^2 - m_1^2}{2p})t] = \sin^2 2\theta \sin^2(\pi x/\ell) \tag{39}$$

where the characteristic oscillation length is given by

$$\ell = \ell_v = \frac{4\pi p}{m_2^2 - m_1^2} = 2.5 \ meters \ \frac{p(Mev)}{\Delta m^2(ev^2)} \ . \tag{40}$$

It is convenient for what follows to express the oscillation phenomenon as the time evolution of a two-component vector in flavor space $\nu(t)$ with ν_e and ν_μ components. Then

$$i\frac{d}{dt}\begin{pmatrix}\nu_e \\ \nu_\mu\end{pmatrix} = \frac{1}{2p}\begin{pmatrix}M_{ee}^2 & M_{e\mu}^2 \\ M_{e\mu}^2 & M_{\mu\mu}^2\end{pmatrix}\begin{pmatrix}\nu_e \\ \nu_\mu\end{pmatrix}. \tag{41}$$

The 2×2 matrix M^2 is given by

$$M_{ee}^2 = \frac{1}{2}(\mu^2 - \Delta m^2 \cos 2\theta_v) \tag{42a}$$

$$M^2_{\mu\mu} = \frac{1}{2}(\mu^2 + \Delta m^2 \cos 2\theta_v) \tag{42b}$$

$$M^2_{e\mu} = \frac{1}{2}\Delta m^2 \sin 2\theta_v \tag{42c}$$

where θ_v is the mixing angle (subscript v is for vacuum) and $\mu^2 = m_1^2 + m_2^2$. In Pauli notation this matrix has the form

$$M^2 \sim \mu^2 1 + \Delta m^2(-\cos 2\theta_v\ \sigma_z + \sin 2\theta_v\ \sigma_x)\cdot$$

Neglecting the unit matrix this is exactly the same form as the problem of the precession of a spin $-\frac{1}{2}$ magnet in a magnetic field at an angle $2\theta_v$ to the spin axis. Neutrino oscillations may be considered as a precession in flavor space.

To probe small values of Δm^2 it follows from Eqs. (39) and (40) that one must look for oscillations over very large distances. In practice this leads to studying oscillations of neutrinos passing through the earth or the sun. In such cases one must take into consideration the modification of the oscillations due to the material medium. The essential point is that oscillations have to do with the phases of the flavor components of the propagating neutrinos and one source of change in phase is the index of refraction term

$$exp[ip(n-1)x]\,. \tag{43}$$

The index of refraction is given by the optical theorem

$$p(n-1) = 2\pi N f(0)/p \tag{44}$$

where N is the number of scatterers per unit volume and $f(0)$ is the coherent forward scattering amplitude. It is customary at this point to note that the optical theorem can be found in any book on quantum mechanics. Unfortunately this is not the case. A number of books give the imaginary part of Eq. (44). It is easy to see that

$$iIm\ p(n-1) = iN\sigma/2 \tag{45}$$

since substituting this into (43) gives $exp[-N\sigma x/2]$ which represents the depletion of the amplitude due to the absorption cross section σ. Combining (44) and (45) one obtains

$$\sigma = 4\pi Im f(0)/p \tag{46}$$

which is found in many books. We are interested here, however, in the real part of the index of refraction. For the problems of interest the absorption of the neutrinos is completely negligible. Equation (44) may be derived by coherently adding the sum of the forward scattered waves from all the targets to the transmitted wave; a succinct derivation is given in Fermi's notes on Nuclear Physics.[13] Note that the result does not require a lattice of targets nor does it make any assumption about the ratio of the wave-length of the neutrino to the spacing of the target atoms. Like any coherent effect there are limitations related to the effective size of the neutrino wave packet; in applications these limitations are not generally important.

For our example both n and f(0) must be considered as matrices in flavor space. In the standard model f(0) is diagonal in flavor. If we consider the weak charged current (W boson exchange) one finds for ν_e scattering from electrons

$$f(0) = -\sqrt{2}Gp/2\pi$$

$$p(n-1) = -\sqrt{2}GN_e \tag{47}$$

where N_e is number of electrons per unit volume. For $\bar{\nu}_e$ the sign must be reversed. Of course, ν_μ do not scatter elastically from electrons via the charged current; they scatter elastically from muons but normal media do not contain muons. There is also scattering of ν_e and ν_μ via the neutral current (Z exchange); however, this is the same for all flavors and so only adds an overall phase (not a

relative phase) to the propagating $\nu(t)$. We can now take account of the phase factor (43) by using Eq. (41) but replacing Eq. (42a) by

$$M_{ee}^2 = \frac{1}{2}(\mu^2 - \Delta m^2 \cos 2\theta_v) + 2\sqrt{2}GN_e p. \tag{48}$$

Note that in obtaining Eq. (48) we have set $x = t$, since with the approximation (37) the neutrinos are moving essentially with the velocity of light.

For a fixed value of N_e, oscillations are described by Eq. (39) with θ, ℓ replaced by θ_m, ℓ_m

$$\tan 2\theta_m = \sin 2\theta_v/(\cos 2\theta_v - \ell_v/\ell_o) \tag{49}$$

$$\ell_m = \ell_v[1 - 2(\ell_v/\ell_o)\cos 2\theta_v + (\ell_v/\ell_o)^2]^{-\frac{1}{2}} \tag{50}$$

$$\ell_o = 2\pi/\sqrt{2}GN_e = (1.6 \times 10^7/\rho_e)\ meters \tag{51}$$

where ρ_e is the electron number density in units of Avogadro's number. The value ℓ_o defines a characteristic length in matter; for normal matter it is of the order of the earth's radius. For $\ell_v << \ell_o$, matter effects can be ignored; for $\ell_v >> \ell_o$, oscillations are highly suppressed; of particular interest in the case in which ℓ_v and ℓ_o are comparable. In particular, for

$$\ell_v = \ell_o \cos 2\theta_v \tag{52}$$

θ_m becomes 45^o. The importance of this case was discovered by Mikhaeyev and Smirnov who refer to it as the resonant amplification of neutrino oscillations by matter. For the case of $\bar{\nu}_e$, $\bar{\nu}_\mu$ the sign of the right-hand side of Eq. (47) is reversed, effectively changing the sign of ℓ_o. Thus the resonance condition can be satisfied for ν_e if $m(\nu_e) < m(\nu_\mu)$ but not for $\bar{\nu}_e$. For small values of θ_v Eq. (52) gives

$$E_\nu(Mev)\rho_e = 6.5 \times 10^6 \Delta m^2(ev^2). \tag{53}$$

For most applications the value of N_e varies. Of particular interest is the case in which, as the density decreases, θ_m decreases from a value near 90^o through 45^o down to $\theta_m = \theta_v$ which corresponds to zero density. In this case the eigenstates in matter change as shown in Figure 1. At large density (such as the center of the sun) the upper state is primarily ν_e (θ_m near 90^o). At the resonance where $\theta_m = 45^o$ the two levels come close together; the levels would cross but they are "held apart" by the mixing term $M_{e\mu}^2$. Finally at zero density the upper state is primarily ν_μ. If the density variation is not too rapid the adiabatic approximation can be used, which means that no transition takes place between the eigenstates. As a result the original ν_e remains primarily in the upper state, which is now primarily ν_μ. The probability that ν_e is still ν_e is given by

$$P_{ee} = \cos^2\theta_o \cos^2\theta_v + \sin^2\theta_o \sin^2\theta_v = \frac{1}{2}(1 + \cos 2\theta_v \cos 2\theta_o) \tag{54}$$

where θ_o is the original value of θ_m. (Note that in deriving Eq. (54) we have not included any interference between the ν_1 and ν_2 components since this is a rapidly oscillating term and averages to zero.) For θ_o near $\pi/2$ and θ_v small we have almost a complete conversion of ν_e to ν_μ. For values of θ_v too small (this means $M_{e\mu}^2$ is small by Eq. (42c)) the mass eigenstates get too close together at the resonance ($\theta_m = 45^o$) and the adiabatic approximation fails. Formulas for P_{ee} that go beyond the adiabatic approximation are given in Refs. 14 and 15.

There are three important cases in which matter effects play an important role:

(1) Neutrinos originating in the atmosphere as a result of collisions of cosmic rays and passing through a major portion of the earth before being detected.

(2) Neutrinos originating near the center of the sun and traversing a radius of the sun.

(3) Neutrinos originating in the core of a collapsing star (supernova) and passing through the dense outer layers.

6. *Neutrino Oscillations : Experiments*

We first summarize briefly our present knowledge obtained from laboratory neutrino oscillation experiments. We distinguish two types of experiments.

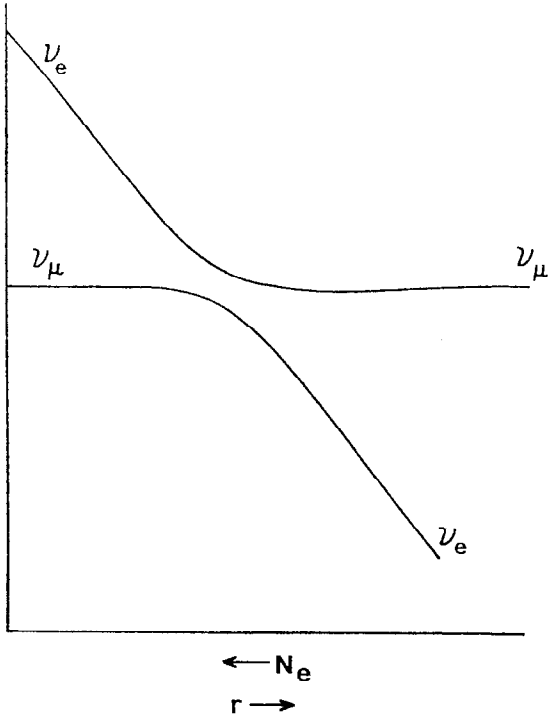

Figure 1 Eigenvalues of the M^2 matrix as a function of electron density N_e or distance r from the center of the sun

Appearance experiments measure quantities like $P_{\mu e}$ of Eq. (39) in which a new flavor (like ν_μ) appears in a beam originally a different flavor (like ν_e). *Disappearance* experiments measure quantities like P_{ee} of Eq. (54) in which one measures the flux of a given flavor some distance from the source. In the case of only two flavors

$$P_{\mu e} + P_{ee} = 1.$$

However, in general, disappearance experiments are sensitive to oscillations from the original flavor to any new flavor. As can be seen from Eq. (39) the oscillation probabilities at a given distance x depend on both Δm^2 and θ_v so that experiments provide only a correlated limit between these quantities. The examples for which most information is available are $\nu_\mu - \nu_\tau$ oscillations and $\nu_e - \nu_\mu$ oscillations. Our prejudices suggest that $\nu_e - \nu_\tau$ oscillations may be very small; in any case $\nu_e - \nu_\tau$ oscillations are the most difficult to probe experimentally.

Our present knowledge of $\nu_\mu - \nu_\tau$ oscillations is summarized in Figure 2. The results shown come from two experiments. For the larger values of Δm^2 they come from E531, an emulsion experiment at Fermilab.[16] It is interesting to note that this important result was simply a byproduct of a study of charm production by neutrinos. The lower branch of the curve comes from the CDHS ν_μ disappearance experiment at CERN.[17] Since this was a disappearance experiment it also provides limits on $\nu_\mu - \nu_e$ oscillations; however, better limits are available in that case. If we assume θ in this case equals or is greater than the Cabibbo angle (indicated by the dashed line) then we conclude $m(\nu_\tau) < 1ev$ (assuming $m(\nu_\mu) << m(\nu_\tau)$). On the other hand if $\sin^2 2\theta < 10^{-2}$ there is no constraint on $m(\nu_\tau)$. As we have noted a value of $m(\nu_\tau)$ between 25 and 50 ev would be of enormous interest for cosmology. Further efforts on oscillations involving ν_τ are certainly worthwhile.

There is also shown in Figure 2 a dashed cross that represents a possible interpretation of the preliminary data on atmospheric neutrinos presented here by Koshiba. If the effect were as large as indicated large mixing angles between ν_μ and ν_e or ν_μ and ν_τ would be required. The effect appears for both upward and downward neutrinos so it is necessary to assume a vacuum oscillation

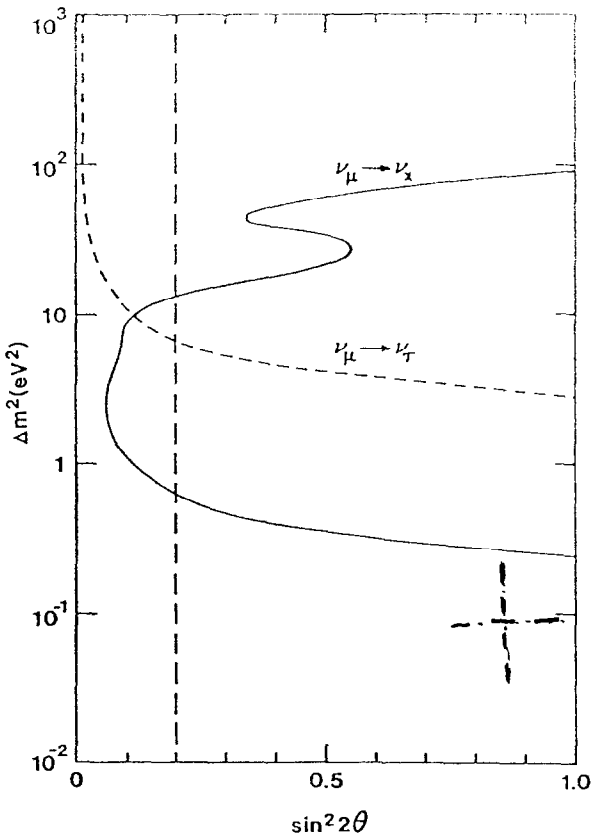

Figure 2 Limits on ν_μ-ν_τ oscillations

length short enough to affect the downward neutrinos. Thus matter effects are negligible with this solution.

There is a much greater body of knowledge on $\nu_\mu - \nu_e$ oscillations. The best present laboratory limits on Δm^2 and $\sin^2 2\theta$ are shown schematically by the solid line in Fig. 3. For large mixing angles the best limits come from disappearance experiments using $\bar{\nu}_e$ from reactors.[18] These limits, of course also apply to $\nu_e - \nu_\tau$ oscillations. These disappearance experiments are not sensitive to values of $\sin^2 2\theta$ less than 0.1. The remaining limits come from looking for the appearance of ν_e in ν_μ beams at the CERN PS and the Brookhaven AGS. While occasional experiments have seen signs of oscillations they have disappeared with the acquisition of better data. For a review of accelerator experiments see Reference 19.

Our theoretical prejudices discussed above suggest $m(\nu_\mu) < 1ev$ with $m(\nu_e)$ much less so that $\Delta m^2 < 1ev^2$ with $\sin^2 2\theta$ of the order 10^{-1}. We see from Fig. 3 that very little of this parameter range has been explored. The dashed lines in Fig. 3 are indications of discovery possibilities or limits that could be achieved by future laboratory experiments of the type already done. These have been abstracted from various conference reports[18,20] and proposals (including those discussed by Koshiba) but there is no assurance that the experiments will be done in the near future.

To go further one needs to go to still larger distances and we turn to the sources listed at the end of Section 5. One result has already been obtained using atmospheric neutrinos passing through the earth; this is shown by the little dash-dot curve in Figure 3. The result[21] comes from the IMB group using their large H_2O Cerenkov detector comparing ν_μ and ν_e arriving from below with those coming from above. For neutrino energies around 300 Mev there would be a large enhancement of neutrino oscillations inside the earth because Eq. (53) is approximately satisfied.

Future large detectors can further explore the oscillations of atmospheric neutrinos. In principle because neutrinos coming in different directions have gone different distances and through different amounts of earth these experi-

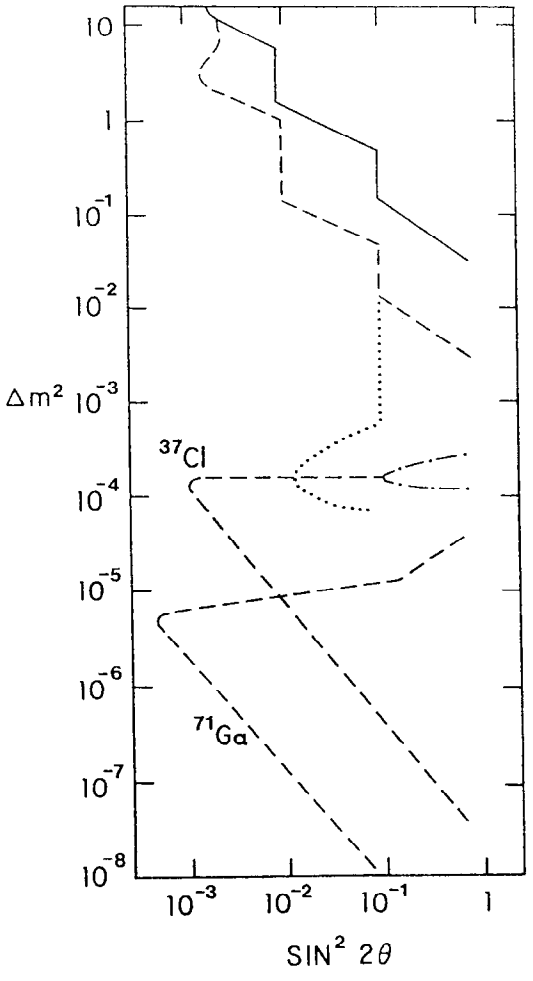

Figure 3 Existing limits and possible future experiments on ν_μ-ν_e oscillations

ments can explore a wide range of parameters. Their sensitivity is limited by uncertainties in the incident flux as well as by statistics. The dotted curve in Figure 3 is a schematic indication of the possible values that would be explored by the proposed Super Kamiokande detector. In principle the possibility exists[22] to explore smaller mixing angles for values of Δm^2 of the order 10^{-2} to $10^{-3} ev^2$ by exploiting the resonant amplification. However, from Eq. (53) applied to the earth this requires detecting neutrinos up to 10 Gev. This can practically be done only by using rock as the target and then detecting the resultant muons. Since the matter effect holds only for ν_μ (and not $\bar{\nu}_\mu$ or conceivably the other way around) the detector should be able to distinguish μ^+ from μ^-.

To go to values of Δm^2 below $10^{-4} ev^2$ we must turn to solar neutrinos. The nuclear reactions that are responsible for providing energy in the sun give off a portion of the energy in the form of neutrinos. The study of these neutrinos provides a way of probing our understanding of what goes on in the solar interior and also provides a way of exploring neutrino oscillations over distances larger than the size of the earth. The three major reactions yielding neutrinos are shown in Table 3 with the calculated relative fluxes. While the predominant flux comes from the weak pp reaction that is the first step in nuclear burning in the sun, the lower energy of these neutrinos makes them difficult to detect. In contrast ^{8}B is the product of the very rare PPIII chain of reactions and so produces a very low flux but the high energy of these neutrinos make them much easier to detect. For the standard introduction to these reactions see Reference 23.

Table 3 - Major Sources of Solar Neutrinos			
NAME	REACTION	ENERGY SPECTRUM	RELATIVE FLUX
$pp\nu$	$p + p \rightarrow d + e^+ - \nu_e$	Continuous to 420 kev	1
^{7}Beν	$e^- + {}^7Be \rightarrow {}^7Li + \nu_e$	Line Mainly 860 kev	.08
^{8}Bν	$^8B \rightarrow {}^8Be + e^+ + \nu_e$	Continuous to 14 Mev	10^{-4}

The first (and for more than 15 years only) attempt to detect solar neutrinos was carried out by Ray Davis using ^{37}Cl as the target material. The ^{37}Cl is

converted to ^{37}A by the reaction

$$\nu_e + {}^{37}Cl \rightarrow e^- + {}^{37}A. \qquad (55)$$

The experiment requires detecting the production of less than 30 argon atoms produced per month. Very elegant radiochemical methods have been developed for this purpose. The threshold of the reaction (55) is too high to detect the $pp\nu$ and almost too high for $^7Be\nu$. The calculated rate[24] of detected neutrinos given in SNU (solar neutrino units, the definition of which is irrelevant) for the ^{37}Cl detector is 3.9 to 8.4 SNU for ^{8}Bν, 0.9 to 1.3 SNU for ^{7}Be ν, and 5.3 to 10.5 SNU for the sum over all neutrinos. (This includes small amounts from the CNO cycle). In contrast the result of the Davis experiment carried out from 1970 to 1985 was 2.1 ± 0.3 SNU.

How serious is this discrepancy? The calculations are based on the standard solar model (SSM). Fundamental laws of physics are applied to describe the sun over the period of 4.5×10^9 years with the boundary conditions (initial radius, etc.) varied until the present radius, luminosity, etc. are fit. Input parameters are taken from laboratory measurements of nuclear reaction rates, calculations of the opacity due to complex atoms, and observation of solar element abundances. The range of values given above includes all the values obtained from one thousand calculations in which the input parameters were varied in accordance with their uncertainties. Excluding exotic possibilities involving unlikely new particles (special kinds[25] of WIMPS) the relevant laws of physics are well understood. The major question is whether some reasonable approximations made (such as neglect of diffusion or convective mixing in the solar interior) might be wrong. The ^{8}B flux is extremely sensitive to the calculated central temperature T_c, varying approximately[24] as T_c^{18}.

In the last year there have been two new results reported on solar neutrinos. The Davis experiment ended in 1985 because Brookhaven, in its infinite wisdom, would not support it. However, with a new source of support Davis, now at Penn, continued the experiment in 1987 and the result for that year reported at the Baltimore APS meeting is 5 ± 1 SNU. Davis believes this could be a real time dependence. His data for the last ten years show an anti-correlation with sunspots, but no reasonable explanation for this is known. As discussed here by Koshiba the first electronic detection has been carried out using the Kamiokande detector. This experiment is sensitive only to ^{8}Bν above 10 Mev. The result is equal to 0.45 times the SSM prediction and three standard deviations away from zero. Given the experimental and theoretical uncertainty, however, it cannot be said definitively to disagree with the SSM prediction.

In Figure 3 the dashed curve labeled ^{37}Cl encloses the region in the $\sin^2\theta_v$, Δm^2 plane for which there would be a reduction of about a factor of two or more in the detected flux of ν_e in the Davis or the Kamiokande solar neutrino experiments. The possibility of detecting small values of θ_v is due to the enhancement of the oscillations by the material medium traversed by the neutrino as it emerges from the center of the sun (MSW effect).

There are at least two way of distinguishing the oscillation hypothesis from the assumption that something is wrong with the SSM. One is a study of the energy spectrum of the ^{8}B neutrinos. Neutrino oscillations are an energy-dependent phenomenon. Thus in general the spectrum of ^{8}Bν is modified if neutrino oscillations are the cause of a reduced flux. For example, for $\Delta m^2 \sim 10^{-4} ev^2$ the high-energy part of the ^{8}B spectrum is depleted but the lower energy neutrinos get through. This is because the resonance condition of Eq. (53) cannot be satisfied for low values of E_υ even near the center of the sun. In contrast if the SSM is wrong and less ^{8}B exists in the sun the total flux is reduced but the spectrum remains unchanged. The detection of a distorted ^{8}B spectrum would also distinguish different regions in the $\Delta m^2 - \sin^2 2\theta$ space that give the same reduction in flux. It is possible[26] to distinguish different spectra in an H_2O detector like Kamiokande if the threshold can be reduced; however, it is difficult because the detected electrons from $\nu_e + e \rightarrow \nu_e + e$ have a continuous energy spectrum even for a fixed ν_e energy. It would be much better to have an electronic detector that detects electrons from inverse beta reactions like (55). There are at least two proposals that aim at this. One called ICARUS planned for the Gran Sasso Tunnel consists of a large liquid argon detector.[27] The other

is a large D_2O detector[28] planned to be placed in a mine in Sudbury, Ontario.

The second possibility is the detection of the ν_μ or ν_τ into which the neutrinos oscillate. In principle ν_μ or ν_τ could be detected via their scattering from electrons in detectors like Kamiokande or ICARUS. However, this cross section for scattering from electrons (due to the neutral current) is only about 0.15 times that of ν_e (which also scatters via the charged current). A more difficult but more distinctive method of detecting ν_μ or ν_τ would be via neutral current interactions on nucleons which have the same cross section for all flavors. Thus a measurement of the neutrino flux in this way should give the total flux independent of oscillations to be compared with the flux of ν_e measured using inverse beta reactions. One possibility is the D_2O detector if one can detect the neutron from the disintegration reaction

$$\nu + d \rightarrow \nu + n + p.$$

A special detector using ^{11}B has also been proposed[29] for this purpose.

Of great importance is the detection of the $pp\nu$ since their flux can be calculated to a high degree of accuracy. A radiochemical experiment for this purpose uses ^{71}Ga in place of ^{37}Cl. It is being planned with 30 tons of gallium in the Gran Sasso and with 60 tons in the Soviet Union. Results should be coming out in the early 1990's. It should be emphasized that the theoretical calculations indicate that only 54% of the events expected in ^{71}Ga are due to $pp\nu$ so that there is still some uncertainty ($\sim$ 15%) in the prediction. The major other contribution (26%) is the ^{7}Be ν. We also show in Fig. 3 the values of Δm^2 and $\sin^2\theta_v$ that would result in greater than a factor of two reduction in the ν_e flux detected in the gallium detector.

The major conclusion to be reached by staring at Fig. 3 is that for reasonable values θ, of the order of the Cabibbo angle, solar neutrino experiments provide the possibility for exploring values of $m(\nu_\mu)$ between 10^{-2} and 10^{-4} ev (assuming $m(\nu_e) << m(\nu_\mu)$). This range is of great interest since it corresponds roughly to masses M in the see-saw formula from 10^{11} to 10^{13} Gev. Of course, the solar neutrino experiments are also sensitive to $\nu_e - \nu_\tau$ oscillations. Even though we expect the mixing angle between ν_e and ν_τ to be smaller it is possible that most of the range of $m(\nu_\tau)$ between 10^{-2} and 10^{-4} ev can also be explored. Thus we can get close to values of M of 10^{15} Gev.

Detailed results of calculations of the MSW effect for solar neutrinos can be found in Ref. 30. A discussion of prospects for solar neutrino experiments is given in Ref. 31.

The transformation of ν_e to ν_μ or ν_τ due to the MSW effect could also take place for ν_e emerging from a supernova and passing through the outer layers of the exploding star where the density conditions are similar to those of the sun. The problem in detecting this is that the major portion of the neutrino flux from a supernova consists of an approximately equal mixture of all flavors of neutrinos. Thus in the first approximation neutrino oscillations have no effect. It is expected, however, that the very first neutrinos coming from the supernova consist of a short pulse containing only ν_e, the neutronization burst. Since the energies of these ν_e are similar to those ^{8}B ν from the sun, most of these would be transformed[32] if the values of Δm^2 and θ were within the region labeled ^{37}Cl in Fig. 3. In fact a study of this neutronization burst would explore much larger values of Δm^2 (with very small values of θ) up to 1000 ev^2 or more since the ν_e emerging from the supernova neutrinosphere pass through regions of very high density ($> 10^9$ gm/cc). Indeed as seen from Fig. 3 the region of Δm^2 above $10^{-4} ev^2$ with small values of θ is almost impossible to explore in any other way. This emphasizes once again the great importance of establishing a program with a variety of detectors for seeing the neutrinos from the next supernova.

In spite of a huge number of papers on the subject no conclusions can be drawn from the very limited observations of SN 1987a. It is quite possible that the first event observed in the Kamiokande detector came from the neutronization burst, but those who draw statistical inferences from a single event do so at their own peril.

7. *Conclusion*

Neutrinos may be massless. Nevertheless the search for a non-zero mass is

exciting for many reasons. The most reasonable explanation of a non-zero mass would be new physics at a large mass scale M. Values of M up to 10^{15} Gev might be explored in this way. A mass of the heaviest neutrino, presumably ν_τ, of 25 to 50 ev would mean that relic neutrinos provide enough dark matter to close the universe. Neutrino masses and mixings consistent with expectations from grand unified theories could explain an apparent disagreement between observation and prediction of the solar neutrino flux.

Arguments from cosmology combined with ideas from particle theory focus our attention on relatively small neutrino masses and not very large mixing angles. From this point of view we find that only a small portion of the range of interesting values of Δm^2 and $\sin^2 2\theta$ have been explored by neutrino oscillation experiments. To extend the range it is necessary to do experiments over longer distances and we hope that new experiments at accelerators and reactors will be carried out to explore values of Δm^2 down by a factor of ten or more.

To go much further one must use atmospheric, solar, or supernova neutrinos. In particular, solar neutrinos provide a unique opportunity to study a large range of values accessible in no other way. This is possible because if ν_e is the lightest neutrino there can be a large enhancement of the oscillation (MSW effect) due to the effect of the solar material. Conclusions from any one solar neutrino experiment must be qualified because of possible uncertainties in the calculated flux. Only a concerted effort using a variety of different detectors can yield some definite conclusions. At least one new experiment, the radiochemical gallium experiment, is about to get underway and a number of other exciting possibilities have been proposed.

This work was supported in part by the U.S. Department of Energy under contract number DE-AC02-76ER03066.

References

1. S. M. Bilenky and S. T. Petcov, Rev. Mod. Phys., 59, 671 (1987).

2. K. Fujikawa and R. E. Shrock, Phys. Rev. Lett., 45, 963 (1980) and references therein.

3. G. B. Gelmini and M. Roncadelli, Phys. Lett. 99B, 411 (1981).

4. D. Dearborn et al, Phys. Rev. Lett., 56, 26 (1986); M. Fukugita et al, Phys. Rev. Lett., 48, 1522 (1982), Phys. Rev. D26, 1840 (1982); L. M. Krauss et al, Phys. Lett., 144B, 391 (1984).

5. H. Georgi et al, Nuc. Phys., 193B, 297 (1981).

6. S. Weinberg, Phys. Rev. Lett., 43, 1566 (1979); Phys. Rev., D22, 1694 (1980).

7. M. Gell Mann, P. Ramond, and R. Slansky, in Supergravity (eds. P. van Nieuwenheizen and D. Freedman) in North Holland (1979), 317; T. Yanagida in Proc. KEK Workshop (eds. A. Sawada and A. Sugimoto), KEK (1979), p. 95.

8. P. Langacker, Phys. Reports, 72, 185 (1981) and references therein.

9. M. Gronau et al, Phys. Rev., D37, 2597 (1988) and references therein.

10. Massive Neutrinos 86 (eds. O. Fackler and J. J. Van) Editions Frontieres (1986), pp. 441-584.

11. D. N. Spergel and J. N. Bahcall, Phys. Lett., B200, 366 (1988) and references therein.

12. J. Bernstein and G. Feinberg, Phys. Lett., 101B, 39 (1981).

13. E. Fermi, Nuclear Physics, University of Chicago (1950), p. 201.

14. W. C. Haxton, Phys. Rev. Lett., 57, 1271 (1986); S. J. Parke, Phys. Rev. Lett., 57, 1275 (1986).

15. S. T. Petcov, Phys. Lett., 200B, 373 (1988) and references therein.

16. N. Ushida et al, Phys. Rev. Lett., 47, 1694 (1981).

17. F. Dydak et al, Phys. Lett., 134B, 34 (1984).

18. F. Boehm, in Neutrino 86 (T. Kitagaki and H. Yuta, eds.) World Scientific (1986), p. 135.

19. M. Shaevitz in Reference 10, p. 259 or Neutrino 86 (Reference 18); pp. 148-176.

20. Proc. BNL Neutrino Workshop (M. J. Murtaugh, ed.) Brookhaven National Laboratory (1987).

21. J. Lo Secco et al, Phys. Lett., B184, 305 (1987).

22. G. Auriemma, et al., Phys. Rev. D37, 605 (1988).

23. D. O. Clayton, Principles of Stellar Evolution and Nucleosynthesis (McGraw Hill) 1968, pp. 366-390.

24. J. N. Bahcall and R. K. Ulrich, Rev. Mod. Phys., 60, 297 (1988).

25. W. H. Press and D. N. Spergel, Ap. J., 296, 679 (1985); J. Faulkner and R. L. Gilliland, Ap. J., 299, 994 (1985).

26. J. N. Bahcall, J. M. Gelb and S. P. Rosen, Phys. Rev., D35, 2976 (1987).

27. J. N. Bahcall et al, Phys. Lett., B178, 324 (1986).

28. G. Aardama et al, Phys. Let., 194, 321 (1987).

29. R. S. Raghavan et al, Phys. Rev. Lett., 57, 1801 (1986).

30. S. P. Rosen and J. M. Gelb, Phys. Rev., D34, 969 (1986); S. J. Parke and T. P. Walker, Phys. Rev. Lett., 57, 2322 (1986); M. Cribier et al, Phys. Lett., 182, 891 (1986).

31. J. N. Bahcall, R. Davis, and L. Wolfenstein, to be published in Nature.

32. T. P. Walker and D. N. Schramm, Phys. Lett., 195B, 331 (1987).

The Bottom Quark: A Key to "Beyond Standard" Physics

Haim Harari

Weizmann Institute

No paper was received from the author in time for printing.

b - Physics in Fixed Target Experiments

Jack Sandweiss

Yale University

No paper was received from the author in time for printing.

A.J.S Smith

"Experimental Searches for Rare Decays"

Paper was not submitted

Recent Results from CUSB-II

CHIAKI YANAGISAWA
Physics Department, SUNY at Stony Brook, NY 11794
Representing CUSB-II collaboration†

Invited talk at
1988 SLAC Summer Institute

ABSTRACT

Recent results obtained by CUSB-II collaboration are presented. The topics covered in this talk are: 1) Υ decay to $\mu^+\mu^-$, 2) Fine-structure and spin dependent potential, 3) Higgs and gluinium searches and 4) $\Upsilon(5S)$ decays.

† U. Heintz, T. Kaarsberg,J. Lee-Franzini, D.M.J. Lovelock, M. Narain, R.D. Schamberger, S.B. Sontz, J. Willins and C. Yanagisawa
Physics Department, SUNY at Stony Brook, NY 11794
P. Franzini, P.M. Tuts
Columbia University, New York, NY 10027

1. Introduction

For many years the accumulated data taken in the Υ energy region has provided us a good understanding of the Υ system. Yet there are still many things to learn. Figure 1 shows a sketch of the Υ system which has been experimentally known so far together with major decay modes. Between the $\Upsilon(2S)$ and the $\Upsilon(3S)$ as well as between the $\Upsilon(1S)$ and the $\Upsilon(2S)$ there are two triplet P-states (^3P_J) which provide us the information on the fine structures. These states can be accessed only via E1 transitions from the triplet S-states ($^3S_1$). Just below the $\Upsilon(4S)$ there is the flavor threshold and the $\Upsilon(4S)$ therefore almost always decays to $B_{u,d}\overline{B}_{u,d}$. The $\Upsilon(5S)$ is heavy enough to allow the decays to $B_{u,d}\overline{B^*_{u,d}} + \overline{B}_{u,d}B^*_{u,d}$ and $B^*_{u,d}\overline{B^*_{u,d}}$ and even $B_s\overline{B}_s$, $B_s\overline{B^*_s} + B_s\overline{B^*_s}$ and $B^*_s\overline{B^*_s}$ as will be discussed in this talk.

CUSB-II is the upgraded version of CUSB-I which had contributed to the understanding of the Υ system for many years. The main feature of CUSB-II detector is the BGO cylinder which provides us an excellent energy resolution better than that of CUSB-I by a factor of two. The detail of the detector is described elsewhere.[1]

2. Υ decay to $\mu^+\mu^-$

The study of this decay mode gives useful information on interesting quantities such as the total width Γ_{tot}, the QCD running coupling constant α_s and the QCD scale parameter $\Lambda_{\overline{MS}}$.

Using the timing, the vertex and dE/dx information, the events from this decay are easily identified and the backgrounds from cosmic rays and other sources are negligible. The following analysis is based on the data taken at the $\Upsilon(3S)$ (86 pb^{-1}) and at the $\Upsilon(1S)$ (23 pb^{-1}).

The branching ratios for the $\Upsilon(3S)$ and for the $\Upsilon(1S)$ are:

$$B_{\mu\mu}(\Upsilon(1S)) = (2.58 \pm 0.09 \pm 0.21)\%$$

$$B_{\mu\mu}(\Upsilon(3S)) = (1.73 \pm 0.16 \pm 0.19)\%.$$

The total width Γ_{tot} is then obtained using the measured width Γ_{ee} [2] [3] :

$$\Gamma_{tot}(\Upsilon(1S)) = (51.6 \pm 2.1 \pm 4.3)\text{keV}$$

$$\Gamma_{tot}(\Upsilon(3S)) = (24.9 \pm 2.2 \pm 3.2)\text{keV}.$$

Knowing the branching ratios $B_{\gamma gg}$, $B_{\pi\pi}$,[4] B_{E1}[5] and R where $B_{\gamma gg}$ is for

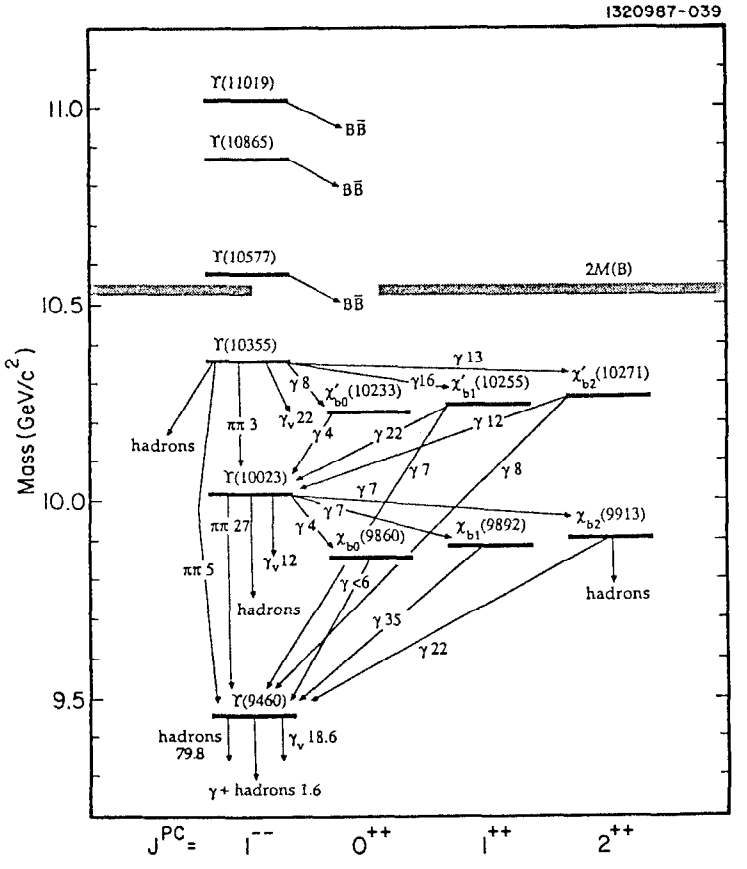

Fig. 1 The Υ system.

the decay to a photon and two gluons,[6] $B_{\pi\pi}$ for the $\pi\pi$ transitions and B_{E1} for E1 transitions (the last two are applicable only to the $\Upsilon(3S)$) and R(=3.63) is the ratio of the hadronic cross section to the lowest order QED dimuon cross section,[7] one can calculate the width Γ_{ggg} normalized to $\Gamma_{\mu\mu}$ by the formula:

$$\frac{\Gamma_{ggg}}{\Gamma_{\mu\mu}} = \frac{1}{B_{\mu\mu}}(1 - B_{\mu\mu}[3 + R) - B_{\gamma gg} - B_{\pi\pi} - B_{E1}).$$

The values for this ratio are found to be:

$$\frac{\Gamma_{ggg}(1S)}{\Gamma_{\mu\mu}(1S)} = 31.2^{+1.3+3.2}_{-1.2-2.7}$$

$$\frac{\Gamma_{ggg}(3S)}{\Gamma_{\mu\mu}(3S)} = 30.2^{+3.7+4.0}_{-3.1-3.3}.$$

The relation between this ratio and α_s allows us to evaluate α_s from which $\Lambda_{\overline{MS}}$ is also obtained. The formula is[8] :

$$\frac{\Gamma_{ggg}}{\Gamma_{\mu\mu}} = \frac{10(\pi^2 - 9)}{81\pi e_b^2}\frac{\alpha_s^3(q)}{\alpha^2}(1 + c(q)\frac{\alpha_s(q)}{\pi}),$$

where e_b is the b-quark charge in unit of the electron charge and c(q) is the first order QCD radiative correction which is zero for q=0.48M_Υ. This relation is interesting in the sense that a 50% error in the radiative correction corresponds only to a 4% error in α_s. The values for this ratio are:

$$\alpha_s(4.54GeV) = 0.176 \pm 0.003^{+0.006}_{-0.005}$$

$$\alpha_s(4.97GeV) = 0.174^{+0.007+0.007}_{-0.006-0.007}.$$

Finally we calculate the QCD scale parameter[9] :

$$\Lambda_{\overline{MS}} = 151^{+9+20}_{-8-17} \text{ MeV at } \Upsilon(1S)$$

$$\Lambda_{\overline{MS}} = 158^{+26+27}_{-21-23} \text{ MeV at } \Upsilon(3S).$$

Our results agree with the values of $\alpha_s(m_b) = 0.179^{+0.009}_{-0.008}$ and $\Lambda_{\overline{MS}} = 175 \pm 31$ MeV obtained by Kwong et al.,[10] and with the value of $\Lambda_{\overline{MS}} = 137^{+28}_{-21}$ MeV obtained by Duke and Roberts.[11]

3. Fine structure and spin dependent potential

3.1 SPIN DEPENDENT POTENTIAL

In general, the spin dependent potential consists of three terms[12] :

$$V_{SD} = \frac{2}{3m^2}\bigtriangledown^2 V_v \vec{s}_1 \cdot \vec{s}_2 + \frac{1}{2m^2 r}(3\frac{dV_v}{dr} - \frac{dV_s}{dr})\vec{L}\cdot\vec{S} + \frac{1}{3m^2}(\frac{1}{r}\frac{dV_v}{dr} - \frac{d^2V_v}{dr^2})S_{12},$$

where V_v and V_s are a vector and a scalar potentials respectively, $\vec{s}_1$ and $\vec{s}_2$ are the spins of the quarks, $\vec{S} = \vec{s}_1 + \vec{s}_2$ and

$$S_{12} = 2[3\frac{(\vec{s}_1\cdot\vec{r})(\vec{s}_2\cdot\vec{r})}{r^2} - \vec{S}^2].$$

The first term represents the spin-spin (hyperfine), the second term the spin-orbit (fine) and the third the tensor (fine) interactions. Since we are concerned about the fine structure of χ_b' states(2^3P_J), we can forget about the first term which is responsible for the mass splitting between $^3S_1$ and $^1S_0$ states. Then if we define two parameters a and b as:

$$a = \frac{1}{m^2}\langle\frac{1}{r}(3\frac{dV_v}{dr} - \frac{dV_s}{dr})\rangle$$

$$b = \frac{1}{12m^2}\langle\frac{1}{r}\frac{dV_v}{dr} - \frac{d^2V_v}{dr^2}\rangle,$$

we can write down the mass formula for the triplet P states[13] :

$$M(^3P_2) = M + a - 2/5b$$

$$M(^3P_1) = M - a + 2b$$

$$M(^3P_0) = M - 2a - 4b.$$

3.2 EXPERIMENTAL METHODS

Experimentally there are two methods to study the fine structure of ^3P_J states. The first method is the analysis of, what we call, 'exclusive' events where one identifies all the particles in the final state of the decay chain: $\Upsilon(3S) \to \gamma\chi_{bJ}'(\chi_{bJ}) \to \gamma\gamma\Upsilon(1S or 2S) \to \gamma\gamma l^+l^-$ where l^+l^- are either e^+e^- or $\mu^+\mu^-$. The events of this type are clean because of the low multiplicity and therefore one can achieve the optimal energy resolution. One drawback is that these events are rare because there are three decays involved and the product branching ratio is small. The analysis of the 'exclusive' events is based on the data taken at the $\Upsilon(3S)$ with the integrated luminosity of 140 pb^{-1}.

The second method is the analysis of, what we call, 'inclusive' events where only photons are identified and their energies are measured: $\Upsilon(3S) \rightarrow \gamma X$. In this method the detailed study of the peak structure in the photon spectrum allows us to obtain the information on E1 transitions as shown later. Since the event multiplicity is high in these events, it is hard to achieve the optimal energy resolution but one can get large data sample. The analysis is based on the data taken at the $\Upsilon(3S)$ corresponding to the integrated luminosity of 106 pb^{-1}.

3.3 'EXCLUSIVE' EVENTS

Figure 2a shows the scatter plot of energies of two photons in the final state $\gamma\gamma l^+l^-$. There are three clear clusters of events. The events in the cluster at the bottom-left corner ($E_{\gamma low}$ ~100 MeV, $E_{\gamma high}$ ~230 MeV) come from the decay chain: (1) $\Upsilon(3S) \rightarrow \gamma\chi'_b \rightarrow \gamma\gamma\Upsilon(2S)$, the events at the top-left corner ($E_{\gamma low}$ ~100 MeV, $E_{\gamma high}$ ~780 MeV) from the decay chain: (2) $\Upsilon(3S) \rightarrow \gamma\chi'_b \rightarrow \gamma\gamma\Upsilon(1S)$ and the events in the cluster at the center ($E_{\gamma low}$ ~430 MeV, $E_{\gamma high}$ ~430 MeV) from the decay chain: (3) $\Upsilon(3S) \rightarrow \gamma\chi_b \rightarrow \gamma\gamma\Upsilon(1S)$.

The projection of Fig. 2a onto the x-axis is shown in Fig. 2b. In this figure there are four peaks as indicated by arrows which correspond to photons from the E1 transitions: (1) $\Upsilon(3S) \rightarrow \chi'_b(2^3P_2)\gamma$, (2) $\Upsilon(3S) \rightarrow \chi'_b(2^3P_1)\gamma$, (3) $\Upsilon(3S) \rightarrow \chi'_b(2^3P_0)\gamma$ and (4) $\Upsilon(3S) \rightarrow \chi_b(1^3P_J)\gamma$ and $\chi_b(1^3P_J) \rightarrow \Upsilon(1S)\gamma$. A similar spectrum with a cut on the sum of two photon energies (280 MeV $\langle E_{\gamma low}+E_{\gamma high}\langle$ 360 MeV) to pick up the transitions $\Upsilon(3S) \rightarrow \Upsilon(2S)$ is shown in Fig. 3. In this figure the fit result with three Gaussians and a linear background is also shown. The energy resolution σ_E/E at 100 MeV is found to be 3.2%. Table 1 summarizes the level splitting of χ'_{bJ} states and Table 2 is the summary of the product branching ratios and branching ratios for the E1 transitions.

Table 1. Level splitting of χ'_{bJ} states.

χ'_{bJ}	E_γ(MeV)	No.of events
J=2	86.1±0.5	104.9±11.7
J=1	101.5±0.6	122.5±12.5
J=0	122.4±2.6	12.3± 5.1

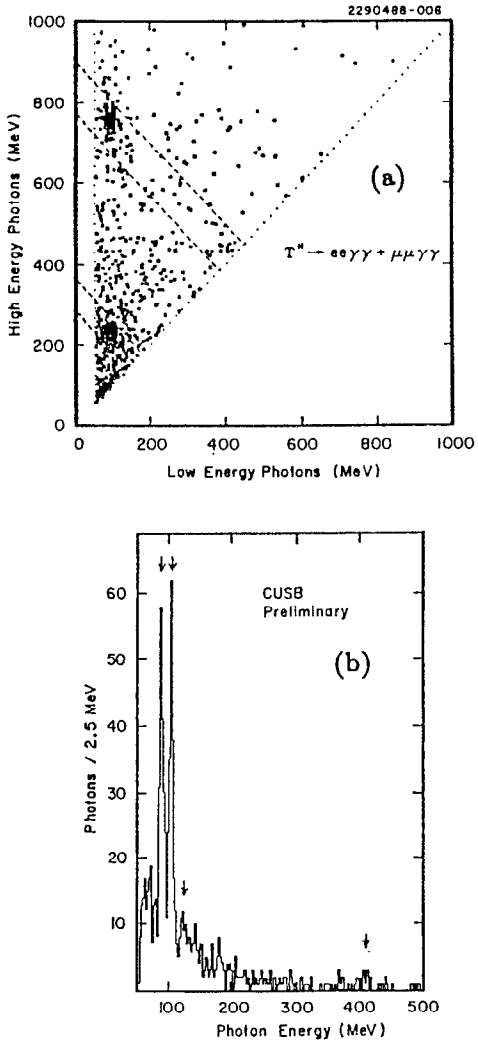

Fig. 2 (a) Scatter plot of $E_{\gamma high}$ vs $E_{\gamma low}$, (b) Projection of scatter plot on $E_{\gamma low}$ axis.

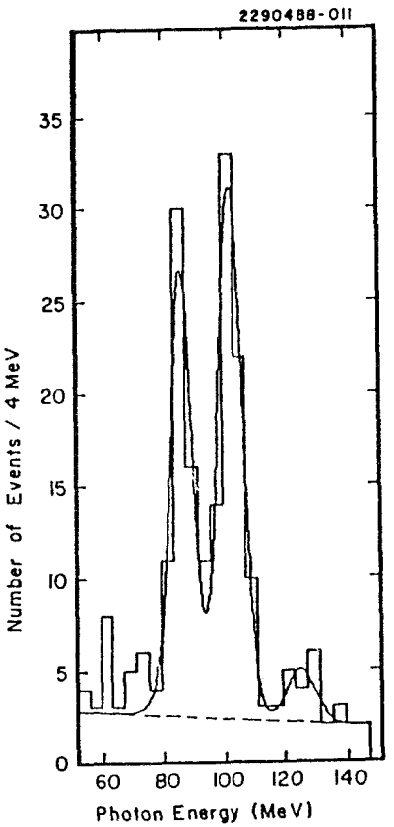

Fig. 3 Spectrum of $E_{\gamma low}$ for 280 MeV $<E_{\gamma low}+E_{\gamma high}<$ 360 MeV.

Table 2. Product branching ratios ($\Upsilon'' \to \chi_b' \to \Upsilon'$) and branching ratios ($\chi_b' \to \Upsilon'$)*

χ_{bJ}'	BR($\Upsilon'' \to \chi_b' \to \Upsilon'$)	BR($\chi_b' \to \Upsilon'$)*
J=2	2.46±0.65 %	21.9±6.1 %
J=1	3.14±0.78 %	26.8±7.1 %
J=0	0.39±0.21 %	9.8±5.6 %
χ_{bJ}'	BR($\Upsilon'' \to \chi_b' \to \Upsilon$)	BR($\chi_b' \to \Upsilon$)*
J=2	1.07±0.21 %	9.5±2.1 %
J=1	0.89±0.17 %	7.6±1.6 %
J=0	0.13±0.08 %	3.1±2.0 %

* BR($\Upsilon'' \to \chi_b'$) from the inclusive photon spectrum are used.

Figure 4 is the photon spectrum with a cut on the sum of two photon energies (770 MeV $<E_{\gamma low}+E_{\gamma high}<$ 900 MeV) to pick up the transitions $\Upsilon(3S) \to \Upsilon(1S)$. The events in the peak around 400 MeV come from the decay chain: $\Upsilon(3S) \to \chi_b(1^3P_J)\gamma \to \Upsilon(1S)\gamma\gamma \to l^-l^-\gamma\gamma$. Taking it into account that one of two photons can be Doppler broadened by ±20 MeV, we find 8 events are consistent with these transitions, 2.4 out of which are background events from the continuum and from the $\pi^0\pi^0$ transitions. The product branching ratio is found to be $Br(\Upsilon(3S) \to \chi_b\gamma)\times Br(\chi_b \to \Upsilon(1S)\gamma) = (0.9 \pm .5) \times 10^{-3}$. This result is compared with three model predictions by Eichten et al.(EI),[14] by Kwong and Rosner (KR)[15] and by Gupta et al. (GRR)[16] in Table 3. The EI model is nonrelativistic and uses the Cornell potential, the KR model uses the inverse scattering method and the GRR model includes the relativistic effects. From the table the KR model's prediction agrees with our result best.

Table 3. $BR(\Upsilon'' \to \chi_b\gamma)\times BR(\chi_b \to \Upsilon\gamma) \times 10^3$.

Experiment	EI	KR	GRR
0.9±0.5	10±2	0.45±0.09	0.08±0.02

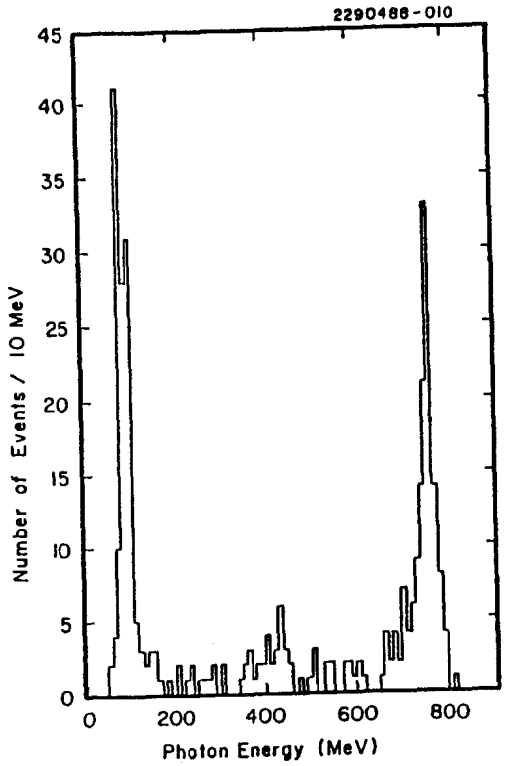

Fig. 4 Photon spectrum for 770 MeV $<E_{\gamma low}+E_{\gamma high}<$ 900 MeV.

3.4 'INCLUSIVE' EVENTS

Figure 5 is the inclusive photon spectrum obtained by a photon search program optimized to have high photon detection efficiency at cost of optimum energy resolution in order to study rarer E1 transitions. The acceptance× efficiency is determined by adding photons generated by 'EGS' to real hadronic events. For the photons of energy between 70 and 1000 MeV the energy resolution is well described by $\sigma_E/E = 2.4\%/\sqrt[4]{E_\gamma(GeV)}$ which is about 30% worse than the optimal one obtained from the analysis of the 'exclusive' events. Figure 5 also shows a part of the background from the resonance decay to gluons and from the continuum $q\bar{q}$ which is simulated by an appropriate combination of the $\Upsilon(1S)$ and the continuum data and this is subtracted. Then the remaining background from the $\pi^0\pi^0$ transitions is removed using a polynomial curve. The photon spectrum after the above background subtractions is shown in Fig. 6. Figure 6 also shows the complete set of $b\bar{b}$ bound states below the $\Upsilon(3S)$ including yet unobserved states together with all possible electromagnetic transitions accessible from the $\Upsilon(3S)$. There are nine groups of E1 transitions: (1) $3^3S_1 \rightarrow 2^3P_{2,1,0}$, (2) $3^3S_1 \rightarrow 1^3P_{2,1,0}$, (3) $2^3P_{2,1,0} \rightarrow 2^3S_1$, (4) $2^3P_{2,1,0} \rightarrow 1^3S_1$, (5) $1^3P_{2,1,0} \rightarrow 1^3S_1$, (6) $2^3S_1 \rightarrow 1^3P_{2,1,0}$, (7) $2^3P_{2,1,0} \rightarrow 1^3D_{3,2,1}$, (8) $1^3D_{3,2,1} \rightarrow 1^3P_{2,1,0}$ and (9) $1^1P_1 \rightarrow 1^1S_0$.

We fit the background subtracted photon spectrum in Fig. 6 including all E1 transitions in the nine groups above. The parameters for some transitions are not free and free parameters are:

- Six parameters for position and intensity of the three lines from 3^3S to 2^3P.
- Six parameters for the summed position and intensity for 2^3P to 2^3S and 1^3S transitions, and for 3^3S to 1^3S decays via 1^3P.
- The overall photon energy resolution.

The parameters for all other lines are fixed. The fit result is also shown in Fig. 6. The first three tall peaks around 100 MeV are from the transitions (1). The small bold curve underneath them is the contribution from the transitions (7). The three little peaks in the same region are from the transitions (6). The tall peak around 200 MeV are three merged peaks from the transitions (3) and the peak in bold line are from the transitions (8). The first two peaks around 450 MeV in thin line are the contributions from the transitions (5) (tall one) and from the transitions (2) (small one). The third peak in bold line is from the transition (9). The last peak around 780 MeV is from the transitions (4).

The peaks corresponding to the transitions (2), (3) and (4) are 4.7 σ, 3.1 σ and 6.3 σ signals respectively and are measured for the first time in an inclusive spectrum. Their rates are consistent with those obtained from the analysis of 'exclusive' events.

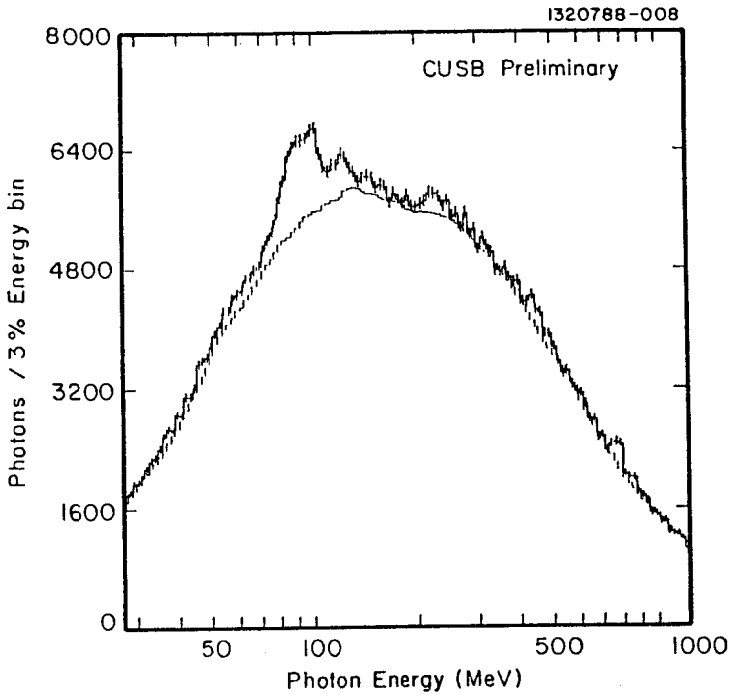

Fig. 5 Inclusive photon spectrum in Υ'' decays.

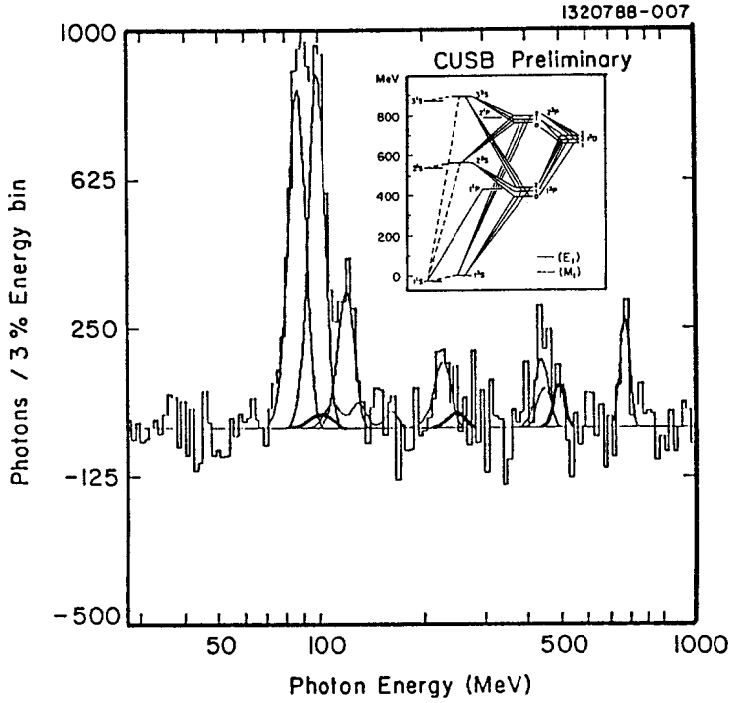

Fig. 6 Background subtracted photon spectrum together with complete possible Υ system below $\Upsilon(3S)$. The curves are described in the text.

Kuang and Yan[17] have suggested that the best way to look for the η_b is to find monochromatic photons from the decay chain: $\Upsilon(3S) \to \pi\pi^1P_1 \to \pi\pi\gamma\eta_b$. Their prediction for the product branching ratio is about 5×10^{-3}. Although the present poor statistics does not allow us to say anything definite, if we suppose that the signal at 496 MeV (~300 photons) is from the transition (9), this signal implies a product branching ratio $Br(\Upsilon(3S) \to \pi\pi^1P_1)\times Br(^1P_1 \to \gamma\eta_b)$ of $(6.4 \pm 3.9) \times 10^{-3}$ and an $\Upsilon(1S) - \eta_b$ splitting of 54±4 MeV. We begin to be sensitive to this decay chain.

Table 4 summarizes the level splitting of χ_b' states and the branching ratios for the decays $\Upsilon(3S) \to \chi_b'(2^3P_J)\gamma$ where the numbers with brackets are the results from CUSB-I and the third number in the second column (peak position) for each transition is the combined result from the analyses of 'inclusive' and 'exclusive' events.

Table 4. Level splitting and branching ratios.

Transition	Energy (MeV)	No.of events	BR(%)
$\Upsilon'' \to \chi_{b2}'$	87.6±0.5 ± 1.5	4061±379	11.2±1.0 ± 0.8
	(84.2±2)		(11.2±4.1)
	86.8±0.3 ± 1.5		
$\Upsilon'' \to \chi_{b1}'$	100.1±0.5 ± 1.5	4049±372	11.7±1.1 ± 0.8
	(101.4±3)		(15.6±4.2)
	100.8±0.4 ± 1.5		
$\Upsilon'' \to \chi_{b0}'$	121.0±1.6 ± 1.5	1485±279	4.0±0.8 ± 0.3
	(122.1±5)		(7.6±3.5)
	121.5±1.2 ± 1.5		
$\langle E_\gamma \rangle$	95.5±0.4 ± 1.5		
	(94±0.5 ± 1.6)		
	95.3±0.3 ± 1.5		
$\langle M(\chi_{bJ}') \rangle$	10259.6±0.4 ± 1.5		
	(10260.8±0.3 ± 1.0)		
	10259.7±0.3 ± 1.5		

One way to study the fine structure is to look at the ratio $r = (M(^3P_2) - M(^3P_1))/(M(^3P_1) - M(^3P_0))$ which can be written in terms of the parameters a and b defined before by $(2a-(12/5)b)/(a+6a)$. The comparison of r for $c\bar{c}$ and $b\bar{b}$ states is made in Table 5 between the experimental values[18] and theoretical predictions of three models by Gupta et al.(GRR),[19] by Moxhay and Rosner (MR)[20] and by McClary and Byers (MB).[21] The GRR model prediction is favored.

Table 5 The fine structure ratio r.

	χ_c	χ_b	χ_b'
Experiments	0.48±0.01	0.67±0.06	0.67±0.05
GRR	0.50	0.64	0.67
MR	0.42	0.42	0.42
MB	0.35	0.45	0.48

4. Higgs and gluinium searches

4.1 HIGGS SEARCH

If the Higgs mass is smaller than the Υ mass one can look for Higgs via Wilczek mechanism[22] by finding a monochromatic photon peak. The decay width normalized to the width for $\Upsilon \to \mu\mu$ including the first order QCD correction is described by :

$$\frac{\Gamma(\Upsilon \to \gamma H)}{\Gamma(\Upsilon \to \mu\mu)} = \frac{G_F M_\Upsilon^2}{4\sqrt{2}\alpha\pi}(1 - \frac{m_H^2}{M_\Upsilon^2})x^2(1-\delta)$$

where $x = \langle\phi_1\rangle/\langle\phi_2\rangle$ which equals one in the standard model, $\langle\phi_i\rangle$ is the vacuum expectation value of the Higgs fields and δ is the order α_s QCD radiative correction which is as large as 50% for $\alpha_s = 0.2$.[23]

Experimentally one looks for a narrow peak in the inclusive photon spectrum. The analysis is based on the data taken at the $\Upsilon(3S)$ and at the $\Upsilon(1S)$ corresponding to the $\Upsilon(3S)$ 3×10^5 and the $\Upsilon(1S)$ 8×10^5 decays respectively. The acceptance×efficiency varies from 12 % to 30 % for photons with energies between 1 GeV and 5 GeV. Since we don't find any signal above 1 GeV, for $x = 1$, namely the minimal Higgs in the standard model, we set the upper limit on the Higgs mass at 5 GeV (90% C.L.). The limit for other values of x can be read off from Fig. 7a. One remark to be mentioned is that from our analysis the Higgs which is lighter than two-muon mass (0.21 GeV) cannot be excluded because we require at least one nonelectromagnetic shower in an event.

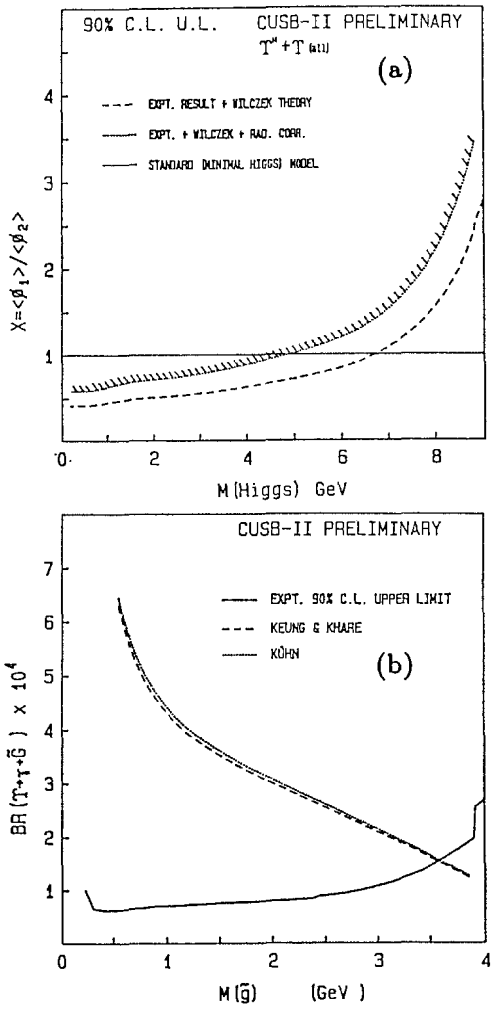

Fig. 7 (a) Ninety percent confidence level upper limit for x vs. Higgs mass,
(b) Ninety percent confidence level upper limit for branching ratio vs. gluino mass.

4.2 GLUINIUM SEARCH

Gluinium are bound states of two gluinos. Using the same method as for the Higgs search, we set the lower limit on the gluino mass at 3.6 GeV (90% C.L.), assuming that its mass is a half of the gluinium mass. The lower limit can be read off from Fig. 7b where two theoretical predictions[24] [25] are shown. The same remark on the sensitivity of our method to the smaller mass region also applies to this case. But in general the gluinium almost always decays to two gluons. Therefore the gluino mass cannot be smaller than the two-pion mass.

5. Physics above $B\bar{B}$ threshold

5.1 COUPLED CHANNEL MODELS

The first coupled channel model was developed by E. Eichten et al.[26] to understand the complicated resonance structure above the $D\bar{D}$ threshold. These models take into account two-body decays such as $B_{u,d}\bar{B}_{u,d}$, $B_{u,d}\bar{B}^*_{u,d} + \bar{B}_{u,d}B^*_{u,d}$, $B^*_{u,d}\bar{B}^*_{u,d}$, $B_s\bar{B}_s$, $B_s\bar{B}^*_s + B_s\bar{B}^*_s$ and $B^*_s\bar{B}^*_s$. In this model different states can be mixed with other states via closed two-body decays. Therefore the wave function of a physical resonance state can be described by a linear combination of bare resonance states and two-body decay channels:

$$|\Upsilon(nS)\rangle_{physical} = \sum_m a_m |m^3S_1\rangle_{bare} + \sum_m b_m |m^3D_1\rangle_{bare} + \sum_i c_i |B\bar{B}\rangle_i.$$

A simplified version of the coupled channel model originally by Eichten et al. was used successfully by CUSB-I collaboration[27] to explain the resonance structure of R, the hadronic cross section normalized to the lowest order QED muon pair production, on and above the $\Upsilon(4S)$ as far as $\sqrt{s}$=11.25 GeV. In this simplified model, the following assumptions are made:

- No S-D mixing, therefore, $b_m = 0$.
- Only two-body decays considered as described above.
- A smooth step in R for decays such as $B\bar{B}+n\pi's$.

According to this model the contribution of each two-body decay to R is written by:

$$R_i = \frac{32\pi^2}{W^3} p_i E_1 E_2 f_q^2 \sum_{n,n'} \Psi_n(0) G^*_n s_i I_n(p_i) I_{n'}(p_i) G_{n'} \Psi_{n'}(0),$$

where $\Psi_n(0)$ is the wave function of the $\Upsilon(nS)$ at the origin, $I_n(p_i)$ is the decay amplitude, s_i is the spin factor which depends on the spin combination of the

decay, namely 1 for $B\bar{B}$, 4 for $B\bar{B}^*+B^*\bar{B}$ and 7 for $B^*\bar{B}^*$, and f_q^2 is the kinematical factor defined by

$$f_q^2 = \frac{3}{\pi}(m_q \frac{m_b m_q}{m_b + m_q})^{-2},$$

G_n is the Green's function given by

$$G_n = \sqrt{\frac{\Gamma_n}{2\pi M_n}} \frac{1}{(W - M_n) + i\Gamma_n/2},$$

and p_i is the momentum of a meson given by

$$p_i = \frac{\sqrt{[W^2 - (M_{i1} + M_{i2})^2][W^2 - (M_{i1} - M_{i2})^2]}}{2W}$$

Then $R = \sum_i R_i$ where i goes through all possible two-body decays. As inputs, the following quantities and their values were used:

- Resonance parameters for the $\Upsilon(nS)$: The positions of resonances are M(4S)=10.5774 GeV, M(5S)=10.845 GeV and M(6S)=11.02 GeV and their widths are Γ(4S)=27 MeV, Γ(5S)=110 MeV and Γ(6S)=90 MeV.
- Quark masses: m_u=0.335 GeV, m_s=0.45 GeV and m_b=5.17 GeV.
- B meson masses: M_B=5.2725 GeV, M_{B^*}=5.328 GeV, M_{B_s}=5.375 GeV and $M_{B_s^*}$=5.425 GeV.
- Wave functions: $|\Psi_{4S}(0)|^2$ calculated by Eichten et al. and for the higher resonances $|\Psi_{nS}(0)|^2$ scales as $1/n$.
- Decay amplitudes: $I_{nS}(p_i)$ calculated by Eichten.[28]

Figure 8a shows the measured $R_{visible}$ values by CUSB-I as a function of energy together with the prediction of the simplified coupled channel model which is in good agreement with the data. Figure 8b is the resonance decomposition according to the model. We took the data with CUSB-II detector at the $\Upsilon(5S)$ this year corresponding to the integrated luminosity of 138 pb^{-1}. Figure 9 is the $R_{visible}$ measured by CUSB-II around the $\Upsilon(5S)$ together with the model prediction which reproduces the data well. This model predicts not only R but also the contribution of each decay to R as described earlier. Table 6 summarizes the contribution of each decay to R as well as the average velocity β of $B^*_{u,d}$ or B^*_s at the $\Upsilon(5S)$.

Table 6. ΔR and $\langle\beta\rangle$ at the Υ(5S)

	$B_{u,d}\bar{B}_{u,d}$	$B_{u,d}\bar{B}^*_{u,d} + \bar{B}_{u,d}B^*_{u,d}$	$B^*_{u,d}\bar{B}^*_{u,d}$	$\sum$B	$B_s\bar{B}_s$	$B_s\bar{B}^*_s + B_s\bar{B}^*_s$	$B^*_s\bar{B}^*_s$	$\sum B_s$
ΔR	0.055	0.11	0.082	0.247	0.017	0.008	0.097	0.121
$\langle\beta\rangle$	–	0.22	0.20	0.21	–	0.11	0.05	0.052

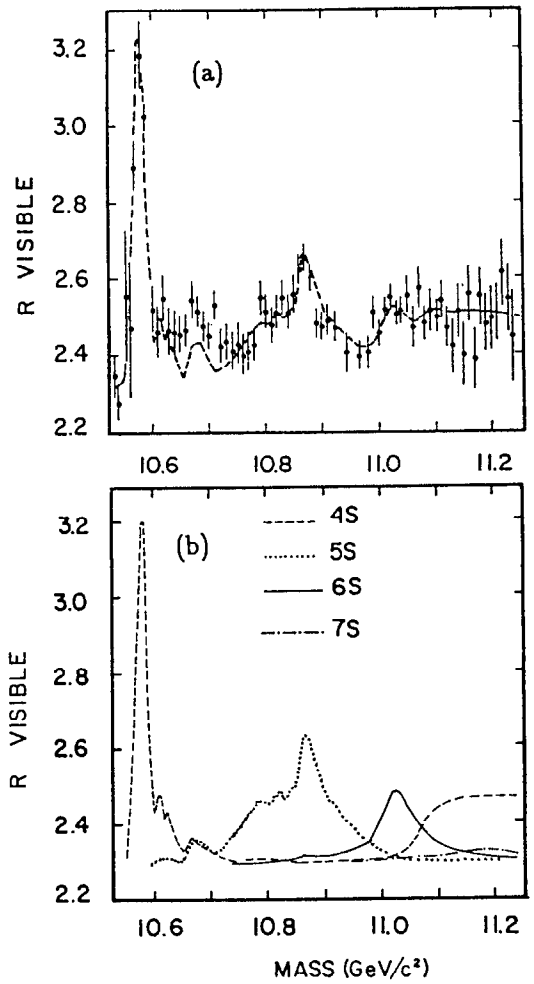

Fig. 8 (a) $R_{visible}$ measured by CUSB-I with model prediction superimposed; (b) Resonance decomposition by the model calculation.

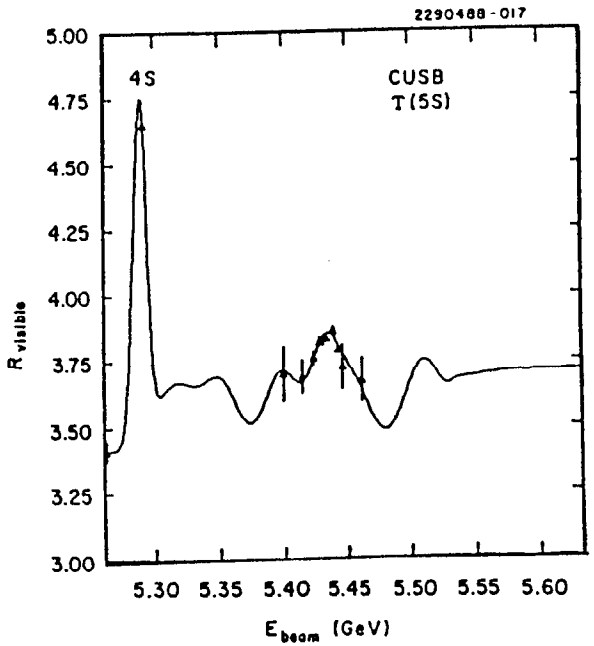

Fig. 9 $R_{visible}$ measured by CUSB-II.

The average velocity $\langle\beta\rangle$, number of photons from the decays $B^*_{u,d,s} \rightarrow B_{u,d,s}\gamma$ and the fraction of B_s at the $\Upsilon(5S)$ are predicted to be 0.14, 1.3 per $\Upsilon(5S)$ decay and 0.3 respectively. Note that a finite value of β implies that photons from the decays $B^*_{u,d,s} \rightarrow B_{u,d,s}\gamma$ are Doppler broadened. Therefore if the intrinsic energy resolution is much better than the effect of the Doppler broadening, one can actually deduce the value of β from the photon spectrum, which turns out to be true in our case.

5.2 PHOTONS FROM THE DECAY $B^* \rightarrow B\gamma$

Figure 10a is the cluster energy distribution at the $\Upsilon(5S)$. If the same distribution at the $\Upsilon(4S)$ shown in Fig. 10b is compared with that at the $\Upsilon(5S)$, one can see even by naked eyes an enhancement around 50 MeV in the distribution at the $\Upsilon(5S)$.

In order to simulate the background shape, an appropriate combination of the data at the $\Upsilon(4S)$ and in the continuum is used. The photon energy spectrum after the background subtraction is shown in Fig. 11.

We use 50 MeV photons generated by 'EGS' which are added to the real hadronic events to estimate the intrinsic energy resolution as well as the acceptance×efficiency. Figures 12a and 12b are the 50 MeV photon peaks after the background subtraction without and with Doppler broadening of β of 0.2. With the help from Figs. 12a and 12b, we obtain the values for the average β, the average peak position and number of photons from $B^* \rightarrow B\gamma$ per $\Upsilon(5S)$ decay:

$$\langle E_\gamma \rangle = (47.4 \pm 0.6) MeV,$$

$$\langle \gamma/\Upsilon(5S) \rangle = 1.12 \pm 0.12, \text{and}$$

$$\langle \beta \rangle = 0.16 \pm 0.015.$$

These values are in good agreement with the simplified coupled channel model predictions, which leads us to the conclusion that the fraction of B_s at the $\Upsilon(5S)$ is 0.3.

5.3 FURTHER STUDIES ON B_s PRODUCTION

Encouraged by the good agreement between our data and the predictions of the simplified coupled channel model, we make more elaborate studies on the fraction of B_s at the $\Upsilon(5S)$ using the three measured quantities $\langle\gamma/\Upsilon(5S)\rangle$,$\langle E_\gamma\rangle$ and $\langle\beta\rangle$. These quantities depend on the relative production rates for the decays $B_{u,d}\overline{B}_{u,d}$, $B_{u,d}\overline{B^*_{u,d}} + \overline{B}_{u,d}B^*_{u,d}$, $B^*_{u,d}\overline{B^*_{u,d}}$, $B_s\overline{B}_s$, $B_s\overline{B^*_s} + B_s\overline{B^*_s}$ and $B^*_s\overline{B^*_s}$, and the meson masses. For this purpose we construct four models in which there are four free parameters.

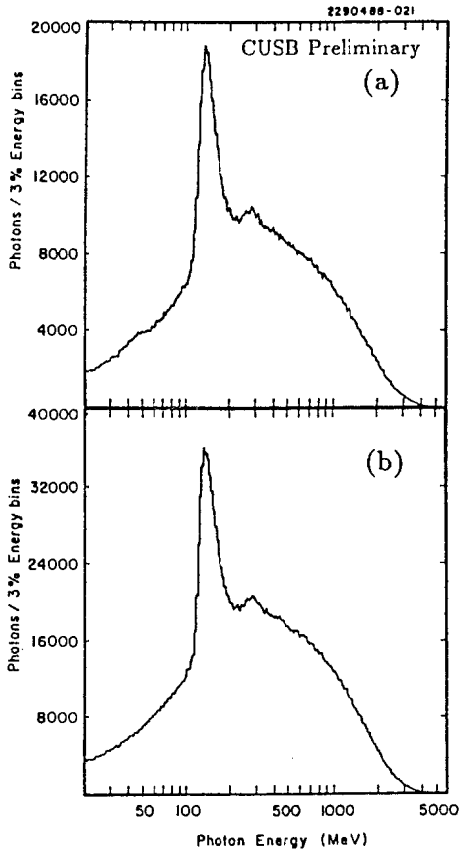

Fig. 10 (a) The cluster energy distribution at $\Upsilon(5S)$, (b) The cluster energy distribution at $\Upsilon(4S)$.

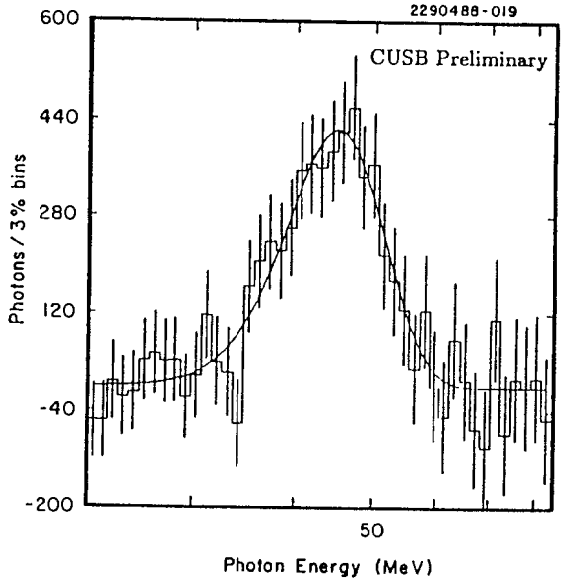

Fig. 11 Subtracted photon spectrum from $B^{*}_{u,d,s} \rightarrow B_{u,d,s}\gamma$ at $\Upsilon(5S)$.

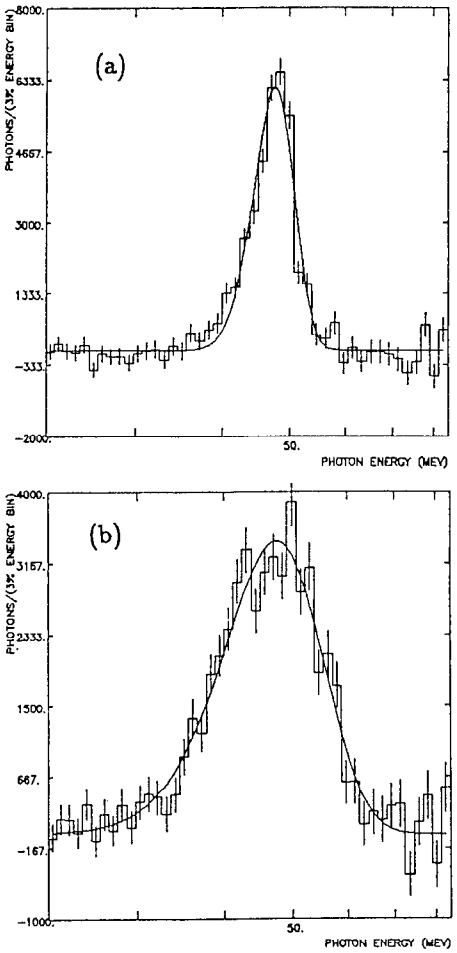

Fig. 12 The 50 MeV EGS photon peaks after background subtraction (a) without and (b) with Doppler broadening of β of 0.2.

They are $D \equiv M_{B_s} - M_{B_{u,d}}$, $U \equiv M_{B_d^*} - M_{B_d}$, $R \equiv (M_{B_s^*} - M_{B_s})/(M_{B_d^*} - M_{B_d})$ and F, the fraction of B_s (including B_s^*). Before going into the detail of the models, we first describe the physical motivation for the choice of parameter ranges.

Estimates for the parameter ranges

(1) 80 MeV$\leq D \leq$ 104 MeV.

The upper limit is based on the simplest assumption that:

$$M_{B_s} - M_{B_{u,d}} = M_{D_s} - \langle M_{D_{u,d}} \rangle = 1970.5 - 1867.0 = 103.5\text{MeV},$$

where we use $\langle M_{D_{u,d}} \rangle$=1867.0 from the average of the measured D_u and D_d masses. The lower limit comes from the expectation that any correction to this value would tend to be small and would lower it. An example is the formula by Eichten and Gottfried given by[29] :

$$M_{B_q} = M_{D_q} + m_b - m_c + (3/4)(1 - m_c/m_b)(M_{D_q^*} - M_{D_q})$$

which gives $M_{B_s} - M_{B_d} = M_{D_s} - M_{D_d} + .48 \times [(M_{D_s^*} - M_{D_s}) - (M_{D_d^*} - M_{D_d})]$. If one uses a naive quark model estimate $M_{D_s^*} - M_{D_s} = m_d/m_s \times (M_{D_d^*} - M_{D_d}) \simeq 103MeV$ which is much lower than the measured value, one gets $M_{B_s} - M_{B_d}$ as small as ~83 MeV. On the other hand if one uses the measured value for $M_{D_s^*} - M_{D_s}$ of 142 MeV, then the above formula gives essentially no correction. To be conservative we use the wider range.

(2) 25 MeV$\leq U \leq$ 75 MeV

The simplest assumption is $M_{B_s^*} - M_{B_s} = M_{B_u^*} - M_{B_u}$. In this case, since we observe the average photon energy of about 47 MeV, U=47 MeV which is close to a naive quark model estimate:

$$M_{D_s^*} - M_{D_s} = \frac{m_d}{m_s}(M_{D_d^*} - M_{D_d}) \simeq 50MeV$$

for $m_d/m_s = 1.84/5.17$. An empirical observation, which has been successful so far to describe the mass difference between the vector(M_v) and the pseudo-scalar (M_{ps}) masses, $M_v^2 - M_{ps}^2 \simeq .54$ to $.58$ GeV^2 predicts 50 MeV$\leq U \leq$ 55 MeV. Here again we use the wider range.

(3) $.7 \leq R \leq 1.0$.

According to the empirical observation R≃1. A naive quark model predicts

$$M_{B_s^*} - M_{B_s} = \frac{m_d}{m_s}(M_{B_d^*} - M_{B_d})$$

where $m_d/m_s = .33/.75 = .73$.

(4) $0 \leq F \leq 1$.

This is clear from the definition.

Model building

Knowing the meson masses in the decays and the relative fraction of each decay one can calculate the values for three quantities experimentally measured. The relative fraction of each decay channel is proportional to the weight w_i given by:

$$w_i = K_i \cdot s_i \cdot I_{5S}^2(p_i),$$

where the subscript refers to one of decay channels, K_i is the kinematical factor, s_i is the same spin factor used in the simplified coupled channel model and $I_{5S}(p_i)$ is the decay amplitude.

(1) Model 1

The kinematical factor for Model 1, which is simplest of all, is β^3. This threshold behavior is motivated by the fact that the mesons are produced in a P-wave. The spin factor is common to all four models. The decay amplitude in this model is simply assumed to be one.

(2) Models 2, 3 and 4

The kinematical factor K_i is given by $p_i E_1 E_2$ for all three models as in coupled channel models, where p_i is the momentum of one of the mesons and E_i is the energy of the meson i. The decay amplitudes for Models 2, 3 and 4 are obtained by Eichten et al.(EI),[30] by Martin and Ng (MN)[31] and by Byers and Hwang (BH).[32] These three models are essentially three coupled channel models at a fixed energy except that the couplings between resonances are neglected, which is a reasonable assumption for the $\Upsilon(5S)$ as justified from Fig. 8b.

Fit results

In order to find solutions and errors on parameters for the models, we define the 'chi-square' as follows:

$$\chi^2 = \frac{(E_\gamma - E_\gamma^{obs})^2}{\sigma_{E_\gamma}^2} + \frac{(N_\gamma - N_\gamma^{obs})^2}{\sigma_{N_\gamma}^2} + \frac{(\beta_\gamma - \beta_\gamma^{obs})^2}{\sigma_{\beta_\gamma}^2}.$$

The solutions to the three constraint equations give the χ^2 values of zero. As shown in Table 7, we actually find the solutions for all four models within the parameter ranges described above. Table 8 summarizes the best fit parameters.

Table 7. Fit values for potential models.

	$\langle E_\gamma \rangle$ (MeV)	$\langle \beta \rangle$	$\langle \gamma/\Upsilon(5S) \rangle$	χ^2
Expt	47.4 ± 0.6	0.16 ± .015	1.122 ± .121	
β^3	47.4	0.161	1.120	0.004
EI	47.4	0.160	1.122	0.006
MN	47.4	0.159	1.126	0.005
BH	47.4	0.160	1.120	0.001

Table 8. Best fit parameters for four models.

Parameter	β^3	EI	MN	BH
$(M_{B_s} - M_{B_{u,d}})$	105 MeV	90 MeV	75 MeV	65 MeV
$(M_{B_d^*} - M_{B_d})$	46.7 MeV	50.4 MeV	48.4 MeV	50.3 MeV
$(M_{B_s^*} - M_{B_s})/(M_{B_d^*} - M_{B_d})$	1.0	.85	.95	.90
Fraction of strange	.38	.49	.68	.71

We define the '1σ' contour as the contour which encloses the region where the χ^2 has increased by one from its minimum value of zero in order to infer the allowed ranges of the parameter values. As an example, the 1σ contours in F-$(M_{B_s^*} - M_{B_s})$ space for Models 2,3 and 4 are shown in Fig. 13.

All the models again predict that the fraction of B_s is at least 30% in the $\Upsilon(5S)$ decays, from which we reach the conclusion that the B_s/B_s^* has been produced. This conclusion agrees with an intuitive argument that if there is no B_s^* produced a wider width of the 50 MeV photon peak is expected.

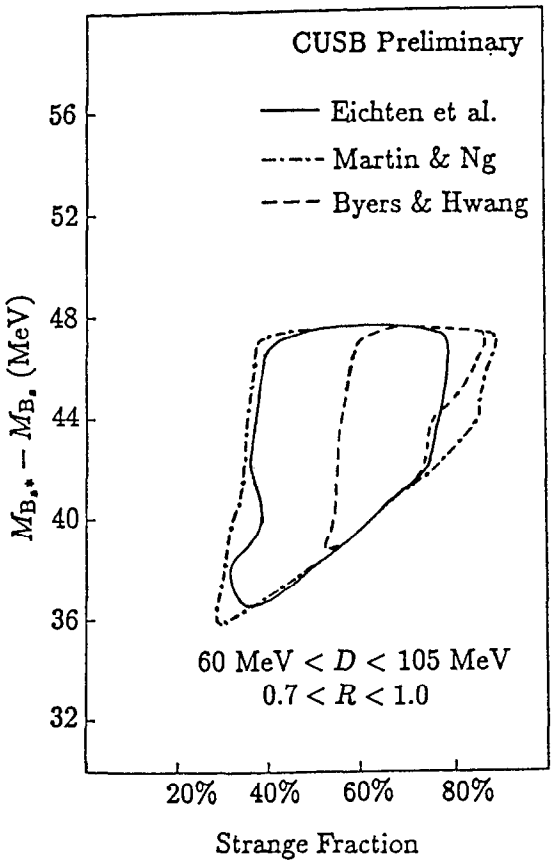

Fig. 13 The overlap of all 1σ contours for the Eichten (solid line), Martin and Ng (dot-dashed line), and Byers and Hwang (dashed line) models for $M_{B_s^*} - M_{B_s}$ vs. the strange fraction ($\equiv F$). The other two parameters cover the regions 60 MeV $< D <$ 105 MeV, and $0.7 < R < 1.0$.

6. Conclusions

We have

- measured $B_{\mu\mu}$ with improved accuracy,
- improved the measurement on the fine structure of the χ'_{bJ} states,
- more detailed knowledge on the E1 transitions in the Υ system,
- the first significant limits on the Higgs and gluino masses and
- found B^*, B_s and B_s^* are produced and the fraction of B_s is at least 30% at the $\Upsilon(5S)$.

ACKNOWLEDGEMENTS

The author thanks all members of the CUSB-II collaboration for their contributions. Special thanks to Professors J. Lee-Franzini, P. Franzini, P.M. Tuts and Dr. R. D. Schamberger for their help during the preparation of this talk. CUSB-II is supported by the U.S. National Science Foundation.

REFERENCES

1. J. Lee-Franzini, Nucl. Inst. Meth. **A263** 35 (1988).
2. Contributed paper by Crystal Ball Collaboration, Proceedings of International Symposium on Lepton and Photon Interaction, Hamburg, F. R. Germany, July 1987.
3. S. Cooper, Proceedings of the XXIII International Conference on High Energy Physics, Berkeley, California, p. 67, July 1986.
4. U. Heinz et al., Contributed paper to the XXIV International Conference on High Energy Physics, Munich, F. R. Germany, August 1988.
5. I. Brock et al., Contributed paper to the XXIV International Conference on High Energy Physics, Munich, F. R. Germany, August 1988.
6. R. D. Schamberger et al., Phys. Rev. Lett. **138**B 225 (1982).
7. E. Rice, Ph. D. Thesis, Columbia University (1982).
8. P. B. Mackenzie and G. P.Lepage, Phys. Rev. Lett. **47** 1244 (1981).
9. W. A. Bardeen et al., Phys. Rev. D**18** 3998 (1978).
10. W. Kwong et al., Phys. Rev. D**37** 3210 (1988).
11. D. W. Duke and R. G. Roberts, Physics Reports **120** 275 (1985).
12. See for example D. Gromes, Nucl. Phys. B**131** 80 (1977).
13. J. L. Rosner, in Experimental Meson Spectroscopy-1983, ed. by S. J. Lindenbaum, AIP, New York, 461 (1984).

14. E. Eichten et al., Phys. Rev. D**17** 3090 (1979); ibid. D**21** 203 (1980).
15. W. Kwong and J. L. Rosner, Enrico Fermi Institute Preprint EFI 88-02.
16. S. N. Gupta, S. F. Radford and W. W. Repko, Phys. Rev. D**30** 2425 (1984).
17. Y. P. Kuang and T. M. Yan, Phys. Rev. D**24** 2874 (1981).
18. The χ_c and χ_b values are from Reference 2 and the χ_b' value is from the CUSB experiment.
19. See Reference 13.
20. P. Moxhay and J. L. Rosner, Phys. Rev. D**28** 1132 (1983).
21. R. McClary and N. Byers, Phys. Rev. D**28** 1692 (1983).
22. F. Wilczek, Phys. Rev. Lett. **40**, 220 (1978).
23. M. I. Vysotsky, Phys. Lett. **97**B 159 (1980); J. Ellis et al., ibid., **158**B 417 (1985); P. Nason, ibid., **175**B 223 (1986).
24. J. H. Kühn and S. Ono, Phys. Lett. **142**B 436 (1984).
25. W. Y. Keung and A. Khare, Phys. Rev. D29 2657 (1984).
26. See Reference 11.
27. D. M. J. Lovelock et al., Phys. Rev. Lett. 54 377 (1985).
28. E. Eichten, Phys. Rev. D**22** 1819 (1980).
29. E. Eichten and K. Gottfried, Phys. Lett. **66**B 286 (1977).
30. See Reference 11.
31. A. D. Martin and C. K. Ng, DPT Preprint, DPT/88/6.
32. N. Byers and D. S. Hwang, Proceedings of the Workshop on Beauty Physics at FNAL and UCLA preprint UCLA/87/TEP/44 (1988).

Recent Results from CLEO

—An Observation of $B^0 - \overline{B}^0$ Mixing and a Search for Charmless B Meson Decays, $B^- \to p\bar{p}\pi^-$ and $\overline{B}^0 \to p\bar{p}\pi^+\pi^-$—

Nobu Katayama

State University of New York at Albany

Representing the CLEO Collaboration

ABSTRACT

I review recent results on the B physics from the CLEO detector at the Cornell Electron Storage Ring (CESR). Using the data containing 484,000 B meson decays CLEO has observed $B\overline{B}$ mixing. The preliminary results for the mixing parameter is $r = 0.182 \pm 0.055 \pm 0.056$, where the first error is statistical and the second systematic. We have searched for charmless decays, $B^- \to p\bar{p}\pi^-$ and $\overline{B}^0 \to p\bar{p}\pi^+\pi^-$ and set 90% upper limits of 1.4×10^{-4} and 2.9×10^{-4} for the branching fractions for $B^- \to p\bar{p}\pi^-$ and $\overline{B}^0 \to p\bar{p}\pi^+\pi^-$.

1. Status of the CLEO Experiment

1.1. Cornell Electron Storage Ring

The Cornell Electron Storage Ring (CESR) is an electron-positron collider located at the Wilson Synchrotron Laboratory at Cornell University, New York. CESR has had an intensive research program aimed at maximizing the integrated luminosities provided to the two experimental areas. CESR has obtained peak luminosities of $10^{32} cm^{-2} s^{-1}$ at the $\Upsilon(5S)$ resonance, or accumulated luminosities of 4.1 pb^{-1} per day at the $\Upsilon(4S)$ resonance.

1.2. CLEO DETECTOR

The CLEO collaboration has 90 physicists from 11 institutions. It operates a general purpose detector at the south interaction region at CESR. The detector has been described in detail elsewhere.[1] In the summer of 1986 a new drift chamber system for the CLEO II detector was installed. We will briefly describe the new tracking system with which the majority of the data discussed here were collected.

Data samples. Thanks to the diligent efforts of the CESR operations crew, CLEO has been able to accumulate impressive amounts of data over the years. Since the summer of 1986 (the '87 run), it has accumulated 21 pb^{-1} at the $\Upsilon(1S)$ resonance, 64 pb^{-1} at the $\Upsilon(3S)$ resonance, 101 pb^{-1} just below the $B\overline{B}$ threshold, 214 pb^{-1} at the $\Upsilon(4S)$ resonance, and 114 pb^{-1} at the $\Upsilon(5S)$ resonance. I will be presenting the results on the $B\overline{B}$ mixing[2] which comes from the data taken at the $\Upsilon(4S)$ and below the $B\overline{B}$ threshold, and on the charmless B meson decays, $B^- \to p\overline{p}\pi^-$ and $\overline{B}^0 \to p\overline{p}\pi^+\pi^-$ from the same data supplemented by the data collected in 1985 (the '85 run) using the original tracking chamber (78 pb^{-1} on the $\Upsilon(4S)$ and 40 pb^{-1} below the $B\overline{B}$ threshold). Since there are significant differences in resolution for the two data samples, we have analyzed them independently as well as giving combined results. The integrated luminosities used for the analyses here are summarized in Table 1.1.

Table 1.1

Integrated luminosities and # of $B\overline{B}$ pairs.

	CLEO '87	CLEO '85	ARGUS
At the $\Upsilon(4S)$ (pb^{-1})	212	78	103
Below $B\overline{B}$ threshold (pb^{-1})	101	36	42
# of $B\overline{B}$ pairs	242,000	90,000	88,000

New tracking system. Charged particle tracking is done inside a super conducting solenoid of radius 1.0m which produces a 1.0T magnetic field. The three nested cylindrical drift chambers measure momenta and specific ionization for charged particles. The innermost chamber is a three layer straw tube vertex detector, the middle a ten layer drift chamber with two layers of z measurements using cathode strips, and the main drift chamber contains 51 layers (41 axial 11 stereo) with two layers of cathode strips. With $3 + 10 + 40$ layers of r-ϕ and $11 + 4$ layers of z tracking, the r. m. s. momentum resolution is

$$\left(\frac{\delta p}{p}\right)^2 = (0.7)^2 + (0.23p)^2, (\%, p \; in \; GeV/c)$$

and the r. m. s. resolution in ionization is 6.5%. These are superior to those of the original CLEO central tracking chambers used until the summer of 1986. The resolutions in ionization and momentum of the new and original CLEO tracking chambers and those of the ARGUS detector[3] are summarized in Table 1.2.

Table 1.2

Drift chamber parameters.

	CLEO '87	CLEO '85	ARGUS
# of Anode layers	3+10+51	10+17	36
$(\frac{\delta p}{p})^2$ (%, p in GeV/c)	$(0.7)^2 + (0.23p)^2$	$(0.6)^2 + (0.7p)^2$	$(0.9)^2 + (1.2p)^2$
dE/dx resolution(%)	6.5	11	4.2*

* The ARGUS drift chamber is operated with Propane.

Particle identification capability of the central drift chamber. Figure 1.1 shows the lowest 50% of the pulse heights measured in the central drift chamber (inner dE/dx) as a function of momentum. The bands for electrons, pions, kaons and protons are clearly visible. Using the dE/dx measurements a proton or antiproton with momentum less than 1.1 GeV/c can be unambiguously identified. As seen in Figure 1.1 the dE/dx distributions for pions and protons are the same at 1.5 GeV/c. However, above 1.8 GeV/c the expected proton dE/dx is one to two standard deviation below that for pions. Proton and kaon distributions are almost identical above 1.5 GeV/c.

Electron identification. Although the outer detector elements of CLEO such as time-of-flight counters, electromagnetic shower counters, and outer dE/dx chambers were unchanged the electron identification capability has been improved by combining information from the inner dE/dx and from the outer detectors (mainly calorimetry). While retaining the same efficiency as for the '85 run (about 90%) the hadron (kaon and pion) fake rates have come down to 0.2% from 0.8% in the '85 run for a track with a momentum greater than 1.4 GeV/c in the 47% of solid angle covered by the calorimetry modules and by

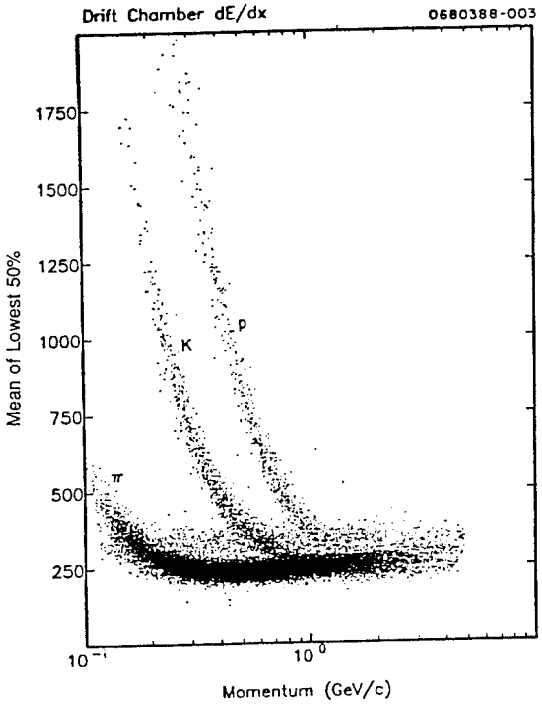

Figure 1.1 The most probable ionization energy loss vs. measured momentum for the CLEO II central drift chamber.

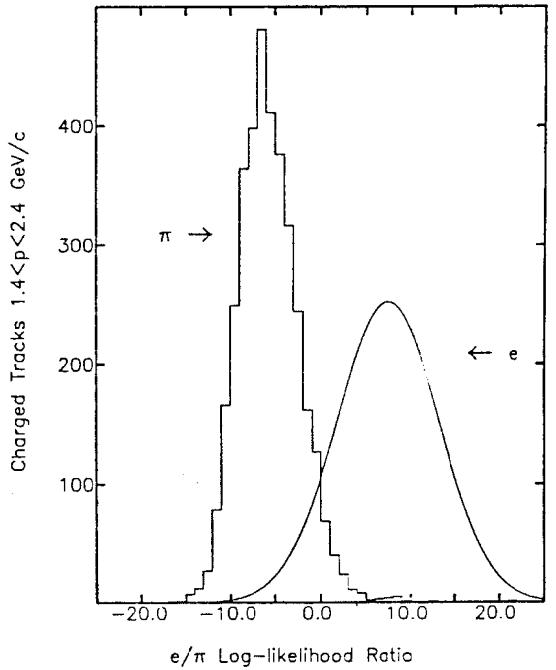

Figure 1.2 Electron/pion log likelihood ratio by the inner dE/dx.

the drift chamber. Outside of the coverage of the calorimetry modules the electrons are identified by the inner dE/dx information alone up to 80% of 4π. The hadron fake rates are 0.6% (not available for '85) for a track with a momentum greater than 1.4 GeV/c. Figure 1.2 is a demonstration of e/π separation by the dE/dx information in the drift chamber. This resulted an increase in the fiducial volume of the electron identification from 47% to 80% of 4π and approximately doubled our number of observed electrons per pb^{-1} in the '87 run.

2. Charmless B Meson Decays, $B^- \rightarrow p\bar{p}\pi^-$ and $\overline{B}^0 \rightarrow p\bar{p}\pi^+\pi^-$

2.1. Introduction

In the Standard Model the weak decay of the b quark proceeds through the charged current coupling to the c quark or to the u quark. The relative amplitudes are proportional to the Cabibbo–Kobayashi–Maskawa matrix elements V_{cb} and V_{ub}. Data on the inclusive production of charmed mesons and baryons in B meson decays[4] and on the lepton momentum spectrum in semileptonic B meson decays[5] are consistent with charm dominance; $|V_{ub}/V_{cb}| << 1$. Ninety percent confidence level upper limits on the branching fractions for many charmless B meson decay modes of the order of 10^{-4} have been published.[6,7] In the summer of 1987 the ARGUS collaboration reported an observation of a signal in the charmless B meson decays $B^- \rightarrow p\bar{p}\pi^-$ and $\overline{B}^0 \rightarrow p\bar{p}\pi^+\pi^-$.[8] They have observed 34 events in total, only 9 ± 4 events out of which are considered to be the background and obtained the branching fractions,

$$B(\bar{B}^- \rightarrow p\bar{p}\pi^-) = (5.2 \pm 1.4 \pm 1.9) \times 10^{-4}, \; and$$
$$B(\bar{B}^0 \rightarrow p\bar{p}\pi^+\pi^-) = (6.0 \pm 2.0 \pm 2.2) \times 10^{-4}.$$

If these are true signals it is the first observation of B meson decays into charmless states caused by the $b \rightarrow u$ transition (See Figure 2.1).

The resulting *lower* limit on the CKM matrix element, V_{ub}, calculated from their measurements in their paper

$$|\frac{V_{ub}}{V_{cb}}| > 0.08,$$

is inconsistent with some of theoretical predictions. Needless to say, it is a very important observation and has to be confirmed by other experiments. Currently, the CLEO experiment is the only other experiment which can search for these charmless decays of B mesons. We report an attempt to confirm this observation using the larger data sample with the improved detector described in the previous chapter.

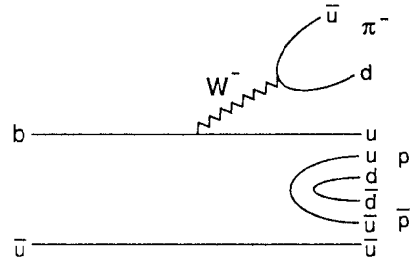

Figure 2.1 B meson decay diagrams through $b \rightarrow u$ transition.

2.2. Data analysis

In order to observe exclusive decays of B mesons into rare modes it is crucial to suppress the background of spurious chance combinations of particles for both B meson decays to other modes and non-$B\overline{B}$ continuum ($e^+e^- \rightarrow q\bar{q}$) events. Three essential techniques: kinematic constraints, topological cuts, and particle identification are used to suppress the backgrounds.

Kinematic constraints and cuts. The fact that the $\Upsilon(4S)$ decays into two B mesons constrains the energy and momentum of each B meson. Since the energy of the B meson should be half of the mass of the $\Upsilon(4S)$, we require that the sum of the measured energies of the candidate decay products be within 50 MeV of the beam energy (65 MeV for the '85 data). This balance is sensitive to the correctness of the mass assignment for each of the presumed decay products. In the '87 data the r. m. s. resolution in the sum of measured energies is determined to be 25 to 30 MeV from the Monte Carlo detector simulation.

Since we calculate the mass of the candidate B meson from the beam constrained formula

$$M^2 = E_{beam}^2 - (\Sigma p_{obs})^2,$$

the momentum constraint is re-expressed as the requirement that the correctly reconstructed candidates show a narrow peaking at the known B meson mass. The reconstructed mass is not sensitive to the mass assignments of the decay products. Because the Q value of $\Upsilon(4S) \rightarrow B\overline{B}$ is small (18 MeV) and the β of the produced B mesons is small (0.06), the contribution from the momentum resolution to the mass resolution is small (calculate a partial derivative of M by

p_{obs}). The resolution is dominated by the energy resolution of the accelerator.[9] Therefore the expected r. m. s. mass resolution is as small as 2.6 MeV which is 10 times better than that of a mere invariant mass.

The direction of the B momentum is not constrained but should be distributed as $sin^2\theta_B$ with respect to the beam axis since the two B mesons (spin zero) are produced from the longitudinally polarized $\Upsilon(4S)$ (spin unity). To suppress background from chance reconstructions, which tend to be isotropic in reconstructed B direction, we require $|cos\,\theta_B| < 0.8$. This results in a 5.6% loss in efficiency for correctly reconstructed B meson decays and 20% suppression for isotropically distributed random combinations.

Topological cut. Particles in background events from non-$B\overline{B}$ continuum ($e^+e^- \rightarrow q\bar{q}$) events tend to align close by with the jet axis of the event, while any axis calculated for the products of a candidate B meson decay should be uncorrelated with the axis for the rest of the particles in the same events. (Notice that the remaining tracks make up the other B meson in the event.) For each event which contains a candidate decay we therefore compute two sphericity axes, one for the candidate decay and the other for all remaining charged particles, and require that the angle α between the two sphericity axes satisfy $|cos\,\alpha| < 0.7$. This is illustrated in Figure 2.2.

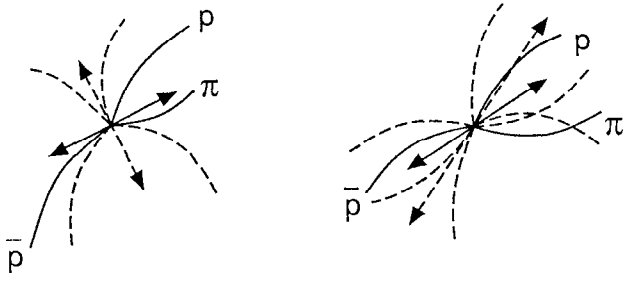

Figure 2.2 Event topology and sphericity axes in the $B\overline{B}$ events and the non $B\overline{B}$ continuum ($e^+e^- \rightarrow q\bar{q}$) events.

Can we see B's ? Figure 2.3 is a demonstration of the mass resolution and statistical power of the '87 data sample, using the charmed decay modes $B^- \rightarrow D^0\pi^- \rightarrow (K^-\pi^+)\pi^-$ and $B^- \rightarrow \psi K^- \rightarrow (e^+e^-)K^-$ or $(\mu^+\mu^-)K^-$. The figure shows the reconstructed mass distribution for events on the $\Upsilon(4S)$ with the kinematic and topological cuts just described, *plus* the requirement that the $K^-\pi^+$ mass be close to the D^0 mass or that the dilepton mass to the ψ mass. The lepton candidates are not required to be identified as leptons using information available from dE/dx, outer calorimetry modules and muon chambers. The product

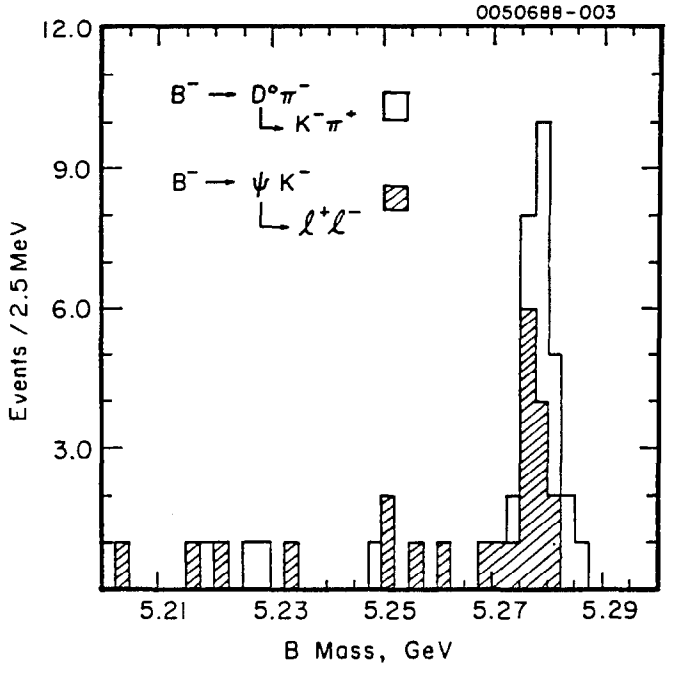

Figure 2.3 Distribution in reconstructed mass for candidates for the decay $B^- \rightarrow D^0\pi^- \rightarrow (K^-\pi^+)\pi^+$ and $B^- \rightarrow \psi K^- \rightarrow (\ell^+\ell^-)K^-$, from the '87 data sample.

branching fractions for these modes are measured by CLEO[10,11] and ARGUS,[12]

$$B(B^-\to D^0\pi^-)\times B(D^0\to K^-\pi^+) = (0.43\pm 0.14\pm 0.06)\%\times(4.2\pm 0.6)\%,$$
$$B(B^-\to \psi K^-)\times B(\psi\to \ell^+\ell^-) = (0.05\pm 0.02)\%\times 2\times(6.9\pm 0.9)\%,$$

which are three to five times smaller than those of $B^-\to p\bar{p}\pi^-$ and $\overline{B}^0\to p\bar{p}\pi^+\pi^-$ as reported by ARGUS. Furthermore the improved detector and the larger data sample enable us to use a 2.5 MeV binning for the mass distribution instead of a 5 MeV binning, which was used in all previous publications of exclusive B meson decays from CLEO.

Particle identification. For the decay modes $B^-\to p\bar{p}\pi^-$ and $\overline{B}^0\to p\bar{p}\pi^+\pi^-$ we require that the $\pi^\pm$ candidates have ionization within two standard deviations of the expected value, and that the combined χ^2 for the proton and antiproton ionization be less than 4. The latter cut corresponds to an efficiency of about 86% for the real p and $\bar{p}$ combinations to pass the cut. Even though there is only a one to two standard deviation separation between the expected values of the ionization for pions and protons above 1.8 GeV/c due to the fact that there are many more pions than protons, this cut reduces the amount of the combinatoric background by a factor of about four. Tracks with poor dE/dx measurements (usually because of steep dip angles) are rejected. We have checked the dE/dx distributions for pions and protons using secondaries from kinematically reconstructed Λ and K^0_S decays. We also require that none of the candidate decay products be identified as an electron or muon. Misidentified high momentum pions or kaons can cause a background of spurious B meson decay reconstructions, since the discrepancy in ΔE caused by assigning a proton mass to a pion or kaon can be compensated by the loss of a low momentum decay product so that the kinematic constraints can still be satisfied even though all candidate tracks are produced by the decay of one B meson into other decay modes in a $B\overline{B}$ event.

Multiple combination in an event. A true $B^-\to p\bar{p}\pi^-$ or $\overline{B}^0\to p\bar{p}\pi^+\pi^-$ decay may make more than one candidate combinations if, for example, a pion mass is assigned to a proton and a proton mass to a pion and both right and misassigned combinations still satisfy the required ΔE cut. Therefore we accept only the one that has the lowest $|\Delta E|$ for each of the two modes if there is more than one candidate decay in an event after all data cuts have been applied (including ones mentioned later).

Mass distributions for the "phase space search." Figures 2.4(a) and 2.5(a) show the plots of the reconstructed mass for $B^-\to p\bar{p}\pi^-$ and $\overline{B}^0\to p\bar{p}\pi^+\pi^-$ combinations in the '87 data sample satisfying the above cuts, for the $\Upsilon(4S)$ resonance (data points) and for the below $B\overline{B}$ threshold data, scaled to the same integrated

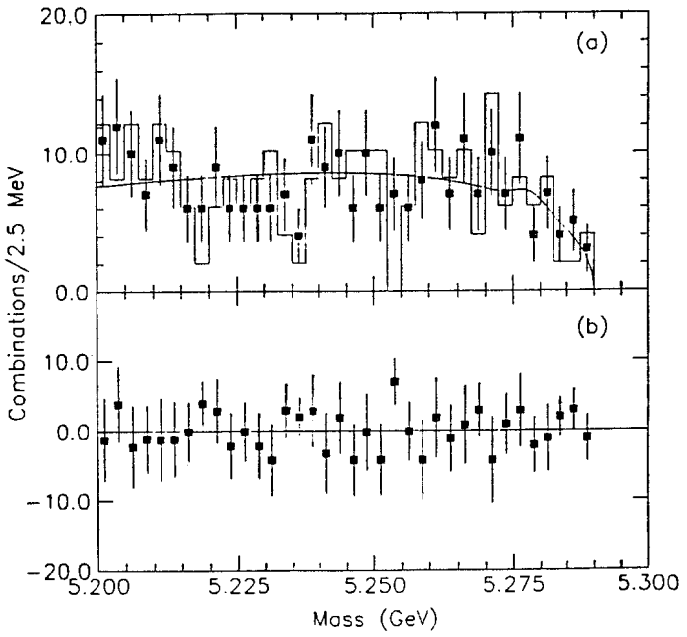

Figure 2.4 Distribution in reconstructed mass for $B^-\to p\bar{p}\pi^-$ candidates from the phase space search, using the '87 data sample: (a) data taken on the $\Upsilon(4S)$ resonance (points), scaled data taken below $B\overline{B}$ threshold (histogram), with the fit to the signal and background function described in the text (curve); (b) the net contribution from the $B\overline{B}$ events, by taking the difference between the $\Upsilon(4S)$ data and the below $B\overline{B}$ threshold data.

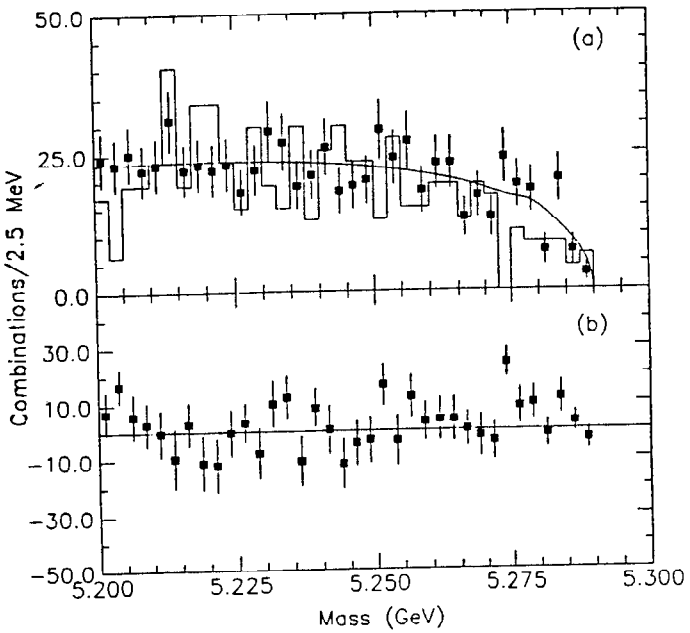

Figure 2.5 Distribution in reconstructed mass for $\overline{B}^0 \to p\bar{p}\pi^+\pi^-$ candidates from the phase space search, using the '87 data sample: (a) data taken on the $\Upsilon(4S)$ resonance (points), scaled data taken below $B\overline{B}$ threshold (histogram), with the fit to the signal and background function described in the text (curve); (b) the net contribution from the $B\overline{B}$ events, by taking the difference between the $\Upsilon(4S)$ data and the below $B\overline{B}$ threshold data.

luminosity and beam energy. For this search we used all available decay phase space. Figures 2.4(b) and 2.5(b) show the difference, corresponding to the net yield from $B\overline{B}$ decays. In addition to any signal, this difference includes background from other B and $\overline{B}$ decay modes incorrectly reconstructed as $B^- \to p\bar{p}\pi^-$ or $\overline{B}^0 \to p\bar{p}\pi^+\pi^-$. Although there may be an excess near the B meson mass for each of the two modes, the mass spectrum does not have the expected shape for a correctly reconstructed mass peak. To derive upper limits on the branching fractions which do not depend on any model of background we count the net number of events (resonance data minus continuum data) within 5 MeV of the B mass, then divide by the total number of produced B's of the appropriate charges (assuming[6]

$$\frac{N(B^0\overline{B}^0)}{N(B^0\overline{B}^0) + N(B^+B^-)} = 0.43),$$

and by the acceptance computed by Monte Carlo with a phase space decay distribution. We form weighted averages of the '87 and '85 data, but because of the smaller event sample and larger background due to poorer resolution in ΔE and dE/dx the '85 data have less weight. The resulting 90% confidence level upper limits are given in Table 2.1.

Kinematic cut in the phase space. In our phase space search for $B^- \to p\bar{p}\pi^-$ or $\overline{B}^0 \to p\bar{p}\pi^+\pi^-$ the sensitivity is limited by the statistical error in the background, mainly from the continuum events. It is conceivable that there are particular configurations of the final state in the phase space that are favored by the decay dynamics or disfavored in the continuum background, so that a search with a kinematical constraint in the phase space may be more successful. The kinematic cuts should be justified in terms of physics otherwise it is like turning knobs in order to enhance the signal. The possible configurations are most easily pictured for the $B^- \to p\bar{p}\pi^-$ mode by drawing the Dalitz plot (Figure 2.6). For the $\overline{B}^0 \to p\bar{p}\pi^+\pi^-$ mode in the limit of quasi three-body decay (for example, $p\bar{p}\rho^0$, $\Delta^0\bar{p}\pi^+$) the decay kinematics are similar to the $B^- \to p\bar{p}\pi^-$ mode. In addition to the cuts mentioned above we make the following kinematic cuts in the decay phase space for both modes.

Proton or antiproton at low momentum. We require that either the p or $\bar{p}$ have a momentum below 1.1 GeV/c. This is motivated by the inclusive baryon momentum spectrum in B meson decay,which is consistent with all baryon momenta being below 1.0 GeV/c, and by the fact that low momentum protons can be unambiguously identified by dE/dx. Region I of the $B^- \to p\bar{p}\pi^-$ Dalitz plot for which this search is sensitive covers 34% of the total phase space. No signal is seen in either of the decay modes and the upper limits are given in Table 2.1. For the detection efficiency we have assumed that all of the decays satisfy the proton momentum requirement. In other words, we did not divide the obtained branching fraction by 34%.

Table 2.1

90% confidence level limits for the branching fractions.

	$B(B^- \to p\bar{p}\pi^-)$ (10^{-4})	$B(\overline{B}^0 \to p\bar{p}\pi^+\pi^-)$ (10^{-4})
"Phase space" search	3.0	11.9
p or $\bar{p}$ at low momentum	2.8	8.4
Collinear p and $\bar{p}$ (ARGUS cut)	1.6	3.3
$\bar{p}\Delta^0$, $\Delta^0\overline{\Delta}^0$	1.3	1.2
$p\overline{\Delta}^{--}$, $\Delta^{++}\overline{\Delta}^{--}$	1.2	1.3
$\bar{p}N^{*0}$, $N^{*0}\overline{N}^{*0}$	1.1	2.5
$p\overline{N}^{*--}$, $N^{*++}\overline{N}^{*--}$	1.7	1.7
$\Delta^0\overline{N}^{*0}$ or $N^{*0}\overline{\Delta}^0$		2.8
$\Delta^{++}\overline{N}^{*--}$ or $N^{*++}\overline{\Delta}^{--}$		2.4

In units of 10^{-4}, from the various searches described in the text, combining the '85 and '87 data samples, and averaging charge conjugate modes. The limits are obtained from the number of candidates within 5 MeV of the B meson mass in the subtracted distribution: data on the $\Upsilon(4S)$ minus scaled data from below $B\overline{B}$ threshold. The "Δ" and "N^*" refer to $p\pi$ mass ranges defined in the text.

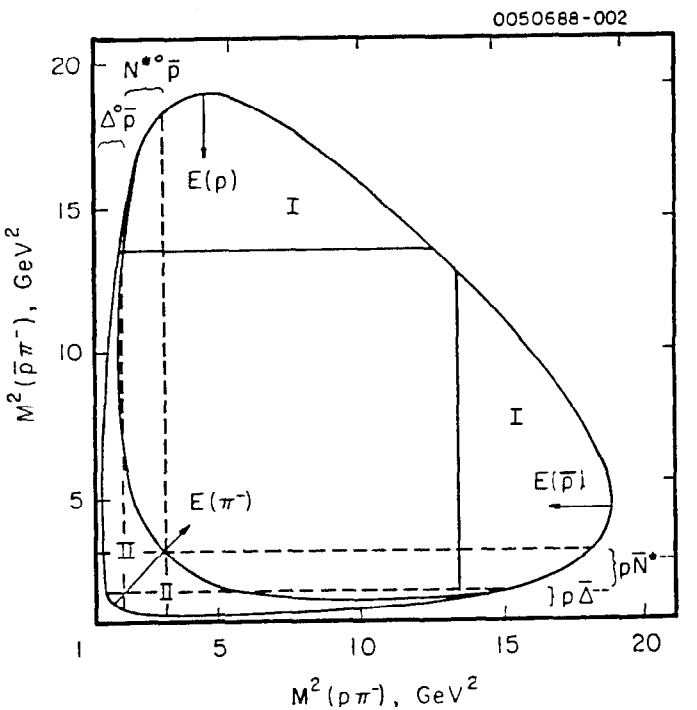

Figure 2.6 Dalitz plot for the decay $B^- \to p\bar{p}\pi^-$ at rest. Region I corresponds to the requirement that either the p or $\bar{p}$ have momentum less that 1.1 GeV/c. In region II the angle β between the p and $\bar{p}$ satisfies $\cos\beta < -0.98$ (almost collinear, the ARGUS cut). The bands corresponding to Δ (M < 1.4 GeV) and N^* (1.4 < M < 1.8 GeV) are bounded by dashed lines. Note that for $B\overline{B}$ produced from a $\Upsilon(4S)$ at rest in the laboratory, the B will be moving and the boundary curve will be smeared somewhat.

Nucleon isobar submasses. For this analysis we define a "Δ" as any $p\pi(\overline{p}\pi)$ combination with invariant mass below 1.4 GeV, and an "N^*" as any such combination between 1.4 and 1.8 GeV. After combining charge conjugates there are two distinct charge pairings, opposite-sign (e.g., Δ^0) and like-sign (e.g., $\overline{\Delta}^{--}$), corresponding to vertical and horizontal bands in the $B^-\to p\overline{p}\pi^-$ Dalitz plot. We see no significant signal in any combination. The upper limits (Table 2.1) are calculated using an acceptance obtained with Monte Carlo isobar events.

Almost collinear p and $\overline{p}$ (ARGUS cut). Following the original search by the ARGUS collaboration we require that $cos\,\beta < -0.98$, where β is the angle between the p and $\overline{p}$ momenta in the Lab frame. For the $B^-\to p\overline{p}\pi^-$ mode this cut includes a 10% region of the Dalitz plot corresponding to high p and/or $\overline{p}$ momenta (region II in Figure 2.6). Again we see no signal (Figures 2.7 and 2.8, with dashed curves showing the size of the mass peak expected from the ARGUS results.) As in the other searches we calculate a model-independent upper limits (Table 2.1) from the difference between the mass distribution for the $\Upsilon(4S)$ resonance data and for the scaled below $B\overline{B}$ threshold data.

ARGUS background. In order to make a closer comparison to the ARGUS result in this search, we also estimate an upper limit using the model dependent ARGUS technique. That is, we fit the mass spectrum taken on the $\Upsilon(4S)$ resonance to a background of the assumed form

$$\frac{dN}{dM_B} = A \times M_B \times \sqrt{x} \times exp(\alpha x),$$

where $x = 1 - M_B^2/E_{beam}^2$, plus a Gaussian at the B meson mass with the expected resolution. The parameter α and the magnitude factors for the background and Gaussian are varied to obtain the best fit, and the upper limits on the branching fractions are determined from the areas of the Gaussians. Our measured branching fractions as well as resulting upper limits for the ARGUS cut and background model are summarized in Table 2.2. The background from incorrectly reconstructed $B\overline{B}$ events is subtracted as well as the background from the $e^+e^-\to q\overline{q}$ events, provided that the background follows the assumed mass distribution. In calculating the detection efficiency for this search we have assumed that all decays satisfy the $cos\,\beta$ collinearity cut, but in order to make a fair comparison we have scaled the ARGUS results in Table 2.2 by a factor of 0.7, since they have assumed a 70% acceptance for the collinearity cut.

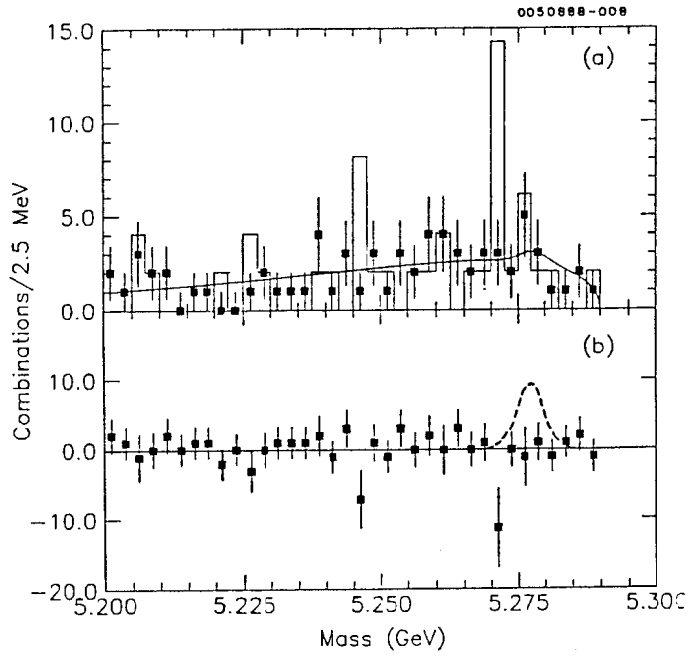

Figure 2.7 Distribution in reconstructed mass for $B^-\to p\overline{p}\pi^-$ candidates from the collinear search (the ARGUS cut), using the '87 data sample: (a) data taken on the $\Upsilon(4S)$ resonance (points), scaled data taken below $B\overline{B}$ threshold (histogram), with the fit to the signal and background function described in the text (curve); (b) the net contribution from the $B\overline{B}$ events, by taking the difference between the $\Upsilon(4S)$ data and the below $B\overline{B}$ threshold data, and the signal expected from the ARGUS branching fraction (dashed curve).

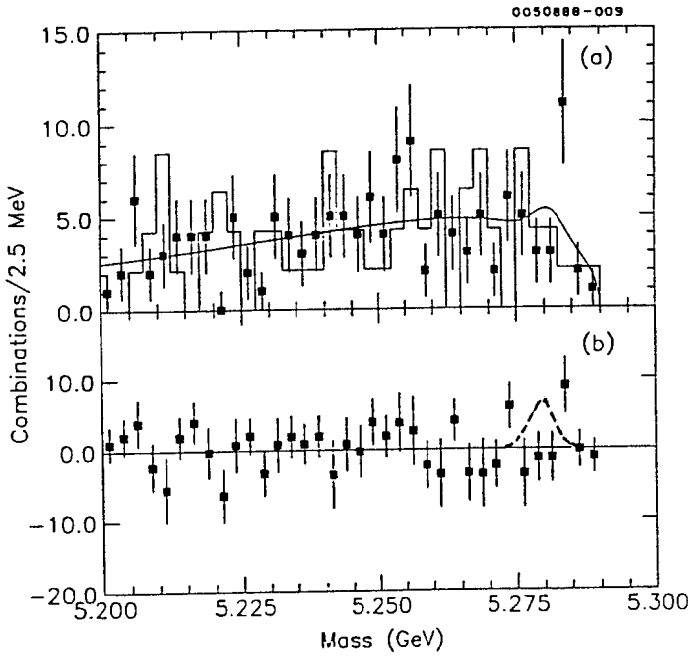

Figure 2.8 Distribution in reconstructed mass for $\overline{B}^0 \to p\bar{p}\pi^+\pi^-$ candidates from the collinear search (the ARGUS cut), using the '87 data sample: (a) data taken on the $\Upsilon(4S)$ resonance (points), scaled data taken below $B\overline{B}$ threshold (histogram), with the fit to the signal and background function described in the text (curve); (b) the net contribution from the $B\overline{B}$ events, by taking the difference between the $\Upsilon(4S)$ data and the below $B\overline{B}$ threshold data, and the signal expected from the ARGUS branching fraction (dashed curve).

Table 2.2

CLEO and ARGUS branching fractions.

	$B(B^- \to p\bar{p}\pi^-)$ (10^{-4})	$B(\overline{B}^0 \to p\bar{p}\pi^+\pi^-)$ (10^{-4})
CLEO '85 (90% C.L. upper limits)	< 4.5	< 5.6
CLEO '87 (90% C.L. upper limits)	< 1.4	< 3.3
CLEO '85 & '87 B.F.	0.4 ± 0.6	1.0 ± 1.3
CLEO '85 & '87 U.L.	< 1.4	< 2.9
ARGUS (ref. 8)	$5.2 \pm 1.4 \pm 1.9$	$6.0 \pm 2.0 \pm 2.2$
ARGUS (scaled)	$3.7 \pm 1.0 \pm 1.3$	$4.3 \pm 1.4 \pm 1.6$

In units of 10^{-4} for the $B^- \to p\bar{p}\pi^-$ and $\overline{B}^0 \to p\bar{p}\pi^+\pi^-$ modes with p and $\bar{p}$ almost collinear (the ARGUS cut). The branching fractions and 90% confidence level upper limits are calculated from a least squares fit of the mass distribution taken on the $\Upsilon(4S)$ to the ARGUS background model (see text) plus a Gaussian at the B meson mass. To compensate for different assumptions about the acceptance of the collinearity cut we have scaled the ARGUS results by a factor of 0.7 in making the comparison.

2.3. Discussions and conclusions

We have searched the charmless decays of B mesons, $B^- \to p\bar{p}\pi^-$ and $\overline{B}^0 \to p\bar{p}\pi^+\pi^-$ and set upper limits on the branching fractions of 1.4×10^{-4} and 2.9×10^{-4}, respectively. Our upper limits are below the scaled ARGUS result. We cannot tell why two results are inconsistent. The most significant differences in the CLEO and ARGUS analyses are probably in the momentum resolution of the detector (Table 1.2) and the size of the data sample (Table 1.1). In conclusion we see no evidence for the decays, $B^- \to p\bar{p}\pi^-$ and $\overline{B}^0 \to p\bar{p}\pi^+\pi^-$. Therefore our *lower* limit on V_{ub} is still zero.

3. Observation of $B^0 - \bar{B}^0$ Mixing

3.1. INTRODUCTION

With the discovery of K^0–$\overline{K}^0$ mixing[14] it was found that the particles with definite mass and lifetime (mass eigenstates) were not the K^0 and $\overline{K}^0$ mesons (flavor eigenstates) but linear combinations of them. This is due to flavor changing oscillations between K^0 and $\overline{K}^0$ which are allowed in the Standard Electroweak Model via the box diagrams illustrated in Figure 3.1.

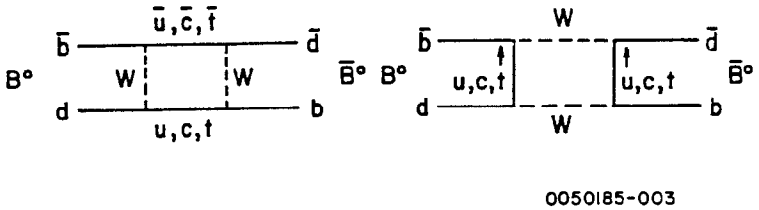

Figure 3.1 $B^0 - \overline{B}^0$ Mixing Diagrams.

A similar thing might happen in the case of the neutral B meson system. The strength of $B\overline{B}$ mixing is described by

$$x = \frac{\Delta M}{\Gamma},$$

with $2\Gamma = \Gamma_1 + \Gamma_2$ where ΔM is the difference between the two mass eigenstates, B_1 and B_2 and Γ_1 and Γ_2 denote their widths. The rate for a particle created as a B^0 meson to transform to a $\overline{B}^0$ meson before its decay divided by the rate that it decays as a B^0 meson is the "mixing parameter," r,

$$r = \frac{\Gamma(B^0 \to \overline{B}^0 \to X)}{\Gamma(B^0 \to X')}.$$

If $\Delta\Gamma << \Gamma$ can be assumed[15] one then has

$$r = \frac{x^2}{2 + x^2}.$$

In the $\Upsilon(4S)$ decay into B mesons, one does not know which type of B meson one starts with, *i.e.*, B^0 or $\overline{B}^0$, so r cannot be measured directly. Instead we can measure

$$y = \frac{N(B^0 B^0) + N(\overline{B}^0 \overline{B}^0)}{N(B^0 \overline{B}^0)},$$

which is the number of *events* that mixed divided by the number that did not. Because we are examining the decay products from $e^+e^- \to \Upsilon(4S) \to B^0\overline{B}^0$, one has to include effects due to Bose-Einstein statistics when calculating y. The $B^0\overline{B}^0$ pair is produced in a p-wave state (ℓ=1). Since two identical bosons must always have a completely symmetric wavefunction, it is not possible to have a B^0B^0 or $\overline{B}^0\overline{B}^0$ state unless one of the mesons has decayed already. Thus one finds

$$y_{(\ell=1)} = r.$$

So far experiments have searched for semileptonic B meson decays where the lepton emerges with the "wrong" charge :

$$r = \frac{\Gamma(B^0 \to \ell^- X)}{\Gamma(B^0 \to \ell^+ X)},$$

and therefore

$$y = \frac{N(\ell^+\ell^+) + N(\ell^-\ell^-)}{N(\ell^+\ell^-)},$$

in the $\Upsilon(4S)$ decaying into $B^0\overline{B}^0$ events or in $b\bar{b}$ events at higher energies. The charge of the lepton in semileptonic decay (See Figure 3.2) is the most useful for tagging the flavor of B meson because (a) it is efficient (our efficiency is about 6% for both e and μ, 1% for D^{*+} tag) and (b) the probability of tagging the wrong flavor B meson due to other sources of leptons from B meson decay can be reduced by imposing a minimum cut on lepton momentum as described in later sections.

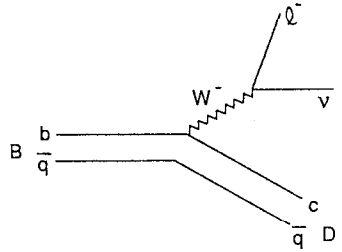

Figure 3.2 Diagram for semileptonic decay of B meson.

3.2. Previous measurements of $B\overline{B}$ mixing

So far a 90% confidence level upper limit of $r < 0.24$ was published by CLEO[2] in 1987, based on 120 pb^{-1} of data collected on the $\Upsilon(4S)$ in 1982 and 1985. A measurement of r was published by the ARGUS collaboration[16] in 1987. Their result, $r = 0.21 \pm 0.08$, is consistent with CLEO's upper limit. Other measurements of and upper limits on r at higher energies have been made by the MARK II,[17] MAC,[18] and UA1[19] collaborations.

3.3. Data analysis

Sources of leptons. The main sources of leptons from B meson decay are,

a) the semileptonic decay of the B meson;

b) the cascade decay of the B meson to a $\overline{D}$ meson, followed by the semileptonic decay of the $\overline{D}$ meson.

Figure 3.3 shows the measured muon and electron momentum spectra. The solid histogram is a fit to the electron spectrum using the Altarelli model[20] for $B \to \ell^+ \nu_\ell X_c$, and the DELCO spectrum[21] for $D \to \ell^+ \nu_\ell X$, folded with the D meson momentum spectrum from B meson decays measured by CLEO.[4] This determines the branching fraction $B(B \to \ell^+ \nu_\ell X)$ and the product branching fraction $B(B \to DX) \times B(D \to \ell^+ \nu_\ell Y)$. From this fit we find

$$B(B \to DX) \times B(D \to \ell^+ \nu_\ell Y) = 0.118 \pm 0.007 \pm 0.015.$$

Combining this fit with an independent fit to the muon spectrum, we obtain a preliminary value for the semileptonic branching fraction,

$$B(B \to \ell^+ \nu_\ell X) = 0.100 \pm 0.002 \pm 0.012,$$

which can be compared with the value $0.110 \pm 0.003 \pm 0.005$ obtained from the '85 run.[5] The systematic error, 0.012, is larger than that for the 1985 result, because we have not yet made a detailed investigation of the lepton detection efficiencies.

Other sources of leptons from B meson decay are:

c) the decay $B \to \psi X$, $\psi \to \ell^+ \ell^-$;

d) $B \to \tau^+ \nu_\tau X$, $\tau^+ \to \ell^+ \nu_\ell X$.

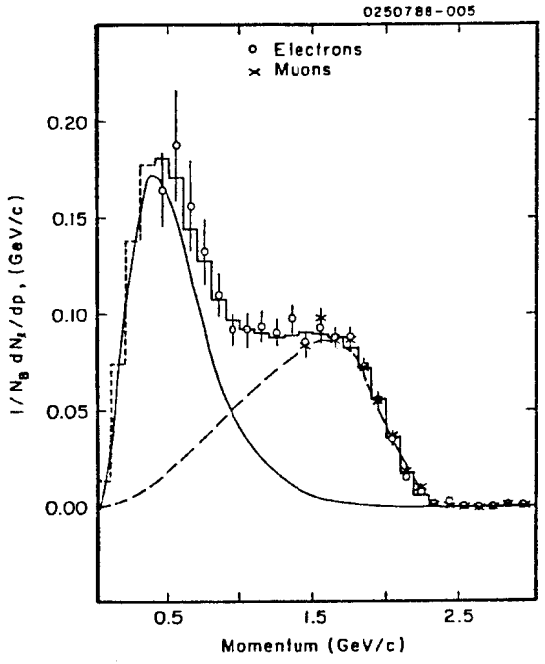

Figure 3.3 Lepton momentum spectrum from B meson decay. The momentum spectrum of lepton is shown as data points for electrons (circle) and muons (cross). The data have been corrected for misidentification of hadrons, acceptance and efficiency, and the contribution from the $e^+e^- \to q\bar{q}$ continuum. The solid histogram is a fit to this spectrum as described in the text. Contributions from the primary leptons, $B \to \ell^+ \nu_\ell X_c$ (dashed curve) and cascade leptons, $B \to \overline{D} \to \ell^- \overline{\nu}_\ell X$ (solid curve) are shown separately.

Since the product branching fraction[10] for the process c),

$$B(B\to\psi X)\times B(\psi\to\ell^+\ell^-) = (0.86\pm 0.07\pm 0.16)\%\times(6.9\pm 0.9)\%,$$

is small compared to the processes a) and b) it does not produce a significant *single* lepton background, and it can be eliminated from dilepton events by using a ψ mass cut which will be described later. We estimate the contribution from the process d) to be $(0.6\pm 0.4)\%$ but it has a much softer lepton momentum spectrum and can be eliminated by the minimum lepton momentum cut.

Minimum lepton momentum cut. To reduce the cascade contribution, we require the lepton momentum to be greater than 1.4 GeV/c. From the fit mentioned above we estimate that the cascade lepton contribution is about 3% above 1.4 GeV/c. Variations of the value of this cut produce similar final results. The single lepton yields are shown in Table 3.1.

Table 3.1

Single lepton yield for momentum between 1.4 and 2.4 GeV/c.

	On the $\Upsilon(4S)$	below $B\overline{B}$ threshold	net $B\overline{B}$
# of Hadronic events	764,309	259,781	222,666*
# of Electron candidates	21,110	2,694	15,493
# of Tracks into electron fiducial	380,280	143,593	80,889
# of Fake corrected Electrons	19,537	2,102	15,154
# of Muon candidates	13,755	2,045	9,491
# of Tracks into Muon fiducial	378,304	145,328	75,004
# of Fake corrected Muons	10,960	903	9,076

* We use a slightly different hadronic event selection criteria from the charmless B decay analysis.

Background from continuum e^+e^- annihilation. Leptons produced in the continuum events are mostly due to $c\bar{c}$ production, followed by the semileptonic decay of the c quark (D meson). Since the lepton spectrum from B meson decay ends around 2.4 GeV/c, we use a maximum momentum cut of 2.4 GeV/c to eliminate continuum leptons that cannot come from B meson decays. We estimate the contribution from the continuum background between the momentum cuts using the data taken below $B\overline{B}$ threshold.

Fake leptons. Fake leptons are non-electron (muon) tracks which project into electron (muon) fiducial volume and are identified as electrons (muons). We calculate the fake probability per track from data taken at the $\Upsilon(1S)$ resonance because hadronic decays of the $\Upsilon(1S)$ ($\Upsilon(1S)\to ggg$) are expected to contain no leptons. The fake probability is checked by using pions (protons) from kinematically reconstructed $K^0_S(\Lambda)$ decays.

Topological cut for dilepton events. To suppress continuum background dilepton events (See Figure 3.4) we require the angle Ω, between two leptons must satisfy

$$-0.8 < cos\,\Omega < 0.9.$$

This cut also removes converted photons.

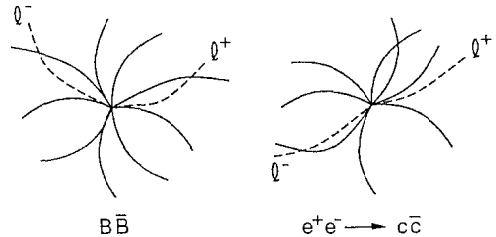

Figure 3.4 Dileptons in $B\overline{B}$ events and $e^+e^-\to c\bar{c}$ events.

ψ mass cut. To reject leptons from $B\to\psi X$, $\psi\to\ell^+\ell^-$, a lepton candidate is not used if it has an invariant mass between 3.06 and 3.14 GeV with any other opposite-sign track in the event, unless the other track is definitively identified as non-leptonic.

Fake dilepton events. Fake dilepton events consist mainly of one real lepton and one hadron that has been misidentified as an electron or muon. To estimate the number of fake dilepton events, we count the number of tracks that satisfy all kinematic cuts in the sample of single lepton events and weigh by the fake probability per track.

Cascades in the dilepton events. Cascade dilepton events mainly consist of one lepton from B meson decay and the second from the cascade decay of a D meson. The cascade like-sign dileptons are from $B\to\ell^+\nu_\ell X$ and $\overline{B}\to D$, $D\to\ell^+\nu_\ell Y$. In this case the directions of the two leptons are uncorrelated. The cascade opposite-sign dileptons are mostly from $B\to\overline{D}\ell^+\nu_\ell X$, $\overline{D}\to\ell^-\overline{\nu}_\ell Y$. Due to the decay kinematics and the requirement that leptons have high momenta, the two leptons tend to be back to back. This type of cascade dilepton events can be eliminated by the angle cut mentioned before. Furthermore if there is

$B^0\overline{B}^0$ mixing, another kind of opposite-sign cascade dilepton events ($B^0 \to \ell^+ \nu_\ell X$ and $\overline{B}^0 \to B^0 \to \overline{D}$, $\overline{D} \to \ell^- \overline{\nu}_\ell Y$) must be taken into account. Cascade backgrounds are calculated from the momentum spectra of D^0 and D^+ mesons from B meson decays folded by the lepton momentum spectrum in the semileptonic decay of D mesons. There are, however, significant uncertainties in the shape of the high momentum end of these spectra, affecting the number of cascade leptons having momentum above 1.4 GeV/c. We have obtained a relative error of 30% in the calculated cascade background due to these uncertainties.

Observed dilepton events. The number of dilepton events found and our estimates of the various backgrounds are given in Table 3.2. As we have discussed, the major background sources are fakes and cascades. The "Signal" row in Table 3.2 is calculated by subtracting the "non-continuum" background and below $B\overline{B}$ threshold events which have already been scaled by luminosity and $1/s$. All the like-sign events in the below $B\overline{B}$ threshold data are explained as fakes as we do not expect like-sign dilepton events from the continuum e^+e^- annihilation process. Therefore, we did not subtract them. However, the error in the signal reflects the statistical uncertainty of this contribution. After subtracting all backgrounds, the "Signal" row gives the numbers of dilepton events in which the two B mesons decayed semileptonically.

3.4. Mixing parameter r

From the net signal given in the "Signal" row (i) of Table 3.2 the mixing parameter r can be calculated. Since opposite-sign dileptons can be obtained from the B^+B^- events as well as $B^0\overline{B}^0$ events, the formula for r in terms of the number of observed dilepton events is non-trivial. The mixing parameter r is

$$r = \frac{N(B^0B^0) + N(\overline{B}^0\overline{B}^0)}{N(B^0\overline{B}^0)} = \frac{N(\ell^\pm\ell^\pm)}{N(\ell^+\ell^-) - N(B^+B^- \to \ell^+\ell^-)},$$

where $N(\ell^\pm\ell^\pm)$and $N(\ell^+\ell^-)$ are the number of various dilepton events from semileptonic decays of both B and $\overline{B}$. "Signal" and $N(B^+B^- \to \ell^+\ell^-)$ is the number of dilepton events from B^+B^- semileptonic decays. The fraction of dilepton events from B^+B^- decays is

$$f = \frac{(b_\pm)^2 f_{+-}}{(b_\pm)^2 f_{+-} + (b_0)^2 f_{00}},$$

where f_{+-} and f_{00} are the fraction of charged and neutral $B\overline{B}$ events produced from $\Upsilon(4S)$ decays, respectively, and $b_\pm$ and b_0 are the charged and neutral B meson semileptonic branching fractions, respectively. The contribution from the

Table 3.2

Unlike-sign and like-sign dilepton rates.

Dilepton types	e^+e^-	$\mu^+\mu^-$	$e^\pm\mu^\mp$	$e^\pm e^\pm$	$\mu^\pm\mu^\pm$	$e^\pm\mu^\pm$
Observed Events						
a) On the 4S	186	66	223	28	6	39
b) Below $B\overline{B}$ threshold	4	2	0	1	1	0
Calculated bkgrnds						
c) $\Upsilon(4S)$ Fakes	9.4±2.7	6.3±2.1	17.2±5.2	3.8±1.1	2.2±0.7	6.7±2.0
d) Cascades	2.0±0.8	0.5±0.2	1.9±0.8	11.6±3.2	2.8±0.8	11.4±3.2
e) ψ+Primary	0.7±0.3	0.3±0.2	1.0±0.5	0.7±0.3	0.3±0.2	1.0 ±0.5
f) Continuum fakes	0.9±0.3	0.8±0.3	1.8±0.6	0.4±0.2	0.5±0.2	0.8 ±0.3
g) $\Upsilon(4S)$ bkgrnd	12.1±2.8	7.1±2.1	20.1±5.3	16.1±3.4	5.3±1.1	19.1±3.8
h) Continuum bkgrnd	6.5±4.2	2.4±3.0	- 3.7±1.3	1.2±1.2	0.0±1.1	-1.6±0.6
i) Signal	167±15	57±9	207±16	11.9±5.3	0.7± 2.5	19.9 ±6.2
Systematic error				±3.6	±1.6	±3.8

The total background on the $\Upsilon(4S)$ g), is calculated by summing items c), d), and e). The below $B\overline{B}$ threshold background, h), is calculated by subtracting the continuum fakes, f), from the continuum events, b), and scaling to compensate for the luminosity. The signal, i), represents the net $B\overline{B}$ contribution. For the opposite-sign dilepton events, this is calculated by subtracting items, g) and h) from the observed events, a). For the like-sign dilepton events, the continuum background is not subtracted because it is statistically equal to zero.

$N(B^+B^-\to\ell^+\ell^-)$ can be calculated from the *total* number of observed dileptons by

$$N(B^+B^-\to\ell^+\ell^-) = f \times (N(\ell^\pm\ell^\pm) + N(\ell^+\ell^-)).$$

Therefore the mixing parameter

$$r = \frac{N(\ell^\pm\ell^\pm)}{(1-f)N(\ell^+\ell^-) - fN(\ell^\pm\ell^\pm)},$$

using this dilepton technique, depends on $b_0/b_\pm$ and f_{00}/f_{+-}, which are not well known. Currently, the restrictions on these are approximately (0.5 – 2.0) and (0.66 – 1.0), respectively.[2] For comparison with the ARGUS results,[16] we will use the same ratios which yield f = 0.55.

Since the detection efficiencies for ee, $\mu\mu$, and $e\mu$ events are not identical, we calculate r separately for each set of combinations and average them. The results are

$$r_{ee} = 0.167 \pm 0.085 \pm 0.056,$$
$$r_{\mu\mu} = 0.027 \pm 0.098 \pm 0.062,$$
$$r_{e\mu} = 0.242 \pm 0.088 \pm 0.051.$$

We calculate a weighted average of these three values,

$$r = w_{ee}r_{ee} + w_{\mu\mu}r_{\mu\mu} + w_{e\mu}r_{e\mu}$$

where the weights, $w_{ee}, w_{\mu\mu}$ and $w_{e\mu}$, respectively 0.38, 0.15, and 0.47, are proportional to the expected number of dileptons. The expected number of dileptons are calculated from the products of the single lepton yields

$$w_{ee} : w_{\mu\mu} : w_{e\mu} = \sigma_e\sigma_e : \sigma_\mu\sigma_m u : 2 \times \sigma_e\sigma_\mu$$
$$= (15,154)^2 : (9,076)^2 : 2 \times (15,154)(9,076)$$

where 15,154 and 9,076 are the number of electrons and muons in the momentum range between 1.4 and 2.4 GeV/c (Table 3.1). We obtain

$$r = 0.182 \pm 0.055 \pm 0.056,$$

for this weighted average. The weighted statistical errors have been combined in quadrature and the systematic errors have been combined linearly.

3.5. Discussions and conclusions

Understanding the background subtraction to the like-sign dileptons is critical to knowing that we are observing B^0– $\overline{B}^0$ mixing. In particular, the calculation of the cascade contribution is not easy to confirm. In an attempt to minimize the background effects, we have looked for dilepton events with identified charged kaons and reconstructed D^{*+}'s. If the like-sign dilepton events were all coming from $\overline{B}^0\overline{B}^0$ (or B^0B^0) semileptonic decays, we would expect DD (or $\overline{DD}$) mesons (resulting in an excess of D^{*+}(or D^{*-}) and an excess of K^- (or K^+). Although I will not discuss these methods in detail we have seen excesses consistent with B^0– $\overline{B}^0$ mixing of $r = 0.182$.

In conclusion, we have observed B^0– $\overline{B}^0$ mixing. Our result is consistent with that published by ARGUS[16] and our previous upper limit.[2] These observations of B^0– $\overline{B}^0$ mixing are the first evidence for the existence of flavor changing oscillations beyond $K^0\overline{K}^0$ system. Our measurement of r translates into

$$x = \frac{\Delta M}{\Gamma} = 0.66 \pm 0.13 \pm 0.13.$$

This oust a constraint on the parameters in the relation among the CKM matrix elements, V_{cb}, V_{tb}, and V_{td} as well as the B meson structure parameters, the QCD correction parameter, and quark masses m_t, m_b, and the W boson mass, M_W.[22]

REFERENCES

1. D. Andrews *et al.*, (CLEO), *Nucl. Instrum. Meth.* **211,** 747 (1983).
2. The results based on the previously collected data sample has been published. A. Bean *et al.*, *Phys. Rev. Lett.* **58,** 183 (1987).
3. H. Albrecht *et al.*, (ARGUS), *Phys. Lett.* **134B,** 137 (1984).
4. D. Bortoletto *et al.*, (CLEO), *Phys. Rev. D* **35,** 19 (1987).
5. S. Behrends *et al.*, (CLEO), *Phys. Rev. Lett.* **59,** 407 (1987).
6. C. Bebek *et al.*, (CLEO), *Phys. Rev. D* **36,** 1289 (1987).
7. P. Avery *et al.*, (CLEO), *Phys. Lett.* **B183,** 429 (197).
8. H. Albrecht *et al.*, (ARGUS), "Observation of Charmless B Meson Decays," DESY preprint 88-056.
9. Precisely speaking, the resolution is dominated by half the resolution of the $\Upsilon(4S)$ mass, which is $\sqrt{2}$ times the resolution of the energy of the single beam (beam energy spread).
10. C. Bebek *et al.*, (CLEO), "The Decay of B Mesons to ψ," submitted to XXXIV International Conference on High Energy Physics at Munich, 1988.
11. P. Baringer *et al.*, (CLEO), "Limits on Rare Exclusive Decays of B Mesons," submitted to XXXIV International Conference on High Energy Physics at Munich, 1988.
12. H. Albrecht *et al.*, *Phys. Lett.* **199B,** 541 (1987).
13. M.S. Alam *et al.*, *Phys.* Rev. Lett. **51,** 1143 (1983).
14. A. Pais and O. Piccioni, *Phys.* Rev. **100,** 1487 (1955).
15. V. Khoze *et al.*, *Yad. Fiz.* **46,** 181 (1987).
16. H. Albrecht *et al.*, (ARGUS), *Phys. Lett.* **192B,** 245 (1987).
17. T. Schaad *et al.*, (MARK II), *Phys. Lett.* **160B,** 188 (1985).
18. H. Band *et al.*, (MAC), Phys. Lett. **200,** 221 (1988).
19. C. Albajar (UA1), *et al.*, *Phys. Lett.* **186B,** 247 (1987).
20. G. Altarelli, *et al.*, *Nucl. Phys.* **B208,** 365 (1982).
21. W. Bacino *et al.*, *Phys Rev. Lett.* **43,** 1073 (1979).
22. J. S. Hagelin, *Phys. Rev.* **D20,** 2893 (1979).

B Decay Studies from ARGUS

David B. MacFarlane
McGill University
Montreal, Quebec

(representing the ARGUS collaboration*)

Abstract. Recent results on B decays are reported from the ARGUS experiment, operating in the e^+e^- storage ring DORIS II at DESY. Studies of Λ-lepton charge correlations lead to interesting conclusions about baryon production in B decays. Evidence from the reconstruction of B mesons in the channels $D\pi\pi$ points to the dominance of $D\rho$ modes. Searches have been made for one-loop weak decay processes with a radiative photon or gluon. The rates for such "Penguin" diagrams are sensitive to the top quark mass and experimental limits are approaching a level which limits extensions of standard model physics. The endpoint region of the semileptonic spectrum in B decays has long been used to place limits on the ratio of KM matrix elements $|V_{ub}/V_{cb}|$. The theoretical foundations for this work has been put on a sounder footing by the ARGUS determination of the polarization of the D^* in the dominant semileptonic decay $\overline{B} \to D^*\ell\nu$. A search for the corresponding $b \to u$ transition, $\overline{B} \to \rho\ell\nu$, is reported. Finally, the current status of the ARGUS study of the charmless B decays to $p\overline{p}\pi(\pi)$ is presented, now made controversial with the non-observation of the same modes by CLEO.

A selection of recent results from ARGUS in the field of B physics are presented. These studies were made using a data sample containing 96,000 $\Upsilon(4S)$ decays obtained in running at the DORIS II e^+e^- storage ring at DESY between 1982 and 1986. Approximately 42 pb^{-1} of data taken at centre-of-mass energies in the continuum below the open beauty threshold were also available. ARGUS is a general purpose 4π detector with an 8 kΓ solenoidal magnetic field. The experiment has an excellent capability for charged particle detection, and includes a electromagnetic calorimeter with good granularity and reasonable resolution. As such, the experiment has been optimized for B studies on the $\Upsilon(4S)$. Details concerning the detector and some of the analysis techniques which have been developed are available in Reference [1].

1 Lambda-lepton charge correlations

Inclusive rates for proton and Λ production in B decays have already been shown to be sizable [2,3]. However, the mechanism for baryon production is not yet understood. The dominant $b\to c$ weak decay mode must occasionally result in a charmed baryon in the final state. ARGUS has presented direct evidence for Λ_C production in B meson decays [4]. Picturing the decay process as shown in Figure 1, it is expected that stable baryons are either the decay products of the charmed baryon, or arise from hadronization processes including the spectator quark, which conserve baryon number. The small difference in the proton and Λ inclusive rates indicates that Λ production in B decays is not dominated by the hadronization process. This is consistent with the expectation that strange baryon production is suppressed relative to nonstrange, since the former requires an $s\bar{s}$ pair from the vacuum.

Additional information about the source of stable baryons can be obtained through the study of Λ-ℓ charge correlations. In B decays the sign of Λ_C baryon, as well as the sign of the primary lepton produced by semileptonic decays, identifies whether the decaying meson was a B or $\overline{B}$. A charmed baryon and a high momentum primary lepton observed in the same $\Upsilon(4S)\to B\overline{B}$ event must originate from the decays of different B mesons, because of energy conservation. Therefore there exists a strong charge correlation between a primary lepton and a Λ baryon resulting from the charmed baryon decay; one should

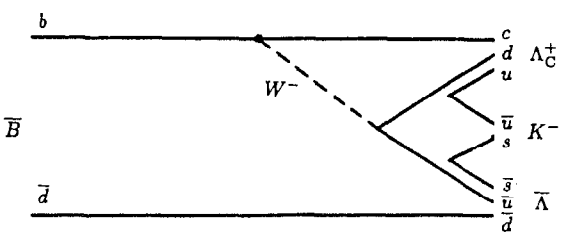

Figure 1. Diagram for baryon production in B decays.

observe only $\Lambda\ell^+$ pairs. In contrast, the hadronization process contributes to $\Lambda\ell^-$ combinations. The $B\overline{B}$ mixing reverses the sign correlation between the primary lepton and a Λ baryon from a charmed baryon decay, thus also resulting in the production of $\Lambda\ell^-$ pairs. Therefore, the study of Λ-ℓ charge correlations could provide additional information on $B\overline{B}$ mixing.

The identification of electrons and muons, as well as the reconstruction of Λ baryons, is performed in the ARGUS detector with high efficiency and low misidentification probability [5-7]. For lepton identification, information from all detector components is used coherently by combining the measurements into an overall likelihood $\mathcal{L}$ [6,7]. The available information consists of specific ionization (dE/dx) and time-of-flight (TOF) measurements, and the magnitude and topology of energy depositions in the shower counters. For muons a hit in an outer muon chamber is required, and information on the hit-impact point distance is used.

The basic strategy for event selection was to suppress continuum Λ-ℓ sources, keeping high acceptance for the decays of $B\overline{B}$ pairs. First, cuts on the second Fox-Wolfram moment [8], H_2, and the total multiplicity of the event were applied:

- $H_2 \leq 0.5$
- $n_{tot} = n_{ch} + \frac{1}{2}n_\gamma \geq 5.5$, where n_{ch} is the charged multiplicity and n_γ is the number of photons with an energy of greater than 80 MeV in the shower counters.

Exactly one particle in the event had to be well identified as a lepton, with $\mathcal{L} \geq 80\%$. The momentum of this lepton was then required to be between 1.5 GeV/c and 2.8 GeV/c. Such a cut suppresses almost all secondary leptons originating from the decays of charmed mesons produced in B meson decays. Electrons originating from photon conversion were suppressed by requiring that the invariant mass of the fast electron and any other positron candidate be greater than 100 MeV/c^2.

The Λ candidates were selected by a soft cut on the χ^2 for the fit of $p\pi^-$ combinations to secondary vertices. Proton and pion hypotheses for charged tracks were accepted if the likelihood ratio constructed from the combined dE/dx and TOF measurements exceeded 1%. Vertices consistent with a K^0_S or a photon conversion were excluded. The Λ baryons can be produced by kaon interactions in the inner detector material ($\overline{\Lambda}$ baryons are not produced in such reactions). However, in this case the flight direction of the Λ and the vector $\vec{r}$ connecting the main to the secondary vertex do not necessarily coincide. In B decays the fraction of Λ baryons produced in these reactions is increased due to the enhanced kaon yield. In order to suppress this source of background, we applied a cut on the angle, $\theta(\vec{p}_\Lambda, \vec{r})$, between the Λ momentum vector and $\vec{r}$, requiring $\cos\theta(\vec{p}_\Lambda, \vec{r}) \geq 0.95$. Since the kinematical bound in B decays for the momentum of the Λ is 2.7 GeV/c, the Λ candidates were required to have momenta below this value.

In continuum events, or where the Λ is produced by kaon interactions, the lepton and Λ tend to travel in opposite directions. On the $\Upsilon(4S)$, a lepton and Λ produced in the decay of different B mesons exhibit no such correlation. The distribution of the opening angle, $\theta_{\ell-\Lambda}$, between the momentum vector of the lepton and of the Λ are shown in Figure 2*a* and 2*b*, for $\Upsilon(4S)$ and continuum events respectively. On the basis of these observations, further suppression of the contribution from continuum events and charge-exchange interactions was accomplished by requiring $\cos\theta_{\ell\Lambda} \geq -0.7$. This cut was applied for both $\Lambda\ell^+$ and $\Lambda\ell^-$ combinations in order to maintain the same selection efficiencies.

Figure 3 shows, for both $\Upsilon(4S)$ and continuum data, the $p\pi^-$ invariant mass spectrum for the remaining events containing $\Lambda\ell^+$ and $\Lambda\ell^-$ pairs. After subtraction of the continuum data, scaled by a factor of 2.5 to account for the ratio of luminosities, clear signals remain for both Λl^+ and Λl^- events from $\Upsilon(4S)$ decays. There are 39.3 Λl^+ and 26.1 Λl^- events with $p\pi^-$ invariant masses within ± 3.5 MeV/c^2, or approximately ± 2 standard deviations, of the nominal Λ mass. The remaining background to the Λ signal was estimated by studying the $p\pi^-$ mass distribution outside the signal region. If the average background level within ± 3.5 MeV/c^2 of the Λ mass is assumed to be equal to the level in the sideband intervals from 1.090 to 1.110 GeV/c^2 and from 1.120 to 1.140 GeV/c^2, estimates of 2.4 and 1.4 background events in the Λ region are obtained for $\Lambda\ell^+$ and $\Lambda\ell^-$ combinations respectively.

The $\Lambda\ell$ events also include contributions from backgrounds due to lepton-hadron misidentification, secondary leptons from charm decays, J/ψ decays, asymmetrical photon conversion, and Λ baryons produced in charge-exchange

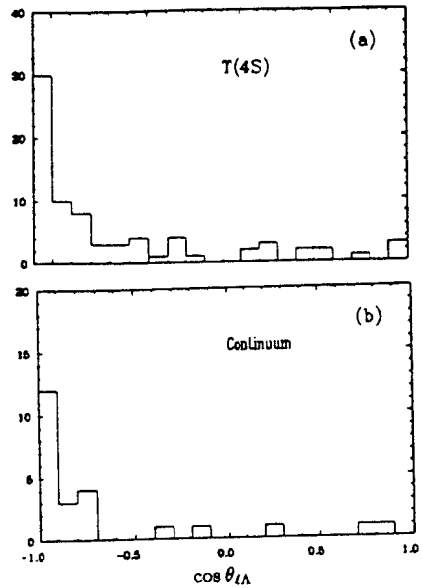

Figure 2. Distribution of the opening angle between the Λ and ℓ^- for (a) the $\Upsilon(4S)$ and (b) the continuum data samples.

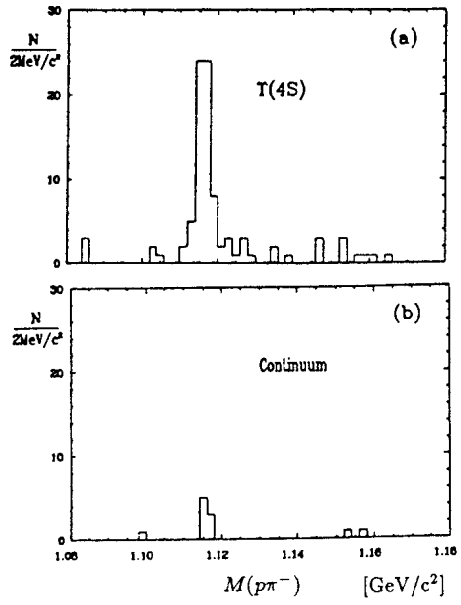

Figure 3. Distribution of $p\pi^-$ invariant mass for $\Lambda\ell^+$ events in (a) the $\Upsilon(4S)$ and (b) the continuum data samples.

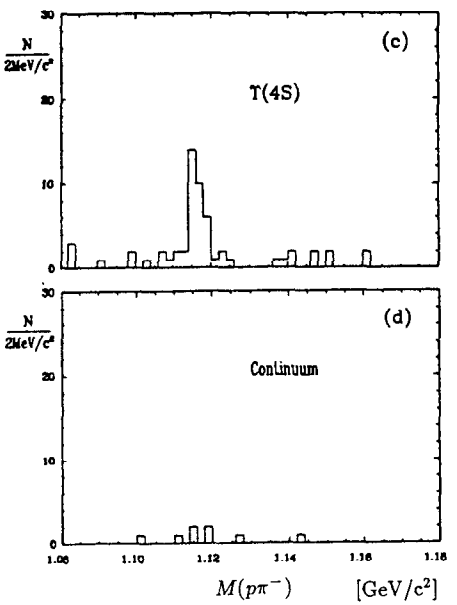

Figure 3. The corresponding distributions for $\Lambda\ell^-$ events in (c) the $\Upsilon(4S)$ and (d) the continuum data samples.

reactions in the inner detector material.

The background due to lepton-hadron misidentification was extracted directly from the data by folding the known lepton-hadron misidentification probabilities [9] with the observed hadron momentum spectrum in events with Λ-hadron pairs. Since the fake rates per track coincide, within errors, for pions and kaons, it was not necessary to account for their relative fractions. The background due to secondary leptons, J/ψ decays and converted photons were determined by Monte Carlo simulation of B decays. A spectator model [10] was used to describe the decay of the b quark, with the final state hadrons produced using the Lund string fragmentation model [11]. The fraction of Λ baryons produced in charge-exchange reactions was estimated from the difference in the numbers of Λ and $\overline{\Lambda}$ baryons in $\Upsilon(4S)$ decays, taking into account the approximately 5% larger absorbtion of $\overline{\Lambda}$ baryons in the inner detector material.

Table 1. Rates for $\Lambda\ell$ events.

	$\Lambda\ell^+$ events	$\Lambda\ell^-$ events
$\Upsilon(4S)$	59	31
Continuum	8×2.45	2×2.45
Backgrounds		
Fake leptons	0.9	0.4
Conversions	0.2	0.2
Secondary decays	0.3	0.3
$J\psi$ decays	0.2	0.2
$\overline{K} \to \Lambda$ interactions	2.6	1.0
Λ sidebands	2.4	1.4
Total	32.7 ± 9.9	22.6 ± 7.3

The results are summarized in Table 1. After subtraction of the continuum contribution and backgrounds, there remains a signal of 32.7 ± 9.9 and 22.6 ± 7.3 $\Lambda\ell^+$ and $\Lambda\ell^-$ events respectively. The distribution of the opening angle between the lepton and the Λ for these events is consistent with being flat, in agreement with the expectation for particles produced in the decays of different B mesons.

As an independent check, the total number of $\Lambda\ell$ events was estimated from the inclusive Λ and inclusive lepton branching ratios. Taking into account the efficiency of event selection and the efficiencies of Λ and lepton identification, the calculated number of $\Lambda\ell$ events is 53 ± 13. This is in agreement with the sum of 55 ± 12 events obtained for $\Lambda\ell^+$ and $\Lambda\ell^-$ pairs. To check the stability of the result, the lepton momentum cut was varied between 1.4 and 1.6 GeV/c. Within statistical errors, the ratio of $\Lambda\ell^+$ to $\Lambda\ell^-$ events did not change.

In contrast to the observation of a strong $\Lambda\ell$ charged correlation reported by CLEO [2], we observe comparable numbers of $\Lambda\ell^+$ and $\Lambda\ell^-$ events. There are several mechanisms for the production of $\Lambda\ell^+$ and $\Lambda\ell^-$ pairs:

1. The Λ baryons from the decay of charmed baryons can only be accompanied by a positively charged primary lepton. $B\overline{B}$ mixing manifests itself in the production of $\Lambda\ell^-$ pairs.
2. Spectator hadronization processes would lead to the production of $\Lambda\ell^-$ events.
3. Baryon anti-baryon pairs produced along with the charmed meson would lead to the production of $\Lambda\ell^-$ and $\Lambda\ell^+$ events.
4. Cabibbo-suppressed decays contribute to the production of $\Lambda\ell^-$ pairs.
5. The penguin diagram, $b\to s$, results in the production of $\Lambda\ell^+$ pairs.
6. Λ baryons produced in $b\to u$ transitions can be accompanied by both positively and negatively charged leptons. The rate for such processes is expected to be negligible.

In principle, all these processes can contribute to baryon production in B decays. If it is assumed that the main sources are mechanisms (1) and (2), the fraction of Λ baryons produced by mechanism (2) can be determined. Subtracting the contribution to the $\Lambda\ell^-$ sample due to $B\overline{B}$ mixing [9], this fraction is $38 \pm 19\%$ of all Λ baryons. One can also express this as:

$$\frac{\mathrm{Br}(B\to\Lambda_C\Lambda X)}{\mathrm{Br}(B\to\Lambda_C X)\cdot\mathrm{Br}(\Lambda_C\to\Lambda X)} = 0.69 \pm 0.31$$

which is the ratio of $\Lambda\ell^-$ to $\Lambda\ell^+$ after correction for $B\overline{B}$ mixing. Contributions from mechanisms (3), (4) or (6) would decrease this value. Thus there seems to be substantial Λ production from hadronization processes. The result is also consistent with the observed level of $B\overline{B}$ mixing, but the large hadronization contribution to $\Lambda\ell^-$ events will not allow a quantitative statement to be made.

2 Reconstruction of $B\to D\pi\pi$

While D mesons are a dominant decay product of B decays, the soft inclusive momentum spectrum [3,12] and the high multiplicity of final state particles [12], suggest that B decay rates to resonant two-body low invariant mass states are rather small. Since large combinatorial backgrounds are encountered in the reconstruction of high multiplicity decays, only a small fraction of hadronic B decay modes have so far been reconstructed [13-16]. Fortunately, the modes most favorable for reconstruction are also of importance for testing theoretical models for weak decays.

ARGUS has already presented the results on the reconstruction of B decays to a D^{*+} and up to three pions [13]. These studies have now been extended to the following additional channels:

$$\begin{aligned} B^- &\to D^0\pi^- & \overline{B}^0 &\to D^+\pi^- \\ B^- &\to D^0\pi^-\pi^0 & \overline{B}^0 &\to D^+\pi^-\pi^0. \end{aligned}$$

The π^0's were reconstructed by detecting both photons from the decay $\pi^0\to\gamma\gamma$; each photon was required to have an energy $E_{sh} > 50$ MeV contained in two or more adjacent shower counters [17]. The D mesons were reconstructed from the following decays:

$$\begin{aligned} D^0 &\to K^-\pi^+ & D^+ &\to K^0_S\pi^+ \\ D^0 &\to K^0_S\pi^+\pi^- & D^+ &\to K^-\pi^+\pi^+ \\ D^0 &\to K^-\pi^+\pi^-\pi^+ & D^+ &\to K^0_S\pi^+\pi^-\pi^+ \end{aligned}$$

which account for 16.5% of D^0 decays and 14.0% of D^+ decays [18]. Combinatorial background was reduced by a cut on the angle θ_K between the K and the D flight direction in the D rest frame, namely $\cos\theta_K < 0.8$. The K^0_S's were reconstructed from the decay $K^0_S\to\pi^+\pi^-$ in which a distinct secondary vertex was resolved. Mass constraint fits were performed on each intermediate state in the B decay chain in order to improve the B mass resolution.

The selection criteria for B candidates were then as follows:

- The angle α_{thrust} between the thrust axes of the B candidate and the remainder of the event was required to satisfy

  $$|\cos\alpha_{thrust}| < 0.8 \text{ for } D\pi \qquad \text{and} \qquad |\cos\alpha_{thrust}| < 0.7 \text{ for } D\pi\pi.$$

  This cut removes a large part of the background from two-jet continuum events, which peak sharply at $\cos\alpha_{thrust} = \pm 1$. In contrast, since B mesons from $\Upsilon(4S)$ decays are produced nearly at rest in the lab, their decay products are essentially uncorrelated, and yield an isotropic distribution.

- The energy E_{meas} of each $D\pi$ or $D\pi\pi$ combination was required to satisfy $|E_{meas} - E_{beam}| \leq 2\sigma_E$, where σ_E is the energy measurement resolution.* This cut is applicable on the $\Upsilon(4S)$, where the beam energy E_{beam} is also the energy of the B meson, or one-half the measured $\Upsilon(4S)$ mass of 10580 MeV [15]. An energy constraint fit was then applied, resulting in a B mass resolution, determined largely by the DORIS beam spread, of approximately 4 MeV/c^2.

- The total probability for the sum of all χ^2 obtained from particle identification and kinematical mass-constraint fits was required to exceed 1%. Only one candidate per event per decay mode was selected on the basis of highest total probability. This requirement suppresses multiple counting in which particles exchange position in the decay chain, or in which very low momentum particles in the event are interchanged, both of which can artificially enhance the B signal.

The modes $D^0\pi^-$ and $D^+\pi^-$ are quite distinctive in that the D and the π are nearly back-to-back with lab momenta sharply peaked at 2.3 GeV/c, and thus have low backgrounds. Figure 4 shows the combined invariant mass distribution of both modes, together with a fit with a Gaussian of 4 MeV/c^2

*For modes with only charged particles in the final state σ_E is typically 30 MeV and is required to be no greater than 60 MeV. For the π^0 modes with $P(\pi^0) < 900$ MeV/c, σ_E is typically 45 MeV.

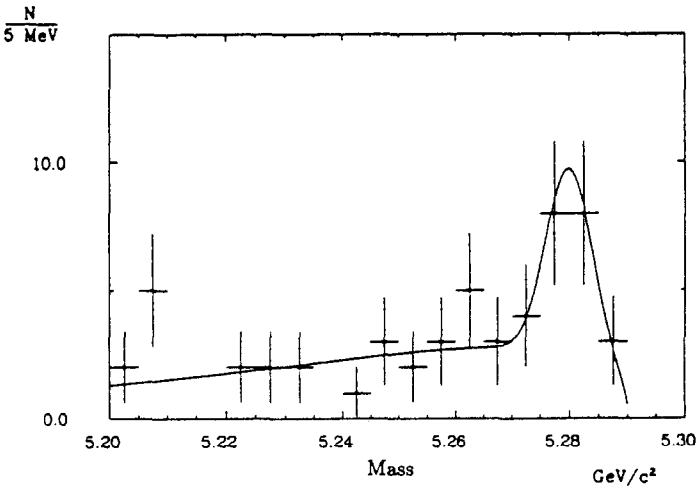

Figure 4. Invariant mass for $D^0\pi^-$ and $D^+\pi^-$ candidates.

width and a background function described below. The signal was found to contain 15 ± 5 events over a background of 8 ± 3 events.

The background for the modes $D^0\pi^-\pi^0$ and $D^+\pi^-\pi^0$ is much larger. The $\pi^-\pi^0$ subsystem was examined for evidence of two-body production. If one selects $D\pi^-\pi^0$ candidates in the B-mass region $5.27 < M < 5.29$ GeV/c^2, the $\pi^-\pi^0$ invariant mass shows a clear ρ^- signal, as is evident in Figure 5a. A fit with a Breit-Wigner of fixed mass and width and a smooth polynomial background yields 16 ± 6 signal events over a background of 11 ± 4 events in the ρ^- region (i.e., within $\pm 1.75\Gamma$ of the ρ^- mass). Conversely, selecting events with $\pi^-\pi^0$ invariant mass in this same ρ^- region yields a clear B signal, shown in Figure 5b with a fit yielding 16 ± 5 signal events over 11 ± 4 background.

Further evidence supporting the interpretation of these events as $\overline{B} \to D\rho^-$ may be found in the angular distribution of the pions from the ρ^- decay. Assuming that the B meson has spin 0, the ρ^- produced in the decay must have helicity 0; its subsequent decay to two pseudoscalar mesons should therefore have a characteristic $\cos^2\theta_\pi$ distribution, where θ_π is the angle between the ρ^- helicity axis and one of the π's, measured in the ρ^- rest frame. The acceptance-corrected distribution shown in Figure 6 is in good agreement with the $\cos^2\theta_\pi$ expectation, when a flat component is also included with a level determined from the number of signal and background events in the mass plot. The statistics for $\cos\theta_\pi > 0$ are poor because in this region the π^0's have high lab momentum and the clusters in the calorimeter for the two photons tend to be spatially unresolved. A study using single-cluster π^0's gave a signal in good agreement with the rate obtained from two-cluster events, although the resolution was somewhat worse.

A search was also made for the "colour-suppressed" decay $\overline{B}^0 \to D^0\rho^0$. In contrast to the strong evidence for $\overline{B} \to D\rho^-$, no evidence for a B signal was found. An analysis similar to the previous one gave a 90% confidence level upper limit of 4 signal events.

The combined $D\pi^-$ and $D\rho^-$ samples are shown in Figure 7. The measured masses of the charged and neutral B mesons were $5279.4 \pm 1.7 \pm 3.0$ MeV/c^2 and $5280.8 \pm 1.6 \pm 3.0$ MeV/c^2 respectively. These values are in good agreement with recently updated values from other channels [15,16]. The systematic uncertainty comes primarily from the scale dependence of the value taken for

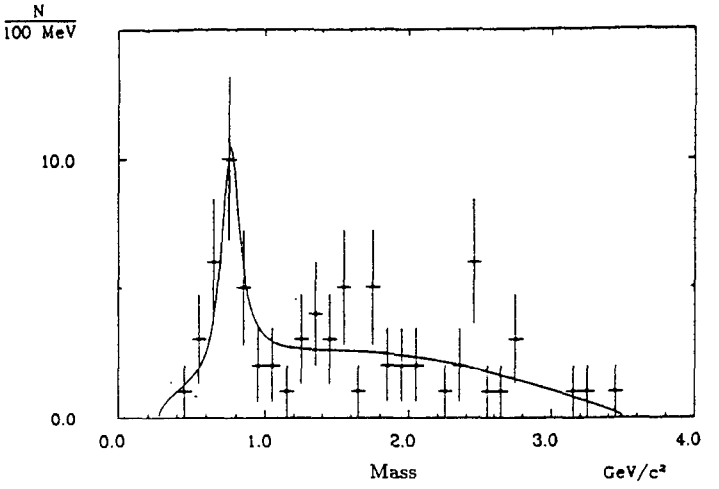

Figure 5a. Invariant mass distributions for the $\pi^-\pi^0$ system from $D\pi^-\pi^0$ candidates in the B signal region.

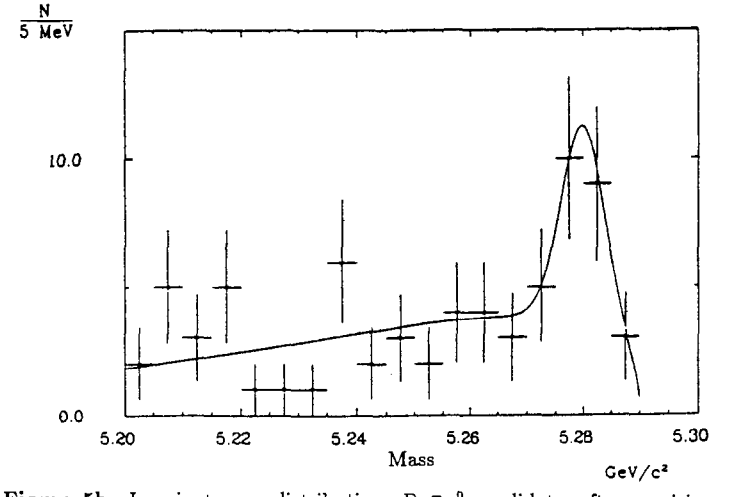

Figure 5b. Invariant mass distributions $D\pi^-\pi^0$ candidates after requiring that the $\pi^-\pi^0$ mass lie in the ρ^0 region.

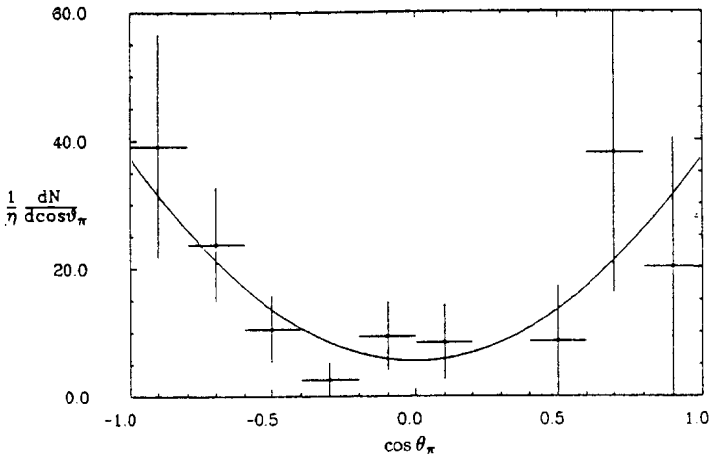

Figure 6. Acceptance-corrected distribution for the helicity angle $\cos\theta_\pi$ of the π^0 from the ρ^- decay.

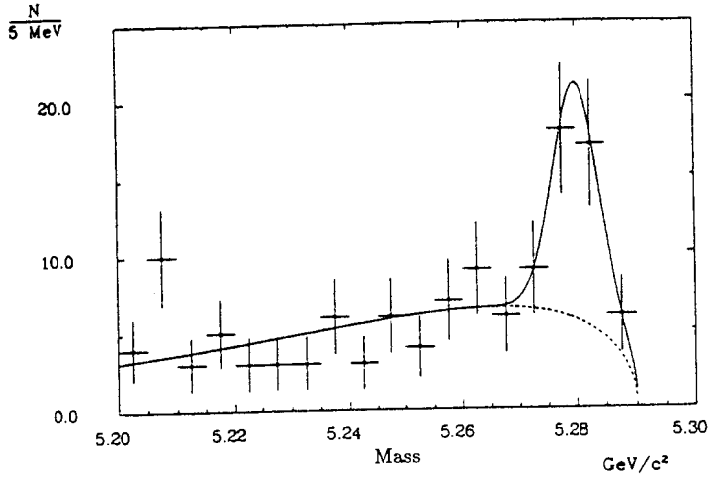

Figure 7. Combined mass distribution for $D\pi^-$ and $D\rho^-$ events.

the mass of the $\Upsilon(4S)$.

The background shape was studied using four separate methods: continuum data, D-sideband combinations, Monte Carlo, and event mixing. By scaling the continuum data by the luminosity ratio, the background from continuum events was found to account for $(74 \pm 20)\%$ of the entries in the B-sideband region (5.20 to 5.27 GeV/c^2) for the $\Upsilon(4S)$ data. However, the statistics of the continuum sample were too limited to derive a background shape and so instead a D-sideband method was used for this information. Such an approach is justified by the observation that the D signal rides on a background which is about 20 times larger than the signal, and hence fake D mesons are the dominant part of the background. Therefore, the same analysis for B decays to $D\pi^-$ and $D\rho^-$ was repeated using a D sideband centred at a mass of 1750 MeV/c^2. The distribution from the D sideband was used to estimate the background shape from continuum events and fake D mesons from $\Upsilon(4S)$ events. Background from correctly reconstructed D mesons in $\Upsilon(4S)$ events, which tend to populate the region near the B mass, was estimated using the Monte Carlo. The sum of both contributions is shown in Figure 8. The fitted curve is a two-parameter function having a square-root threshold behaviour at E_{beam}. The distribution obtained by event mixing in good agreement with this shape. This form was then used to fit the B-candidate distributions and assigned a 25% systematic error.

A potentially dangerous background source, referred to as feeddown, arises from actual B decays in which one or more particles in the decay chain have been missed or ignored. This has been investigated in separate Monte Carlo studies. Among the sources considered were B decays to $D^*\pi^-$ and $D^*\rho^-$. For the $D\pi^-$ modes, which contain only charged particles in the final state, σ_E is typically 30 MeV, and from the requirement $|E_{meas} - E_{beam}| \leq 2\sigma_E$ such feeddown sources were found to be negligible. However, for the $D\rho^-$ modes, σ_E is highly correlated with the π^0 momentum, due to a nearly linear rise in the shower energy resolution [17] at high energies. If we restrict the analysis to well-measured candidates in which the π^0 momentum is less than 900 MeV, we retain 75% of the $\overline{B}\to D\rho^-$ decays (reconstructed from two-cluster π^0 decays), while feeddown is reduced to less than one event in our data sample. Applying this cut to the data reduced the signal from 16 ± 5 $D\rho^-$ events to 12 ± 4 events;

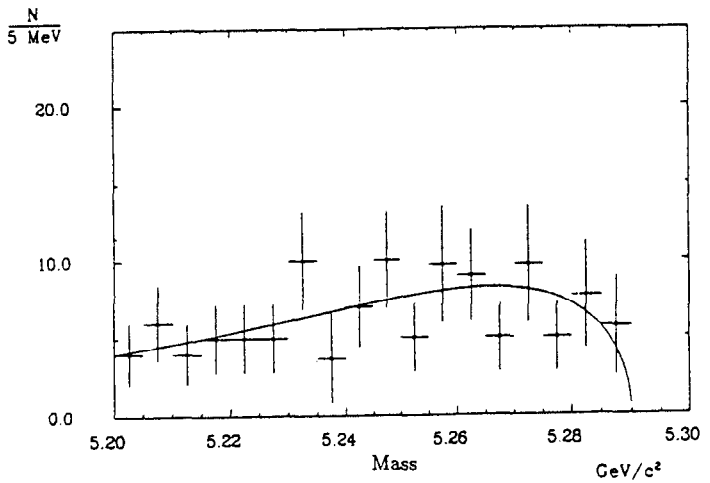

Figure 8. Background distribution for $D\pi^-$ and $D\rho^-$ events obtained by using a D sideband.

this is entirely consistent with the 75% retention expected if the initial sample were free of feeddown.

Table 2. Branching ratios for $B \to D\pi$ and $D\rho^-$ channels.

Decay mode	Signal	Bkgd	Efficiency	Branching Ratio (%)
$B^- \to D^0\pi^-$	7	6 ± 3	0.036	$0.19 \pm 0.10 \pm 0.06$
$B^- \to D^0\rho^-$	10	6 ± 3	0.0047	$2.1 \pm 0.8 \pm 0.9$
$\overline{B}^0 \to D^+\pi^-$	7	3 ± 2	0.027	$0.31 \pm 0.13 \pm 0.10$
$\overline{B}^0 \to D^+\rho^-$	6	5 ± 3	0.0033	$2.2 \pm 1.2 \pm 0.9$
$\overline{B}^0 \to D^0\rho^0$	< 4	6 ± 3	0.022	< 0.3 at 90% CL

The fitted signals, background levels within $\pm 2.5\sigma$ of the measured masses, B reconstruction efficiencies, and resulting branching ratios with statistical and systematic errors are listed in Table 2. While the results show rough agreement with the theoretical predictions of Reference [19], the measured decay rates of the vector modes $D\rho^-$ relative to the pseudoscalar modes $D\pi^-$ are large.

3 Searches for rare B decays

In recent years there has been considerable interest in penguin decays of B mesons, either with a radiated photon or gluon. Such transitions probe the electroweak interaction at the one-loop level and provide a possible window on physics well beyond the directly accessible mass-scale [20-31]. Penguin decays are also potentially important in gaining an understanding of the ΔI=1/2 rule in K decays, since it is possible that a mechanism enhancing these diagrams for B mesons might also enhance those for K mesons. Such information is valuable in attempts to understand whether or not CP violation in the K^0-$\overline{K}^0$ system can be accommodated by the Kobayashi-Maskawa formalism [32,33].

Estimates of the inclusive $b \to s\gamma$ rate receive a substantial correction for hard QCD processes, possibly by as much as two orders of magnitude for small top quark masses [25]. This leads to predicted branching ratios for the inclusive rate which range from 4.8×10^{-5} [31] to 1.4×10^{-3} [25] for $m_t = 50$ GeV/c^2. Final states are assumed to be dominated by the K^* resonances, but the relative strength of the allowed exclusive channels is not well understood.

For $B \to K^*(892)\gamma$ estimates range from 99.8% of the inclusive rate [24] to as low as 4.5% [26]. The influence of a fourth generation has been considered [29,30] and increases the range of allowed branching ratios for $b \to s\gamma$ by another order of magnitude. Typically estimates for the $b \to s$ *gluon* inclusive rate range from about 10^{-4} to 10^{-3}. There are, to date, no reliable theoretical estimates of the exclusive rates.

3.1 $b \to s\gamma$ transitions

Radiative B decays have been studied [34] in the decay channels:

$$B^0 \longrightarrow K^{*0}\,\gamma \qquad \Big\lfloor \to K^+\pi^-$$

$$B^+ \longrightarrow K^{*+}\,\gamma \qquad \Big\lfloor \to K^0_S\pi^+$$

where K^* refers to the $K^*(892)$, the $K_2^*(1430)$ or the $K_3^*(1780)$ resonance. In addition, the decay of B mesons into the $K_1(1400)$ resonance with $J^P = 1^+$ has been investigated in the following mode:

$$B \longrightarrow K_1(1400)\,\gamma \qquad \Big\lfloor \to K^*\pi$$

for both charges.

All $K^+\pi^-$ or $K^0_S\pi^+$ combinations were accepted as $K^*(892)$, $K_1(1400)$, $K_2^*(1430)$ or $K_3^*(1780)$ mesons if their invariant masses lay within $\pm 1.2\Gamma$ of the appropriate nominal values. Photons were reconstructed in a fine-grained electromagnetic calorimeter [17], made of lead-scintillator sandwich modules with wavelength shifter readout. The energy resolution is approximately given by $\sigma_{E_{sh}}/E_{sh} = 7\%\sqrt{1/E_{sh}+1}$, where E_{sh} is in GeV.

The usual energy constraint fit was applied to those candidates whose measured energy was within $\pm 2\sigma_E$ of the known beam energy. The background from continuum events was greatly reduced by a topological cut, which required that the opening angle between the thrust axis for the B candidate and that for the remaining particles in the event satisfy $|\cos\alpha_{thrust}| \leq 0.8$.

Figure 9a shows the invariant mass distribution of the $K^*(892)\gamma$ combinations passing these cuts. There is no evidence for a signal from B decays. An examination of the same mass distribution, obtained using a sideband of the $K^*(892)$ centered at 1.05 GeV/c^2, showed that the level entries in the mass distribution is fully explained as combinatorial background. In order to derive upper limits for the various branching ratios, the mass distributions were fitted using a Gaussian distribution centred at the B mass with a width derived from Monte Carlo simulation (including the effect of the width of the $\Upsilon(4S)$ resonance and the spread in the beam energy at DORIS), plus the following function to model the background:

$$\frac{\mathrm{dN}}{\mathrm{d}M} \sim M\sqrt{1-\frac{M^2}{E^2_{beam}}}\cdot e^{-\alpha\left(1-\frac{M^2}{E^2_{beam}}\right)}$$

where α is a free parameter. The first term represents the expected distribution of background uniformly distributed in phase space, while the second term empirically accounts for the drop in acceptance toward lower masses. The result was a limit of 4.1 signal events (90% CL). Using a constant background level instead leads to an even lower limit.

Table 3. Branching ratio limits for $b \to s\gamma$ modes.

Decay mode	Events (90% CL)	Br (90% CL)
$B \to K^*(892)\gamma$	< 4.1	$< 2.4 \times 10^{-4}$
$B^0 \to K^{*0}(892)\gamma$	< 3.9	$< 2.9 \times 10^{-4}$
$B^+ \to K^{*+}(892)\gamma$	< 3.4	$< 8.5 \times 10^{-4}$
$B \to K_1(1400)\gamma$	< 4.4	$< 4.1 \times 10^{-4}$
$B \to K_2^*(1430)\gamma$	< 6.4	$< 8.3 \times 10^{-4}$
$B \to K_3^*(1780)\gamma$	< 9.1	$< 3.0 \times 10^{-3}$

The mass distribution for the decays $B^0 \to K^{*0}(892)\gamma$ and $B^+ \to K^{*+}(892)\gamma$ were fitted separately. The results of the fit can be found in Table 3. The

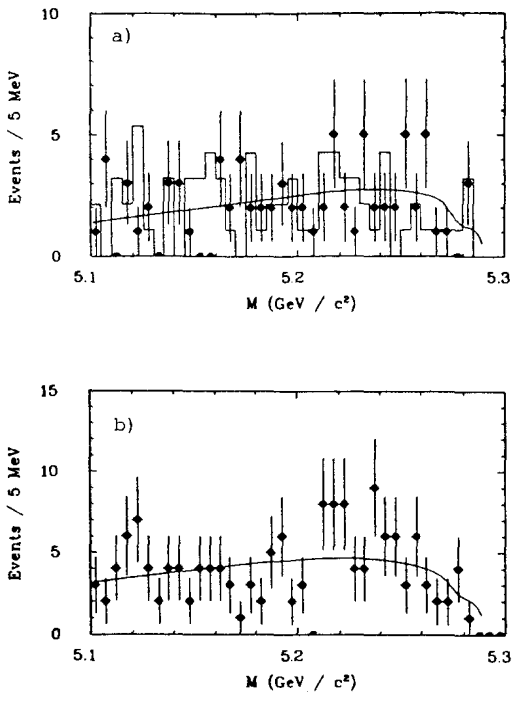

Figure 9. Mass distributions for (a) $K^*(892)\gamma$ and (b) $K_1(1400)\gamma$ searches. The curves shown are the result of the maximum likelihood fits described in the text.

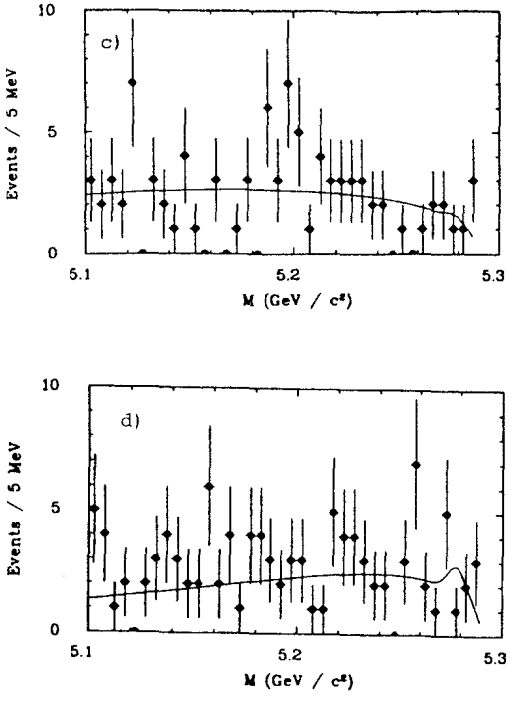

Figure 9. Mass distributions for (c) $K_2^*(1430)\gamma$ and (d) $K_3^*(1780)\gamma$ searches. The curves shown are the result of the maximum likelihood fits described in the text.

search for decays involving the higher mass K^* resonances has been performed in the same way (Figures 9b,c,d). In all cases the invariant mass spectrum was well described by a background distribution obtained from a sideband of the K^*. The results are summarized in Table 3. In order to determine the reconstruction efficiency, $\Upsilon(4S)$ decays were simulated using the LUND 6.2 model [11], adjusted to describe the general properties of B meson decays. The ratio of neutral and charged B mesons produced in $\Upsilon(4S)$ decays was assumed to be 0.45:0.55. The generated events were passed through a detailed detector simulation [35], where the description of electromagnetic calorimeter was carefully checked, and then were reconstructed in the same manner as the data. The upper limits on the number of events have been obtained by integrating the likelihood distributions, including the errors on efficiency and K^* branching ratios. Our result for the $B\to K^*(892)\gamma$ decay represents an improvement by an order of magnitude over the previous best limit [36].

3.2 $b\to s$ *gluon* transitions

The search for $b\to s$ *gluon* transition was made using the channels $B\to\pi$, ρ, or ϕ and one of K, $K^*(892)$, $K_1(1400)$, or $K_2^*(1430)$. No evidence for a signal was seen in any of these channels either, leading to a further 24 upper limits. These form a significant addition to the existing limits on standard and electromagnetic penguin decays [36,34]. While all of these decays can proceed via penguin diagrams, it should be noted that some (such as $B^0\to K^+\pi^-$) can occur via spectator diagrams, which are suppressed by small Kobayashi-Maskawa matrix elements, or via flavour-changing neutral currents, which are not allowed in the standard model. However, standard model predictions for penguin-mediated decay rates involving the stable K meson are about two orders of magnitude larger than those for the spectator processes.

For this analysis, the mass bands used to select candidates for K^*, K_1, or K_2^* mesons were a slightly more restrictive $\pm\Gamma$ around the appropriate nominal mass. The ϕ mesons were taken from K^+K^- combinations within ± 6 MeV/c^2 of the nominal ϕ mass. The ρ mesons were all neutral and taken from $\pi^+\pi^-$ combinations with a mass lying between $-\Gamma$ and $+1.2\Gamma$ of the nominal ρ^0 mass. In order to suppress background, no decay channels involving neutral pions were used.

Table 4. Summary of the results on $B\to K^{(*)}\pi$.

Decay mode	Events (90% CL)	Br (90% CL)
$B^0\to K^+\pi^-$	< 9.8	$< 2.8\times10^{-4}$
$B^+\to K_S^0\pi^+$	< 3.0	$< 1.2\times10^{-4}$
$B^0\to K^{*+}(892)\pi^-$	< 3.7	$< 1.1\times10^{-3}$
$B^+\to K^{*0}(892)\pi^+$	< 5.5	$< 4.1\times10^{-4}$
$B^0\to K_1^+(1400)\pi^-$	< 3.6	$< 6.6\times10^{-4}$
$B^+\to K_1^0(1400)\pi^+$	< 3.2	$< 2.3\times10^{-3}$
$B^0\to K_2^{*+}(1430)\pi^-$	< 3.5	$< 3.1\times10^{-3}$
$B^+\to K_2^{*0}(1430)\pi^+$	< 6.8	$< 1.0\times10^{-3}$

Table 5. Summary of the results on $B\to K^{(*)}\rho^0$.

Decay mode	Events (90% CL)	Br (90% CL)
$B^0\to K_S^0\rho^0$	< 2.3	$< 2.0\times10^{-4}$
$B^+\to K^+\rho^0$	< 5.3	$< 2.1\times10^{-4}$
$B^0\to K^{*0}(892)\rho^0$	< 5.6	$< 5.0\times10^{-4}$
$B^+\to K^{*+}(892)\rho^0$	< 2.3	$< 5.4\times10^{-4}$
$B^0\to K_1^0(1400)\rho^0$	< 2.6	$< 3.1\times10^{-3}$
$B^+\to K_1^+(1400)\rho^0$	< 8.4	$< 1.7\times10^{-3}$
$B^0\to K_2^{*0}(1430)\rho^0$	< 7.3	$< 1.6\times10^{-3}$
$B^+\to K_2^{*+}(1430)\rho^0$	< 2.3	$< 1.9\times10^{-3}$

In addition to the usual energy requirement, cuts were made on the production and helicity angle distributions. Assuming B mesons are spinless, their production angular distribution should be proportional to $\sin^2\theta_B$, where θ_B is the angle between the momentum of the B and the beam axis. We therefore required that $|\cos\theta_B| \le 0.5$ in order to reduce the background. In addition, for decays of a B meson into a spin-1 and a spin-0 particle, the spin-1 particle must be in a helicity-0 state. If we define α_V as the angle between the decay axis of the spin-1 particle in its rest frame and the boost direction, one expects a $\cos^2\alpha_V$ distribution for signal events. Requiring $|\cos\alpha_V| \le 0.5$ improved background rejection. Background from continuum events was largely

removed by the requirement $|\cos\alpha_{thrust}| \leq 0.8$. After these cuts, no evidence for a signal was seen in any of the channels. The upper limits given in Tables 4-6 were obtained by the same method as for the $b\to s\gamma$ results.

Table 6. Summary of the results on $B\to K^{(*)}\phi$.

Decay mode	Events (90% CL)	Br (90% CL)
$B^0\to K^0_S\phi$	< 2.3	$< 4.5\times10^{-4}$
$B^+\to K^+\phi$	< 3.6	$< 3.1\times10^{-4}$
$B^0\to K^{*0}(892)\phi$	< 2.3	$< 4.7\times10^{-4}$
$B^+\to K^{*+}(892)\phi$	< 2.3	$< 1.1\times10^{-3}$
$B^0\to K^0_1(1400)\phi$	< 2.3	$< 5.9\times10^{-3}$
$B^+\to K^+_1(1400)\phi$	< 3.8	$< 1.6\times10^{-3}$
$B^0\to K^{*0}_2(1430)\phi$	< 2.3	$< 1.1\times10^{-3}$
$B^+\to K^{*+}_2(1430)\phi$	< 2.3	$< 4.1\times10^{-3}$

In summary, no evidence for radiative $b\to s\gamma$ or $b\to s$ *gluon* decays was found. If the fraction of $B\to K^*(892)\gamma$ decays is 7% [25] of the inclusive rate, we derive an upper limit of:

$$\mathrm{Br}(b\to s\gamma) < 3.4\times10^{-3}$$

This is just at the limit of sensitivity for constraining the top quark mass. The same conclusion holds for the influence of a possible fourth generation, where a slightly improved sensitivity would allow the exclusion of a wide range of values for mixing with a new generation.

4 D^* polarization in $\overline{B}\to D^*\ell\nu$

ARGUS demonstrated some time ago that the decay $\overline{B}^0\to D^{*+}\ell^-\overline{\nu}$ ($\ell^- = e^-$, μ^-) has a large branching ratio and can be cleanly reconstructed [37]. This mode therefore provides an ideal laboratory for studying the quark dynamics of the weak $b\to c$ transition as probed by the fundamental vector and axial vector currents.

The major problem for theoretical calculations of the semileptonic decay widths for exclusive channels is a model for the hadronic part of the interaction. This can be handled, for example, by introducing form factors [38-45]. The predicted values for these form factors have important consequences for the helicity decomposition of the $\overline{B}^0\to D^{*+}\ell^-\overline{\nu}$ decay width [44], which affect not only the estimates for the integrated rates, but also the shape of the lepton momentum spectrum. Since the decay $\overline{B}^0\to D^{*+}\ell^-\overline{\nu}$ constitutes about 60% of the inclusive semileptonic rate, it is important to compare theoretical predictions with experimental measurements, because the same models are used to determine $|V_{ub}|/|V_{cb}|$ from the measured inclusive lepton spectrum in B decays [46].

As pointed out in References [43] and [44] the average D^{*+} polarization in $\overline{B}^0\to D^{*+}\ell^-\overline{\nu}$ determines the ratio Γ_L/Γ_T of the longitudinal and transverse component of the decay width. Thus a polarization measurement is a powerful tool for checking the validity of model predictions for semileptonic B decays.

The polarization of the D^{*+} is determined using the strong two-body decay $D^{*+}\to D^0\pi^+$. The distribution of the angle $\theta^*_{\pi^+}$ of the slow pion in the rest frame of the D^{*+} with respect to the D^{*+} boost direction discriminates between the allowed helicity contributions. For longitudinally polarized D^{*+} mesons will exhibit a $\cos^2\theta^*_{\pi^+}$ distribution, while for transversely polarized D^{*+} mesons a $\sin^2\theta^*_{\pi^+}$ behavior is expected. In the D^{*+} rest frame the angular distribution can be parametrised by:

$$N(\theta^*_{\pi^+}) \sim 1 + \alpha\cdot\cos^2\theta^*_{\pi^+}$$

where

$$\alpha = \frac{2\Gamma_L - \Gamma_T}{\Gamma_T}\,.$$

The allowed values for the asymmetry parameter α range from -1, corresponding to fully transverse polarized D^{*+} mesons, to infinity, corresponding to full longitudinal polarization. For $\alpha = 1$ both polarizations are equal in magnitude. Note that the predicted value for α depends on the lepton momentum cut.

In order to maximize the size of the sample, D^{*+} mesons were reconstructed using the decay chain $D^{*+}\to D^0\pi^+$, followed by $D^0\to K^-\pi^+$ or $K^-\pi^+\pi^+\pi^-$. Both the D^0 and D^{*+} final states were kinematically constrained to the appropriate masses. The combinatorial background from multiple counting was reduced by selecting only one D^{*+} candidate per event. This was accomplished

by accepting the combination which maximised the χ^2 probability from kinematical fitting and particle identification. In addition, the χ^2 probability was required to exceed 5% for the $D^0 \to K^-\pi^+$ channel and 10% for the $K^-\pi^+\pi^+\pi^-$ final state. The continuum contribution was suppressed by requiring the D^{*+} candidates satisfy $x_p < 0.5$ ($x_p = p/\sqrt{E_B^2 - M_{D^*}^2}$), which is the kinematic limit for D^{*+} mesons from B decays on the $\Upsilon(4S)$.

Leptons were identified, as previously described, by using information from all detector components combined into an overall likelihood, $\mathcal{L}$. An e^- or μ^- candidate was accepted if the likelihood ratio exceeded 70% and the momentum was larger than 1 GeV/c. The fake rates due to lepton-hadron misidentification are 0.5% for electrons and 1.5% for muons with these requirements.

The partial reconstruction of the decay $\overline{B}^0 \to D^{*+}\ell^-\overline{\nu}$ is possible because $\overline{B}^0$ mesons produced in $\Upsilon(4S)$ decays are nearly at rest. The neutrino is unobserved, but can be inferred if the recoil mass against the $D^{*+}\ell^-$ system, M^2_{Recoil}, is consistent with zero, where:

$$M^2_{Recoil} = [E_{beam} - (E_{D^{*+}} + E_{l^-})]^2 - [\vec{p}^{\,*+}_D + \vec{p}_{l^-}]^2.$$

The M^2_{recoil} distribution obtained from the data is shown in Figure 10. A prominent peak at $M^2_{recoil} \sim 0$ can be seen, due to the decay $\overline{B}^0 \to D^{*+}\ell^-\overline{\nu}$. The position and shape of the signal are well described by the Monte Carlo prediction for $\Upsilon(4S) \to B^0\overline{B}^0$ followed by the semi-leptonic decay $\overline{B}^0 \to D^{*+}\ell^-\overline{\nu}$. The contribution of individual background sources has been evaluated in detail. The estimates for the total $D^{*+}\ell^-$ sample, as well as the number of combinations in the signal region defined by $|M^2_{recoil}| < 1$ GeV^2/c^4, are listed in Table 7.

The background level from the continuum component of the $\Upsilon(4S)$ data sample was determined from continuum data recorded at centre-of-mass energies below the open beauty threshold. The contribution from fake leptons was obtained by extracting D^{*+}-hadron events, where the hadron was not compatible with either the electron or muon hypothesis, and rescaling using the known hadron misidentification rates. The upper D^{*+} mass sideband was used to determine the background from fake D^{*+} combinations, normalised to the fitted background level under the signal. Background sources (1-3) were found to have the same dependence on M^2_{recoil}. For backgrounds (4-6) the shapes

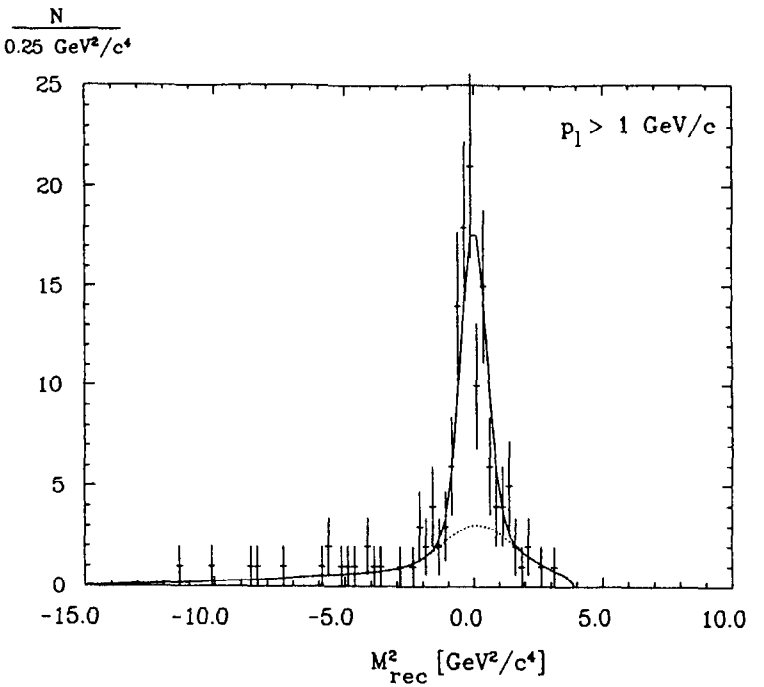

Figure 10. Distribution of M^2_{recoil} for $D^{*+}\ell^-$ combinations with lepton momentum above 1 GeV/c. The solid line is the result of a fit using a Gaussian plus the background parametrisation described in the text.

were obtained by Monte Carlo simulation.

The fit to the M^2_{recoil} distribution (Figure 10) was then performed as follows. The shapes of all the background sources were fixed. The absolute contributions of (4-5) were varied within the range shown in Table 7. The normalisations of (1-3) and (6) were free parameters in the fit. The solid line is the fit result using a Gaussian of width $\sigma = 0.5$ GeV^2/c^4 for the signal, above the described background shown as a dotted line. The number of signal events was found to be 75 ± 11 and was stable against variations of the background shape and the normalisations of (4-5). The total number of background combinations obtained from the fit is 66 ± 14, in good agreement with the sum of (1-5) given in Table 7. The contribution of the decay $\overline{B} \to D^*(2420)\ell^-\overline{\nu}$ with $D^*(2420) \to D^{*+}\pi$ (6) was consistent with zero, leading to the upper limits quoted in Table 7. In the signal region the background was 23 ± 5 events, giving a signal-to-background ratio of about 3:1.

Table 7. Background sources to the signal for $\overline{B}^0 \to D^{*+}\ell^-\overline{\nu}$ with lepton momentum greater than 1 GeV/c.

Background source	Total sample	$\lvert M^2_{recoil}\rvert$ $< 1\ GeV^2/c^4$
1. Continuum events	13 ± 6.5	8 ± 4
2. Fake leptons	4 ± 2	2 ± 1
3. Fake D^{*+} signal	35 ± 10	13 ± 4
4. $B \to \overline{D}^0(D^-)X$, $\overline{B} \to D^{*+}X$, with $\overline{D}^0(D^-) \to \ell^- X$	4 ± 1.5	1 ± 0.4
5. $B^0 \to \overline{B}^0 \to \ell^- X$, $\overline{B}^0 \to D^{*+}X$	12 ± 5	2 ± 1
6. $\overline{B} \to D^*(2420)\ell^-\overline{\nu}$, with $D^*(2420) \to D^{*+}\pi$	< 13 @ 90% CL	< 7 @ 90% CL
Total (1-5)	68 ± 13	26 ± 6

The $\cos\theta^*_{\pi^+}$ distribution was extracted from the events in the signal region ($|M^2_{recoil}| < 1$ GeV^2/c^4). For background sources (1-3) the shape in $\cos\theta^*_{\pi^+}$ was obtained from the data, while sources (4-6) were assumed to have a flat distribution in $\cos\theta^*_{\pi^+}$. The kinematics for the process $\overline{B}^0 \to D^{*+}\ell^-\overline{\nu}$, as well as the acceptance in $\cos\theta^*_{\pi^+}$, have been studied using a Monte Carlo programme, where the generated events were passed through a detailed detector simulation, and then all analysis cuts. The simulation includes the measured lepton and D^{*+} spectra as obtained in Reference [37]. The smearing of the $\cos\theta^*_{\pi^+}$ distribution due to the motion of the B meson was found to be negligible. Note that the acceptance in $\cos\theta^*_{\pi^+}$ is determined largely by the acceptance for the slow pion.

After acceptance correction and normalisation, the $\cos\theta^*_{\pi^+}$ distribution in Figure 11a was obtained. The solid line is the result of a least-squares fit with

$$\frac{dN}{N \cdot d\cos\theta^*_{\pi^+}} = \frac{1 + \alpha \cdot \cos^2\theta^*_{\pi^+}}{2 \cdot (1 + \alpha/3)}$$

where the denominator on the right-hand side accounts for the proper normalisation and α is a free parameter. The fitted value for α was $0.3 \pm 0.6 \pm 0.3$. The first error is statistical, the second the estimated systematic uncertainty. The systematic error has been investigated by varying the $\cos\theta^*_{\pi^+}$ shape of the background sources, as well as the acceptance function. In addition, a consistency check was made by obtaining the $\cos\theta^*_{\pi^+}$ distribution from fits to the M^2_{recoil} spectrum in bins of $\cos\theta^*_{\pi^+}$. The result for α was found to be compatible within the statistical errors. For lepton momenta larger than 1.2 GeV/c (Figure 11b), we obtained $\alpha = 0.3 \pm 0.8 \pm 0.3$.

From the value for α one can deduce the ratio of the longitudinal and transverse component Γ_L/Γ_T in the decay width. We obtain

$$\frac{\Gamma_L}{\Gamma_T} = 0.65 \pm 0.3 \pm 0.15$$

$p_\ell > 1$ GeV/c. The measured average polarisation of the D^{*+} mesons shows that there is a substantial contribution of the transverse helicity component to the decay width of $\overline{B}^0 \to D^{*+}\ell^-\overline{\nu}$ in the selected region of phase space.

A comparison between our measured values for α and the model predictions of Pietschmann and Schöberl (PS) [41], Grinstein, *et al.* (GIW) [42], and Körner and Schuler (KS) [44] is shown in Figure 12, where the asymmetry parameter α is plotted versus the lower lepton energy cut off (computation taken from Reference [44]). The data points are the ARGUS result, where statistical and systematic errors have been added in quadrature. We find

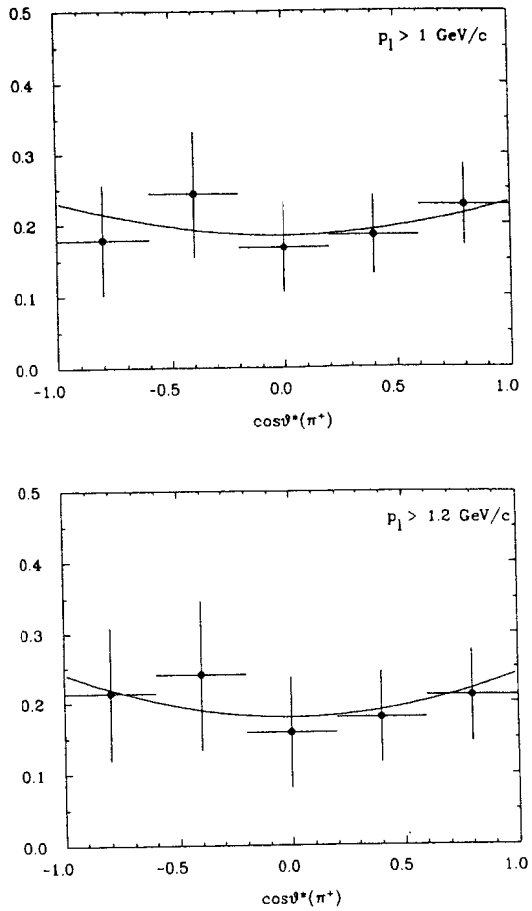

Figure 11. Distribution of $\cos\theta^*_{\pi^+}$ for events with $|M^2_{recoil}| < 1$ GeV^2/c^4, after background subtraction, acceptance correction and normalisation: (a) for lepton momentum greater than 1 GeV/c, and (b) greater than 1.2 GeV/c.

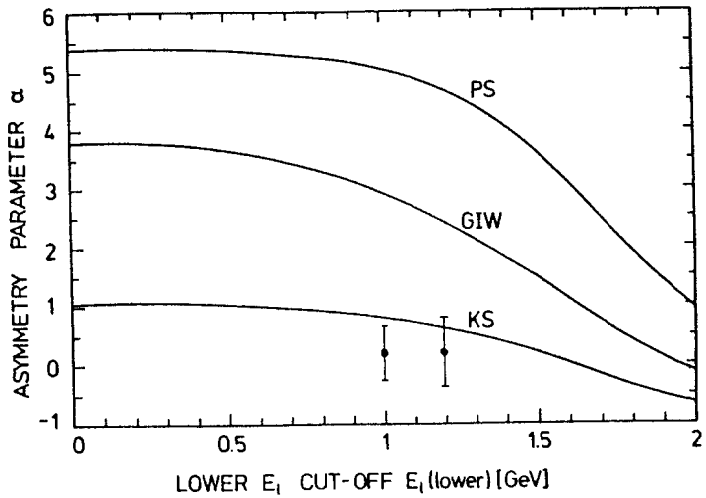

Figure 12. Comparison between measured values of the asymmetry parameter α (statistical and systematic errors added in quadrature) with the model predictions of Pietschmann and Schöberl (PS) [41], Grinstein, *et al.* (GIW) [42], and Körner and Schuler (KS) [44]. The curves are taken from Reference [44].

good agreement with the KS model, whereas the GIW and PS models can be excluded by more than 3 and 6 standard deviations respectively.

5 Search for $\overline{B}\to\rho\ell\nu$

The best method for extracting a reliable value for $|V_{ub}|$, from the standpoint of theoretical prediction and experimental accessibility, appears to be a measurement of an exclusive noncharm B decay in a semileptonic mode. In this context, the channel $B^-\to\rho^0\ell^-\overline{\nu}$ seems particularly suitable, especially in the light of the success with $\overline{B}^0\to D^{*+}\ell^-\overline{\nu}$. For this reason, ARGUS undertook a study of the decay $B^-\to\rho^0\ell^-\overline{\nu}$, using the recoil mass technique. The channel $B^-\to\rho^0\ell^-\overline{\nu}$ is of course intrinsically more difficult to observe, since it is suppressed by the small size of the KM matrix element V_{ub}. This is compounded by the large width of the ρ^0 resonance and, particularly relevant for the recoil mass approach, the fact that many ρ^0 mesons are produced in the dominant $b\to c$ decay modes. The compensating factor for these difficulties is the high reconstruction efficiency for the ρ^0, about 50 times larger than that for the D^{*+}.

In the search for the decay $B^-\to\rho^0\ell^-\overline{\nu}$, ρ^0 candidates were selected from $\pi^+\pi^-$ combinations lying within 150 MeV/c^2 of the nominal ρ^0 mass. In addition, the ρ^0 momentum was required to exceed 1.0 GeV/c. Leptons were selected by the usual cut on the global likelihood ratio ($\mathcal{L} > 75\%$), and were required to have momenta above 1.5 GeV/c. Continuum background was suppressed by a cut on the angle between the lepton and the thrust axis of the event with the lepton and ρ^0 tracks removed. Again, the two-jet nature of the continuum events leads to a strong forward-backward correlation in this variable for the continuum background (Figure 13). The requirement that $|\cos\alpha_{thrust}| < 0.5$ retains about 50% of the potential signal.

The resulting spectrum for the mass recoiling against the $\rho^0\ell^-$ system, M^2_{recoil}, is shown in Figure 14. No signal is observed at zero recoil mass. The backgrounds are substantially larger for this analysis than for $\overline{B}^0\to D^{*+}\ell^-\overline{\nu}$, because of the larger combinatorial background under the broad ρ^0, as well as the substantial number of ρ^0 mesons from higher mass states produced in $b\to c$ or $b\to u$ transitions. An upper limit of 46 events (90% CL) can be

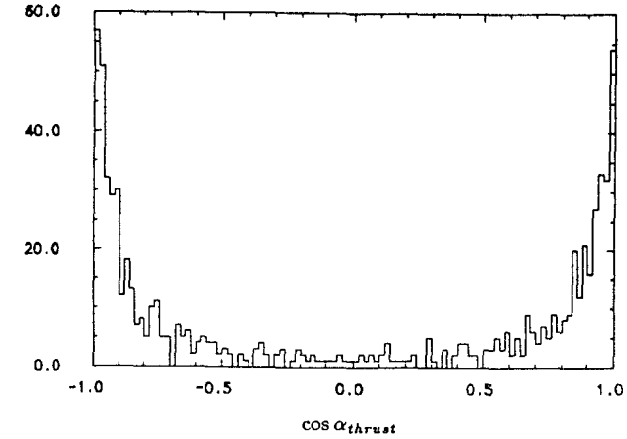

Figure 13. Distribution of the opening angle between the lepton and the thrust axis for the event with lepton and ρ^0 tracks removed.

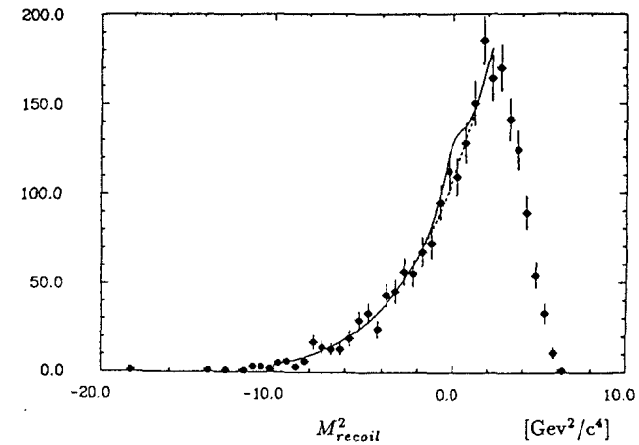

Figure 14. Distribution of M^2_{recoil} for $\rho^0\ell^-$ events with lepton momentum above 1.5 GeV/c.

attributed to the decay $B^- \to \rho^0 \ell^- \overline{\nu}$ (shown by the solid curve in Figure 14). This corresponds to a limit on the branching ratio for $B^- \to \rho^0 \ell^- \overline{\nu}$ of 0.22% (90% CL).

A direct comparison with the decay $\overline{B}^0 \to D^{*+} \ell^- \overline{\nu}$ in the same data, gave a limit of:

$$R = \frac{\mathrm{Br}(B^- \to \rho^0 \ell^- \overline{\nu})}{\mathrm{Br}(\overline{B}^0 \to D^{*+} \ell^- \overline{\nu})} < 3.2\%$$

where some experimental errors cancel in the ratio. It is also expected that this quantity can be reasonably well predicted using the available theoretical models. Assuming equal lifetimes for charged and neutral B mesons, and:

$$\frac{\Gamma(\overline{B}^0 \to \rho^+ \ell^- \overline{\nu})}{\Gamma(B^- \to \rho^0 \ell^- \overline{\nu})} = \frac{1}{2}$$

one obtains from References[39] and [44]:

$$R = \frac{\Gamma(\overline{B}^0 \to \rho^+ \ell^- \overline{\nu})}{\Gamma(\overline{B}^0 \to D^{*+} \ell^- \overline{\nu})} \approx 0.63 \times \frac{|V_{ub}|^2}{|V_{cb}|^2} .$$

The measured limit on R translates, with these assumptions, into a restriction of the ratio:

$$\frac{|V_{ub}|}{|V_{cb}|} < 22\% .$$

This result is not quite at the level obtained from the full inclusive lepton spectrum, but brings with it less theoretical uncertainty.

6 Status of charmless B decays

Last year, ARGUS reported [16,47] the observation of hadronic B decays to charmless final states. This was part of a systematic effort to establish the existence of weak $b \to u$ transitions. Upper limits for the ratio $\Gamma(b \to u)/\Gamma(b \to c)$ have been obtained from the analysis of inclusive lepton spectra in semileptonic decays of B mesons [46], from the study of the reaction $B^- \to \rho^0 \ell^- \overline{\nu}$ described above, and from searches for charmless hadronic B meson decays, largely into multipion final states [48]. A common feature of all such analyses is the strong model dependence of the upper limits derived for the Kobayashi-Maskawa matrix element V_{ub}. However, the observation of a charmless B meson decay would provide evidence for a finite $b \to u$ coupling.

The successful search for charmless B decays came in channels containing baryons. Originally this was motivated by the fact that with baryons more of the available phase-space would be absorbed as mass, with the possible consequence that branching ratios would be larger for low multiplicity channels. The specific channels investigated were:

$$\begin{aligned} B^+ &\to p\bar{p}\pi^+ \\ B^0 &\to p\bar{p}\pi^+\pi^- . \end{aligned}$$

Particle identification information for this study was applied in the usual fashion, by using as protons or pions those particles with a likelihood ratio [1] for the proton or pion hypothesis which exceeded 1%. In addition, the probability for the sum of all χ^2 contributions from particle identification was required to exceed 2% for the $p\bar{p}$ system. Given the limited discrimination available from the ARGUS dE/dx and TOF systems in the relevant momentum regions, these requirements effectively mean that the protons and antiprotons only satisfy a consistency requirement. However, the pions have low momentum, and are uniquely identified by this procedure.

The B candidates were required to satisfy $|E_{meas} - E_{beam}| < 2\sigma_E$, where σ_E is the measured energy error. Typically, σ_E is 40 MeV and candidates with an error greater than $\sigma_E > 60$ MeV were rejected. For the accepted candidates, an energy constraint fit was applied.

Background from continuum events was reduced by three topological cuts. The first was the previously described cut on the opening angle between the B thrust axis, and the thrust axis of the recoiling $\overline{B}$, where for this analysis the requirement was $|\cos\alpha_{thrust}| \leq 0.8$. Second, the multiplicity of charged particles in the remainder of the event, excluding the particles contributing to the B candidate, was required to be larger than three. This cut exploits the fact that the multiplicity in $\Upsilon(4S)$ decays is larger than in the continuum. In addition, it is a precondition for the implementation of the third cut: the Fox-Wolfram moment H_2 [8] of the remaining charged and neutral particles in the event was required to be less than 0.3, thereby selecting spherical events.

The distribution of the opening angle between proton and antiproton $\theta_{p\bar{p}}$ for candidates which passed these cuts, and had an invariant mass in the B mass region, can be seen to be strongly peaked at 180° (Figure 15a). This behaviour

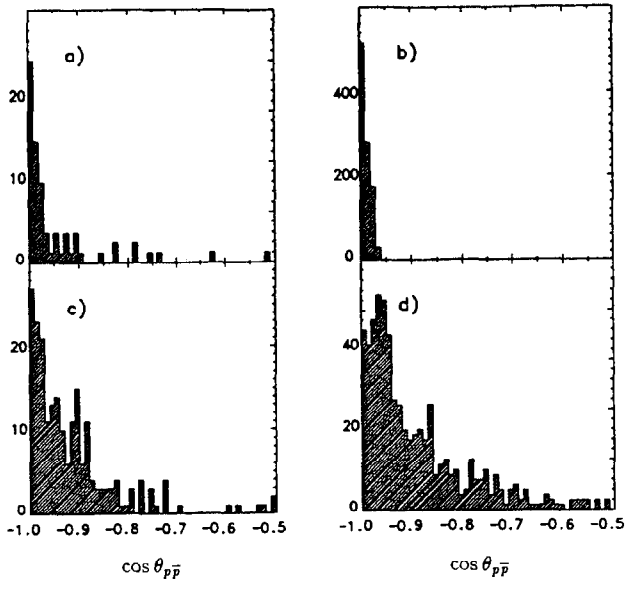

Figure 15. Distribution of the opening angle, $\theta_{p\bar{p}}$, between the proton and antiproton for (a) candidates in the B mass region ($5.272 < M < 5.285$ GeV/c^2), (b) Monte Carlo generated decays $B \to \Delta\bar{p}$. (c) continuum data with and ($5.100 < M < 5.290$ GeV/c^2), and (d) a sideband interval below the B mass ($5.100 < M < 5.260$ GeV/c^2).

is readily understood if two-body channels, consisting of protons and low mass baryonic resonances, dominate the studied final states. As an example, the $\theta_{p\bar{p}}$ distribution for Monte Carlo generated $B \to \bar{p}\Delta$, $\Delta \to p\pi$ decays, shown in Figure 15b, exhibits the same back-to-back peaking as the B candidates. In contrast, the $\theta_{p\bar{p}}$ distribution for candidates below the B mass region in $\Upsilon(4S)$ sample (Figure 15d), as well as for continuum data (Figure 15c), shows a significantly less pronounced peaking at 180°. Restricting our search to such quasi two-body channels, we required $\cos\theta_{p\bar{p}} \leq -0.98$.

After applying these cuts, in the mass range between 5.1 GeV/c^2 and the kinematic limit at 5.29 GeV/c^2, 18% of the events contained more than one B candidate in one of the decay channels and 7% contained candidates in both channels. Only one candidate per channel was accepted by choosing the candidate with the smallest χ^2 from the beam energy constraint fit.

The resulting mass spectrum for the $\Upsilon(4S)$ data (Figure 16) shows a pronounced peak in the B mass region. The shape of the background was described by the form introduced previously:

$$\frac{\mathrm{dN}}{\mathrm{d}M} \sim M\sqrt{1-\frac{M^2}{E^2_{beam}}}\cdot e^{-\alpha\left(1-\frac{M^2}{E^2_{beam}}\right)}.$$

However, since the level of background is small, the results are not sensitive to the specific choice.

Table 8. Comparison of fitted mass values for B^0 and B^+. The $D^{*+}n\pi$ mass values are from Reference [13], adjusted to a $\Upsilon(4S)$ mass of 10580 MeV/c^2.

[MeV/c^2]	$p\bar{p}\pi^+(\pi^-)$	$D^{*+}\mathrm{n}\pi$
$M(B^0)$	$5278.8 \pm 1.7 \pm 3.0$	$5279.7 \pm 1.0 \pm 3.0$
$M(B^+)$	$5277.8 \pm 1.2 \pm 3.0$	$5277.3 \pm 1.3 \pm 3.0$
$M(B^0) - M(B^+)$	$1.0 \pm 2.1 \pm 1.0$	$2.4 \pm 1.6 \pm 1.0$

From a fit with a Gaussian for the signal plus this background form, the signal was found to have a mass of $5278.3 \pm 1.1 \pm 3.0$ MeV/c^2 and a width, consistent with expectation, of 4.2 ± 1.0 MeV/c^2. In a ± 1.5 sigma region around the B mass, we observed in total 34 events. Only 9 ± 4 of these events were attributed to the background, where the error includes a systematic

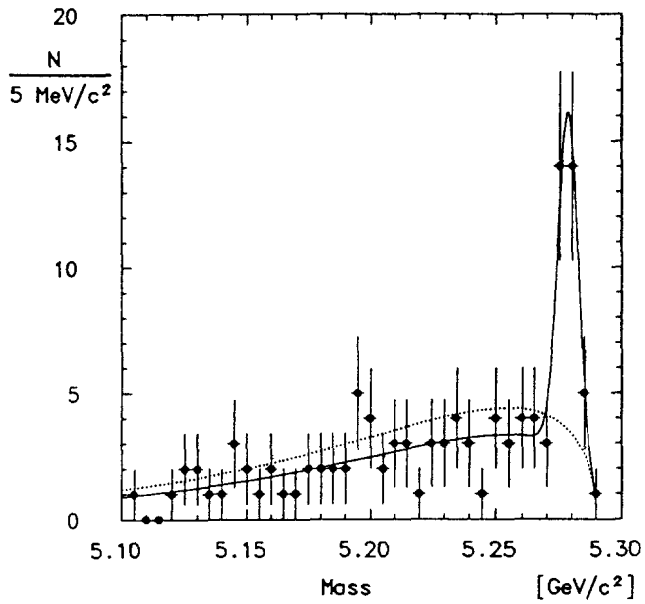

Figure 16. Invariant mass distribution for both channels in the $\Upsilon(4S)$ data sample. The dotted line is the fitted curve from the same distribution in the continuum sample, scaled by luminosity.

contribution from the uncertainty of the background shape. The probability that the observed excess of events is a statistical fluctuation of the background corresponds to more than five standard deviations.

The sample can be divided into neutral and charged B mesons (Figure 17). The masses obtained by separate fits to these distributions are given in Table 8. They agree nicely with previous measurements in the decay channels $B \to D^{*+} n\pi$, $n = 1,2,3$ [13]. In order to determine branching ratios, we assumed that 55% of the time the $\Upsilon(4S)$ decays into B^+B^- pairs and 45% into pairs of neutral B mesons. A Monte Carlo simulation was used to calculate the geometrical acceptance. Since the $|\cos\alpha_{thrust}|$ distribution is expected to be flat, the acceptance for the cut on the thrust axes angle was taken to be 0.8. Fitting the invariant mass distribution in separate bins, the angular distribution shown in Figure 18 was determined for our data. Within errors, the data is consistent with expectation. The acceptance for the cut on the opening angle between the proton and antiproton was evaluated by fitting the observed signal without this requirement. The correction for this cut was found in this way to be $(70 \pm 30)\%$. The losses due to the other cuts were determined similarly, taking into account possible correlations between the different requirements. By this means we found:

$$\begin{aligned} \mathrm{Br}(B^+ \to p\bar{p}\pi^+) &= (5.2 \pm 1.4 \pm 1.9) \times 10^{-4} \\ \mathrm{Br}(B^0 \to p\bar{p}\pi^+\pi^-) &= (6.0 \pm 2.0 \pm 2.2) \times 10^{-4} \end{aligned}$$

where the first is the statistical and the second the systematic error, including a contribution introduced by our assumed background function.

Table 9. Branching ratios for the decay channels $B \to p\bar{p}n\pi$.

Decay mode	Br
$\mathrm{Br}(B^0 \to p\bar{p})$	$< 1.3 \times 10^{-4}$ (90% CL)
$\mathrm{Br}(B^+ \to p\bar{p}\pi^+)$	$(5.2 \pm 1.4 \pm 1.9) \times 10^{-4}$
$\mathrm{Br}(B^0 \to p\bar{p}\pi^+\pi^-)$	$(6.0 \pm 2.0 \pm 2.2) \times 10^{-4}$
$\mathrm{Br}(B^+ \to p\bar{p}\pi^+\pi^+\pi^-)$	$< 4.7 \times 10^{-4}$ (90% CL)

A comparison of these values with upper limits for branching ratios of the decay channels $B^0 \to p\bar{p}$ and $B^+ \to p\bar{p}\pi^+\pi^+\pi^-$ in our data is given in Table 9.

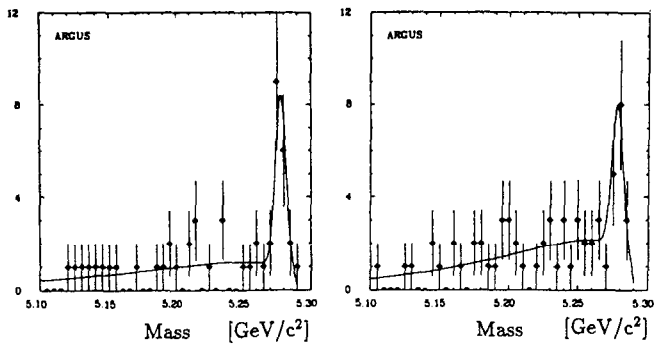

Figure 17. Invariant mass distributions for (a) $B^- \to p\bar{p}\pi^-$ and (b) $\overline{B}^0 \to p\bar{p}\pi^-\pi^+$.

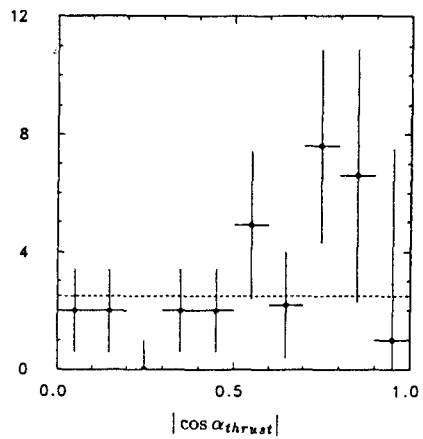

Figure 18. Distribution of $|\cos\alpha_{thrust}|$ from fits to the invariant mass distribution in bins of $|\cos\alpha_{thrust}|$. The dashed line is the expected behaviour.

The analysis of the two-prong and five-prong channels was identical to that described above, except that the cut on the angle between the p and $\bar{p}$ was not applied.

In general, background arises from resonant $e^+e^- \to \Upsilon(4S)$ and from continuum $e^+e^- \to q\bar{q}$ events. The continuum mass distribution (Figure 19a) does not show any excess of events at the B mass. Thus, the observed signal originates from $\Upsilon(4S)$ decays and cannot be faked by any background from continuum events. Outside the B mass region, continuum and $\Upsilon(4S)$ data agree in magnitude within one standard deviation. This is shown in Figure 16 where the continuum data were normalised by the ratio of luminosities taken on and off the $\Upsilon(4S)$. Thus, the background in the $\Upsilon(4S)$ sample is mostly from nonresonant $e^+e^- \to q\bar{q}$ events, and, at least outside the enhancement at the B mass, the contribution from $e^+e^- \to \Upsilon(4S)$ resonance decays must be small.

The only remaining background sources which could produce a peak are reflections from other B decay channels. Reflections may occur if particles are used with a wrong mass hypothesis (particle misidentification) or if particles are added to or removed from the true final state (adding or losing particles).

While it is not too surprising that continuum events produce a smooth background, it is not so obvious that the same will be true for background from $B\overline{B}$ pairs. To appreciate the potential difficulty, one should recall the peculiar topology of the signal events. The momentum of the two proton candidates is outside the region where either dE/dx or TOF can provide positive identification. If the tracks were not actually protons, the requirement of consistency with the proton hypothesis would be roughly equivalent to selecting only high-momentum particles. Moreover, after the opening angle cut there would be reasonable acceptance only if the two fast tracks had come from a single B decay. What needs to be demonstrated is that, despite the implicit correlation introduced by the selection criteria, B decays to charm cannot produce a narrow peak at the observed rate.

One simplification is that particle misidentification alone cannot be a source of reflection in this analysis. This is because the mass difference between protons and kaons (pions) is large enough to kinematically separate related final states where kaons (pions) are misidentified as protons. Combinations with a wrong mass assignment do not pass the energy cut, provided everything else is

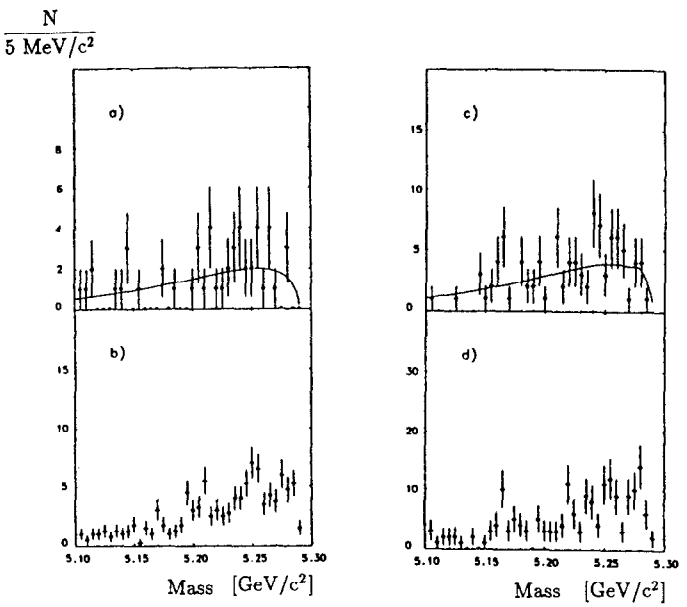

Figure 19. Background studies showing the mass distribution obtained from (a) the continuum data sample, (b) wrong-energy combinations, using $E_B = E_{beam} \pm 300$ MeV/c^2 and ± 500 MeV/c^2, (c) wrong-charge combinations forbidden by baryon number conservation, and (d) Monte Carlo generated $\Upsilon(4S)$ events containing eleven times as many B decays as in the data, all via ($b \to c$) transitions.

interpreted correctly. Similarly, adding or losing a single particle is excluded as a source of reflections as long as only one of these misinterpretations takes place. Again, these combinations are rejected by the energy cut.

As a consequence, only those reflections need be considered where two or more simultaneous mistakes are made (particle misidentification and adding or losing particles) affecting the energy balance in different directions and fulfilling the energy constraint, thereby producing a peak with the expected mass and narrow width.

Nevertheless an explicit search was made among the candidates for known charmed mesons or baryons, or a Λ or K^0_S with an undetected decay vertex. The invariant mass distributions of appropriate subsystems were examined under all possible mass assignments for the candidate tracks. Both Cabibbo-allowed and suppressed channels were considered. Only one candidate was found to be consistent with the hypothesis that it originated from a charmed particle decay. As it appears in the Cabibbo-suppressed decay mode $\Lambda_C \to p\pi^+\pi^-$, it can be readily discarded as an accidental combination.

This leaves correlated backgrounds where particles are taken from both B decays. Two empirical tests have been used to establish the level of contribution for such processes. For the majority of channels, the phase space for a B decay to produce two fast same-charge tracks is roughly equal to that for two oppositely charged. Consider as an example: $B^- \to \pi_1^- \pi^0 D^+$ followed by $D^+ \to K_3^- \pi_2^+$. For this decay the probability that π_1^- and π_2^+ have momentum greater than 1.5 GeV/c (and, hence, are consistent with the proton hypothesis) is actually smaller than that for π_1^- and K_3^-. With this argument in mind, the same analysis has been repeated for combinations forbidden by baryon number conservation: $pp\pi^-$ and $pp\pi^-\pi^-$. The resulting invariant mass distribution (Figure 19c) shows no evidence for an enhancement in the B mass region.

An alternative approach is to conduct the analysis with the B candidates intentionally selected with the wrong energy requirement. This technique leads to the mass plot shown in Figure 19b, if sideband energies of $E_{beam} = \pm 300$ and ± 500 MeV/c^2 are used and averaged. These energies were chosen because the signal itself can reflect into the nearest sidebands. In general the method tends to overestimate the background level, since particle misidentification

alone, or adding or losing a particle alone, can fulfill the energy constraint for the sideband analysis. However, this study reinforces the conclusion that reflections from B decays are not responsible for the observed peak.

These arguments are naturally confirmed in a more general way by Monte Carlo simulation. An event generator was used that incorporates the weak decay $b \to cW^-$, with the c, spectator quark and W^- decay products dressed into hadrons using the Lund model [11]. A total of 2.1×10^6 $\Upsilon(4S)$ decays were generated, passed through a detector simulation and reconstructed with the standard analysis programs. After applying the same cuts as used for the data, the invariant mass distribution shown in Figure 19d was obtained. Although the predicted form of the background peaks toward the B mass, the estimated level of contribution from $\Upsilon(4S)$ backgrounds is less than one event per bin. This result is quite consistent with the observation made earlier that the background rate is saturated by the continuum component alone. All these tests point to the same conclusion: there is no indication for any background source which could be responsible for a peak at the B mass, in particular for a peak with the observed narrow width.

As a check of the validity of the identification of the protons and antiprotons in our sample of events, we compared the ensemble properties of the candidate particles to those of a sample of uniquely identified protons and antiprotons of similar momenta, produced from Λ and $\overline{\Lambda}$ decays respectively. To demonstrate the level at which such a method can distinguish protons and pions, a sample of uniquely identified pions from K^0_S decays was also obtained, again in an appropriate momentum region.

For the shower counters, comparisons were made of both the energy deposited and the lateral shower development. The mean energy seen in the shower counters was 1.10 ± 0.02 GeV and 0.62 ± 0.02 GeV for the identified antiproton and pion samples. The antiprotons from our B candidates had a mean energy deposition of 0.95 ± 0.11. The candidate tracks and the mean pion response are therefore three standard deviations apart.

The mean value of the specific ionization in the drift chamber and of mass computed from the time-of-flight measurements were also determined for each of the ensembles. The mean dE/dx response for pions between 2.0 and 2.5 GeV/c was found to be $6.1 \pm 1.4\%$ higher than the response to the candidate tracks with the same momentum restriction, the difference corresponding to over four standard deviations. TOF provided similar evidence. The ensemble values for the proton and antiprotons in the B candidates are therefore in excellent agreement with expectation, and are clearly distinct from the response to pions.

Thus, the only viable interpretation of our observation is to attribute these decays to $b \to u$ transitions. However, the ARGUS result is at present controversial, despite the internal consistency of this analysis. In a data sample containing 484,000 B decays, CLEO has not observed a signal in either channel using approximately the same selection criteria [49]. This has lead to the upper limits shown in Table 10. For comparison the ARGUS measurements are also shown, with the acceptance for the $\theta_{p\bar{p}}$ cut removed from both the central value and the systematic error.

Table 10. Comparison of ARGUS measurements and CLEO limits for charmless B decays. No acceptance correction for the $p\bar{p}$ opening angle cut is applied.

	$\mathrm{Br}(B^+ \to p\bar{p}\pi^+)$	$\mathrm{Br}(B^0 \to p\bar{p}\pi^+\pi^-)$
ARGUS	$(3.6 \pm 1.0 \pm 0.9) \times 10^{-4}$	$(4.2 \pm 1.4 \pm 1.1) \times 10^{-4}$
CLEO, 1987	$< 1.4 \times 10^{-4}$ (90% CL)	$< 3.8 \times 10^{-4}$ (90% CL)
Average	$(1.0 \pm 0.7) \times 10^{-4}$	$(2.7 \pm 1.4) \times 10^{-4}$

A statistical test of the consistency of these four measurements can be made by computing the weighted average of each pair of measurements and then determining the χ^2 for a fit of the four measurements to the two common branching ratios. For this purpose, the central value of the CLEO results was taken as zero, and the 90% CL upper limits interpreted as equal to 1.64 standard deviations. The weighted averages are listed in Table 10. The χ^2 obtained is 7.2 for two degrees of freedom, which has a probability of almost 3%, equivalent to 2.2σ. Thus, the ARGUS and CLEO observations are discrepant, but not seriously so. A final resolution of this question therefore awaits further data from both experiments.

*Current members of the ARGUS collaboration are: H.Albrecht, P.Böckmann, R.Gläser, G.Harder, A.Krüger, A.Nippe, M.Reidenbach, M.Schäfer, W.Schmidt-Parzefall, H.Schröder, H.D.Schulz, F.Sefkow, J.Spengler, R.Wurth, A.Yagil (DESY), R.D.Appuhn, A.Drescher, C.Hast, D.Kamp, H.Kolanoski, A.Lindner, R.Mankel, H.Scheck, G.Schweda, B.Spaan, A.Walther, D.Wegener (Dortmund), W.Funk, J.C.Gabriel, J.Stiewe, S.Werner (Heidelberg), K.W.Edwards, W.R.Frisken, H.Kapitza, R.Kutschke, D.B.MacFarlane, K.W.McLean, A.W.Nilsson, R.S.Orr, J.A.Parsons, P.M.Patel, J.D.Prentice, S.C.Seidel, J.D.Swain, G.Tsipolitis, T.-S.Yoon (IPP Canada), R.Ammar, S.Ball, D.Coppage, R.Davis, S.Kanekal, N.Kwak (Kansas), T.Ruf, S.Schael, K.R.Schubert, K.Strahl, R.Waldi (Karlsruhe), B.Boštjančič, G.Kernel, P.Križan, E.Križnič, M.Pleško (Ljubljania), H.I.Cronström, L.Jönsson (Lund), A.Babaev, M.Danilov, B.Fominykh, A.Golutvin, I.Gorelov, V.Lubimov, A.Rostovtsev, A.Semenov, S.Semenov, V.Shevchenko, V.Soloshenko, V.Tchistilin, I.Tichomirov, Yu.Zaitsev (ITEP Moscow), R.Childers, C.W.Darden, R.C.Fernholz (South Carolina).

References

[1] ARGUS Collab., H.Albrecht *et al.*, "ARGUS: a universal detector for DORIS II", DESY preprint DESY 88-080, to appear in Nucl. Instr. Meth.

[2] CLEO Collab., M.S.Alam *et al.*, Phys.Rev.Lett. **59** (1987) 22.

[3] ARGUS Collab., D.B.MacFarlane, Proc. of the 15^{th} SLAC Summer Institute on Particle Physics, SLAC Report 328 (1987) 411.

[4] ARGUS Collab., H.Albrecht *et al.*, Phys.Lett. **210B** (1988) 263.

[5] ARGUS Collab., H.Scheck, Ph.D. Thesis, University of Dortmund, 1988.

[6] ARGUS Collab., A.Golutvin, Ph.D. Thesis, Institute of Theoretical and Experimental Physics, Moscow, 1987.

[7] ARGUS Collab., S.Weseler, Ph.D. Thesis, University of Dortmund, 1986.

[8] G.C.Fox and S.Wolfram, Phys.Lett. **82B** (1979) 139.

[9] ARGUS Collab., H.Albrecht *et al.*, Phys.Lett. **192B** (1987) 245.

[10] G.Altarelli, N.Cabibbo and L.Maiani, Nucl.Phys. **B100** (1975) 313.

[11] B.Anderson *et al.*, Phys.Rep. **97** (1983) 31.

[12] B.Gittelman and S.Stone, "B meson decay", Cornell preprint CLNS 87/81 (1987).

[13] ARGUS Collab., H.Albrecht *et al.*, Phys.Lett. **185B** (1987) 218.

[14] CLEO Collab., S.Behrends *et al.*, Phys.Rev.Lett. **50** (1983) 881. Most B candidates reported here were not fully reconstructed, resulting in shifted masses and incorrect branching ratios.

[15] CLEO Collab., C.Bebek *et al.*, Phys.Rev. **D36** (1987) 1289.

[16] W.Schmidt-Parzefall, Proc. of the International Symposium on Lepton and Photon Interactions at High Energy, Hamburg (1987) 257.

[17] ARGUS Collab., A.Drescher *et al.*, Nucl.Instr.Meth. **A249** (1986) 277.

[18] MARK III Collab., J.Adler *et al.*, Phys.Rev.Lett. **60** (1988) 89.

[19] M.Bauer, B.Stech and M.Wirbel, Z.Phys. **C34** (1987) 103.

[20] G.Eilam and J.P.Leveille, Phys.Rev.Lett. **44** (1980) 1648.

[21] B.Guberina, R.D.Peccei, and R.Rückl, Phys.Lett. **90B** (1980) 169.

[22] G.Eilam, Phys.Rev.Lett. **49** (1982) 1478.

[23] M.B.Gavela *et al.*, Phys.Lett. **154B** (1985) 425.

[24] P.J.O'Donnell, Phys.Lett. **175B** (1986) 369.

[25] N.G.Deshpande *et al.*, Phys.Rev.Lett. **59** (1987) 183, N.G.Deshpande, P.Lo and J.Trampetic, Z.Phys. **C40** (1988) 369.

[26] S.Bertolini *et al.*, Phys.Rev.Lett. **59** (1987) 180.

[27] T.Altomari, Phys.Rev. **D59** (1988) 677.

[28] L.L.Chau and H.-Y.Cheng, Phys.Rev.Lett. **59** (1987) 958.

[29] W.-S.Hou, A.Soni and H.Steger, Phys.Rev.Lett. **59** (1987) 1521.

[30] J.L.Hewett, Phys.Lett. **193B** (1987) 327.

[31] B.Grinstein and M.Wise, Phys.Lett. **201B** (1988) 274;
Phys.Lett. **202B** (1988) 138.

[32] F.Gilman and J.S.Hagelin, Phys.Lett. **126B** (1983) 111; Phys.Lett. **133B** (1984) 443.

[33] L.L.Chau *et al.*, Phys.Rev. **D32** (1985) 1837.

[34] ARGUS Collab., H. Albrecht *et al.*, Phys.Lett. **210B** (1988) 258.

[35] ARGUS Collab., H.Gennow, "SIMARG, A program to simulate ARGUS", DESY Internal Report, DESY F15-85-02 (1985).

[36] CLEO Collab., P.Avery *et al.*, Phys.Lett. **183B** (1987) 429.

[37] ARGUS Collab., H.Albrecht *et al.*, Phys.Lett. **197B** (1987) 452.

[38] A.Ali, J.G.Körner, G.Kramer and J.Willrodt, Z.Phys. **C1** (1979) 269.

[39] M.Wirbel, B.Stech and M.Bauer, Z.Phys. **C29** (1985) 637.

[40] S.Chao *et al.*, Phys.Rev. **D31** (1985) 1756.

[41] F.Schöberl and H.Pietschmann, Europhys.Lett. **2** (1986) 583.

[42] B.Grinstein, M.B.Wise and N.Isgur, Phys.Rev.Lett. **56** (1986) 298;
Phys.Lett. **197B** (1987) 249;
"Quark model predictions for the electron energy spectrum in semileptonic D and B decays", Caltech preprint CALT-68-1311 (1986).

[43] T.Altomari and L.Wolfenstein, Phys.Rev.Lett. **58** (1987) 1583;
Phys.Rev. **D37** (1988) 681;
"Calculation of the rates for semileptonic B decays", Carnegie-Mellon preprint CMU-HEP86-17.

[44] J.G.Körner and G.A.Schuler, Z.Phys. **C38** (1988) 511.

[45] M.A.Shifman and M.B.Voloshin, "On the production of D and D^* mesons in B meson decays", ITEP (Moscow) preprint ITEP-87-64 (1987).

[46] CUSB Collab., C.Klopfenstein *et al.*, Phys.Lett. **130B** (1983) 444;
CLEO Collab., A.Chen *et al.*, Phys.Rev.Lett. **52** (1984) 1084;
CUSB Collab., G.Levman *et al.*, Phys.Lett. **141B** (1984) 271;
CLEO Collab., S.Behrends *et al.*, Phys.Rev.Lett. **59** (1987) 407;
ARGUS Collab., K.R.Schubert, Proc. XXIIIrd Int. Conf. on High Energy Physics, Berkeley (1986);
Crystal Ball Collab., K.Wachs *et al.*, "The electron spectrum from B meson decays", DESY preprint DESY 88-111 (1988).

[47] ARGUS Collab., H.Albrecht *et al.*, Phys.Lett. **209B** (1988) 119.

[48] CLEO Collab., C.Bebek *et al.*, Phys.Rev. **D36** (1987) 1289.

[49] CLEO Collab., N.Katayama, these proceedings.

EVIDENCE FOR $D_s^+ \to e^+X$ †

DALE PITMAN

Representing the Mark III Collaboration ‡

Stanford Linear Accelerator Center

Stanford University, Stanford, California 94309

Abstract

We have searched for the inclusive reaction $D_s^\pm \to e^\pm X$ using a tagged sample of 73 $D_s^\pm$ produced in the reaction $e^+e^- \to D_s^\pm D_s^{*\mp}$. The data were collected by the Mark III experiment at SPEAR at a center-of-mass energy of 4.14 GeV. The tagged sample consists of the decays $D_s^+ \to \phi\pi^+$, $D_s^+ \to \overline{K^{*}}^0 K^+$ and $D_s^+ \to K_s^0 K^+$. We determine $B(D_s^+ \to e^+X) = 0.09^{+0.09}_{-0.07} \pm 0.02$.

† Work supported in part by the Department of Energy, contract numbers DE-AC03-76SF00515, DE-AC02-76ER01195, DE-AC03-81ER40050, DE-AM03-76SF00034, and by the National Science Foundation.

‡ **Stanford Linear Acccelerator Center**: J. Adler, T. Bolton, J.-C. Brient, K. Bunnell, R. Cassell, D. Coward, K. Einsweiler, C. Grab, P. Kim, R. Mozley, A. Odian, D. Pitman, R. Schindler, W. Stockhausen, W. Toki, F. Villa, S. Wasserbaech, D. Wisinski. **California Institute of Technology**: D. Coffman, F. DeJongh, G. Dubois, G. Eigen, J. Hauser, D. Hitlin, C. Matthews, A. Mincer, J. Richman, W. Wisniewski, Y. Zhu. **University of Illinois at Urbana-Champaign**: J. Becker, G. Blaylock, B. Eisenstein, T. Freese, G. Gladding, J. Izen, S. Plaetzer, C. Simopoulos, A. Spadafora, I. Stockdale, B. Tripsas, A. Wattenberg. **University of Iowa at Iowa City**: U. Mallik. **University of California at Santa Cruz**: M. Burchell, D. Dorfan, J. Drinkard, C. Gatto, R. Hamilton, C. Heusch, L. Köpke, W. Lockman, R. Partridge, H. Sadrozinski, M. Scarlatella, T. Schalk, A. Seiden, A. Weinstein, S. Weseler, R. Xu. **University of Washington**: J. Brown, T. Burnett, V. Cook, A. Duncan, A. Li, R. Mir, P. Mockett, B. Nemati, L. Parrish, H. Willutzki.

INTRODUCTION

Though the existence of the charmed-strange D_s^+ meson (formerly the F^+)[1] has been known for close to a decade, fewer than 30% of its decay modes have been observed. In fact, only the branching fractions of the various modes (which number a half-dozen or so) relative to the decay $D_s^+ \to \phi\pi^+$ have been well-measured.[2-5] Absolute branching ratios are obtained only through an estimate of the ratio of D_s^+ to total charm production. Furthermore, no observation of the leptonic decay of the D_s^+ has been made to date.

The Mark III experiment recently took data at SPEAR at a center-of-mass energy of 4.14 GeV. At this energy, the D_s^+ is produced in association with its vector meson partner, the D_s^{*-}; the production rate of $D_s^+D_s^-$ appears to be suppressed[4] at this center-of-mass energy. Several hadronic modes have already been studied. This analysis now addresses the subject of the semileptonic decays, and in particular, the inclusive semi-electronic branching ratio, $D_s^+ \to e^+X$.

While the spectator decay mechanism is considered too naive a picture of hadronic charm decay, which may be affected by final state interactions, the same does not apply for the semileptonic decay. In fact, the measured partial widths $\Gamma(D^0 \to e^+X)$ and $\Gamma(D^+ \to e^+X)$ are approximately equal.[6] The semileptonic spectator decays of the D_s^+, D^0, and D^+ are shown in Fig. 1. Assuming that the partial electronic width of the D_s^+ is approximately equal to that of the D^0 or D^+, the inclusive electronic branching fraction $B(D_s^+ \to e^+X)$ can then be estimated:[7] it is $\approx 8\%$.

THE TAGGED SAMPLE

Three channels were used to tag the $D_s^+D_s^{*-}$ sample: $D_s^+ \to \phi\pi^+$, $K_S^0K^+$, and $\overline{K^{*0}}K^+$. The Mark III detector has been described in detail elsewhere.[8] Particle identification techniques, briefly summarized below, are similar for the three decay modes. Invariant mass calculations and kinematic fits have been used to extract the tagged signals, depending upon the background contamination in a given mode. Throughout the analysis, the goal has been to maximize the signal-to-noise without losing too much of the data.

Kaons are identified primarily using the TOF system, which resolves kaons and pions at 3 σ for $p < 1$ GeV/c. For momenta less than 650 MeV/c, dE/dx information from the drift chamber can be used when TOF data is lacking. Electrons are identified primarily using a lead-proportional chamber gas sampling calorimeter. Charged tracks are also required to pass reasonably close to the reconstructed vertex, within 0.015 m for pions and within 0.030 m for kaons. (This requirement is lifted in the case of detached vertices such as K_S^0.)

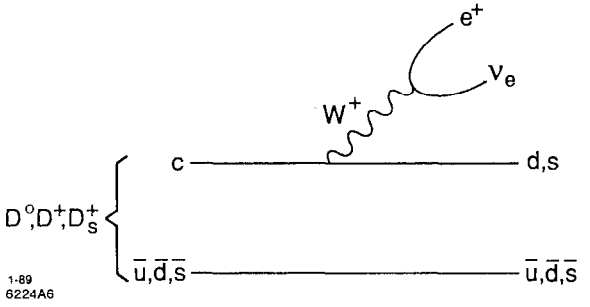

Figure 1: The spectator picture of semileptonic decay of the D^0, D^+, and D_s^+ showing the expected (right-sign) charge of the electron relative to the charm of the parent particle.

$D_s^+ \to \phi\pi^+$

Invariant mass combinations of K^+K^- pairs are formed and those which fall within ± 10 MeV/c^2 of the nominal ϕ mass are retained. Mass combinations of the ϕ with all $\pi^\pm$ in the event are then calculated. Figure 2 shows $M_{\phi\pi}$ vs. the recoil mass calculated using the constraint on the total event energy (4.14 GeV). Events which satisfy $1.92 < M_{\phi\pi} < 2.02$ GeV/c^2 and $2.04 < M_{recoil} < 2.18$ GeV/c^2 are selected for the tagged sample. There are 42 such events. The estimated number of signal tagged events is 36 ± 3.

$D_s^+ \to K^{*0}K^+$

For this channel, particle identification is done using only TOF. A 1-C fit is performed with the recoil mass constrained to equal the value of the D_s^* mass. Additional criteria are applied: that the 1-C fit probability be ≥ 0.10; that the $K\pi$ mass be within 60 MeV/c^2 of the nominal K^* mass; and that the angle of the K in the K^* rest frame, $|\cos\theta_{K^*}| \geq 0.3$.

Figure 3 shows the K^*K mass after the constrained fit and the above criteria are applied. This channel is particularly plagued with D-related backgrounds. To maximize the signal-to-noise ratio, those events which satisfy $1.96 \leq M_{K^*K} \leq 1.98$ GeV/c^2 are selected for the tagged sample. This yields 24 events, of which 18 ± 3 are estimated to be signal.

$D_s^+ \to K^0K^+$

A 2-C fit is performed using the K^0 mass and the recoil D_s^* mass as constraints. For the tagged sample, events with a fit probability ≥ 0.10 and $1.92 \leq M_{K^0K} \leq 2.02$ Gev/c^2 are retained. The reconstructed decay length of the K^0 is required to be greater than zero. Figure 4 shows M_{K^0K} after these selection criteria are applied. There are 27 events which satisfy this criteria; the estimated number of signal events is 19 ± 3.

THE RECOIL SYSTEM

Tracks which pass within 0.015 m of the vertex and which have not been used in the "tag" are examined for possible electron identification. For tracks with momenta less than 300 MeV/c, the identification is made using TOF. For tracks with momenta greater than 300 MeV/c, a recursive partitioning algorithm[9] is employed, which makes use of information from the TOF and the electromagnetic calorimeter. Kaons identified using TOF are first excluded. In addition, to eliminate electrons due to photon conversions, tracks which have an opening angle $\leq 14°$ with any other oppositely-charged track are also excluded. The remaining recoil tracks are then assigned one of three identifications: electron, pion or ambiguous identification.

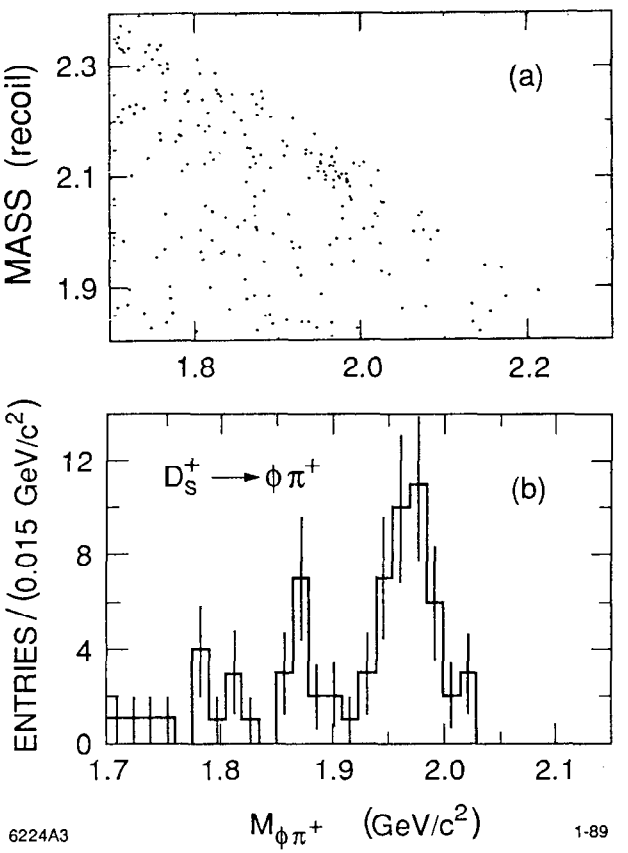

Figure 2: (a) The calculated M_{recoil} vs. $M_{\phi\pi}$, and (b) $M_{\phi\pi}$ when M_{recoil} is required to lie in the range $2.04 - 2.18$ GeV/c^2.

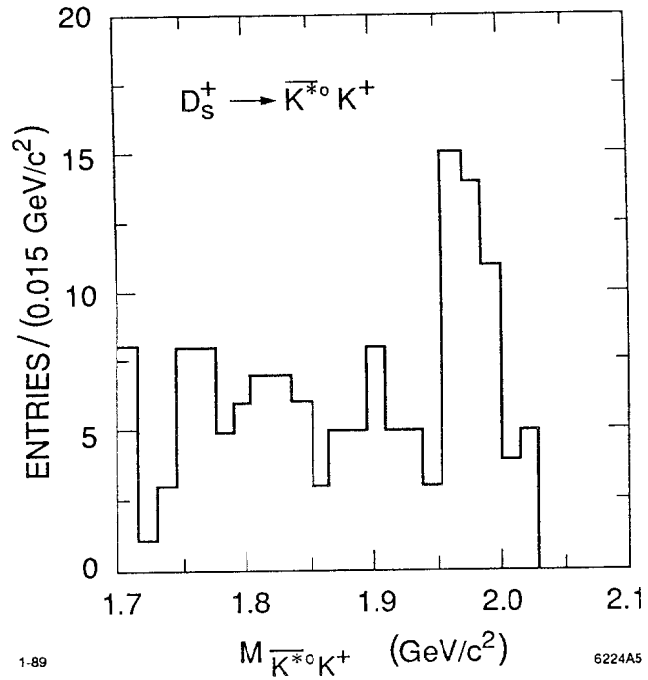

Figure 3: $M_{K^{*}K}$ following a 1-C fit and the selection criteria described in the text.

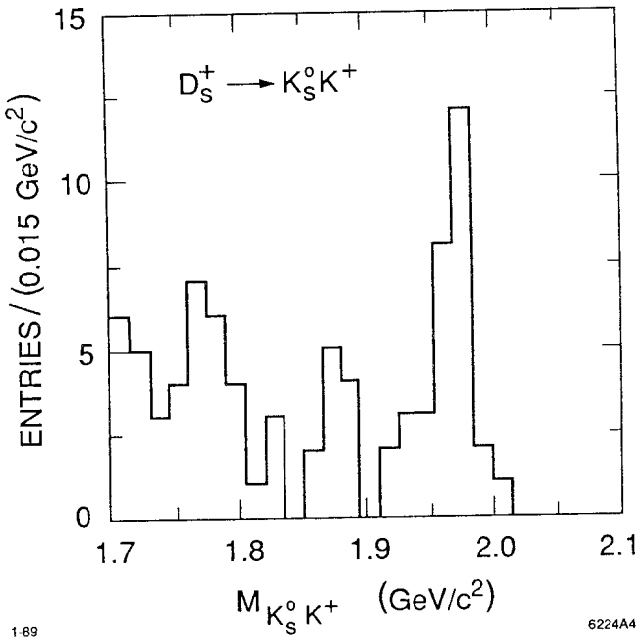

Figure 4: M_{K^oK} following a 2-C fit and the selection criteria described in the text.

The numbers of electrons and pions found for each of the tagged channels are shown in Table 1. The probability for misidentification of tracks is momentum-dependent. For the purposes of the branching ratio calculation, we have used seven momentum bins. Table 2 shows the numbers of electrons and pions found in each momentum bin.

Table 1. The tagged D_s channels and the total numbers of right- and wrong-sign electrons and pions found in the recoil, where, for example, n_e^R denotes the number of right-sign electrons.

Channel	Tagged Events	Signal Events	n_e^R	n_e^W	n_π^R	n_π^W
$\phi\pi$	42	36 ± 4	4	1	32	14
K^0K	27	19 ± 3	2	1	32	16
K^*K	24	18 ± 3	3	1	18	6
Totals	93	73 ± 10	9	3	82	36

Table 2. Momentum distribution of observed electrons and pions in the recoil against a D_s tag.

	< 0.3 GeV/c	0.3-0.4 GeV/c	0.4-0.5 GeV/c	0.5-0.6 GeV/c	0.6-0.8 GeV/c	0.8-1.0 GeV/c	> 1.0 GeV/c
n_e^R	5	2	1	1	0	0	0
n_e^W	1	1	0	0	1	0	0
n_π^R	30	11	14	8	12	4	3
n_π^W	15	6	8	4	3	0	0

The numbers of right- and wrong-sign electrons were also tabulated for mass sideband regions. The sideband for each channel was the mass range $1.72 - 1.92$ GeV/c^2. The region above the D_s mass contains insufficient numbers of events to be of use. The masses for those events, both in the signal and sideband regions, which contain an electron in the recoil are shown in Fig. 5.

BRANCHING RATIO

The number of observed electrons has two components: electrons which have been correctly identified and pions which have been misidentified. The probabilities for identification and misidentification are momentum-dependent. There

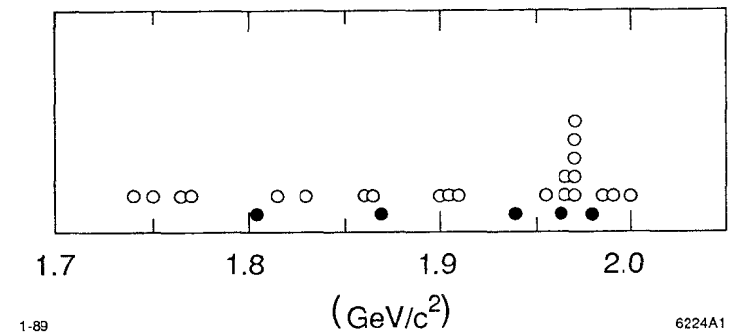

Figure 5: The masses for tagged events, both in the D_s^+ signal and sideband regions, which contain an electron of either right or wrong sign in the recoil.

are four identification/misidentification probabilities for a given momentum bin. These we call: $P_{e\to e}$, $P_{e\to\pi}$, $P_{\pi\to\pi}$, and $P_{\pi\to e}$, where for example, $P_{e\to\pi}$ is the probability that an electron is called a pion. Thus for each momentum bin, where we have *observed* pions and electrons (n_π and n_e), we have the *true* (or produced) numbers of pions and electrons ($\tilde{n}_\pi$ and $\tilde{n}_e$):

$$\begin{aligned} n_e^R &= P_{e\to e}\,\tilde{n}_e^R + P_{\pi\to e}\,\tilde{n}_\pi^R \quad , \\ n_e^W &= P_{e\to e}\,\tilde{n}_e^W + P_{\pi\to e}\,\tilde{n}_\pi^W \quad , \\ n_\pi^R &= P_{\pi\to\pi}\,\tilde{n}_\pi^R + P_{e\to\pi}\,\tilde{n}_e^R \quad , \\ n_\pi^W &= P_{\pi\to\pi}\,\tilde{n}_\pi^W + P_{e\to\pi}\,\tilde{n}_e^W \quad , \end{aligned}$$

where the superscripts denote right- and wrong-sign. The total number of right-sign electrons is assumed to be due to semileptonic D_s decay and to charge-symmetric background, such as photon conversions. The number of wrong-sign electrons is assumed to be due solely to charge-symmetric background. The effects of D semileptonic background have been ignored. We estimate the number of semileptonic decays due to misidentified D decays to be at most one (right-sign) event. Of the three tagged channels, only the $\overline{K^*}^0K^\pm$ channel suffers substantial background contamination: hence the more stringent requirement on the invariant tagged mass. The branching ratio is:

$$B(D_s \to eX) = \frac{\sum(\tilde{n}_e^R - \tilde{n}_e^W)/\epsilon}{n_{tags}}$$

where ϵ, the momentum-dependent efficiency, is a product of the geometric acceptance (0.80 ± 0.05) and the ability to classify a track as a pion or electron. The numerator is summed over the seven momentum bins.

The probability to correctly classify an electron ranges from 0.78 to 0.90. The probability to misclassify a pion as an electron varies between 0.03 and 0.06.

Using the numbers of right- and wrong-sign electrons and pions given in Table 2, and the momentum-dependent identification probabilities, we obtain $B(D_s^+ \to e^+X) = 0.09$.

ERROR CALCULATIONS

In general, the numbers of produced electrons and pions arise from parent distributions:

$$\tilde{N}_e^R \ , \ \tilde{N}_e^W \ , \ \tilde{N}_\pi^R \ , \text{ and } \tilde{N}_\pi^W \ .$$

Likewise, the number of tags can be considered to arise from a parent distribution, N_{tags}. We then construct a probability function using Poisson statistics for the numbers of electrons and Gaussian statistics for the numbers of pions. (Again, n_e^R is the number of observed right-sign electrons.) We have averaged over the momentum bins. The number of tags is treated like a Gaussian, with σ being equal to the error on the number of tags, which is due to background fluctuation. We have:

$$\begin{aligned} P_1 &= \frac{e^{-(P_{e\to e}\,\tilde{N}_e^R + P_{\pi\to e}\,\tilde{N}_\pi^R)} \cdot (P_{e\to e}\,\tilde{N}_e^R + P_{\pi\to e}\,\tilde{N}_\pi^R)^{n_e^R}}{n_e^R!} \\ P_2 &= \frac{e^{-(P_{e\to e}\,\tilde{N}_e^W + P_{\pi\to e}\,\tilde{N}_\pi^W)} \cdot (P_{e\to e}\,\tilde{N}_e^W + P_{\pi\to e}\,\tilde{N}_\pi^W)^{n_e^W}}{n_e^W!} \\ G_1 &= \frac{1}{\sqrt{2\pi n_\pi^R}} e^{-((P_{\pi\to\pi}\,\tilde{N}_\pi^R + P_{e\to\pi}\,\tilde{N}_e^R) - n_\pi^R)^2/2n_\pi^R} \\ G_2 &= \frac{1}{\sqrt{2\pi n_\pi^W}} e^{-((P_{\pi\to\pi}\,\tilde{N}_\pi^W + P_{e\to\pi}\,\tilde{N}_e^W) - n_\pi^W)^2/2n_\pi^W} \\ G_3 &= \frac{1}{\sqrt{2\pi}\Delta n_{tags}} e^{-(N_{tags} - n_{tags})^2/2n_{tags}} \end{aligned}$$

We then construct the negative log-likelihood function:

$$-\ln\mathcal{L} = -\ln(P_1 \cdot P_2 \cdot G_1 \cdot G_2 \cdot G_3) \quad .$$

The five parameters, N_e^R, N_e^W, N_π^R, N_π^W, and N_{tags}, are varied. Using MINUIT, the minimum of $-\ln\mathcal{L}$ was found for each value of the branching ratio. This is plotted in Fig. 6.

The 1 σ errors on the branching ratio are obtained by moving along the vertical axis by 0.5 units. This gives:

$$B(D_s^+ \to e^+X) = 0.09^{+0.09}_{-0.07} \quad .$$

The systematic error, ± 0.02, arises from the error on the geometric acceptance and the errors on the classification probabilities. The latter are determined from a study of electrons from radiative Bhabha events and charged pions from K^0 decays.

DISCUSSION

We have obtained the first evidence of semileptonic decay of the D_s^+ meson, using a sample of 73 tagged hadronic events. Though the result is not statistically

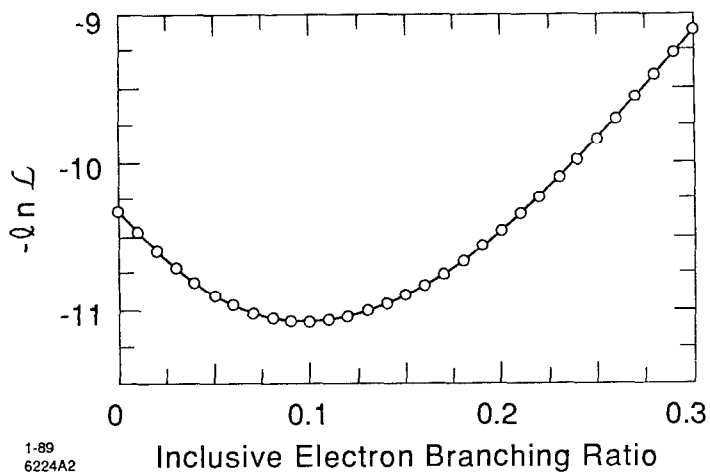

Figure 6: The likelihood function $\mathcal{L}$ shown vs. the branching ratio, $B(D^+ \to e^+X)$.

compelling, it also represents the first measurement of an absolute branching ratio of the D_s^+, whose hadronic decays have previously been measured in terms of relative branching ratios. The value of $B(D_s^+ \to e^+X)$ agrees with that predicted assuming equal semileptonic partial decay widths for the D^0, D^+, and D_s^+. This may lend support to the theory that interference effects play a significant role in hadronic charm decay, leading to the differing charm lifetimes, rather than to suggestions of the importance of annihilation/exchange diagrams.

ACKNOWLEDGEMENTS

The efforts of the SPEAR staff are gratefully acknowledged. The author also wishes to thank the organizers of the very pleasant SLAC Summer Institute.

REFERENCES

1. Throughout this paper, reference to a charged state implies the charge conjugate state as well.
2. H. Albrecht *et al., Phys. Lett.* **153B** (1985) 343, H. Albrecht *et al., Phys. Lett.* **179B** (1986) 393, and H. Albrecht *et al., Phys. Lett.* **195B** (1987) 102.
3. J. C. Anjos *et al., Phys. Rev. Lett.* **60** (1988) 897.
4. G. Blaylock *et al., Phys. Rev. Lett.* **58** (1987) 2171.
5. G. Wormser *et al., Phys. Rev. Lett.* **61** (1988) 1057.
6. These are calculated using the inclusive electronic branching fractions for the D^+ and D^0 of R. M. Baltrusaitis *et al., Phys. Rev. Lett.* **54** (1985) 1976, and the values of the D^0 and D^+ lifetimes of J. C. Anjos *et al., Phys. Rev. Lett.* **58** (1987) 311.
7. The estimate uses the value of the D_s^+ lifetime of J. C. Anjos *et al., Phys. Rev. Lett.* **58** (1987) 1818, and the average of the semi-electronic partial widths for the D^+ and D^0.
8. D. Bernstein *et al., Nucl. Instr. Meth.* **226** (1984) 301.
9. D. M. Coffman, Ph.D. thesis, California Institute of Technology, 1986 (unpublished).

RECENT RESULTS FROM TRISTAN

Junpei Shirai

KEK, National Laboratory for High Energy Physics
1-1, Oho, Tsukuba-shi, Ibaraki-ken, 305 JAPAN

Abstract

Recent results from four experiments, VENUS, TOPAZ, AMY and SHIP at the e^+e^- colliding beam accelerator TRISTAN at KEK, Japan are presented. Each detector has accumulated more than $11pb^{-1}$ at center-of-mass energies between 50 and 56 GeV. For hadronic events the measured values of R-ratio indicate no signal of the top quark. Analyses for other new particle searches extended the mass limits on sequential heavy leptons, excited leptons and magnetic monopoles. The differential cross sections for processes $e^+e^- \to e^+e^-$ and $e^+e^- \to \gamma\gamma$ are in good agreement with QED, and the forward-backward charge asymmetries for reactions $e^+e^- \to \mu^+\mu^-$ and $e^+e^- \to \tau^+\tau^-$ show good agreement with the standard electroweak theory.

Talk presented at the 16th SLAC Summer Institute on Particle Physics,
Stanford, California, July 18–29, 1988.

1 Introduction

Since the first Bhabha event was observed by VENUS at $\sqrt{s}$= 48 GeV on the 19th of November 1986, stable machine operation and increasing beam energy enabled the four TRISTAN experiments VENUS, TOPAZ, AMY and SHIP to do well. All the experiments have accumulated total integrated luminosities of more than $11pb^{-1}$ at $\sqrt{s}$ of 50, 52, 55 and 56 GeV. Figure 1 shows the integrated luminosity per day accumulated by VENUS. During this spring run at $\sqrt{s}$ = 56 GeV, the total beam current reached 13.6 mA and the luminosity reached a level of $300nb^{-1}$/day. The machine operation and integrated luminosities are summarized in Table 1. At the time of this conference the experiments are running at $\sqrt{s}$= 57 GeV.

In this paper results from the data of 50 to 56 GeV are reported. The contents are arranged in the following way: A brief explanation of the major detectors (VENUS, TOPAZ and AMY) is made in section 2. Section 3 describes the top quark search based on the R-ratio, event-shape analysis and the study of inclusive lepton events. Results of other new particle searches such as sequential heavy leptons and excited leptons (e^* and μ^*) are described in section 4, together with a magnetic monopole search which was done by a special purpose detector SHIP. Tests of QED by $e^+e^- \to e^+e^-$ and $e^+e^- \to \gamma\gamma$ processes and those of electroweak theory by $e^+e^- \to \mu^+\mu^-$ and $e^+e^- \to \tau^+\tau^-$ processes are given in sections 5 and 6. Finally a summary and a brief description of future plans are given.

2 Detectors

Since detailed descriptions of the three major detectors VENUS, TOPAZ and AMY are given elsewhere [1], it is sufficient to give the features and performance of major components. They are all general purpose detectors with tracking devices in a magnetic field supplied by a superconducting solenoid and electromagnetic shower counters and a muon chamber system which is placed outside the return yoke. Table 2 summarizes the characteristics of the detectors.

VENUS is characterized by uniform and hermetic calorimeters (barrel lead glass and endcap liquid argon counters) with good energy resolution. The acceptance is greater than 99% of 4π. The components of the calorimeters (lead glass blocks of barrel and lead plate modules of endcap calorimeters) point to the interaction region in order to make shower reconstruction easy. Figure 2(a)

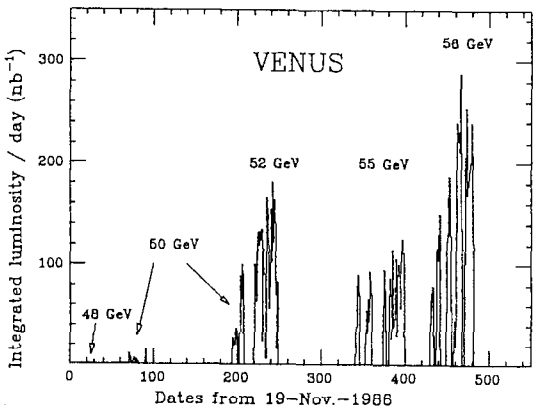

Figure 1. Integrated luminosity per day from Nov.1986 to Mar.1988 measured by VENUS.

Table 1. Machine operation and integrated luminosities.

Period	$\sqrt{s}$ (GeV)	Oper.Time (h)		Integrated Luminosities (pb^{-1})			
		tot.	exp.	VENUS	TOPAZ	AMY	SHIP
1986 Dec	48	182	104				
1987 Jan-Feb	50	596	281	} 0.7	0.4	0.6	0.8
1987 May-Jun	50	737	368				
1987 Jun-Jul	52	707	530	2.9	3.6	4.0	4.0
1987 Oct-Dec	55	1310	724	2.4	2.9	3.3	4.0
1988 Jan-Mar	56	1170	650	5.4	5.6	6.0	7.5
			total	11.4	12.5	13.9	16.3
1988 Jun	56.5			0.9	0.9	1.0	–
1988 Jul	57			3.7	3.7	4.4	4.5

shows a mass spectrum of two clusters in hadronic events measured by the barrel lead glass calorimeter. A clear neutral pion peak is seen with a r.m.s width of 17 MeV. In Fig. 2(b) the energy cluster spectrum is shown for endcap Bhabha events at $\sqrt{s}$= 56 GeV measured by the liquid argon counter. The resolution σ_E/E is 3.5 % at 27.5 GeV. The momentum resolution σ_{p_t}/p_t of the central drift chamber in a magnetic field of 7.5kG is about $0.008p_t$ which is shown in Fig. 2(c).

TOPAZ is characterized by a powerful central tracking device, a time projection chamber (TPC) [2], in a magnetic field of 1.0 tesla for three-dimensional tracking and particle identification by the dE/dx method. Figure 3(a) and (b) show the performance of the TPC for real data. Clear separation of electron, pion, kaon and proton in momentum up to a few GeV/c is seen in Fig. 3(a) and the effective mass of $\pi^+\pi^-$ in multihadronic events is presented in Fig. 3(b) in which a clear K^0_s peak is seen.

AMY is a compact detector with a high magnetic field of 3 tesla. The momentum resolution σ_{p_t}/p_t of the central tracking chamber is about $0.007p_t$. The effective mass of $\pi^+\pi^-$ in hadronic events is shown in Fig. 4(a) in which a sharp K^0_s peak with a r.m.s width of 8 MeV/c^2 is seen. The barrel calorimeter is placed inside the superconducting coil. The calorimeter is made up of alternating layers of lead and gas proportional tubes with angular resolution of 5 mrad to obtain good identification capability of electrons or gammas in the high multiplicity hadronic events. Figure 4(b) shows the shower spread of 26 GeV electrons and that of neutral clusters with energies between 8 and 15 GeV in hadronic events. Considering that the opening angle of two gammas from π^0 with an energy of 10 GeV is typically two degrees, it is clear that a single gamma can be distinguished from π^0 with an energy up to 10 GeV. The compactness of the detector enhances muon identification capability by reducing the background muons from pion and kaon decays. Figure 4(c) shows the distance between the hit position of the muon chamber and the extrapolated position of the track with the momentum greater than 2.5 GeV/c by the central drift chamber for inclusive muon events together with μ-pair events produced from two-photon process $e^+e^- \to e^+e^-\mu^+\mu^-$. The two distributions are in good agreement with each other except for some backgrounds in the distance greater than 50 cm. Figure 4(d) shows the detection efficiency for primary muons and fraction of the background estimated by a Monte Carlo as a function of the

Table 2. Characteristics of AMY, TOPAZ and VENUS detector.

	AMY	TOPAZ	VENUS
Magnetic Field	30kG	10kG	7.5kG
Central Tracker	MWDC	TPC	MWDC
coverage	$35-145°$	$30-150°$	$30-150°$
$\sigma_{p_t}/p_t(\%)$	$\simeq 0.7p_t$	$\sqrt{(1.5p_t)^2+(1.6)^2}$	$\sqrt{(0.79p_t)^2+(1.29)^2}$
dE/dx resol.	–	4.6%	–
E.M.Calorimeter			
Barrel part	lead-PWC	lead glass	lead glass
coverage	$43-137°$	$32-148°$	$37-143°$
readout	strips	4300ch	5160ch
$\sigma_E/E(\%)$	$\frac{21}{\sqrt{E}}+6$	$\sqrt{(\frac{8}{\sqrt{E}})^2+(4.2)^2}$	$3.7_{@27.5GeV}$
Endcap part	lead-scint.PWC	lead-PWC	lead-liq.Ar
coverage	$15-26.5°$	$12-32°$	$8-38°$
readout	strips	towers	towers
$\sigma_E/E(\%)_{@27.5GeV}$	13	6.7	3.5
Muon Detector	drift tube	drift tube	drift tube
layers	4	8	8
coverage(barrel)	$42-138°$	$49-131°$	$48-132°$
coverage(endcap)	–	–	$22-43°$
iron thickness	9λ	5λ	5λ

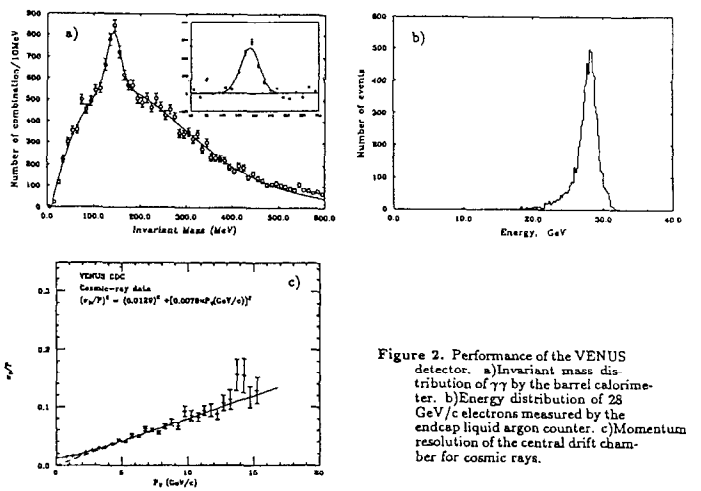

Figure 2. Performance of the VENUS detector. a)Invariant mass distribution of $\gamma\gamma$ by the barrel calorimeter. b)Energy distribution of 28 GeV/c electrons measured by the endcap liquid argon counter. c)Momentum resolution of the central drift chamber for cosmic rays.

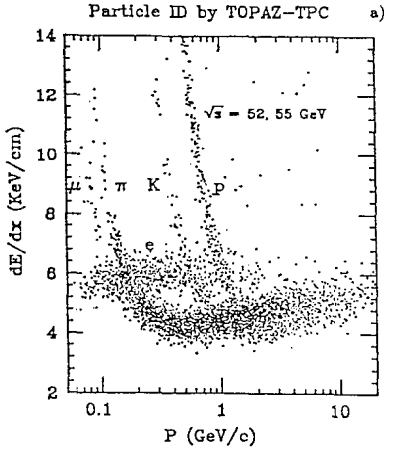

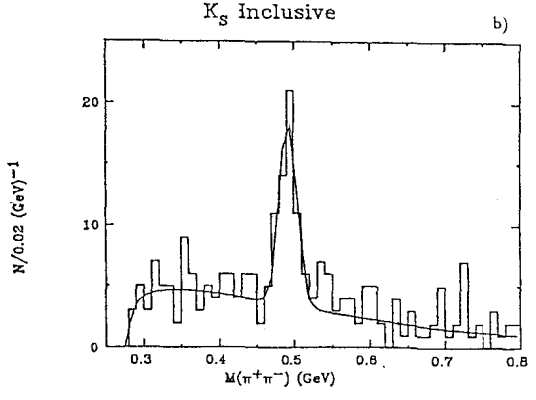

Figure 3. Performance of the TOPAZ TPC. a) dE/dx versus momentum. b) Invariant mass distribution of $\pi^+\pi^-$ in hadronic events.

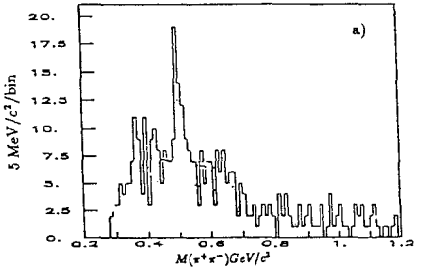

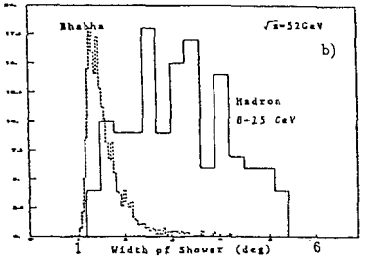

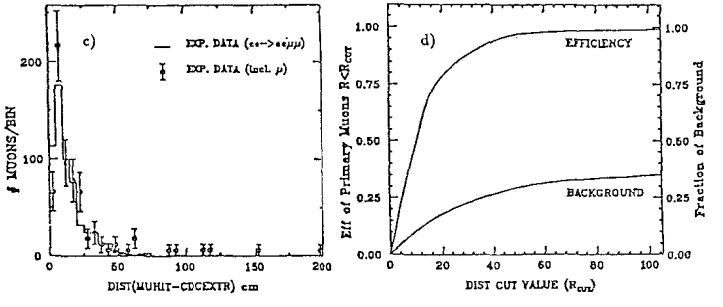

Figure 4. Performance of the AMY detector. a) Invariant mass distribution of charged particles in hadronic events by the central chamber. b) Shower width ($\Delta\theta$) of neutral clusters ($\geq 8GeV$) in hadronic events (solid line) and electrons (26 GeV/c, dotted line). c) Distance between the hit position of the muon detector and the extrapolated track by the central tracking chamber for inclusive muon events (dots with error bar) and two-photon events (histogram). d) Efficiency and fraction of the backgrounds for the muon detector.

distance between the hit and extrapolated points at the muon chamber. With the cut at 40 cm, the detection efficiency is 90% and the background level is about 25%. This corresponds to a hadron rejection ratio of 1/500.

3 Search for Heavy Quark Flavors

One of the most interesting physics objects at TRISTAN is to search for heavy quarks especially for the top quark. The search was made by three types of analysis for hadronic events; measurement of the R-ratio, event-shape analysis and study of inclusive lepton production.

3.1 R-ratio

According to the standard model [3] the ratio R, the total production cross section of hadrons divided by the lowest order QED cross section of μ pair production, is expressed by (including the quark mass effect and the QCD correction terms up to α_s^2 [4]),

$$R = 3\sum_f [\frac{1}{2}\beta(3-\beta^2)\left\{1 + C_1^V\frac{\alpha_s}{\pi} + C_2^V(\frac{\alpha_s}{\pi})^2\right\}C_{VV}^f$$

$$+\beta^3\left\{1 + C_1^A\frac{\alpha_s}{\pi} + C_2^A(\frac{\alpha_s}{\pi})^2\right\}C_{AA}^f],$$

where f indicates flavor of quarks, β is the quark velocity and C_{VV}^f and C_{AA}^f are functions of the electric charge Q_f of the quark with flavor f and the vector and axial vector coupling constants (v_e, v_f, a_e, a_f), respectively. The functions C_{VV}^f and C_{AA}^f are given as follows:

$$C_{VV}^f = Q_f^2 - 2Q_f v_e v_f Re\chi(s) + (v_e^2 + a_e^2)v_f^2|\chi(s)|^2,$$

$$C_{AA}^f = (v_e^2 + a_e^2)a_f^2|\chi(s)|^2,$$

$$v_e = -1 + 4\sin^2\theta_W, \qquad a_e = -1,$$

$$v_{u,c} = +1 - \frac{8}{3}\sin^2\theta_W, \qquad a_{u,c} = +1,$$

$$v_{d,s,b} = -1 + \frac{4}{3}\sin^2\theta_W, \qquad a_{d,s,b} = -1,$$

$$\chi(s) = \frac{G_F}{8\sqrt{2}\pi\alpha}\frac{sM_Z^2}{s - M_z^2 + iM_Z\Gamma_Z},$$

where G_F is the Fermi coupling constant and M_Z and Γ_Z are the mass and width of the weak neutral boson. The functions of β are C_1^V and C_1^A are expressed by [5]:

$$C_1^V = \frac{4}{3}\pi\left\{\frac{\pi}{2\beta} - \frac{3+\beta}{4}(\frac{\pi}{2} - \frac{3}{4\pi})\right\},$$

$$C_1^A = \frac{4}{3}\pi\left\{\frac{\pi}{2\beta} - (\frac{19}{10} - \frac{22}{5}\beta + \frac{7}{2}\beta^2)(\frac{\pi}{2} - \frac{3}{4\pi})\right\},$$

and C_2^V and C_2^A depend on the number of the quark flavors N_f,

$$C_2^V = C_2^A = 1.986 - 0.115N_f.$$

For five known quarks (u,d,c,s,b), β is nearly equal to unity in the TRISTAN energy region and C_1^V and C_1^A are very close to unity; R is then written as

$$R = 3\sum_f\left\{1 + \frac{\alpha_s}{\pi} + C_2^V(\frac{\alpha_s}{\pi})^2\right\}(C_{VV}^f + C_{AA}^f)$$

$$= 3\sum_f Q_f^2(1 + "QCD")(1 + "Weak").$$

For example, at $\sqrt{s} = 56GeV$ a simple calculation for R with parameters $M_Z = 92.6GeV/c^2$, $\sin^2\theta_W = 0.226$ [6], $\Gamma_Z = 2.5GeV$ and $\alpha_s = 0.15$ leads to

$$R = \frac{11}{3}("QPM") + 0.78("Weak", 20\%) + 0.23("QCD", 6\%) = 4.67.$$

If the top quark threshold opened, the value of R increases by 4/3 and if the threshold of the b' quark opened, the value increases by 1/3. This level of increase will easily be observed.

Experimentally R is calculated by the following expression:

$$R = \frac{N_{obs} - N_{bg}}{L\epsilon(1+\delta)\sigma_0},$$

where N_{obs} is the number of observed hadronic events, N_{bg} is the number of background events, L is the integrated luminosity determined from Bhabha events, ϵ is the detection efficiency which was estimated by the LUND Monte Carlo program [7], δ is the radiative correction factor which was obtained by full calculation up to α^3 order processes [8] and σ_0 is the lowest order QED cross section of μ pair production $4\pi\alpha^2/3s$. Though the value of δ depends on the maximum energy of the radiated photon, $\epsilon(1+\delta)$ is found to be stable and typically 0.95.

Event selection for hadronic events was done by the characteristics of high multiplicity, a large visible energy and a small momentum imbalance. Main backgrounds come from τ pair production and two-photon processes like $e^+e^- \rightarrow e^+e^- + hadrons$. The following were the selection criteria applied to the VENUS data:

1) total deposit energy in the calorimeter E_{cal} was greater than 5 GeV, where E_{cal} was the energy sum of the barrel and endcap calorimeters in the polar angle region of $|cos\theta| \leq 0.91$,

2) number of tracks with $|cos\theta|$ less than 0.85 and transverse momentum greater than 0.2 GeV/c was equal to or greater than five,

3) invariant masses of particles in both hemispheres defined by a normal plane to the thrust axis were greater than 2 GeV/c^2. (Thrust axis was defined as the direction of a unit vector $\mathbf{e}_T$ which gave thrust T, the maximum value of $\sum_i |\mathbf{p}^i \cdot \mathbf{e}_T| / \sum_i |\mathbf{p}^i|$ where $\mathbf{p}^i$ is the momentum of the i'th particle.)

Criteria 2) and 3) were effective for rejection of τ pair production. Backgrounds from two-photon processes were characterized by a small visible energy E_{vis} which was the sum of E_{cal} and momentum P_{track} of charged particles, and large longitudinal momentum imbalance which was defined by $P_{bal} \equiv (\Sigma E_{cal,z} + \Sigma P_{track,z})/E_{vis}$, where $E_{cal,z}$ and $P_{track,z}$ were z-components of E_{cal} and P_{track} respectively. To reject them, they applied the following cuts:

4) the absolute value of P_{bal} was less than 0.4,

5) E_{vis} was greater than the beam energy E_{beam}.

Figure 5(a) is a scatter plot of P_{bal} vs. E_{vis}/E_{beam} at $\sqrt{s} = 56GeV$ for events which passed the criteria 1) to 3). The corresponding E_{vis}/E_{beam} and P_{bal} are shown in Fig. 5(b) and (c) together with histograms of solid lines generated by Monte Carlo simulations both for hadronic events and backgrounds from two-photon processes. It is clear that criteria (4) and (5), which are indicated by a dotted line in Fig. 5(a), are effective to reject two-photon processes. The estimated fraction of backgrounds in the remaining events were 0.5% from two-photon processes and less than 0.1% from τ pair production. Other backgrounds

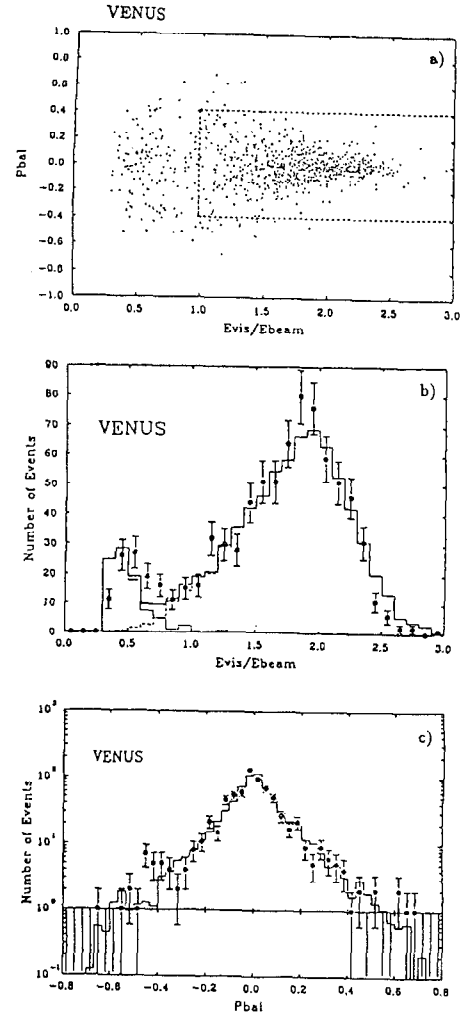

Figure 5. a)Momentum imbalance P_{bal} versus visible energy E_{vis} normalized by beam energy. b) E_{vis}/E_{beam} for events with $|P_{bal}| < 0.4$. c) P_{bal} for events with E_{vis} greater than beam energy.

were found to be negligible.

A summary of N_{obs} and R from the three experiments are given in Table 3. The values for 55 and 56 GeV are preliminary. The results at 50 and 52 GeV have been published [9]. The first and the second errors in R are statistical and systematic ones, respectively.

Table 3. Number of hadronic events and R.

	VENUS	TOPAZ	AMY
Nobs			
$\sqrt{s}$ =50 GeV	96	61	87
52 GeV	399	508	478
55 GeV	274	381	364
56 GeV	681	589	727
R			
50 GeV	$4.4 \pm 0.5 \pm 0.4$	$4.08 \pm 0.53 \pm 0.28$	$4.34 \pm 0.45 \pm 0.30$
52 GeV	$4.7 \pm 0.3 \pm 0.5$	$4.40 \pm 0.20 \pm 0.28$	$4.23 \pm 0.20 \pm 0.21$
55 GeV	$4.24 \pm 0.30 \pm 0.18$	$4.64 \pm 0.24 \pm 0.30$	$4.50 \pm 0.24 \pm 0.27$
56 GeV	$4.92 \pm 0.22 \pm 0.21$	$4.99 \pm 0.22 \pm 0.31$	$5.15 \pm 0.19 \pm 0.31$

The values of R are plotted in Fig. 6 together with previous experiments at PETRA [4,10,11]. A clear increase of R due to the Z^0 effect is seen at the TRISTAN energy. The results are in good agreement with the prediction by the standard model with five quark flavors. The dashed lines in the figure show the level of the top and b' quark production. It is clear that full opening of the top quark is excluded at 95% confidence level. Production of the b' quark, however, cannot be excluded at the present level of statistics. A fit of R was applied within a framework of the standard model to the VENUS data to obtain $\sin^2\theta_W$. The result is that $\sin^2\theta_W$ is 0.22 ± 0.03 and the corresponding Z^0 mass is 93.0 ± 5.0 GeV/c^2 which are consistent with the world average values [6]. The fitted value of R is shown by a solid line in Fig. 6.

3.2 Shape Analysis

Production of a new heavy quark would be studied by a difference of momentum distribution of the final state particles. The low velocity of the heavy quark would produce more "spherical" events than ones from the light quark production which have jet-like topologies. Figure 7 shows scatter plots of Q_1

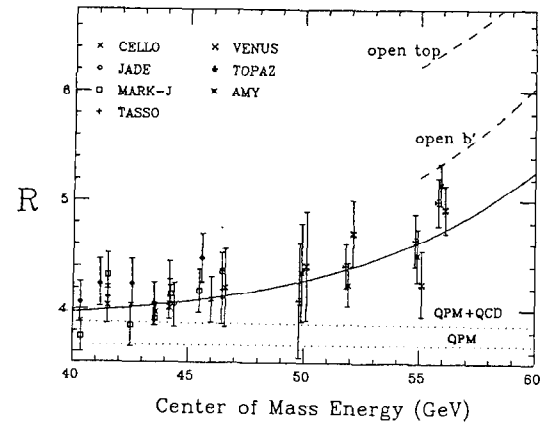

Figure 6. R ratios measured by TRISTAN and previous experiments.

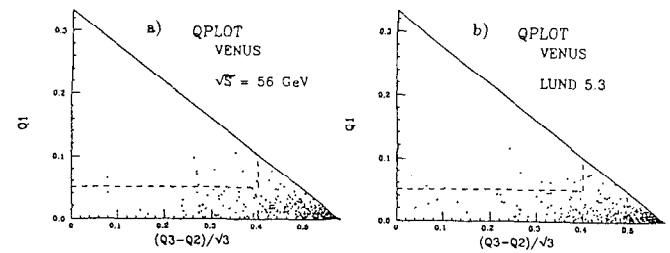

Figure 7. $Q1$ versus $(Q3 - Q2)/\sqrt{3}$ by VENUS. a) data at $\sqrt{s} = 56GeV$. b)Monte Calro with five quark flavors. Dashed line indicates cut to select spherical events.

vs. $(Q_3 - Q_2)/\sqrt{3}$ for hadronic events at $\sqrt{s}$=56 GeV from VENUS, where Q_i's are eigenvalues ($Q_1 < Q_2 < Q_3$) of the sphericity tensor $T_{\alpha\beta}$ defined by

$$T_{\alpha\beta} = \sum_{ij} \frac{\mathbf{p}_\alpha^i \cdot \mathbf{p}_\beta^j}{|\mathbf{p}^i| \cdot |\mathbf{p}^j|}.$$

The number of "spherical" events passing through conditions $Q_1 > 0.05$ and $(Q_3 - Q_2) < 0.4$ was 8 (Fig. 7(a)). This number agrees very well with the predicted value of 7.9 ± 2.9 from the Monte Carlo simulation (LUND5.3) with five quark flavors (Fig. (7b)). Subtracting the predicted number from the data, the upper limit on the production cross section of the top quark with mass M_{top} of 27.5 GeV/c^2 was obtained to be 4.9pb at 95% confidence level. Figure 8 shows aplanarity ($= \frac{3}{2}Q_1$) distribution at $\sqrt{s}$=55 GeV from TOPAZ in which data points (rectangles with error bars) are compared with histograms from a Monte Carlo estimation with five flavors (solid line) and six flavors ($M_{top} = 26GeV/c^2$, dashed line). The number of "spherical" events with aplanarity greater than 0.1 was $5 \pm 2.2(stat.) \pm 2.2(syst.)$. Comparing this number with 3.9 (5 flavors) and 17.0 (6 flavors) from the Monte Carlo estimation, the observed event number is in good agreement with the expected number from 5 flavor Monte Carlo. The lower limits on the top quark mass was calculated to be 27.1 GeV/c^2 at 95% confidence level. The AMY group examined the thrust distribution at $\sqrt{s}$=56 GeV as shown in Fig. 9. By comparing the number of "spherical" events with low thrust ($T < 0.7$) between data (dots with error bars) and the Monte Carlo estimation with (solid line) and without (dashed line) the top quark, they set a lower mass limit for the top quark as $27.3GeV/c^2$ at 95% confidence level. They also made similar analysis for the b' quark and set the lower mass limit to be 25 GeV/c^2 at 95% confidence level.

3.3 Inclusive leptons

Signals of heavy quark production could be observed as a form of isolated leptons from jets. In addition to this, a recent MARK-J result [11] indicated some excess with isolated muons in a low thrust region at $\sqrt{s}$ around 46 GeV, although it has been controversial comparing with other experiments. It is thus important to study the inclusive lepton events at higher energy region to confirm the existence of the possible new signals. VENUS, TOPAZ and AMY examined hadronic events with electrons and muons at $\sqrt{s}$=50 to 56 GeV. Identification

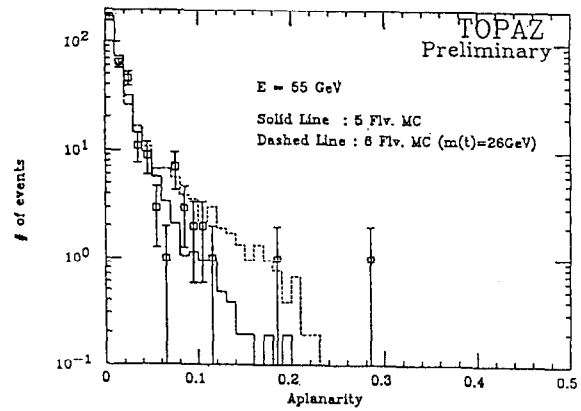

Figure 8. Aplanarity distribution by TOPAZ.

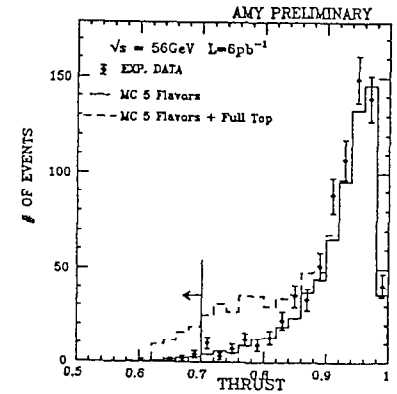

Figure 9. Thrust distribution by AMY.

of muons were done from the matching of hit positions of the muon chambers with extrapolated tracks from the central tracking device. Major backgrounds from the decay and punch-through of pions and kaons were estimated by generating hadron tracks having consistent momentum spectrum with real data and using a detector simulation program. Electrons were identified by using the information of the barrel calorimeter and the central tracking chamber. The ratio of the cluster energy in the calorimeter to the momentum of the associated charged track was required to be around unity. TOPAZ also used the dE/dx information from the TPC to reject pions form electron samples. Figures 10(a) and (b) show results from AMY for inclusive muon events. In Fig. 10(a) the thrust distribution of inclusive muon events (dots with bar) at $\sqrt{s}$ =56 GeV is shown together with histograms by a Monte Carlo estimation with and without the top quark. It is clear that the observed thrust distribution agrees well with predictions without the top quark and it was concluded that M_{top} is greater than 27.7 GeV/c^2. Figure 10(b) is the scatter plot of $|cos\delta|$ (δ is the angle between the lepton track and the thrust axis) vs. thrust (T) for 121 inclusive muon events from 14 pb^{-1} data. There remained no events in the area with $|cos\delta| < 0.7$ and $T < 0.8$ which are the same conditions applied by MARK-J. Results for inclusive electrons from TOPAZ are shown in Figs. 11(a),(b) and (c). Again, the data is consistent with results from five flavor Monte Carlo. The thrust distribution and its correlation with $|cos\delta|$ were also examined by VENUS [12] for both electron and muon inclusive events at $\sqrt{s}$ between 50 and 55 GeV. They also confirmed that the data is consistent with five quark flavors. For events with $|cos\delta| < 0.7$ and $T < 0.8$, the observed number of events are presented in Table 4 together with those from PETRA experiments [13].

Table 4. No. of observed events with T<0.8 and $|cos\delta| < 0.7$.

	AMY	TOPAZ	VENUS	MARK-J	JADE	CELLO
$\sqrt{s}$(GeV)	50-56	52-55	50-55	46.3-8	46.3-8	46.3-8
$\int L(pb^{-1})$	11.3	6.5	6.0	2.8	1.8	2.1
$ee \rightarrow \mu X$						
observed	0	0	1	7	5	1
expected	2.4	0.8 ± 0.3	< 1.4	0.8	0.7	0.65
$ee \rightarrow eX$						
observed	2	0	1	–	0	0
expected	1.9	0.5 ± 0.9	< 1.3	–	0.7	0.5

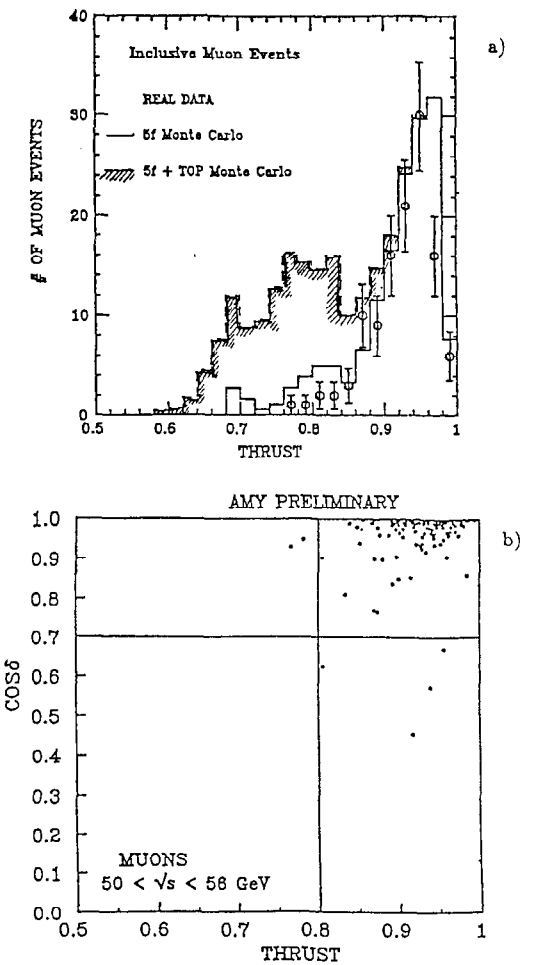

Figure 10. a) Thrust distribution and b) $|cos\delta|$ versus thrust for $ee \rightarrow \mu X$ events by AMY.

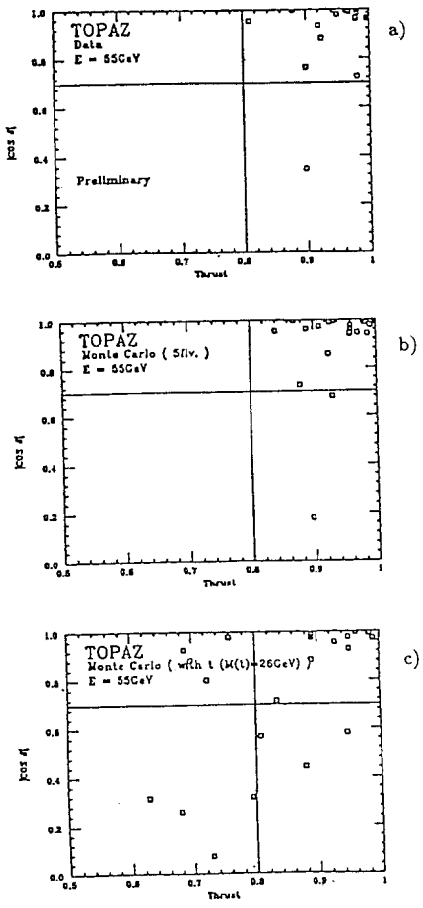

Figure 11. Scatter plots of $|cos\delta|$ versus thrust for $ee \rightarrow eX$ events at $\sqrt{s} = 55GeV$ by TOPAZ. a) Data. b) and c) Monte Carlo with five and six quark flavors, respectively.

In conclusion, we can say that for both electron and muon inclusive events the thrust distribution was well reproduced by the Monte Carlo with five quark flavors and no excess was found in the low $|cos\delta|$ and low thrust region.

4 Search for New Particles

4.1 Sequential heavy lepton

The number of observed generations of quarks and leptons is at present three, though the top quark has not been found yet. It is very important to find a sequential charged heavy lepton ($L^{\pm}$) because it is a direct evidence of the next generation. Previous analysis [14] from TRISTAN extended the lower limit on the mass of charged heavy leptons M_L up to 25.5 GeV/c^2 (at 95% confidence level) under the assumption of the mass of the associated neutrino (ν_L) to be zero. The present search was made by taking account of the finite mass of the neutrino. The VENUS group analyzed $5.3pb^{-1}$ data taken at $\sqrt{s}$ of 56 GeV considering the following two possible cases [15]:

Case (1) $L^{\pm}$ decaying into a weak doublet and $\nu_L(\overline{\nu_L})$ with finite mass in which ν_L has long life time and does not decay within the detector volume,

Case (2) $L^{\pm}$ being stable, and ν_L heavier than L and not mixing with other neutrinos.

In case (1) an examination was done for pair-produced heavy leptons both of which decaying into multihadrons plus an associated neutrino, in other words, an acoplanar two-jets event with large missing energy. Event selection was done to remove τ pair production, beam-gas and beam pipe interactions. Figure 12(a) shows E_{vis}/E_{beam} distribution of 686 events passing through the selection criteria of $N_{track} \geq 5$, $E_{barrel} > 3GeV$, and $|cos\theta_T| < 0.7$ (θ_T is the polar angle of the thrust axis). Backgrounds from two-photon and multihadronic events were estimated by a Monte Carlo simulation and results are shown by histograms in Fig. 12(a). Figure 12(b) shows the E_{vis}/E_{beam} distribution which was estimated by a Monte Carlo for pair produced heavy leptons with the mass of 27 GeV/c^2 assuming the associated neutrino mass of 0, 10 and 15 GeV/c^2. From this study, they set a condition of $0.3 < E_{vis}/E_{cm} < 0.8$ to select the possible

candidates of heavy lepton production. The condition is indicated by arrows in Fig. 12. There remained 150 events and they were examined by looking at an acoplanarity angle distribution which was defined by

$$cos\theta_{acop} = -\frac{(\mathbf{n}_1 \times \mathbf{z}) \cdot (\mathbf{n}_2 \times \mathbf{z})}{|\mathbf{n}_1 \times \mathbf{z}| \cdot |\mathbf{n}_2 \times \mathbf{z}|},$$

where $\mathbf{n}_1$ and $\mathbf{n}_2$ are the unit vectors of the momentum sum of two jets given by the thrust axis and $\mathbf{z}$ is the unit vector parallel to the direction of the electron beam. Figure 13 shows the acoplanarity angle distribution. The histograms represent expected yields from heavy lepton production of $M_L = 27 GeV/c^2$ with the associated neutrino mass of zero (dotted line) and 15 GeV/c^2 (dashed line) and from conventional multihadron events (solid line). The number of simulated events were normalized to the integrated luminosity of $5.3 pb^{-1}$. They took the events with θ_{acop} greater than 40 degrees as the $L^{\pm}$ production candidates and there remained no events in the data. This is consistent with the expected number of 0.7±0.4 from multihadron events. The systematic error of the acceptance calculation was 13 to 21% depending not only on the value of M_L or m_{ν_L} but also on the uncertainties from the fragmentation model, radiative correction [8], decay branching ratio, cuts for the event selection, statistics in the Monte Carlo simulation and luminosity measurement. The 95% confidence level upper limit for observed zero events was compared with the numbers of the expected $L^{\pm}$ production events with the systematic error taken into account. The obtained limits on M_L and m_{ν_L} are presented in Fig. 14 together with previous results from PEP, PETRA [16] and UA1 experiments (at 90% confidence level) [17].

In case (2) the search was made for collinear two track events using a time-of-flight (TOF) information. Selection criteria were as follows:

1) each track had a momentum greater than 1 GeV/c,

2) the acollinearity angle θ_{acol} of the two tracks satisfied $cos\theta_{acol} > 0.98$,

3) time difference of the two tracks was less than 5.0 nsec,

4) the energy calculated from the momentum and velocity (E=pc/β) exceeded 5 GeV for at least one of the two tracks,

5) difference between the z-position measured by the TOF counter and the central tracking chamber was less than 18 cm.

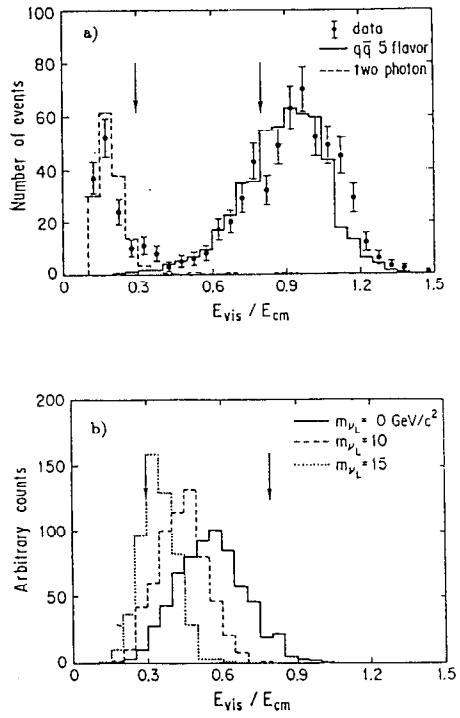

Figure 12. E_{vis}/E_{cm} from VENUS: a)Selected 686 events (dots with error bar) and backgrounds estimated by a Monte Carlo from multihadronic events (solid line) and two-photon processes (dashed line). The backgrounds are normalized to the integrated luminosity of $5.3 pb^{-1}$. b) Monte Carlo estimation of heavy lepton production with $M_L = 27 GeV/c^2$ and $m_{\nu_L} = 0$, 10 and 15 GeV/c^2.

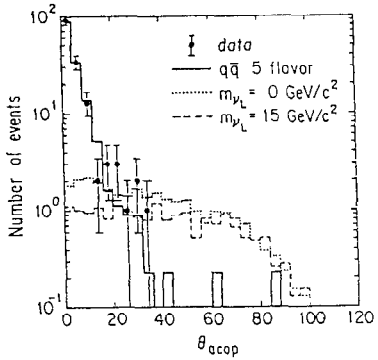

Figure 13. Acoplanarity angle distribution for the final sample of 150 events and Monte Carlo estimation of multihadronic events (solid line) and heavy lepton production ($M_L = 27 GeV/c^2$) with associated neutrino mass of 0 and 15 GeV/c^2.

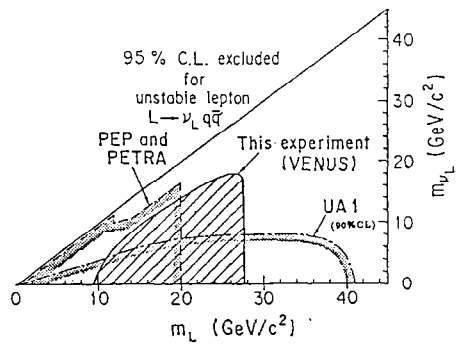

Figure 14. Limits on M_L at 95% confidence level as a function of the associated neutrino mass. Shaded area shows excluded region by VENUS.

There remained 1520 events from the selection. The searched region was $1.5 < \frac{1}{\beta} < 6.0$ where no events remained. A particle with $\frac{1}{\beta} > 6.0$ could not be detected because of its short range. This fact corresponds to a mass of 27.6 GeV/c^2. The mass range from 18.4 to 27.6 GeV/c^2 was thus excluded for spin 1/2 stable charged leptons at 95% confidence level.

The AMY group searched for pair-produced heavy lepton events [18] in which one of the heavy leptons decays leptonically and the other one decays hadronically (lepton-hadron mode) as well as those in which both heavy leptons decay hadronically (hadron-hadron mode). The analysis was made on $6.0 pb^{-1}$ data sample taken at $\sqrt{s}$=56 GeV. In lepton-hadron mode, the requirements were as follows:

1) within a 20° cone (half angle) around the lepton (e or μ) there was no energy deposit greater than 2 GeV,

2) the effective mass of hadrons was less than $\sqrt{s}/2$,

3) thrust T and the transverse momentum imbalance P_t divided by the visible energy satisfied

$$T \leq 0.9, \quad P_t/E_{vis} \geq 0.2 \quad and \quad P_t/E_{vis} \geq (2T - 1.3).$$

The requirement 2) eliminated most of the multihadronic events and 3) eliminated hadronic events with a large amount of energy lost into the beam pipe or carried away by neutral hadrons, two-photon events in which one of the electrons had wide angle to be detected and τ pair production whose thrust value was close to unity. The scatter plot of P_t/E_{vis} vs. thrust is shown in Fig. 15. There remained no events. A 95% confidence level lower limit on M_L is 27.3 GeV/c^2 for massless ν_L in this mode. Considering both hadron-hadron and lepton-hadron modes, they concluded that M_L should be greater than 27.6 GeV/c^2 for massless ν_L. For a finite mass of ν_L, the excluded region (at 95% confidence level) of M_L and m_{ν_L} is presented in Fig. 16. In the figure the results from the hadron-hadron mode and from stable charged leptons are also shown together with those from other experiments [16,17].

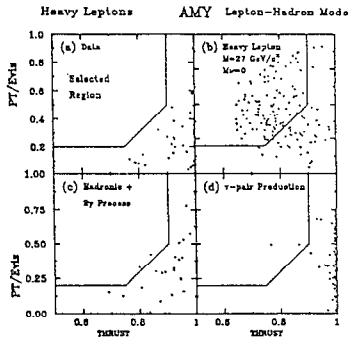

Figure 15. Scatter plots of P_t/E_{vis} versus thrust for the events that passed the selection criteria (in the text) for lepton-hadron mode by AMY: a) the data (6 pb^{-1}); b) simulated heavy lepton production (80.6pb^{-1}); c)simulated multihadron events together with simulated two-photon events (26.3pb^{-1}); d) simulated τ pair production (60.4 pb^{-1}). The selected region is on the upper left side surrounded by the solid line in each plot.

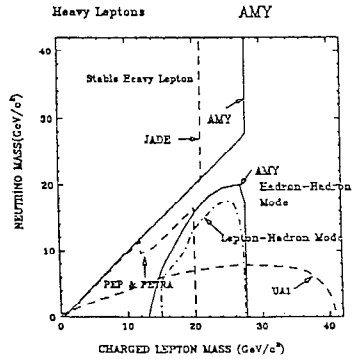

Figure 16. Excluded region of the heavy lepton mass and neutrino mass at 95% confidence level obtained by AMY together with those from other experiments.

4.2 Excited Leptons

One of the signatures from possible sub-structure of leptons [19] is the existence of excited leptons. They would be expected to be found in e^+e^- colliding beam experiments. The VENUS group searched for excited electrons (e^*) with the assumption that e^* is of spin 1/2 and couples to $e\gamma$ with the effective lagrangian given by [20]

$$L_{eff} = \frac{\lambda e}{2M_{e^*}}\overline{\psi_{e^*}}\sigma_{\mu\nu}\psi^e F^{\mu\nu} + hc,$$

where λ is a dimensionless parameter for the relative coupling strength to the electromagnetic coupling. The pair production process, $e^+e^- \rightarrow e^{*+}e^{*-} \rightarrow e^+e^-\gamma\gamma$, and single production process, $e^+e^- \rightarrow e^*e \rightarrow e\gamma(e)$ were searched.

For pair production, the 5.3pb^{-1} data sample taken at $\sqrt{s}$=56 GeV was analyzed. The selection criteria were:

1) there were four clusters in the barrel calorimeter with an energy greater than 5 GeV,

2) there were two tracks with momenta greater than 2 GeV/c and pointing to the energy clusters,

3) there was no other track reconstructed,

4) the opening angle of any pair out of the four particles was greater than 15^o,

5) the polar angle of all the particles satisfied $|cos\theta| \leq 0.743$.

After the selection no events remained. The number of events for given mass of e^* was calculated by the cross section formula for spin-1/2 fermion production via single photon annihilation expressed by,

$$\frac{d\sigma}{d\Omega} = \frac{\alpha^2}{4s}\beta\left\{1 + cos^2\theta + (1-\beta^2)sin^2\theta\right\},$$

where β is the velocity of e^* and is given by $\beta = \sqrt{1-(4M_{e^*}^2/s)}$. The pair production by t-channel process was neglected because of the small coupling strength of λ. The effects of the form factor and the small contribution from the Z^o-exchange process (less than 4%) were also neglected. The results are presented in Fig. 17 in which the hatched area shows the ambiguity of $\pm$10%

coming from systematic errors in event selection, geometrical cuts, radiative correction and luminosity measurements. The lower limit on the mass of e^* is 27.9 GeV/c^2 at 95% confidence level.

For single production, the quasi-real Compton scattering is the dominant contribution [21,22] in which a quasi-real photon radiated from a beam particle is scattered by another particle. The initial particle which radiated the quasi-real photon is not observed in most cases at large angles. In this process, e^* with mass up to $\sqrt{s}$ can be produced. The analysis was made on data at $\sqrt{s}$ from 50 to 56 GeV whose luminosity amounted to $11.4pb^{-1}$. To select event samples that an electron and a photon were observed and the other electron was not observed at a large angle, the following conditions were required:

1) there were two clusters in the barrel calorimeter with energy greater than 10 GeV,

2) there was one and the only one track with transverse momentum greater than 2 GeV/c and pointing to the clusters,

3) the track and the cluster were in a polar angle region of $|cos\theta| \leq 0.743$,

4) the acollinearity angle between the electron and the photon was greater than 3°,

5) the acoplanarity angle θ_{acop} (the acollinearity angle viewed from the beam axis) was less than 3°.

There remained 109 events. The effective mass of $e\gamma$ is plotted in Fig. 18 together with a histogram of QED expectation calculated with the Weizsäcker-Williams approximation and the Compton scattering cross section [22]. The distribution and total number of 110 ± 9 (systematic) expected from QED show good agreement with the data. The upper limit on λ was obtained from the expected number of single e^* production which was calculated from the cross section formula [19,21],

$$\frac{d\sigma}{dt} = -\frac{2\pi\alpha^2\lambda^2}{M_{e^*}^2 s^2}\left(\frac{s^2+(s-M_{e^*}^2)^2}{t} + m_e^2\frac{2M_{e^*}^4}{t^2}\right),$$

where a small contribution from s-channel process was neglected. Comparing with the QED expectation, the upper limit at 95% confidence level on λ for

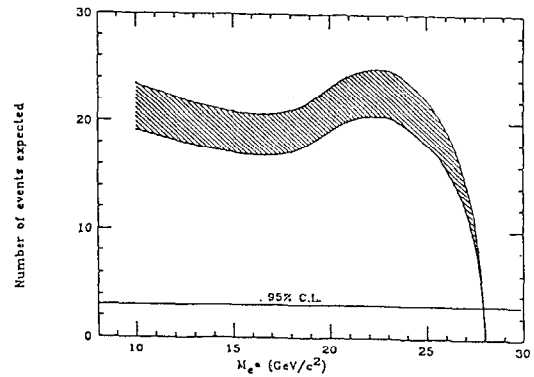

Figure 17. Number of expected events for e^* pair production, $ee \rightarrow ee\gamma\gamma$ by VENUS as a function of e^* mass.

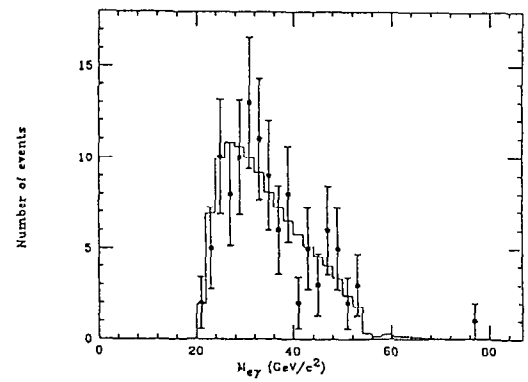

Figure 18. Effective mass of $e\gamma$ from $ee \rightarrow e\gamma(e)$ measured by VENUS. Histogram shows QED expectation.

M_{e^*} between 23 and 54 GeV/c^2 was obtained. The systematic error (18% in average) was taken into account to give conservative results for the upper limit. For M_{e^*} greater than 54 GeV/c^2, the limit on λ was derived from $\lambda = M_{e^*}^2/\Lambda_+^2$, where Λ_+ was the lower limit on the cut-off parameter for $e^+e^- \to \gamma\gamma$ and was 80 GeV from VENUS analysis. As indicated in Fig. 19, the present result significantly extended the previous limits from CELLO [23] and DELCO [24].

The AMY group searched for excited muons μ^* as well as excited electrons from $\mu^+\mu^-\gamma$ and $\mu^+\mu^-\gamma\gamma$ event samples in which all the particles in the final state were observed in the central tracking chamber ($|cos\theta| \leq 0.87$) for charged particles and the barrel calorimeter ($|cos\theta| \leq 0.73$) for shower clusters. The analysis was based on the $14pb^{-1}$ data samples taken at $\sqrt{s}$ from 50 to 56 GeV. The effective mass of the muon and photon are plotted in Fig. 20 for pair production together with those of the electron and photon. Two combinations are entered for each event. There are no events in the diagonal region where pair-produced μ^* or e^* events would appear. The lower limit on M_{μ^*} and M_{e^*} of 27.8 GeV/c^2 was obtained. For single production of μ^*, the estimated QED backgrounds were subtracted from the data in the $\mu\gamma$ effective mass distribution. The remainder was compared with the expected number of μ^* which was calculated from the cross section of the s-channel process [19,21],

$$\frac{d\sigma}{dt} = -\frac{2\pi\alpha^2\lambda^2}{M_{e^*}^2 s^2}\left(\frac{M_{\mu^*}^2(s-M_{\mu^*}^2)+2tu}{s}\right),$$

and a 95% confidence level upper limit on λ was extracted. The limit on M_{μ^*} was 55.5 GeV/c^2. From this and the study of the pair production of μ^*, the upper limits at 95% confidence level on λ for $\mu\gamma$ coupling are presented in Fig. 21.

4.3 Magnetic Monopoles

The SHIP (*Search* for *Highly Ionizing Particles*) experiment has searched for magnetic monopoles with magnetic charge in units of $g_D \equiv \frac{e}{2\alpha} \sim 68.5e$ which would explain the quantization of electric charge [25]. The detector [26] consists of two types of etchable track-recording solids, CR-39 plastic [27] and UG-5 glass [28]. They are characterized by high ionization thresholds and are completely insensitive to relativistic singly charged particles. A stack of UG-5 was installed inside the 1.5 mm thick aluminum vacuum beam pipe and at 7 cm below the interaction point to search for particles with short range and very high ionization. Outside the area of the beam pipe was covered by stacks of

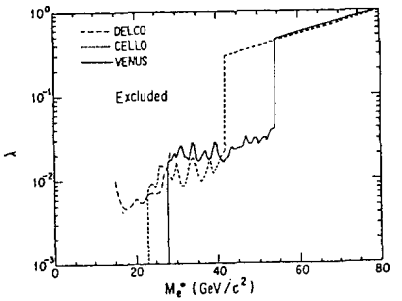

Figure 19. Upper limits at 95% confidence level on coupling strength λ of e^* to $e\gamma$ by VENUS as a function of e^* mass.

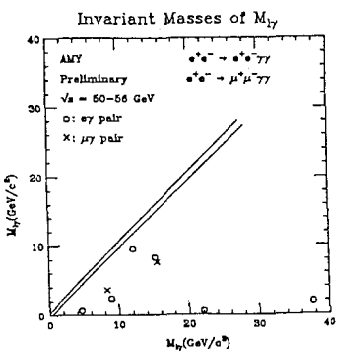

Figure 20. The invariant mass of lepton-photon pairs in $e^+e^- \to e^+e^-\gamma\gamma$ and $e^+e^- \to \mu^+\mu^-\gamma\gamma$ events measured by AMY. A diagonal band shows the mass resolution.

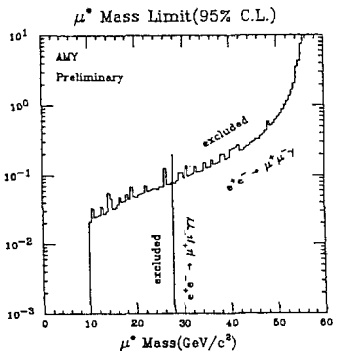

Figure 21. Upper limits on coupling strengh λ of μ^* to $\mu\gamma$ by AMY as a function of μ^* mass.

the more sensitive CR-39. Table 5 represents the integrated luminosity, the geometric acceptance and the cut-off mass M_n. The cut-off mass M_n was defined as a mass where the detector efficiency becomes half the geometric acceptance for magnetic monopoles with charge ng_D.

Table 5. Integrated luminosity, geometric acceptance,and cut-off masses.

Run($\sqrt{s}$)	$\int Ldt$	$\Delta\Omega/4\pi, M_1, M_2(GeV/c^2)$								
(GeV)	(pb^{-1})	CR-39(A)			CR-39(B)			UG-5		
I(50)	0.8	0.40*	23.2	12.1	0.40*	22.0	5.6	0.05	–	21.0
II(52)	4.0	0.40*	24.1	13.2	0.40*	23.3	7.3	0.05	–	22.0
III(55)	4.0	0.43*	25.7	15.1	0.43*	24.9	9.9		–	
VI(56)	7.5	0.43*	26.3	15.7	0.43*	25.4	10.6		–	

* Solid angle overlapping UG-5 has been subtracted.

The detectors from all exposures have been etched and scanned and the search was made for pairs of collinear tracks produced by penetrating particles. The null result from runs I and II has already been published [26]. In runs III and IV, there were no tracks satisfying the scanning criteria. The ratio R_D was defined as the upper limit on the production cross section σ_{lim} of magnetic monopoles at 95% confidence level divided by that of the muon pair normalized by their charge,

$$R_D \equiv \frac{\sigma_{lim}(m)}{\sigma_{\mu\mu}(>2m)(\frac{g_D}{e})^2}.$$

Figure 22 shows limits on R_D for magnetic monopoles with charge g_D and $2g_D$ together with limits from other accelerator searches [29] and from cosmic rays [30]. The present search is classified as "direct" since no assumption have been made about the properties of monopoles except for the magnitude and magnetic nature of the charge. The present experiment has established the upper limits on the production cross section of Dirac magnetic monopoles with masses up to 26.3 GeV/c^2 for charge g_D and up to 22.0 GeV/c^2 for charge $2g_D$.

5 Tests of QED

The study of the $e^+e^- \to e^+e^-$ and $e^+e^- \to \gamma\gamma$ processes at TRISTAN is of great importance for a direct and clean check of the validity of QED with

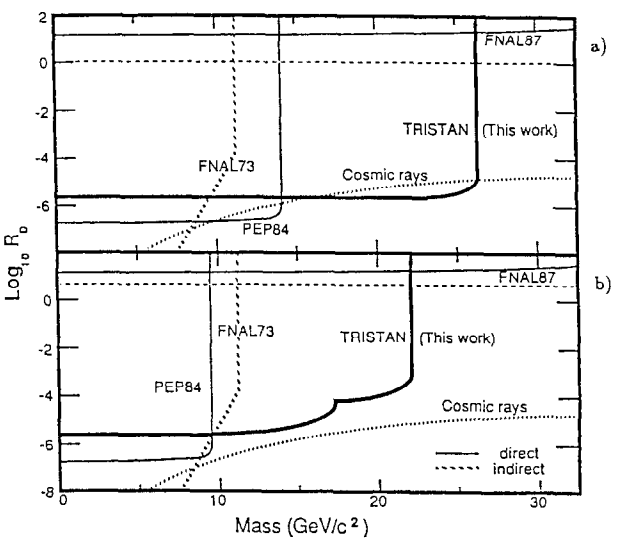

Figure 22. Upper limits at 95% confidence level on $R_D \equiv \sigma_{lim}(m)/\sigma_{\mu\mu}(g_D/e)^2$ for isotropic exclusive production of magnetic monopoles with charge a) g_D and b) $2g_D$.

the highest sensitivity at the highest possible e^+e^- energy. The measured differential cross sections for both processes were compared with QED and the deviation from QED was simply parameterized by the conventional cut-off parameters $\Lambda_\pm$ [31].

For $e^+e^- \to e^+e^-$, the event selection was made by requiring two collinear tracks with corresponding energy deposits in the barrel calorimeter or two energetic and collinear clusters in the endcap calorimeters. The event selection for the $e^+e^- \to \gamma\gamma$ process was done by requiring two collinear energetic clusters without associated tracks. The observed numbers of events for both processes are summarized in Table 6. Note the excellent operation of the endcap liquid argon counter enabled VENUS to obtain $e^+e^- \to \gamma\gamma$ events with small polar angle region ($0.82 \leq |cos\theta| < 0.93$).

Table 6. Number of observed events of $e^+e^- \to e^+e^-$ and $e^+e^- \to \gamma\gamma$ by AMY, TOPAZ and VENUS.

	AMY	TOPAZ	VENUS	
$e^+e^- \to e^+e^-$ (Barrel)				
$\|cos\theta\|$	< 0.73	< 0.8	< 0.74	
$\sqrt{s} = 50$ GeV	264	–	306	
52 GeV	1488	1654	1192	
55 GeV	1187	1261	646	
56 GeV	2042	2621	1861	
$e^+e^- \to e^+e^-$ (Endcap)				
$\|cos\theta\|$	$0.91 - 0.96$	$0.87 - 0.98$	$0.82 - 0.97$	
$\sqrt{s}$ =50 GeV	2592	–	–	
52 GeV	15059	9880	–	
55 GeV	11384	7046	6945	
56 GeV	19993	13196	21496	
$e^+e^- \to \gamma\gamma$ (Barrel)				
$\sqrt{s}$ =50 GeV	26	–	44	VENUS
52 GeV	188	177	165	endcap
55 GeV	144	136	99	71
56 GeV	272	270	269	199

After the correction of the acceptance, backgrounds and event loss, radiative corrections from calculation of electroweak processes up to the order of α^3 were made [32]. Figure 23 shows the ratio of the measured differential cross section

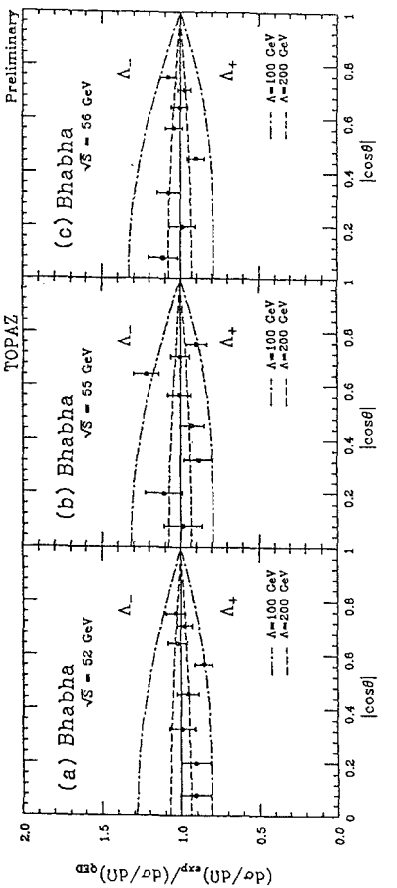

Figure 23. The ratio of the differential cross section of $e^+e^- \to e^+e^-$ to that of the lowest order QED at $\sqrt{s}$=52, 55 and 56 GeV by TOPAZ. Dashed and dot-dashed lines indicate the ratio with finite values of cut-off parameters of 200 and 100 GeV, respectively.

of $e^+e^- \to e^+e^-$ at $\sqrt{s}$=52, 55 and 56 GeV from TOPAZ to the lowest QED cross section. Dashed and dot-dashed lines in the figure are cross sections with finite values of the QED cut-off parameters Λ_+ and Λ_- expressed by

$$\frac{d\sigma}{d\Omega} = \frac{\alpha^2}{4s}[\frac{10+4x+2x^2}{(1-x)^2}F^2(t) - \frac{2(1+x)^2}{1-x}F(t)F(s) + (1+x^2)F^2(s)],$$

where

$$F(q^2) = 1 \pm \frac{-q^2}{q^2-\Lambda_\pm^2}, \quad x = cos\theta \quad and \quad t = \frac{-s(1-x)}{2}.$$

A simultaneous fit of this equation to the data gave the lower limits of 183 GeV for Λ_+ and 265 GeV for Λ_- at 95% confidence level. In Fig. 24 are presented the differential cross sections for $e^+e^- \to \gamma\gamma$ at $\sqrt{s}$=55 and 56 GeV from VENUS and the ratio to the lowest order QED prediction. The deviation from QED was introduced as

$$\frac{d\sigma}{d\Omega} = \frac{\alpha^2}{s}\frac{1+x^2}{1-x^2}[1 \pm \frac{s^2}{2\Lambda_\pm^4}(1-x^2)].$$

The simultaneous fit gave the lower limits on Λ_+ and Λ_- of 80 GeV and 76 GeV at 95% confidence level, respectively. Table 7 is a summary of the lower limits on the QED cut-off parameters (at 95% confidence level) from the three experiments together with those of previous experiments [33].

Table 7. Summary of Lower Limits on QED Cut-off Parameters (Λ_+ and Λ_-). (GeV, at 95% confidence level)

	$e^+e^- \to e^+e^-$		$e^+e^- \to \gamma\gamma$	
Exper.	Λ_+	Λ_-	Λ_+	Λ_-
AMY	130	330	76	77
TOPAZ	183	265	104	74
VENUS	164	218	80	76
CELLO	83	155	85	44
JADE	267	200	61	57
MARKJ	165	235	72	–
PLUTO	184	162	46	–
TASSO	435	590	61	56
HRS	154	220	59	59
MAC	–	–	66	67

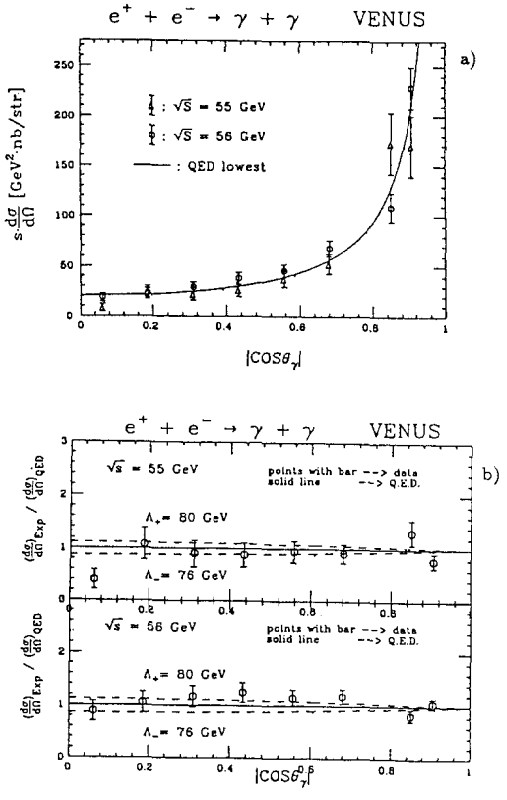

Figure 24. a)Differential cross section of $e^+e^- \to \gamma\gamma$ measured at $\sqrt{s}$= 55 and 56 GeV by VENUS. b) The ratio of the measured cross section to that of the lowest order QED.

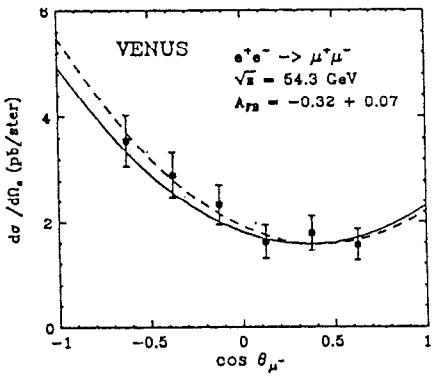

Figure 25. Differential cross section of $e^+e^- \to \mu^+\mu^-$ at $\sqrt{s} = 54.3GeV$ by VENUS (combined for $\sqrt{s}$ =50, 52, 55 and 56 GeV).

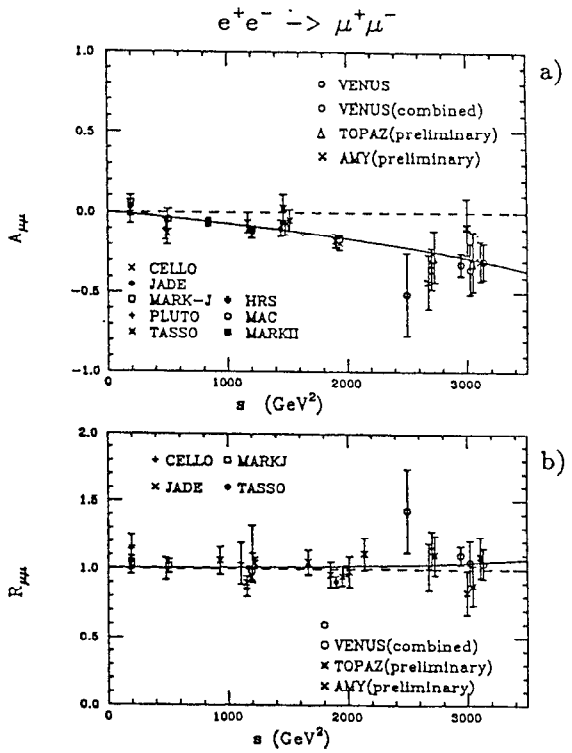

Figure 26. The observed values of a) forward-backward asymmetry $A_{\mu\mu}$ and b)cross section ratio $R_{\mu\mu}$ at TRISTAN and the previous experiments. Solid lines are the prediction of the standard model and dashed lines indicate pure QED.

As a result no deviation from QED was found in TRISTAN at present. In spite of the lower statistics than PEP and PETRA, TRISTAN with its higher center-of-mass energy, has obtained the comparable limits with the previous experiments.

6 Tests of Electroweak Theory

From the standard electroweak theory the interference between the electromagnetic current and the weak current becomes large in the TRISTAN energy region and significant forward-backward charge asymmetry is expected in the $e^+e^- \to \mu^+\mu^-$ and $e^+e^- \to \tau^+\tau^-$ processes. So studying these processes is a powerful check of the standard model.

6.1 $e^+e^- \to \mu^+\mu^-$

Selection criteria made by VENUS were two collinear tracks (with acollinearity angle less than 10 degrees) with large momenta (greater than half of the beam energy) and small energy deposit (less than 5 GeV) in the barrel calorimeter ($|cos\theta| \leq 0.75$). The small time difference of the two tracks (less than 5 nsec) measured by the TOF counters was also required to reject cosmic ray muons. The observed numbers of events by the three detectors are summarized in Table 8. The lowest order electroweak differential cross section was obtained by $d\sigma/d\Omega = (N_{obs} - N_{bg})/(L\epsilon(1+\delta)d\Omega)$, which is the number of observed events (N_{obs}) subtracted by that of backgrounds (N_{bg}) divided by the integrated luminosity (L) and corrected by the detection efficiency (ϵ) and the radiative correction factor (δ) which was calculated by a Monte Carlo program [34]. Typically $\epsilon(1+\delta)$ was 0.89. Figure 25 shows the differential cross section at $\sqrt{s}$=54.3 GeV from VENUS for the combined data taken at $\sqrt{s}$ of 50, 52, 55 and 56 GeV. Clear asymmetry is seen. The asymmetry parameter $A_{\mu\mu}$ was obtained by fitting the following expression for the lowest order differential cross section to the measured angular distribution by adjusting parameters $A_{\mu\mu}$ and $R_{\mu\mu}$,

$$\frac{d\sigma}{d\Omega} = \frac{\alpha^2}{4s} R_{\mu\mu}(1 + cos^2\theta + \frac{8}{3} A_{\mu\mu} cos\theta).$$

The solid line in Fig. 25 is the prediction by the standard model with the parameters of the world average [6] and the dashed line is the result of the fitting. The results were $A_{\mu\mu} = -0.32 \pm 0.07$ and $R_{\mu\mu} = 1.10 \pm 0.07$. In the standard model R_{ll} and $A_{ll}(l = \mu, \tau)$ are expressed by

$$R_{ll} \equiv \frac{\sigma_{ee\to ll}}{\sigma_{QED}} = 1 + 2v_e v_l Re\chi + (v_e^2 + a_e^2)(v_l^2 + a_l^2)|\chi|^2,$$

$$A_{ll} = \frac{3}{2} a_e a_l \chi (1 + 2v_e v_l Re\chi)/R_{ll},$$

where $v_e = v_\mu = v_\tau = -1 + 4sin^2\theta_W$, $a_e = a_\mu = a_\tau = -1$ and χ is given in section 3.1. At $\sqrt{s} = 56GeV$, $A_{\mu\mu} = -0.27$ and $R_{\mu\mu} = 1.03$ which are in good agreement with measured values. The values of $A_{\mu\mu}$, $R_{\mu\mu}$ and the product of the axial vector coupling constants $a_e a_\mu$ from TRISTAN experiments are summarized in Table 8 and plotted in Fig. 26 together with the previous ones from PEP and PETRA [35]. The errors indicated are statistical only.

Table 8. Summary of $e^+e^- \to \mu^+\mu^-$ (preliminary for 55 and 56 GeV).

	VENUS	TOPAZ	AMY	st.theory
Nobs				
$\sqrt{s}$ = 50 GeV	21	–	–	
52 GeV	65	58	71	
55 GeV	46	38	44	
56 GeV	91	35	101	
total	223	131	216	
$\int L(pb^{-1})$	11.4	11.3	13.3	
$< \sqrt{s} >$(GeV)	54.3	54.5	54.5	
$A_{\mu\mu}$	-0.32 ± 0.07	-0.29 ± 0.13	-0.28 ± 0.09	-0.27
$R_{\mu\mu}$	1.10 ± 0.07	0.91 ± 0.10	1.02 ± 0.09	1.03
$a_e a_\mu$	1.18 ± 0.26	1.12 ± 0.50	1.03 ± 0.32	1.00

6.2 $e^+e^- \to \tau^+\tau^-$

The event selection of this process by the three experiments at TRISTAN was made to search for τ-pairs in the barrel region with a topology of $1+n(1 \leq n \leq 5)$. The selection criteria of VENUS were as follows:

1) the number of tracks N_{track} in the polar angle region of $|cos\theta| \leq 0.72$ satisfied $2 \leq N_{track} \leq 6$.

2) there was a charged track whose isolation angle θ_{iso} between the track and the other charged tracks satisfied $cos\theta_{iso} \leq -0.8$,

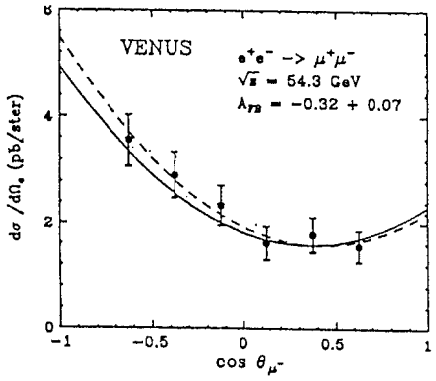

Figure 25. Differential cross section of $e^+e^- \rightarrow \mu^+\mu^-$ at $\sqrt{s} = 54.3GeV$ by VENUS (combined for $\sqrt{s}$ =50, 52, 55 and 56 GeV).

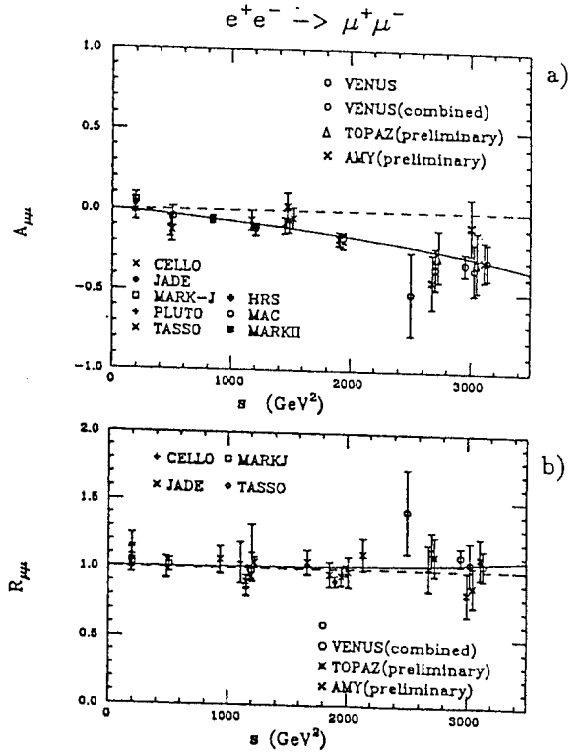

Figure 26. The observed values of a) forward-backward asymmetry $A_{\mu\mu}$ and b)cross section ratio $R_{\mu\mu}$ at TRISTAN and the previous experiments. Solid lines are the prediction of the standard model and dashed lines indicate pure QED.

3) the sum of the absolute values of the charged particle momentum was greater than a quarter of the beam energy (for reduction of the beam-gas and two-photon events),

4) the visible energy was greater than the beam energy or the magnitude of the transverse momentum imbalance of the charged particles ($=|\Sigma p_t|$) was greater than 15% of the beam energy (rejection of two-photon events),

5) the energy deposit in the barrel calorimeter was less than 1.5 times the beam energy (to reduce Bhabha events),

6) the charged particles were divided into two groups by a normal plane to the thrust axis. One of the highest momenta was to be less than a half of the beam energy (for rejection of μ-pair events),

7) the effective mass of the particles in each group was less than 3 GeV/c^2 (rejection of hadronic events),

8) the acoplanarity angle for two-track events was required to be greater than one degree. Events were rejected if both particles were identified as electrons (to reject $e^+e^- \to \gamma\gamma$ and $e^+e^- \to e^+e^-(\gamma)$ events),

9) the production angle defined by the polar angle of the thrust axis satisfied $|cos\theta| < 0.70$.

The number of events after the selection is summarized in Table 9 with those from TOPAZ and AMY. The same analysis procedure as that for μ pair production was made to obtain the lowest order electroweak differential cross section. Figure 27 shows the angular distribution from VENUS by combining data at the four energy points. The asymmetry parameter $A_{\tau\tau}$ and the cross section ratio $R_{\tau\tau}$ from the three groups are listed in Table 9 and are presented in Fig. 28 with previous experiments at PEP and PETRA [35]. They are in good agreement with the standard model prediction. As to the axial vector coupling constants, the ratio of the a_μ/a_τ is consistent with unity at the present level of statistics. We cannot say anything about the deviation from the $\mu - \tau$ universality.

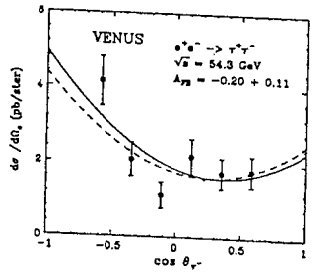

Figure 27. Differntial cross section of $e^+e^- \to \tau^+\tau^-$ at $\sqrt{s}$ = VENUS (combined for $\sqrt{s}$ =50, 52, 55 and 56 GeV).

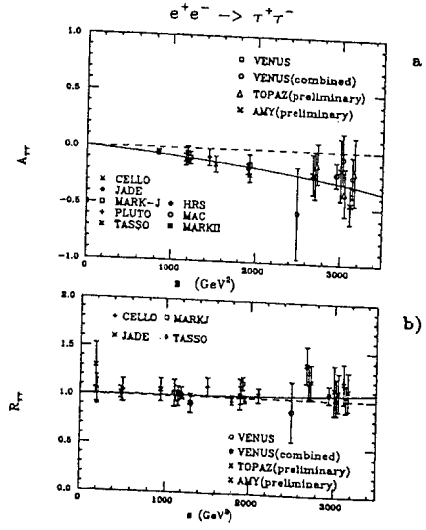

Figure 28. The observed values of a) forward-backward asymmet b)cross section ratio $R_{\tau\tau}$ at TRISTAN and the previous experim lines are the prediction of the standard model and dashed lin pure QED.

Table 9. Summary of $e^+e^- \to \tau^+\tau^-$ (preliminary for 55 and 56 GeV).

	VENUS	TOPAZ	AMY	st.theory
Nobs				
$\sqrt{s}$ = 50 GeV	8	–	–	
52 GeV	42	44	64	
55 GeV	29	29	36	
56 GeV	57	30	74	
total	136	103	174	
$\int L(pb^{-1})$	11.4	11.3	13.3	
$< \sqrt{s} >$(GeV)	54.3	54.5	54.5	
$A_{\tau\tau}$	-0.20 ± 0.11	-0.20 ± 0.14	-0.31 ± 0.11	-0.27
$R_{\tau\tau}$	1.06 ± 0.09	1.17 ± 0.14	1.24 ± 0.12	1.03
$a_e a_\tau$	0.73 ± 0.40	0.77 ± 0.54	1.11 ± 0.41	1.00
a_μ / a_τ	0.62 ± 0.37	0.69 ± 0.57	1.08 ± 0.25	1.00

7 Summary

1) All the TRISTAN experiments have been doing very well and have accumulated total integrated luminosities of 11 to 16pb^{-1} at the center-of-mass energy between 50 and 56 GeV during the first year of operation.

2) The R-ratio, shape analysis and study of inclusive e/μ production process in multihadronic events show that the threshold of the top quark is not opened up to the center-of-mass energy of 56 GeV. No anomalous enhancement like MARK-J type events is observed.

3) A new limit on the mass of new charged heavy leptons with massive neutrino has been obtained. For the mass of new stable charged leptons, the lower mass limit is 27.6 GeV/c^2 at 95 % confidence level.

4) No signal of excited electrons and muons has been observed. The lower limits on M_{e^*} and M_{μ^*} have been obtained at 95% confidence level. The upper limits on the coupling strength λ of e^* and μ^* have been obtained for M_{e^*} and M_{μ^*} up to 55.5 GeV/c^2.

5) No candidates of highly ionizing particles have been found. For Dirac magnetic monopoles, new upper limits have been obtained on the pair-production cross section up to the mass of 26.3 and 22.0 GeV/c^2 for magnetic charge g_D and $2g_D$.

6) No deviation from QED has been observed in the differential cross sections of $e^+e^- \to e^+e^-$ and $e^+e^- \to \gamma\gamma$ processes.

7) The measured cross section and the forward-backward charge asymmetries for $e^+e^- \to \mu^+\mu^-$ and $e^+e^- \to \tau^+\tau^-$ processes are in good agreement with the standard electroweak theory.

TRISTAN is now operating at $\sqrt{s}$=57 GeV. After the installation of 16 units of superconducting cavities in one of the RF sections of the main ring, the next physics experiments will start in November at $\sqrt{s}$=62 GeV. The center-of-mass energy will be further increased to 66 GeV by installing another 16 units of superconducting cavities in 1989. In addition, each colliding section will be equipped with a set of superconducting quadrupoles for mini-β operation to get twice the present luminosity. As for the detectors, several improvements are proposed. Some of them are: vertex chambers (VENUS, TOPAZ) for direct detection of short lived particles, a transition radiation detector (VENUS) and an X-ray chamber (AMY) to increase electron identification capability and a set of calorimeters for better hermeticity (TOPAZ, AMY).

In conclusion, tests of the standard model and new particle searches are being done at the highest e^+e^- energy at TRISTAN. At present new phenomena have not been observed. However, with future increases in energy and luminosity together with upgrades in the detector systems, we may find new signals if they exist.

Acknowledgements

The author gives special thanks to the organizing committee for inviting him to the conference and to the secretary E.Brennan for the excellent administration throughout the conference. His thanks also goes to the TRISTAN accelerating crews for their excellent machine operation and the members of TRISTAN experimental groups for their warm help in his preparation of this talk. Finally the author wishes to give his appreciation to professors K.Takahashi and S.Iwata for their helpful discussion and encouragement.

References

[1] F.Takasaki, Nucl. Phys. **B**(Proc. Suppl.) 3 (1988) 17.

[2] A.Shirahashi et al., IEEE Trans. NS-35 (1988) 414.

[3] S.L.Glashow, Nucl. Phys. **22** (1961) 579;
A.Salam, Phys. Rev. **127** (1962) 331;
S.Weinberg, Phys. Rev. Lett. **19** (1967) 1264.

[4] CELLO Collab., H.-J.Behrend et al., Phys. Lett. **183B** (1987) 400.

[5] T.W. Appelquist and H.D.Politzer, Phys. Rev. Lett. **34** (1975) 43;
S.Güsken et al., Phys. Lett. **155B** (1985) 185.

[6] Particle Data Group (Review of Particle Properties): Phys. Lett. **170B** (1986) 1.

[7] T.Sjöstrand, Comput. Phys. Commun. **39** (1986) 347;
T.Sjöstrand and M.Bengtsson, Comput. Phys. Commun. **43** (1987) 367;
B.Anderson et al., Phys. Rep. **97** (1983) 31.

[8] F.Berends, R.Kleiss and S.Jadach, Nucl. Phys. **B202** (1982) 63;
Comput. Phys. Commun. **29** (1983) 185.

[9] VENUS Collab., K.Abe et al., Jour. Phys. Soc. Japan **56** (1987) 3763;
H.Yoshida et al., Phys. Lett. **198B** (1987) 570.
TOPAZ Collab., I.Adachi et al., Phys. Rev. Lett. **60** (1988) 97.
AMY Collab., Sagawa et al., Phys. Rev. Lett. **60** (1988) 93.

[10] CELLO Collab., H.-J.Behrend et al., Phys. Lett. **144B** (1984) 297;
JADE Collab., W.Bartel et al., Phys. Lett. **160B** (1985) 337;
Phys. Lett. **129B** (1983) 145.
MARK-J Collab., B.Adeva et al., Phys. Rep. **109** (1984) 131;
Phys. Rev. Lett. **50** (1983) 799.
TASSO Collab., M.Althoff et al., Phys. Lett. **138B** (1983) 441; R.Brandelik et al., Phys. Lett. **113B** (1982) 499.

[11] MARK-J Collab., B.Adeva et al., Phys. Rev. **D34** (1986) 681.

[12] VENUS Collab., K.Abe et al., Phys. Lett. **207B** (1988) 355.

[13] JADE Collab., W.Bartel et al., Z. Phys. **C36** (1987) 15.
CELLO Collab., H.-J.Behrend et al., Phys. Lett., **193B** (1987) 157.

[14] VENUS Collab., H.Yoshida et al., Phys. Rev. Lett. **59** (1987) 2915.
TOPAZ Collab., I.Adachi et al., Phys. Rev. **D37** (1988) 1339.
AMY Collab., S.Igarashi et al., Phys. Rev. Lett. **60** (1988) 2359.

[15] VENUS Collab., K.Abe et al., Phys. Rev. Lett. **61** (1988) 915.

[16] D.P.Stoker and M.L.Perl, in Electroweak Interactions and Unified Theories, edited by J.Tran Thanh Van (Editions Frontiers, Gif-sur-Yvette, 1987); S.L.Wu, Cern Report No. CERN-EP/87-235, 1987 (unpublished) and references therein.

[17] R.M.Barnett and H.E.Haber, Phys. Rev. **D36** (1987) 2042. The data analyzed in this reference were originally presented in C.Albajar et al., Phys. lett. **B185** (1987) 241.

[18] AMY Collab., G.N.Kim et al., Phys. Rev. Lett. **61** (1988) 911.

[19] H.Terazawa et al., Phys. Lett. **112B** (1982) 387.

[20] F.E.Low, Phys. Rev. Lett. **14** (1965) 238.

[21] K.Hagiwara, S.Komamiya and D.Zeppenfeld, Z. Phys. **C29** (1985) 115.

[22] A.Courau and P.Kessler, Phys. Rev. **D33** (1986) 2024.

[23] CELLO Collab., H.-J. Behrend et al., Phys. Lett. **168B** (1986) 420.

[24] DELCO Collab., G.R.Bonneaud et al., Phys. Lett. **177B** (1986) 109.

[25] P.A.M.Dirac, Proc. Roy. Soc. London **133** (1931) 60.

[26] K.Kinoshita et al., Phys. Rev. Lett. **60** (1988) 1610.

[27] B.G.Cartwright, E.K.Shirk and P.B.Price, Nucl. Instr. Meth. **153** (1978) 457.

[28] P.B.Price, L.M.Cook and A.Marker, Nature **325** (1987) 137.

[29] R.A.Carrigan et al., Phys. Rev. **D8** (1973) 3717;
D.Fryberger et al., Phys. Rev. **D29** (1984) 1524;
P.B.Price et al., Phys. Rev. Lett. **59** (1987) 2523.

[30] R.R.Ross et al., Phys. Rev. **D8** (1973) 698.

[31] S.D.Drell. Ann. Phys. **4** (1958) 75.
N.M.Kyoll, Nuovo Cimento **A45** (1966) 65.

[32] K.Tobimatsu and Y.Shimizu, Prog. Theor. Phys. **74** (1985) 567; ibid. **75** (1986) 905; ibid. **76** (1986) 334.
S.Kuroda, T.Kamitani, K.Tobimatsu, S.Kawabata and Y.Shimizu: Comput. Phys. Commun. **48** (1988) 335.
J.Fujimoto and M.Igarashi, Prog. Theor. Phys. **74** (1985) 791;
J.Fujimoto, M.Igarashi and Y.Shimizu, Prog. Theor. Phys. **77** (1987) 118.
S.Kawabata, Comput. Phys. Commun. **41** (1986) 127.

[33] CELLO Collab., H.-J.Behrend et al., Phys. Lett. **103B** (1981) 143; Phys. Lett. **123B** (1983) 127.
JADE Collab., W.Bartel et al., Z. Phys. **C19** (1983) 197; Z. Phys. **C30** (1986) 371.
MARK-J Collab., B.Adeva et al., Phys. Lett. **152B** (1985) 439; Phys. Rev. Lett. **53** (1984) 134.
PLUTO Collab., Ch.Berger et al., Z.Phys. **C27** (1985) 341; Phys. Lett. **94B** (1980) 87.
TASSO Collab., M.Althoff et al., Z. Phys. **C26** (1984) 337; W.Braunshweig et al., Z. Phys. **C37** (1988) 171.
HRS Collab., M.Derrick et al., Phys. Lett. **166B** (1986) 463; Phys. Rev. **D34** (1986) 3286.
MAC Collab., E.Fernandez et al., Phys. Rev. **D35** (1987) 10.

[34] M.Igarashi et al., Nucl. Phys. **B263** (1986) 347.

[35] CELLO Collab., H.-J.Behrend et al., Z. Phys. **C14** (1982) 283; H.-J.Behrend et al., Z. Phys. **C16** (1983) 301.
JADE Collab., Bartel et al., Z. Phys. **C26** (1985) 507; B.Naroska, Phys. Rep. **148** (1987) 67.

MARK-J Collab., B.Adeva et al., Phys. Rev. Lett. **55** (1985) 665; B.Adeva et al., Phys. Rep. **109** (1984) 131.
TASSO Collab., M.Althoff et al., Z. Phys. **C22** (1984) 13.
HRS Collab., D.Bender et al., Phys. Rev. **D30** (1984) 515; M.Derrick et al., Phys. Rev. **D31** (1985) 2352; K.K.Gan et al., Phys. Lett. **153B** (1985) 116.
MAC Collab., W.W.Ash et al., Phys. Rev. Lett. **55** (1985) 1831; E.Fernandez et al., Phys.Rev. Lett. **54** (1985) 1620.
MARKII Collab., M.E.Levi et al., Phys. Rev. Lett. **51** (1983) 1941.

PROSPECTS FOR B PHYSICS
(ca. The late 1990's)

M.S. Witherell

Department of Physics
University of California
Santa Barbara, CA. 93106

ABSTRACT

The Snowmass Workshop this summer was dedicated to a look at particle physics 10 years from now. Two groups studied the prospects for high-rate B physics. This is a summary of that work.

Lectures given at the SLAC Summer Institute on Particle Physics, Stanford, CA., July 18–29, 1988.

INTRODUCTION

As Haim Harari[1] pointed out in his lectures last week, we are closing in on the parameters of the standard model. Except for the measurement of the top quark mass the crucial information will come from B decays. In addition, Harari emphasized that the bottom quark is a key to physics beyond the standard model.

The main goals in the study of B-meson decays are (1) measuring the remaining elements of the Kobayashi-Maskawa matrix, (2) understanding the nature of CP violation, and (3) searching with great sensitivity for various rare decays. Recent experimental results[2] suggest that ϵ'/ϵ is consistent with the three-generation K–M model for CP violation. Measurements of B_d mixing reported at this conference[3] confirm that $x_d \simeq 0.7$, which is almost ideal for large CP-violating asymmetries. The consistent picture that is taking shape gives us a clear goal for the next generation of B physics experiments—to be able to decisively test this model of CP violation.

For these reasons, it is a propitious time to look at the long-range prospects for B decay experiments. This was a major focus of the Weak Decays group at Snowmass '88. Three subgroups worked in this area, and I will be reporting on their results and conclusions. Roberto Peccei led a group studying the theory and phenomenology. Dave Cassel, Gary Feldman, and Bob Siemann led a combined group on B-physics at e^+e^- colliders, including both experimental issues and accelerator designs. Michael Schmidt led a group looking at B physics at hadron machines. This summary will draw heavily on the summary talks given at Snowmass. The subgroup reports will appear in the Snowmass proceedings, and will contain more detail than I am able to supply here.

PARAMETERS OF THE STANDARD MODEL

The Kobayashi-Maskawa (KM) matrix describes the weak coupling between the quarks:

$$V = \begin{pmatrix} V_{ud} & V_{us} & V_{ub} \\ V_{cd} & V_{cs} & V_{cb} \\ V_{td} & V_{ts} & V_{tb} \end{pmatrix}.$$

There are many simplifying notations available, but I will use the one used by Peccei, but with the normal sign for the phase of V_{ub}:

$$V = \begin{pmatrix} 1-\lambda^2/2 & \lambda & A\rho\lambda^3 e^{-i\delta} \\ -\lambda & 1-\lambda^2/2 & A\lambda^2 \\ A\lambda^3(1-\rho e^{i\delta}) & -A\lambda^2 & 1 \end{pmatrix}.$$

In this parameterization, unitarity is built in and for the off-diagonal terms, only the leading term is kept. The well-measured parameters are $\lambda = \sin\theta_c$ and $A = V_{cb}/V_{us}^2$. The ratio $V_{ub}/V_{cb}\lambda$ is $\rho e^{-i\delta}$. The CP-violating phases are nonzero for V_{ub} and V_{td}: $V_{ub} = |V_{ub}|e^{-i\delta}$ and $V_{td} = |V_{td}|e^{-i\phi}$.

The unitarity of the K–M matrix applied to the first and third columns lead to the equation

$$V_{ub}^* V_{ud} + V_{cb}^* V_{cd} + V_{tb}^* V_{td} = 0.$$

By setting the diagonal terms to 1, and using $V_{cd} = -\lambda$, we get

$$V_{ub}^* + V_{td} = \lambda V_{cb}^*.$$

This can be demonstrated graphically with the triangle in Fig. 1(a). By dividing out the length of the base of the triangle, we get Fig. 1(b), which explicitly demonstrates the relationship between the two CP-violating phases. Accurate measurements of the lengths of all three sides could show that the triangle does not close and the three-generation model does not work, or that all amplitudes are real and the K–M model of CP violation is wrong.[4] In practice, we assume the three-generation model to predict the size of CP-violating effects.

EXPERIMENTAL DETERMINATION OF PARAMETERS

The parameter which is best determined is $\lambda = \sin\theta_c = 0.221 \pm 0.002$,[5] as measured in strange particle decays. The next parameter is $A = V_{cb}/V_{us}^2 = 1.0 \pm 0.2$.[6] This is determined by the measurements of the B lifetime and the semileptonic branching ratio. The limiting errors are due to the theoretical uncertainties in choosing m_b and in accounting for the effects of exclusive channels.

The measurement of $|V_{ub}/V_{cb}|$ is the most important immediate goal of experiments studying B decays. The ratio can be measured by fitting the lepton energy spectrum from semileptonic B decays. The most conservative limit from this technique is $|V_{ub}/V_{cb}| < 0.20$.[7] A recent CLEO limit[8] using the exclusive decay mode $B \to \pi e\nu$ is $|V_{ub}/V_{cb}| < 0.17$. Because of the inconsistency between

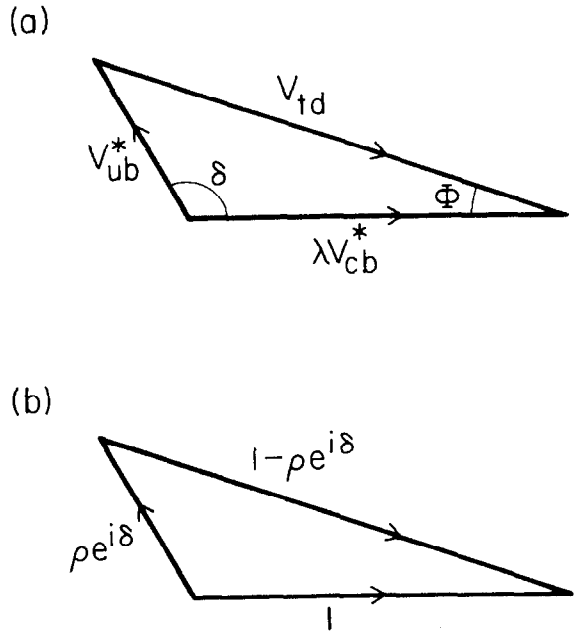

Fig. 1(a). The triangle relation in the complex plane for elements of the K–M matrix. (b) The same triangle, scaled to unit length for the base.

results on the decay modes $p\bar{p}\pi$ and $p\bar{p}\pi\pi$,[9] it is impossible to put a lower bound on the ratio. The parameter $\rho = |V_{ub}|/\lambda|V_{cb}|$ is less than 0.8.

The final parameter in the K–M matrix is the phase δ, for which we have no direct measurement. The observation of CP-violation implies $\sin\delta \neq 0$. The CP parameter $|\epsilon|$ is proportional to $B_K\ \rho\sin\delta\ [1 + \frac{1}{2}A^2(1-\rho\cos\delta)(m_t/50\ \mathrm{GeV})^2]$, where m_t is the mass of the top quark and B_K is the B parameter for kaon decays. Since we know $1/3 \leq B_K \leq 1$ and $m_t > 40$ GeV, we can indirectly limit δ to be in the range 0.5–3 radians.

For predicting the level of CP violation it is important to improve our knowledge of m_t and x_d. The lower limit on m_t is 40 GeV from UA1.[10] An upper limit can be inferred from the parameters M_w, M_z and θ_w, and is around 180 GeV.[8,11] The mixing parameter in B_d decays is defined as $x_d = \Delta m_d/\Gamma_d$. To a good approximation, $x_d \propto m_t^2\ |1-\rho e^{i\delta}|^2$, and is therefore very dependent on m_t. The average measurement is now $x_d = 0.73 \pm 0.18$.[3]

All of these experimental results can be summarized in Fig. 2(a), which shows the allowed regions of the parameters, ρ and δ. This allows the full range of uncertainty: 40 GeV $< m_t <$ 180 GeV, $1/3 < B_K < 1$, and 100 MeV $\leq B_B^{1/2} f_B \leq$ 200 MeV.[11] The two measurements which can restrict this range are m_t and x_s. Figure 2(a) shows the ranges allowed for various values of x_s. For these values of x_s, it is not enough to measure the integrated number of mixed events, which will be very close to 50%. The time dependence must be measured to determine x_s.

Figure 2(b) shows the restriction on the allowed range for two values of top quark mass. Either an observation of the top quark or an improved lower limit will significantly restrict the allowed parameter space. The present runs of CDF and UA2 will be able to do one of these two in the present run.

To go back to the triangle of Fig. 1, the length of the side $|V_{ub}|$ is determined by the decay $b \rightarrow ue\nu$, and knowledge of x_d fixes $|V_{td}|$. The length of the base is determined by τ_B and the Cabibbo angle. As Harari pointed out, for small ρ, δ does not have much effect. For large ρ, δ cannot be small, or else x_d would be too small.

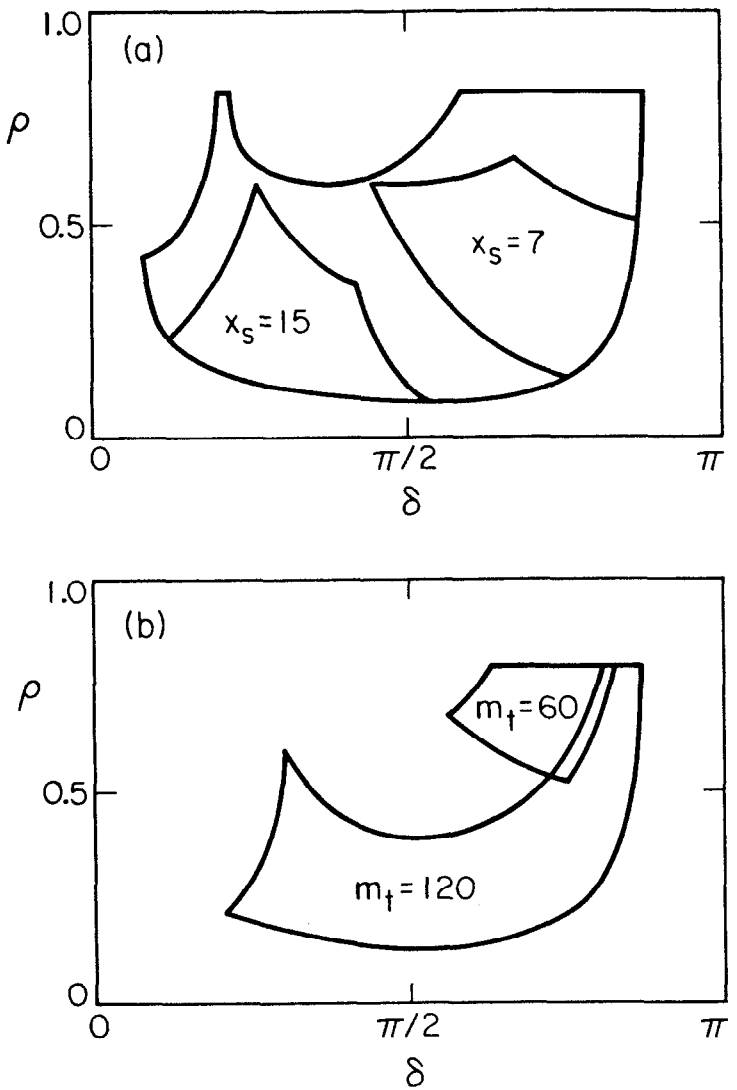

Fig. 2. (a) Allowed region for the two parameters characterizing V^{ub}, ρ and δ. The restricted regions allowed for two values of x_s are shown. (b) The allowed regions for two values of M_t. These are adapted from reference 11.

CP VIOLATION

The CP violating asymmetries always have the form

$$\Gamma - \overline{\Gamma} \propto |V_{us}||V_{cb}|\ Im(V_{ub}) \propto A^2\lambda^6\rho\sin\delta.$$

In K decay the rates are proportional to $A^2\lambda^4\rho\sin\delta \simeq 10^{-3}$; which agrees with the measured value of $|\varepsilon|$. The case in B decay is quite different. Then the decay rates for the dominant modes are proportional to $A^2\lambda^4$ and asymmetries are around $\lambda^2\rho\sin\delta \simeq .02$. In addition, one can study asymmetries in K–M suppressed modes involving b → u transitions, for example, for which the asymmetry can be around $\sin\delta$. The price of such a large asymmetry is a small branching ratio, however.

Table 1. Estimates of branching ratios and asymmetries for CP violation studies in B decays

Class	Modes	Branching Ratio	Asymmetry
I. Charge Asymmetry in Same Sign Dileptons	$B_d\overline{B_d} \to \ell^\pm\ell^\pm + X$	0.001	10^{-3}
	$B_s\overline{B_s} \to \ell^\pm\ell^\pm + X$	0.002	10^{-4}
II. Mixing with Decay* to a CP Eigenstate	$B \to \psi K_s$	5×10^{-4}	0.05 – 0.3
	$B \to \psi K_s X$	2×10^{-3}	0.05 – 0.3
	$B \to D\overline{D}K_s$	5×10^{-3}	0.05 – 0.3
	$B \to \pi^+\pi^-$	5×10^{-5}	0.05 – 0.5
	$B \to D^{+*}D^-,\ D^+D^-,\ D^*D^*$	3×10^{-3}	0.05 – 0.3
III. Mixing with Decay* to a CP Non-Eigenstate	$B_d \to D^+\pi^-$	6×10^{-3}	0.001
	$B_d \to D^0K_s$	6×10^{-5}	0.01
	$B_s \to D_s^+K^-$	3×10^{-4}	0.5 ?
IV. Cascade Decays to the Same Final State	$B^- \to D^0K^- + X$, $D^0 \to K_s + Y$	10^{-5}	0.1 ?
V. Interference of Spectator and Annihilation Graphs	$B^- \to D^{0*}\overline{D}$	3×10^{-3}	0.01
VI. Interference of Spectator and Penguin Graphs	$B^- \to K^-\rho^0$	$\sim 10^{-5}$	0.1
	$\overline{B_d} \to K^-\pi^+$	$\sim 10^{-5}$	0.1

* The asymmetry is integrated over the entire time evolution, and is equal to $\alpha\ x/(1+x^2)$. Thus the parameter α is about twice the listed asymmetry for the B_d.

Table 1 shows the estimates of asymmetries made at the Berkeley SSC study in 1987.[12] There were seven classes of CP-violating asymmetries that were studied. The first of these is the charge asymmetry in dilepton events. Although this mode is the easiest experimentally, and is the one in which mixing is measured, the asymmetry is probably unobservably small. Class VI, interference of spectator and penguin graphs, may have a large asymmetry of 10%, but the size of the penguin graph is not yet known. These modes have the experimental advantage

that they are often self-tagging, with no need to observe the other B decay in the event. There is the theoretical disadvantage that effects of hadronization are important in extracting the K–M parameters, even if the asymmetry was measured.

Most of the work at Snowmass was focused on class II, mixing with decay to a CP eigenstate. A CP-violating asymmetry requires two amplitudes to interfere. In this case the interference is between the unmixed B_d and mixed $\bar{B}_d$ states decaying to the same CP eigenstate. Because the mixing is so large, the amplitudes are comparable and the asymmetry is large. The asymmetry depends only on K–M matrix parameters, so the theoretical interpretation is straightforward.

Two modes which illustrate the available information are $B_d \to \psi K_s$ and $B_d \to \pi^+\pi^-$. The mixing diagram, shown in Fig. 3(a), involves two vertices with factor V_{td}. The ψK_s decay diagram in Fig. 3(b) involves only V_{cb} and V_{cs} and introduces no additional phases. Thus the asymmetry parameter $\alpha = \sin 2\phi$. The diagram for $B_d \to \pi^+\pi^-$, shown in Fig. 3(c) includes an extra factor of V_{ub} and has asymmetry parameter $\alpha = \sin 2(\phi + \delta)$. The time dependence of the decays will be

$$\Gamma(B^0 \to f) = e^{-\Gamma t}[1 + \alpha \sin(\Delta m t)]$$
$$\Gamma(\overline{B^0} \to f) = e^{-\Gamma t}[1 - \alpha \sin(\Delta m t)],$$

where the α parameters are given above.

Measurements of the asymmetries in these two modes would specify the shape of the triangle. This shape can be determined independently by measuring the three sides, although theoretical and experimental uncertainties are still large. The asymmetry parameter for the ψK_s mode is restricted to be positive, but the parameter for the $\pi^+\pi^-$ is completely unlimited. Knowledge of these two asymmetries will provide a detailed test of the three-generation model of CP violation.

STATUS OF B DECAY STUDIES

It is useful to recall the experimental status of B decays, reviewed by Karl Berkelman in his lectures at this conference.[8] ARGUS collected about $0.9 \cdot 10^5$ $B\overline{B}$ events, and CLEO collected $2.5 \cdot 10^5$ in its 1987 run. The goal of CESR and

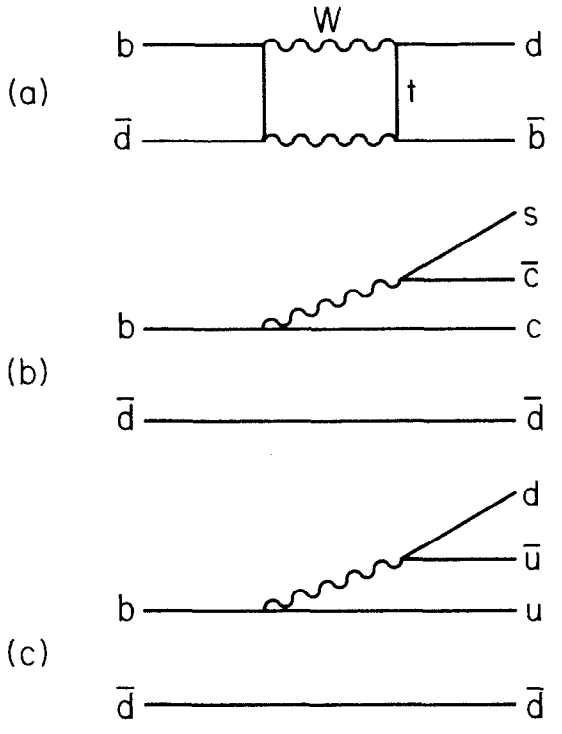

Fig. 3. The quark diagram for (a) $B_d - \overline{B_d}$ mixing, (b) $B_d \to \psi K_s$ and (c) $B_d \to \pi^+\pi^-$.

CLEO II is to raise this number to 10^6 in the near future and 10^7 by 1994 or so. In the modes which have large branching ratios and are relatively easy to see, such as $D^{*+}\pi^-$ and $D^{*+}\pi^+\pi^-\pi^+$, CLEO saw 10's of events. This corresponds to efficiencies of about 30% for the low multiplicity modes, not including D branching ratios, and efficiencies of about 3% for high multiplicity modes in which more cuts are required.

In the benchmark mode $B^0 \to \psi K_s$, the branching ratio is .03% based on two events. This is consistent with the ratio of .08% for $B^- \to \psi K^-$, which comes from a sample of 20 events. To be able to do a definitive CP-violation experiment on the ψK_s mode, one would need about 3000 events with the time dependence measured and tagging of the opposite sign B. With no improvements in efficiencies, this would take almost 10^9 $B\overline{B}$ events, but produced not at rest. This comparison gives some feeling for how far we need to go.

There is one existing proposal for a storage ring to improve on existing machines in the 10 GeV region. The PSI proposal is based on two rings, each carrying 0.5 A of current at full luminosity. With parameters $\Delta Q = 0.04$, $\beta^* = 2$ cm, and 1 MW of R.F. power, the luminosity is designed to be about $1.2 \cdot 10^{33}$ $cm^{-2}s^{-1}$ at 5 GeV per beam. The detector design in this proposal is a prototype of the next generation for such detectors. It includes a ring imaging Cherenkov counter (RICH) with liquid radiator to provide improved particle identification. In addition, there is a silicon vertex detector (SVD) which includes strips in both the z and r–ϕ directions. The beam pipe has a radius of 1.5 cm, which is crucial to the performance of the vertex detector. The vertex detector will be used to separate the tracks from the D decay vertices and improve background suppression for many modes. If the radius of the first silicon planes is significantly increased, the resolution is degraded by multiple scattering.

The existing experiments designed to study B physics, both at the $\Upsilon(4s)$ and at higher energy, will have a great deal of physics to do in the coming years. A partial list of important topics are:

1) lifetimes of the B^+, B_d, and B_s.

2) measurement of $B^0 \to \pi^+ e^- \nu_e$ and $B^0 \to \pi^+\pi^-$ (V_{bu}).

3) measurement of x_s (mixing parameter for B_s).

4) measurement of $B \to \tau\nu_\tau$.

5) measurement of $\ell^+\ell^+/\ell^-\ell^-$ ratio.

6) measurement of $\bar{B}_d \to K^-\pi^+/B_d \to K^+\pi^-$.

All of these will sharpen our picture of B decays along with the measurement of the top quark mass. The last two would be early searches for anomalous CP violation. Clearly there is new, important physics at each new order of magnitude. Finally, the goal will be to look for CP violation at the level it is expected in the standard model.

MEASURING CP VIOLATION IN B DECAYS AT e^+e^- MACHINES

The strategy of studying CP violation depends on the decay time information that is available. In this discussion, I will assume that we are looking at CP violation in CP eigenstate modes such as ψK_s and $\pi^+\pi^-$. There are three situations, each with its own time dependence.

1) $\underline{\Upsilon(4s) \to B^0\overline{B^0}}$. Most of our information on B physics comes from e^+e^- machines operating at the $\Upsilon(4s)$. Since the relative angular momentum (L) of the two B mesons is odd, they will always be a particle-antiparticle pair at the time of the first decay. Although there is mixing, the mixing is coherent to maintain this condition. Assume that one B decays into $X\ell^+\nu$ at time t, and the other into a hadronic final state at time $\bar{t}$. Then the two-dimensional time dependence will be

$$e^{-\Gamma(t+\bar{t})}[1 \pm \alpha \sin x\Gamma(t-\bar{t})]$$

where x is the mixing parameter. If the decay time is not measured, the asymmetry integrates to 0. The only relevant time for the asymmetry is $t - \bar{t}$, the difference in proper decay times.

2) $\underline{\Upsilon(4s+) \to B\overline{B^*}}$. This is the case of running above the threshold for BB^* production. If the BB^* mode dominates then the two B mesons are in a $L = +1$ state, and Bose symmetry has an opposite effect. Using the same notation as above, the time dependence is

$$e^{-\Gamma(t+\bar{t})}[1 \pm \alpha \sin x\Gamma(t+\bar{t})].$$

In this case the CP asymmetry integrates to a nonzero value even with no time measurement.

3) Incoherent $B\overline{B^0}$. This is the case that pertains for production at the Z^0, in the continuum, or at hadron machines. It assumes an incoherent sum of L = +1 and L = −1 states, giving a time dependence

$$e^{-\Gamma(t+\bar{t})}[1 \pm \alpha \cos(x\Gamma t) \sin(\bar{x}\Gamma\bar{t})].$$

In addition, the B is a mix of B^+, B_d, B_s and Λ_b. The distribution in $\bar{t}$, the time of the decay to the CP eigenstate, exhibits the usual time dependence of the asymmetry. The asymmetry is simply diluted by the average value of $\cos(x\Gamma t)$, where t is the decay time of the semileptonic (tagging) mode.

To compare the luminosity required to study CP violation at various machines, the group at Snowmass looked at six cases of B production at e^+e^- machines. The main advantages and disadvantages are listed here:

Case 0: Symmetric $\Upsilon(4s)$

Case 0 is the special case of the $\Upsilon(4s)$ at rest. The advantages are well known, and have led to the great success in studying B decay physics at CESR and DORIS. The beam-energy constraint improves the mass resolution and thereby reduces the background for exclusive decay modes, as long as it is used carefully. There is a factor of three increase in the B cross section at the $\Upsilon(4s)$. The total final state is $B^0\overline{B^0}$, with no additional particles, which is useful for completely reconstructed final states. Finally, if one observes a neutral B, the other side must be neutral as well.

The disadvantage for the symmetric $\Upsilon(4s)$ is a large one, however. Because the B's are almost at rest, the time development cannot be measured. For CP-conserving B physics this is a hindrance, because it is impossible to reduce combinatoric backgrounds by using vertex information. For the study of CP violation, this is a catastrophic problem. I pointed out above, the asymmetry integrates to 0 with no time information. It is still possible to look for CP violation in dileptons, but the asymmetry should be small. It is also a good place to study CP violation in decays such as $B^- \to K^-\rho^0$, which have no mixing and therefore no time dependence in the asymmetry. Because of the uncertainty in calculating penguin diagrams, however, the branching ratios and asymmetries are difficult to calculate.

Case 1: Asymmetric $\Upsilon(4s)$

It is an attractive possibility to combine the advantages of the $\Upsilon(4s)$ with the ability to measure time development with good resolution. This can be done using an asymmetric collider operating at the resonance. The monochromatic B's then travel down the beam line, a distance of 0.4 mm or so, which can be resolved by a SVD. This information can be used to separate decay products and reduce backgrounds. It also affords a measurement of $t - \bar{t}$, the difference in decay times, which is the proper time variable for mixing studies.

Possibly the main disadvantage of this approach is the difficulty of building the detector. There are two new and crucial design criteria. Because of the small transverse momenta of the charged particles, the beam pipe must be very small ($\sim$ 1 cm) to obtain the required position resolution. In addition, the particles are folded forward, so that good measurements must be made to very small angles. An additional difficulty lies in the fact that such a machine has not been built, and the performance is still not known. Designs have been made using the PETRA and PEP rings, and will be discussed later.

There has been a Monte Carlo study at SLAC[13] to look at the ability to do the desired physics at an asymmetric collider. The results are quite encouraging, assuming that the beam pipe can be made with 1 cm radius and the silicon can be kept thin. Figure 4 shows a drawing of the detector design for an asymmetric B-factory that resulted from the Snowmass study.

Case 2: Symmetric $\Upsilon(4s+)$

For this case, the Snowmass group assumed running a symmetric collider above $B\bar{B}^*$ threshold. The advantage is that the asymmetry survives integrating over time. The disadvantages are that there is no cross section peak, and that the asymmetry is reduced in the integration.

Case 3: Continuum

At a center-of-mass energy in the range 20–30 GeV, the B's have sufficiently high velocity to allow precise measurement of their decay times. The decay products of the two B's are well separated. Since the exact energy is not important, there is no need of a narrow spread in beam energy. This is important for the case of linear colliders. The disadvantages are loss of the beam constraint, more particles in the event, and, most importantly, small cross section.

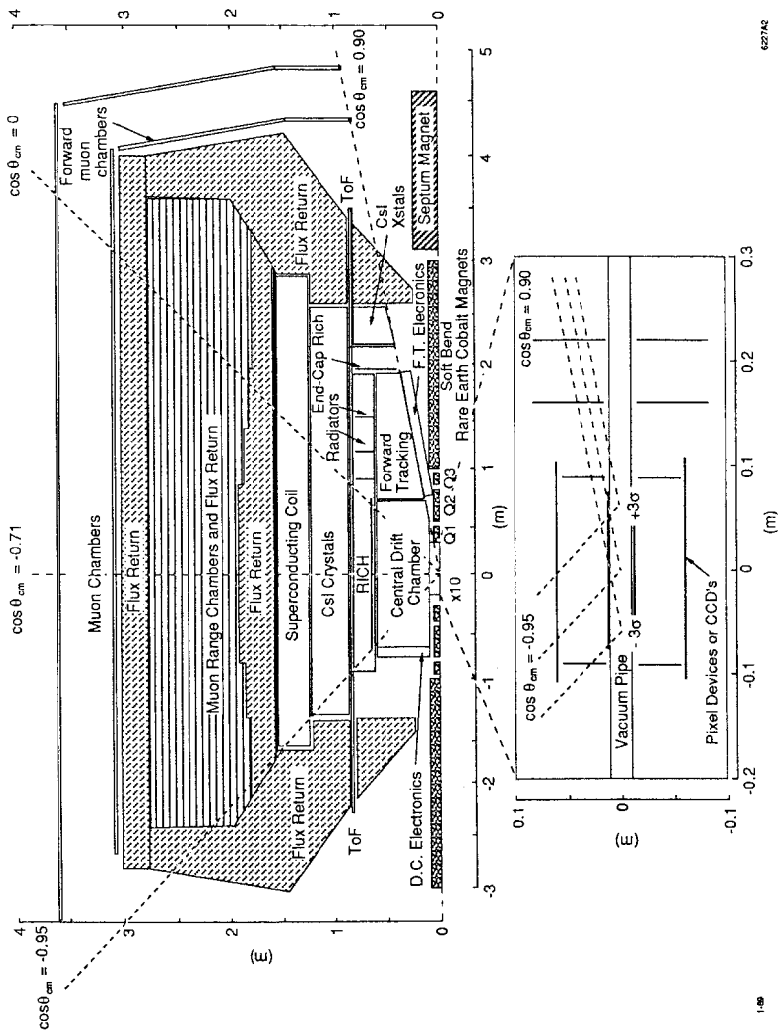

Fig. 4. Detector design for an asymmetric collider.

Cases 4 and 5: Z^0 Factory (unpolarized and polarized)

The large value of R at the Z^0 peak more than cancels the drop in dimuon cross section. The $b\bar{b}$ cross section is 5.3 times as large as at the $\Upsilon(4s)$, and no continuum subtraction is necessary. There is a significant advantage for the use of vertex detectors at the Z. The high p_T of the B-mesons means that the beam pipe can be larger and the vertex detector thicker before resolution is degraded by multiple scattering. The disadvantage is the high multiplicity of the event, although this may be completely overcome by three-dimensional vertex information.

For CP violation studies, it is important to tag the flavor of the B. Usually this is done by detecting the opposite sign lepton. With polarized Z^0's, however, there is a large asymmetry in the $b\bar{b}$ decay. This removes the need to detect the other B.

The Snowmass group calculated the needed integrated luminosity to observe CP violation for case 1–5. Many assumptions were made about predicted asymmetries, tagging efficiency, etc. Many of these cancel out when comparing two techniques, however. Thus it should give a fairly good indication of the relative strengths of the various machines, if they could be built with the same luminosity.

The goal is to detect the mode $B^0 \to \psi K_s$, $\psi \to \ell^+\ell^-$, and tagging the opposite B by various techniques. The needed luminosity can be calculated using the formula

$$\left[\int L dt\right]^{-1} = \sigma(e^+e^- \to b\bar{b}) f^0 2B\varepsilon_r\varepsilon_t(1-2w)^2 d^2\delta^2(\alpha).$$

Here f^0 is the fraction of b quarks which are bound in B^0's, and B is the branching ratio, assumed to be $5 \cdot 10^4$ for $B \to \psi K_s$ and 0.14 for $\psi \to \ell^+\ell^-$. The ψK_s reconstruction efficiency is ε_r, and the tagging efficiency is ε_t. There are different techniques assumed for tagging: lepton (ℓ), kaon (K), D-meson (D), or forward-backward asymmetry (A_{FB}). A wrong fraction of tags w is assumed, and d is the dilution factor of the asymmetry to take into account such factors as mixing of the tagging B. The required accuracy on the CP asymmetry parameter is $\delta(\alpha)$, which was set to be 1/3 of the expected asymmetry, for a 3σ effect. The assumed value of α is in the range 0.1–0.6.

The results of this comparison are shown in Table 2. There is probably some amount of overoptimism in the tag efficiency, but it applies to all of the first four columns. The resulting $\int L dt$ needed to see such an effect is in the last column. Symmetric $\Upsilon(4s+)$ requires a factor of 6 more luminosity, and continuum running a factor of 40, than the asymmetric case. The Z^0 factory requires comparable luminosity, and less if it has high polarization.

Table 2. Comparison of B-Factory Techniques

Case / Factor	Asym. $\Upsilon(4s)$	Sym. $\Upsilon(4s+)$	$\sqrt{s}$ = 16 GeV	Z P = 0	Z P = 0.9 (P = 0.45)
$b\bar{b}$ cross section σ (nb)	1.2	0.3	0.11	6.3	6.3
Fraction of B^0, f^0	0.43	0.34	0.35	0.35	0.35
ψK_s reconstruction efficiency, ε_r	0.61	0.61	0.61	0.46	0.46
Tag efficiency, ε_t (& method)	0.48 (l,K)	0.48 (l,K)	0.30 (l,D)	0.18 (l,D)	0.61 (A_{FB})
Wrong tag fraction, w	0.08	0.08	0.08	0.08	0.125 (0.27)
Asymmetry dilution, d	0.71	0.63	0.52	0.52	0.71
$\int L$ dt needed for 3σ effect (10^{40} cm^{-2}) *	0.3 – 12.	2.2 – 78.	14. – 490.	0.5 – 19.	0.1 – 3.6 (0.3 – 9.6)
Relative $\int L$ dt needed	1.0	6.4	40.	1.5	0.3 (0.8)

* = the peak luminosity needed in units of 10^{33} cm^{-2}sec^{-1} for 10^7 seconds of fully efficient running at peak luminosity.

A number of conclusions are evident from the results of this study. For the same luminosity, an asymmetric $\Upsilon(4s)$ and unpolarized Z^0 factory are about equally powerful for CP-violation studies in the B system. Polarized Z^0's do somewhat better. More luminosity is required if symmetric $\Upsilon(4s+)$ operation is used, and substantially more at the continuum. If one wanted to reach the level of probably seeing CP violation, one would design for a 4σ peak at $\alpha = 0.2$. Then one needs a luminosity of about $5 \cdot 10^{40}$ cm^{-2}, or 10^{41} if the efficiency estimates are somewhat optimistic. Using a "Snowmass year" of running 10^7 seconds at peak luminosity, this would take a machine with peak luminosity of 10^{34} cm^{-2}s^{-1} in the most favorable cases. It should be understood that it would normally take many years of running the new machine to obtain a Snowmass year.

I also looked quickly at the self-tagging modes (e.g. class 6 in Table 1). These are decays such as $B^0 \to K^+\pi^-$ or $B^+ \to K^+\rho^0$ which reveal the sign of the parent B, but still have large asymmetries. The expected branching ratios are about 10^{-5}, and they have not yet been seen. The integrated luminosity needed for a 3σ effect is about $2 \cdot 10^{41}$ cm^{-2}, which is roughly comparable to running a symmetric machine at the $\Upsilon(4s+)$ to look for $B \to \psi K_S$. If the branching ratios are larger than the assumed values, we will know soon from CLEO II.

e^+e^- COLLIDERS AS INTENSE B SOURCES

The accelerator physics group working on intense e^+e^- machines in the 10–100 GeV region worked with the physics group looking at B physics at these machines. There were six cases looked at, roughly matched to the cases mentioned in the last section, with the extra choice of linear or circular colliders. I will give a brief summary of the results and refer the reader to the Snowmass summary of Bob Siemann.[14]

1. B-Factories

The first type of B-factories includes equal energy rings at $\sqrt{s} = 10$ GeV. The existing record is held by CESR with $\mathcal{L} = 10^{32}$ cm^{-2}s^{-1}. There are proposals and ideas to upgrade to a luminosity of $5 \cdot 10^{32}$ in three years or so. The limits are beam currents and r.f. power. In addition, there is the PSI proposal discussed earlier, with a design luminosity of over 10^{33} cm^{-2}s^{-1}. In five years these machines will be able to run at the $\Upsilon(4s+)$ with luminosity just below or at 10^{33}. This is not in the range where CP violation is accessible.

There was extensive discussion of asymmetric rings at $\sqrt{s} = 10$ GeV, based on a design of A. Garren. He assumes a 2 GeV ring with 0.54 A in six bunches colliding with a 12 GeV ring with 0.27 A in 85 bunches, which is PEP. The design luminosity is $5 \cdot 10^{32}$ cm^{-2}s^{-1}. Such colliders have been studied at the level of scaling arguments and lattice designs. They are promising and there will be detailed design work in the coming year. The main topics are the stability of high current, low energy beams, the beam-beam effect for unequal energies, and the interaction region design. Since a beam pipe with radius 1–1.5 cm is necessary, the last topic is crucial. This design reaches the lower end of the range specified for CP violation studies. It is using the most optimistic estimates for asymmetry and experimental efficiency, however.

Another possibility is a linear collider, operating either at the $\Upsilon(4s)$ or in the continuum. One of the most developed projects is ARES at Frascati. According to its design, the luminosity at the $\Upsilon(4s)$ is $1.3 \cdot 10^{33}$ cm^{-2}s^{-1}, which grows to $1.1 \cdot 10^{34}$ cm^{-2}s^{-1} at an energy of 15 GeV, but with a spread in energy of 90 MeV. This correlation of increased luminosity with increased spread in energy is a fundamental feature of such designs. The luminosities are large, and reach the lower end of the range specified for CP studies. There must be a great deal of research and development before it is known whether they are realistic. The areas for R & D are positron production and damping, effects of large disruption parameters, and the power source. The proposed R & D program for ARES is to cost $80 million over five years.

2. Z-Factories

The existing storage ring at the Z^0 is LEP, which is supposed to operate at $\mathcal{L} = 1.6 \cdot 10^{31}$ cm^{-2}s^{-1}, with 4 bunches per beam. The RF upgrade for LEP II will be enough for 80 bunches, corresponding to $3 \cdot 10^{32}$ cm^{-2}s^{-1}. There are questions of how to separate the orbits, and whether this can be done in one ring. Other improvements might raise this luminosity to $5 \cdot 10^{32}$ cm^{-2}s^{-1}. With this luminosity at the Z^0, LEP would be at the lower end of the range specified for CP violation.

There are also many papers describing linear Z-factories. One was presented by R. Palmer at Snowmass giving a luminosity of $2.3 \cdot 10^{34}$ cm^{-2}s^{-1}, which he derated to $6 \cdot 10^{33}$ cm^{-2}s^{-1}. This is the only machine, even on paper, which reaches the upper end of the range needed for CP violation in the B system. The R & D issues are similar but not identical to those for the B-factory linear collider. An R & D project of similar scale would be needed to pursue this option.

B PHYSICS IN HADRON COLLISIONS

The main advantage of using hadron collisions as a source of B mesons is the high rate of B production. The main disadvantage is the low fraction of all interactions containing a $b\bar{b}$ pair. New calculations of the $b\bar{b}$ cross sections to terms of order $(\alpha_s^2 + \alpha_s^3)$ show that this is not as low as previously thought, however. The cross sections are predicted to be 45 μb at $\sqrt{s} = 2$ TeV and $\sigma = 500$ μb at $\sqrt{s} = 40$ TeV, which is about 0.5% of the total cross section. For comparison, charm hadroproduction at fixed target energies has a cross section about 0.1% of the total cross section. Similar calculations are correct for charm photoproduction and hadroproduction. They are expected to be even more reliable for bottom production.

The rates of $b\bar{b}$ production are shown in Table 3. The present Tevatron with expected upgrades for the next few years produces $2 \cdot 10^9$ $b\bar{b}$ per Snowmass year. This would go to $8 \cdot 10^{10}$ with a proposed pp machine at $\mathcal{L} = 2 \cdot 10^{32}$ cm^{-2}s^{-1}, or slightly less at RHIC. The SSC would produce a whopping 10^{12} $b\bar{b}$ events in this time, even assuming a "low" luminosity region with $2 \cdot 10^{32}$ cm^{-2}s^{-1}. In this case one would need a factor greater than 10^{-4} for geometrical acceptance, and efficiencies for trigger, tracking, vertex separation, and particle identification.

Table 3. Rates for $b\bar{b}$ production

Source	$\sqrt{s}$ (TeV)	$\sigma_{b\bar{b}}$	$\mathcal{L}$	Rate sec^{-1}	Rate $(10^7$ sec$)^{-1}$
TeV	1.8	40	$5 \cdot 10^{30}$	200	$2 \cdot 10^9$
TeV′ (pp)	1.8	40	$2 \cdot 10^{32}$	8000	$8 \cdot 10^{10}$
RHIC	0.6	13	$2 \cdot 10^{32}$	2600	$2.6 \cdot 10^{10}$
SSC	40	500	$2 \cdot 10^{32}$	100,000	10^{12}

A possible configuration for a B spectrometer at the SSC is shown in Fig. 5. It stretches to 40 m in one direction, allowing acceptance in pseudorapidity to $\eta = 5$, or an angle of 13.5 mr. The coverage extends down in to the central region to $\eta = -3$. This version draws on the forward B detector from the Berkeley SSC Workshop[12] and the design of the Bottom Collider Detector for TeV I,[15] which operates in the central region.

The important features of a B spectrometer for the SSC are: large acceptance, excellent momentum resolution, good electron and muon identification wherever possible, hadronic particle identification by Cherenkov counters, and a very powerful trigger. To study CP violation, it would be necessary to use decay modes with low multiplicity and no neutrals, such as ψK_s or $\pi^+\pi^-$. The opposite side B would be tagged by a semileptonic decay, and the mixing of the B gives the wrong sign tag about 15% of the time.

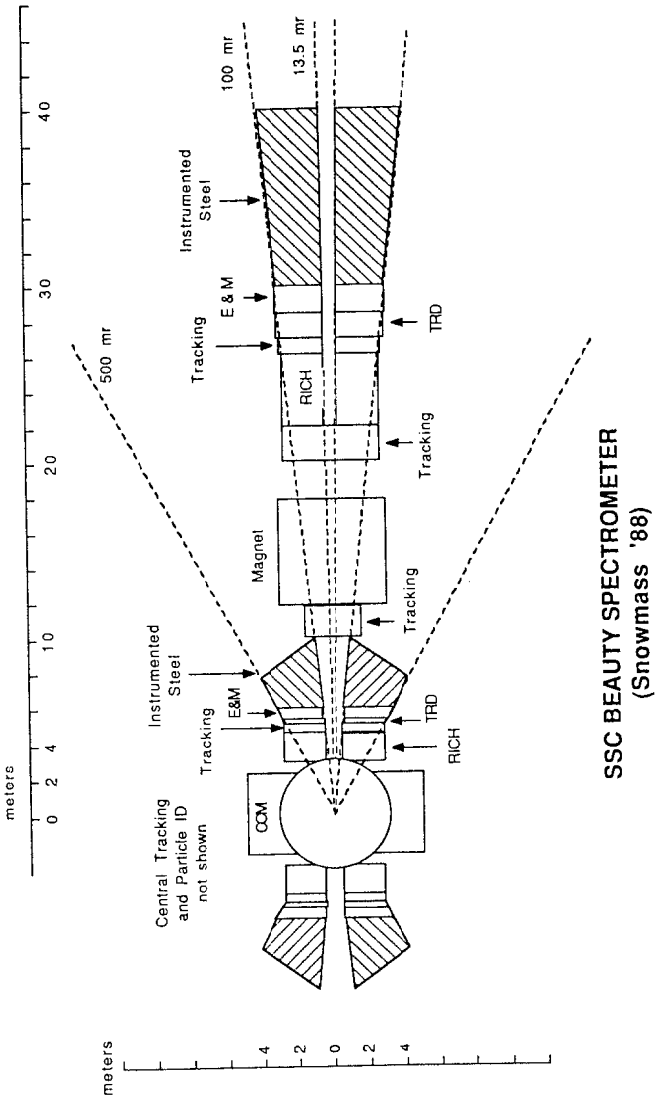

Fig. 5. Detector design for the 1988 Snowmass version of the SSC B spectrometer.

The most difficult problems for designing and building such an experiment are the lepton trigger, the high-rate capability, and the vertex detector. If the two leptons from the ψ decay are used in the trigger, one can probably make an acceptable trigger either with muons or electrons. To completely study the B-decay physics however one wants to trigger on the single lepton from the opposite side B, and be able to study decay modes such as $\pi^+\pi^-$. To trigger on leptons with $P_T \gtrsim 2$ GeV/c is extremely difficult, and a fast-tracking capability is necessary.

There is not the time here to go into the detailed design considerations for such an experiment at the SSC.[16] It is obvious, however, that the requirements go beyond existing hadron collider experiments in many respects. There needs to be a large, continuing R & D effort to work on the problems identified by the Snowmass group.

This group also worked on the design of a B physics experiment for the Tevatron collider. There the $\bar{b}b$ rate is .01–.1 as large, and the signal-to-noise ratio is significantly smaller. Such an experiment needs large acceptance and the full luminosity of a proposed pp upgrade. The length over which the interactions are distributed is much smaller for the pp upgrade as well, and that is crucial for operation of the vertex detector. Of course the time scale of the Tevatron upgrade could be closer than the other experiments considered. A large group is now carrying out the first serious study of the design problems for such an experiment. They are planning on proposing such an experiment in the near future.

There is also a future for B physics in fixed target hadron experiments. Sergio Conetti[17] is talking at this conference about Fermilab E–771, an experiment designed to look for $B \to \psi X$ in pp interactions at $\sqrt{s} = 40$ GeV. This will provide a test of many aspects of the collider experiment; operation of a vertex detector at high rates, and the muon trigger are two examples. Other experiments are proposed to look for two-body modes of B mesons and B production in photon and hadron beams. After the first round of these experiments, it will be possible to see with what sensitivity one can study B physics at fixed target.

SUMMARY

The effort to study CP violation in B decays will be a central focus for

particle physics for some time to come. In addition there are new levels of physics available in B physics at every new order of magnitude leading up to the level needed for CP violation. We are in an unusual situation. At e^+e^- machines, we know how to build the experiments, but the accelerator that can provide sufficient intensity is not yet designed. At hadron machines, accelerators can produce enough B's, but a new type of experiment is needed.

My own guess is that it will take a 10-year program to reach definitive experimental results on CP violation in B decay. It is also one of the problems in physics important enough to deserve such an effort.

REFERENCES

1. H. Harari, these proceedings.
2. H. Burkhardt *et al.*, *Phys. Lett.* **206**, 169 (1988); also see M. Woods *et al.*, *Phys. Rev. Lett.* **60**, 1695 (1988).
3. H. Albrecht *et al.*, *Phys. Lett.* **192**, 245 (1987); N. Katayama, D. MacFarlane, and H. Harari, these proceedings.
4. F.J. Gilman, Proceedings of Rencontres de Physique de al Vallée d'Aoste and SLAC–PUB–4598.
5. H. Leutwyler and M. Ross, *Z. Phys.* **C25**, 91 (1984).
6. F.J. Gilman, K. Kleinknecht, and B. Renk, "The Kobayashi–Maskawa Mixing Matrix", in the 1988 Review of Particle Properties (to be published in Rev. of Mod. Phys.).
7. S. Behrends *et al.*, *Phys. Rev. Lett.* **59**, 407 (1987).
8. K. Berkelman, these proceedings.
9. H. Albrecht *et al.*, *Phys. Lett.* **209**, 119 (1988); also see Ref. 8.
10. P. Jenni, in Proceedings of the 1987 International Symposium on Lepton and Photon Interactions at High Energies, ed. by W. Bartel and R. Rückl (North-Holland, Amsterdam, 1988).
11. R. Peccei *et al.*, to appear in Proceedings of the 1988 Snowmass Conference; and *Nucl. Phys.* **B307**, 19 (1988).
12. K.J. Foley *et al.*, in "Experiments, Detectors, and Experimental Areas for the Supercollider", ed. by Rene Donaldson and M.G.D. Gilchriese (World Scientific, Singapore, 1988).
13. R. Aleksan *et al.*, SLAC preprint SLAC–PUB–4673, 1988.
14. R. Siemann *et al.*, to appear in Proceedings of the 1988 Snowmass Conference.
15. Bottom Collider Detector group, Letter of Intent submitted to Fermilab (1988).
16. See the report of M. Schmidt *et al.*, to appear in the 1988 Snowmass Proceedings.
17. S. Conetti, these proceedings.

Hadroproduction of ψ and χ States

Sergio Conetti

McGill University

No paper was received from the author in time for printing.

RECENT RESULTS ON S=-3 BARYON SPECTROSCOPY FROM THE LASS SPECTROMETER*

BRIAN T. MEADOWS†
University of Cincinnati

ABSTRACT

Data demonstrating the existence of two Ω^{*-} resonances produced in K^-p interactions at 11 GeV/c in the LASS spectrometer are presented. The first state is seen in the $\Xi^{*0}K^-$ decay channel with mass 2253 ± 13 MeV/c^2 and width 81 ± 38 MeV/c^2 and the second in the $\Omega^-\pi^+\pi^-$ system with mass 2474 ± 12 and width 72 ± 33 MeV/c^2. Inclusive cross sections corresponding to these decays corrected for unseen charge modes are estimated to be respectively 630 ± 180 and 290 ± 90 nb.

Presented at the SLAC Summer Institute on Particle Physics,
Stanford, California, July 17-28, 1988.

1. Introduction

Even though the Ω^- hyperon was discovered more than two decades ago, data showing the existence of any of its excited states have become available only very recently [2-4]. Such data have required the use of K^- or hyperon beams in fixed target experiments. They also require detectors with the acceptance and resolution necessary to deal efficiently with the complex topologies that events involving such particles entail, the capability to perform good particle identification necessary in the recognition of the relevant final states, and the ability to acquire and process huge data samples. These qualities have been admirably matched by the Large Aperture Superconducting Solenoid (LASS) spectrometer at SLAC. In this talk, I shall present the data of the LASS E135

* Work supported in part by the Department of Energy under contract No. DE-AC03-76SF00515, the National Science Foundation under grant Nos. PHY82-09144, PHY85-13808, and the Japan U.S. Cooperative Research Project on High Energy Physics.

† Representing the LASS E135 collaboration [1].

collaboration [1] which were accumulated in a large exposure to a beam of 11 GeV/c K^-. These data clearly demonstrate the existence of Ω^{*-} resonances in two channels:

$$K^-p \rightarrow \Xi^-\pi^+K^- + \text{anything} \quad \hookrightarrow \Lambda\pi^- \tag{1}$$

$$K^-p \rightarrow \Omega^-\pi^+\pi^- + \text{anything} \quad \hookrightarrow \Lambda K^- \tag{2}$$

2. The Experiment

The LASS spectrometer is shown in Fig. 1. Full descriptions of the hardware, triggering and data processing algorithms and other experimental details are given in Reference [5]. Details associated with extraction of the Ξ^- and Ω^- samples discussed here are also given in Reference [6].

The spectrometer was situated in an RF-separated beam of 11 GeV/c K^- with a K/π ratio of 70/1, tagged by beam Cherenkov counters. Important features of LASS were its uniform acceptance over almost the full 4π solid angle, excellent momentum and angular resolution, azimuthal symmetry, and good particle identification. Momentum measurement was accomplished with the superconducting solenoid with 22.4 kG field in the beam direction, and with the 30 kG-m dipole with vertical field. Low momentum particles were well measured by the solenoid vertex detector which was instrumented with proportional wire chambers (PWC's) having $200\mu m$ spatial resolution. High momentum particles travelling close to the beam axis were accurately measured in the dipole spectrometer.

Particle identification was accomplished by two threshold Cherenkov counters (C_1 and C_2) and a time-of-flight (TOF) hodoscope placed behind C_1 at a distance of five meters downstream from the target. The pulse heights measured in the cylindrical PWC's surrounding the target provided dE/dx information for low momentum particles having wide recoil angles. This was useful in distinguishing $\pi/K/p$ hypotheses in the $1/\beta^2$ region.

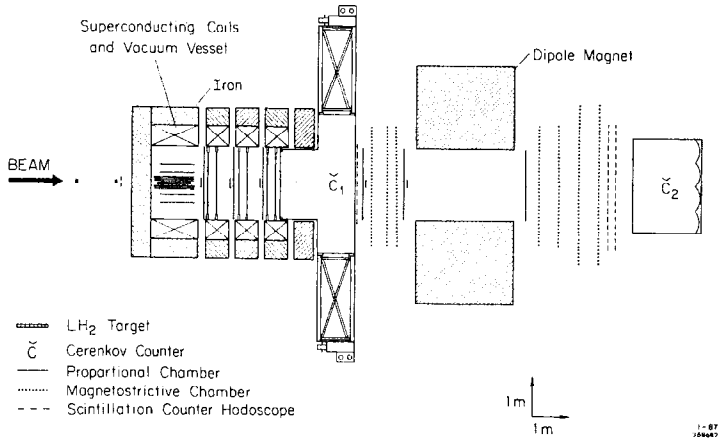

Fig. 1 The LASS Spectrometer.

A very loose trigger required two or more charged particles to emerge from the hydrogen target. For the channels of interest here this represented a completely negligible bias.

The raw data sample contained $\sim$ 113 million triggers, and the resulting useful K^- beam flux corresponded to a sensitivity of 4.1 events/nb. After track reconstruction, a sample of events consistent with the $\Xi^- \to \Lambda\pi^-$ or $\Omega^- \to \Lambda K^-$ decay topologies, illustrated in Fig. 2, was identified. A pair of oppositely charged tracks which met within a few mm in space was required to yield a $p\pi^-$ effective mass consistent with the nominal Λ mass. The Λ momentum vector was further required to point back within a few mm of a negative track candidate which was chosen such that the effective mass formed with the Λ was compatible with either of the above decay modes.

Finally, the composite track formed from this negative with the Λ was, in turn, required to extrapolate back to within 1 cm of a primary vertex whose position was determined by a fit to the incoming beam and the primary charged track candidates. A sample of $\sim$ 1.5 million events satisfying these requirements was defined.

3. The $\Xi^- K^- \pi^+$ Channel

A clean sample of Ξ^- events was readily extracted. Particle identification was used to reject events inconsistent with a Ξ^- interpretation and also events with identified protons at the primary vertex. Kinematic overlap between γ and Λ often occurred. Such misidentified γ's were removed from the remaining Λ sample by eliminating events with Λ decay helicity cosine greater than 0.98. Finally, only events with a Ξ^- track length greater than 3 cm were retained. The resulting $\Lambda\pi^-$ effective mass distribution shown in Fig. 3 exhibited a strong Ξ^- signal. Approximately 82,000 Ξ^- events with a background of approximately 10% in the mass range $1310 < M_{\Lambda\pi^-} < 1332$ MeV/c^2 were selected for further study.

These events were then tested for existence of a K^-. Clearly, a negative track produced in $K^- p$ induced Ξ^- reactions was more likely to be a π^- than a K^-, since the latter required production of an additional unit of strangeness. Clear identification of the K^- was therefore necessary, and to this end negative tracks entering the geometrically efficient regions of C_1 or C_2 at momenta above 2.9 GeV/c were required to give no light.

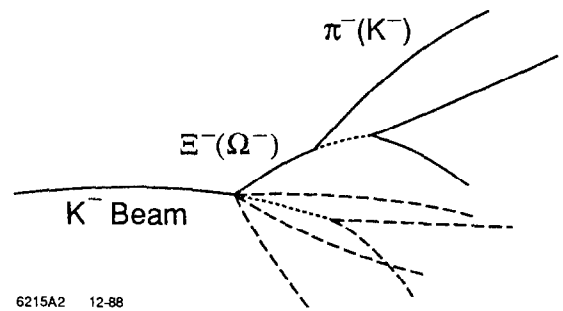

Fig. 2 Basic V^- event topology. Solid lines indicate tracks required in the primary selection process described in the text.

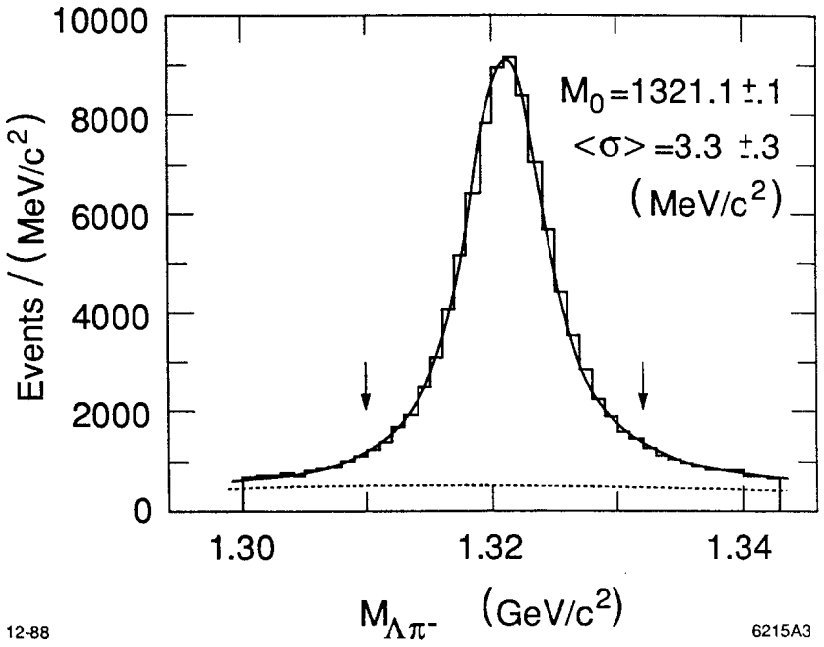

Fig. 3 Distribution of the $\Lambda\pi^-$ effective mass for events selected as Ξ^- candidates as described in the text. The arrows indicate the selected mass range.

To reduce background from poorly measured π^-'s below threshold, K^- candidates were also required to have momenta at least two standard deviations above threshold.

Since K^- identification required a negative signature (no light) from the Cherenkov counters, it was essential to obtain an accurate estimate of the "punch through" contamination in the K^- sample produced by π^-'s (or e^-'s) failing to produce light due to Cherenkov inefficiency. This estimate was derived from the particles which did give Cherenkov light. The momentum distributions for negative particles from primary vertices of events in the Ξ^- sample were examined, and are shown in Fig. 4. These distributions were weighted, on a particle by particle basis, by factors depending upon the Cherenkov efficiencies (ϵ), which in turn depended upon the particle momentum and hit position. The points on the dotted curve corresponded to particles which produced light in at least one C, and were weighted by the factor ϵ^{-1}. This distribution was taken to represent the π^- (and e^-) sample. The threshold near 2.6 GeV/c was clearly seen, and events below this were presumed to be due to e^-. Also in Fig. 4 (points on the solid line) was the distribution representing those particles which gave no light in either C_1 or C_2. This was corrected for efficiency by taking the difference between the momentum distribution for all negative particles (whether giving light or not) and the distribution described above. The sharp fall with increasing momentum near threshold arose because the efficiency increased in this region. Above threshold, this could be taken to represent the K^- momentum distribution. The points on the dashed curve resulted from plotting the momenta of the negative particles giving light, weighted by the factor $\epsilon^{-1}(1-\epsilon)$. This curve represented, therefore, the punch-through contamination. Comparing this with the K^- distribution, it was clear that above the 2.9 GeV/c cut, a rather clean K^- sample was separated.

In this way, a sample of 814 events was extracted, yielding 1,259 $\Xi^-K^-\pi^+$ mass combinations shown in the distribution in Fig. 5. No clear resonant structure was seen in this $S=-3$ baryon system. However, the mass distribution for the $\Xi^-\pi^+$ subsystems (Fig. 6) showed a strong $\Xi^{*0}(1530)$ signal. Selection of an enriched $\Xi^{*0}(1530)$ sample ($1510 < M_{\Xi^-\pi^+} < 1555$ MeV/c^2) resulted in the $\Xi^-K^-\pi^+$ mass histogram of Fig. 7. A clear signal (~ 4 standard deviations) at a mass of approximately 2250 MeV/c^2 was apparent, and could be interpreted to correspond to the decay of an Ω^{*-} to $\Xi^{*0}(1530)K^-$.

An estimate of the behaviour of the non-resonant background beneath the Ξ^{*0} peak

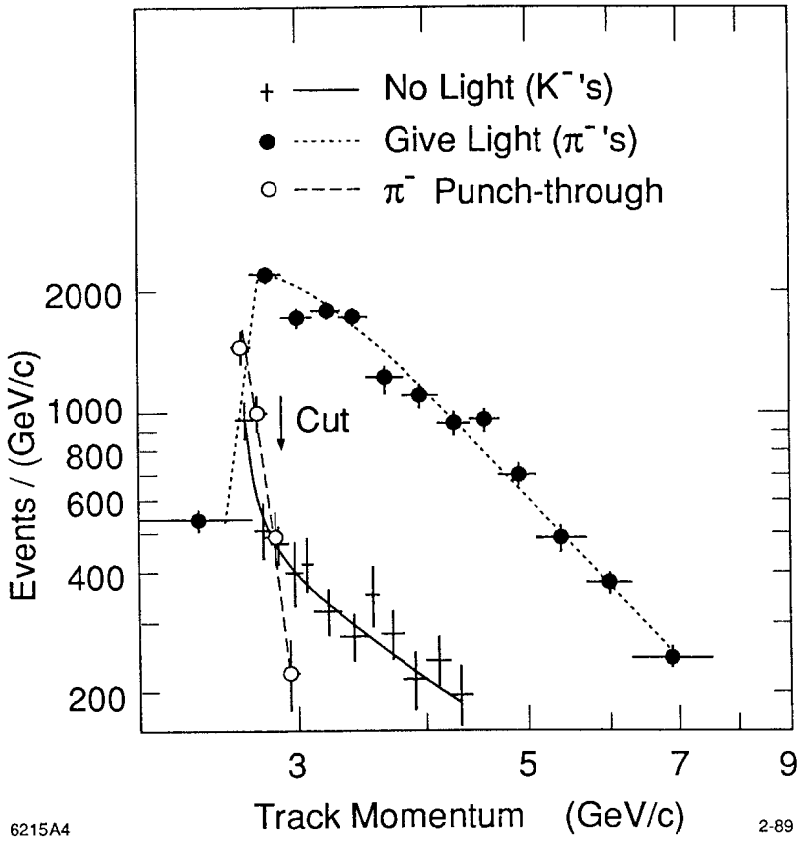

Fig. 4 Momentum distributions for three classes of negative charged particles produced in conjunction with Ξ^-'s. The curves are drawn to aid in distinguishing the three classes. The solid line indicates those tracks which gave no Cherenkov light; the dotted curve connects data points for the tracks which did give light. The latter data are weighted by a factor ϵ^{-1} where ϵ is the momentum dependent Cherenkov efficiency. The dashed line shows the same data plotted instead with a weight $\epsilon^{-1}(1-\epsilon)$.

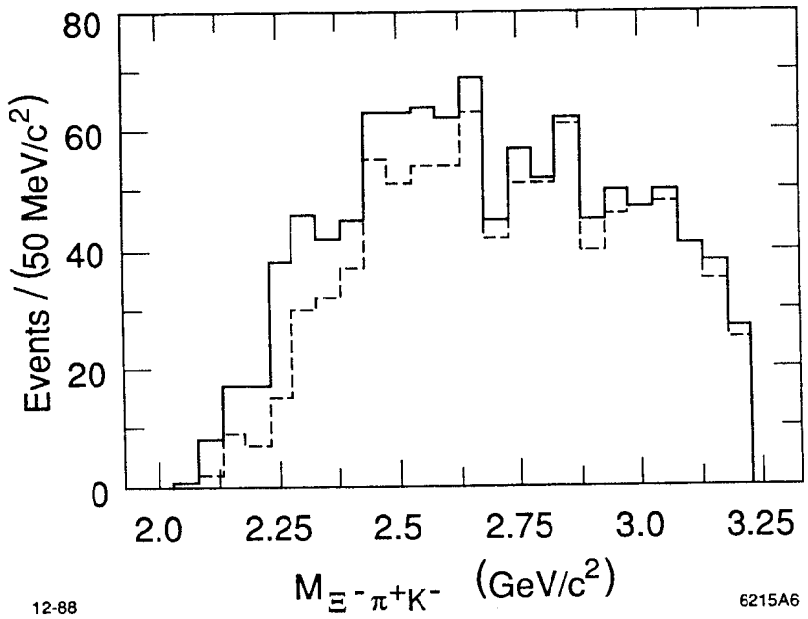

Fig. 5 Distribution of $\Xi^-K^-\pi^+$ effective masses for all 1,259 combinations. The dashed histogram contains events outside the $\Xi^{*0}(1530)$.

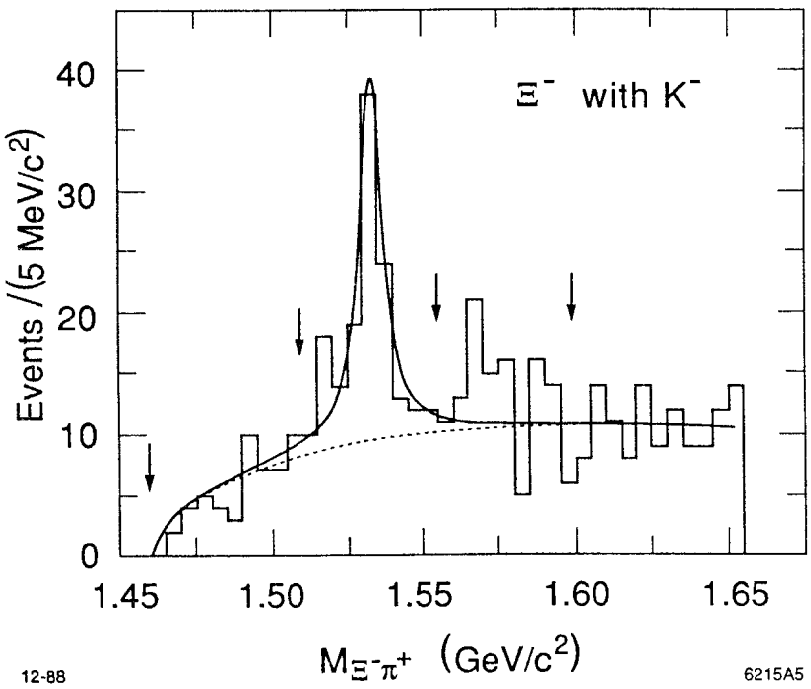

Fig. 6 Distribution of $\Xi^-\pi^+$ effective masses for 814 events with both a Ξ^- and a K^-. The limits used to define both $\Xi^{*0}(1530)$ and the control regions on either side are marked by arrows.

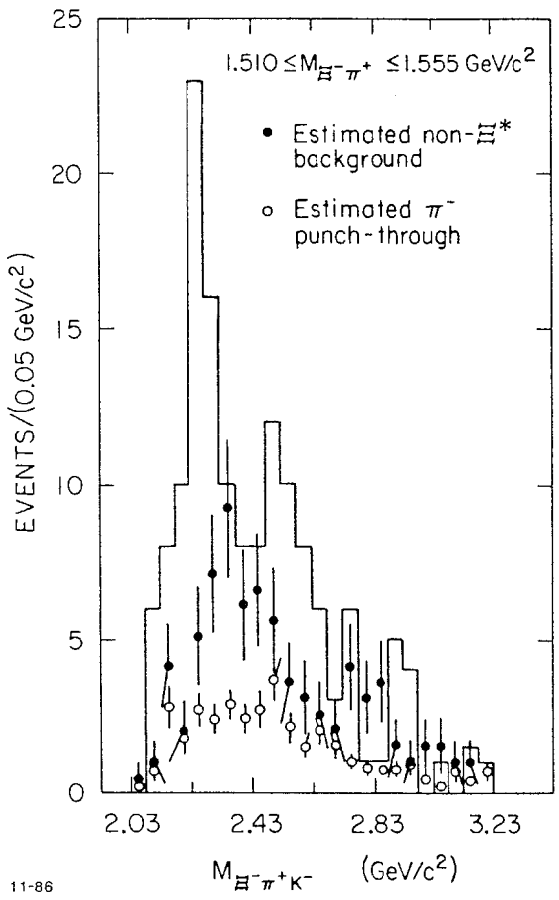

Fig. 7 Distribution of $\Xi^-K^-\pi^+$ effective masses for events having both a K^- and $\Xi^-\pi^+$ mass in the range $1510 < M_{\Xi^-\pi^+} < 1555 \mathrm{MeV/c^2}$ (outer histogram); or in the control bands defined by $M_{\Xi^-\pi^+} < 1510$ or $1555 < M_{\Xi^-\pi^+} < 1600 \mathrm{MeV/c^2}$ (solid dots). The open circle distribution is for events with $\Xi^-\pi^+$ mass in the former range and a negative track giving light in either C_1 or C_2. In this distribution, each event is weighted by the factor $(1-\epsilon)/\epsilon$, in which ϵ is the Cherenkov efficiency.

in Fig. 6 was made using the events in the sideband regions defined by ($M_{\Xi^-\pi^+} < 1510$ or $1555 < M_{\Xi^-\pi^+} < 1600$ MeV/c^2). The $\Xi^-K^-\pi^+$ mass distribution for these events, normalised to the number of events under the $\Xi^{*0}(1530)$ signal was plotted in Fig. 7 with solid dots. The striking absence of any peak near 2250 MeV/c^2 was a clear indication that the observed structure was associated purely with $\Xi^{*0}(1530)$.

In order to investigate the possibility that the effect arose from π^-'s being misidentified as a result of Cherenkov inefficiency, a study was made using events which were selected exactly as above, except that the "K^-" tracks were required to give light in either C_1 or C_2. All momentum requirements were as before, and the tracks were still assigned a K^- mass. The $\Xi^{*0}(1530)$"K^-" mass distribution that resulted (Fig. 8), contrasted with the true K^- distribution, showing no structure suggestive of a peak in the 2250 MeV/c^2 region. In addition to demonstrating that the peak was not due to misidentified pions, this also showed that it was not a kinematic effect due to the acceptance limitations placed upon the negative track by the Cherenkov identification requirement. An estimate of the mass distribution corresponding to punch-through was also obtained from these "K^-" events by plotting them, each weighted by a factor $(1-\epsilon)/\epsilon$ (where ϵ was the π^- Cherenkov efficiency). This distribution, indicated by open dots in Fig. 7, showed that such punch-through contributed negligibly to the signal.

The significance of the Ω^{*-} signal was estimated from the background subtracted $\Xi^{*0}(1530)K^-$ spectrum in Fig. 9. This was obtained from the data of Fig. 7 by subtraction of the Ξ^{*0} sideband distribution (black dots) representing the non-Ξ^{*0} background from the data in the histogram.

The solid curve of Fig. 9 was the result of a fit to the data using the expression:

$$\frac{dN}{dM} = q\left[\frac{c_1}{\left(M_0^2 - M^2\right)^2 + M_0^2\Gamma^2} + c_2 + c_3 M\right]$$

$$\text{with} \quad \Gamma = \Gamma_0\left(\frac{q}{M}\right)\left(\frac{M_0}{q_0}\right)$$

where M_0 and Γ_0 were the Ω^{*-} mass and width respectively; q (q_0) was the K^- momentum in the rest frame of a Ξ^*K^- system of mass $M(M_0)$, and the c_i were fit parameters.

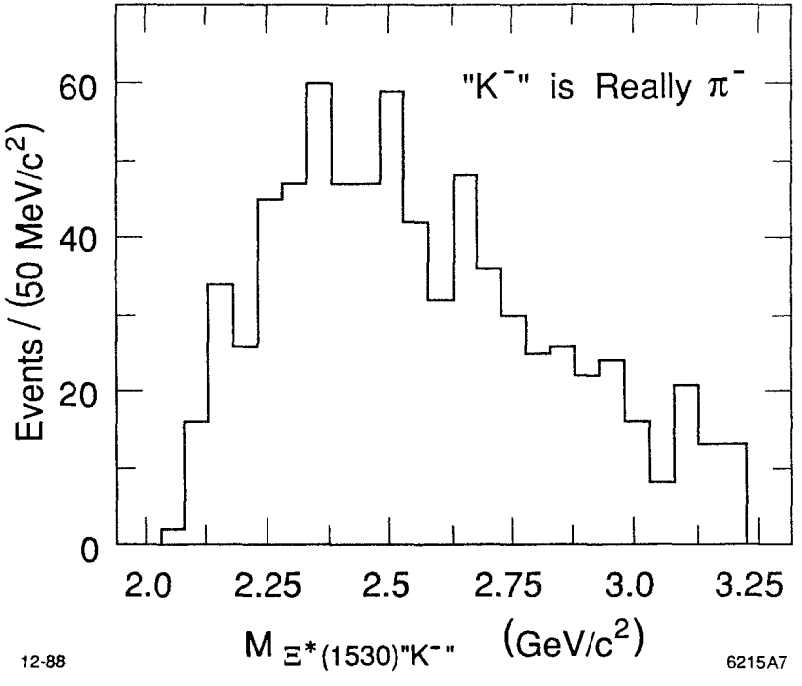

Fig. 8 Distribution of $\Xi^-K^-\pi^+$ effective masses for events with a $\Xi^-\pi^+$ mass in the range $1510 < M_{\Xi^-\pi^+} < 1555$ MeV/c^2 and a negative track giving light in either C_1 or C_2 with a a K^- mass assignment. This sample contains no events contributing to the outer histogram in Fig. 7, but when each event is weighted by the factor $(1-\epsilon)/\epsilon$, yields the distribution with open circles in that figure.

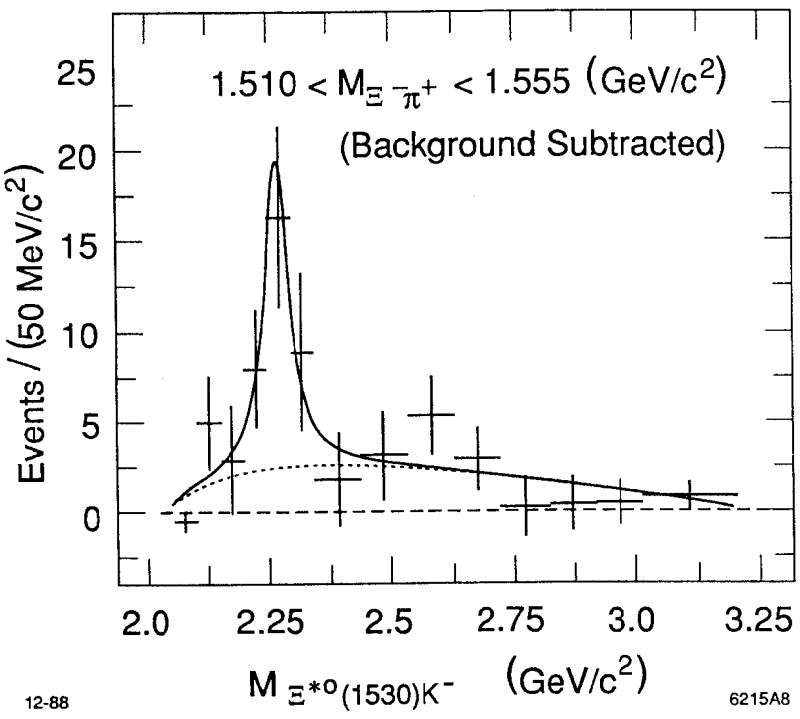

Fig. 9 Background subtracted $\Xi^{*0}(1530)K^-$ mass distribution.

The fit, which resulted in a χ^2 of 8.5 for 9 degrees of freedom, yielded Ω^{*-} parameter values:

$$M_0 = 2253 \pm 13 \quad \mathrm{MeV/c^2}$$
$$\Gamma_0 = 81 \pm 38 \quad \mathrm{MeV/c^2}$$

and a corresponding signal of 41.2 ± 10.2 events (~ 4.1 standard deviations). The dotted curve represented the non-resonant background, and appeared to agree well in magnitude and shape with the corresponding π^- punch-through distribution.

4. The $\Omega^-\pi^+\pi^-$ Channel

The inclusive production cross section of Ω^- was only $\sim 3\%$ of that for Ξ^- [7] and the decay length was approximately three times smaller. These facts made the separation of the Ω^- events in reaction (2) somewhat less straightforward than the selection of the Ξ^- sample discussed above. All events considered as Ω^- candidates were therefore processed through a fitting procedure which was designed to achieve the improvement in resolution of vertex positions necessary to distinguish between those relatively rare events with genuine Ω^- topologies and the more plentiful ones in which the Λ originated directly from the nearby primary vertex. In this procedure, measured coordinates for an event were matched to an Ω^- topological template in which constraints in three-momentum conservation at each decay vertex and in Λ mass were built in. The χ^2 quality of this fit and the information it provided on both the Ω^- track length and its uncertainty were required to match criteria which, when added to a set of requirements similar to those used to define the Ξ^- sample, made it possible to identify a clean Ω^- signal which was seen in the ΛK^- mass plot of Fig. 10. A total of about 600 Ω^- were in the peak. In all, approximately 350 Ω^- events, each with at least one $\pm$ charged track combination, were seen above $\sim 9\%$ background within $\pm$ 10 MeV/c^2 of the Ω^- mass, and were considered as candidates for reaction (2).

The $\Omega^-\pi^+\pi^-$ effective mass distribution, shown in Fig. 11(a), showed evidence for a strong signal at ~ 2470 MeV/c^2. In making this plot, all combinations of $\pm$ track pairs were included, as long as they were not inconsistent with a pion identity with respect to the various particle identification devices. An estimate of the background under this peak was obtained from the wrong sign combinations $\Omega^-\pi^\pm\pi^\pm$. These were plotted in

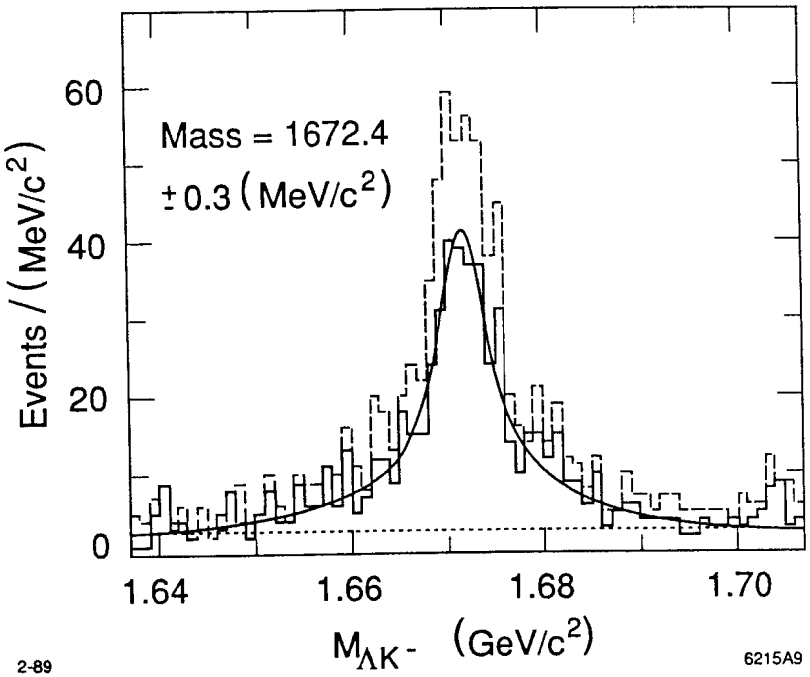

Fig. 10 The ΛK^- mass distribution for the inclusive Ω^- events; the solid histogram corresponds to those events having at least one pair of oppositely-charged primary vertex tracks consistent with a $\pi^+\pi^-$ interpretation; the dashed curve is for all events. The curve is a fit to the resolution function, determined from a Monte Carlo sample, with a linear background.

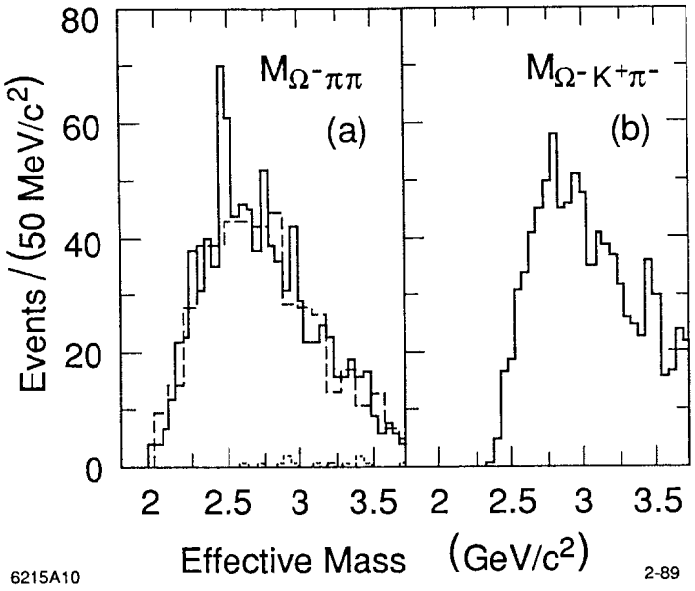

Fig. 11 (a) The inclusive $\Omega^-\pi^+\pi^-$ mass distribution for those events within ± 10 MeV/c^2 of the nominal Ω^- mass in the solid histogram of Fig. 10; for the $\pi^\pm$ tracks, any available particle identification information was required to be consistent with the pion mass assignment. The dotted histogram corresponds to Cherenkov-identified π^+'s. The dashed histogram represents the $\Omega^-\pi^\pm\pi^\pm$ distribution weighted as described in the text. (b) The mass distribution obtained from the solid histogram of Fig. 11a when the π^+ track is given the K^+ mass.

Fig. 11(a) normalised to the sample outside the peak region by a linear mass factor and indicate that the peak was more than five standard deviations above this background.

An obvious problem in these events was that, because of strangeness conservation, the existence of the Ω^- implied that the positive track was likely to be a K^+. The strong possibility existed, therefore, that the peak could be due to production of a Ξ^{*-} decaying to $\Omega^- K^+ \pi^-$. To investigate this possibility, the combinations in Fig. 11(a) were also plotted with a K^+ mass assigned to the positive track. This $\Omega^- K^+ \pi^-$ mass distribution, shown in Fig. 11(b) had no evidence for a peak, indicating that the Ξ^{*-} interpretation was not correct. Other mass hypotheses such as $\Omega^- e^+ e^-, \Omega^- K^+ K^-$ were also studied, and failed to show any significant peak structure, further suggesting that the signal was due to $\Omega^- \pi^+ \pi^-$ combinations.

In order to establish that the peak at 2470 MeV/c^2 corresponded to an $S = -3$ baryon system, it was essential to associate it with those events in which some evidence of the identity of the π^+ existed. The dotted distribution in Fig. 11(a) contained events for which Cherenkov identification of π^+ was possible and showed clearly that such information was of rather limited use. This contrasted with the $\Omega^{*-}(2250)$ situation in which the Cherenkov counters gave important information on an event by event basis of K^- identification. It was found, however, that for a significant number of positive particles in reaction (2), information from either the dE/dx or time-of-flight (TOF) devices was available, and some K/π separation was possible. The momentum spectra of these particles was such that though discrimination between K and π interpretations for individual events was possible in only a few cases, a statistical analysis did provide effective distinction.

Clean samples of $K^\pm$ and $\pi^\pm$ were selected with which to study the behaviour of both dE/dx and TOF devices at various momenta. In Fig. 12, the ΛK^- mass distribution from the tightly constrained reaction

$$K^- p \rightarrow \Lambda K^- K^+ \qquad (3)$$

observed in the present experiment showed a strong signal demonstrating that baryon exchange production of $\Xi^{*-}(1830)$ was present. These events were chosen to provide

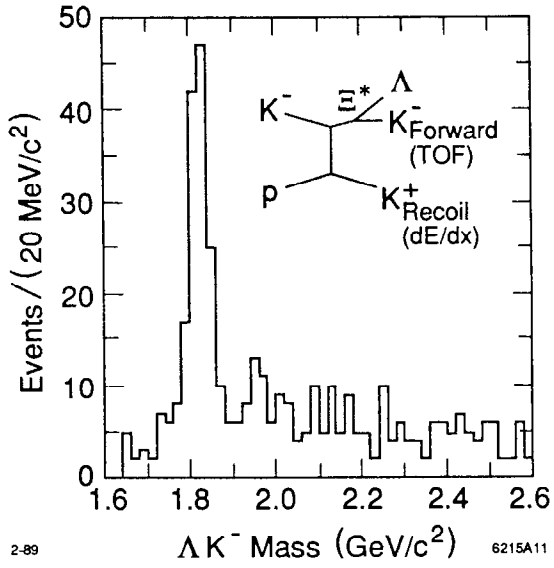

Fig. 12 The ΛK^- effective mass from the reaction $K^- p \rightarrow \Lambda K^+ K^-$.

a small, but very clean, sample of K^-'s with TOF measurement (Fig. 13(a)), and a somewhat larger, high purity sample of K^+'s having dE/dx information (Fig. 13(d)).

In Fig. 13(a), the difference (in standard deviations) between the TOF calculated under the kaon mass assumption, t^K_{calc}, and the measured value, t_{meas}, was plotted as abscissa, with K^- momentum as ordinate. The plot showed a vertical band of points localised within $\sim \pm 2\sigma$ of the origin, as would be expected for a pure K^- sample. In Fig. 13(d), the abscissa was the natural logarithm of the kaon to pion probability ratio, P_K/P_π, as derived from the induced cathode pulse height signals in the cylindrical PWC's [5]. In this plot, for momenta less than ~0.4 GeV/c, the kaon interpretation was clearly preferred; at higher momenta, the distribution was a vertical band centered at the origin.

Figures 13(b) and 13(e) were similar TOF and dE/dx plots, respectively, for negative primaries from our Ω^- sample. These particles were almost certain to be π^- with a very small contamination from e^-. There was virtually no chance they were either K^- or $\bar{p}$. The distribution of Fig. 13(b) was confined almost entirely to the region of positive abscissa, in contrast to that observed in Fig. 13(a). Furthermore, when the expected TOF was re-calculated using the pion mass, the distribution became a narrow, vertical band centered at the origin, demonstrating that these negative tracks were almost entirely π^-'s, as expected. The dE/dx data in Fig. 13(e) for these particles also contrasted with the K^+ population of Fig. 13(b), and showed a clear bias towards negative abscissa at all momenta, as expected for π^-.

The plots for the positive primary particles from the Ω^- sample, shown for TOF and dE/dx data respectively in Figs. 13(c) and (f), could clearly be described by a superposition of the two sets of plots discussed above. This agreed exactly with what would be expected for an admixture of both K^+ and π^+. The required separation of the π^+ population could, however, be accomplished in each case.

It was clear from Figs. 13(a) and (b) that the sample having positive abscissa in Fig. 13(c) should contain almost all of the π^+'s together with approximately half the K^+'s, whereas that with negative abscissa should also contain approximately half the K^+'s but only a small fraction of the π^+'s. In Fig. 14 (a), the $\Omega^-\pi^+\pi^-$ masses were plotted separately for combinations containing π^+'s from the above two samples. The solid

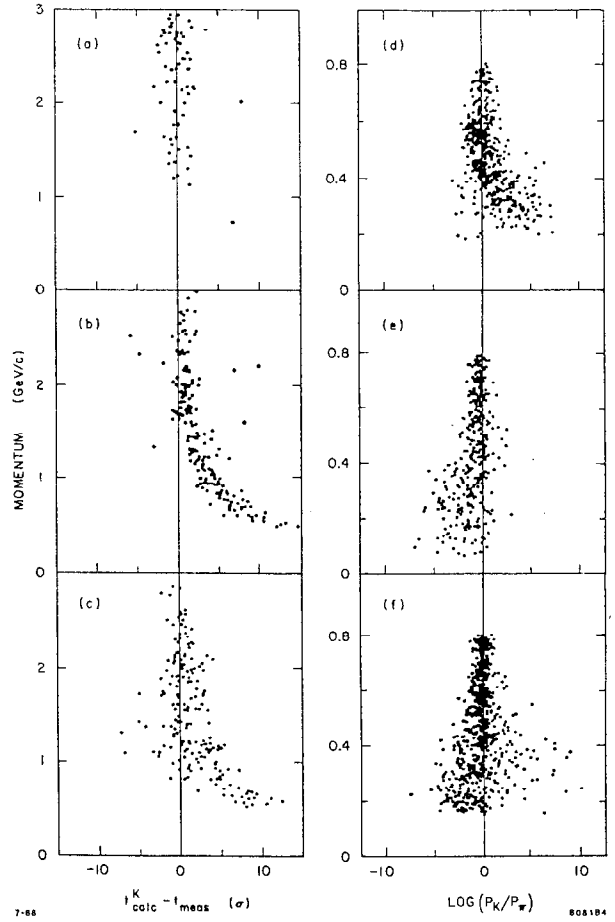

Fig. 13 (a)-(c) The momentum dependence of the difference between time-of-flight calculated on the assumption of the kaon mass (t^K_{calc}) and the measured value: (a) for K^-'s from reaction (2); (b) for negative, and (c) for positive primary tracks produced in association with an Ω^-. (d)-(f) The momentum dependence of the natural logarithm of the kaon to pion probability ratio for tracks having dE/dx information from the cylindrical PWC package surrounding the target: (d) for K^+'s from reaction (2); (e) for negative, and (f) for positive primary tracks produced in association with an Ω^-.

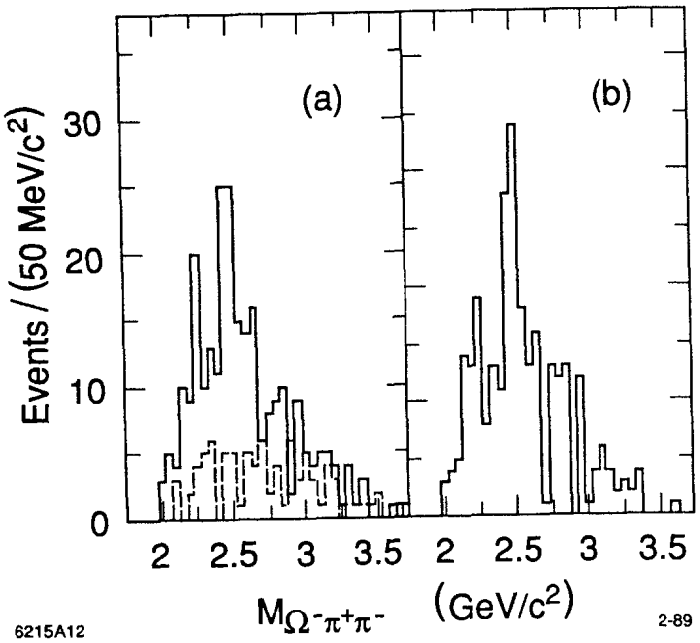

Fig. 14 (a) The $\Omega^-\pi^+\pi^-$ mass distribution corresponding to those π^+ tracks having TOF information such that $t^K_{calc} \geq t_{meas}$; the dashed histogram is for those having $t^K_{calc} \leq t_{meas}$. (b) The $\Omega^-\pi^+\pi^-$ mass distribution for the "net identified π^+" sample described in the text.

histogram corresponded to those $\Omega^-\pi^+\pi^-$ combinations for which the positive track was predominantly π^+, and indicated a signal similar in position, shape and significance to that of Fig. 11(a). The dashed histogram, constructed from positive tracks from the left side of Fig. 13(c) showed no evidence of a signal. This showed that the signal was associated with genuine $\pi^+\pi^-$ pairs. Furthermore, in the difference between the solid and dashed histograms of Fig. 14(a), the contribution from misidentified K^+'s should cancel, within statistics, thereby yielding a "net TOF-identified π^+" distribution. This distribution also constituted one contribution to the histogram of Fig. 14(b).

A second contribution to Fig. 14(b) was obtained by following a similar procedure with regard to the dE/dx distributions. It was clear from Figs. 13(d) and (e) that the positive particles in Fig. 13(f) could be split into a sample which was predominantly K^+ in the region with momenta below 0.4 GeV/c and positive abscissae, and the remaining sample which was predominantly made up from π^+. In the latter sample, the K^+ contamination would be distributed approximately symmetrically about the ordinate axis. Subtraction of the distribution of $\Omega^-\pi^+\pi^-$ mass combinations formed with positive tracks in this sample with positive abscissae from the corresponding distribution with negative abscissae could, therefore be taken to represent the "net π^+" distribution. This was found to contain a signal with 10 more events in the 2470 MeV/c^2 region, and was added into Fig. 14(b) giving an aggregate signal which contained approximately 60% of that in Fig. 11(a). The remaining 40% of the signal came from combinations in which the positive track missed both the TOF and dE/dx systems. No combinations were found in which both TOF and dE/dx identification of the π^+ was made.

In addition to establishing the identity of the π^+, the Ω^{*-} hypothesis for the peak in Fig. 11(a) also required that the system had isospin ($I = 0$). This, in turn, required that the $\pi^+\pi^-$ also be in an $I = 0$ state. The effective mass distributions $M_{\pi^+\pi^-}$ in Fig. 15 indicated a broad, structureless form concentrated at low mass values for events in the $\Omega^-\pi^+\pi^-$ peak region [Fig. 15(b)] as well as in the low and high side bands (Figs. 15(a) and 15(c), respectively). In particular, no clear evidence for ρ^0 ($I = 1$) was seen.

A large Monte Carlo sample of events corresponding to production of an $\Omega^-\pi^+\pi^-$ system in this mass range was generated, with the simulated dipion system in an $s-$wave. Recoil mass and transverse momentum distributions of the $\Omega^-\pi^+\pi^-$ systems were produced to simulate the data as closely as possible. These events were then subjected to

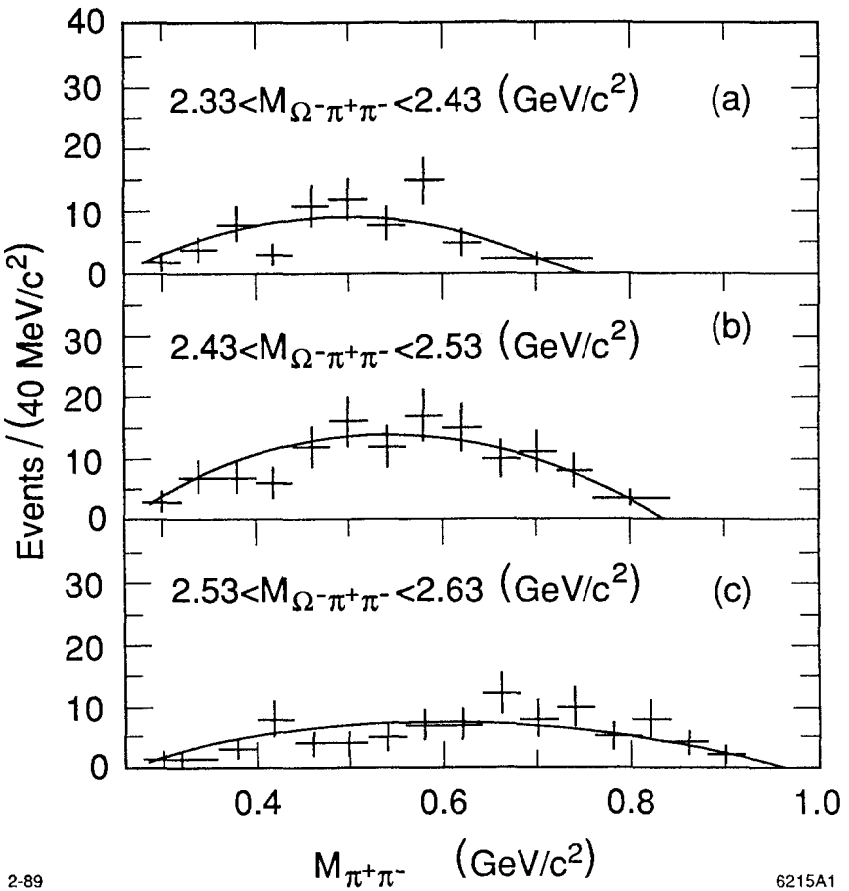

Fig. 15 Distributions of $\pi^+\pi^-$ effective mass in three $\Omega^-\pi^+\pi^-$ mass ranges: (a) below; (b) in; (c) above the peak at $\sim$ 2470 MeV/c^2. The curves are from Monte Carlo data with purely s—wave dipion systems.

the identical analysis to the data, and curves indicating the dipion mass shapes were drawn, suitably normalised upon the distributions in Fig. 15. This s—wave behaviour clearly described the data well, indicating therefore a predominance of $I = 0$ in the $\Omega^-\pi^+\pi^-$ peak region, and providing further evidence of Ω^{*-} production.

A fit to the $\Omega^-\pi^+\pi^-$ mass distribution in Fig. 11(a), similar to that for the $\Xi^{*0}K^-$ plot, led to a mass of 2474$\pm$12 MeV/c^2 and a width of 72$\pm$33 MeV/c^2 for this Ω^{*-}. This is shown in Fig. 16. The acceptance of LASS was computed using the Monte Carlo event sample discussed above, and the cross section for inclusive production of $\Omega^{*-}(2470)$ from 11 GeV/c K^-p interactions with decay to $\Omega^-\pi^+\pi^-$ corrected for unseen charge modes was determined to be 290 $\pm$ 90 nb. A similar computation was made to determine the cross section for production of the $\Omega^{*-}(2250)$ with decay to $\Xi^{*0}(1530)K^-$, also corrected for unseen charge modes. The result was 630 $\pm$ 180 nb.

5. Discussion

Evidence for Ω^{*-} production has been reported in only one other experiment. Using a charged hyperon beam from the CERN SPS, WA42 observed a significant signal at 2251 MeV/c^2 and a further, less compelling signal at 2384 MeV/c^2, both in $\Xi^-K^-\pi^+$ systems from 116 GeV/c Ξ^-Be collisions [3]. In the same experiment no clear evidence for structure in the $\Omega^-\pi^+\pi^-$ system was seen [8]. A comparison of data between the two experiments is given in Table I below.

In making comparisons between the two experiments, we note that in addition to considerable differences in acceptance, the very different nature of K^-p and Ξ^-Be production mechanisms forces us to conclude that no conflict exists with respect to signals observed. In particular, the $\Omega^{*-}(2470)$ observed as a five standard deviation effect in LASS and not in WA42 could be explained as a difference in observable cross section. A similar conclusion might be made for the signal in $\Xi^-\overline{K^{*0}}(890)$ seen by WA42 and not LASS.

Evidence for at least one state near 2250 MeV/c^2 appears to be very solid. Both E135 and WA42 observed signals with similar mass and width values, and in both cases a significant $\Xi^{*0}(1530)K^-$ decay mode was evident. However, it is somewhat speculative to equate the states seen, since:

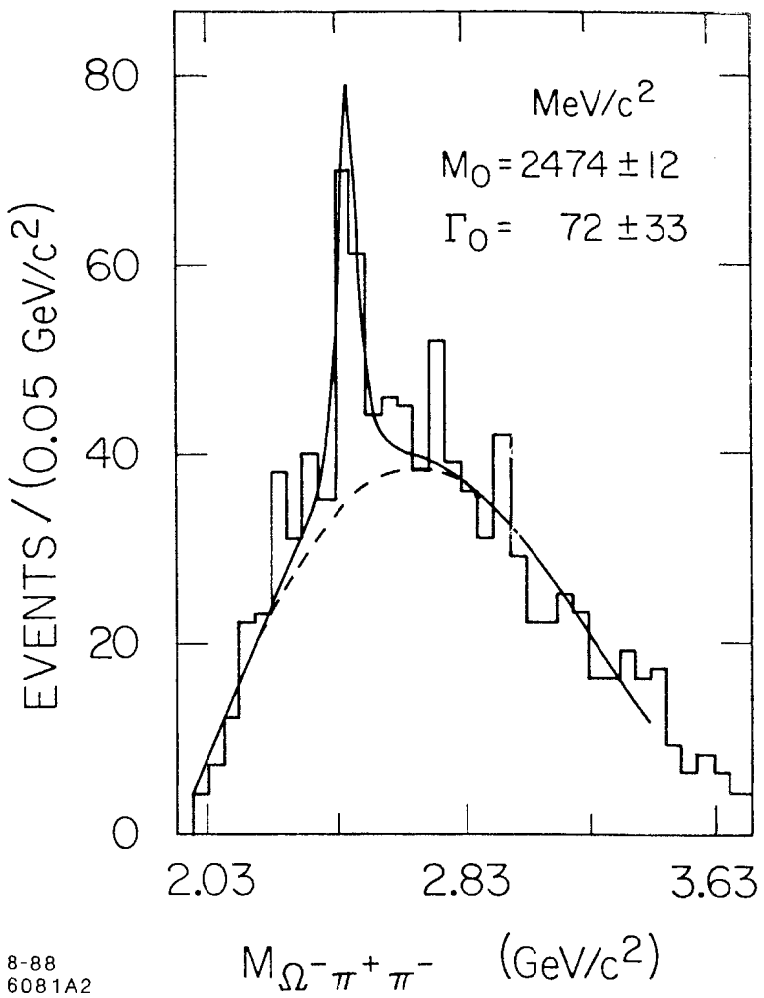

Fig. 16 The histogram is the solid histogram of Fig. 11a; the curve is obtained from a fit using an S-wave Breit-Wigner line-shape plus a polynomial background (dashed curve); the resulting mass and width values are as indicated.

	LASS E135	SPS WA42
Reaction	$K^- p$ at 11 GeV/c	Ξ^-Be at 116 GeV/c
State 1:		
M_o(MeV/c^2)	2253 ± 13	2251 ± 12
Γ_o(MeV/c^2)	81 ± 38	48 ± 20
Events in signal	44 ± 11	78 ± 23
Decay modes	$\Xi^{*0}(1530)K^-$ dominant.	
	$\Xi^-K^-\pi^+/\Xi^{*0}K^- < 0.2$(90%c.l.)	$\Xi^{*0}K^-/\Xi^-K^-\pi^+ = 0.7 \pm 0.2$
State 2:		
M_o(MeV/c^2)	2474 ± 12	not observed
Γ_o(MeV/c^2)	72 ± 33	"
Events in signal	52 ± 10	"
Decay modes observed	$\Omega^-\pi^+\pi^- > 0.075$	"
State 3:		
M_o(MeV/c^2)	not observed	2384 ± 12
Γ_o(MeV/c^2)	"	26 ± 23
Events in signal	"	45 ± 10
Decay modes observed	"	
		$\Xi^-\overline{K^{*0}}/\Xi^-K^-\pi^+ = 0.5 \pm 0.3$

Table I Summary of Ω^{*-} Data.

- The two experiments differ somewhat in estimated three-body $\Xi^-K^-\pi^+$ decay rates.
- Neither experiment was able to identify the J^P of states observed since both were

subject to acceptance and statistical limitations imposed by K^- identification criteria.

and finally

- Several states near this mass are expected in the $\Xi^{*0}(1530)K^-$ decay mode.

Predictions for excited Ω^- states exist. Most obviously, the known Δ and Σ baryon spectra have led to the expectation of several such states. For example, pairing up the six best established Δ's with Σ states having the same spin-parities and using the Gell-Mann-Okubo equal spacing rule, leads to Ω^- baryons, at:

$\sim 2000 \pm 100(\mathrm{MeV/c^2})$	$(1/2^-)$
$\sim 2200 \pm 50(\mathrm{MeV/c^2})$	$(7/2^+, 1/2^-)$
$\sim 2400 \pm 100(\mathrm{MeV/c^2})$	$(1/2^+, 5/2^+, 3/2^-)$

A calculation using a $q-q$ interquark potential $A + Br^{0.1}$ with A and B derived from the meson spectrum has been made by J.M. Richard [9]. By including spin-spin forces, he computed, in addition to the ground state $(3/2^+)$ Ω^- at 1672 MeV/c^2 the expectation of radially excited Ω^- states at:

$2244(\mathrm{MeV/c^2})$	$(3/2^+)$
$2358(\mathrm{MeV/c^2})$	$(1/2^+, 3/2^+, 5/2^+)$

The most detailed prediction of the Ω^- spectrum, and of the expected decay rates was made by Chao, Isgur and Karl (CIK) [10]. This model included elements of QCD and confinement in describing flavour independent $q-q$ forces in a simple harmonic oscillator potential. Parameters in the model were determined from other sectors of the baryon spectrum and decay rates. Orbitally excited states with masses above 2100 MeV/c^2 were predicted at:

$2020(\mathrm{MeV/c^2})$	$(1/2^- 3/2^-)$
$2225(\mathrm{MeV/c^2})$	$(5/2^+)$
$2265(\mathrm{MeV/c^2})$	$(3/2^+, 5/2^+)$

However, no radial excitations were calculated.

It is interesting to observe that the two states at 2265 MeV/c^2 were predicted to have predominant decay to $\Xi^{*0}(1530)K^-$. Obviously, without measuring J^P, however, spectroscopic assignment of the signals seen in this system in both the LASS and WA42 experiments is not possible.

The $\Omega^{*-}(2470)$ has a mass above the range computed in Reference [10]. This fact alone suggests it is a radial excitation. Further evidence supporting such interpretation might be found in the large $\Omega^-\pi^+\pi^-$ decay mode observed, and the lack of any evidence for a two-body decay, for instance, to $\Xi^{*0}K^-$ or $\Xi^-\overline{K^{*0}}$. The decay branching ratio to $\Omega^-\pi\pi$ appears to be at least 7.5 %. The cross section we observed, corrected for the unseen $\Omega^-\pi^0\pi^0$ was $290nb$ while the inclusive cross section for Ω^- production at this energy was $3.9 \pm 0.6\mu b$ [7]. A large decay to dipion states has been a recognised characteristic of radially excited states in both K^* and quarkonium systems. The suppression of two-body decays relative to such modes is expected, under certain circumstances, on the basis of the dynamics of radially excited quark systems [11].

The lowest Ω^- excitations expected have masses below 1900 MeV/c^2, and have yet to be observed. Within the framework of the CIK model, they are expected to decay mostly to $\Xi^-\overline{K^0}$ or Ξ^0K^-. For states below 1808 MeV/c^2, decay to $\Omega^-\gamma$ would be most likely. None of these modes is easily accessible to either LASS or to WA42.

6. Summary

Excited Ω^{*-} states at 2250 and 2470 MeV/c^2 have been seen in LASS. The former state may also have been seen in experiment WA42 in an entirely different production reaction. Some evidence exists that $\Omega^{*-}(2470)$ is a radial excitation. This state was not seen in WA42. No evidence for $\Omega^{*-}(2380)$ reported by the WA42 collaboration has been seen in LASS data. The experimental situation is not yet completely satisfactory. In particular, the lowest Ω^- excitations have not yet been observed since statistically significant samples of events containing $\Xi\overline{K}$ and $\Omega^-\gamma$ systems (the expected decay modes) have been too difficult to accumulate. Also, more data are still required to corroborate evidence for $\Omega^{*-}(2470)$ and $\Omega^{*-}(2380)$, and to make J^P measurements necessary in making spectroscopic assignments. Nonetheless, almost 30 years after the discovery of

the Ω^-, the data presented here have been able to show clearly that excited Ω^- states do indeed exist.

REFERENCES

1. The members of the LASS E135 collaboration were: D. Aston,[1] N. Awaji,[2] T. Bienz,[1] F. Bird,[1] J. D'Amore,[3] W. Dunwoodie,[1] R. Endorf,[3] K. Fujii,[2] H. Hayashii,[2] S. Iwata,[2] W.B. Johnson,[1] R. Kajikawa,[2] P. Kunz,[1] D.W.G.S. Leith,[1] L. Levinson,[1] T. Matsui,[2] B.T. Meadows,[3] A. Miyamoto,[2] M. Nussbaum,[3] H. Ozaki,[2] C.O. Pak,[2] B.N. Ratcliff,[1] D. Schultz,[1] S. Shapiro,[1] T. Shimomura,[2] P. K. Sinervo,[1] A. Sugiyama,[2] S. Suzuki,[2] G. Tarnopolsky,[1] T. Tauchi,[2] N. Toge,[1] K. Ukai,[4] A. Waite,[1] S. Williams[1]
   [1] *Stanford Linear Accelerator Center, Stanford University,*
   [2] *Department of Physics, Nagoya University,*
   [3] *University of Cincinnati,*
   [4] *Institute for Nuclear Study, University of Tokyo*
2. D. Aston et al., contributed talk given by B. Ratcliff in session P09 at the International Europhysics Conference on High Energy Physics, Bari, Italy, July 1985; see S. Cooper, Rapporteur Talk in the Proceedings of that conference, p. 947 and SLAC-PUB-3819.
3. S.F. Biagi et al., Zeits. Fur Physik, C31 (1986) 33 .
4. D. Aston et al, Phys. Lett. B194 (1987) 579.
5. D. Aston et al., SLAC-REP-298 (1986).
6. J. D'Amore, Ph. D. Thesis, University of Cincinnati (1988), (unpublished).
7. D. Aston et al., Phys. Rev. D32 (1985) 2270.
8. P. Rosselet, Proceedings of the Second International Conference on Hadron Spectroscopy, KEK, Tsukuba, Japan, April 1987.
9. J.M. Richard, Phys. Lett. 100B (1981) 515.
10. N. Isgur and G. Karl, Phys. Rev. D19 (1979) 2653.
11. A. Bradley, J. Phys. G4 (1978) 1517.
    E. Eichten et al., Phys. Rev. D21 (1980) 203.
    S.B. Gerasimov et al., Z. Phys. C13, (1982) 43.

CALCULATIONS OF HADRONIC WEAK MATRIX ELEMENTS: A STATUS REPORT*

STEPHEN R. SHARPE
Physics Department, FM-15, University of Washington
Seattle, WA 98195

ABSTRACT

I review the calculations of hadronic matrix elements of the weak Hamiltonian. My major emphasis is on lattice calculations. I discuss the application to weak decay constants (f_K, f_D, f_B), $K^0 - \overline{K^0}$ and $B^0 - \overline{B^0}$ mixing, $K \to \pi\pi$ decays, and the CP violation parameters ϵ and ϵ'. I close with speculations on future progress.

1. Introduction

This is a talk about calculations in QCD. You might wonder, therefore, what is it doing in an Institute devoted to "Probing the Weak Interaction." The fact is that, while we understand the weak interactions in terms of forces acting between quarks, we cannot make direct measurements with quarks. The quarks are bound into mesons and baryons, and it is the decay rates of these bound states that we measure. Thus we have to be able to disentangle the effects of QCD, which cause the binding, from those of the weak interactions, which cause the decays. This is why it is crucial that we develop the ability to calculate, if not fully understand, the non-perturbative effects of QCD.

The parameters we really want to get our hands on are those of the Kobayashi-Maskawa (KM) matrix, and the top quark mass. I will use the Harari-Leurer notation[1] for the Maiani parameterization of the KM matrix:

$$\begin{pmatrix} c_{12}c_{13} & c_{13}s_{12} & s_{13}e^{i\delta} \\ -s_{12}c_{23} - c_{12}s_{23}s_{13}e^{i\delta} & c_{12}c_{23} - s_{12}s_{23}s_{13}e^{i\delta} & s_{23}c_{13} \\ s_{12}s_{23} - c_{12}c_{23}s_{13}e^{i\delta} & -c_{12}s_{23} - s_{12}c_{23}s_{13}e^{i\delta} & c_{23}c_{13} \end{pmatrix} . \tag{1.1}$$

To very good approximation, one can use the form

$$\begin{pmatrix} c_{12} & s_{12} & s_{13}e^{i\delta} \\ -s_{12} - s_{23}s_{13}e^{i\delta} & c_{12} & s_{23} \\ s_{12}s_{23} - s_{13}e^{i\delta} & -s_{23} & 1 \end{pmatrix} . \tag{1.2}$$

* Work supported in part by DOE contracts DE-AC03-76SF00515 and DE-AT06-88ER40423.

For a summary of the present determinations of the parameters see the lectures of Harari.[2] The poorly known parameters are s_{13} and s_δ. The former determines the $b \to u$ decay rate. It is sometimes more convenient to use $q = s_{13}/s_{23}$. The angle δ is the sole CP violating parameter.†

To illustrate the importance of non-perturbative QCD calculations, I will use two examples. Both will be discussed in more detail in following sections. The first is a very old problem in kaon and hyperon non-leptonic decays: the $\Delta I = 1/2$ rule.[3] In kaon decays, this rule summarizes the fact that the decay $K^+ \to \pi^+\pi^0$ is roughly 600 times slower than $K_S^0 \to \pi^+\pi^- + \pi^0\pi^0$. Only in the latter decay can the pions be in an $I = 0$ state, so only in this decay can the weak Hamiltonian transform as an $I = 1/2$ operator. For the K^+ decay the Hamiltonian must transform as $I = 3/2$ or $5/2$. Combining all three decay widths one finds, in fact, that the the $\Delta I = 5/2$ amplitude can be neglected. The usual way of summarizing the results is that the amplitude $A_0 = A(K_0 \to \pi\pi(I = 0))$ is 22 times larger than $A_2 = A(K_0 \to \pi\pi(I = 2))$.

This enormous difference has remained largely a mystery for 34 years. At the level of non-interacting quarks, the decay is caused by simple W-exchange diagrams. These contain both $\Delta I = 1/2$ and $3/2$ parts, with no significant enhancement of one over the other. Indeed, if one uses vacuum saturation approximation one finds $A_0/A_2 \sim 1$. To do better, one must include QCD corrections. The short-distance, perturbative part was calculated long ago.[4] One finds an enhancement of A_0, and a suppression of A_2. If one uses perturbation theory to bring one down from the W scale to $\mu \sim m_c$, and uses $\Lambda_{QCD} = 100\,\mathrm{MeV}$ and $m_t = 70\,\mathrm{GeV}$, the enhancement is by 1.55, and the suppression by 0.8. The remainder of the enhancement in A_0/A_2, i.e. roughly a factor of 10, must come from long distance, non-perturbative QCD. Thus, if the $\Delta I = 1/2$ rule is any guide, non-perturbative effects can be the source of large factors.

My second example of the importance of non-perturbative effects is CP violation in kaon decays. This is parameterized by ε', and it is the ratio ε'/ε that is actually measured. Over the years a series of experiments has pushed down the limits on $|\varepsilon'/\varepsilon|$, but now we finally have a measurement from the NA31 collaboration.[5] They find $\varepsilon'/\varepsilon = .0033(11)$. There is also the prospect of the errors being reduced by a factor of two or more.[6] The measurement of ε'/ε is particularly important because it promises a stringent test of the standard model. This is because there is a single source of CP violation, i.e. δ. In principle, once one CP violating quantity, say ε, has been measured, one can fix δ. All other CP violating quantities, e.g. ε', can then, in principle, be predicted.

Unhappily, this is not yet possible. Let me focus for the moment on the difficulties with using the experimental measurement of ε'/ε. A schematic formula for ε'/ε is

$$\frac{\varepsilon'}{\varepsilon} \approx \text{(known factors)}\ \ s_{13}\, s_\delta\, \tilde{c}_6(\mu)\, \langle K^0|\mathcal{O}_6|\pi^+\pi^-\rangle. \qquad (1.3)$$

This takes the form that will occur repeatedly in the following: a product of poorly known KM angles, a coefficient which is calculable in QCD perturbation theory, but which depends on m_t, and a non-perturbative matrix element of a known operator between hadronic states. Here the dependence on the top quark mass is hidden in $\tilde{c}_6$, which depends logarithmically on m_t. The operator $\mathcal{O}_6$ is the penguin operator.[7] The scale μ divides the momentum range into that which can be calculated perturbatively ($p > \mu$), and that which is non-perturbative ($p < \mu$). One must use $\mu \geq m_c$.

Even if one knew the KM angles and m_t, one needs to know the hadronic matrix element of the penguin operator in order to predict ε'/ε. A non-perturbative QCD calculation is required for this. Indeed, one might expect non-perturbative enhancements, since the penguin operator $\mathcal{O}_6$ has $I = 1/2$. Be that as it may, we need to learn how to calculate the matrix element to a level of accuracy comparable to that of the experimental measurements.

As Haim Harari has stressed in his lectures here,[2] pinning down the parameters of the standard model (including the top quark mass m_t) will not be the simple procedure I outlined above. One measures as many relevant experimental quantities as possible. The examples discussed below are ε, ε', the $B - \overline{B}$ mixing parameter x_d, and the $b \to u$ amplitude. Each depends upon the unknown KM matrix elements , upon m_t, and upon some non-perturbative QCD factors. There will always be some error in the both the experimental measurement, and in determination of the QCD factors. One has to gradually reduce the errors in both, and perform ever more refined global fits to determine the unknown parameters.

The situation now is that the uncertainty in the non-perturbative QCD calculations is larger than that in the experimental measurements for almost all quantities of interest. This is why it is so important to learn how to do non-perturbative QCD calculations.

Having provided the motivation for the calculations, the remainder of this talk is devoted to details. The next section discusses the break-up of the calculation into perturbative and non-perturbative pieces. It sets up a non-technical

† Strong CP violation, though possible in principle, is constrained by the limit on the neutron electric dipole moment to have a negligible effect in hadronic decays.

explanation of how lattice QCD provides a non-perturbative method for calculating matrix elements. This is followed by a discussion of the status of lattice calculation. These sections can be skipped by someone interested only in the present status of the results of the calculations. The bulk of the talk deals with the various hadronic matrix elements that are being calculated on the lattice. Each matrix element merits its own section, and these are relatively self contained. Those interested only in results from a complete calculation in QCD will be disappointed. Such hard-liners should skip straight to the conclusions, where I give my view of the future progress of the field.

2. Ingredients for a calculation of matrix elements

In this section I spell out how one breaks up the calculation of a hadronic matrix element. As alluded to above, there are three ingredients: the weak interaction operators, short-distance QCD, and long-distance QCD.

The electroweak interactions can be treated reliably using perturbation theory. Radiative corrections involving higher order electroweak diagrams are small, at least as long as the top quark and the Higgs boson are not too heavy. In fact, these radiative corrections are bounded by experiment in such a way as to limit the top quark mass to be less than $\sim 200\,\mathrm{GeV}$. Thus we know the fundamental quark interactions occurring in all weak processes. For example, in the decay $K^+ \to \pi^+\pi^0$, one of the diagrams has the $\bar{s}u$ pair, which make up the K^+, annihilating into a virtual W^+, which then produces a $\bar{d}u$ pair. The vertices are

$$\bar{s}\gamma_\mu^L u\, W_\mu^+ \quad \text{and} \quad W_\mu^-\, \bar{u}\gamma_\mu^L d\,, \tag{2.1}$$

where the superscript L indicates that only left-handed quarks take part in the interaction: $\gamma_\mu^L = \gamma_\mu(1+\gamma_5)$.

The electroweak vertices are the most fundamental of the ingredients needed to calculate a weak amplitude. From the point of view of a weak interaction physicist, things go downhill from here on. We must introduce the interactions between the quarks caused by QCD. Fortunately, we can do this in two stages. This is because QCD has the remarkable property of asymptotic freedom. If one measures the strong coupling constant using momentum transfers μ, then one finds a scale dependent result, $\alpha_s(\mu)$, which decreases as μ increases. At large momenta, i.e. short distances, the quarks and gluons are weakly interacting, and one can use perturbation theory. A beautiful demonstration of this is the emergence of jets in high energy e^-e^- and $p\bar{p}$ collisions. These jets are the physical manifestation of the underlying quark and gluon jets, as is shown by the fact that their angular distributions agree with perturbative QCD predictions.

The second ingredient in a matrix element calculation is the effects of quark and gluon loops with momenta large enough that perturbation theory is valid.* The diagrams that one actually calculates are the standard vertex corrections and wave function renormalizations of the textbooks. I will not discuss these calculations here, and I refer you to the literature.[9] The net effect of these calculations is to replace the few diagrams involving the W boson by a number of four-fermion operators involving only light quarks. "Light" means those lighter than the scale, μ, above which perturbation theory is being used. Thus if $\mu \sim 2\,\mathrm{GeV}$, the value taken for most of the following, then the u, d, s and c quarks are kept. The light quark operators are multiplied by coefficients which are calculable in perturbation theory. These coefficients depend on μ, and upon the heavy quark masses m_t and m_b.

The final ingredient in the calculation of matrix elements is QCD interactions at scales below μ. For these scales α_s grows quickly large, and perturbation theory cannot be used. Non-perturbative effects cause the strong binding of quarks into mesons and baryons, and of gluons into glueballs. In fact, quarks and gluons are thought to be absolutely confined. It is perhaps peculiar that it is simple to write down the theory which we think explains these complicated effects:

$$\begin{aligned} \mathcal{L} &= -\frac{1}{4}G_a^{\mu\nu}G_{a\mu\nu} + \sum_q \bar{q}(i\not{D} - m_q)q \\ D^\mu &= \partial^\mu - igT_aA_a^\mu \\ G_a^{\mu\nu} &= \partial^\mu A_a^\nu - \partial^\nu A_a^\mu - gf_{abc}A_b^\mu A_c^\nu. \end{aligned} \tag{2.2}$$

Here A_a^μ is the gluon field strength, a, b, c are color indices, T_a are the fundamental representation matrices of SU(3), and f_{abc} are the structure constants. The coupling g is more familiar as $\alpha_s = g^2/4\pi$. To fully define the theory we must include a cut-off μ, momenta above which are not allowed. The cut-off

* The reliability of QCD perturbation theory has recently been thrown into question by a calculation of the $O(\alpha_s^3)$ term in $R(e^-e^-)$.[8] This term is larger by 2-3 than the α_s^2 term. One way of interpreting this result is that the reliability of the asymptotic series has ended. If so, one should only keep the α_s term. With one exception, all the calculations relating to weak amplitudes have only been done to $O(\alpha_s)$. I shall take the view that these calculations are reliable down to scales $\mu \sim 2\,\mathrm{GeV}$. Of course, a leading correction term is not sufficient to determine the scale at which to evaluate α_s, so there are remaining uncertainties. For the moment, though, these are smaller than the other errors which I discuss below.

theory is that which results when all physics above μ is integrated out. Because QCD is renormalizable, the theory retains the form given in Eq. (2.2) as μ is lowered, as long as one uses a running coupling constant $g = g(\mu)$. However, μ has to be large enough so that perturbation theory applies. If not, we cannot calculate the form of the cut-off theory.

So the problem boils down to calculating the matrix elements of certain operators in a cut-off version of QCD. There have been various attempts to do this, which I would divide into three classes. First, there are the models, e.g. the non-relativistic quark model and the bag model. These are set up so as to reproduce hadron masses. They have confinement built in. They do remarkably well at fitting much data with few parameters. However, their ultimate drawback is that they are not connected to QCD in any rigorous way. Thus it is hard to know how to improve upon them. Similarly, it is hard to know what error to assign to any result. Nevertheless, such models are useful if one wants a rough estimate of a matrix element.

The second class of methods are more closely related to QCD. I have in mind the QCD sum rules, and the large N_c (number of colors) approximation. The former represents low momentum physics by a few phenomenological parameters: $\langle G_a^{\mu\nu} G_{a\mu\nu} \rangle$, $\langle \bar{\psi}\psi \rangle$, ... Various technical approximations must be made to get an answer, and it is not clear what errors these introduce. For a discussion which highlights the strengths and weakness of the method see the recent talk by Pich.[10] The large N_c approximation has been studied in a series of papers by Bardeen, Buras and Gerard, and I recommend reading the review of Buras.[11] It has been applied with success to D meson decays, and to the properties of kaons and pions. Here one does have a systematic way of improving the method: one can keep higher order terms in N_c. In practice, though, this is very complicated. Futhermore, in the application to kaon properties, one has to assume that one can use perturbative QCD down to $0.6 - 0.8\,\mathrm{GeV}$, which is highly questionable. Nevertheless, this method has had some significant successes, in particular in the explanation of the $\Delta I = 1/2$ rule.

These are the methods I will not talk about much in the following. I will concentrate on the final class of methods. This has one member only: lattice calculations. These have the advantage that they are derived directly from QCD. They have the disadvantage of being numerical, so that there is always a statistical error. Lattice calculations have matured to the point of being competitive with the other methods. Unless there are some new developments, I expect that lattice calculations will, in a few years, be the method of choice.

3. Basics of Lattice QCD

Lattice QCD was first invented by Wilson in 1974.[12] The idea is very simple: replace space with a grid of points, typically a cubic lattice. It turns out that one must put the quarks on the sites of the lattice, while the gluon fields live on the links between the sites. In the numerical applications I will discuss, one works in Euclidean space (imaginary time), and discretizes the time as well as space directions. One also has to restrict the theory to a finite box in space and time.

The approximations of finite lattice spacing and finite box size reduce the problem to something that can be put on a computer. Using Euclidean space allows one to use Feynman's path integral to do quantum mechanics. Since there are only a finite number of variables, one ends up doing a very large numerical integral. To be sure, this is done using various tricks. But it should not be forgotten that, at base, this is a brute force numerical method of calculation.

I should mention that the term "lattice QCD" includes not only the method just outlined, but also various analytical approaches.[13] In particular, one can keep time continuous, and use Hamiltonian methods. These all turn out to be strong coupling expansions – expansions about $g = \infty$. For certain quantities (e.g. the masses of exotic glueballs) these methods are competitive, or perhaps superior, to the Euclidean numerical calculations. But they suffer from the difficulty of estimating reliable errors. In any case, for the matrix elements to be discussed below, the numerical approach is the only one being used.

I have mentioned two major approximations that are made in numerical lattice calculations: finite lattice spacing (a), and finite box size (L). I think we are at the point where these approximations are not too serious. First let me discuss the lattice spacing. This cut-off in position space corresponds roughly to a momentum space cut-off of $\mu \sim \pi/a$ – no higher momenta than this are allowed on the lattice. One's first thought might be to set $a = 1/m_W$ and directly put the weak interactions on the lattice, including the W and the Z. This is not only hopelessly impractical given the available computer time, but it also runs into serious theoretical difficulties. These are caused by the handedness of the weak interaction couplings. It turns out to be very hard to just put a left-handed fermion on the lattice; this is called the fermion doubling problem. There appear to be schemes which get around this,[14] but they are too complicated to use. Thus one is forced to integrate out the weak bosons, and work in terms of effective operators in QCD. Then handedness is not an issue, since QCD is parity invariant. An operator and its parity transform have the same matrix elements, so one can form the average and obtain an operator which can be put on the lattice. There still remain problems of principle when putting the

fermions on the lattice, but these can be overcome. There are two methods that are simple to use numerically, Wilson fermions and staggered fermions. Both have been used in the matrix elements discussed below. They should yield the same results for small enough a.

Present computer power allows us to work with lattice spacings no smaller than $a^{-1} \sim 2.0 - 2.5\,\mathrm{GeV}$. In physical units this is $a \sim 0.1$ fm. However, this is probably small enough. All that matters is that perturbation theory is reliable down to this scale. For then the standard renormalization group machinery can be used to calculate the effective operators and coefficients. One then performs a separate perturbative calculation to match the continuum and lattice regularizations. Although 2 GeV doesn't seem like a very large scale, one might argue that the equivalent momentum scale is not $1/a$ but more like π/a. In any case, one can test the assumption that a given a is small enough. This is done by calculating for a few values of a, using the appropriate values for the coefficients of the various operators, and checking that the total result is independent of a. For the most part, this has not been done for the matrix elements themselves. Calculations of other quantities, however, lend support to the conjecture that the presently accessible lattice spacings are small enough, if one wants an accuracy of 10-20%.[15]

Given $1/a \sim 2$ GeV one cannot simulate the b quark directly. This is because there are always lattice artifacts which are suppressed by powers of $m_q a$. For example, a free fermion propagator on a cubic lattice differs from the continuum result by terms of size $(m_q a)^2$. For a b quark, one has $m_b a \sim 2.5$, a value so large that lattice artifacts will dominate. This means that results for B mesons have to be obtained by extrapolation. The c quark, however, is a borderline case, and one has to perform tests to determine the size of lattice artifacts.

The second major approximation is the use of a finite size box. The number of sites in the spatial directions is limited to about 20 by the available computer power. Thus, given $1/a \sim 2\,\mathrm{GeV}$, the spatial size is 2 fm or less.* There are four ways in which this is a limitation. First, it puts a lower limit on the masses of the hadrons that can be simulated. For example, if the spatial boundary conditions are periodic, each particle is surrounded by images in adjacent boxes. The interaction with these images changes the mass (M) of the particle by an amount $\propto \exp(-ML)$. (For pions the fall off is power law rather than exponential.[16]) In practice, one finds that finite size effects are reduced to a tolerable level if $ML > 3 - 5$, with the effects being worse for baryons than for mesons. For $L \sim 2$ fm this means a lower limit of about 300 MeV, about twice the physical pion mass. In fact most calculations only go down to masses of $\sim 400\,\mathrm{MeV}$, since the computer time grows inversely with the pion mass squared.

The second limitation is on the number of particles which can be accommodated in the finite box. For example, if one puts two pions in the box, then there will be an interaction energy which falls as $1/L^3$. This means that in processes such as $K \to \pi\pi$ decay, there can be corrections due to the finite volume. In the case of pions, soft pion theorems imply that the interaction is small if the pions are light, and have small relative momentum. But, as described in the last paragraph, the lattice pions are heavier than their continuum counterparts, and large final state interactions are possible. Detailed studies of these effects are only just beginning.[17,18]

The third limitation is on the momenta of the particles. With periodic boundary conditions the allowed particle momenta are $|\vec{p}| = 0, 2\pi/L, \ldots \sim 0, 0.6\,\mathrm{GeV}, \ldots$. This makes it hard to do studies of momentum dependence since the step size is so large.

The final limitation is due to the finiteness of the time direction. In Euclidean space, the mass of a particle is determined by examining the fall-off of a correlation function in which the particle is created at say $t = 0$ and destroyed a time T later. The correlator falls off as $\exp(-E|T|)$, where E is the energy of the state. For zero spatial momentum states $E = M$. However, the operators can also create and destroy excited states with the same quantum numbers. These give an additive positive contribution to the correlator $\propto \exp(-M'|T|)$, where M' is the mass of the excited state. If the time distance is not long enough then there can be contamination from the excited states, and the mass M can be overestimated. This is why all lattices have more points in the time direction than in the spatial directions.

The main effect of all these limitations on the calculations discussed below is that one cannot use quark masses as small as those of the physical up and down quarks. One has to extrapolate to reach the physical pion mass. One also has to extrapolate to get the properties of the physical kaon, since it contains one light quark. These extrapolations may be problematical.

The approximations of finite a and L are, in my view, either under control, or close to being so. Furthermore, it is straightforward to improve upon them. The remaining approximation which is employed by current calculations is much more serious. This is the so-called "quenched" approximation, in which the internal quark loops are left out. The creation of $\bar{q}q$ pairs is simply switched off. This is an uncontrolled approximation, which cannot be systematically improved except by removing it altogether.

* Of course, for a given computer power, one has to reach a compromise between lattice spacing and physical box size. The quoted values are the result of such a compromise.

The reason for this approximation is lack of computer time. To include fermions in any simulation one must deal with the fact that they are represented by anticommuting variables. This is a notorious problem, and much effort has gone into designing algorithms suitable for QCD.[19] Although much progress has been made, the cost of including dynamical fermions is a factor of 100-1000, and gets worse for smaller quark masses. Thus only studies on small lattices have been done.

The quenched approximation does not actually represent a unitary theory when rotated back to Minkowski space. For example, one can calculate the $\rho \to \pi\pi$ decay amplitude (from a three point function), but the ρ propagator does not contain the absorptive part due to the $\pi\pi$ cut: Physically this means that the ρ is not a resonance, but a pole. This neglect of the decay can have an effect on the mass of order the width, i.e. 100 MeV. Other effects of the quenched approximation are that baryons will have a much reduced pion cloud, and will not contain any strange quarks in the sea. The strange quark content of the proton is known to be significant, however, both from the value of the pion-nucleon sigma term, and from the recent EMC measurements of the polarized structure functions. Pion physics will also be affected, because the chiral loops which are responsible for the non-analytic corrections to the leading current algebra formulae are mostly absent in the quenched approximation.

Thus we should not expect the quenched results to agree with those of the full theory. Nevertheless, on the positive side, certain essential elements of QCD are included. In particular, quark confinement and chiral symmetry breaking have been convincingly established in numerical simulations of the quenched theory (see below). Furthermore, one might hope that ratios, such as the kaon B parameter, might be less sensitive to the approximation. I think, however, it is best to view the quenched calculations as semi-quantitative. In many cases, it is a significant achievement that they can be done at all.

Before describing how well lattice calculations fare, I should explain a point which will repeatedly come up. To fix the lattice spacing in a lattice calculation one has to choose the coupling constant g. Recall that in cut-off QCD the coupling constant is evaluated at a scale $\mu \sim 1/a$. For small enough a, we know from perturbation theory how $g(1/a)$ depends on a. Thus we can invert, and find the dependence of a on g. The smaller we choose g, the smaller a. In practice, we do not know exactly what a we get when we choose a certain g. This is partly because we do not know exactly which scale to use as the argument of g ($1/a$ versus π/a). Also, experiments still have not pinned down the value of Λ_{QCD}, i.e. the value of α_s at some particular scale. And finally, if we use the quenched approximation, we are not allowed to compare with the real world anyway. So there is an overall ambiguity in the scale of lattice results. One measures a mass in lattice units, i.e. Ma, with a definite statistical precision, but there is a much larger systematic error involved in converting this to a value for M in physical units.

4. Tests of lattice calculations

I will give a brief overview of the present status. For more details see the reviews by myself (least technical),[20] Gupta (more details),[21] or Marinari (most technical).[22]

First, I should say that the theory without fermion loops is a perfectly sensible theory as long as one considers only gluonic quantities. This is the pure SU(3) gauge theory, which has a spectrum of glueballs alone. One can also add infinitely heavy quarks, and the theory still is consistent, since there is no amplitude to create $\bar{q}q$ pairs. Since it is the gluonic sector that causes confinement, one can learn a lot by calculations in this theory.

Confinement is, perhaps, the most esoteric of the phenomena attributed to QCD. Though we have learnt to live with it, there is still no derivation of confinement from first principles. The best "proof" available is the numerical evidence from quenched lattice calculations. Here one measures the potential between an infinitely heavy quark and antiquark, as a function of the distance between them. If quarks are confined, the potential should grow linearly with separation, and grow without bound. The coefficient of the linear term is called the string tension, $V = \sigma r + O(1)$. The physical picture associated with this is a tube of color-electric flux running between the quark and antiquark. If the flux is confined to a tube of constant cross section then the energy density stored in the flux tube will grow proportional to its length.

For calculations of the potential the use of the quenched approximation is actually an advantage. In the full theory, when the heavy $\bar{q}q$ pair are far enough apart, it would become energetically favorable to create a light $\bar{q}q$ pair, and form a pair of heavy-light mesons. Thus confinement would be masked, and the potential would flatten out beyond a certain distance. A compilation of results for the quenched potential[23] is shown in Fig. 1. The plot shows the result in dimensionless units, the dimensions being carried by the string tension. As discussed below, one uses $\sqrt{\sigma} \sim 420\,\mathrm{MeV}$ to convert to physical units. Thus the potential is being measured over the range $0.1 - 1.0$ fm. The plot also shows the Cornell potential,[24] which consists of a linear and $1/r$ terms, and which is tuned to fit the charmonium data. The long distance behavior of the lattice potential is consistent with linear growth. The large errors at the largest separations are indicative of the fact that it is very hard to measure the string tension accurately.[21] Nevertheless, the qualitative result is clear. The

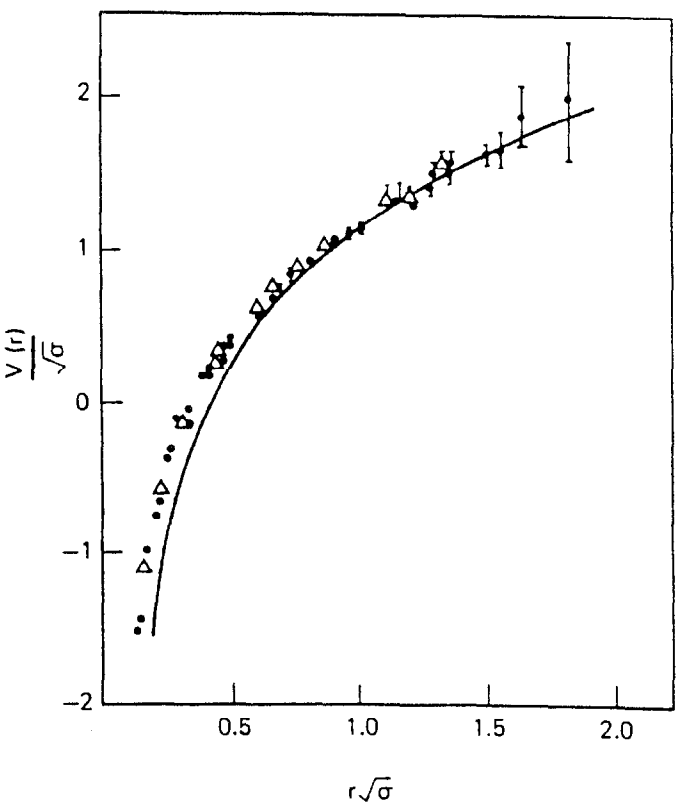

Fig. 1

Comparison of Monte-Carlo results for the heavy quark potential with the Cornell potential.[23] The results are put into dimensionless units using the string tension. The normalization is chosen to make the two curves agree at $r\sigma = 1$.

disagreement between the data and the phenomenological potential at small distances may be an effect of the quenched approximation.

Another calculation that can be done in the pure gauge theory is that of the glueball spectrum. These calculations have proved much more difficult than first expected. The major difficulty has been inventing operators with a large enough overlap with the glueball states. One has to use large operators, say 0.5 fm across, involving a tangled web of gauge links. One should think about this as a complicated mess of flux. These new techniques have made it possible to calculate masses for the scalar and tensor glueball on lattices with the spacings I discussed in the previous section, i.e. $1/a \sim 2\,\mathrm{GeV}$. Furthermore, there are results from a variety of lattice spacings, and for a variety of box sizes. Thus a systematic study of the error due to the approximations is underway.

It turns out that there are very large finite size effects in glueball masses. For very small volumes (one glueball Compton wavelength across or less) the tensor glueball is slightly lighter than the scalar glueball. For volumes up to five glueball Compton wavelengths the tensor representation (five states) splits up into two parts, one lighter than the scalar, the other heavier. For larger volumes, the two components of the tensor representation come together, as they must if full rotational invariance is to be restored, and they lie significantly higher than the scalar glueball. This provides a salutary lesson in the possibility of finite size effects.

I quote the numbers from the review talk of Andreas Kronfeld at the Lattice-88 symposium.[25] He has kept only results for small lattice spacings ($6/g^2 \gtrsim 5.9$), and for large volumes ($m(0^{++})L > 8$). The tensor to scalar ratio is $m(2^{++})/m(0^{++}) = 1.56(7)$, the error being statistical only. To quote a number for the scalar glueball one must know what value of the lattice spacing to choose. Since this is not the real theory of the world, there is no obvious choice. The standard procedure is to use the string tension to set the scale. The result is $m(0^{++})/\sqrt{\sigma} = 3.24(16)$. To convert this into a rough estimate in physical units one uses the estimate of σ from the Regge slope: the slope of the linear relationship between the meson mass-squared and angular momentum. This gives $\sqrt{\sigma} = 420\,\mathrm{MeV}$, and thus $m(0^{++}) \sim 1.36\,\mathrm{GeV}$.

I stress that this physical value is only a very rough estimate. To obtain it one has to assume that the string picture of high angular momentum states works in detail, and that the inclusion of fermion loops will not change the ratio $m(0^{++})/\sqrt{\sigma}$. In fact, a scalar glueball will decay copiously into two pions in an S-wave, and is likely to have a very large width, which in turn will effect its mass. There is no reason to expect an exactly similar effect in the string tension. Thus I take the pure gauge result as indicative that the scalar glueball will probably be more massive than 1 GeV, and that the tensor glueball might

well be heavier than 2 GeV. However, for the glueball hunters amongst you, it is far too early to rule out that the $f_2(1720)$ (a.k.a. $\theta(1720)$) is a tensor glueball.

The importance of these results is not so much the numbers themselves, but rather that reliable calculations in pure gauge theory are now possible. These calculations appear to have the systematic errors from the finite size of the lattice, and the finite lattice spacing, down at the 10% level.

A similar level of accuracy has also been attained in the calculations including quenched fermions. This was not so when I gave the talk, but the very recent results from the APE collaboration[26] have drastically improved the situation. The APE machines are home-built parallel computers, designed with QCD in mind. They are dedicated to lattice QCD and statistical mechanics calculations.

Figure 2 shows their results for proton, rho and pion masses on a modified Edinburgh plot: m_p/m_ρ versus $(m_\pi/m_\rho)^2$. Since only dimensionless ratios are plotted, one can directly compare to experiment. Two points on this plot are known: the physical values, and the infinite quark mass limit. (For $m_q = \infty$ the particle mass is just proportional to the number of quarks and antiquarks.) Also shown are a sample of the "old" results from the Tsukuba group.[27] The improvement in the errors is dramatic.

The two sets of results from the APE group are from calculations at $6/g^2 = 5.7$ and $6/g^2 = 6.0$. The lattice spacings are respectively ~ 1.2 GeV and ~ 2 GeV (using the string tension to set the scale). The smaller spacing is too small for perturbation theory to apply, so, following the discussion of the previous section, one would expect differences between the two sets of results. This is clearly confirmed by the data. The merit of the $6/g^2 = 5.7$ data is that it extends to smaller quark masses, and shows that there is no dramatic curvature in the data. Thus it seems fairly certain that the $6/g^2 = 6.0$ data will extrapolate to a prediction for m_p/m_ρ which is greater than 1.4.

The finite size effects in this calculation appear to be small.[27] I also think it unlikely that going to smaller lattice spacing will change the result significantly. Thus it seems to me that we are fairly certain of the value of m_p/m_ρ in the quenched approximation, and that it differs significantly from the physical value. As discussed above, this is not unexpected. What is important is whether the difference should be considered large or small. This is important because the matrix element calculations will be using the quenched approximation for the next two or three years, and we want to have some idea of the errors this implies.

I do not know whether one should treat the deviations as large or small. One can either say that there is a 10-20% effect (comparing the actual values of m_p/m_ρ), or one could compare the difference of the ratio from the $m = \infty$ value 1.5. In the latter case the effect of the quenched approximation is very large. This is not a facetious comparison, because some quantities vanish in the

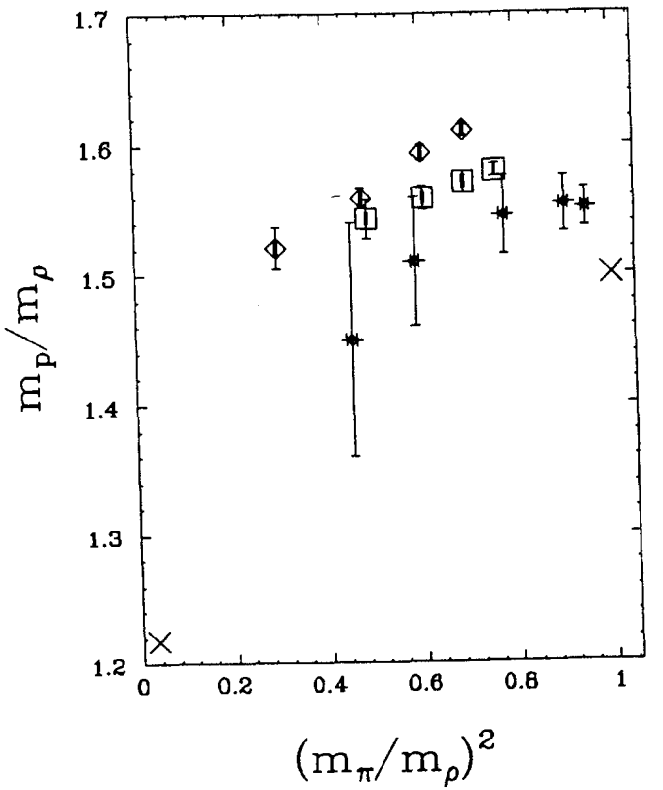

Fig. 2

Quenched QCD results for the mass spectrum. The ratio m_p/m_ρ (m_p is the proton mass) is plotted against $(m_\pi/m_\rho)^2$. The diamonds are the APE data[26] at coupling $6/g^2 = 5.7$, the squares are APE data at $6/g^2 = 6.0$, and the plusses are the TSUKUBA results[27] at $6/g^2 = 5.85$. The errors shown have been reconstructed from the papers, and while not exactly correct, are nearly so. The "X"s mark the known points for *full* QCD: the physical values and the infinite quark mass limit.

infinite mass limit, and yet are expected to be large for physical quark masses. An example is the "eye diagram" contribution to the $\Delta I = 1/2$ rule. What would be very helpful is a crude model of the effect of the quenched approximation.

The final test of lattice QCD I want to mention concerns chiral symmetry breaking. Aside from confinement, this is the most striking feature of the low lying spectrum of QCD. The Lagrangian of QCD almost has a chiral symmetry in which the left-handed and right-handed light quarks (u, d and s) are multiplied by independent phases. This symmetry would be exact if the quarks were massless. This symmetry of the Lagrangian is broken by the vacuum of the theory. The broken vacuum can freely convert a left-handed quark into a right-handed quark, and visa versa. Thus the quarks propagating through the vacuum have an effective mass – the constituent mass of $\sim 300\,\mathrm{MeV}$. A second consequence of the breaking of the symmetry is the appearance of Goldstone bosons. These are the pions, kaons and η, which would be massless were it not for the current quark masses. The Gell-Mann–Oakes–Renner[28] formula states, in fact, that $m_\pi^2 \propto m_q$. The interactions of the pseudo-Goldstone bosons with one another, and with other particles, are constrained by chiral symmetry.

Chiral symmetry breaking is a non-perturbative property of full QCD, for which there is considerable evidence in the real world. A simple picture of how it happens was given by Nambu and Jona-Lasinio many years ago.[29] The attractive interaction between a quark and antiquark increases as the momentum scale decreases, and eventually becomes strong enough that it is energetically favorable for the vacuum to fill with $\bar{q}q$ pairs. This picture suggests that internal quark loops are not essential to the phenomenon. On the contrary, they would partially screen the attraction between quark and antiquark. Thus the quenched approximation is a good place to search for chiral symmetry breaking.

There is now considerable evidence that chiral symmetry breaking does occur in quenched QCD. Here the fact that lattice calculations can vary the quark mass allows one to map out the functional form of quantities in much more detail than in the real world. The condensate $\langle\bar{\psi}\psi\rangle$ is found to be non-zero. The mass formula $m_\pi^2 \propto m_q$ works extremely well. More detailed predictions of the broken chiral symmetry picture are now beginning to be tested, and work within quite large errors.[18,30]

So the qualitative features which we observe in nature are indeed reproduced by quenched QCD. The differences are at the quantitative level. Given this situation, the only reasonable way to proceed is to use a three pronged attack. (1) Continue trying to improve algorithms for including fermion loops. (2) Develop methods to calculate measured, non-perturbative quantities, that can then give an indication of the accuracy of the quenched approximation. (3) Learn how to calculate matrix elements which will allow one to test the standard model, and use the wisdom obtained from (2) to give reasonable estimates of the errors. It has proved quite hard to figure out how to calculate certain matrix elements, such as the kaon decay amplitudes. Once the methods are in place, however, they can be used directly on the full theory, when computer time allows.

I now turn to the various weak hadronic matrix elements for which lattice calculations are underway. I should also mention various other matrix elements on which considerable progress has been made, but which I will not discuss. These are the low moments of meson and nucleon structure functions, quark distribution amplitudes, proton decay rates, and the form factors of the pion and nucleon. The status of these calculations has been recently reviewed by Martinelli.[31]

There are a relatively small number of people working on this particular branch of lattice gauge theory. In order to have convenient labels to use below, I will list the groups now. The choice of identifying geographical institution has become standard, and I cannot be blamed for it. In alphabetical order, there is the BOULDER group consisting of Tom DeGrand and Richard Loft; the FNAL (/IBM) group of Estia Eichten, Paul Mackenzie and Jim Sexton; the LANL (/BROWN/CERN/UW) group of Gerry Guralnik, Rajan Gupta, Greg Kilcup, Apoorva Patel, and yours truly; the ROME (/CERN/MADRID/ORSAY/SOUTHAMPTON) group of Belen Gavela, Luciano Maiani, Guido Martinelli, O. Pene, S. Petrarca, F. Rapuano and Chris Sachrajda; the TRIUMF (/BAYLOR/KENTUCKY) group of Terry Draper, K.F. Liu, Walter Wilcox and R.M. Woloshyn; and finally the UCLA (/TRIUMF) contingent of Claude Bernard, Terry Draper, George Hockney, Aida El-Khadra, and Amarjit Soni. It appears that, much as with experimental high energy physics, the collaborations span countries, continents and even oceans!

5. Decay constants

The meson decay constants are determined by the simplest of all matrix elements. For example,

$$\langle 0|\bar{u}\gamma_\mu\gamma_5 s|K^0(p)\rangle \equiv i f_K p_\mu \,, \tag{5.1}$$

is the normalization in which $f_\pi = 135\,\mathrm{MeV}$. It is simplest to do the calculations with $\vec{p} = 0$, and use $\mu = 0$.

The present interest is in decay constants of heavy-light mesons. This interest is for two main reasons. The first is the possibility that f_F ($F = \bar{s}c$) might

be measured directly, from the rate of the decay $F \to \mu^+\nu$. The second is the measurement of $B^0 - \overline{B^0}$ mixing, the amplitude for which is proportional to f_B^2.

The range of quark masses at our disposal is roughly from $\frac{1}{2}m_s$ up to 2 GeV. We can calculate with both quarks equal in mass, or with unequal masses. To calculate decay constants for mesons containing up or down quarks we must extrapolate. However, this extrapolation seems quite smooth. For example, one can fit f_K to the form $b + c(m_d + m_s)$, with b and c constants. Thus one can extract quite reliable values for f_π and f_K. The ratio f_K/f_π should be free from dependence on the overall scale, and might have reduced sensitivity to the quenched approximation. This ratio is ~ 1.22 experimentally. The lattice results are consistent with this, though with quite large errors. For example, a staggered fermion calculation[32] finds $f_K/f_\pi = 1.20(6)$, while Wilson fermions[33] give $1.22 \pm .05^{+.28}_{-.12}$ (the second error is an estimate of systematics). This gives some confidence in the predictions for heavy-light systems.

Table 1 contains a compilation of the available data on the heavy-light decays constants. The second column shows the coupling constant used ($\beta = 6/g^2$), and the type of fermions used. I have only included results with $\beta \geq 6.0$, i.e. with small lattice spacing. Roughly speaking for $\beta = 6.0$, 6.1, 6.2, the inverse lattice spacings are $a^{-1} = 2.0$, 2.3, 2.6 GeV. The errors quoted are only statistical. The decay constants in the first four rows have been converted into physical units by first calculating the ratio f/f_π and then multiplying by the physical value of f_π. This is probably the most reliable method. For the BOULDER data[35] I have done this conversion by hand, using the results in the paper. In the last three rows conversion is made to physical units using a value for the lattice spacing $1/a(g = 1) = 1.9$ GeV. This is the method that has to be used if light quark extrapolations are not available.

Table 1. Decay constants

Reference	$\beta^\star$	Method	f_{cd}	f_{cs}	f_{bd}	f_{bs}
ROME[34]	6.2(W)	f/f_π	181(27)	218(27)	~ 120	~ 150
UCLA[33]	6.1(W)	f/f_π	174(26)	234(46)	105(17)	155(31)
ROME[34]	6.0(W)	f/f_π	197(14)	214(19)	-	-
BOULDER[35]	6.0(W)	f/f_π*	232	272	-	-
BOULDER[35]	6.0(W)	a^{-1}	190(33)	222(16)	-	-
TRIUMF[36]	6.0(W)	a^{-1}	-	225(25)†	-	-
TRIUMF[36]	6.0(S)	a^{-1}	-	290(20)†	-	-

⋆ S=staggered fermions, W=Wilson fermions

* Calculated indirectly from information in paper

\- Results read off figure, error unreliable

Let me first discuss the results for the decay constants of the mesons containing charm quarks. Comparison of these numbers indicates that there is relatively good agreement between the Wilson fermion results. The exception is the BOULDER data using the f/f_π method. These are the results that I have estimated, and they have very large errors because of the error in f_π. Thus the numbers are probably not inconsistent, although this needs to be checked. There is a substantial difference, however, between the results for the two types of fermion. In principle, as $a \to 0$, these two types of fermion should give the same answers. In fact, the TRIUMF group find that the divergence between the two types of fermion increases as the mass of the meson increases. This suggests that there are large $O(Ma)$ (M is the meson mass) corrections. This is what one might naively expect since, for the charmed mesons, $Ma \sim 1$. Nevertheless, for the Wilson fermion calculations, the UCLA group has found that various ways of estimating the effect of $O(Ma)$ corrections indicates that they are small. Thus it is possible that the difference between the two types of fermion is mainly a problem for staggered fermions. However, the evidence for this is not convincing, and more work remains to be done.

The most detailed study of systematic errors has been done by the UCLA group. They find that the dominant systematic is the uncertainty in the overall scale. They estimate that the error in f_D and f_F is ~ 50 MeV. Given the differences between Wilson and staggered fermions, this may be a slight underestimate, but is probably not off by too much. A very rough estimate of the effect of the quenched approximation can be obtained from the size of the contribution of pion, kaon and η loops to f_π and f_K. In the large N_c approximation,[11] this turns out to be a 10-20% effect. Thus the quenched approximation is probably not the dominant source of error, at present.

One can avoid the large error due to the uncertainty in the scale by considering the ratios f_{cd}/f_π, f_{cs}/f_π, and f_{cs}/f_{cd}. It is a firm result of the quenched approximation that these are greater than 1.

To make an estimate of the decay constants for B mesons one must extrapolate well beyond the reach of the lattice. For heavy-light mesons, it has be shown[37] that, if the mesons are heavy enough, $f \propto 1/\sqrt{M}$. There are actually small multiplicative corrections to this of the form $\alpha_s(m)^\gamma$, where γ is a known anomalous dimension. Given the size of the errors in present lattice estimates, however, these corrections can be ignored. Thus to estimate $f\beta$ one has to know when the asymptotic form begins to apply.

The UCLA group has addressed this question by calculating the decay constant, for fixed light quark mass, for a large number of heavy quark masses. I show in Fig. 3 their data for light quarks of masses $\sim .4m_s$, $.7m_s$ and $1.4m_s$. The heavy quark masses range up to values greater than m_c. I have taken the

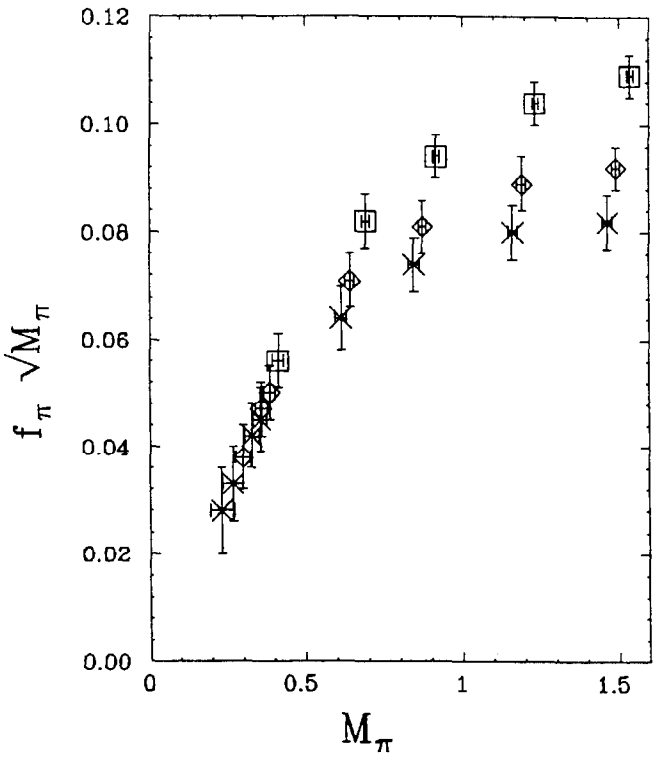

Fig. 3

Quenched QCD results for heavy-light meson decay constants. The data is from the UCLA group.[33] The plot shows $f_\pi\sqrt{M_\pi}$ versus M_π, where all quantities are in lattice units. Three sets of data points are shown, each corresponding to a fixed light quark mass. The crosses, diamonds and squares are for light quark masses $\sim .4m_s$, $.7m_s$, and $1.4m_s$. For the technically minded the actual parameters are κ = 0.154, 0.153 and 0.151 respectively. The data are from $12^3 \times 33$ lattices at β = 6.1. The errors are statistical.

data (for $6/g^2 = 6.1$) quoted in their paper, and multiplied the decay constant (in lattice units) by $\sqrt{Ma}$, and plotted against Ma. The errors are statistical only. The curves clearly show a tendency to flatten as M increases. This is what one expects if the asymptotic formula applies. Nevertheless, this flattening is occurring for Ma>1, at which mass lattice artifacts may be significant. Furthermore, one knows[33] that, for $Ma >> 1$, the lattice fa drops exponentially with the meson mass, and so eventually the curves must turn over. Thus, without independent confirmation I find this is a tantalizing, but not convincing, result.

To proceed, the UCLA group assume that the asymptotic behavior has set in by the last two points, and extrapolate to obtain f_{bu} and f_{bs}. These are the results shown in Table 1. The ROME group have not done such a detailed study, but if they extrapolate from their heaviest mass, assuming the asymptotic formula, then they obtain the estimates in the table. If the asymptotic behavior does not set in until higher masses, these will be underestimates of f_B. Clearly, in addition to the error in the scale, and the possible Ma corrections, there is a significant extrapolation error in these results. Thus I think it is too early to say whether f_B is less than f_π, though it begins to seem likely that $f_B/f_D < 1$.

Although the results for f_D will improve, it is less clear that those for f_B will get better. This is because it would take a considerably smaller lattice spacing to test if the glimpse of asymptotia shown in Fig. 3 is a real effect. But the size of the heavy-light mesons does not decrease as the heavy quark mass increases, since the size is determined by the light quark mass. Thus one cannot decrease the physical size of the lattice by much, without running into finite size effects. So one is forced to use lattices with more points in all directions, and this is beyond the powers of present computers.

To do better for f_B an alternative approach is needed. This is provided by a method suggested by Estia Eichten.[37] The idea is to expand about a heavy-light meson in which the heavy quark has infinite mass. In this limit the heavy quark does not move in space, and is easy to deal with. The light quark is allowed to propagate around the fixed heavy quark. It turns out that the calculation of the decay constant in this limit automatically has the $1/\sqrt{M}$ behavior as an overall kinematic factor. It is also possible to calculate non-leading terms suppressed by $O(1/M)$. Unfortunately, the calculations have proved difficult so far in practice.[38] But, in the future this may be the best way of determining f_B. Related ideas have been discussed by Lepage and Thacker.[39]

It is interesting to compare the lattice results with those of the QCD sum rules. Narison[40] finds 172(15), $\sim$ 220, and 187(17) MeV for f_{cd}, f_{cs} and f_{bd} respectively, while Dominguez and Paver[41] quote 224(26), 277(13) and 150-210 MeV respectively. The spread in the sum rule values is similar to the estimate of the systematic error in the lattice estimates. The sum rule values are, however, systematically higher, particularly for f_{bd}. Thus it is all the more important to press ahead with the lattice calculations of this quantity.

6. $B^0 - \overline{B^0}$ mixing

From the point of view of probing the weak interactions, the most pressing need for f_B is in order to predict $B - \overline{B}$ mixing. This has been measured for $\bar{b}d$ mesons both by ARGUS and CLEO. The result is $x_d \equiv |\Delta M|/\Gamma \sim 0.7$. The dominant contribution to ΔM comes from the box diagram in which both internal lines are top quarks. Because of this, the dominant momenta in the loop are $p \sim m_t$, and one can use perturbation theory to do the loop integral. The classic renormalization group analysis of Gilman and Wise[42] for $K - \overline{K}$ mixing can be carried over. This replaces the box diagram by a calculable QCD coefficient multiplying the four fermion operator $\mathcal{O} = \bar{b}\gamma_\mu^L d\ \bar{b}\gamma^{\mu L} d$. The coefficient is to evaluated at a scale at which perturbation theory applies, and the matrix element $\langle B|\mathcal{O}|\overline{B}\rangle$ is to be evaluated in QCD cut-off at the same scale. Schematically one has

$$x_d \;=\; (\text{known factors})\; f(m_t)\; s_{23}^2 \left(s_{12}^2 + q^2 - 2 s_{12} q \cos(\delta)\right) \langle B|\mathcal{O}|\overline{B}\rangle \;. \qquad (6.1)$$

Although s_{23} is measured from the B semileptonic width, and thus should be part of the "known factors", the error is still quite large. Thus I have displayed the factor of s_{23}^2 explicitly. The function of m_t is known, and is proportional to m_t^2 for most of the range of interest (40-200 GeV). The more-or-less completely unknown factor is the combination of angles in parentheses. The lack of observed $b \to u$ semileptonic decays limits $q < 0.17$. The ARGUS observation of $b \to u$ decays would provide a lower limit of $q > 0.08$, but this observation has not been confirmed by CLEO. Knowledge of the last factor in Eq. (6.1), i.e. the hadronic matrix element, would enable us to determine some combination of the parameters m_t, q and δ.

An oft-used parameterization of the matrix element is

$$\langle B|\mathcal{O}|\overline{B}\rangle \;=\; \frac{8}{3} f_{bd}^2 M_B^2 B_{bd} \;. \qquad (6.2)$$

This introduces a fudge factor B_{bd}. In vacuum saturation approximation, this factor is 1, by construction. This approximation is not sufficient to provide an answer, because of the uncertainty in f_B. I should also mention that in the large N_c approach, the leading order result is the same as vacuum saturation, except that $8/3 \to 2$.

The fudge factor B_{bd} is the ratio of the full matrix element to that in vacuum saturation approximation. Such a ratio can be measured directly on the lattice. Since it is dimensionless, there is no systematic error due to the uncertainty in the scale. Also, one might hope that there is less sensitivity to the quenched approximation. The measurement has been performed by both ROME[34] and UCLA[33] groups. As with the decay constants the results have to be extrapolated to the B mesons. However, this extrapolation seems very straightforward as B is close to 1 for all meson masses greater than $\sim$ 1GeV. One finds $B_{bd} \sim B_{bs} \sim 1.0(2)$. The error here is not from the extrapolation, nor from the statistics, but from the variation of the result as a is varied, and the uncertainty in the matching between continuum and lattice scales.[33] Similar values have been obtained by the FNAL group.[37] Thus the major uncertainty in the theoretical estimation of x_d comes from the factor of f_{bd}^2.

7. The kaon B parameter and ε

At the other end of the mass range it is also very important that we measure a mixing matrix element. The fudge factor for $K - \overline{K}$ mixing is defined as for the B system

$$\langle K|\bar{s}\gamma_\mu^L d\ \bar{s}\gamma^{\mu L} d|\overline{K}\rangle \;=\; \frac{8}{3} f_K^2 m_K^2 B_K \;. \qquad (7.1)$$

The uncertainties here are just the reverse of those in the B system. We know f_K from experiment, but there are considerable uncertainties in B_K.

We need to know B_K because it is a crucial ingredient in the standard model prediction of CP violation in $K - \overline{K}$ mixing. This is parameterized by ε, which is measured to have a value 0.00228. The theoretical analysis of ε is similar to that for $B - \overline{B}$ mixing. The box diagrams with internal top quarks dominate, although charm quark contributions cannot be neglected in a complete analysis. The box can be replaced by the matrix element displayed in Eq. (7.1), multiplied by a QCD coefficient which can be calculated perturbatively. Both matrix element and coefficient are to be evaluated at a scale μ at which perturbation theory is still valid. For the internal charm quark contributions to be replaced by an effective operator this scale must be comparable to m_c.

The detailed analysis has been done by Gilman and Wise,[42] with the result

$$\varepsilon \;=\; (\text{known factors})\; s_{23}^2\; q\; s_\delta\; g(m_t) B_K \;. \qquad (7.2)$$

Only the top quark contribution has been displayed. The function $g(m_t)$ is proportional to m_t^2 for most values of m_t. Clearly it is essential to know B_K to a level comparable to the experimental accuracy if we are to make full use of the data.

The various approximate methods have given values for B_K. To compare these values I will use scale $\mu \sim 2\,\text{GeV}$; B_K is defined so as to be 1 in vacuum saturation approximation, but this corresponds to a cutoff $\mu < 1\,\text{GeV}$. When one uses the renormalization group to run from this scale up to 2 GeV, one finds

$B_K(2\,\mathrm{GeV}) \sim 1.3$.* Using $SU(3)_L \times SU(3)_R$ chiral symmetry one can relate B_K to the $K^+ \to \pi^+\pi^0$ amplitude.[43] One finds $B_K(2\,\mathrm{GeV}) \sim 0.5$. QCD sum rules give values[11] in the range 0.33-1.2. Finally, the large N_c approximation[11] gives $B_K(2\,\mathrm{GeV}) \sim 0.8$.

There is clearly a great need for improvement. Superficially it might seem that lattice calculations should be as simple for B_K as for B_B. This is not so. The difficulty is that the behavior of the matrix element as a function of m_K is determined by chiral symmetry as $m_K \to 0$. One should find that $B_K = b + cm_K^2$, with b and c constants. To put it another way, the actual matrix element ($\propto m_K^2 B_K$) should vanish when $m_K = 0$.

For this result to hold in a lattice calculation, chiral symmetry must be respected. But with the Wilson formulation of lattice fermions, this symmetry is explicitly broken, and only recovered in the limit that $a \to 0$. This means, in practice, that one cannot simply measure the matrix element displayed in Eq. (7.1). One must perform subtractions on the operator, and, since these subtractions are calculated in lowest order perturbation theory, they are not exact. For a discussion see the review of Bernard.[44] The end result is that one doesn't expect that $B_K m_K^2$ will extrapolate to the origin. Indeed, the results from the ROME and UCLA groups show this.[44,45] Since this indicates contamination in the data, one has to assume something about the behavior of this contamination in order to extract an answer. Making a reasonable assumption, the ROME group quotes $B_K(2.5\,\mathrm{GeV}) = 0.65(15)$. The conversion from $\mu = 2\,\mathrm{GeV}$ to $\mu = 2.5\,\mathrm{GeV}$ is a small effect.

The other lattice calculation has been done by the LANL group, using staggered fermions. We calculate a different matrix element from that in Eq. (7.1), but one which is simply related to it. The advantage is that enough chiral symmetry is retained to guarantee, directly on the lattice, that the matrix element will vanish when $m_K = 0$. Actually, this derivation only holds in the infinite volume limit, as stressed to me by Claude Bernard. It is not clear how finite volume corrections will alter the prediction. I show our latest results in Fig. 4 (from 15 configurations of an $18^3 \times 42$ lattice at $6/g^2 = 6.2$ using the wall source method[46]). We measure B_K directly, but it is better to display $B_K m_K^2$. This is the middle set of points. The linear fit extrapolates quite close to the origin, and if one allows a little curvature, one can easily make the curve pass through the origin. The linear fit shown in the figure gives the value $B_K = .86$.

* Perturbation theory is not trustworthy below $\mu \sim 2\mathrm{GeV}$, so this estimate is somewhat untrustworthy. A similar comment applies to the chiral symmetry and large N_c calculations.

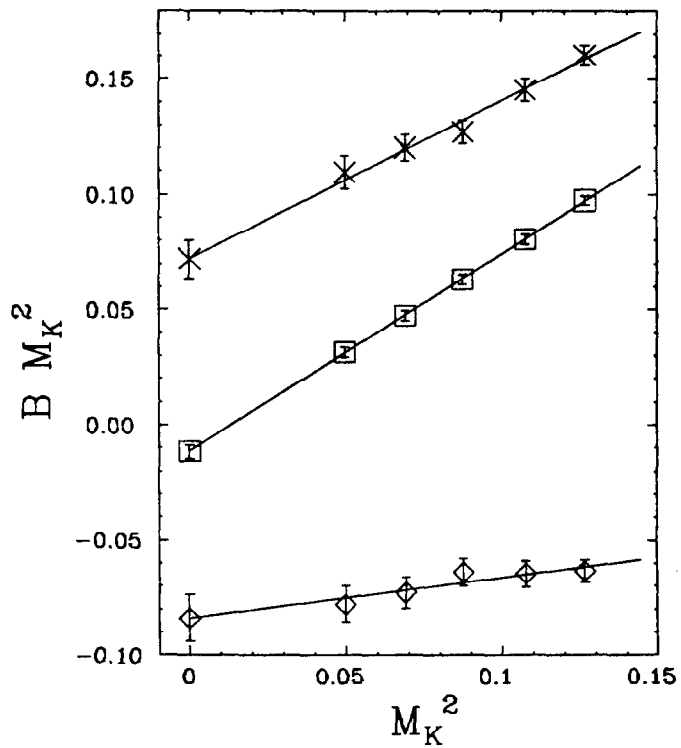

Fig. 4

Matrix elements of four-fermion operators in quenched QCD, obtained by the LANL group using staggered fermions.[46] The data are from 15 lattices of size $18^3 \times 42$, generated with $\beta = 6.2$. The squares show $B_K m_K^2$ plotted against m_K^2. All masses are in lattice units. The lines show linear fits to the data (i.e. those points with $m_K^2 \geq 0.05$), and the points at $m_K = 0$ are the corresponding extrapolated values. The upper and lower curves show other matrix elements. (They are, respectively, the V and A curves of Ref. 46.)

This result by itself is very pleasing. However, the other two sets of points in Fig. 4 are different matrix elements, each of which should also pass through the origin! One can imagine adding enough curvature to make this happen, but this looks very contrived. Such a large curvature corresponds to the breakdown of the lowest order chiral symmetry predictions. But if it is not present, and the intercepts are non-zero, then there is something amiss in the staggered fermion calculation. Similar results are obtained on two other lattices ($16^3 \times 40$ at $\beta = 6.0$ and $12^3 \times 30$ at $\beta \sim 5.9$), using different codes, so I do not think there is a bug in the programs. Clearly the problem requires further study. In particular, we are adding another mass point at $m_\pi^2 \sim .0035$.

For the moment, all one can say is that the lattice favors values towards the high end of the range of previous estimates. But substantial progress has been made in setting up the calculation theoretically, and in understanding the systematics, and I expect improvement in the next year.

Of course, it must not be forgotten that these are calculations in the quenched approximation. This means that pion, kaon and η loop diagrams are not properly included (one can actually still draw some such diagrams, but not all). Using the chiral Lagrangian one can actually calculate the effect of these loops. Although some of the contribution simply renormalizes f_K, there is a significant effect on B_K. One has to make assumptions to actually evaluate the size of the correction, and this is a controversial subject. Using the large N_c approach, one finds a 12% reduction in B_K due to these loops.[11] This suggests that the systematic errors due to quenching are not too large. There are also finite size corrections due to pion loops, which are probably calculable. Since the interactions of pions is weak, however, I do not expect these to be very large.

8. The $\Delta I = 1/2$ rule

Calculating the CP conserving parts of the kaon decay amplitudes is an important benchmark for lattice calculations. If the quenched approximation gives values close to those observed experimentally, then we can have more confidence in other results. To date, only the large N_c approximation has come close to explaining the large ratio of the K^0 decay amplitude to that for the K^+. This is a very nice piece of work,[11] but it involves stretching various approximations beyond their range of validity. In particular, perturbative calculations are used down to a scale $\mu = 0.6 - 0.8\,\mathrm{GeV}$. Despite these caveats, it is a challenge to the lattice calculations to do as well.

The lattice calculations are now closing in on an answer. The calculation of the $\Delta I = 3/2$ amplitude turns out to be relatively straightforward, plagued only by the perturbative subtractions similar to those for B_K. The $\Delta I = 1/2$ amplitude, however, is much more difficult to calculate. The problem is non-perturbative mixing with lower dimension operators. The solution to this theoretical problem has now been found, both for Wilson[47] and for staggered fermions.[48] I will not go into the details here.

The general method for the calculation of the amplitudes is the same as in the calculations described above. One starts with the W exchange diagram in terms of quarks, and then uses QCD perturbation theory to calculate the effect of loop momenta greater than some scale μ. The full analysis involves six operators, and has been described in the papers of Gilman and Wise.[42,49] As discussed in the introduction, QCD corrections enhance the operators with $\Delta I = 1/2$ and suppress those with $\Delta I = 3/2$. There is only a factor of two enhancement in A_0/A_2 if one stops using perturbation theory at $\mu \sim 2\,\mathrm{GeV}$.*

The non-perturbative part of the problem is the calculation of matrix elements of the operators between the kaon and the two pion final state. Of course, one has to extrapolate from the heavier lattice quarks to the physical quark masses. Chiral symmetry dictates how the amplitudes should vary as the meson masses approach zero. It is very important that the expected behaviors are observed, so that the extrapolation can be done reliably.

In fact, things are not so simple. It turns out that one has to do an off-shell calculation. There are three reliable ways of doing this. The first[50] is to calculate

$$K(\vec{p} = 0) \to \pi(\vec{p} = 0)\pi(\vec{p} = 0)\ ; \qquad m_u = m_d = m_s\ . \tag{8.1}$$

The use of equal quark masses (so that the kaon is degenerate with the pion) is essential. Having calculated this amplitude one uses chiral symmetry to extrapolate, both in mass and momentum, to the physical, on-shell point. The particular problem facing this method is the possible final state interactions between the two pions.

The second method[47] uses chiral symmetry to relate the $K \to \pi\pi$ matrix element to the $K \to \pi$ transition amplitude. It turns out that, with Wilson fermions, one has to calculate this transition amplitude for both $\vec{p} = 0$ and $\vec{p} \neq 0$. One is not forced, however, to use degenerate quarks.

With staggered fermions one has the possibility of using a third method. Here one need only measure the $K \to \pi$ transition amplitude at $\vec{p} = 0$, as long as one also measures the K to vacuum amplitude.[51,48]

* In such a calculation, charm quarks are not integrated out. This means that the penguin operators do not appear. Thus the question of whether these operators are the source of the $\Delta I = 1/2$ rule is meaningless.

All methods must eventually agree. To date, only Wilson fermion calculations have reported results, using the first two methods. Only the third method has been attempted with staggered fermions, and the calculation is in progress. I would summarize the present situation as hopeful, but a lot more work needs to be done. Most calculations have been done with quite heavy quark masses (not much lighter than m_s), and many have used large lattice spacings ($\beta = 5.7$). The final state interaction effects appear to be large in the $\Delta I = 1/2$ amplitudes. There are simply many more checks to be done.

To give an idea of the quantitative situation I will simply quote the latest results from the two groups. The numbers are given in Table 2, as well as the experimental values. (More data exists than is shown in the table, but it has not been fully analyzed.[44]) The $\Delta I = 3/2$ amplitude seems to come out too large, while the $\Delta I = 1/2$ amplitude has very large statistical errors. It is very likely that the statistical precision of the results will improve dramatically in the next year, and that the staggered fermion results will appear, since all three groups have access to considerably more computer time than previously available.

9. ε'/ε

The final matrix elements that I will discuss pertain to ε'/ε. As discussed in the introduction, ε'/ε allows us to test the understanding of CP violation in the standard model. For ε' to be non-zero, there must be CP violation in kaon decay amplitudes. In a phase convention in which all amplitudes are real if $\delta = 0$, it is necessary that the decay amplitudes develop an imaginary part. This can occur in so-called penguin diagrams in which the top quark is in the loop. This is a short distance loop, and can thus be replaced by a set of light quark operators, multiplied by known coefficients.[49] The dominant operator is $\mathcal{O}_6 = \bar{s}_a \gamma_\mu^L d_b \sum_{q=uds} \bar{q}_b \gamma_\mu^R q_a$ (a and b are color indices). The final equation for ε'/ε is given schematically in Eq. (1.3). The challenge for the lattice is to

Table 2. Kaon decay amplitudes

Reference	Method	β	$\frac{A(K_S \to \pi^-\pi^-)}{10^{-6} m_K}$	$\frac{A(K^+ \to \pi^+\pi^0)}{10^{-8} m_K}$	$\frac{A(K_S \to \pi^+\pi^-)}{A(K^+ \to \pi^+\pi^0)}$
UCLA[52]	$K \to \pi\pi$	5.7	1.0(6)	9(2)	11(6)
ROME[53]	$K \to \pi^*$	6.0	$\frac{1.2(1.3)}{2.5(1.8)}$	16(6)	$\frac{8(24)}{15(40)}$
ROME[53]	$K \to \pi\pi$	6.2	2.1(1.3)	5.9(1.4)	35(31)
Experiment	$K \to \pi\pi$	∞	0.78	3.8	21.2

* Two different methods of extrapolation were used for $K \to \pi$ amplitudes

calculate the matrix element of $\mathcal{O}_6$. This is of similar difficulty to the calculation of the $\Delta I = 1/2$ decay amplitude.

It turns out that ε' is sensitive to isospin breaking. This enters through the difference $m_u - m_d$, and from electromagnetic interactions. Naively one would expect these to give small contributions, but they are magnified by the $\Delta I = 1/2$ rule, and by the constraints of chiral symmetry. For more details see the original papers on the subject.[54] One of the electromagnetic contributions is obtained by replacing the gluon in the penguin diagram by a photon. Because of this, the electromagnetic terms have become known as being due to electromagnetic penguins (EMP).

For the full calculation of ε'/ε one needs the matrix elements of $\mathcal{O}_6$ for the strong penguins, and of two new operators $\mathcal{O}_7$ and $\mathcal{O}_8$ for the EMP. All three matrix elements can be estimated using the vacuum saturation approximation. Let me illustrate this for $\mathcal{O}_6$

$$\langle K^0 | \mathcal{O}_6 | \pi^+\pi^- \rangle = -i4\sqrt{2} f_\pi (m_K^2 - m_\pi^2) \frac{m_K^2}{m_s(\mu)^2} \left(\frac{f_K}{f_\pi} - 1 \right) B_6 \,. \qquad (9.1)$$

As always, the fudge factor (B_6) is defined so as to be 1 in vacuum saturation approximation. Similar equations define B_7 and B_8.[55] Notice the appearance of the strange quark mass, a parameter which is not very well known.

Lattice calculations in the quenched approximation can attempt to calculate these three B parameters. They cannot, however, expect to calculate the full matrix element. This is because the value of m_s in the quenched approximation is two to three times smaller than the physical value. Any matrix element that depends sensitively on m_s will be poorly measured in the quenched approximation. The matrix element of $\mathcal{O}_6$ is indeed sensitive to m_s, as shown by Eq. (9.1). It makes much more sense to measure the ratio B_6, so that the dominant dependence on m_s cancels. Of course, this problem will not be present in the full theory. But until we can simulate this theory on large lattices, we must live with the factors of m_s, and the uncertainty that they introduce.

When all the factors are put in, one finds that

$$\frac{\varepsilon'}{\varepsilon} = .028(10) |q| |s_\delta| \left| \frac{\hat{c}_6}{0.1} \right| \left(\frac{125\,\mathrm{MeV}}{m_s} \right)^2 B_6 (1 - \Omega_{\eta-\eta'} + \Omega_{EMP}). \qquad (9.2)$$

All quantities are to be evaluated at a common scale, which will be about 2 GeV for the lattice calculations; $\Omega_{\eta+\eta'}$ is the correction due to isospin breaking mass differences. It is proportional to the strong penguin contribution, and is fairly

well known. The range of reasonable values is $0.27 - 0.4$. The electromagnetic contribution is parameterized by Ω_{EMP}. This is defined to be

$$\Omega_{EMP} = 0.23 \frac{B_8}{B_6} \left(\frac{\frac{1}{3}\tilde{c}_7 B_7 + \tilde{c}_8}{\tilde{c}_6} \right). \tag{9.3}$$

Notice that if Ω_{EMP} is positive, which turns out to be so, then the two isospin breaking effects partly cancel.

The coefficients $\tilde{c}_{6,7,8}(\mu)$ are evaluated in perturbation theory. All depend logarithmically on m_t. Typical values[55] ($\mu = 2\,\mathrm{GeV}$, $\Lambda_{QCD} = 0.1\,\mathrm{GeV}$, $m_t = 70\,\mathrm{GeV}$) are $\tilde{c}_6 \sim -0.1$, $\tilde{c}_7 \sim -0.21$ and $\tilde{c}_8 \sim -0.03$. With these values, if one assumed vacuum saturation ($B_6 = B_7 = B_8 = 1$), then $\Omega_{EMP} \sim 0.23$, and there is a large cancellation with $\Omega_{\eta+\eta'}$.

Lattice calculations of B_7 and B_8 have been done by all three groups, and there is good agreement. All find that both B parameters are within 20% of unity.[44] These are relatively easy calculations that do not involve large subtractions.

The calculation of B_6 is much harder. The only result is that from the LANL group, using the third method discussed in the previous section, and using staggered fermions.[30] This result has some encouraging features, e.g. the dependence of the matrix element on the meson masses is consistent with expectations from chiral symmetry. But there are significant problems with the calculation. Certain terms are simply assumed to be small, and are not calculated.[44] Furthermore, the statistical errors are large. The actual number found is $B_6 \sim 0.5$, but, given the errors, I would only take this to indicate that B_6 may deviate substantially from unity.

It was at first thought to be very hard to calculate B_6 with Wilson fermions, but recently the UCLA group has pointed out that the $K \to \pi\pi$ method can be used.[52] They are in the process of doing the calculation. I expect much improved results from both types of fermion in the next year.

The situation for ε'/ε is thus quite unclear.[56] I should mention that the large N_c approximation, in leading order, has $B_6 = B_8 = 1$ and $B_7 = 0$. The suppression of B_7 is shown in Eq. (9.3) by the factor of $1/3$ multiplying B_7. However, since $\tilde{c}_8$ turns out to be very small, one must keep the non-leading terms in the approximation, and one would expect that $B_7 \sim 1$. The non-leading calculation has not been done. I hope that it will be attempted, because the size of the pion, kaon and η loop diagrams, which are a part of the calculation, will give an indication of the corrections to the quenched approximation.

Since the NA31 group has now a 3 standard deviation measurement of ε'/ε, I should make some comment on the theoretical expectations. Let me run through the uncertainties in Eq. (9.2). Moving from right to left, I begin with Ω_{EMP}. A reasonable range seems to be $0.2 - 0.5$. Thus the last parenthesis will probably not differ from 1 by more than 20%. As just discussed $B_6 \sim \mathcal{O}(1)$; $m_s(2\,\mathrm{GeV})$ is unlikely to be smaller than 125 MeV, but may be larger; $\tilde{c}_6$ always lies close to -0.1. The only solid result on q is the CLEO bound $q < 0.17$. Putting the factors together, if $q \sim 0.1$ (i.e. the observation of $b \to u$ decays by ARGUS is correct), and if $B_6 \sim 1$, and if $m_s \sim 125\,\mathrm{MeV}$, then the NA31 value is compatible with theory. But if $q < 0.1$, and the lattice finds $B_6 < 1$, and if $m_s > 125\,\mathrm{MeV}$, then theory cannot get as large a value as 0.003.

Thus there is a strong incentive to push hard on the lattice calculation of B_6. The Fermilab group is hoping to make a measurement within an error of 0.0005. If the NA31 result ($\varepsilon'/\varepsilon = .0033(11)$) is confirmed, this would be an accuracy of 20%. An interesting question for the future is whether it is worth reducing the experimental errors beyond this level. It is hard for me to judge how well q can eventually be measured, but over a time scale of 5-10 years, I expect that a calculation of B_6 and m_s to 10% accuracy is not unlikely.

10. Future progress

I hope to have given the impression of guarded optimism for the future. The machinery for the calculations is now in place. Either we need a major analytical breakthrough, or we need more Gigaflops.

Let me set out a possible progression. Present calculations (such as the $\beta = 6.0$, $1/a \sim 2\,\mathrm{GeV}$, $16^3 \times 40$ lattice that the LANL and UCLA groups are collaborating on) use, say, a CRAY-2 processor (of which there are four per machine) for one sixth of a real year (i.e. 1500 hours), and run at 100 Mflops. Let me define a unit calculation to be one requiring 10^{15} floating point operations. Present calculations, i.e. those leading to the results quoted above, take $\sim .5$ units.

The next step up is to have an entire year (nearly 9000 hours) of a CRAY-2 processor, i.e. 3 units of computation. This would allow one to increase the lattice volume to say $20^3 \times 40$, and to reduce the smallest quark mass accessible to $\sim m_s/4$. One has to do both at once, because smaller quark masses imply smaller meson masses, which require large volumes to avoid finite size effects. The lattice spacing would be unchanged, and the quenched approximation would still be used. Given the importance of testing the small meson mass behavior, it is better to use any increase in resources to decrease the quark mass rather than the lattice spacing. This amount of computer time has been granted for the next year to a merger of the LANL and UCLA groups, under the Department of

Energy's "Grand Challenge" program. The ROME group hopes to get at least as much time on the APE computers.

With present technology it is possible to do better. The fastest commercial supercomputer is the Connection Machine-2 (CM-2). A full CM-2 can probably run lattice QCD programs at 2 Gflops. The home-built machines at Columbia University, at Fermilab and the APE machine[57] will to soon be as fast or faster. Given a dedicated 1Gflop machine for an entire year, one has 30 units of computation. The extra factor of 10 allows one to increase the lattice size to $30^3 \times 50$ and to decrease the quark mass by roughly a factor of 2 to $m_s/8$. This assumes that the computer time scales as V/m, where V is the space time volume. Such a small quark mass would correspond to a pion of mass $\sim 250\,\mathrm{MeV}$. This should be small enough to definitively test the chiral behavior of amplitudes. Such a calculation is only a year or so away.

The next step may follow quickly afterwards. Don Weingarten at IBM is building a 10Gflop machine that will be dedicated to QCD. Parts of this machine are working. There are also other proposals with similar computer power.[57] This gives another factor of 10, assuming it can be used efficiently. Thus one could do a 300 unit computation each year. At this point one has gained enough to be able to try an unquenched calculation on a lattice comparable to those now used for quenched calculations (i.e. $16^3 \times 40$ with $1/a \sim 2\,\mathrm{GeV}$).

This takes us a few years hence, and I hope that the progression will continue. The APE collaboration are discussing a machine which would gain another factor of 10. There is the yet to be unveiled Connection Machine-3. It seems to me not too rash to expect that 5-10 years from now we will be able to do calculations in full QCD with 10-20% reliability.

Thus I foresee monotonic, though not fast, progress. In addition to improving the calculations that I have discussed in this talk, there are many other quantities that can be calculated which are important for probing the electroweak interactions. One project that is already underway is the calculation of the vector form factors relevant in exclusive semileptonic decays.[52] The idea is to calculate the form factors for $D \to Ke\nu$, and, by extrapolation, for decays such as $B \to \rho e\nu$. Eventually, when experimental and theoretical uncertainties have become small enough, this will allow a direct determination of KM angles.

Acknowledgements

I thank Claude Bernard, Terry Draper, Rajan Gupta, Greg Kilcup, Luciano Maiani, Guido Martinelli, Apoorva Patel, Amarjit Soni and Walter Wilcox for discussions, Andreas Kronfeld and Enzo Marinari for providing information at very short notice, and Eileen Brennan for patience.

References

1. H. Harari and M. Leurer, *Phys. Lett.* **181B** (1986) 123.
2. H. Harari, these proceedings.
3. M. Gell-Mann and A. Pais, Proc. Glasgow Conf. (1954) 342, Pergamon London (1954).
4. M.K. Gaillard and B.W. Lee, *Phys. Rev. Lett.* **33** (1974) 108; G. Altarelli and L. Maiani, *Phys. Lett.* **52B** (1974) 351.
5. H. Burkhardt *et al.*, *Phys. Lett.* **206B** (1988) 169.
6. M. Woods *et al.*, *Phys. Rev. Lett.* **60** (1988) 1695.
7. A.I. Vainshtein, V.I. Zakharov and M.A. Shifman, *JETP* **45** (1977) 670.
8. S.G. Gorishny, A.L. Kataev and S.A. Larin, *Phys. Lett.* **212B** (1988) 238.
9. Particularly useful is H. Georgi, *"Weak Interactions and Modern Particle Theory"*, Benjamin/Cummings, 1984.
10. A. Pich, CERN preprint TH.5102/88, to be published in Proc. Ringberg Workshop on hadronic matrix elements and weak decays, Ringberg Castle, Germany, April 1988.
11. A.J. Buras, in *"CP violation"*, Ed. C. Jarlskog, World Scientific, 1988.
12. K.G. Wilson, *Phys. Rev.* **D10** (1974) 2445.
13. For a very nice introduction see M. Creutz, *"Quarks, Gluons and Lattices"*, Cambridge University Press, 1983.
14. H. Quinn and M. Weinstein, *Phys. Rev. Lett.* **57** (1986) 2617.
15. R. Gupta, G. Kilcup, A. Patel and S.R. Sharpe, *Phys. Lett.* **211B** (1988) 132.
16. J. Gasser and H. Leutwyler, *Nucl. Phys.* **B307** (1988) 763.
17. G.W. Kilcup, S.R. Sharpe, R. Gupta, G. Guralnik and A. Patel, *Phys. Lett.* **164B** (1985) 347.
18. E. Franco, L. Maiani, G. Martinelli and A. Morelli, CERN preprint TH.5101/88.
19. For a very recent review see D. Weingarten, Proc. 1988 Lattice Symposium, Fermilab, September 1988.
20. S.R. Sharpe, talk at the Brookhaven Workshop on *"Glueball, hybrids and exotics"*, August 1988, to be published in the proceedings.

21. R. Gupta, Proc. 1st CCAST workshop/symposium on *"Lattice Gauge Theory using Parallel Processors,"* Beijing, China, 1987, Gordon and Breach, 1987.

22. E. Marinari, talk at the 1988 Symposium on Lattice Field Theory, Fermilab, September 1988, to be published in the proceedings.

23. C. Peterson, talk at DPF-85, Eugene, Oregon, 1985.

24. E. Eichten *et al.*, *Phys. Rev.* **D17** (1978) 3090; **D21** (1980) 203.

25. A. Kronfeld, talk given at the 1988 Symposium on Lattice Field Theory, Fermilab, September 1988, to be published in the proceedings.

26. P. Bacilieri *et al.*, the APE collaboration, preprints ROM2F-88-019 and ROM2F-88-021, July 1988.

27. Y. Iwasaki and T. Yoshie, preprint UTHEP-182, June 1988.

28. M. Gell-Mann, R.J. Oakes and B. Renner *Phys. Rev.* **175** (1968) 2195.

29. Y. Nambu and G. Jona-Lasinio, *Phys. Rev.* **122** (1961) 345.

30. S.R. Sharpe, R. Gupta, G. Guralnik, G.W. Kilcup and A. Patel, *Phys. Lett.* **192B** (1987) 149.

31. G. Martinelli, talk given at the 1988 Symposium on Lattice Field Theory, Fermilab, September 1988, to be published in the proceedings.

32. R. Gupta, G. Guralnik, G.W. Kilcup, A. Patel, S.R. Sharpe and T. Warnock, *Phys. Rev.* **D36** (1987) 2813.

33. C. Bernard, T. Draper, G. Hockney and A. Soni, preprint IUHET 141, UCLA/87/TEP/28, May 1988, to be published in *Phys. Rev.* **D**.

34. M.B. Gavela, L. Maiani, S. Petrarca, G. Martinelli and O. Pene, *Phys. Lett.* **206B** (1988) 113.

35. T.A. DeGrand and R.D. Loft, *Phys. Rev.* **D38** (1988) 954.

36. R.M. Woloshyn, T. Draper, K.F. Liu and W. Wilcox, TRIUMF preprint, 1988.

37. E. Eichten, Nucl. Phys. B, Proc. Suppl. **4** (1988) 170.

38. E. Eichten, J. Sexton and H. Thacker, work in preparation.

39. G.P. Lepage and B.A. Thacker, Nucl. Phys. B (Proc. Suppl.) 4 (1988) 199.

40. S. Narison, *Phys. Lett.* **198B** (1987) 104.

41. C.A. Dominguez and N. Paver, *Phys. Lett.* **197B** (1987) 427; **199B** (1987) 596 (E).

42. F. Gilman and M.B. Wise, *Phys. Rev.* **D27** (1983) 1128.

43. J.F. Donoghue, E. Golowich and B.R. Holstein, *Phys. Lett.* **119B** (1982) 412.

44. C. Bernard, talk given at the 1988 Symposium on Lattice Field Theory, Fermilab, September 1988, to be published in the proceedings.

45. L. Maiani, talk given at the 1988 Symposium on Lattice Field Theory, Fermilab, September 1988, to be published in the proceedings.

46. S. Sharpe, SLAC-PUB-4711, September 1988, to be published in Proc. Ringberg Workshop on Hadronic Matrix Elements and Weak Decays, Ringberg Castle, Germany, April 1988;
G. Kilcup, talk given at the 1988 Symposium on Lattice Field Theory, Fermilab, September 1988, to be published in the proceedings.

47. L. Maiani, G. Martinelli, G.C. Rossi and M. Testa, *Nucl. Phys.* **B289** (1987) 505.

48. G.W. Kilcup and S.R. Sharpe, *Nucl. Phys.* **B283** (1987) 493.

49. F.J. Gilman and M.B. Wise, *Phys. Rev.* **D20** (1979) 2392.

50. C. Bernard, T. Draper, G. Hockney and A. Soni, Proc. Nucl. Phys. B (Proc. Suppl.) 4 (1988) 483.

51. C. Bernard, T. Draper, D. Politzer, A. Soni and M.B. Wise, *Phys. Rev.* **D32** (1984) 2343.

52. C. Bernard, A. El-Khadra and A. Soni, preprint UCLA/88/TEP/31, to be published in Proc. Ringberg Workshop on hadronic matrix elements and weak decays, Ringberg Castle, Germany, April 1988.

53. M.B. Gavela, L. Maiani, S. Petrarca, G. Martinelli and O. Pene, preprint CERN-TH.5032/88, La Sapienza-Roma n.599, FTUAM 88/13, May 1988.

54. J. Bijnens and M.B. Wise, *Phys. Lett.* **137B** (1984) 245;
J.F. Donoghue, E. Golowich, B.R. Holstein and J. Trampetic, *Phys. Lett.* **179B** (1986) 361; **B188** (1987) 511 (E).

55. S. Sharpe, *Phys. Lett.* **194B** (1987) 551.

56. For a recent review see S. Sharpe, talk at DPF-88, Storrs, Connecticut, August 1988, to be published in the proceedings.

57. For a recent review of the various home-brewed machines see N. Christ, talk given at the 1988 Symposium on Lattice Field Theory, Fermilab, September 1988, to be published in the proceedings.

Recent Results from IMB

J.M. LoSecco
University of Notre Dame

The IMB Collaboration

Z.J. Ajaltouni,[10] C.B. Bratton,[4] D. Casper,[2,11] R. Claus,[11] M. Crouch,[8] S.T. Dye,[5]
S. Errede,[9] W. Gajewski,[1] M. Goldhaber,[3] T.J. Haines,[12] T.W. Jones,[6]
D. Kielczewska,[1,7] W.R. Kropp,[1] J.G. Learned,[5] J.M. LoSecco,[10] J. Matthews,[2]
R. Miller,[1] M. Mudan,[6] L.R. Price,[1] F. Reines,[1] J. Schultz,[1] S. Seidel,[2,11] D. Sinclair,[2]
H.W. Sobel,[1] J.L. Stone,[11] L. Sulak,[11] R. Svoboda,[1] G. Thornton,[2]
J.C. van der Velde,[2]

[1] *The University of California, Irvine, Irvine, California 92717*
[2] *The University of Michigan, Ann Arbor, Michigan 48109*
[3] *Brookhaven National Laboratory, Upton, New York 11973*
[4] *Cleveland State University, Cleveland, Ohio 44115*
[5] *The University of Hawaii, Honolulu, Hawaii 96822*
[6] *University College, London WC1E6BT, United Kingdom*
[7] *Warsaw University, Warsaw, Poland*
[8] *Case Western Reserve University, Cleveland, Ohio 44106*
[9] *The University of Illinois, Urbana, Illinois 61801*
[10] *The University of Notre Dame, Notre Dame, Indiana 46556*
[11] *Boston University, Boston, Massachusetts 02215*
[12] *University of Maryland, College Park, Maryland 20742*

Abstract

Revised numbers are presented for the neutrino burst from SN1987A observed by the IMB detector. The new values do not differ significantly from those already published. We also use the revised values and a study of systematic effects caused by a malfunctioning power supply to present and discuss the angular distribution of the observed events. Our present knowledge of systematic errors makes it unlikely that these produce much distortion in the angular distribution.

The angular distribution and energetics support the hypothesis that both neutrinos and antineutrinos were observed in the burst. The Kamioka and IMB experiments have good agreement with each other and with the hypothesis of a 25% forward scattering component of the form expected from $\nu e \rightarrow \nu e$. The nature of the forward scattering component can be inferred from known cross sections and experimental expectations.

This result has implications for models of supernova and for neutrino physics itself.

Introduction

The IMB collaboration has made detailed reports on our neutrino observations[1] of SN1987A. Over the past year we have made extensive studies and simulations of the detector and now have a better understanding of the events recorded in the supernova burst. The purpose of this note is to update the values of the observations to reflect our current best estimates and to explore the implications of the partial detector malfunction on the observed scattering angular distribution of the events.

At the time of the supernova neutrino burst one of the four high voltage power supplies in the detector had tripped off. This supply provided power to 25% of the photosensitive detectors. The detectors are arranged in blocks of 8 by 8 phototubes. These blocks are called patches. The east and west faces have four patches on them. The top, bottom, north and south faces have six patches each. The eight patches affected by the high voltage failure are illustrated in Figure 1. We had presumed that this malfunction reduced detection efficiency and produced a substantial angular distortion. An analysis of the effect of this malfunction is presented here and elsewhere.[2]

Updated Data

Table 1 lists the former best estimate of the parameters for the eight observed interactions. Table 2 lists the current revised values for these observations. There are no major differences to be noted. Most of differences are within measurement errors. A comparison of Table 1 with Table 2 should give the reader a better feeling for the inaccuracies of the measurements.

We have also established a new fiducial volume to have a mass of 6800 metric tons. This represents the entire sensitive volume of the IMB detector in front of the light detecting tube planes. Our published SN1987A results used a fiducial mass of 5000 metric tons. All previous physics results[3] with this device had been done with a 3300 metric ton fiducial volume (or less) obtained from the full sensitive volume by removing the outer 2 meters (or more) of water.

These different fiducial volumes do not yield significantly different physics results since the efficiency drops sharply, at these low energies, in the extended fiducial volume. The total sensitive volume has the dimensions of 22.9 meters in the east-west (x) direction, 16.8 meters in the north-south (y) direction and 17.8 meters in the up-down (z) direction. A table of efficiencies for the full volume and the standard fiducial volume are given in Table 3. The table has an additional 3% systematic error added on to the efficiency error. This reflects Monte Carlo differences between the measured detector response and amongst different Monte Carlo calculations. The reader is warned that

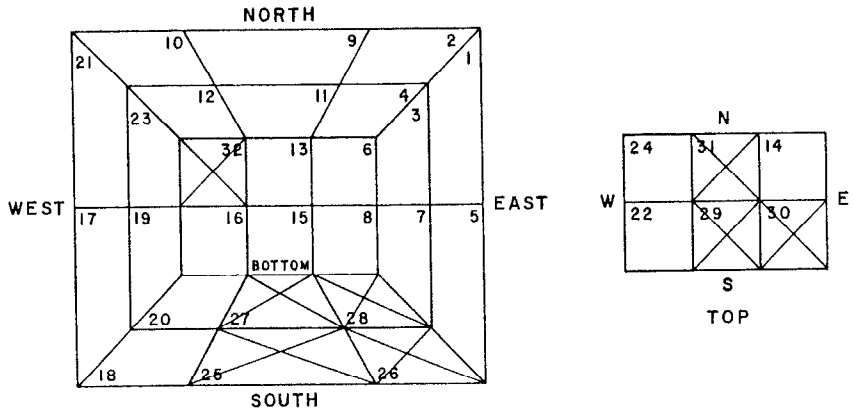

Figure 1: Malfunctioning Trigger Patches

Table 1: Old Distribution of IMB Events (April 1987 PRL)

Event	Time	Vertex (cm)			Direction			Angle	Azimuthal
Number	7:35:40+	X	Y	Z	X cos	Y cos	Z cos	from SN	Angle
1	1.37	-168.	-42.	86.	-0.712	0.697	0.086	75.	82.
2	1.79	717.	-529.	73.	-0.129	0.992	0.008	53.	47.
3	2.02	678.	489.	107.	0.955	0.292	0.060	56.	-59.
4	2.52	-740.	-436.	-236.	-0.480	0.037	0.876	63.	150.
5	2.94	-1017.	298.	-869.	-0.300	0.482	0.823	40.	130.
6	4.06	-670.	207.	-288.	-0.420	0.260	0.869	52.	141.
7	6.38	-531.	76.	284.	-0.327	0.632	0.702	39.	113.
8	6.96	652.	324.	-85.	0.384	0.349	-0.855	102.	-11.

Table 2: New Distribution of IMB Events

Event	Time	Vertex (cm)			Direction			Angle	Azimuthal
Number	7:35:40+	X	Y	Z	X cos	Y cos	Z cos	from SN	Angle
1	1.374	-20.	-62.	59.	-0.810	0.576	0.115	80.	90.
2	1.786	601.	-270.	145.	0.354	0.935	-0.020	44.	10.
3	2.024	583.	460.	101.	0.955	0.291	0.062	56.	-59.
4	2.515	-630.	-446.	-302.	-0.562	0.083	0.823	66.	144.
5	2.936	-982.	235.	-871.	-0.200	0.594	0.779	33.	122.
6	4.058	-628.	81.	-325.	-0.419	0.260	0.870	52.	141.
7	6.384	-513.	172.	247.	-0.344	0.485	0.804	42.	128.
8	6.956	702.	224.	-185.	0.376	0.320	-0.870	104.	-11.

Table 3: 75% IMB Monte Carlo Trigger Efficiencies

Energy	6800 T	3300 T
(MeV)	efficiency †	efficiency †
14	1.8±3.6	3.0±4.1
18	7.3±4.2	10.4±5.0
20	12.0±4.5	19.0±5.5
25	30.2±5.1	44.2±6.2
30	41.6±5.2	57.8±6.3
35	58.1±5.2	74.3±5.8
40	65.1±5.1	83.0±5.3
45	66.3±5.1	86.1±5.1
50	70.1±5.1	93.2±4.7

†Includes 3% systematic error

the efficiencies are calculated for an isotropic event distribution at the specified electron energy. The effect of the 25% missing light collectors is included. If the parent angular distribution is *not isotropic* these efficiencies will *not* accurately reflect the true detector response. These efficiencies are plotted in Figure 2.

Table 4 lists the revised event energies and compares the efficiency corrected event rate for both regions. They agree quite well. On the basis of the seven events actually observed in the 3300 ton fiducial volume we would expect to see an efficiency corrected number of 36±13 events in the full volume. We see 26.4 efficiency corrected events. The error on the expected value is purely statistical and does not reflect any additional errors coming from systematic efficiency errors.

The time distribution of the events is illustrated in Figure 3. The figure represents the cumulative number of events after a specified time. The negative slope of the curve represents the event rate. A major portion of the signal is found in the first two seconds.

In Figure 4 we illustrate the distribution of event vertices in the y-z plane. A similar figure could be constructed for the other two projections using the data from Table 2. In Figure 5 we present the projection of the direction cosines from Table 2 projected onto the y-z plane. Since the direction cosine vectors are normalized to one, this figure contains all of the direction information for these events. Note that four of the events point upward; three of them point horizontally and one points downward.

Angular Distribution

A major concern has been to understand the scattering angular distribution. This is illustrated in Figure 6. If the interactions are dominated by charged current reactions of electron antineutrinos on protons ($\bar{\nu_e} P \rightarrow e^+ n$) one would expect the distribution to be nearly isotropic. The plot of Figure 6 should be flat. In fact we find that all but one event is found in the forward hemisphere and the distribution shows a peak near 60°.

We can assign a statistical significance to the distribution that we find. The Smirnov-Cramer-Von Mises test allows us to compare the observed cumulative distribution function (CDF) for the scattering angle to a theoretically predicted one. Figure 7 illustrates the measured CDF and two predictions. The dotted curve is the CDF for a flat distribution. The data has a probability of about 1.5% to have come from a flat distribution. Due to a small energy dependence the actual distribution at our energy ($< E >= 30$ MeV) is expected to be slightly peaked forward with a distribution of $(1 + .13\cos\theta)$. In addition to this small forward bias the inoperative photomultipliers may have produced some additional distortion. Monte Carlo studies indicate that this distortion is small. It is at most a 10% effect. Conservatively we have compared the measured CDF

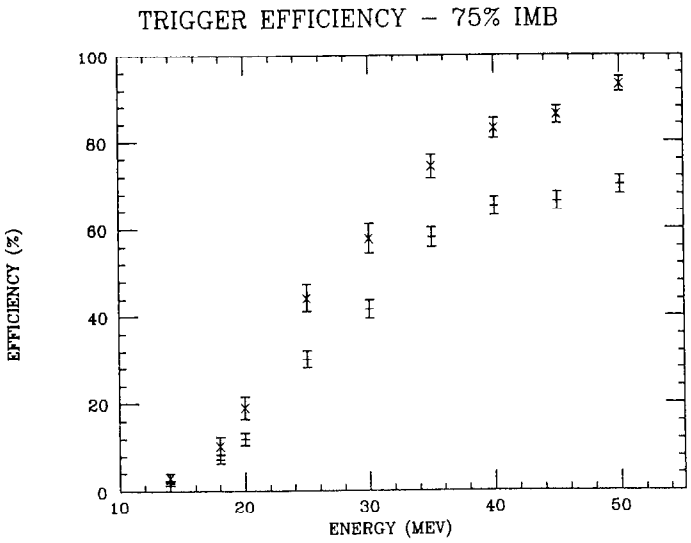

Figure 2: Trigger Efficiency for 75% of IMB

Table 4: Event Energy Summary

Event Number	Energy (MeV)	Inverse 6800 T efficiency	Inverse 3300 T efficiency
1	38±7	1.60	1.26
2	37±7	1.64	1.29
3	28±6	2.70	1.91
4	39±7	1.57	1.23
5	36±9	1.68	— (1.32)
6	36±6	1.68	1.32
7	19±5	10.36	6.80
8	22±5	5.19	3.44
All	26	26.4	17.3

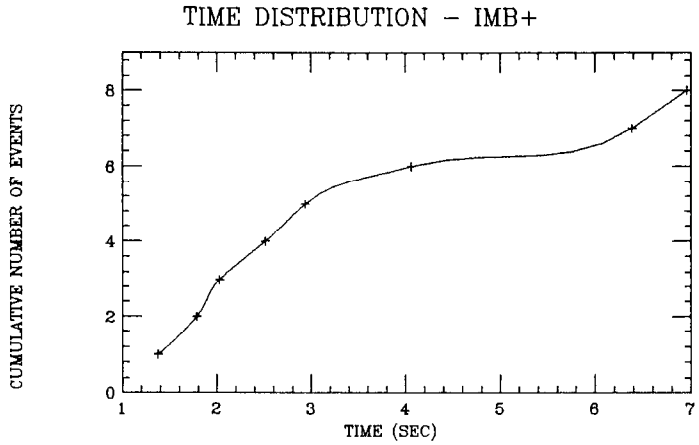

Figure 3: Time Distribution of Supernova Events

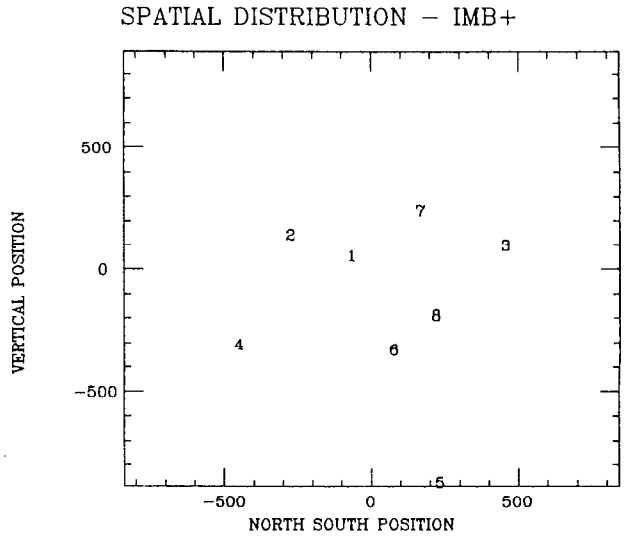

Figure 4: Projected Spatial Distribution of Supernova Events in the IMB Detector

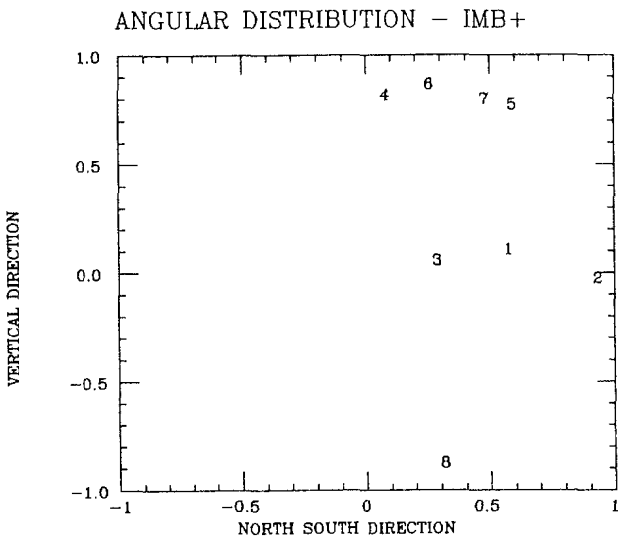

Figure 5: Projected Angular Distribution of Supernova Events. The malfunctioning patches would tend to populate the left side of the plot.

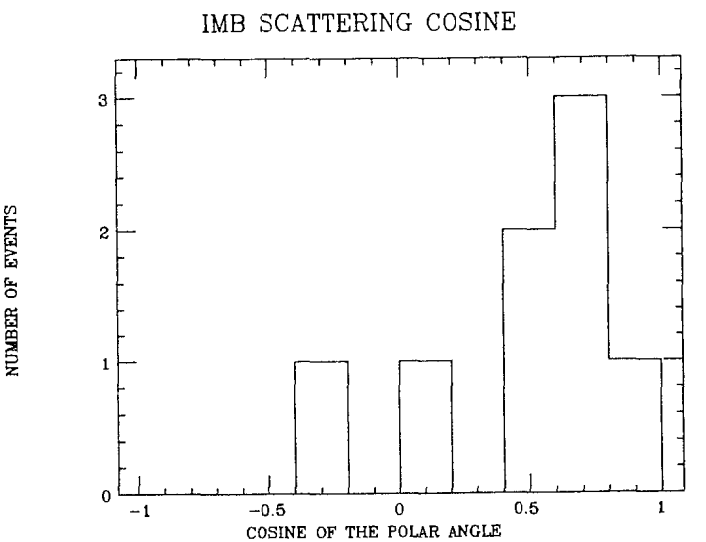

Figure 6: Scattering Angular Distribution

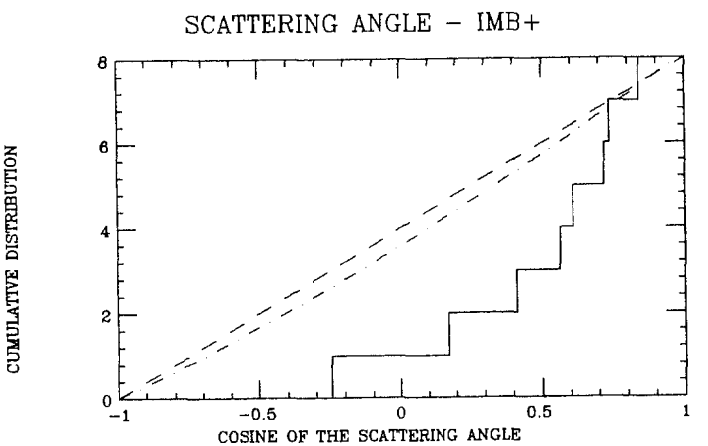

Figure 7: Cumulative Distribution for Scattering Angle

with the dot dashed curve[2] which is the distribution $(1 + .23\cos\theta)$. This includes a reasonable estimate of all systematic biases and physics effects. The probability of our distribution coming from such an initial distribution is about 4.5%. We consider this poor agreement.

The distribution of events in time, energy and scattering angle carries a good deal of information about the nature of the gravitational stellar collapse and the nature of the neutrino itself. The angular distribution is expected to be very different for events induced by electron neutrinos and by electron antineutrinos. The distribution we observe is not representative of either of these.

Beyond the scattering angle discussed above we measure the azimuthal angle of the events. No known physics effects can modulate the azimuthal distribution so any distortion observed here must be attributable to systematic effects. In Figure 8 we show the distribution of events in both scattering angle and azimuthal angle. There is a notable clumping of events within a cone of 20° opening angle. These events 4,5,6,7 occur in sequence. Even with the expected two dimensional distortion coming from missing phototubes such clumping has a probability of less than .7%.

Interpretation of the Observed Angular Distribution

Our detailed understandings of neutrino physics can be used to extract much useful astrophysical information from these data. Many details are revealed in subtleties of the observations. To avoid being led astray, comparison of data from the Kamioka and IMB experiments can be used to reduce systematic errors or the probability of statistical fluctuations. These experiments differ in sensitivity and possible systematic errors.

Tables 5 and 6 contain most of the information reported by IMB and Kamioka. The relative times, observed energy and scattering angles can be used to understand the burst.

Information regarding the types of interactions is limited. Neutrinos of all six types: $\nu_\mu, \nu_\tau, \nu_e, \bar{\nu}_\mu, \bar{\nu}_\tau$ and $\bar{\nu}_e$ are the only known particles that can penetrate the 5000 to 8000 km of earth between the source and detectors, or can escape the interior of the stellar collapse itself. There are only a limited number of reaction channels available to neutrinos on a water target at these energies. Some of these reactions can be distinguished by the angular distribution of the recoiling lepton.[4]

The three possible scatterers of the various types of neutrinos and antineutrinos would produce three distinct angular distributions.

Kinematics dictates that scattering from electrons ($\nu e \rightarrow \nu e$) will be strongly peaked forward. Multiple scattering will smear the sharp forward peak over a region of the

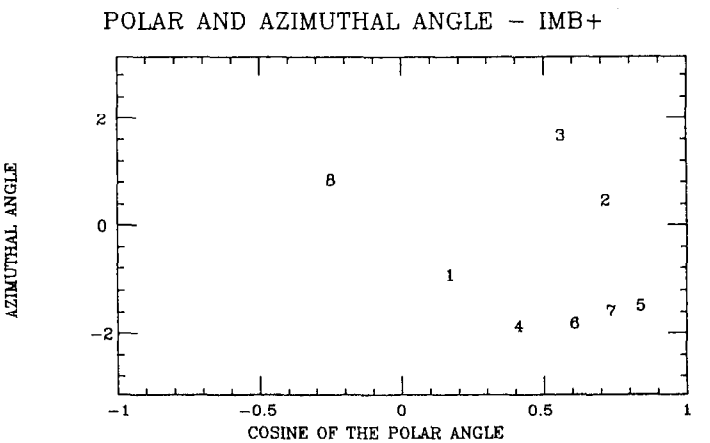

Figure 8: Polar (Scattering) and Azimuthal Angle

Table 5: Summary of IMB Events

Event Time	Relative Time	Cosine from SN	Angle from SN	Energy (MeV)
7:35:41.374	0.000	0.172	80±10	38±7
7:35:41.786	0.412	0.720	44±15	37±7
7:35:42.024	0.650	0.563	56±20	28±6
7:35:42.515	1.141	0.414	65±20	39±7
7:35:42.936	1.562	0.843	33±15	36±9
7:35:44.058	2.684	0.610	52±10	36±6
7:35:46.384	5.010	0.738	42±20	19±5
7:35:46.956	5.582	-0.246	104±20	22±5

Table 6: Summary of Kamioka Events

Event Time	Relative Time	Cosine from SN	Angle from SN	Energy (MeV)
7:35:35	0.000	0.951	18.±18.	20.0±2.9
7:35:35	0.107	0.766	40.±27.	13.5±3.2
7:35:35	0.303	-.309	108.±32.	7.5±2.0
7:35:35	0.324	0.342	70.±30.	9.2±2.7
7:35:36	0.507	-.707	135.±23.	12.8±2.9
7:35:36	0.686	0.375	68.±77.	6.3±1.7
7:35:37	1.541	0.848	32.±16.	35.4±8.0
7:35:37	1.728	0.866	30.±18.	21.0±4.2
7:35:37	1.915	0.788	38.±22.	19.8±3.2
7:35:44	9.219	-.530	122.±30.	8.6±2.7
7:35:45	10.433	0.656	49.±26.	13.0±2.6
7:35:47	12.439	-.017	91.±39.	8.9±1.9

forward scattering angle. At the electron energies observed in these experiments multiple scattering[5] is expected to be about σ=18°-22°. It rises to σ=30° at 10 MeV. This multiple scattering is added to the true scattering angle, which at these energies is as much as 12°-18°. Reconstruction errors will also tend to move the reconstructed track direction away from forward simply due to the larger solid angle available away from the forward direction. The very sharp peak expected for this process by some authors[6] is unrealistic and will not be present. Electron scattering is the only process that can give a forward peak.

Charged current scattering of electron antineutrinos by protons ($\bar{\nu}_e P \rightarrow e^+ n$) is expected to be nearly isotropic with a very small (10%) backward asymmetry at low energies and forward at high energies. This includes the effects of all known form factors.[7] The momentum transfer at these energies is negligible and so scattering is insensitive to the q^2 dependence of the form factors. In this work the asymmetry parameter (a as in $1 + a\cos\theta$) has been calculated from all of the observed interactions using the form factors and energy dependence of Bonetti *et al.*[7] The detectors do not recognize the neutrons resulting from this reaction.

Charged current nuclear scattering from oxygen ($\nu_e\ ^{16}O \rightarrow e^-\ ^{16}F$) or carbon is expected to be predominantly in the backward hemisphere.[8] The oxygen nucleus is tightly bound and requires a large threshold (E > 15.4 MeV) to participate in charged current neutrino or antineutrino reactions. There is no evidence in the data for any backward excess.

Since each of these scattering processes give, in principle, distinguishable final states there will be no interference among them. Experimentally the observed angular distribution will be the sum of the contributions of each of them. Often more than one process could account for a specific event so that it is difficult to distinguish types of interactions on an event by event basis. For example, a given forward event could result from either electron scattering or charged current antineutrino scattering on protons. A study of the overall distribution can be used to determine the fraction of events of the several types mentioned. Since the expected distributions do have some small energy dependence it would be best to identify specific events with specific processes. Since this can't be done we will settle for an average expected distribution using the data as a rough guide.

Figure 6 shows the angular distribution of the IMB observations. Only 1 of 8 events are in the backward hemisphere. Figure 9 shows the angular distribution of the Kamioka observations. The solid curve represents Kamioka events that have energies above the IMB threshold of 19 Mev. Only 4 of 12 Kamioka events are in the backward hemisphere. Figure 10 shows the angular distribution of the combined sample. Again, the solid

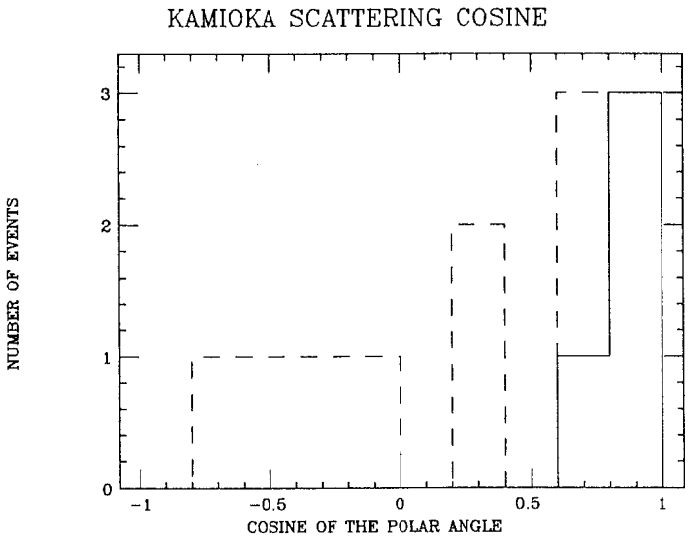

Figure 9: Histogram of the angular distribution of the 12 Kamioka supernova neutrino events. The dashed curve represents all events. The solid curve represents the 4 events above the IMB 19 MeV detection threshold.

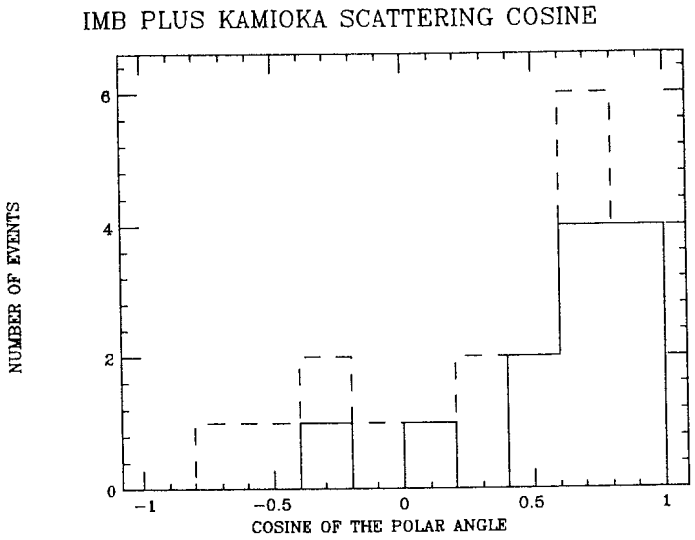

Figure 10: Histogram of the angular distribution of the 20 supernova neutrino events in the combined IMB and Kamioka sample. The dashed curve represents all events. The solid curve represents the 12 events above the IMB 19 MeV detection threshold.

curve represents events above the IMB threshold. Only one high threshold event (out of twelve) is in the backward hemisphere.

The absence of a particularly strong signal in the backward hemisphere is indicative of the absence of any contribution of charged current scattering on nucleii. The data can be understood in terms of charged current reactions of electron antineutrinos on protons and neutrino electron scattering.

A comparison of the raw Kamioka and IMB angular distributions indicates a (Kolmogorov) probability of 81% that they were drawn from the same distribution. This is remarkably good since the different energy thresholds and systematic errors in IMB should produce some differences that are not accounted for in a simple comparison of the raw data.

A reasonable method for studying the angular distribution of a small event sample of this type is to do a maximum likelihood fit to a minimum number of parameters. This has been done with the scattering angles in Tables 5 and 6 using the distribution:

$$\frac{(1-f)}{2}(1+ax)+\frac{2f}{\sqrt{2\pi}\theta_0}\exp(-\frac{(1-x)^2}{2\theta_0^2}),$$

where f is the fraction of forward scattering (in addition to that from the approximately isotropic charged current scattering) present; x is the cosine of the scattering angle; a is the charged current asymmetry $(1+a\cos\theta = 1+ax)$ and is zero at Kamioka energies; a is taken to be .23 for IMB data. This includes the energy dependence of the asymmetry (.13) plus a 10% systematic error resulting from the failed detector components.[2] For the combined sample a is taken as .092 and θ_0 is the appropriate multiple scattering and other angular dispersion effects. At the energy in question $\theta_0 \approx .0875$ which corresponds to $\sigma = 22°$. The angular distribution of a forward peak and the angular distribution of charged current antineutrino scattering are not fit but are imposed on the solution. The best value of f is the most probable fraction of forward scatters present. The fit yields $f = 0.23$ for the 20 event combined sample of IMB and Kamioka data.

The maximum likelihood method permits an even more detailed study of the data. The angles in the tables include an error estimate that accounts for the multiple scattering and reconstruction errors that have been put in by hand in using the value $\theta_0 \approx .0875$ above. A maximum likelihood fit can be done using the PDF given above but with the forward peak reduced to $\theta_0 = 0.025$, that is $\sigma \approx 12°$. This is the width appropriate for just the kinematic spread from electron scattering at the highest energies observed. The PDF was sampled at the central values given in Tables 5 and 6 but was averaged over a $\pm 1\sigma$ Gaussian. The width of the Gaussian was given by the error quoted for the specific measured angle. The Gaussian was folded over at the poles when needed. This fit gives the value $f = 0.25 \pm 0.15$. The result has been estimated two ways. The maximum likelihood value using all 20 events is $f = 0.249$. The variance has been estimated by $\sigma^2(\hat{f}) = -(\frac{d^2\log(L)}{df^2})^{-1}$ which gives $\sigma = 0.147$. A jackknife technique[9] has also been used. In the jackknife technique the mean and variance are estimated by comparing the maximum likelihood fit for the total 20 event sample with the value obtained from the 20, 19 event subsamples produced by removing one event at a time. The jackknife technique yields $f = 0.253 \pm 0.146$.

The statistical significance of this result can be measured by comparing the cumulative distribution function[10] (also known as the integral distribution) of the scattering angle with theoretical distributions containing various fractions of isotropic and forward scattering. The most well known test is the Kolmogorov-Smirnov test[10] which searches for the maximum absolute difference between the experimental and theoretical curves. The comparison is made to the integral of our fit function:

$$f \times (1 - erf(\frac{(1-x)}{\sqrt{2}\theta_0})) + (1-f) \times (\frac{x + \frac{ax^2}{2} + 1 - \frac{a}{2}}{2}).$$

When this theoretical curve is compared with the data, no forward scattering (i.e. $f = 0$) has a Kolmogorov-Smirnov probability of 13% for the Kamioka data and 14% for the IMB data. The combined sample has a probability of only 1.5% of having come from a distribution with no forward scattering component.

To quantify the significance of our fit for f the data has been compared with distributions with f varying from $f = 0$ to $f = .55$. Figure 11 plots the Kolmogorov-Smirnov probability for each of the two experiments as a function of the forward scattering fraction. Both experiments have a peak probability at about $f = .25$. For Kamioka the probability for $f = .24$ is 84%. For IMB the probability for $f = .23$ is 53%. For comparison, a χ^2 of 8 for 8 degrees of freedom has a confidence level comparable to the IMB value quoted here. It is noteworthy that the probability does not drop to as low a value as it had for $f = 0$ until $f = .41$. To put it differently, the probability of having no forward scattering in the sample is comparable to the probability of having 41% forward scattering.

The combined sample (20 events) has a peak Kolmogorov-Smirnov probability at $f = .23$. These tests indicate the most probable value is close to $f = .25$ for each individual experiment as we have found for the combined sample.

This result is relatively robust. It is not very sensitive to a range of reasonable values for the multiple scattering used (θ_0). It is not very sensitive to specific individual events. Variations in the asymmetry, a, do not seriously effect the result.

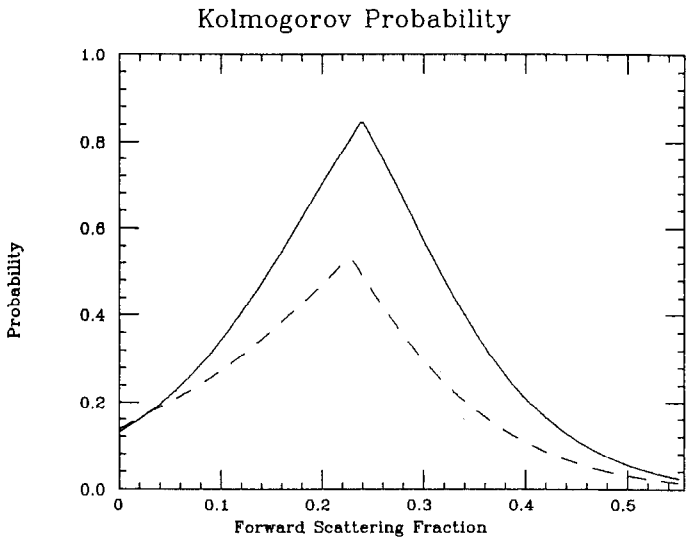

Figure 11: The Kolmogorov-Smirnov probability as a function of the forward scattering fraction. The solid curve is for the Kamioka data. The dashed curve is for the IMB data.

Energy Considerations

The previous result has followed just from a consideration of the angular distribution. The energetics of the events make the rate obtained reasonable too.[11] Many authors have calculated the energy output[6,12] in electron antineutrinos above the Kamioka threshold of 8.1 MeV to be about 8–9 $\times 10^{52}$ ergs. Because of its lower energy detection threshold the Kamioka data gives a better estimate of the total neutrino energy output since there is less need to extrapolate below the observed events. This section will summarize considerations that are not based on the IMB observations.

An energy output of 7 $\times 10^{52}$ ergs in electron neutrinos in any spectrum would produce a single electron scattering of the form ($\nu_e e \rightarrow \nu_e e$) in the Kamioka detector (with $\epsilon(E_\nu)$=0.9). Because the cross section rises linearly with energy this depends only on the total energy output in the form of ν_e's but detection depends on the spectrum being above the energy threshold of about 7 MeV. The forward events seem to satisfy this requirement. The cross sections for electron scattering[13] of other neutrino types are smaller than for ν_e's but the sum of the cross sections for the other five types of neutrinos is comparable to that for ν_e's. If the luminosities are comparable the number of forward scatterings should double. For a luminosity of 9 $\times 10^{52}$ ergs in each neutrino type one would expect 2.6 forward scattering events in Kamioka based on energy considerations alone. This 22% is very close to the 25% found from consideration of the angular distribution alone.

Applications

It is highly probable that forward scattering events are present in the sample of events collected from the February 23, 1987 supernova. The most reasonable interpretation is that these events are produced by scattering of neutrinos on electrons.

This implies a total energy output in all forms of neutrinos in excess of 5 $\times 10^{53}$ ergs. This result would follow from considerations based on the majority of events being induced by electron antineutrinos and with equal luminosities in each of six neutrino types. It is corroborated by the elastic scattering events. This energy is considerably above the expected value of 3 $\times 10^{53}$ ergs.

The concurrent presence of several neutrino types in a short time period implies a major reduction in limits on the muon and tau neutrino mass. The similarity in flight times for neutrino and antineutrino implies that gravitation does not distinguish between them. This is an accurate experimental test comparing freely falling matter and antimatter.[14] The neutrinos and antineutrinos arrive within a burst duration of from 2 to 10 seconds. General Relativity predicts a delay of 2 to 5 months due to

gravitational effects of our Galaxy.[15] All neutrinos and antineutrinos are apparently delayed by the same amount.

Conclusions

The revised IMB data has been presented. Effects of possible systematic errors associated with a detector malfunction at the time of observation have been found to be small. Good agreement is found between the IMB and the Kamioka data.

The facts do not support the hypothesis that the observed events are produced by only the interactions of electron antineutrinos.These calculations have implications for the nature of the neutrino pulse observed from SN1987A. These hypotheses do not necessarily rule out many alternative possibilities.

Acknowledgements

One of us (JML) would like to thank F. Gilman, G. Feldman and D.W.G.S. Leith for their hospitality at the 1988 SLAC Summer Institute. This work was supported in part by the U.S. Department of Energy under contract DE-AC02-87ER40366-A001. We would like to thank D. Arnett, A. Burrows, A. Dar, O. Saavedra, D. Schramm and A. Yahil for helpful discussions. We are grateful to the Morton-Thiokol Company for access to their Fairport mine.

References

1. R.M. Bionta, G. Blewitt, C.B. Bratton, D. Casper, A. Ciocio, R. Claus, B. Cortez, M. Crouch, S.T. Dye, S. Errede, G. Foster, W. Gajewski, K. Ganezer, M. Goldhaber, T.J. Haines, T.W. Jones, D. Kielczewska, W.R. Kropp, J.G. Learned, J.M. LoSecco, J. Matthews, R. Miller, M.S. Mudan, H.S. Park, L.R. Price, F. Reines, J. Schultz, S. Seidel, E. Shumard, D. Sinclair, H.W. Sobel, J.L. Stone, L. Sulak, R. Svoboda, G. Thornton, J.C. Van der Velde, C. Wuest, Phys. Rev. Lett. **58**, 1494 (1987).

2. C.B. Bratton, *et al.*, Phys. Rev. **D37**, 3361 (1988).
J.M. LoSecco, *et al.*, "Update on IMB Observations of SN1987A", Proceedings of the Les Rencontre de Physique de la Vallee d'Aoste 1988, M. Greco editor, UND-PDK-88-3, (to be published).

3. T.J. Haines, *et al.*, Phys. Rev. Lett. **57**, 1986 (1986).
J. LoSecco, *et al.*, Phys. Rev. Lett. **54**, 2299 (1985).
G. Blewitt, J. LoSecco, *et al.*, Phys. Rev. Lett. **55**, 2114 (1985).
R.M. Bionta, *et al.*, Phys. Rev. Lett. **51**, 27 (1983).
S. Errede, *et al.*, Phys. Rev. Lett. **51**, 245 (1983).
J.M. LoSecco, *et al.*, Phys. Lett. **B184**, 305 (1987).
T.W. Jones, *et al.*, Phys. Rev. Lett. **52**, 720 (1984).
B. Cortez, *et al.*, Phys. Rev. Lett. **52**, 1092 (1984).
J.M. LoSecco,*et al.*, Phys. Rev. **D35**, 2073 (1987).
H.S. Park, G. Blewitt, *et al.*, Phys. Rev. Lett. **54**, 22 (1985).
J.M. LoSecco, *et al.*, Phys. Lett. **B188**, 388 (1987).

4. J. LoSecco, Science **224**, 56 (1984).

5. Particle Data Group, Phys. Lett. **170B**, 1-350, (1986).

6. K. Hirata, *et al.*, Phys. Rev. Lett. **58**, 1490 (1987).
K. Hirata, *et al.*, Phys. Rev. **D38**, 448 (1988) has a revised scattering angle for the second Kamioka event. The revised values are used in this paper.

7. T.D. Lee and C.N. Yang, Phys. Rev. **126**, 2239 (1962).
S. Bonetti, *et al.*, Nuov. Cim. **38**, 260 (1977).
C. Llewellyn-Smith, Phys. Rep. **3C**, 261 (1972).

8. J.B. Langworthy, *et al.*, Nuc. Phys. **A280**, 351 (1977).
W.C. Haxton, Phys. Rev. **D36**, 2283 (1987).

9. R.G. Miller, Biometrika **61**, 1 (1974).
R.G. Miller, Ann. Math. Statist. **39**, 567 (1968).

10. W.T. Eadie, *et al.*, Statistical Methods in Experimental Physics, (North Holland, Amsterdam, 1971).

11. J.M. LoSecco, "The Case for Neutrinos from SN1987A", (to be published) UND-PDK-88-7.

12. I. Goldman, *et al.*, Phys. Rev. Lett. **60**, 1789, (1988)
and references therein.

13. B. Kayser, *et al.*, Phys. Rev. **D20**, 87 (1979).
H.H. Chen, *et al.*, "A Study of $\nu_e e$ Elastic Scattering", Proceedings of the Twelfth International Conference on Neutrino Physics and Astrophysics, edited by T. Kitagaki and H. Yuta (World Scientific, Singapore, 1986).

14. J.M. LoSecco, "Limits on CP Invariance in General Relativity", Phys. Rev. D (to be published) UND-PDK-88-2.

15. M.J. Longo, Phy. Rev. Lett. **60**, 173, (1988).
L.M. Krauss and S. Tremaine, Phy. Rev. Lett. **60**, 176, (1988).

THE NEUTRINO ASTROPHYSICS: BIRTH AND FUTURE

SLAC Summer Institute, 28 July 1988

M. Koshiba

CERN and TOKAI University

ABSTRACT

The birth of observational neutrino astronomy/astrophysics is described and its future possibilities are discussed.

1. Introduction

A new born branch of basic science eagerly awaits the active participation of young scientists and this lecture is meant to encourage especially the young scientists to take part in the exploration of this NEU-astrophysics by pointing out the fact that it was born in 1987. I think we can make this statement despite the existence of the pioneering work of R.Davis[1] in the United States on the solar ^{8}B neutrinos, which gave rise to the so-called Solar Neutrino Problem SNP; *i.e. the observed neutrino flux* about one-third of the expected from the Standard Solar Model,[2] SSM. This is because one needs the arrival direction and time of the signal in order to construct an astronomy in addition to the spectrum to construct *an astrophysics experiment. The Davis experiment* using the inverse beta decay ,^{37}Cl to ^{37}Ar, for detecting the solar neutrinos did not satisfy these requirements. The observation of solar ^{8}B neutrinos by KAMIOKANDE-II[3] uses the elastic scattering of these neutrinos off electrons for their *detection and hence it is real-time*, directional, and spectral observation. The observation by the same experiment,[4] and by IMB,[5] of the neutrino

burst from the supernova SN1987a was based on the reaction,($_e$ on proton) to become (positron plus neutron), and it is real-time and spectral, though not directional.

We have learned a lot about our Universe through the long history of optical astrophysics; e.g. the universal expansion and/or the chemical abundance. The post-war development of radio-astronomy has shown, among others, the existence of the cosmic microwave background at 2.7°K thereby making the Big Bang origin of our Universe quite plausible. The X-ray astronomy has given some evidence for neutron stars and possibly for black holes. The more recent infra-red astronomy is beginning to tell us about the birth of stars. Come to think of it, however, all these signals are electromagnetic waves and as such interact rather strongly with matter. This means that only the information on the thin surface of stellar objects and/or on the diffuse gaseous objects can be conveyed by these signals.

If we were to probe deep inside the stellar objects, be it a star or a galaxy, it is clear that we have to use a much more penetrating signal interacting only through the weak force with matter. Such a signal exists in nature and it is the neutrino. What, then, can we expect to learn with this probe?

Before entering this main issue let me spend a few minutes to explain the basics to the non-experts either in elementary particle physics or in astrophysics.

2. Preliminaries on Elementary Particles[6]

At present we seem to have three families of elementary particles. Each family consists of 15, (16 if the neutrinos had non-zero masses) particles. In the first family they are:

$$\begin{pmatrix} u_r^L, & u_g^L, & u_y^L, \\ d_r^L, & d_g^L, & d_y^L, \end{pmatrix} \qquad (u_r^R,\ u_g^R,\ u_y^R,);\ (d_r^R,\ d_g^R,\ d_y^R,);$$

$$\begin{pmatrix} e^{-L}, \\ \nu_e^L, \end{pmatrix};\qquad e^{-R};\qquad (\nu_e^R)?$$

Here u and d are quarks of different flavors, electric charges 2/3 and -1/3 respectively. They come in three different colors, r, g, and y, and in two spin states, right-handed and left-handed denoted by R and L respectively. Also e- and ν_e are electron of charge -1 and electron-neutrino of charge 0. If neutrino had a non-zero mass, there would also be right-handed neutrino.

These particles interact with each other through the four known forces; i.e., gravitational, weak, electromagnetic and strong, mediated by graviton, Z^o and W^{+-}, γ, and eight differently colored gluons, respectively. Notice that the above table contain horizontal triplets (r, g, y) as well as vertical doublets ($_L{}^L$) . The strong interaction has SU(3) symmetry and three colored quarks fit in its basic representation, triplet, and the weak interaction has SU(2) symmetry and work only on L's in doublet. Of course all the electrically charged particles interact each other by exchanging γ's. In the second and third families, (u, d, e^-, and ν_e) are replaced by (c, s, μ^- ,and ν_μ) and (t, b, τ^-, and ν_τ), respectively, although the t-quark has not been detected experimentally yet. The present-day tendency of theoretical particle physics is to convert the dynamics into the geometry. Probably the first successful example of this approach is the general relativity theory of Einstein. At the end of the last century, magnetic and electric forces were unified into the electromagnetic theory of Maxwell which turned out to have the form of a local gauge field theory of U(1) symmetry: a geometry. The fruitfulness of this approach was dramatically demonstrated by the discovery of the Z^o and W^{+-} predicted by the so-called Standard Theory which is a local gauge field theory of SU(2)xU(1) unifying the weak and electromagnetic forces. So it was rather natural to proceed unifying further the strong force, believed to be described by another local gauge field theory of SU(3), into a local gauge field of a large symmetry group containing SU(3)xSU(2)xU(1). This was proposed in the middle 1970's in the form of Grand Unified Theories[7] which aimed at unifying the three forces of nature,electro-magnetic,weak and strong, into a local gauge field theory of some unifying symmetry group; SU(4), SU(5), SO(10), and/or E(6). These GUT's generally predicted a finite life of proton, some in the range of 10^{29}years,[8] existence of magnetic monopole, and possibility of non-zero mass for neutrinos. Later the Super Symmetry, the fermion-boson symmetry, was introduced in order to remedy some of the difficulties of GUT's. Perhaps the ultimate of this theoretical trend is the Superstring theories which aim at the final unification of all the four forces of nature in the form of a space-time geometry. They had some theoretical successes but are not ready to give any experimentally verifiable predictions.

We now discuss the practical problem of detecting the neutrinos. The detection of a neutrino, electrically neutral and with only weak interactions, requires first its conversion into an electrically charged particle by some weak interaction process. For the purpose of obtaining the astrophysical information from the detected neutrinos the conversion process shoud preserve the direction and the energy of the incoming neutrino in those of the resulting electrically charged particle and the detection shoud be real-time. We list some of the processes below. The letters D, S, and/or T in the parentheses imply directional, spectral and/or real-time observation, respectively. We first consider the ν's of energy less than say 50MeV which are typical of astrophysical origin.

$(\nu_x + e^-)$ to $(\nu_x + e^-)$; the elastic scattering off electron. (D, S, and T) (1)

This is a very nice process for detecting the astrophysical neutrinos of energies larger than say 6MeV, greater than 10x(electron rest mass), because of its kinematical forward emission of recoil electron, directional information, and because of the one-to-one correspondence between the energy spectrum of incident neutrinos and that of recoil electrons, spectral information, and furthermore because the detection can be made real-time. The recoil electrons as observed by their Cerenkov emission pattern would furnish these three types of information. The difficulty here is in the small cross section[9] of the process. It is $2.6\times10^{-44}cm^2$ for 10MeV ν_e to produce a recoil electron of greater than 6MeV and it is still six or seven times smaller[10] for other types of neutrinos.

$(\nu_e + p)$ to $(e^+ + n)$; the inverse of neutron β-decay. (S and T) (2a)

This process has a much larger cross section than (1), $5\times10^{-42}cm^2$ for 10MeV anti-ν_e, and it is good for the energy spectrum observation because the emitted positron energy plus the Q-value, 1.3MeV, gives the incident neutrino energy. The angular distribution however is isotropic and does not give any directional information. The positrons can be observed either by their Cerenkov pattern or by their scintillation light in some scintillator.

$(\nu_e + d)$ to $(p + p + e^-)$; (weak D, S, and T) (2b)

Similar to (2a), it has a cross section[11] of $2\times10^{-42}cm^2$ for 10MeV ν_e. There is a weak backward peaking, $(1-(1/3)\cos\theta)$, in the angular distribution of electrons. The p in d above can of course be used as target for detecting anti-ν_e by the process (2a).

$(\nu_x + d)$ to $(p + n + \nu_x)$ - the neutral current disassociation[12] of deuteron. (2c)

This can in principle be a powerful process to detect the total neutrinos flux of any flavor. It has the flavor independent cross section of $8\times10^{-43}cm^2$ for 10MeV neutrinos. The difficulty here is the detection of the liberated neutron through its capture γ-ray in the presence of very severe background. The timing accuracy is limited by the neutron diffusion time.

$(\nu_e + (Z,A))$ to $(e^- + (Z+1,A))$ - the radiochemical method. (3)

The use of ^{37}Cl for (Z,A), extraction of the produced ^{37}Ar, and then the observation of ^{37}Ar decay back to ^{37}Cl was the method utilized by R. Davis in his pioneering work on solar neutrinos. The different choice of (Z,A) gives different detection threshold. In view of the fact that these processes give neither the directional nor the spectral information and that the detection is not real-time, we shall not discuss them further here.

The detection of higher energy ν's are considerably easier.

$(\nu_x\ (\nu_x) + \text{Nucleus})$ to $(l_x\ l_x) + \text{anything})$; (D, T) (4)

The directional and real-time observation of the produced leptons, (e^-,μ^-,τ^-), and/or anti-leptons can be made by their Cerenkov light patterns and the directional accuracy can reach 1 degree.

There is one more thing I should mention here. That is the possibility of neutrino flavor oscillation in the case of non-zero mass neutrinos. The mass eigenstates are in general not identical to the flavor eigenstates and then there arises, even in the absence of material media, the quantum-mechanical evolution of an initially non-existent flavor state as time goes on. This possibility was used by Pontecorvo[13] to explain the SNP; the initially produced ν_e's were converted into other flavor states, ν_μ and ν_τ, which can not produce signals in the ^{37}Cl experiment of R. Davis.

When the neutrinos are traversing matter there is a more efficient way of flavor change. This was pointed out by Mikheyev and Smirnov[14] following the formalism of Wolfenstein.[15] It is quite similar in mechanism to the K_S^o regeneration by K_L^o in matter. The problem of the neutrino

oscillation is also of vital importance and I shall come back to it again in a later part of this lecture.

3. Preliminaries on Astrophysics[16)]

The stars in their main sequence stage, our sun for instance, are supposed to obtain their shining energy by burning four protons into a helium nucleus. The process requires the conversion of two protons into two neutrons by emitting two positrons and two ν_e 's. There are a variety of intermediate channels to complete the process and the resulting energy spectrum of the emitted neutrinos will be a superposition of different energy spectra corresponding to each of these intermediate channels as shown in Fig. 1. Therefore, if we can measure accurately the energy spectrum of the emitted ν_e 's, we can reconstruct the energy generating processes deep inside the star. This, easily said, is indeed a very difficult task and we are just beginning to observe the upper end of the solar ν_e energy spectrum. The better understanding of the sun, our ultimate energy source, is obviously of great importance and a number of solar neutrino experiments are being prepared or projected in the world[17)]; e.g. Ga-detectors for low energy part of the spectrum under construction at Gran Sasso, Italy, and at Baksan, USSR, and/or a heavy water Cerenkov detector proposed in Canada.

When the star accumulates more and more helium in the core, the helium ash contracts by its own gravitational force and the inner part becomes hot and dense enough to start the reaction $3x^4He$ to $^{12}C+\gamma$. The outer H atmosphere is then expanded due to this internal energy source and the star becomes a red supergiant of lower surface temperature. Depending mainly on the initial mass of the star, it may evaporate a considerable amount of mass into space during this red supergiant stage.[18)] The accumulated carbon will eventually react with themselves to produce more fusion energy. The process goes on until the accumulated ash is ^{56}Fe which has the largest nuclear binding energy per nucleon so that no more energy can be generated by further nuclear fusion. At this stage the star will consist of a number of burning onion shells and there may be some nuclear detonation due to instability which could be identified as supernova of type I without neutrino burst. The exact evolutionary path of a star depends on the initial mass, the metalicity, and the angular momentum, etc.

When the mass of the Fe core reaches the Chandrasekhar mass limit, 1.4 solar mass, the pressure of the degenerate electrons can no longer support the gravitational weight of the Fe core and it collapses inward.

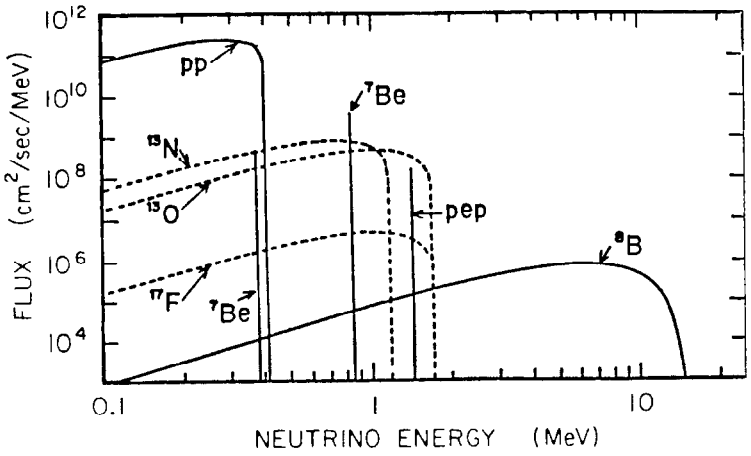

Fig. 1 The calculated energy spectrum of solar neutrinos.

This inward fall of Fe matter raises the temperature and the density at the central region. The photodisintegration of Fe nuclei and the electron captured by the proton will result in a neutron core of about the nuclear density, where the mean free path of neutrinos become small compared to the size of the core and the neutrinos become degenerate with Fermi level at about 10MeV.[19] The emission of ν_e's from this neutrino sphere constitutes the first signal of the stellar collapse which perhaps lasts a few tens of milliseconds. The still infalling Fe matter on the central core are heated by the bouncing shock wave and the neutral current weak interaction produces the neutrinos in pairs irrespective of their flavors.[20] These neutrinos will suffer diffusion process before they come out of the star and this subsequent signal lasts about 10 seconds. The shock wave will blast off the outer layers to show the optical supernova of type II but the actual light curve will critically depend on the conditions of the outer layers.

One of the most important problems in astrophysics is to understand the very early stages of our Universe. Immediately after the Big-Bang the temperature as well as the density must have been very high. We know empirically that nature respects the symmetries of physical laws at sufficiently high temperature. At temperatures of 10^{19} GeV or more all the species of elementary particles, known and yet-unknown, must have been produced and in equilibrium; particles and anti-particles in equal number for example. Namely all the quarks and leptons with their anti's must have been in equilibrium with the force mediating bosons, γ, W, Z, gluon and graviton, and also with their Super Symmetric partners, if they exist at all. We, however, seem to observe a large disparity between matter and anti-matter in our present day universe. If the matter were absolutely stable this asymmetry could not have happened. Inspired by the predictions of GUTs a number of experiments were launched over the world to search for proton decays and our experiment KAMIOKANDE is one of them (see Fig. 2). The unique feature of this experiment is its sensitivity for low energy phenomena, down to several MeV electron, which was accomplished by the very large photomultipliers specifically developed for this experiment in collaboration with HAMAMATSU PHOTONICS INC. This sensitivity not only allowed the best lower limits of partial lifetimes of proton into most of the possible decay modes but also enabled the experiment to observe the solar ^{8}B neutrinos as well as the neutrino burst from SN1987a.

Coming back to the Big-Bang era, the stable particles like monopole and/or the lightest mass particle of Super Symmetry would survive to

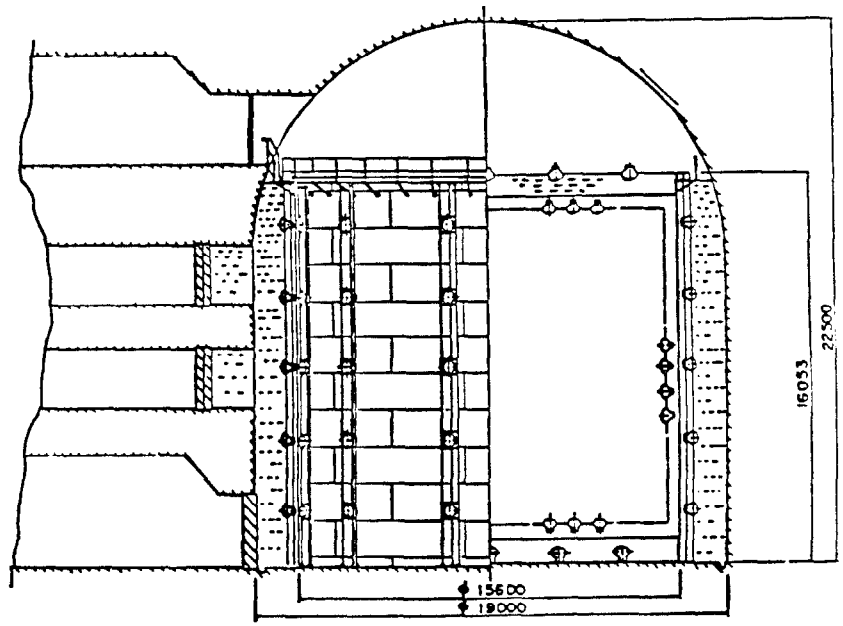

Fig. 2 The schematic drawing of KAMIOKANDE detector. By observing intensity as well as arrival time, the Cerenkov light produced by fast particles one can reconstruct the event vertex, direction of motion and energy. Note that 20% of the entire inner surface of the inner detector is covered by photocathode resulting in 3.4 photoelectrons per 1MeV electron.

this day, though deccelerated by the universal expansion to velocities of the order of 10^{-3} c. Such heavy relic particles would have been captured by the gravitational force of the sun during the last billions of years, and monopoles will catalyze the nucleon decays, Rubakov effect[21], and the lightest supersymmetric particles will annihilate with their anti's in the sun. These processes will emit the neutrinos of the corresponding energy spectrum and, thus, by searching for the neutrinos of appropriate energy coming from the direction of the sun we can look for such Heavy Relic Particles with a great sensitivity. For some years the astrophysicists have been perplexed by the seeming existence of Dark Matter. The Heavy Relic Particles or the finite mass neutrinos could be what is constituting the Dark Matter.[22]

Cosmic rays have been with us for more than half a century but we still do not know where and how they were accelerated though there exists some hint from their chemical abundances that the ion source may be supernovae. Unfortunately we can not use them to point back to their origin because they are electrically charged and, hence, suffered many scatterings by magnetic clouds in the interstellar space. The acceleration of protons and ions, be it due to the off-axis rotation of gigantic magnetic moment of neutron star or due to shock wave Fermi acceleration, to such high energies will result in the interaction of these high energy particles with the nearby tenure gas particles to produce high energy π^{+-} and π^{o}. The π^{o}'s will immediately decay into two γ's and the π^{+-}'s will decay into μ^{+-} and ν_μ /$\overline{\nu_\mu}$ or interact depending on the density of the media there. These ν's and γ's are not electrically charged and their observation will tell us where the acceleration is taking place. The comparison between the two types of signals will further tell us whether the acceleration was indeed of hadrons or not and what physical conditions exist in the media there. Some air shower experiments claimed the observations of very high energy, 10^{15}eV or more, γ's from a point source like Cyg-X-3 and some underground experiments reported high energy μ signal from the same source. However, the situation is far from clear and more sophisticated air shower type experiments are being prepared. The difficulty here is the rejection of the overwhelming background of cosmic ray hadron showers. The observation of high energy neutrinos can be made by the μ's they produce in the earth and the usual practice is to look at only the upward-going μ's to avoid the background of the downward-going μ's produced by cosmic rays in the atmosphere. Even then there are the upward-going μ's produced by the high energy ν's resulting from the cosmic ray interactions in the atmosphere on the opposite side of the earth. The identification of the point source signal thus depends critically on the angular measurement accuracy of the experiment. The angular deviation of the observed μ from the original ν direction is due to two causes. One is the multiple Coulomb scattering of the μ's in traversing the rock and it is inversely proportional to the square root of the threshold detection energy of the μ's; about 1 degree for 5 GeV threshold. The other is the emission angle of the μ in the ν interaction and depends on the energy spectrum of the primary ν's; also about 1 degree or plausible choices of energy spectra and for 5 GeV threshold. Therefore, the experiment aiming at high energy neutrino astronomy has to have the angle measuremental accuracy of about 1 degree.

4. Solar Neutrino Observation by KAMIOKANDE

The most difficult task in this observation is obviously that of background rejection. There are four main causes of background involved here. The first is the Rn dissolved in the water. The second is the low energy delayed β-emitter among the fragments produced by high energy μ interactions in the water and the third is the γ's and the neutrons from the surrounding rocks. The fourth cause is the U and Th contamination in the water.

The Rn has as one of its descendents ^{214}Bi which gives 3.26MeV β. This low energy β triggers the 7.5MeV threshold with about 10^{-5} probability because of the finite energy resolution. In the early days of operation once in a while 10 tons of fresh water was added to compensate for the loss due to evaporation. This addition of 0.3% water resulted in the jump of trigger rate as can be seen in Fig. 3. The 3.8 days decay of the ancestor nucleus ^{222}Rn is clearly seen. This cause of background was taken care of by making airtight the inner water circulating system and by providing the airtight reservoir tank for replenishing the water.

The second cause, ^{12}N and ^{12}B etc. from the oxygen break-ups, had to be deleted in the off-line analyses by using the time- and space-correlations with the parent μ. At this underground depth of 1000 meters the cosmic ray muon rate is 0.37Hz. We can not just kill the detector after every passage of muons; some of the possible radioactive fragments, like ^{11}Be, ^{15}C, and/or ^{16}N, of oxygen have half-lives in seconds. This analysis of fitting the muon-induced low energy events with respect to the time dependence and the energy spectrum gave us one of the absolute

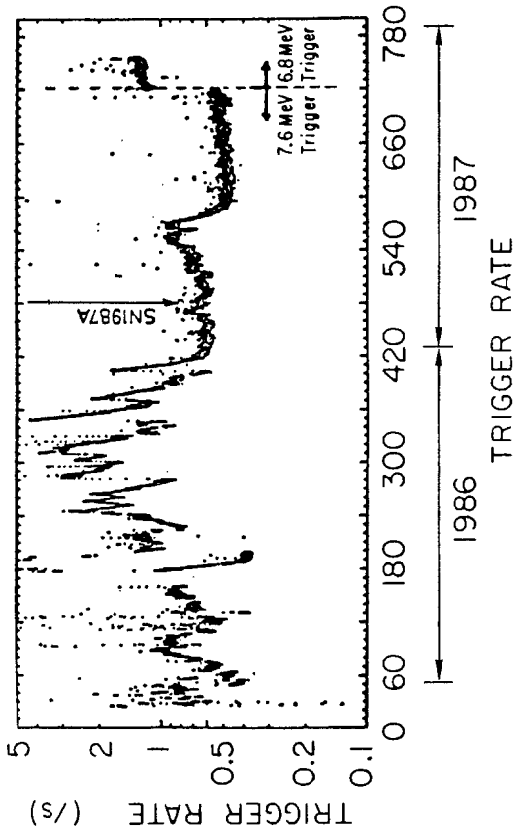

Fig. 3 The improvements in trigger rate of low energy events. See text.

energy calibrations. The absolute energy calibration was supplemented by the observation of μ-e decay electrons and finally by the observation of Compton electrons from the known monochromatic γ-rays resulting from the thermal neutron capture by Ni-foil. The thermal neutrons were from ^{252}Cf fission source immersed in the water. The resulting absolute energy calibration is better than 3%.

The third cause, γ's and n's from the surrounding rocks, has been dealt with by installing Cerenkov anti-counters of water, >1.4m thick, all around the main detector and also deleting the peripheral region, <3.14m from the top and <2.0m from the other boundaries of the inner PMT arrays, in the analysis of solar neutrino events; the resulting fiducial mass 680 tons. There still seem to remain some γ-events even after the fiducial cut and an additional cut was made for those excess events in the direction of normal to and in the vicinity of the container walls.

For the last cause of background, U and Th contamination in the water, we installed the columns of ion-exchange resins and the contamination was reduced from the original 10^{-9} to the present 10^{-12} level and is still improving gradually.

The effect of these background cuts are schematically shown in Fig. 4. The remaining events are shown in Fig. 5 in the form of the angular distribution with respect to the sun-earth direction, which were then fitted by the maximum-likelihood method to estimate the number of solar neutrino events in the sun-earth direction region. Figure 6 shows the latest result of the solar neutrino observation by KAMIOKANDE and one sees that the observed flux is more than 3σ away from the null flux and is definitely smaller than the SSM expectation.

5. Neutrino Burst from Supernova 1987a

The observation of the neutrino burst from this supernova has already been published and discussed in detail.[23] Therefore, I will just show the raw data of the low energy events as printed out by a laser printer. See Fig. 7. Here I wish to point out that with this type of detector the discovery of the supernova signal is quite easy and that if the computer was on the site to analyze the data real-time it would have been possible to give a warning of a supernova explosion to the optical observatories in the world so that they can wait for the early phase flare-up in UV. Note also that with a next generation detector like SuperKAMIOKANDE[24] the number of the direction indicating events, $(\nu_e + e^-)$

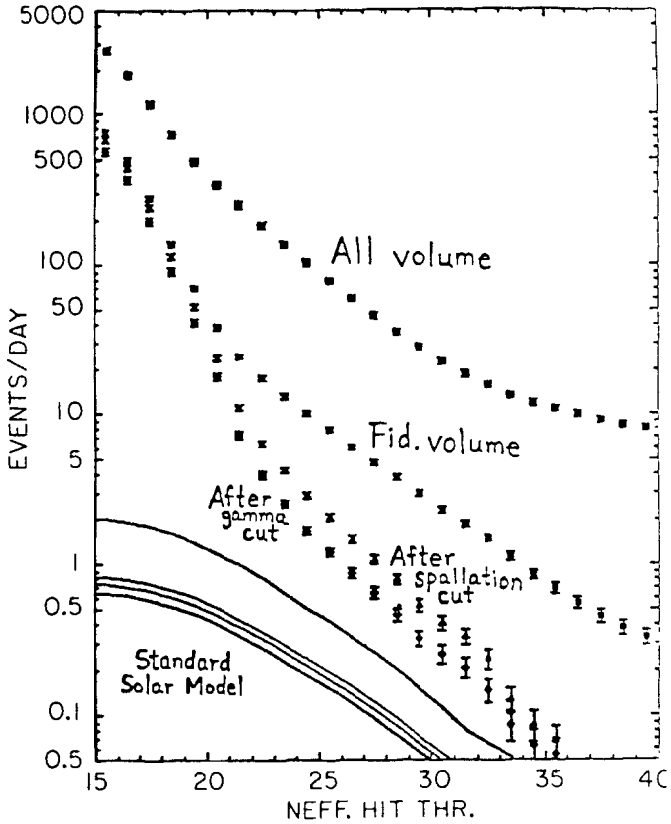

Fig. 4 The reduction of the data to obtain the solar ^{8}B neutrinos. See text.

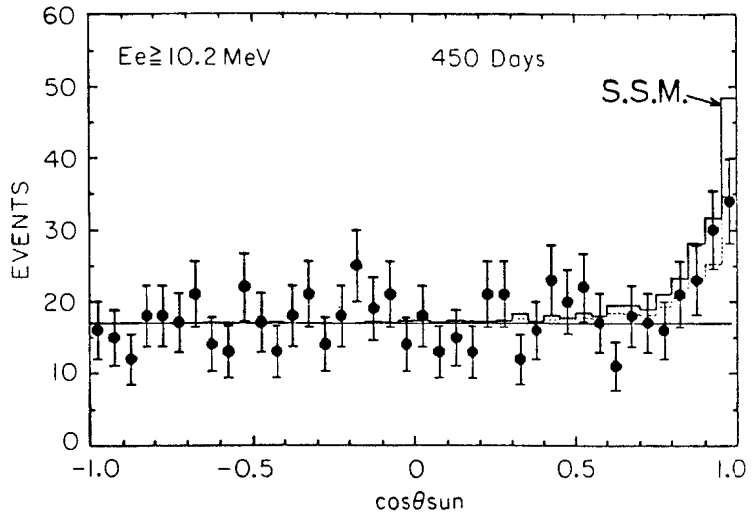

Fig. 5 The use of the directionality of the solar neutrino events.

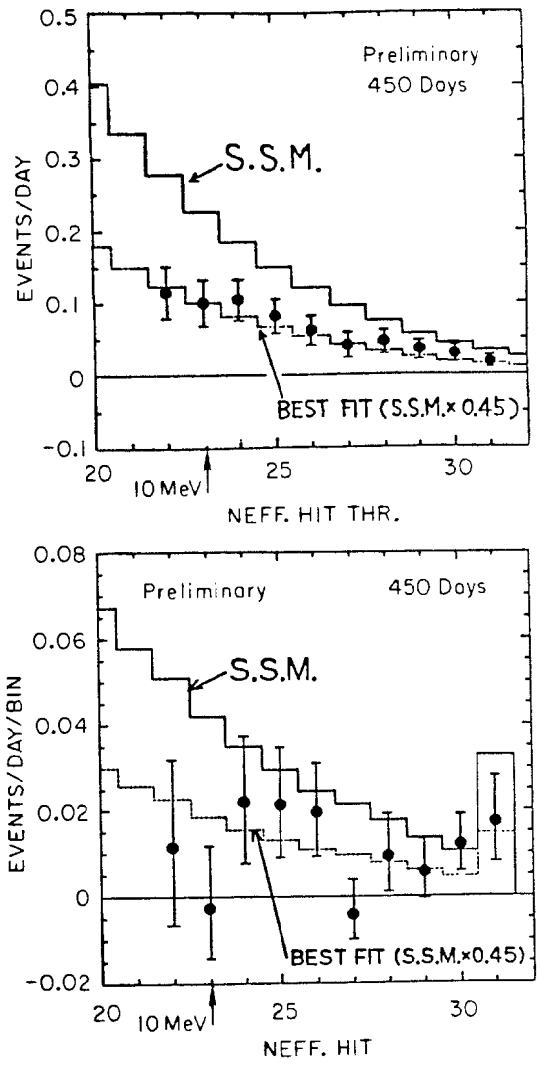

Fig. 6 The latest result on the solar ^{8}B neutrinos. Figure 6a shows the integral energy spectrum of the recoil electrons produced by the solar ^{8}B neutrinos, while Fig. 6b shows the same results in the differential form.

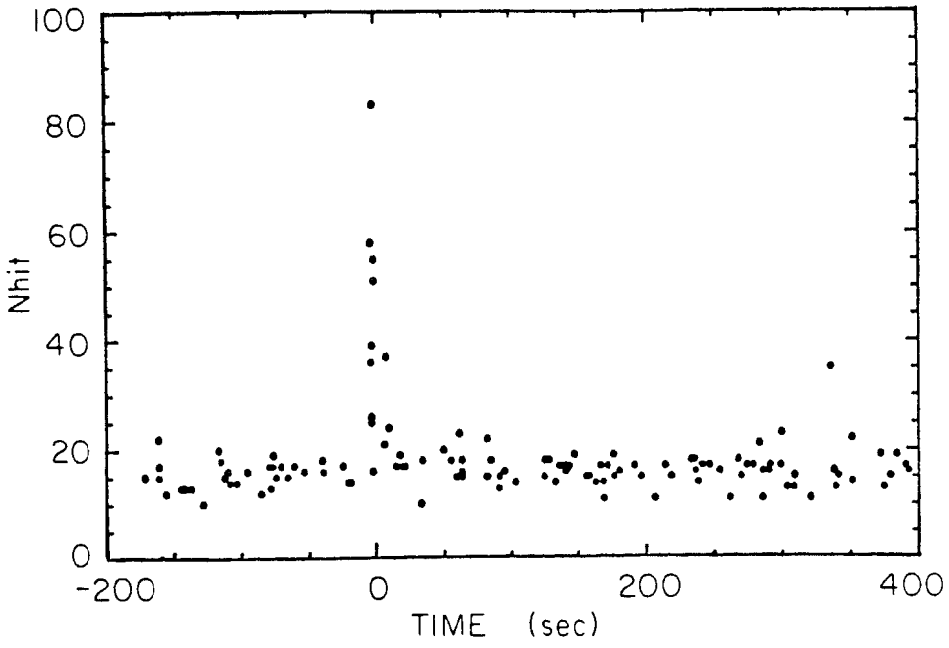

Fig. 7 The neutrino burst signal from SN1987a as observed by KAMIOKANDE. The Nhit on the vertical axis is the number of photomultipliers which gave the light signals and is in good approximation representing the event energy.

elastic scattering, in the first 10 ms would be about 200 for a supernova at the galactic center. This is enough to point the direction with 2 degrees of accuracy that the subsequent observation of neutrino spectrum as function of time does not depend on the optical visibility of the object which can be very bad in the vicinity of the galactic center.

6. Search for Point Sources of High Energy Neutrinos[25]

The search for high energy ν_μs from the direction of SN1987a was made with negative results so far. Also made was the search for point sources of high energy ν_μs with again negative results. The 90% C.L. upper limit fluxes obtained for the neutrino-produced upward-going μ's from the direction of possible sources are in units of $10^{-13}cm^{-2}s^{-1}$; 1.2 for SN1987a, 0.99 for Cyg.- X-3, 1.44 for Her.-X-1, 0.66 for Crab, 0.63 for Geminga, 0.56 for SS433, 0.70 for Gal.Cen., 0.34 for Vel.-X-1, and 0.26 for LMC-X-4. These values are still preliminary and the final results will be published shortly by the KAMIOKANDE collaboration. It is clear, however, that the detectors of sensitive area orders of magnitude larger will be needed to detect the high energy neutrinos from point sources.

7. Search for Heavy Relic Particles in the Sun

The search for possible neutrino signals from the direction of the sun have been made in the contained events as well as in the upward-going μ events. The preliminary results so far obtained by KAMIOKANDE are the 90% C.L. excluded mass regions in GeV: for Majorana ν, >76; for Dirac ν, 10-20 and >60; for scaler ν_e, 3-25; for scaler ν_μ, >3; for scaler ν_τ, 4-25; and for photino no constraint as yet. The final results will appear shortly.[22]

8. Hint of Positive Result on Neutrino Oscillation

Recently a careful analysis of the atmospheric neutrinos by KAMIOKANDE revealed some interesting results.[26] From the early days of operation, both KAMIOKANDE and IMB, a large water Cerenkov detector in the U.S., noticed something unexplicable at the level of two standard deviations. Although the overall flux of atmospheric neutrinos has theoretical uncertainty of about 20%, the number ratio R, at least its lower limit, of $(\nu_\mu + \overline{\nu_\mu})$ to $(\nu_e + \overline{\nu_e})$ can be rather well estimated. Namely, disregarding the difference in the energy, the ratio R is 2 because π-decay gives $1\nu_\mu$ and 1μ, and this 1μ when it decays gives $1\nu_\mu$ and $1\nu_e$ together with 1e. The energy consideration will raise R somewhat and so does the existence of undecayed μ's. On the other hand, the K-decay into electron will increase the number of ν_e thus reducing R. However, the branching ratio of this decay mode is small and even if one assumes the equall production of π and K the reduction of R is less than 5%.

Among the totally contained events, the percentage of those events with μ-e decay electron signal is essentially determined by this ratio R, though the inclusion of the inelastic events with π-μ-e decay will dilute the effect somewhat. The IMB experiment expected (34±1)% and observed (26±3)%, while KAMIOKANDE expected (77±2)% and observed (61±07)%. This seeming reduction of ν_μ events was 2.6σ effect in IMB and was 2.2σ in KAMIOKANDE. IMB quoted as the cause of this effect the following three possibilities:1) the assumed input ν_μ/ν_e too large, 2) the detection efficiency of μ-e decay electrons overestimated, or 3) some as-yet-unaccounted-for physics. The possibility 1) is very unlikely as explained above and the possibility 2) is also unlikely especially in KAMIOKANDE where the detection threshold has been 7.5MeV electron. The effect will be more acutely visible in the pseudo-elastic charged current events. We thus look at the sample of single-ring contained events, 0.2 to 2.0GeV/c, and analyze whether the secondary is an electron or a μ. The μ-e identification was made with 98% efficiency. Now the result is:

$$(\text{No. of } \mu)_{Data} / (\text{No. of } \mu)_{M.C.} = (0.59 \pm 0.06_4), \text{ a } 6\sigma \text{ effect; while}$$

$$(\text{No. of e})_{Data} / (\text{No. of e})_{M.C.} = (1.12 \pm 0.18) \quad \text{which is quite normal.}$$

The comparisons are shown graphically in Fig. 8. In order to get rid of the 20% uncertainty in the overall flux of atmospheric neutrinos, we take the ratio of the two types of events and obtain:

$$(\text{No. of } \mu/\text{No. of e})_{Data}/(\text{No. of } \mu/\text{No. of e})_{M.C.} = (0.56 \pm 0.09), \text{ a } 5\sigma \text{ effect.}$$

One of the promising explanations of this observed anomally can be sought in the neutrino oscillation, in vacua and/or in matter, and the full analysis along this line will appear shortly.[27] The consistency check with the upward-going μ data of the same experiment is being made but if this were the correct explanation, the responsible parameter range of neutrino oscillation would be: Δm^2 of 10^{-2} to 10^{-3} $(eV)^2$ and $\sin^2 2\theta$ of 0.3 or larger, with a hint of preference of ν_μ-ν_τ oscillation over that of ν_μ-ν_e.

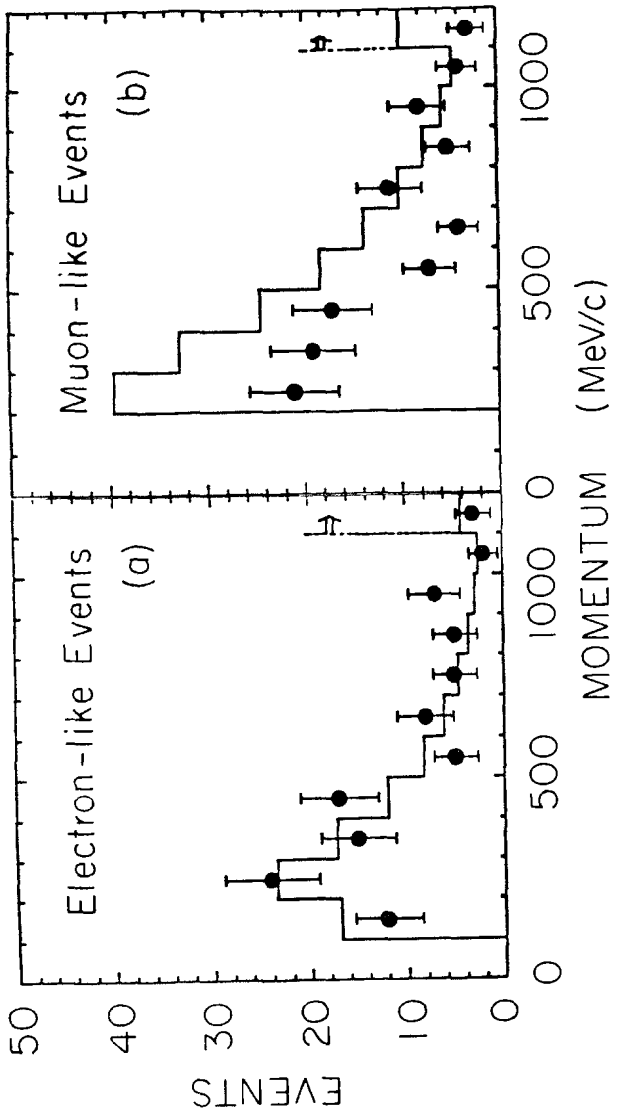

Fig. 8 The momentum spectra of e-events, (a) and of m-events, (b) as observed by KAMIOKANDE.

9. Future Outlook

Various low temperature devices have been and are being studied for possible detection of low energy neutrinos and/or axions by means of low momentum transfer, with large cross sections, processes of neutral current interaction. We shall, however, not go into detail because our primary concern here is the directional, spectral and real-time observation of astrophysical neutrinos. The $^{71}Ga(\nu_e,e^-)^{71}Ge$ experiments with radiochemical extraction of Ge, being constructed one in Gran Sasso of Italy and another in Baksan of USSR, have a low detection threshold of 0.233MeV capable of detecting the neutrinos from the reaction (p+p) to $(d+e^++\nu_e)$ which is supposed to produce more than 99% of the solar energy. The LVD, large volume liquid scintillator, being installed also in Gran Sasso of Italy aims at the detection of $\overline{\nu_e}$ rather than ν_e through the process $(\overline{\nu_e} + p)$ to $(e^+ + n)$ and is sensitive mainly to the future stellar collapse; non-directional but spectral and real-time observation. The large volume liquid Ar drift chamber experiment, ICARUS proposed for Gran Sasso, was recently reduced in size from 200 to 300 ton level for its first phase operation.

The proposed SuperKAMIOKANDE is an upgrade of KAMIOKANDE in the sense of 25 times the fiducial mass and 2 times the photon detection efficiency. It is described elsewhere in detail and I will just mention here again that with this detector one can expect 200 (ν_e+e) elastic scattering events as well as about 4000 $(\overline{\nu_e} + p)$ events for a supernova occurring near the center of our galaxy so that the directional accuracy of 2° and the spectrum change as time would be obtained, not to mention the accurate observation of solar neutrinos and the search for Dark Matter. It is to be noted also that based on the solar neutrino result of KAMIOKANDE the variation of the central temperature of the sun can be monitored with an accuracy of better than 1% every week by this SuperKAMIOKANDE.

A similar water Cerenkov detector but with 1000 tons 0f D_2O rather than H_2O is being proposed in Canada.[28] This experiment not only affords the possibility of observing the solar neutrinos by the $(\nu_e$ + "n") to $(e^-$ + p) reaction of much larger cross section, though not quite directional, but also has the potentiality of observing the neutrinos of all the flavors through the neutral current reaction $(\nu_e$ + d) to $(p+n+\nu_e)$. The last reaction, however, would be very difficult to detect in the presence of tremendous background.

Now we go on to the near future prospect for high energy neutrino astronomy. The proposal of LENA, Lake Experiment on Neutrino Activity, was made along these lines. In what follows, a version of LENA conceived for installation near Gran Sasso is described in some detail. See Fig. 9. The physics aims of the experiment are:

(1) Appearance experiments on ν_μ/ν_e and ν_μ/ν_τ oscillations at the parameter range down to a Δm^2 of 10^{-3} $(eV)^2$ and to a $\sin^2 2\theta$ of 0.1. The CERN neutrino beams,either from SPS or PS, could be directed toward the Gran Sasso. The distance is 730km to be compared with the oscillation length of 1240km for 0.5GeV neutrinos for Δm^2 of$10^{-3}(eV)^2$. The event rate for one Megaton detector is 60 for 10^{19} protons on the target at CERN even for the low energy focussed neutrino beam as used for BEBC experiment and is orders of magnitude larger for the high energy focussed neutrino beam. The identification of electrons and muons are excellent even at the low energy of 200MeV. The identification of τ could probably be made by measuring the invariant masses of π^o, ρ, and A1 mesons in the ν_τ plus 3π decay mode of the produced τ leptons.

(2) Study of atmospheric neutrinos. This type of study by KAMIOKANDE gave the first hint of neutrino oscillation in the parameter range mentioned above. The detector here can expect around 14,000 upward-going muons per year to be compared with 40 in KAMIOKANDE.

(3) One can initiate also the high energy neutrino astronomy with a realistic sensitive area of 3.6 times 10^4 m^2. The angular measurement accuracy is better than 1 degree.

(4) Search for Heavy Relic Particles in the sun by taking advantage of one Megaton fiducial mass together with the μ-e discrimination capability.

(5) Search for the point sources of high energy γ-rays. The top layer modules, which act as the anti-counters for other studies, are good energy flow detectors and with the complete back-up by the inner detector as the muon detector can detect the high energy γ-rays cleanly separated from the otherwise overwhelming background of cosmic ray hadron showers. The accuracy in the angular measurement is better than 1 degree. The threshold energy of γ-rays will be 10^{13}eV at 2000m a.s.l.

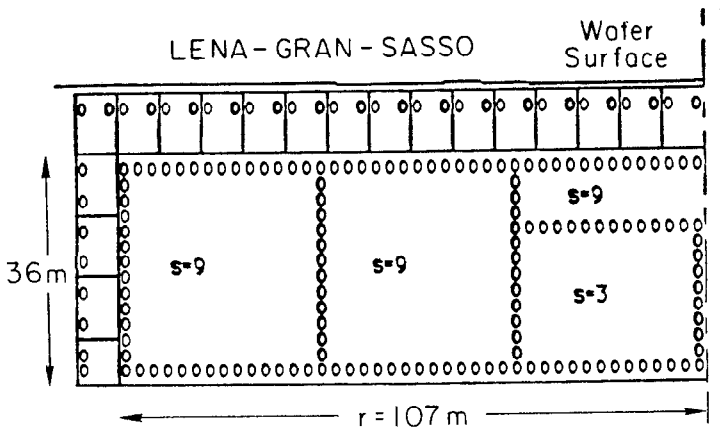

Fig. 9 The schematic cut-out view of LENA-Gran-Sasso. The small ovals represent each 50cmf photomultipliers and s is the area to be covered by a single 50cmϕ photomultiplier on the surface.

(6) Study of the primary cosmic ray composition at and above 10^{16}eV.

(7) If we want to be a little bit more extravagant, we can equip the innermost 10% volume with more PMT's to make it sensitive down to 20MeV electron. This part of the detector is now capable of observing the future supernova neutrinos with 16 times the IMB fiducial mass. This will cost an additional 20% to the instrumentation cost. This last item, however, should be attempted only after all the backgrounds are fully understood.

The detector dimensions would be: Size of the water reservoir: R=113m and D=46m. Size of the inner detector: R=107m and D=36m. Fiducial volume: 3m inside of PMT array: 1.02 times $10^6 m^3$.

The PMTs are installed over the inner surface of the inner detector, as well as over the vertical membranes of concentric cylinders of radii 34 and 69m, at 1PMT per $9m^2$. The inner detector is surrounded on top and side by anti-counter modules of $36m^2$ times10m height containing each 2 PMT's. In the extravagant version, the innermost volume of R=34m and D=26m will be equipped with the additional PMT's to make the surface density 1PMT per $3m^2$.

The threshold detection energy is 60MeV over the entire inner volume of 1.02 times 106 m^3 and is 20MeV over the innermost volume of 83.5 times 10^3 m^3. The approximate cost would be:
15000PMT's with electronic @ SF2500.----------37.5MSF
Civil engineering cost (depends very much on the chosen terrain).

10. Acknowledgement

The experimental data used in this lecture are mostly from the KAMIOKANDE-II and my collaborators in this experiment are as of June '88: K.S.Hirata, T.Kajita, T.Kifune, K.Kihara, M.Nakahata, K.Nakamura, S.Ohara, Y.Oyama, N.Sato, M.Takita, Y.Totsuka and Y.Yaginuma; Institute for Cosmic Ray Research, University of Tokyo; M.Mori, A.Suzuki, K.Takahashi, T.Tanimori and M.Yamada; National Laboratory for High Energy Physics (KEK); T.Suda; Department of Physics, University of Kobe; K.Miyano, H.Miyata and H.Takei; Department of Physics, University of Niigata; K.Kaneyuki, Y.Nagashima and Y.Suzuki; Department of Physics, University of Osaka; E.W.Beier, L.R.Feldscher, E.D.Frank, W.Frati, S.B.Kim, A.K.Mann, F.M.Newcomer, R.Van Berg and W.Zhang; Department of Physics, University of Pennsylvania. It is a pleasure to acknowledge the generous and timely support for KAMIOKANDE given by the Ministry of Education, Culture and Science of Japan. The experiment was supported in part also by the Department of Energy of U.S.A.

It was indeed a pleasure to be at the SLAC Summer Institute where one can meet and discuss with so many active young scientists from all over the world. I am grateful to Professor D. Leith for inviting me to this Institute.

References

1) R. Davis Jr. et al.; Phys. Rev. Lett., 20 (1968) 1205. J.K. Rowley et al.; in "Solar Neutrinos and Neutrino Astronomy," ed. M.L. Cherry, W.A. Fowler, and K. Lande; (AIP Conf. Proc. No. 126), New York, (1985), p.1.

2) J.N.Bahcall and R.K.Ulrich; Rev. Mod. Phys., 60 (1988) 297.

3) For details of this observation, see; M.Nakahata, Ph.D. thesis, Univ. of Tokyo preprint, UT-ICEPP-88-01, Feb. 1988.

4) K.Hirata et al; Phys. Rev. Lett., 58 (1987) 1490 . The full paper will appear shortly in Phys. Rev. D.

5) R.M.Bionta et al; Phys. Rev. Lett., 58 (1987) 1494.

6) See for instance; D.H. Perkins, Introduction to Elementary Particle Physics, Addison-Wesley Pub. Co. Inc., Third edition (1987).

7) See for instance; P.Langacker; Phys. Rep., 72 (1981) 285.

8) H. Georgi and S.L. Grashow; Phys. Rev. Lett., 32 (1974) 438.

9) R.C. Allen et al; Phys. Rev. Lett., 55 (1985) 2401.

10) L.A. Ahrens et al; Phys. Rev. Lett., 51 (1983) 1514; Phys. Rev. Lett. 54 (1985)18.

11) S. Nozawa et al; J. Phys. Soc. Japan, 55 (1986) 2636.

12) H.H. Chen; Phys. Rev. Lett., 55 (1985) 1534.

13) B. Pontecorvo, Sov. Phys. JETP, 26 (1968) 984; V. Gribov and B. Pontecorvo; Phys. Lett. 28B (1969) 495.

14) S.P. Mikheyev and A. Y. Smirnov; Nuovo Cimento C9 (1986) 17.

15) L. Wolfenstein; Phys. Rev. D17 (1978) 2369 and Phys. Rev., D20 (1979) 2634.

16) See for instance, D.D. Clayton; Principles of Stellar Evolution and Nucleosynthesis, McGraw-Hill (1968). See also; E. Burbidge et al, Rev. Mod. Phys., 29 (1957) 547.

17) See for instance, G. Friedlander and J. Weneser; Science 235 (1987) 760 and 755.

18) D. Sugimoto and K. Nomoto; Space Science Rev., 25 (1980) 155. S.E. Woosley and T.A. Weaver; Ann. Rev. Astron. Astrophys. 24 (1986) 205.

19) A. Burrows and J.M. Lattimer; Ap. J., 307 (1986) 178.

20) D.Z. Freedman et al; Rev. Nucl. Sci., 27 (1977) 167.

21) V.A. Rubakov; Nucl. Phys., B203 (1982) 311.

22) N. Sato; Ph.D. thesis, University of Tokyo, (1988).

23) For the implications, on particle physics and on astrophysics, of this event, see for instance, D.N. Schramm; Nucl. Phys., B3 (1988) 471. Also, A. Burrows; Arizona Theoretical Astrophysics Preprint #88-16, University of Arizona.

24) Y. Totsuka; Proc. 7th WOGU/ICOBAN'86, Toyama, Japan, (1987) 118.

25) Y. Oyama et al; Phys. Rev. Lett., 56 (1986) 991 and 59 (1987) 2604.

26) K.S. Hirata et al; Phys. Lett., B205 (1988) 416.

27) M. Takita; Ph.D. thesis, Univ. of Tokyo, (1988). See also: V. Barger and K. Whisnant; Univ. of Wisconsin preprint, MAD/PH/414, March 1988, and J.G. Learned et al; Univ. of Hawaii preprint, UH-511-643- 88, March 10, 1988.

NEUTRINO PRODUCTION of CHARM at FNAL E744

C. Foudas, K. T. Bachmann, R. H. Bernstein, R. E. Blair,
W. C. Lefmann, W. C. Leung, S. R. Mishra, E. Oltman,
P. Z. Quintas, F. Sciulli, M. H. Shaevitz, W. H. Smith
Columbia University

F. S. Merritt, M. Oreglia, H. Schellman, B. A. Schumm
Enrico Fermi Institute, University of Chicago

F. Borcherding, H. E. Fisk, M. J. Lamm,
W. Marsh, K. W. B. Merritt, D. Yovanovitch
Fermi National Accelerator Laboratory

A. Bodek, H. S. Budd, W. K. Sakumoto
University of Rochester

Talk presented by Heidi Schellman.

ABSTRACT

We present data on opposite-sign dimuon production in Fermilab neutrino experiment E744. Opposite-sign dimuons are a clean signature of charm production and provide unique information on the strange component of the nucleon.

I. Introduction

We present data on charm production in neutrino-nucleon scattering from Fermilab experiment E744. This experiment has high statistics and explores the energy range from 30-600 GeV. Charm is produced from d and from s quarks. However, as anti-neutrino charm production from $\bar{d}$ quarks is suppressed by the Cabibbo angle, while production from $\bar{s}$ quarks is not, this is a unique probe of the strange quark component of the nucleon.

II. Charm production

Figure 1 illustrates the basic Feynmann diagrams for charm production in neutrino scattering. In the standard quark parton model the cross section for νN charm production is:

$$\frac{d^2\sigma^{\nu N}}{dxdy} = \frac{G_F^2 s}{2\pi} x' \Big[\sin^2\theta_C d_N(x') + \cos^2\theta_C s_N(x')\Big](1 - \frac{m_c^2}{sx'}) \qquad (1.a)$$

$$\frac{d^2\sigma^{\bar{\nu}N}}{dxdy} = \frac{G_F^2 s}{2\pi} x' \Big[\sin^2\theta_C \bar{d}_N(x') + \cos^2\theta_C \bar{s}_N(x')\Big](1 - \frac{m_c^2}{sx'}) \qquad (1.b)$$

In the limit of massless quarks the momentum fraction carried by the struck quark would be

$$x = \frac{Q^2}{2M\nu}$$

where M is the nucleon mass and ν is the energy of the final state hadronic system in the lab frame. In charm production x is replaced by

$$x' = x(1 + \frac{m_c^2}{Q^2}),$$

where x' is now the momentum fraction carried by the quark with m_c the mass of the charm quark. This is the *slow rescaling* formalism.[1] The additional factor of $(1 - m_c^2/sx')$ assures that there is sufficient center-of-mass energy to produce a heavy quark in the final state.

The variable $y \equiv \nu/E_\nu$ measures the energy transferred to the hadronic system and is directly related to the center-of-mass angle, θ_{CM}, in the quark-ν frame by $y = \frac{1}{2}(1 - \cos\theta_{CM})$.

The functions $d_N(x)$, $s_N(x)$, $\bar{d}_N(x)$ and $\bar{s}_N(x)$ are the probabilities that a given quark type carries x fraction of the total nucleon momentum. The *valence* distributions $d_N(x)$ and $u_N(x)$ are much larger than the *sea* distributions $\bar{d}_N(x)$,

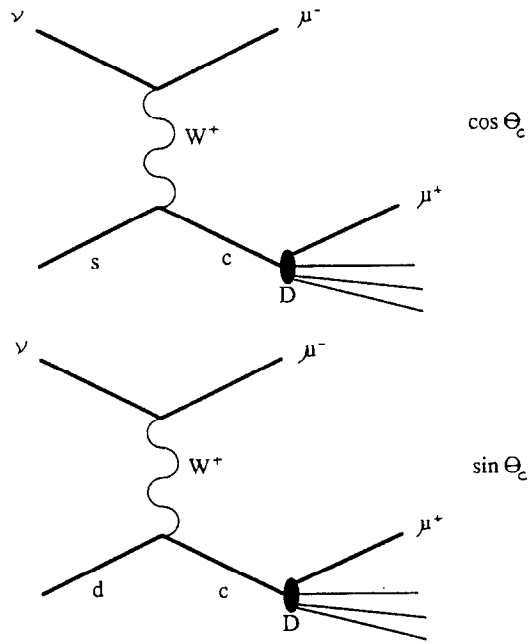

Figure 1: Diagrams for charm production.

$\overline{u}_N(x)$, and $s_N(x) = \overline{s}_N(x)$ which are all of similar magnitude. For simplicity the additional Q^2 dependence of the quark distributions is not shown explicitly.

By convention, quark distribution functions are quoted for the proton. The notation $q_N(x)$ used above is for an isoscalar target such as our iron calorimeter. In the following discussion the unsubscripted function $q(x)$ will refer to the proton distribution. Isospin conservation implies that $d_N = 1/2(d_p + d_n) = 1/2(d+u)$. A similar relation holds for u_N and $\overline{u}_N$, $\overline{d}_N$. We assume that $s_N = \overline{s}_N = s = \overline{s}$. In this analysis we make no correction for Fermi motion or other nuclear effects.

Figure 2 shows the expected relative contributions of the various quark flavors to the charm production rate. These curves are derived from previous measurements of quark distributions.[2,4] Note that, due to charge conservation, charm cannot be produced from u or $\overline{u}$ quarks. The rate for anti-neutrinos is almost directly proportional to $\overline{s}_N(x)$ since the Cabibbo angle suppresses the $\overline{d}_N(x)$ term. The rate for νN scattering is composed of approximately equal contributions from $d_N(x)$ and $s_N(x)$.

We detect charm production via the semi-leptonic decay of the charm hadron which produces a second muon. The signature for charm production in our detector is thus an opposite-sign dimuon with possible additional hadronic energy.

The dimuon cross section is simply related to the total charm cross section:

$$\frac{d^2\sigma}{dxdy}(\nu N \to \mu^-\mu^+ + X) = \frac{d^2\sigma}{dxdy}(\nu N \to \mu^- + c + X) \times B_\mu \qquad (2)$$

where $B_\mu = B(c \to \mu^+ + X)$ is the average charmed hadron branching fraction into muons for the mixture of charmed hadrons produced in neutrino interactions. A study of the shapes and levels of the neutrino and anti-neutrino dimuon rates compared to the charged current rates will yield $xd_N(x)$ and $xs_N(x)$ and hence

(1) the ratio

$$\eta_s = \frac{2\overline{S}}{U+D} = \frac{\int 2x\overline{s}(x)dx}{\int(xu(x) + xd(x))dx}$$

or equivalently, the strange sea suppression factor

$$\kappa = \frac{2\overline{S}}{\overline{U}+\overline{D}} = \frac{\int 2x\overline{s}(x)dx}{\int(x\overline{u}(x) + x\overline{d}(x))dx}$$

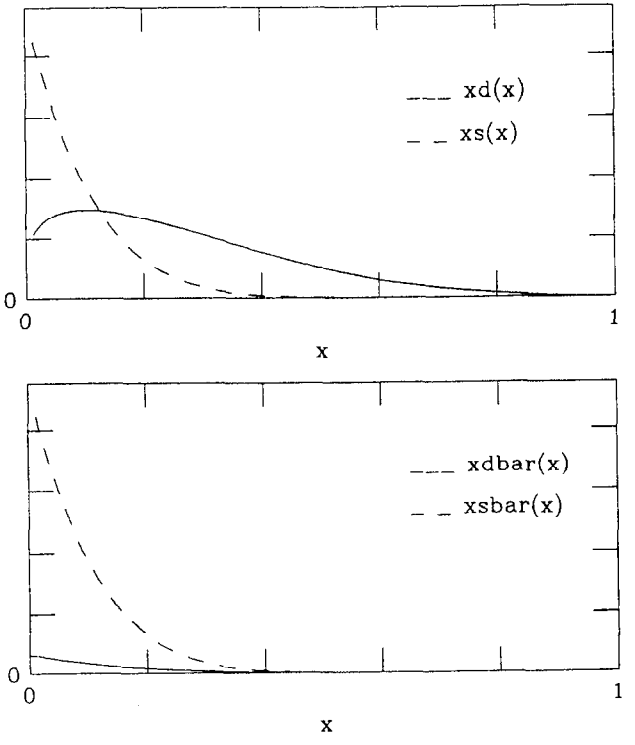

Figure 2: Contributions of partons to the charm production cross section. The solid lines are $xd_N(x)$ and $x\overline{d}_N(x)$ and the dashed lines are $xs_N(x)$ and $x\overline{s}_N(x)$.

given the ratio $\overline{Q}/Q = \int(x\overline{u} + x\overline{d} + x\overline{s})dx / \int(xu + xd + xs)dx = 0.175 \pm 0.012$ determined from the charged current neutrino differential cross section.[2,4] If the sea is SU(3) symmetric ($\overline{u} = \overline{d} = \overline{s}$) then $\kappa = 1$.

(2) a measure of the x dependence of $s(x)$ and $d(x)$.

(3) a measurement of the branching fraction B_μ.

III. Experimental details

Fermilab experiment E744 was run by the CCFR collaboration in 1985. This experiment explored dimuon production with both high statistics and at higher energies than previous experiments. A new wide band quadrupole triplet neutrino beam used the 800 GeV proton energies available at Fermilab to produce detectable neutrinos and anti-neutrinos with energies from 30 – 600 GeV. Figure 3 shows the measured charged current interaction spectra from the 1985 run.

The Lab E detector is composed of an unmagnetized 3×3×16.5 m^3 target calorimeter made up of 42 drift chambers and 84 liquid scintillation counters interleaved between 168 5 cm iron plates, followed by a muon spectrometer made up of 3 magnetized iron toroids with 5 drift chambers after each magnet and an additional 10 drift chambers downstream of the last magnet for an additional lever arm. The total mass of the target calorimeter is 690 tons. In order to ensure shower containment, we use only those events which lie within a fiducial volume which is at least 25 cm from the edges of the detector transversely, and at least 2 m of iron upstream of the spectrometer longitudinally. These cuts reduce the effective fiducial mass to approximately 400 tons. The r.m.s. hadron energy resolution in the calorimeter is $\delta E/E = 89\%/\sqrt{E, \mathrm{GeV}}$ while the r.m.s. muon momentum resolution is $\delta p/p = 11\%$. Due to the long non-magnetized calorimeter, a muon can experience an energy loss of 7 – 15 GeV before momentum analysis in the spectrometer. We therefore impose a lower limit of 9 GeV/c on the momenta of sign analyzed muons to assure reasonable acceptance. All CCFR dimuon rates are quoted with this cut.

In addition to conventional momentum fitting, we perform straight line fits for x and y views separately in each set of 5 drift chambers in the field free regions between the spectrometer magnets. The muon time of passage is left as a free parameter. The time for each muon track can be determined with an accuracy of 5 ns. This allows us to completely eliminate the spurious dimuons from 'accidentals' in which two charged current events occur in the target within the 2 μs drift chamber gate.

In the 1985 run, 800,000 fully reconstructed charged current events passing all cuts were collected in the fiducial volume of the Lab E detector, six times the

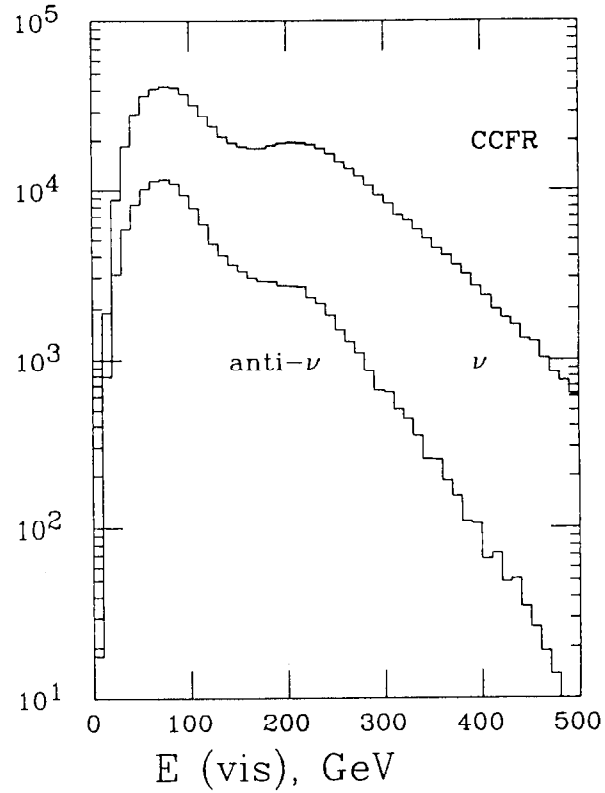

Figure 3: Measured charged current neutrino energy spectra from the 1985 Fermilab run. No acceptance correction has been made. There are 800,000 total neutrino induced events of which 65,000 have energies in the previously unstudied region above 300 GeV.

statistics of previous Fermilab experiments. All events with two calorimeter tracks entering the spectrometer were scanned for dimuons. The measured efficiency for finding dimuons with both momenta above 9 GeV/c is at least 99%. Figure 4 is a typical opposite sign dimuon event.

Crossovers Our beam is a 2:1 mix of ν and $\overline{\nu}$. We distinguish the two by identifying the decay muon as the one with the smallest p_T relative to the hadron shower direction. The sign of the other muon then identifies the type of the incoming neutrino. Monte Carlo studies indicate that this algorithm yields a 2% $\overline{\nu}$ contamination in the neutrino sample but a 26% ν contamination is found in the $\overline{\nu}$ sample. This is due to the different fluxes and kinematics for ν and $\overline{\nu}$ events. We also tried an alternative algorithm in which the muon of lowest momentum was assumed to be the decay muon. This algorithm yielded higher contaminations but caused no significant shift in our results. We find 1529 neutrino induced and 284 anti-neutrino induced dimuon events with the p_T classification scheme. Figure 5 shows the p_T of the decay muon and the current muon relative to the hadron shower.

IV. Model of opposite-sign dimuon production

Charm production model

We wish to study the relative shapes and magnitudes of $s(x) = \overline{s}(x)$ and $\overline{d}(x)$. We use as our model for the total charged current rate a Buras-Gaemers[3] QCD parameterization of charged current data[4] taken with the Lab E detector in Fermilab experiments E616 and E701 at beam energies from 30-250 GeV. This parameterization yields the shapes and levels of $u(x)$, $d(x)$, $\overline{u}(x)$ and $d(x)$.

We describe the strange sea with two parameters, η_s and α such that

$$\overline{s}(x) = s(x) = N_0 \overline{d}(x)(1-x)^{\alpha}$$

where N_0 is set by the requirement that the ratio of the integrals of $2x\overline{s}$ and $(xu + xd)$ is η_s.

We must also assume a mass for the charm quark since this determines the degree of slow rescaling in the cross section. We use a central value of m_c = 1.5 GeV/c^2 and study the range from 1.0 to 1.9 GeV/c^2.

Decay muon kinematics

In order to describe dimuon production in our detector, we must also model the kinematics of the decay muon. The initial charm quark fragments into a D meson or charmed baryon which carries a fraction z of the total quark

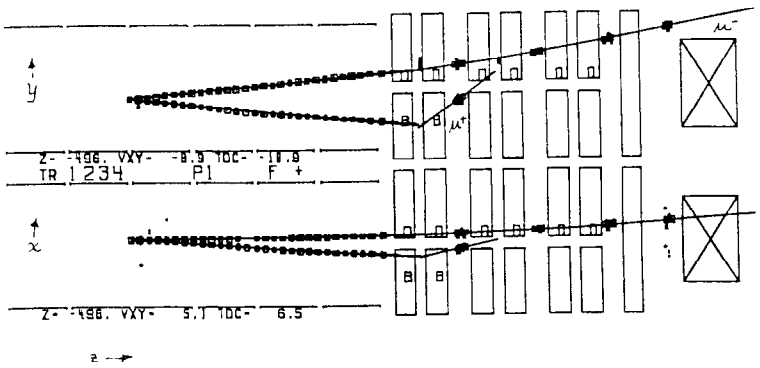

Figure 4: An opposite-sign dimuon event in the Lab E detector. The muon momenta are 57 and 14 GeV/c.

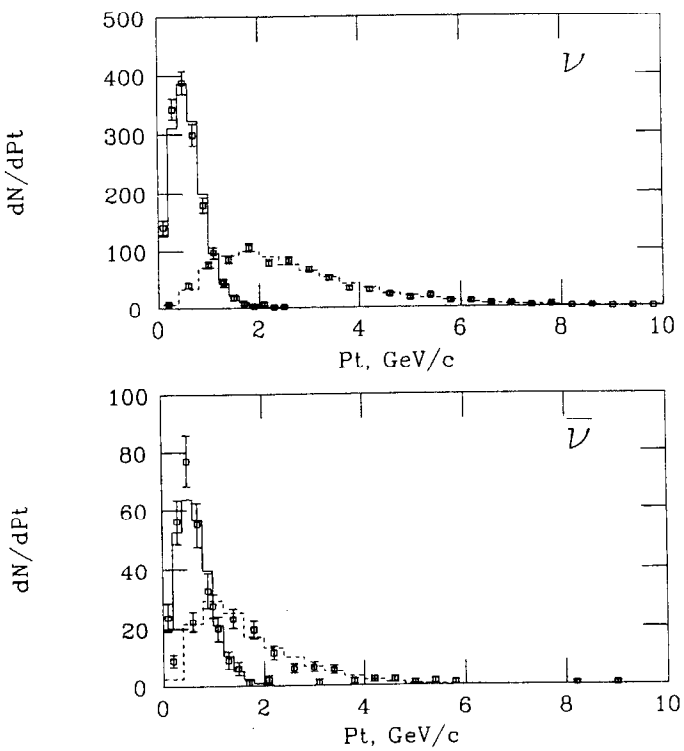

Figure 5: Solid line: p_T of the decay muon relative to the hadron shower direction. Dashed line: p_T of the current muon relative to the hadron shower direction. The squares are the data and the histogram is the Monte Carlo calculation.

momentum and acquires a p_T relative to the quark direction. The D meson then decays to produce the muon.

We use the Peterson[5] fragmentation model:

$$P(z) = \frac{1}{z(1 - \frac{1}{z} - \frac{\epsilon}{1-z})^2}$$

with $\epsilon = .19 \pm .03$ from ARGUS[6] measurements of D fragmentation in e^+e^- scattering. In our estimate of systematic errors we vary ϵ from $0.09 - 0.29$ as the mechanism in νN scattering may differ from that in e^+e^-.

The p_T distribution of the charmed hadrons is:

$$\frac{dN}{dp_T^2} = e^{-1.1p_T^2}$$

from a fit[2] to LEBC hadronic charm production data.[7] The Fermilab ν-emulsion experiment E531[8] finds that the charmed baryon component of charm production is small for $E_\nu > 30$ GeV. We therefore treat all charm particles as D mesons in our acceptance calculation.

We use data from the Mark III collaboration[9] for the D meson decay kinematics. The branching fraction $B_\mu = B(c \to \mu + X)$ is left as a free parameter as the precise mix of D^+ and D^0 mesons is unknown. A calculation based on e^+e^- data[10] and the D^0/D^+ fractions measured in neutrino emulsion experiments[8] indicates that B_μ is $(10.9 \pm 1.4)\%$.[2]

Figure 6 shows a comparison of the fraction of the quark energy carried by the decay muon $z_\mu = E_{\mu_2}/(E_{\mu_2} + E_{had})$ for E744 data and for our production model.

Background

The only significant backgrounds to the charm signal are muon production via π and K decay in flight within the hadron shower and trimuon production in which the third muon is not detected. We have studied these intensively as they contribute to the much rarer same-sign dimuon process.[11] We find that 6% of the opposite sign dimuons can be attributed to decay in flight and trimuons. All subsequent plots have this background subtracted.

Cross sections

Figures 7 and 8 show the energy dependence of the total opposite sign dimuon rate after acceptance correction and background subtraction compared to the total charged current rate. The rise with energy is due to the charm mass

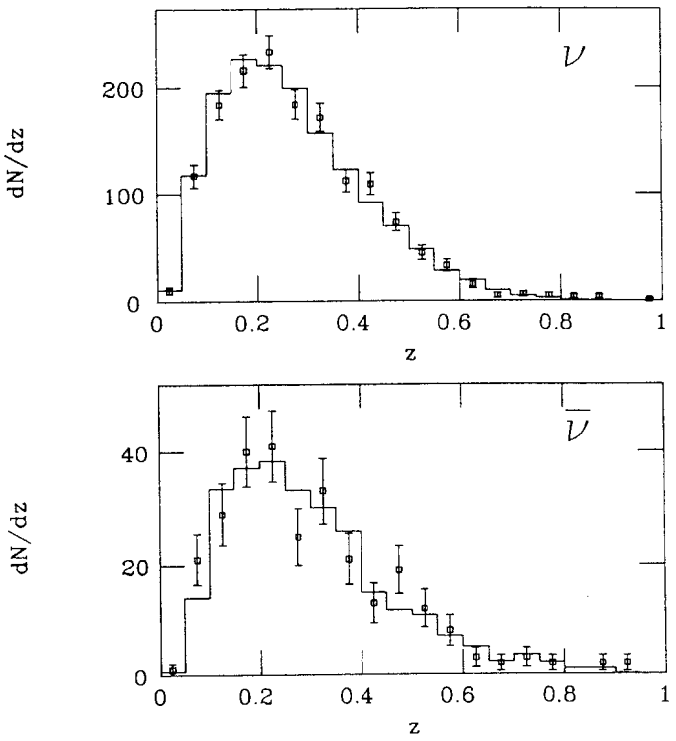

Figure 6: Comparison of z_μ for a) neutrino and b) anti-neutrinos. The curves are the Monte Carlo simulation of dimuon production

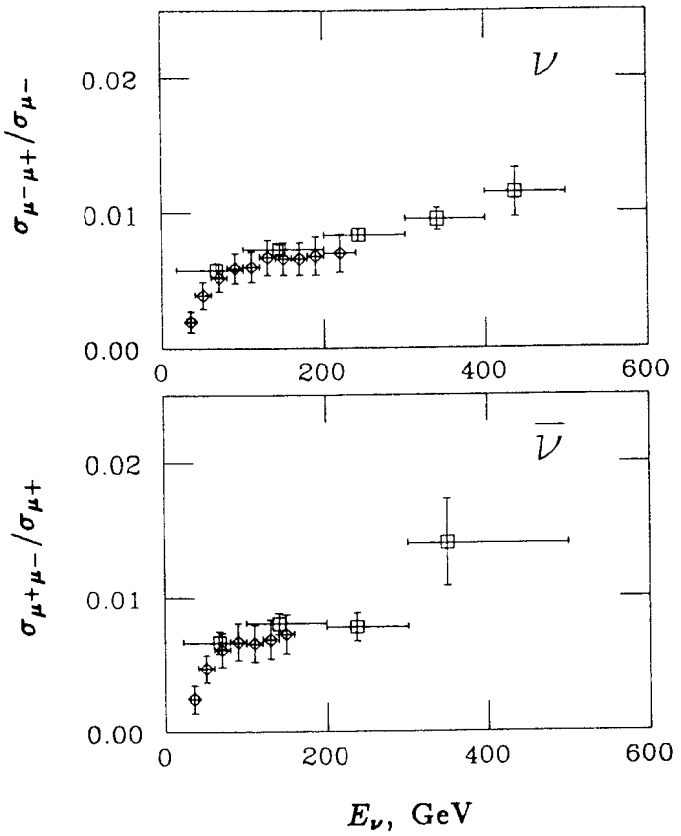

Figure 7: Dimuon rates relative to the total charged current cross section. The squares are this experiment and the diamonds are from the CDHS experiment.[12]

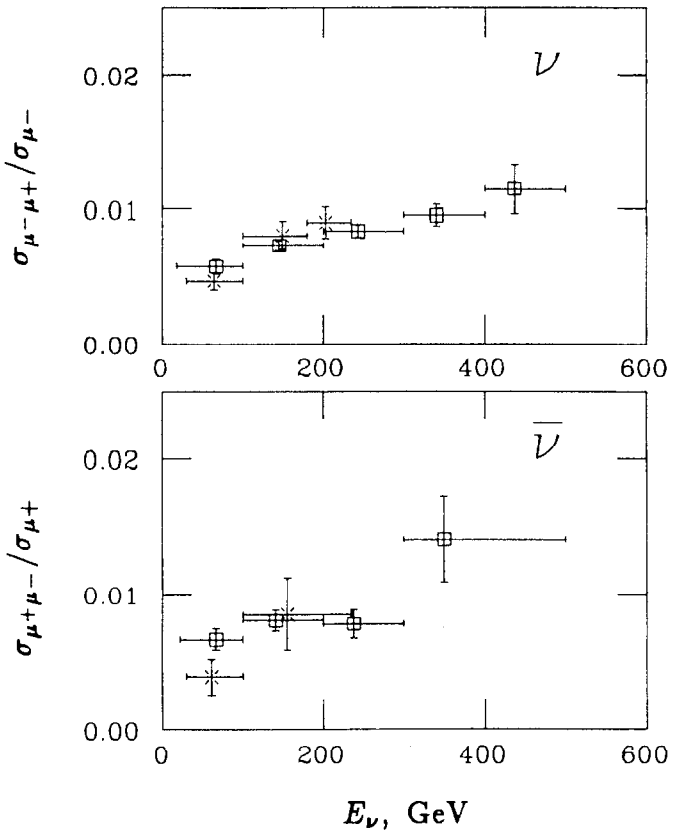

Figure 8: Dimuon rates relative to the total charged current cross section. The squares are this experiment and the crosses are from an earlier run with the same apparatus.[2]

threshold. We have used a charm mass m_c of 1.5 GeV/c^2. This experiment is compared to the CDHS measurement from CERN[12] and a previous measurement with the Lab E detector[2] in Figure 7.

IV. Interpretation

As shown in Equations 1 and 2 the quark distribution functions can be directly related to the dimuon differential cross section $\frac{d\sigma}{dx}$.

We fit the x distribution from the production model to the measured distributions and extract the parameters η_s, α and B_μ. Figure 9 shows such a fit while Figure 10 shows the individual components of the calculated rate, including crossovers from $\nu \to \overline{\nu}$.

The best fit parameters are:

$$\eta_s = 0.068 \pm 0.011 \pm 0.005$$
$$\alpha = 4.8$$
$$B_\mu = 10.2 \pm 1.0\%$$
$$\chi^2 = 9.5 \text{ for } 11 \text{ degrees of freedom.}$$

This implies a κ of $0.46^{+.10+.08}_{-.07-.05} \pm 0.04$ where the first error is statistical, the second is the systematic error on η_s and the third error reflects the error on $\overline{Q}/Q = 0.175 \pm 0.012$ in the conversion from η_s to κ. The details of the systematic errors are discussed below.

A similar fit (Figure 11) with α constrained to zero yields $\kappa = 0.42$ and does not describe the data as well.

Systematic Errors The dominant systematic errors in our measurement of κ are the theoretical assumptions in the acceptance modeling. If we change the charm mass from 1.0 to 1.9 GeV, κ varies from 0.41 to 0.54. If we vary the fragmentation parameter ϵ from 0.09 to 0.29 (the quoted error is $\pm.03$), κ varies by ± 0.01 and B_μ varies by $\pm 0.8\%$.

Comparison with other experiments The CDHS experiment[12] has measured $\kappa = 0.52 \pm 0.09$. Their errors are dominated by systematics and do not include charm mass variations.

We have measured κ previously[2] in earlier runs with our detector to be $\kappa = 0.52^{+0.17}_{-0.19}$ where the dominant error is statistical. As the statistics for this earlier measurement were much less than those for the present measurement, B_μ was fixed at $10.9 \pm 1.4\%$ determined from Mark III branching fractions and particle fractions from ν-emulsion data.

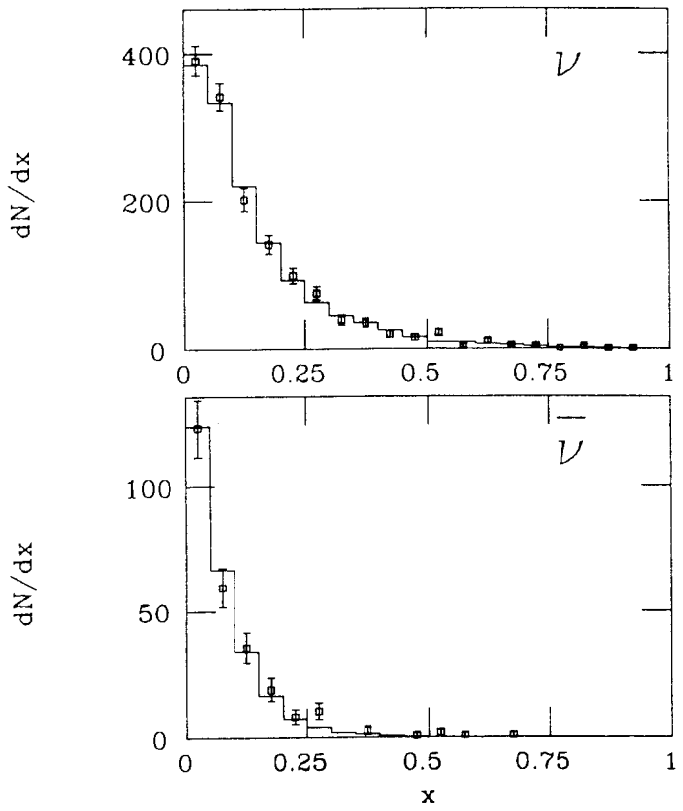

Figure 9: Simultaneous fit to $\frac{d\sigma}{dx}$ for ν and $\bar{\nu}$. The curve is the model.

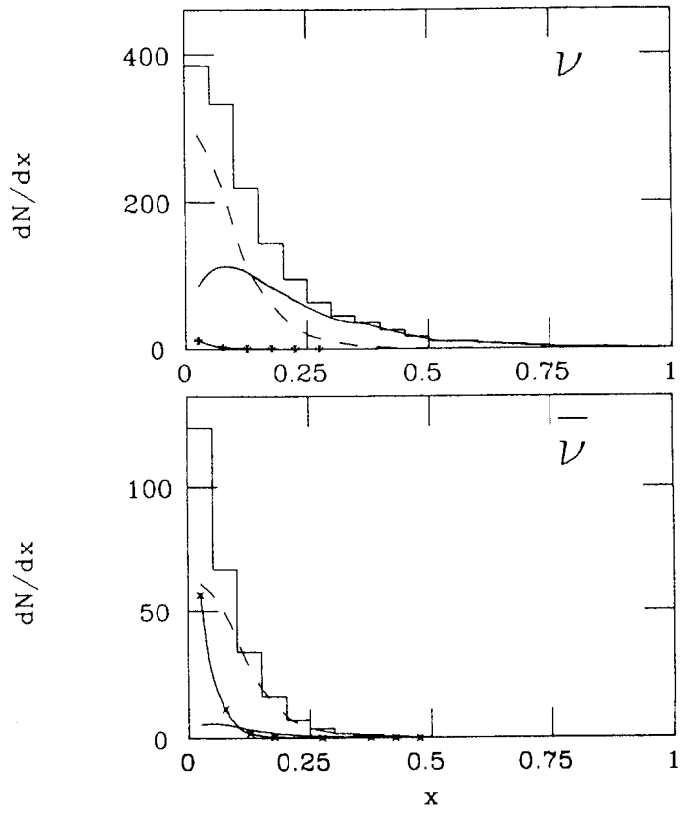

Figure 10: Components of the model. The histogram is the total calculated rate, the solid curve is the d_N quark contribution, the dashed curve is the s_N quark contribution and the curve with dots indicates the crossover component.

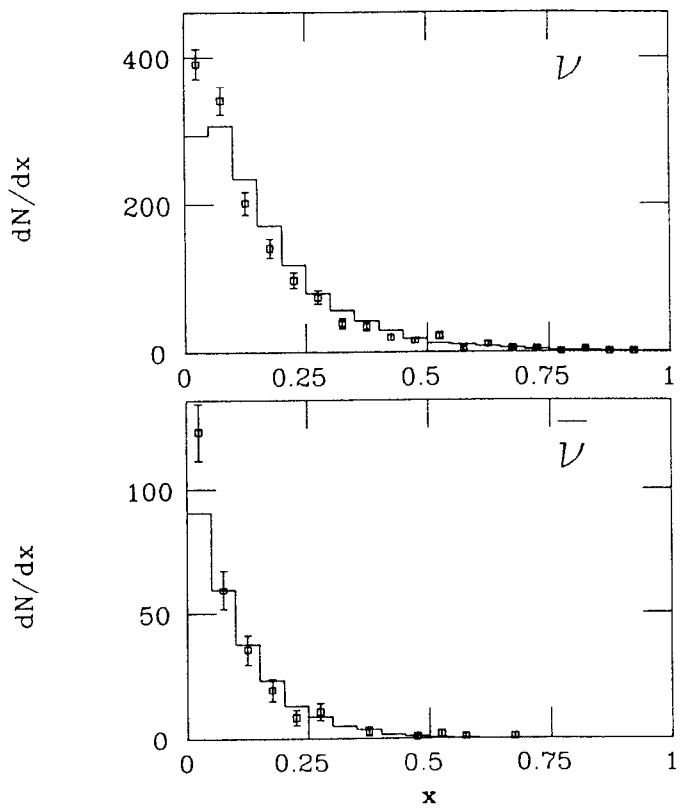

Figure 11: Simultaneous fit to $\frac{d\sigma}{dx}$ for ν and $\overline{\nu}$ with α constrained to zero. The curve is the model.

Conclusion

We have studied the level and x dependence of the strange sea. We find that κ, which would be 1 for SU(3) symmetry is around 1/2. This value is consistent with earlier measurements.

REFERENCES

[1] R.N. Barnett, Phys. Rev. Lett. **36**, 1163 (1976), B.J. Edwards, T.D. Gottschalk, Nucl. Phys. **B186**, 309 (1981), C.H. Lai, Phys. Rev. **D18**, 1422 (1978), H. Georgi, H.D. Politzer, Phys. Rev. **D14**, 1829 (1976), B.J. Kaplan, F. Martin, Nucl. Phys. **B115**, 333 (1976).

[2] K. Lang *et. al.*, Z. Phys. **C33**, 483 (1987).

[3] A.J. Buras, K.J.F. Gaemers, Nucl. Phys. **B132**, 249 (1978).

[4] D. MacFarlane *et. al.*, Z. Phys. **C26**, 1 (1984).

[5] C. Peterson *et. al.*, Phys. Rev. **D27**, 105 (1983).

[6] H. Albrecht *et. al.*, Phys. Lett. **150B**, 235 (1985).

[7] M. Aguilar-Benitez *et. al.*, Phys. Lett. **123B**, 103 (1983).

[8] N. Ushida *et. al.*, Phys. Lett. **121B**, 287 (1983).

[9] D.M. Coffman, Ph.D. Thesis, California Institute of Technology, CALT-68-1415 (1987).

[10] R.M. Baltrusaitis *et. al.*, Phys. Rev. Lett. **54**, 1976 (1985).

[11] B.A. Schumm *et. al.*, Phys. Rev. Lett. **60**, 1618 (1988).

[12] H. Abramowicz *et. al.*, Z. Phys. **C15**, 19 (1982).

TWENTY YEARS OF DRELL-YAN DILEPTONS

C. N. Brown, Fermilab

E605/772 Collaboration

Twenty years ago, Christenson *et al.* exposed a solid uranium target to the highest energy, highest intensity beam available at the time, the AGS 30 GeV external proton beam.[1] Hiding behind a thick steel and concrete absorber, they recorded large angle, high energy muons with a spectrometer consisting of a scintillator hodoscope to measure the production angle and a crude muon range absorber to measure muon momentum. They were hoping to see single high P_t muons possibly from the decay of new particles such as the intermediate vector boson. Instead, they recorded a copious flux of pairs of high P_t muons. The spectrum of apparent dimuon mass for these muon pairs was monotonically decreasing but showed a broad shoulder in the 2.5 to 4.5 GeV mass range. Many theoretical attempts were made to understand this spectrum. The most promising was the paper by S. D. Drell and T. M. Yan,[2] who pointed out that Feynman's parton model implied the existence of parton-antiparton pairs virtually present in the nucleon. These virtual antipartons could annihilate electromagnetically with partons in the incoming nucleon, and the virtual photon thus produced could then decay into a muon pair.

In August of 1974, J. J. Aubert *et al.*[3] constructed at Brookhaven a similar experiment with much better resolution, detecting electron pairs instead of muon pairs in a precision magnetic spectrometer. They resolved the mass spectrum into a sharp peak, the J/ψ at 3.1 GeV mass, on a smooth continuum. The time reversed channel, J/ψ resonance production in electron-positron collisions, was also seen at SLAC.[4] This was of course the October revolution that completed the second generation of quarks and set the stage for the Standard Model as we know it today.

Meanwhile, Lederman and his colleagues had moved to the new 400 GeV synchrotron at Fermilab to investigate the dimuon spectrum at higher energies. From 1974 to 1977 they perfected techniques for studying dileptons at the higher energies, first studying dielectrons and mapping out the production of the J/ψ and ψ' resonances in hadron collisions.[5] In 1977, they reported the observation of yet another narrow resonance, at 9.45 GeV, the Upsilon.[6] The Upsilon, along with the Tau lepton[7] discovered at SLAC, indicated the existence of a third generation of quarks and leptons.

The 200 GeV, 300 GeV, and 400 GeV dimuon yields, Figure 1, also showed clearly the broad continuum predicted by Drell and Yan. The first important test of the Drell-Yan mechanism was the prediction that the cross section would show a universal form if expressed in parton variables, due to the underlying simplicity of the parton annihilation. The scaling curve, Figure 2, beautifully confirmed this prediction.

The subsequent 10 years of dilepton yield measurements in hadron collisions, in many different experiments, have confirmed in detail the many predictions of the Drell-Yan model. Table 1 and the review talks listed in Reference 8 indicate the extent of this work.

Today, I would like to report on two recent contributions to this field carried out by my collaborators at the Fermilab 800 GeV Tevatron. After completing the series of measurements at 400 GeV, it was decided to build a bigger magnetic spectrometer for measurements at 800 GeV.

The steel of the retired Columbia cyclotron was reconfigured into the E605 mass-focusing spectrometer, Figure 3. Both large analysis magnets, SM12 and SM3, used the Columbia steel and were outfitted with new coils. A water cooled copper beam dump in the first magnet defined an upper and lower aperture for an opposite sign pair of high P_t particles to be focussed on the downstream detector planes. The spectrometer was first used in 1984 to measure single and dihadron yields at 800 GeV.[9]

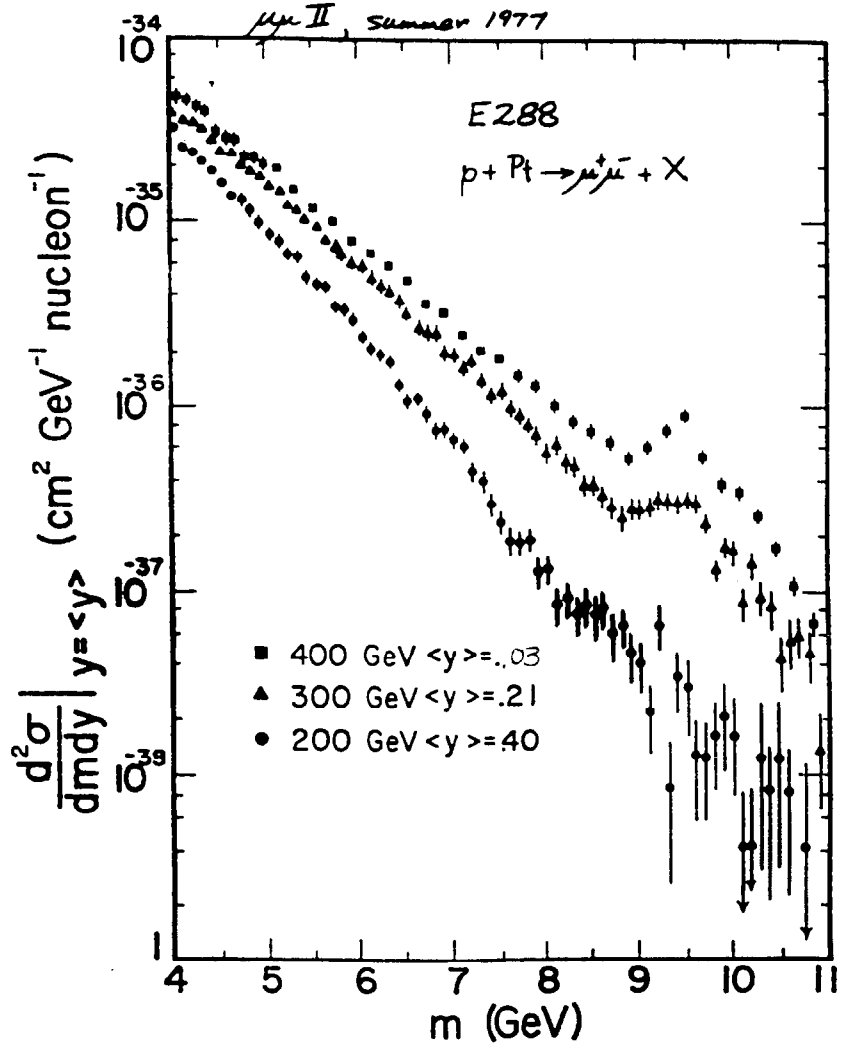

Fig 1. Yield of dimuons at 200 GeV, 300 GeV and 400 GeV observed in proton-nucleus collisions.[6]

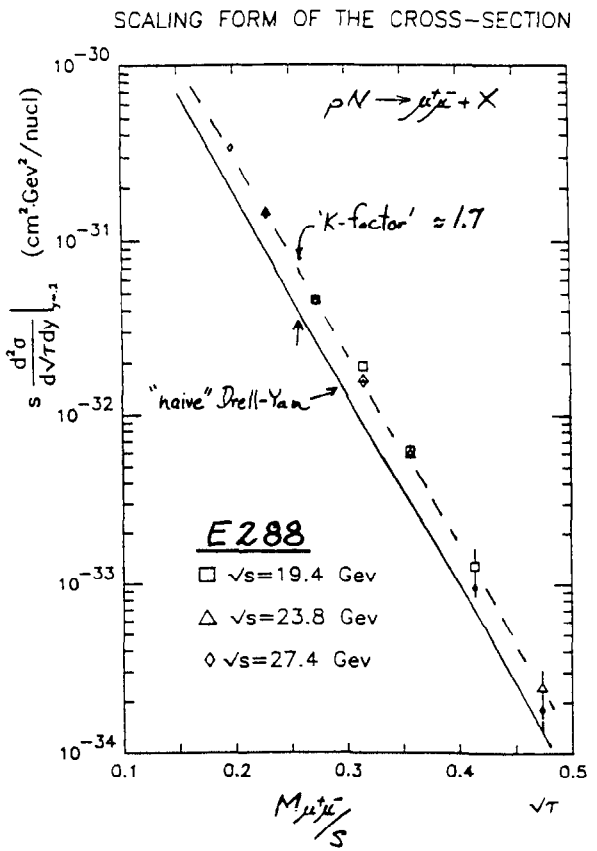

Fig 2. Yield of dimuons plotted in scaling variables.

Table 1. Experimental K-Factors, the Ratio of Experiment to Drell-Yan

Group	Reference	Beam/Target	Energy	K-Factor
CFS	Ito et al.(1981)	p-Pt	400	~1.7
MNTW	Smith et al.(1981)	p-W	400	1.6+.3
CHFMNP	Antreasyan et al.(1981)	p-p	$\sqrt{s}$=44,63	1.6+.2
AABCS	Kourkoumelis et al.(81)	p-p	$\sqrt{s}$=44,63	~1.7
NA3	Badier et al.(1985)	p-Pt	400	3.1+.5+.3
AFMMS	Annassontzis et al.(85)	$\bar{p}$-W	125	2.45+.12+.2
NA3	Badier et al.(1980)	$\bar{p}$,p-W	150	2.3+.4
NA3	Badier et al.(1983)	$\pi^{\pm}$-Pt	150 280	2.49+.37 2.22+.33
CP	Greenlee et al.(1985)	π^--W	225	2.70+.4
NA10	Betev et al.(1985)	π^--W	194	2.8+.1
Goliath	Barate et al.(1979)	π^--Be	150,175	~2.5
Omega	Corden et al.(1980)	$\pi^{\pm}$-W	39.5	2.6+.5
CIP	McDonald et al.(1987)	π^--W	250	2.8+.1

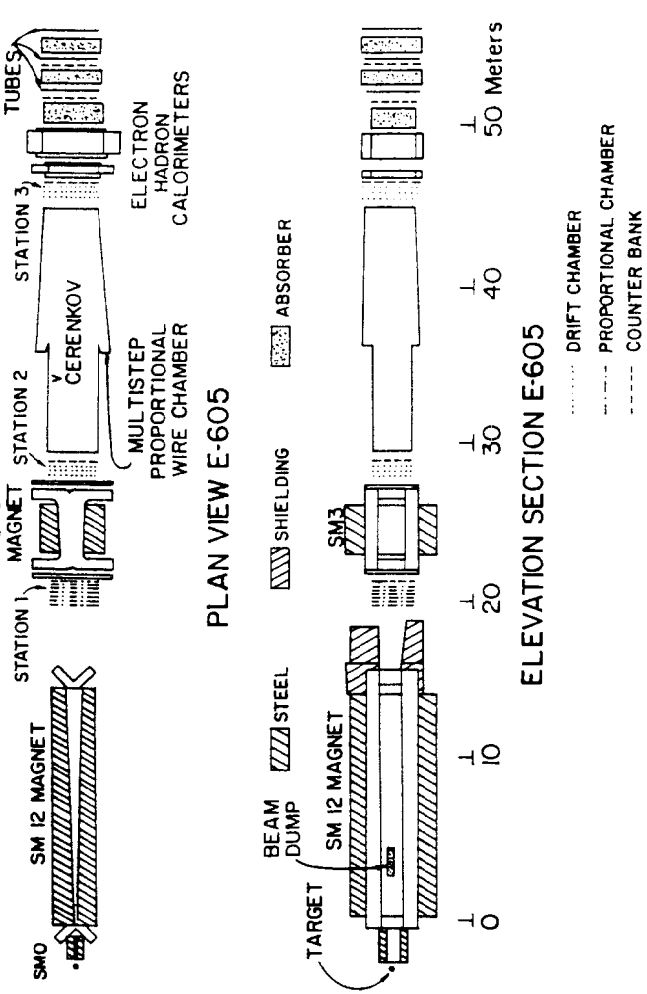

Fig 3. E605 spectrometer in the M-East beamline at Fermilab.

In 1985, a one meter absorber wall of lead was added at the downstream end of the first analysis magnet. This allowed operation of the spectrometer with incident proton intensities up to 2×10 11 protons per second while retaining the excellent mass resolution of the spectrometer. Figure 4 shows the yield of dimuon pairs measured with a copper target. No new resonances, besides the three upsilon s-states, are evident up to 18 GeV.

The scaling form of the cross section, Figure 5, shows good agreement with the previous measurements. The yield is also compared with an absolute prediction based on the quark structure functions as measured by BCDMS folded into a Drell-Yan yield calculation[10] which includes corrections due to various gluon scattering diagrams. The order α_s gluon scattering corrections increase the predicted yield by about 50%. This K-factor of 1.5 seems to be in agreement with the measured yield.

In Figure 6 the measured yield is compared to the measurements of the NA3 group at CERN using their scaling form of the cross section and their binning. The agreement is very good and shows some hint of a scale-breaking decrease in the yield at the higher energy, as predicted by the order α_s Drell-Yan calculation. In Figure 7, the yield as a function of the rapidity of the muon pair is compared with the data of E228. At the higher values of average fractional momentum of the annihilating quarks, $\sqrt{\tau}$, the yield shows a distinct forward peaking. Although the Drell-Yan calculation has some forward peaking due to the asymmetry of the initial state (more d-quarks in the target than in the beam), the data seems to have a larger asymmetry than predicted. This might arise from a non-SU3 asymmetry of the quark-antiquark sea, as first predicted many years ago by Feynman.[11] The present structure function analyses of deep-inelastic scattering data assume symmetry of the sea. An alternate origin of the asymmetry might be a nuclear-target relaxation of the quark momenta in the target nucleus.

In order to investigate nuclear effects on Drell-Yan yields, a new collaboration was formed to carry out a precision A-dependence measurement using the

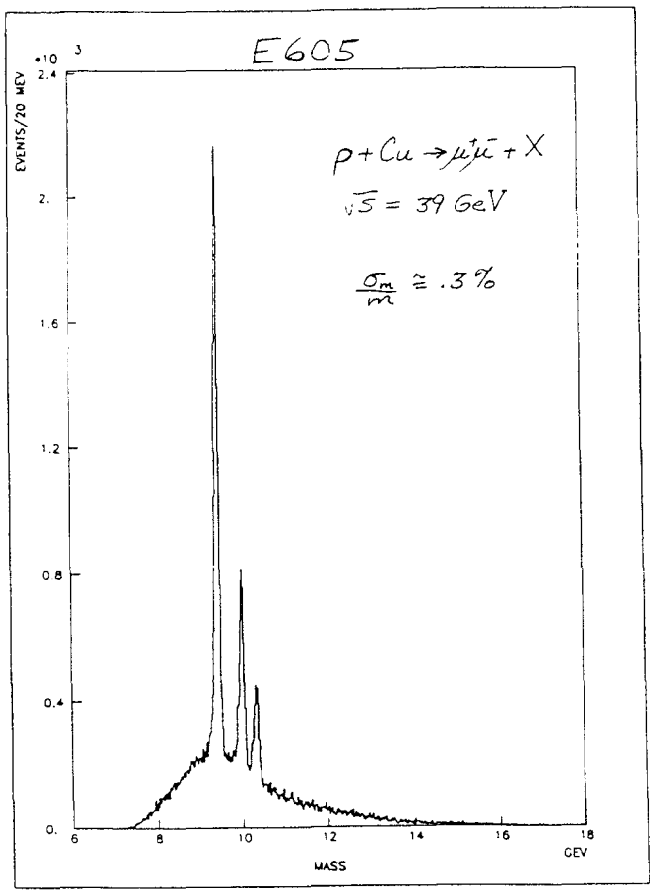

Fig 4. E605 dimuon spectrum observed in 800 GeV proton-copper collisions.

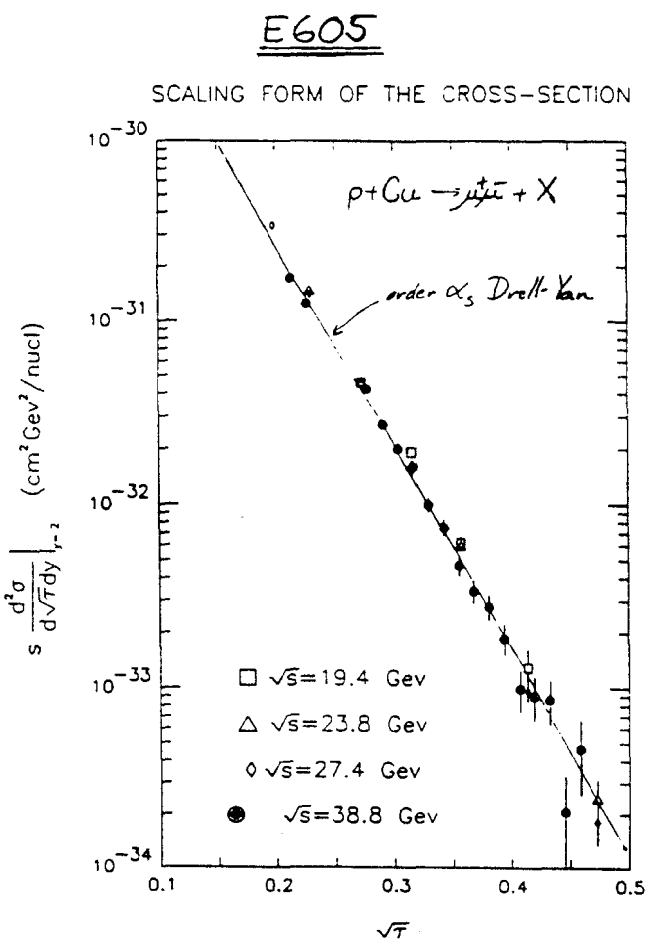

Fig 5. E605 dimuon yields compared with the E228 measurements. The curve is the prediction of the order α_s Drell-Yan calculation.[10]

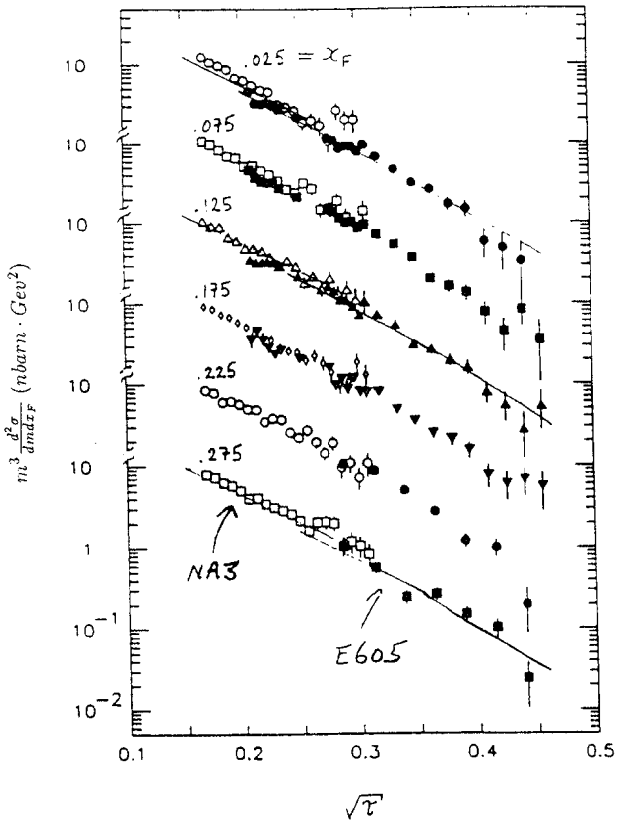

Fig 6. Comparison of E605 and NA3 dimuon yields versus P_t of the dimuon pair. The curve is the prediction of the order α_s Drell-Yan calculation.[10]

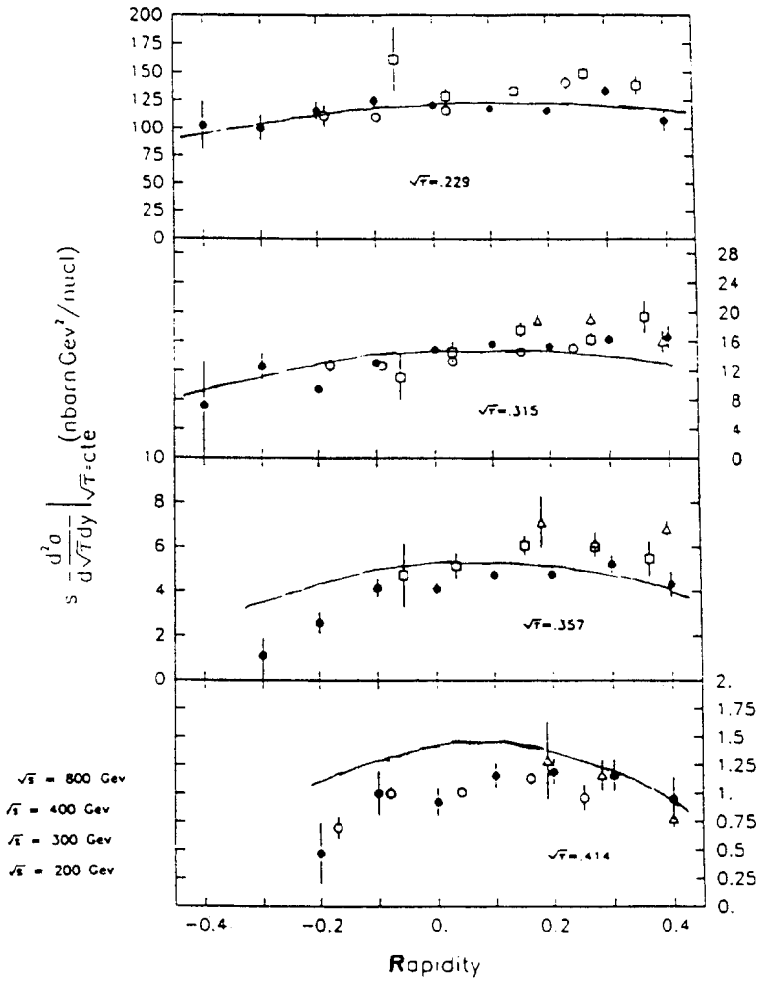

Fig 7. Dimuon yield versus rapidity for E605 and E288 data. The curve is the prediction of the order α_s Drell-Yan calculation.[10]

E605 spectrometer. In 1987, a Los Alamos-Fermilab-UIC-NIU-Texas collaboration, E772, measured dimuon yields from deuterium, carbon, calcium, iron and tungsten targets. Figure 8 indicates the dimuon masses covered by the three magnet settings used. At each setting, targets were alternated every few minutes in order to minimize normalization systematics. The very preliminary ratio of the dimuon yields from calcium and deuterium is shown in Figure 9.

There is a qualitative indication of a vector-meson yield reduction for calcium compared to an A-dependence near unity for the Drell-Yan continuum. Note that the vector meson lifetime is much longer than the time to traverse the nucleus. Thus, it is possible that the absorption of the vector-mesons seen in the calcium nucleus is due to inelastic reactions after the initial production. A preliminary estimate of the absorption needed is of the order of a few mbarns.

In conclusion, after 20 years, the Drell-Yan description of dilepton production in hadron collisions remains one of the simple demonstrations of quark-lepton connections in the Standard Model. The present understanding of dilepton yields is limited to about 25% by: systematic differences between experiments, higher order QCD effects, uncertainties in the data and structure function analyses of deep-inelastic scattering, and possible nuclear effects. Hopefully, the ensemble of new experimental results on both dilepton yields and deep-inelastic scattering will clarify some of these points and lead to a better understanding of the gluon and quark-antiquark structure of nucleons and nuclei.

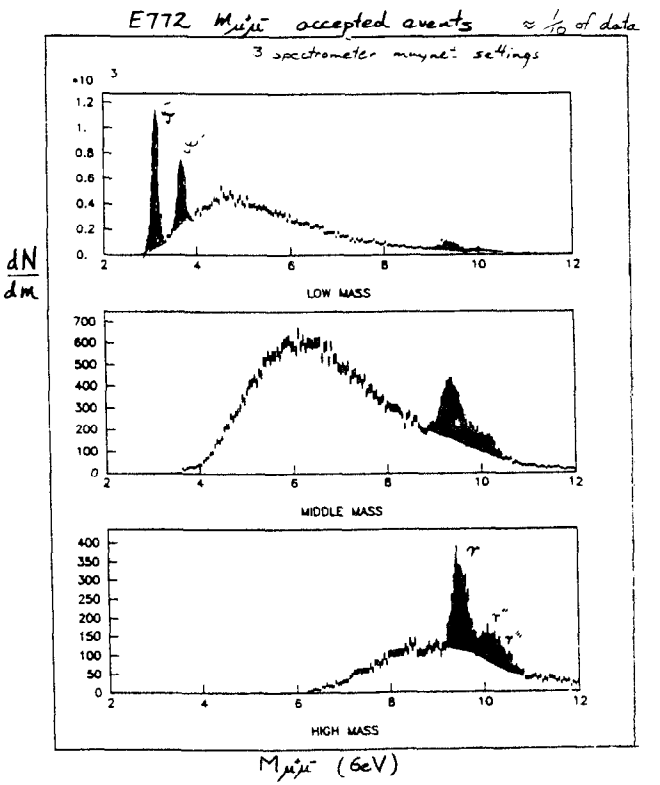

Fig 8. Mass spectrum of dimuons observed at three spectrometer settings in E772.

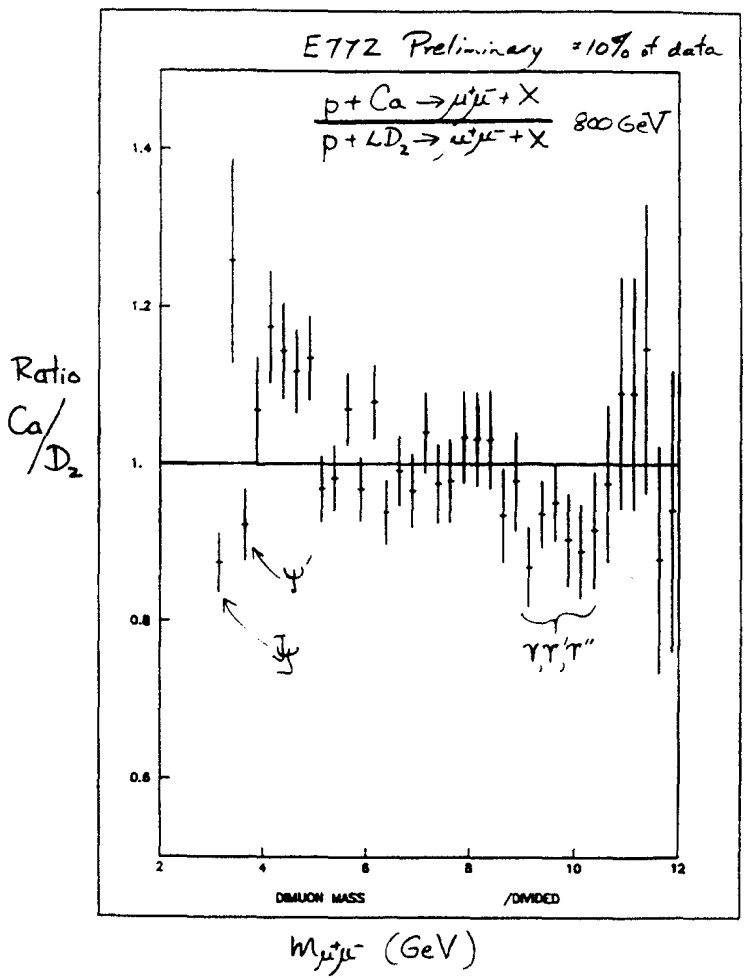

Fig 9. Preliminary ratio of the dimuon yields from calcium and deuterium targets in E772.

REFERENCES

1. J. H. Christenson *et al.*, Phys. Rev. **D8**, 2016 (1973).
2. S. D. Drell and T. M. Yan, Phys. Rev. Lett. **25**, 316 (1970).
3. J. J. Aubert *et al.*, Phys. Rev. Lett. **33**, 1404 (1974).
4. J.-E. Augustin *et al.*, Phys. Rev. Lett. **33**, 1406 (1974).
5. B. C. Brown *et al.*, Fermilab 77/54-EXP, June 1977.
6. S. W. Herb *et al.*, Phys. Rev. Lett. **39**, 252 (1977).
7. M. L. Perl *et al.*, Phys. Rev. Lett. **35**, 1489 (1975); M. L. Perl *et al.*, Phys. Lett. **63B**, 466 (1976).
8. I. R. Kenyon, Rep. Prog. Phys. **45**, 1261 (1982); J. P. Rutherfoord, Proceedings of the 1985 International Symposium on Lepton and Photon Interactions at High Energies, Kyoto (1985).
9. Y.B.Hsiung *et al.*, Phys. Rev. Lett. **55**, 457 (1985); J. A. Crittenden *et al.*, Phys. Rev. **D34**, 2584 (1986).
10. A. D. Martin, R. G. Roberts and W. J. Sterling, University of Durham preprint DTP/88/2, 1988.
11. R. P. Feynman, "Photon-Hadron Interactions," W. A. Benjamin Inc., 1972.

RECENT RESULTS FROM E-691*

Rollin J. Morrison

J.C. Anjos,[3] J.A. Appel,[5] A. Bean,[1] S.B. Bracker,[8]
T.E. Browder,[1,a] L.M. Cremaldi,[4,b] J.E. Duboscq,[1] J.R. Elliott,[4,c]
C.O. Escobar,[7] P. Estabrooks,[2] M.C. Gibney,[4] G.F. Hartner,[8]
P.E. Karchin,[9] B.R. Kumar,[8] M.J. Losty,[6] G.J. Luste,[8]
P.M. Mantsch,[5] J.F. Martin,[8] S. McHugh,[1] S.R. Menary,[8]
R.J. Morrison,[1] T. Nash,[5] P. Ong,[8] J. Pinfold,[2] G. Punkar,[1]
M.V. Purohit,[5,d] J.R. Raab,[1,e] A.F.S. Santoro,[3] J.S. Sidhu, [2,†]
K. Sliwa,[5] M.D. Sokoloff,[5,f] M.H.G. Souza,[3] W.J. Spalding,[5]
M.E. Streetman,[5] A.B. Stundžia,[8] M.S. Witherell,[1]

1. University of California, Santa Barbara, California, USA
2. Carleton University, Ottawa, Ontario, Canada
3. Centro Brasileiro de Pesquisas Fisicas, Rio de Janeiro, Brazil
4. University of Colorado, Boulder, Colorado, USA
5. Fermi National Accelerator Laboratory, Batavia, Illinois, USA
6. National Research Council, Ottawa, Ontario, Canada
7. Universidade de São Paulo, São Paulo, Brazil
8. University of Toronto, Toronto, Ontario, Canada
9. Yale University, New Haven, Connecticut, USA

a. Now at Stanford Linear Accelerator Center, Stanford, CA 94309
b. Now at University of Mississippi, Oxford, MS 38677
c. Now at Electromagnetic Applications, Inc., Denver, CO 80226
d. Now at Princeton University, Princeton, NJ 08544
e. Now at CERN, Division EP, CH-1211 Genève, Switzerland
f. Now at University of Cincinnati, Cincinnati, OH 45221
†Deceased

(The Tagged Photon Spectrometer Collaboration)

* Invited talk given at the 1988 SLAC Summer Institute Topical Conference.

In Fermilab photoproduction experiment E–691 a sample of about 10,000 charm decays has been observed with very little background. A crucial aspect of the experiment was the high precision silicon microstrip vertex detector which allowed the tracks from the downstream weak decay to be clearly identified. A number of results on charm particle lifetimes,[1,2,3,4] $D^0 - \overline{D^0}$ mixing,[5] and D_s^+ decays[6] have already been published.

The results presented here have been chosen primarily to address three physics issues. The measurements of the D^+ and D_s^+ decays to the $\pi^+\pi^-\pi^+$ final state provides crucial information on hadronic decay mechanisms. The exclusive semileptonic D decays address the issue of extracting K–M matrix elements. The third topic is the search for L= 1 charmed mesons. Finally, since there is experimental disagreement on the mass of the Σ_c^0, we briefly present our results for this state.

I. THREE PION DECAYS OF THE D_s^+ AND D^+

If the D_s^+ decays are dominated by the spectator diagram, shown in Figure 1a, the final state contains predominantly $s\bar{s}$ final states such as $\overline{K}K$, $\overline{K^*}K$, $\phi\pi^+$, $\eta\pi^+$, etc. If, on the other hand, the annihilation diagram of Figure 1b is important, we expect large branching ratios to pionic final states, $\pi\rho$, etc.

In order to cleanly detect the rare charm decays to three pions, in the enormous combinatorial background, very stringent vertex cuts are required. These cuts have the effect of requiring that only the three pions of interest emanate from the decay vertex, and that none of the pions associated with the decay vertex could have actually come from the production vertex. In addition we require that the primary and secondary vertices be separated by at least 15 σ. This corresponds roughly to a requirement that the proper decay time be greater than 1.3 lifetimes. The resulting $\pi^+\pi^-\pi^+$ (and charge conjugate) mass plot is shown in Figure 2. In addition to the large peak at low mass, due to misidentified K's in the $D^+ \rightarrow K^-\pi^+\pi^+$ decay, there are clear peaks for the Cabibbo-suppressed $D^+ \rightarrow \pi^+\pi^-\pi^+$ and the $D_s^+ \rightarrow \pi^+\pi^-\pi^+$.

The $\pi^+\pi^-$ resonant substructure for the D_s^+ decay is seen in Figure 3b, where there are two entries per event. The narrow peak is due to the $f_0(975)$ (previously the S(975)). After correcting for background, no evidence for the ρ^0 is seen. To extract the branching ratios, a fit to the Dalitz plot has been carried

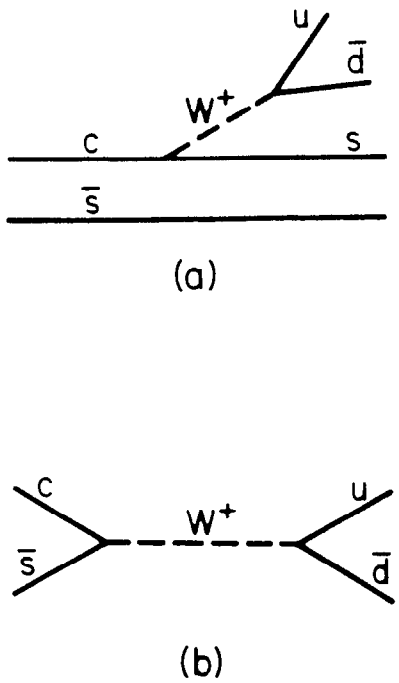

Fig. 1.

Quark diagrams for D_s^+ decay. (a) spectator diagram; (b) annihilation diagram.

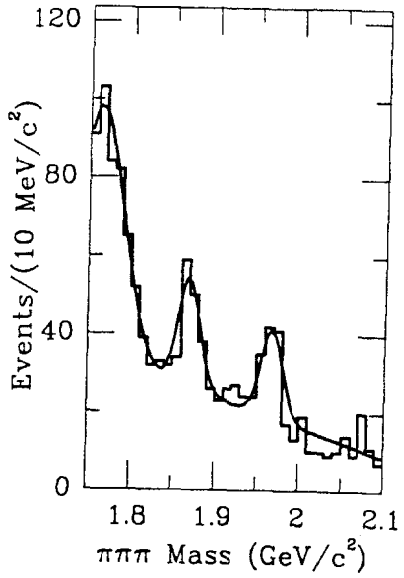

Fig. 2. The three pion mass spectrum.

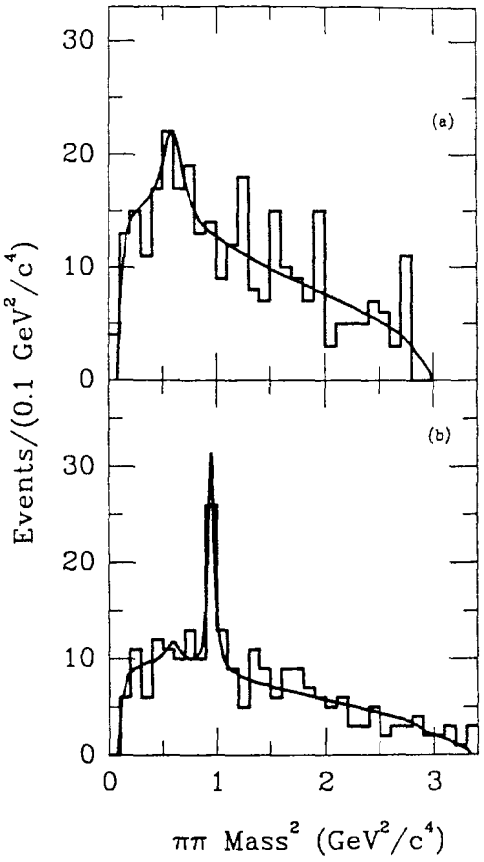

Fig. 3.

The $\pi^+\pi^-$ resonant substructure for (a) the D^+ mass region and (b) the D_s^+ mass region.

out which takes into account interference between the various amplitudes, the identical nature of the two pions, and the angular dependence of the decay particles for the case where the resonance is a vector. The resulting branching ratios, normalized to our most easily observable mode, are given in Table I.

TABLE I. Relative branching ratios (B) for D_s^+ and $D^+ \to$ non-strange states. Errors are given in the form: ± statistical ± systematic.

Decay mode 1	Decay mode 2	B(decay mode 1)/B(decay mode 2)
$D_s^+ \to \pi^-\pi^+\pi^+$	$D_s^+ \to \phi\pi^+$	$0.44 \pm 0.10 \pm 0.04$
$D_s^+ \to (\pi^-\pi^+\pi^+)_{NR}$	$D_s^+ \to \phi\pi^+$	$0.29 \pm 0.09 \pm 0.03$
$D_s^+ \to \rho^0\pi^+$	$D_s^+ \to \phi\pi^+$	< 0.08 (90% C.L.)
$D_s^+ \to f_0\pi^+$	$D_s^+ \to \phi\pi^+$	$0.28 \pm 0.10 \pm 0.03$
$D^+ \to \pi^-\pi^+\pi^+$	$D^+ \to K^-\pi^+\pi^+$	$0.035 \pm 0.007 \pm 0.003$
$D^+ \to (\pi^-\pi^+\pi^+)_{NR}$	$D^+ \to K^-\pi^+\pi^+$	$0.027 \pm 0.007 \pm 0.002$
$D^+ \to \rho^0\pi^+$	$D^+ \to K^-\pi^+\pi^+$	$0.008 \pm 0.005 \pm 0.001$
$D_s^+ \to \pi^-\pi^+\pi^-\pi^+\pi^+$	$D_s^+ \to \phi\pi^+$	< 0.29 (90% C.L.)
$D^+ \to \pi^-\pi^+\pi^-\pi^+\pi^+$	$D^+ \to K^-\pi^+\pi^+$	< 0.019 (90% C.L.)

The observation of the f_0 (975) in this decay is in fact an indication of the non-dominance of the annihilation amplitude. The f_0 is an $s\bar{s}$ state which is prevented from decaying to the KK final state since it is below KK threshold. Subtracting the f_0 contribution, we take the nonresonant $\pi^+\pi^-\pi^+$ as a measure of the annihilation mechanism. This is only 0.14 ± 0.04 of the total branching ratio for $D_s^+ \to K^+K^-\pi^+$,[6] indicating that the annihilation mechanism is unimportant. The five pion branching ratio is also observed to be very small.

The Cabibbo-suppressed D^+ branching ratio to $\rho\pi^+$ and to the nonresonant $\pi^+\pi^-\pi^+$, given in Table I, also illustrates basic features of hadronic charm decay mechanisms. If the Cabibbo-suppression occurs at the upper vertex, as shown in Figure 4a, there is an $s\bar{s}$ final state with no identical quarks. If the Cabibbo-suppression occurs at the charm vertex as seen in Figures 4b and 4c we get pionic final states. In the latter case there are two identical $\bar{d}$ quarks in the final state leading to the possibility of destructive interference. This type of destructive interference in the Cabibbo favored D^+ decays is believed to be the dominant source of the long D^+ lifetime. Using the results of Table I and the previously measured Cabibbo-suppressed $D^+ \to \phi\pi^+$ decay[6] we obtain the ratio

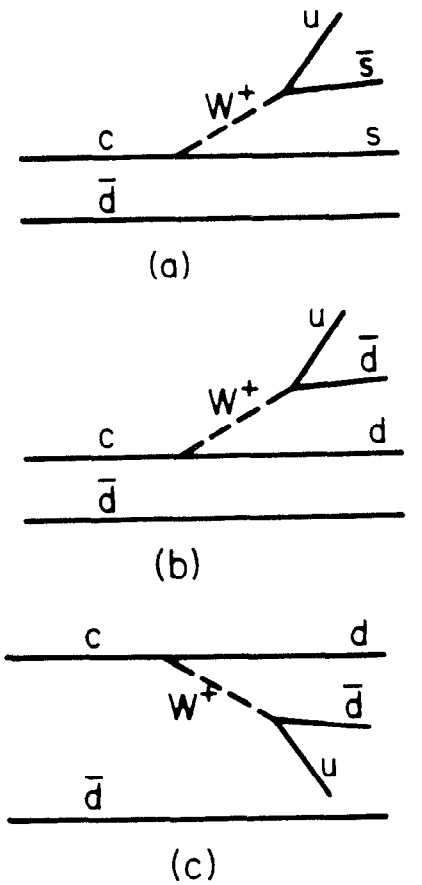

Fig. 4.

Quark diagrams for Cabibbo-suppressed D^+ decays. (a) Cabibbo-suppression at the upper vertex; (b) outer diagram with Cabibbo-suppression at the charm vertex; (c) inner diagram with Cabibbo-suppression at the charm vertex.

of branching ratios for the two types of Cabibbo-suppressed pseudoscalar-vector decays,

$$\frac{B(D^+ \to \rho^0 \pi^+)}{B(D^+ \to \phi \pi^+)} = 0.10 \pm 0.06 \ .$$

We can also make the comparison for the nonresonant case. Here there is a factor of three more phase space for the three pion state as compared with the $KK\pi$. For the ratio of squared amplitudes we have,

$$\left| \frac{Amp(D^+ \to (\pi^+\pi^-\pi^+)_{NR})}{Amp(D^+ \to (K^+K^-\pi^+)_{NR})} \right|^2 = 0.18 \pm 0.06 \ .$$

The comparison of the two types of Cabibbo-suppressed D^+ decays clearly supports the notion of destructive interference between the two diagrams.

II. EXCLUSIVE SEMILEPTONIC DECAYS

The semileptonic decays of heavy quarks are more quantitatively tractable theoretically than the hadronic decays since, as seen in Fig. 5, there are only two quarks in the final state. As a consequence, the semileptonic decays are our main source of information about the K–M matrix.

The Cabibbo-allowed semileptonic decays of charmed mesons are thought to be dominated by the $K\ell\nu$ and $K^*\ell\nu$ final states. In the pseudoscalar case the decay rate is proportional to $|V_{cs}|^2$ and the square of a single transition form factor, which must be evaluated from theoretical models. The branching ratio of $D^0 \to K^- e^+ \nu$ measured by E–691[7] is $3.8 \pm 0.5 \pm 0.6\%$ and is in very good agreement with the Mark III value,[8] $3.9 \pm 0.6 \pm 0.6\%$. The transition rate, the branching ratio divided by the lifetime, is,

$$\Gamma\left(D^0 \to K^- e^+ \nu_e\right) = 9.1 \pm 1.1 \pm 1.2 \ 10^{10} \ \mathrm{sec}^{-1} \ ,$$

in agreement with theoretical expectations.

The main test of the theoretical models is the vector decay, which involves three transition form factors. Experiment E–691 has studied the decay $D^+ \to K^-\pi^+e^+\nu$, which is expected to be dominated by the $\overline{K^{*0}}$ resonance. The main experimental problem is the missing neutrino. Since the mass cannot be reconstructed, there is a problem of signal to background and, in addition, the kinematics is not completely determined.

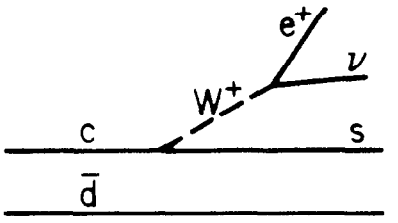

Fig. 5. Quark diagram for the Cabibbo-allowed semileptonic D^+ decay.

To isolate the signal we require the correct decay vertex topology and demand a well identified electron. This decay has the advantage that most backgrounds are charge symmetric with equal numbers of events with the wrong sign combination, $K^+\pi^-e^+$ (and charge conjugate). The $K^-\pi^+e^+$ mass spectrum shown in Figure 6 is obtained with moderately tight vertex cuts. In addition to the 318 right sign events there are 66 of the incorrect combination. The $K\pi$ mass spectrum of these events is shown in Figure 7. To check that the wrong sign data is a reasonable measure of the background, a data sample with tighter vertex and particle identification cuts is shown in Figure 8, where there are 169 right sign and 14 wrong sign events. The number of K^* events, corrected for background and efficiency, is independent of the cuts. The branching ratio, after correcting for the missing $\overline{K^0}\pi^0$ decay, and using the Mark III[9] value for $B(D^+ \to K^-\pi^+\pi^+)$ is found to be,

$$B(D^+ \to \overline{K^{*0}}e^+\nu_e) = (4.5 \pm 0.4 \pm 0.8)\% ,$$

and the nonresonant branching ratio is,

$$D\left(D^+ \to (K^-\pi^+)_{NR}e^+\nu_e\right) = (0.3 \pm 0.2 \pm 0.2)\% ,$$

which is less than 0.7% at the 90% confidence level.

The transition rate for the K^* part is,

$$\Gamma(D^+ \to \overline{K^{*0}}e^+\nu) = (4.1 \pm 0.4 \pm 0.7)\ 10^{10}\ \mathrm{sec}^{-1} ,$$

which is $0.45 \pm 0.09 \pm 0.07$ that of $D \to Ke\nu$.

While the transition rate for the decay $D \to Ke\nu$ is in agreement with theoretical predictions, the small K^* rate is substantially lower than expected.[10] The $D \to Ke\nu$ and $D \to K^*e\nu$ rates measured in E-691 are in agreement with those of Mark III.[8] On the other hand, E-691 finds substantially less $D^+ \to (K^-\pi^+)_{NR}e^+\nu$.

Since the K^* is a vector, we can measure its helicity. In the K^* frame we define the angle θ between the direction of the D^+ and the decay pion. The angular distribution is $W(\theta) = 1 + \alpha\ \cos^2\theta$. The ratio of longitudinal to transverse components, Γ_L/Γ_T, is given by,

$$\Gamma_L/\Gamma_T = \tfrac{1+\alpha}{2} .$$

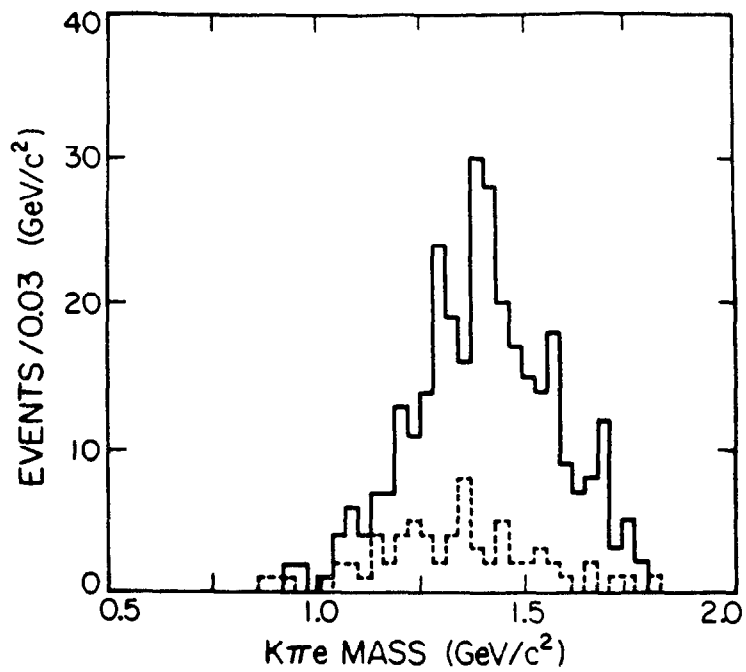

Fig. 6. The $K\pi e$ mass spectra obtained with moderately tight vertex cuts. The solid line corresponds to right sign data $K^{\mp}\pi^{\pm}e^{\pm}$. The dashed curve is for wrong charge combinations $K^{\pm}\pi^{\mp}e^{\pm}$.

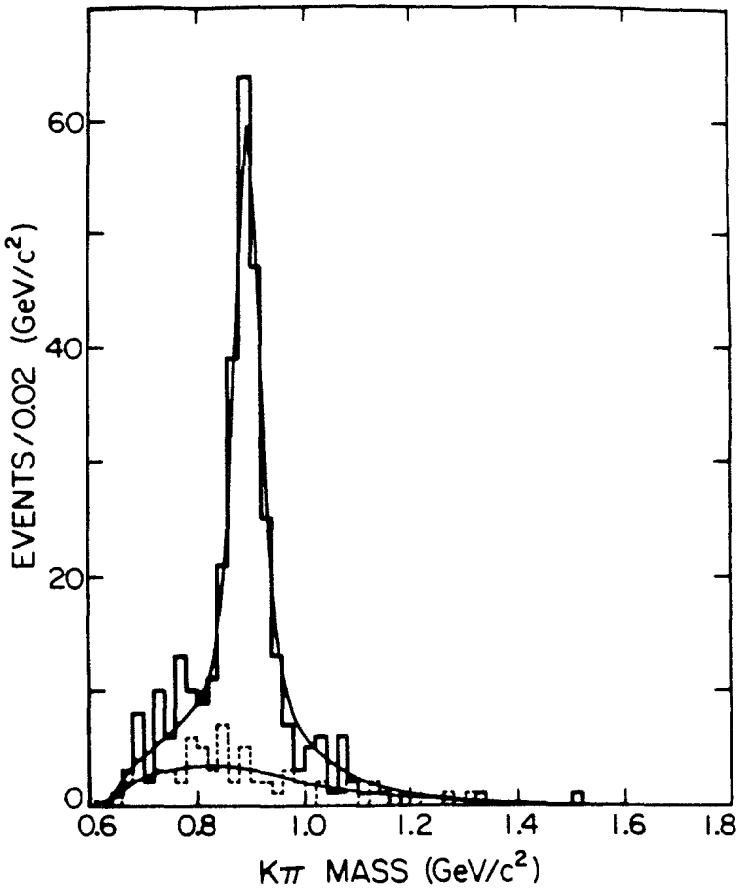

Fig. 7.

The $K^-\pi^+$ mass spectrum of the right sign (solid) and wrong sign (dashed) data of Figure 6. The right sign fit is to a K^* Breit-Wigner plus an S-wave phase space nonresonant contribution. The wrong sign fit is to the same nonresonant shape.

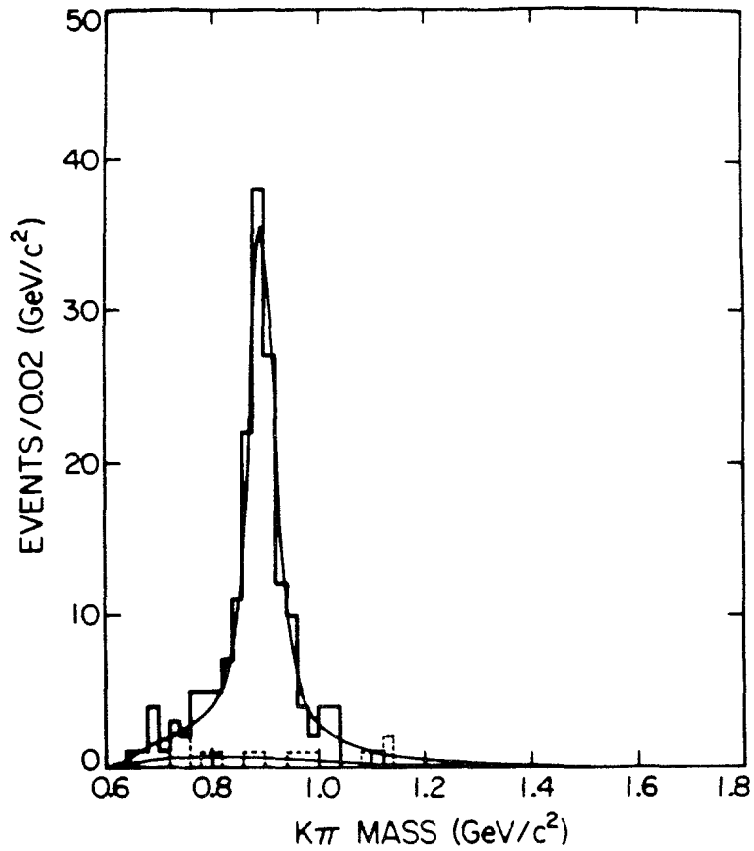

Fig. 8. The same spectra as in Figure 7 but with tighter vertex and particle identification cuts. There are 169 right sign and 14 wrong sign events.

In this notation Γ_T is the sum, $|H_+|^2 + |H_-|^2$, of the individual transverse components referred to in the talk by David MacFarlane.[11] Unpolarized corresponds to $\Gamma_L/\Gamma_T = \frac{1}{2}$, while theoretical predictions tend to give values closer to one.[12]

In order to measure the angle θ, the momentum of the D^+ must be determined. Although the neutrino is undetected, the direction of the D^+ momentum can be evaluated from the locations of the primary and secondary vertices. The D^+ momentum is then determined to within a twofold ambiguity. The solution which has the least momentum for the D^+ has the higher probability of being correct due to the x dependence of D^+ production and the detector acceptance. A Monte Carlo study using simulated events indicates that the mean absolute difference between the true value of $\cos\theta$ and that determined experimentally from the least momentum solution is 0.18. The observed $\cos\theta$ distribution for a distribution which was generated as completely longitudinal is shown in Fig. 9a. The effect of the experimental resolution and the twofold ambiguity is to add a constant to the $\cos^2\theta$ distribution.

The distribution in $\cos\theta$ of the right sign data, in the $K\pi$ mass region, $0.840 < M_{K\pi} < 0.960$ GeV/c^2, is shown in Fig. 9b. Approximately 9% of the events in this plot are background and 3% are nonresonant. The result of a fit to this data is that the ratio of longitudinal to transverse polarization is,

$$\frac{\Gamma_L}{\Gamma_T} = 2.4^{+1.7}_{-0.9} \pm 0.2 \ .$$

In comparing to the ARGUS results[11] for beauty semileptonic decays to the vector, we find two qualitative differences. In the charm case, the fraction of semileptonic decays to the vector is only ~ 0.3, while for beauty it is ~ 0.6. For charm the degree of longitudinal polarization appears to be substantially more than for the case of beauty.

III. OBSERVATION OF L = 1 CHARMED MESONS

The charm quark–light quark system is expected to have L = 1 excited states. These states will have even parity and isospin $\frac{1}{2}$ so that each state has a neutral and charged member. The spectroscopic notation, spin-parity, and the allowed decays to charm plus a single pion are given in Table II. Since the quark spin is not a good quantum number the two 1^+ states are expected to mix.[13]

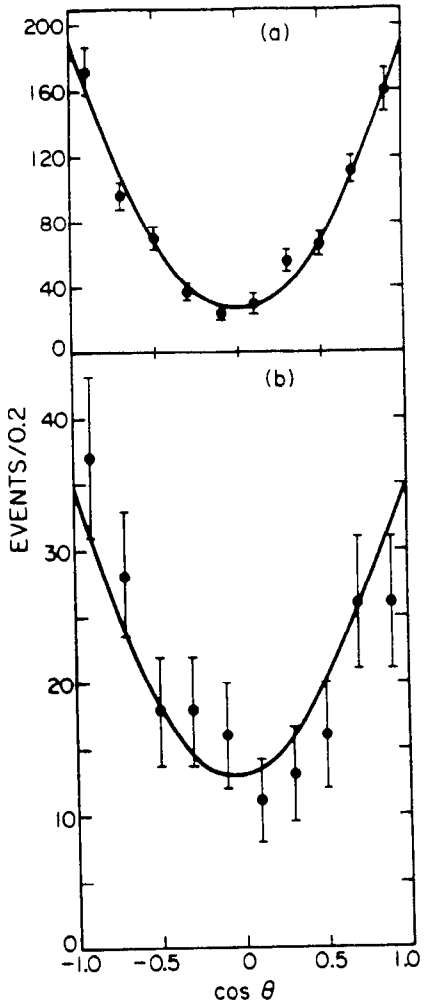

Fig. 9. The distribution in the variable $\cos\theta$, the angle between the decay pion and the D^+ direction in the K^* frame. (a) Monte Carlo simulation for a pure longitudinal ($\cos^2\theta$) distribution. The fit is to $\cos^2\theta$ plus a constant. (b) The data for the mass region $0.840 < M_{K\pi} < 0.960$ GeV/c^2. Approximately 9% of the events are background and 3% are nonresonant.

TABLE II. Spectroscopic notation, spin-parity, and the allowed decays to charm plus a single pion for the L = 1 states.

	J^P	Decays
$^3P_2$	2^+	$D^*\pi$, $D\pi$
$^3P_1$	1^+	$D^*\pi$
$^1P_1$	1^+	$D^*\pi$
$^3P_0$	0^+	$D\pi$

ARGUS[14,15] and CLEO[16] have both seen a broad peak in the $D^{*+}\pi^-$ spectrum at a mass of about 2420 MeV/c^2. For E–691 the sample of 2908 D^*'s shown in Fig. 10 for the modes $D^0 \to K^-\pi^+$ and $D^0 \to K^-\pi^+\pi^-\pi^+$, are used in a search for $D^*\pi$ states. The cuts are defined by studying the efficiency using Monte Carlo simulated events, and by evaluating the background using the wings of the D^+ mass spectrum. The resulting mass difference spectrum, $M_{D^{*+}\pi^-} - M_{D^{*+}}$, is shown in Fig. 11. A 4σ peak is observed at $\Delta M = 419 \pm 8$ MeV corresponding to a mass of 2428 ± 8 MeV/c^2, with a width of 58 ± 14 MeV/c^2. The fraction of D^{*+}'s which came from the decay of this D^{**} (2420) is found to be $0.13^{+0.03}_{-0.04} \pm 0.02$. E–691 confirms the previous observation of this state by ARGUS and CLEO. This state can be either of the 1^+ states or the 2^+ or any combination of the three.

The $D\pi$ spectrum is best studied using the charged D since there is a large background of D^0's from the decays of $D^*(2010)$'s. The D^+ signal used is shown in Fig. 12, which contains 4135 signal events from the mode $D^+ \to K^-\pi^+\pi^+$. The mass difference spectrum, $M_{D^+\pi^-} - M_{D^+}$, is shown in Fig. 13. A 5σ peak is found at a mass difference of 590.7 ± 3.2 MeV/c^2, corresponding to a mass of 2459 ± 3 MeV/c^2. The peak contains 153^{+42}_{-37} events, has a width of 20^{+11}_{-8} MeV/c^2, and corresponds to $0.07 \pm 0.02 \pm 0.02$ of the D^+'s coming from this state. In Fig. 13 the feedthrough from the $D^{**}(2420)$ decay to $D^{*+}\pi^-$ with the D^{*+} decaying to D^+ and unobserved photons or π^0s is seen. Also shown in the figure is the fit, which includes the expected contribution of this feedthrough using the E–691 measurements of the $D^{**}(2420)$. The new state at 2459 is believed to be the 2^+ due to the narrow width and the larger mass.

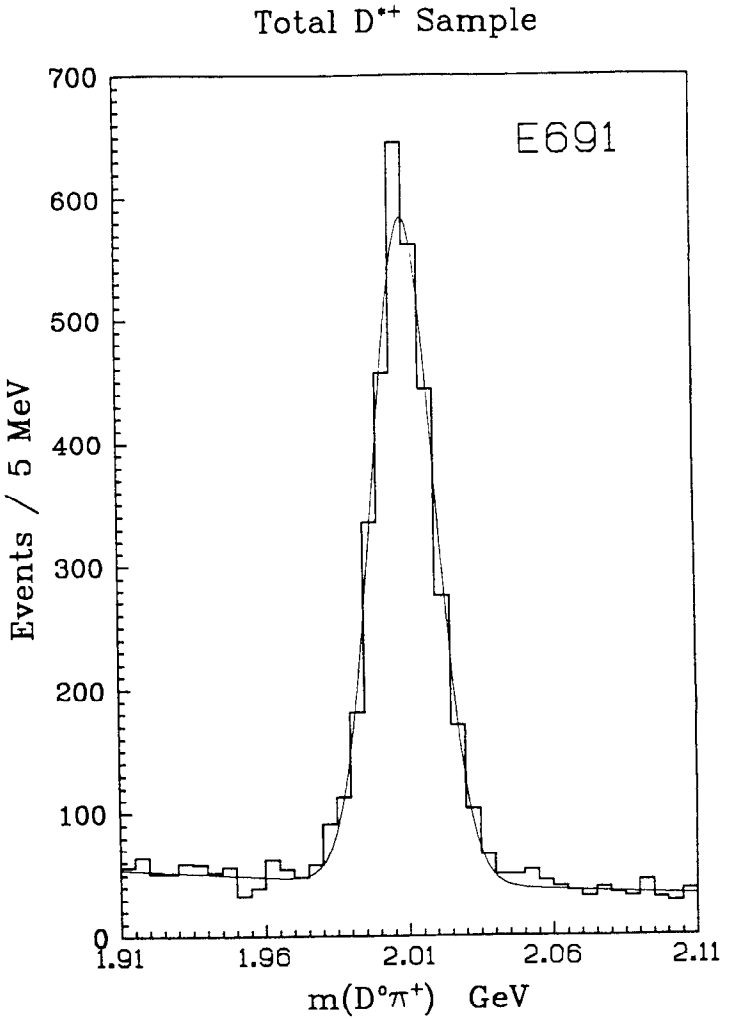

Fig. 10. The sample of 2908 D^{*+}'s used in the search for higher mass resonances decaying to $D^{*+}\pi^-$. The D^{*+}'s decay to a π^+ and a D^0 with the D^0 going to $K^-\pi^+$ or $K^-\pi^+\pi^-\pi^+$.

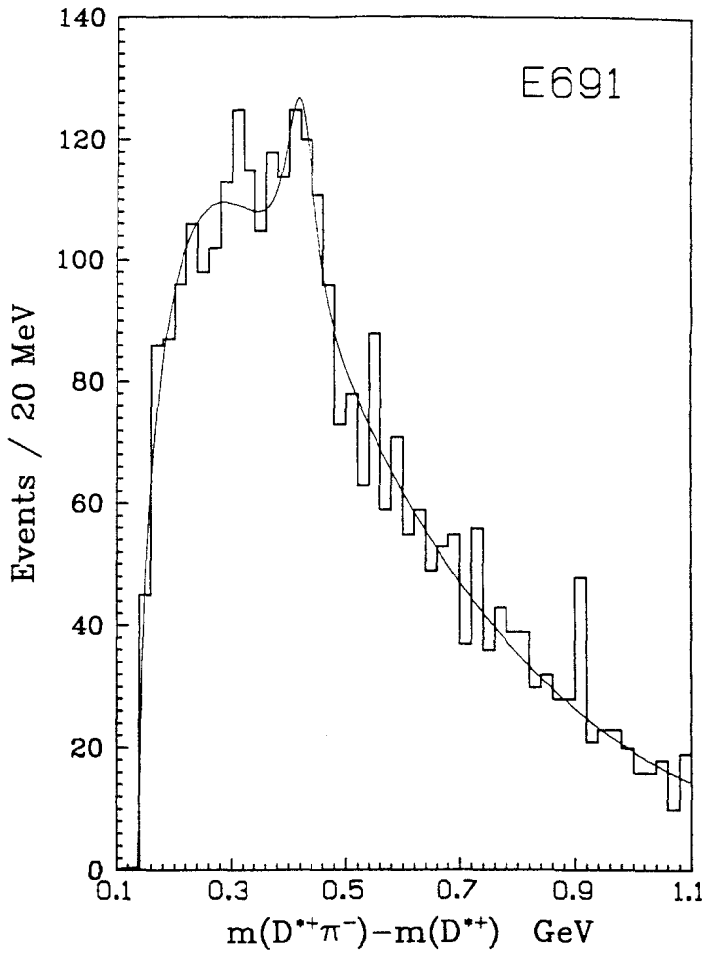

Fig. 11. The mass difference spectrum, $M_{D^{*+}\pi^-} - M_{D^{*+}}$. A 4σ peak is observed at $\Delta M = 419 \pm 8$ MeV confirming the previous observation of this state by ARGUS.

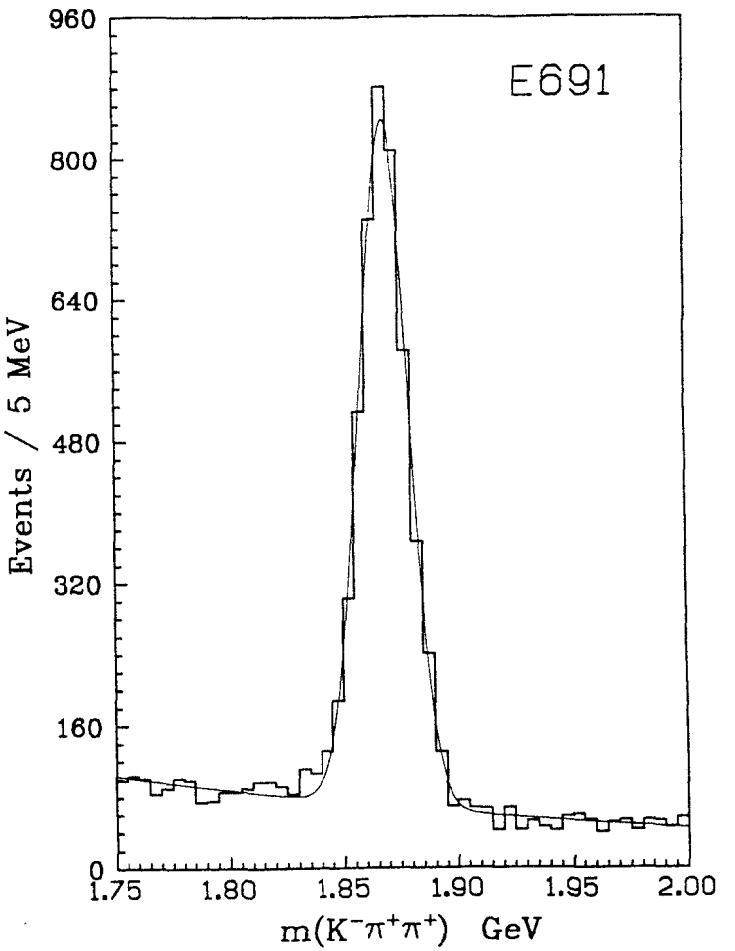

Fig. 12. The sample of 4135 D^+'s used in the $D\pi$ search. The mode is $D^+ \to K^-\pi^+\pi^+$.

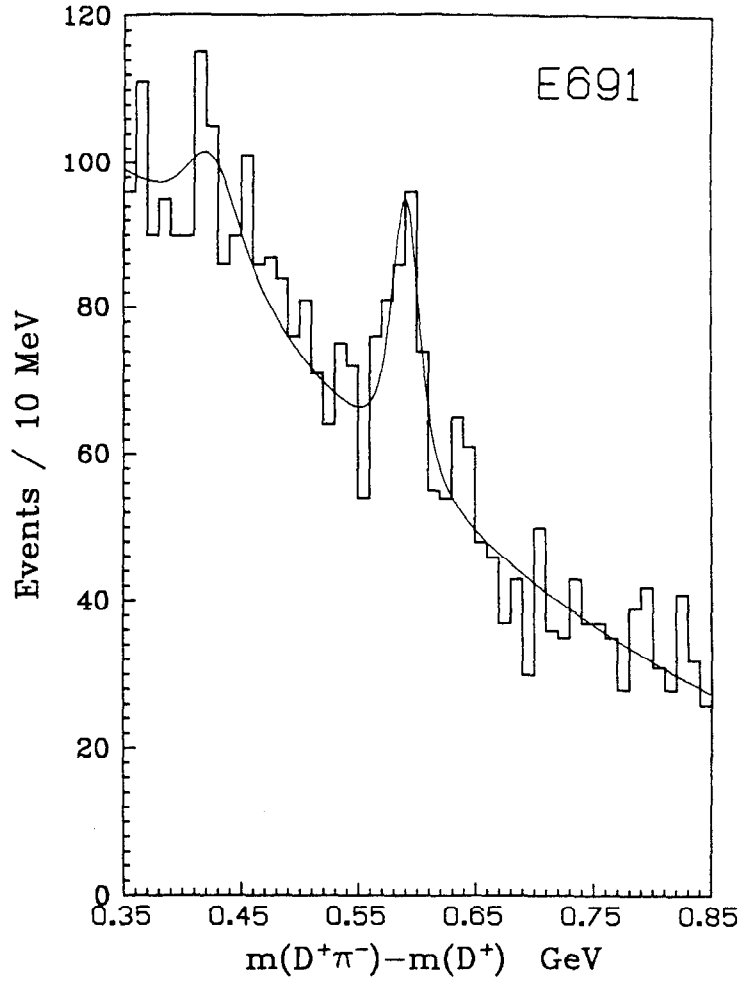

Fig. 13. The mass difference spectrum, $M_{D^+\pi^-} - M_{D^+}$. A 5σ peak is seen with $\Delta M = 590.7 \pm 3.2$ MeV/c^2.

IV. OBSERVATION OF THE Σ_c^0

Finally, since two different values for the mass of the Σ_c have been reported,[17,18] we show the E–691 data on the mass difference $M_{\Lambda_c^+\pi^-} - M_{\Lambda_c^+}$. A clear peak is observed in Fig. 14 at a mass difference of $168.4 \pm 1.0 \pm 0.3$ MeV/c^2. This is in agreement with the previously determined ARGUS value[17] of 167.0 ± 0.5 MeV/c^2 and in disagreement with the value $178.2 \pm 0.4 \pm 2.0$ MeV/c^2 determined by E400.[18]

V. CONCLUSIONS

The three pion decay of the D_s^+ is observed but at a rate indicating that the annihilation process is not dominant. The three pion decay of the D^+ provides clear evidence for destructive interference in Cabibbo-suppressed D^+ decays.

The $D^+ \rightarrow \overline{K^{*0}} e^+ \nu$ semileptonic decay is observed with about 0.5 of the expected branching ratio and with a large longitudinal polarization. Both of these results appear to be qualitatively different from the analogous situation in B decays.

Two higher mass resonances are observed in the D system. In the $D^{*+}\pi^-$ spectrum the state at a mass of 2420 MeV/c^2, previously seen by ARGUS and CLEO, is confirmed. A new and narrower state is seen in the $D^+\pi^-$ spectrum at a mass of 2459 MeV/c^2. This is probably the 2^+. The Σ_c^0 is also observed at a mass $168.4 \pm 1.0 \pm 0.3$ MeV/c^2 above the Λ_c^+ mass.

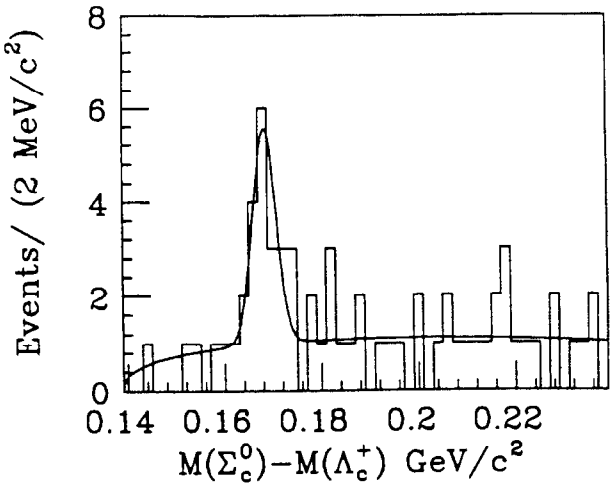

Fig. 14. The mass difference spectrum, $M_{\Lambda_c^+\pi^-} - M_{\Lambda_c}$.

REFERENCES

1) J.C. Anjos *et al.*, *Phys. Rev. Lett.* **58**, 311 (1987).

2) J.C. Anjos *et al.*, *Phys. Rev. Lett.* **58**, 1818 (1987).

3) J.R. Raab *et al.*, *Phys. Rev. D* **37**, 2391 (1988).

4) J.C. Anjos *et al.*, *Phys. Rev. Lett.* **60**, 1379 (1988).

5) J.C. Anjos *et al.*, *Phys. Rev. Lett.* **60**, 1239 (1988).

6) J.C. Anjos *et al.*, *Phys. Rev. Lett.* **60**, 897 (1988).

7) J.C. Anjos *et al.*, Submitted to the XXIVth Conference on High Energy Physics, Munich, Federal Republic of Germany (1988).

8) R. Schindler, Mark III Collaboration, SLAC-PUB-4135, 1986; D. Coffman, Ph.D. Thesis, CALT-68-1415 (1987).

9) J. Adler *et al.*, *Phys. Rev. Lett.* **60**, 89 (1988).

10) M. Wirbel, B. Stech, and M. Bauer, *Z. Phys.* **C29**, 637 (1985).

11) D. MacFarlane, contribution to this conference.

12) The model of Ref. 10 gives $\Gamma_L/\Gamma_T = .92$, although this is not stated in the paper. Other useful references on polarization are: J.G. Körner and G.A. Schuler, *Z. Phys.* **C38**, 511 (1988) and M. Bauer and M. Wirbel, Heidelberg preprint HD-THEP-88-22 (1988).

13) J.L. Rosner, *Comments on Nuclear and Particle Physics* **16**, 109 (1986).

14) H. Albrecht *et al.*, *Phys. Rev. Lett.* **56**, 549 (1986).

15) J.C. Yun, Ph.D. Thesis, Carleton University, Ottawa, Canada (1987). Note that these results are more complete and somewhat different from those of Ref. 14.

16) C. Bebek *et al.*, Proceedings of the 1987 Intl. Symp. on Lepton and Photon Interactions at High Energies, page 215, Hamburg (1987).

17) D.B. MacFarlane, Proceedings of the 23rd International Conference on High Energy Physics, Berkeley, California, 1986; H. Albrecht *et al.*, DESY 88-058 (1988).

18) M. Diesburg *et al.*, *Phys. Rev. Lett.* **59**, 2711 (1987).

Study of $K^+ \to \pi^+ e^+ e^-$, and Search for $K^+ \to \pi^+ \mu^+ e^-$ at BNL

Vladimir Chaloupka
University of Washington

The subject of rare K decays has been thoroughly reviewed at this Summer Institute, both in its theoretical[1] and experimental[2] aspects. Therefore, this written version of my talk will be very brief, and I will try to limit duplication of discussions contained in these reviews, as well as in our first publication.[3]

I will be reporting on the present status and future plans of the E777 Collaboration.[4] Our spectrometer is located in the 5.8 GeV/c positively charged, unseparated secondary beam at the Brookhaven National Laboratory Alternating Gradient Synchrotron. The beam optics is shown on Fig. 1; typically, a primary flux of 6×10^{11} protons per pulse resulted into a secondary flux of some 10^7 K per pulse, accompanied by 2×10^8 π^+/p per pulse. In addition, the spectrometer is exposed to the flux of muons from π^+ and K^+ decays, and to the halo of particles produced at the collimators. It turned out that it is this halo which is the limiting factor for the sensitivity achievable with the present setup. The primary beam is typically 24 - 28 GeV/c with 1 sec acceleration and 1 - 1.6 sec 'flat top'. The quotation marks indicate the problems with microstructure of the beam (at harmonics of 60 Hz), which increase the instantaneous rate; this is a subject of a constant improvement effort at BNL.

The spectrometer in plan view is shown on Fig. 2. The apparatus is optimized for the decay $K^+ \to \pi^+ \mu^+ e^-$. The purpose of the first bending magnet M1 is to direct most of the negative particles to the left side specialized in detection of e^- (i.e. with excellent rejection of π^-). This is accomplished by two atmospheric-pressure H_2 Cerenkov counters C1L and C2L, followed by a lead-scintillator shower calorimeter. The positive particles are deflected towards the right-hand side, which has to provide a good detection of π^+/μ^+ (i.e., a good rejection of e^+). This is done by two atmospheric-pressure CO_2 counters C1R and C2R, followed again by a shower calorimeter. The π^+/μ^+ separation is accomplished by a muon calorimeter consisting of eight alternating layers of

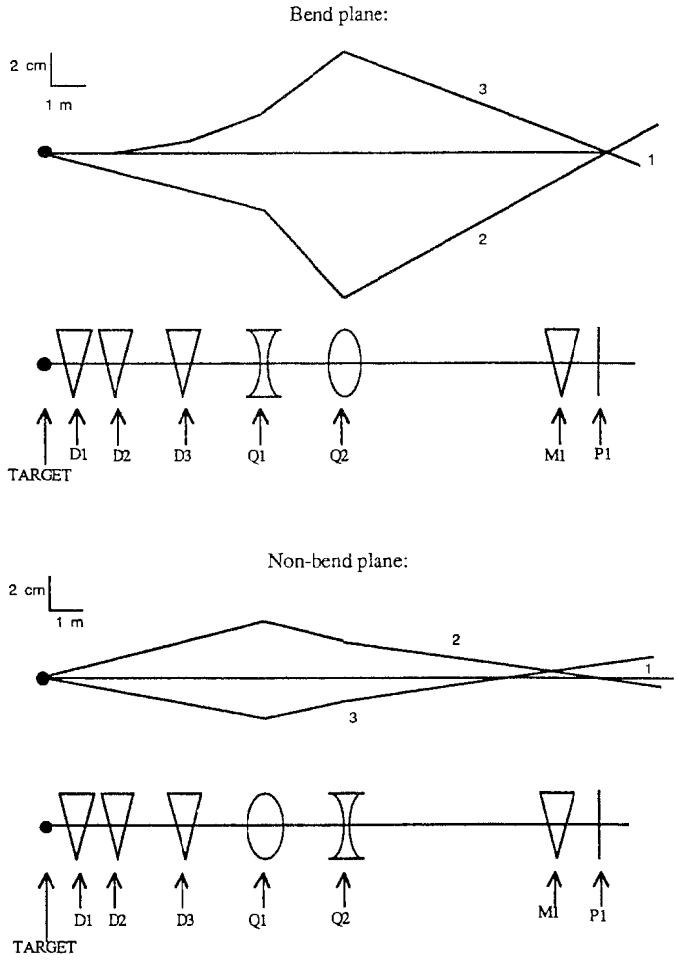

Fig. 1. Schematic view of the D6 beamline, with ray 1 (central momentum, on axis), ray 2 (central momentum, 15 mrad off-axis vertically and horizontally), and ray 3 (5% low in momentum, on axis horizontally, 10 mrad off-axis vertically).

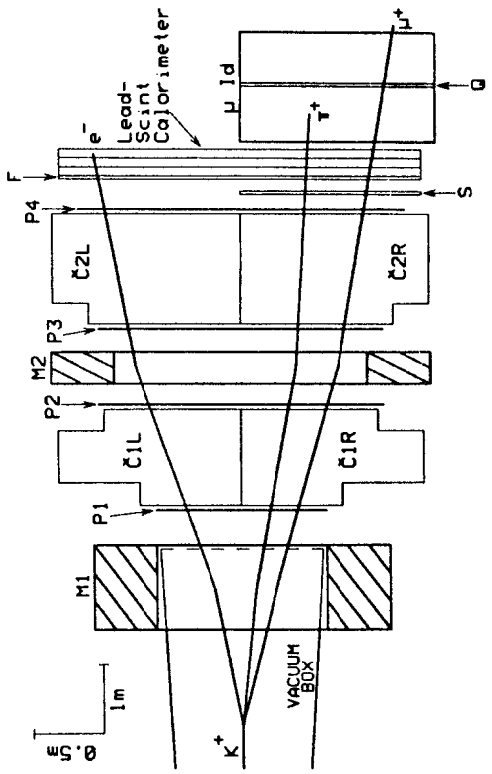

Fig. 2. Plan view of the E777 spectrometer.

9-cm steel plates and proportional-tube chambers. The second bending magnet M2 is preceeded by proportional wire chambers P1 and P2, and followed by the chambers P3 and P4, and provides the momentum analysis of the decay products. Each of the wire chamber stations has three planes of wires (vertical, and at $\pm 18.4^o$ to the vertical), with 2 mm wire spacing. The magnet M2, with its momentum kick of 150 MeV/c , also serves to decouple the delta ray production in C1 from C2, thus enabling an efficient use of the two counters in coincidence. To minimize the amount of material in the beam region, both C1 and C2 were built as a single counter, separated into the right (CO_2) and left (H_2) gas volumes by a 5 mil Mylar membrane. Because of the low index of refraction of hydrogen and resulting low yield of photoelectrons, the phototubes were placed inside the gas volume to avoid light loss at windows. Before installing the phototubes, we performed laboratory tests of the possibility of 'hydrogen poisoning' of the phototubes. We did find some H_2 permeation, but the rate is negligible over the lifetime of the experiment.The scintillator hodoscopes S and F were mainly used for triggering purposes. Through the whole spectrometer, the region containing most of the secondary beam was deadened by standard procedures (baffles etc.).

The most critical demands on the spectrometer are in respect to the particle identification, and the apparatus performed more or less as designed. We have studied the efficiencies and misidentification probabilities of the various components, using the decays $K^+ \to \pi^+\pi^+\pi^-$ and $K^+ \to \pi^-\pi^0, \pi^0 \to e^+e^-\gamma$, in the running environment. The results, at a typical beam intensity and beam spill structure, are shown in Tables 1 and 2.

As far as the mass resolution is concerned, we fell short of the 'inherent' resolution (predicted from the PWC wire spacing, multiple scattering and other known effects) by about factor of two. We believe that this stems from an inadequate knowledge of the magnetic field. Figure 3 illustrates the significant fringe field along the spectrometer axis. The existing field mapping was done without the Cerenkov counters in place, and the iron pipes shielding the 36 phototubes are expected to disturb the field. For the physics addressed by our existing data, the resolution was adequate. For the next experiment (see below), we will remeasure the field — it will have to be done after the experiment, as it will require dismantling the Cerenkovs to a skeleton containing the iron shielding but accessible to the measuring probe. More detailed description

Table 1: Particle Identification Efficiencies

	C1	C2	Shower	μ Identifier	Total
π^+	0.99	0.99	0.96	----	0.94
μ^+	0.99	0.99	> 0.99	0.98	0.95
e^-	0.90	0.90	0.99	----	0.80
e^+	0.98	0.97	0.99	----	0.94

Table 2: Particle Misidentification Probabilities

Misident.	C1	C2	Shower	μ Identifier	Total
π^- as e^-	0.002	0.002	0.14	------	6×10^{-7}
μ^- as e^-	0.002	0.002	> 0.05	------	$<2\times10^{-7}$
e^+ as π^+	0.02	0.03	0.14	------	8×10^{-5}
e^+ as μ^+	0.02	0.03	0.14	< 0.01	$<8\times10^{-7}$
π^+ as μ^+	----	----	----	0.04	0.04

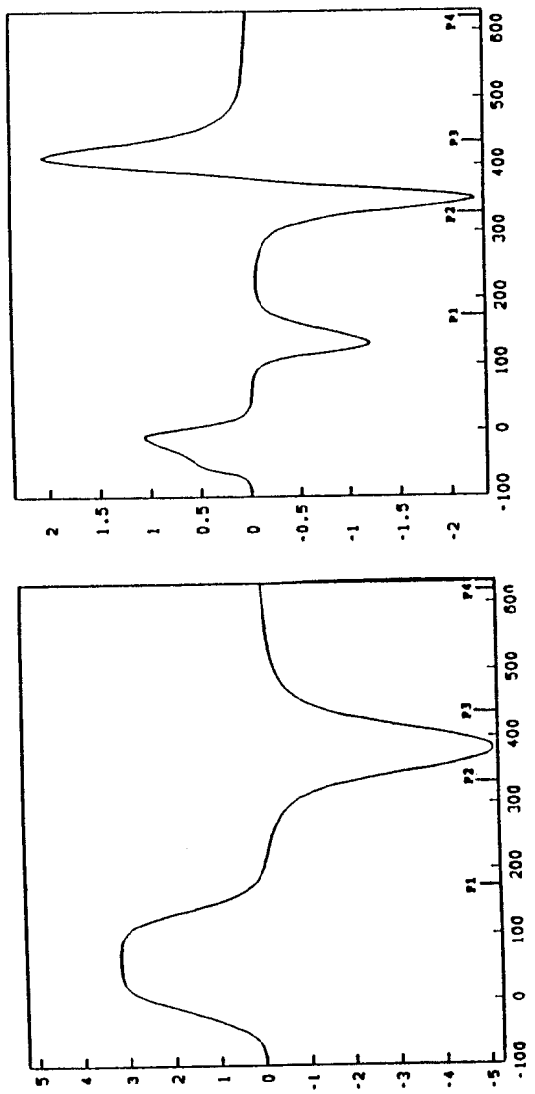

Fig. 3. The field profile (kGauss) along the beam (z) direction (cm). Also indicated are the positions of the PWC's.
a) vertical field at x=0 and y=0.
b) longitudinal field at x=0 and y=20 cm.

of the spectrometer and its performance can be found in Refs. 3,5d '

The data acquisition was accomplished by a multilayered fasctr trigger, followed (as of the 1988 run) by an on-line data processing 'n processor farm'. The fast trigger was a combination of four separrig

- PIMUE trigger, sensitive to the decay $K^+ \to \pi^+\mu^+e^-$(an K $\pi^+\pi^0, \pi^0 \to \mu^+e^-$).
- EE trigger, sensitive to the rare decay $K^+ \to \pi^+e^+e^-$(an K $\pi^+\pi^0, \pi^0 \to e^+e^-$) as well as to the plentiful 'calibration anrm tion' decays $K^+ \to \pi^+\pi^0, \pi^0 \to e^+e^-\gamma$. This trigger was usuares by a factor of 8.
- 'high-mass EE trigger': as above but optimized for detection onts high invariant mass $m(e^+e^-)$. The resulting suppression of :on Dalitz-pair decays enabled accepting all triggers of this kind pre = 1).
- 'TAU' trigger, sensitive to the decays $K^+ \to \pi^+\pi^+\pi^-$, presc by and used for calibration and debugging purposes. The 'miroc farm' consists of 16 ACP (Advanced Computer Project[8]) micoce acquiring data from Smart Crate Controllers, performing c-fi and track-fitting, and writing good events (with 3-4 tracks a vertex) on tape via a microVAX II workstation. Subseqi an (particle identification, stepping through magnetic field etc.)her formed off-line.

Our running record reflects a typical debugging and learningve, ually transforming into efficient running, identification of limitingors proposal for further improvements:

December 1986 - January 1987: first physics data; theult published.[3]

February 1987 - May 1987: first data on the decay $K^+ \to {}^+e^-$ results are submitted for publication.[7]

February 1988 - June 1988: the main data-taking run. The dedi is in progress; physics results are expected in early 1989.

A comprehensive summary of the past, present and possible re s of the E777 physics is shown in Table 3. I will now briefly discuss tdi physics channels.

Table III: Overview of some E777 Physics: Past, Present and Future.

	K+ -> pi+e+e-		K+ -> pi+mu+e-		K+ -> mu+e+e-nu K+ -> e+e+e-nu		pi0 -> e+e-	
	evts	BR*10**7 matrix elem.	evts	BR 90% C.L.	evts	BR*10**7	evts	BR*10**7
previous exps.	41	2.7+-0.5 ?	0	5. *10**-9	14 4	11+-3 2+2-1	8 59 0	2.2+2.4-1.1 1.7+-0.7 1.2 (90% CL)
E777 publ. or ready	200	+-0.4 vector over scalar /also: limits on low m(e+e-) /	0	1.1*10**-9	---		---	
data at hand (1988 run)	700	+-0.2 quantitative study	0 ?	2.*10**-10	~ 150 events ~ 50 -"-		?	
estimate for possible E777 offspring(s)	2700	+-0.1 detailed study with H2 in C1R and C2R (E$51)	0 ?	10**-11 with two-stage beam	~ 600 events ~ 200 events	80 events with the fast beam PWC and optimization of the resolution (E$51)		

The Decay $K^+ \to \pi^+ e^+ e^-$:

In our 1987 data we have obtained about 200 events of this rare decay, compared to 41 events seen in the only previous experiment which has observed this decay.[9] Consequently, we were able to study the nature of the decay mechanism in some detail, and we find the matrix element compatible with the Standard Model (see Fig. 4). The precision in the determination of the branching ratio suffers from the fact that this decay mode was a by-product of an experiment optimized to search for $K^+ \to \pi^+ \mu^+ e^-$; the preliminary value is not incompatible with the previous result, and the final value will be available shortly. We estimate that we have about 700 events of this decay mode in the 1988 data - this will enable us to do a quantitative analysis of the matrix element, and to improve the knowledge of the branching ratio considerably. In order to perform a detailed study of this channel, we have submitted a proposal to BNL to run an experiment optimized for this mode.[10] The main change will be replacing the CO_2 in the right-hand side Cerenkov counters by H_2 — this is expected to decrease the trigger rate significantly, thus enabling us to raise the beam intensity. The other improvements and goals of this proposal are discussed below (the section on $\pi^0 \to e^+ e^-$).

The Decay $K^+ \to \pi^+ \mu^+ e^-$:

From our 1987 data, we have obtained an upper limit of 1.1×10^{-9} on this decay mode[7]; this represent an improvement by a factor of 4.4 on the previous upper limit.[11] As a by-product of this measurement, we have obtained an upper limit of 7.8×10^{-8} (90% C.L.) on the decay $\pi^0 \to \mu^+ e^-$; this is comparable with the upper limit deduced[12] from previous experiments. To illustrate our result, Fig. 5 shows a scatter plot of the effective mass $m(\pi^+ \mu^+ e^-)$ versus the vertex quality of the candidate events. Although there are no events inside the signal area (compare this with Fig. 6 showing similar distribution for the 'TAU' decays), there are a few events which come close, and we might expect a problem when statistical sensitivity will increase. However, for the 1988 run, we have improved the particle identification (Cerenkov mirror realignment, better shower counter calibration etc.), in order to keep our systematics below the level of the statistical sensitivity.

We estimate the statistical sensitivity of our 1988 data for $K^+ \to \pi^+ \mu^+ e^-$to be about 2×10^{-10}. A major upgrade of the setup (including

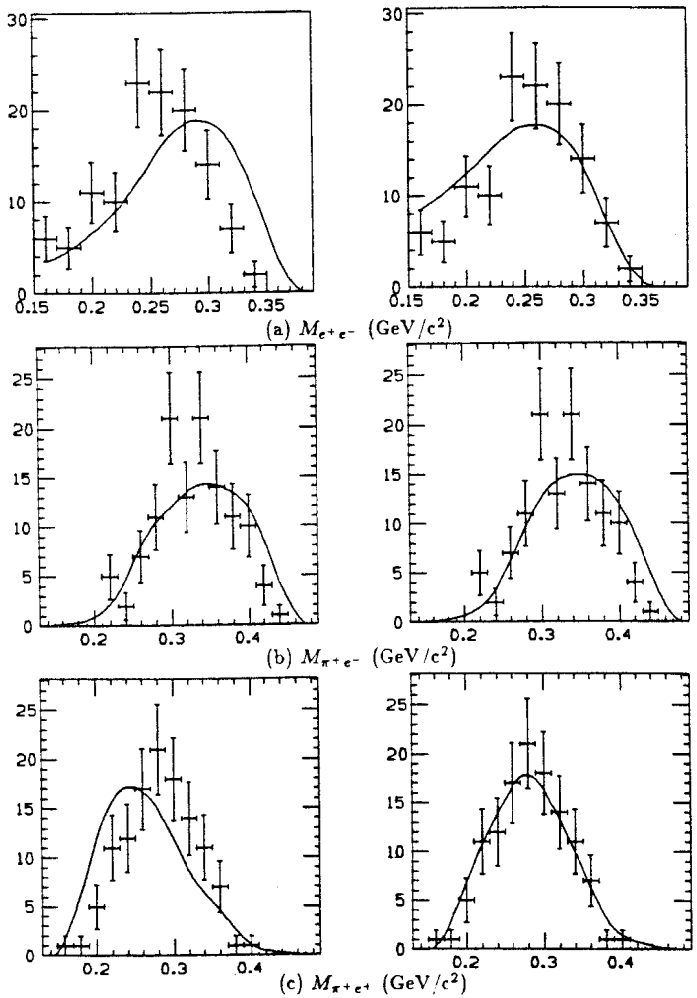

Fig. 4. Distributions of the invariant masses of the two-particle combinations from the decay $K^+ \to \pi^+e^+e^-$, from the May 1987 sample. The scalar (phase-space) simulation is superimposed on the left, the Standard Model (vector) prediction is on the right.

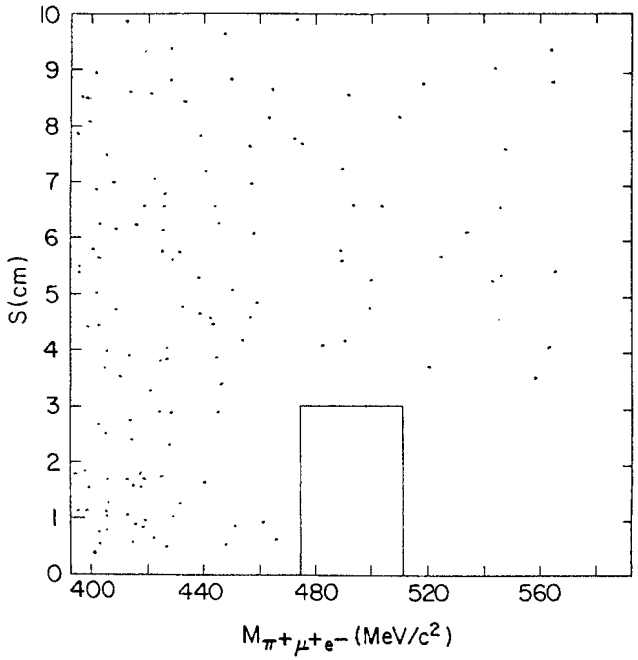

Fig. 5. The scatter plot of the invariant mass $m(\pi^+\mu^+e^-)$ vs. the vertex quality s (cm) (the square root of the sum of squares of the distances of the tracks to a common point), for the candidate events for the decay $K^+ \to \pi^+\mu^+e^-$. The rectangle represents the signal region expected to contain 90% of the signal.

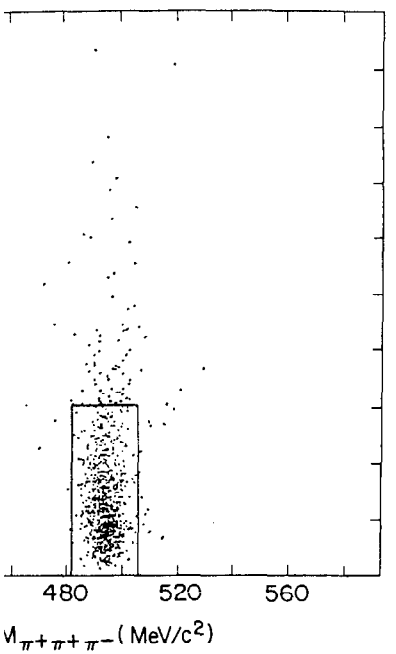

. 5, for the decay $K^+ \to \pi^+\pi^+\pi^-$.

a new two-stage beam) may make it possible to achieve the level of 10^{-11} in 1990/1991; at present, we are investigating this possibility.

The Decays $K^+ \to \mu^+e^+e^-\nu$ and $K^+ \to e^+e^+e^-\nu$:

These allowed but rare decays are expected to proceed through second order weak-electromagnetic interaction. As a by-product of our experiment, we expect to significantly increase the world statistics on these decays. The difficulty of theoretical calculations for these processes reduces somewhat the importance of improving the experimental uncertainties on the branching ratios, but information on the matrix elements may turn out to be of some interest. Obviously, we will also be looking for possible surprises in these final states.

The Decays $K^+ \to \pi^+X^0, X^0 \to e^+e^-$:

A 'non-exotic' but still interesting example of this decay is $\pi^0 \to e^+e^-$. Until recently, the two experiments[13,14] which claimed to have seen this decay provided an indication that the decay rate might be considerably larger than the 'unitarity' prediction[15] of 4.8×10^{-8}. However, recently the SINDRUM group at SIN obtained an upper limit of 1.2×10^{-7} for this branching ratio.[16] In the new experiment E851,[10] we will have an improved mass resolution and detectors optimized for e^+e^- physics. In addition, we plan to take full advantage of a fast PWC installed in the beam during our last run to constrain the measurement of the incident K^+. We estimate that we will be able to obtain 80 events of this decay above a reasonable background, and hopefully resolve the present confusion. In addition to the π^0, there are more 'exotic' possibilities of $X^0 \to e^+e^-$. In our first publication,[3] we have set an upper limit of 5×10^{-7} for the region below 100 MeV/c^2. In the new experiment, with better rejection of the low $m(e^+e^-)$ background from the K^+ Dalitz decays, we hope to achieve a sensitivity at the 10^{-8} level. Last but not least, the same sensitivity will apply to an exploration of the entire region between $2m_e$ and $(m_K - m_\pi)$ for states decaying to e^+e^-.

References:

1. I. Bigi, 'Precious Rarities - On Rare Decays of K, D and B', these Proceedings.
2. S. Smith,'Experimental Searches for Rare Decays', these Proceedings.
3. N.J.Baker **et al**, 'Search for Short-Lived Neutral Particles Emitted in K^+ Decay', PRL **59**,2832 (1987).
4. Experiment E777 is a BNL — SIN — University of Washington — Yale University Collaboration : C.Alliegro, C.Campagnari, V.Chaloupka, P.S.Cooper, J.Egger, H.A.Gordon, N.J.Hadley, W.D.Herold, E.A.Jagel, H.Kaspar, D.M.Lazarus, A.M.Lee, H.J.Lubatti, P.Rehak, M.E.Zeller and T.Zhao.
5. C.Campagnari, 'A Search for the Decay $K^+ \to \pi^+\mu^+e^-$', Ph.D.Thesis, Yale University 1988.
6. E.Jagel, 'An Experimental Study of the Rare K+ Meson Decay $K^+ \to \pi^+e^+e^-$', Ph.D.Thesis, University of Washington 1988.
7. C.Campagnari **et al**, 'Search for the Decay $K^+ \to \pi^+\mu^+e^-$', submitted to PRL (to appear Oct. 31, 1988).
8. I. Gaines **et al**, 'The ACP Multiprocessor System At Fermilab', FERMILAB-Conf-87/21, presented at the Computing in High Energy Physics Conference, Asilomar State Beach, CA Feb. 1987.
9. P.Bloch et **al**, PL **56B**, 201 (1975).
10. H.A.Gordon **et al**, BNL Proposal E851. This proposal has now been approved to run in Winter/Spring 1989 running period.
11. A.M.Diamant-Berger **et al**, PL **62B**, 485 (1976).
12. D.Bryman, PR **D26**, 2538 (1982) P.Herzeg and C.M.Hoffman, PR **D29**, 1954 (1984).
13. J.Fischer **et al**, PL **73B**, 364 (1978).
14. J.S.Frank **et al**, PR **D28**, 423 (1983).
15. L.Bergstrom, Z.Phys. **C14**, 129 (1982).
16. E.Engfer, reported in 3rd Conference on the Intersections Between Particle and Nuclear Physics, Rockport, ME (1988).

Search for Flavor Changing Neutral Currents $K^0_L \to \mu^\pm e^\mp$, e^+e^- and $\pi^0 e^+e^-$

W.M. Morse, E. Jastrzembski, R.C. Larsen, and L.B. Leipuner
Department of Physics
Brookhaven National Laboratory, Upton, NY 11973

H.B. Greenlee, H. Kasha, E.B. Mannelli, M. Mannelli,
K.E. Ohl, S.F. Schaffner, and M.P. Schmidt
Department of Physics
Yale University, New Haven, CT 06511

ABSTRACT

We report on a search for the flavor-changing neutral-current decays $K^0_L \to \pi^0 e^+e^-$, $K^0_L \to e^+e^-$ and $K^0_L \to \mu^\pm e^\mp$. Limits obtained for these processes are $BR(K^0_L \to \pi^0 e^+e^-) < 3.2 \times 10^{-7}$, $BR(K^0_L \to e^+e^-) < 1.2 \times 10^{-9}$, $BR(K^0_L \to \mu^\pm e^\mp) < 1.9 \times 10^{-9}$.

The decays $K^0_L \to \pi^0 e^+e^-$ and $K^0_L \to e^+e^-$ occur as a consequence of strangeness changing neutral currents and are highly suppressed in the Standard Model. The decay $K^0_L \to \mu^\pm e^\mp$ is forbidden by lepton generation number conservation. The decay $K^0_L \to \pi^0 e^+e^-$ through one photon exchange is a CP violating process. Decays to $\pi^0 e^+e^-$ can proceed through vector or scalar currents, while decays to e^+e^- are mediated by axial vector or pseudoscalar currents.

The decay $K^+ \to \pi^+ e^+e^-$ is known to occur[1] with a branching ratio of $(2.7 \pm 0.5) \times 10^{-7}$. Theoretical estimates[2] of the decay rate for the CP-conserving decay $K^0_S \to \pi^0 e^+e^-$ range from one-tenth of the rate for $K^+ \to \pi^+ e^+e^-$ to 2.5 times that rate while the rate for similar $K^0_L \to \pi^0 e^+e^-$ decays is expected to be reduced by the factor ε^2 in the absence of any direct CP-violating amplitude. Theoretical estimates[2] of the transition $K^0_L \to \pi^0 e^+e^-$ range from $2 \cdot 10^{-12}$ to $3 \cdot 10^{-11}$. The branching ratio for a CP-conserving decay transition through two virtual photons is expected to be below 10^{-11}. The decay $K^0_L \to \pi^0 e^+e^-$ is then an excellent window to search for light scalar particles that couple to e^+e^-. In such searches the K^0_L branching ratio is expected to be about 8.4 times the K^+ branching ratio to π^+ and a light scalar.[3] Furthermore, some non-standard models of CP-invariance violation[4] predict branching ratios higher than $3 \cdot 10^{-11}$. The present 90% confidence level limit[5] for this decay is $BR(K^0_L \to \pi^0 e^+e^-) < 2.3 \cdot 10^{-6}$.

The decay $K^0_L \to e^+e^-$ is suppressed in the standard model with respect to the observed rare decay $K^0_L \to \mu^+\mu^-$ because of the small value of m_e/m_K. The unitarity limit[6] for $K^0_L \to e^+e^-$ is $BR(K^0_L \to e^+e^-) > 2.5 \times 10^{-12}$. This decay is then particularly sensitive to new interactions proceeding through pseudoscalar currents. The present limit[7] is $BR(K^0_L \to e^+e^-) < 4.5 \times 10^{-9}$. The unitarity limit for $K^0_L \to \mu^+\mu^-$ is $BR(K^0_L \to \mu^+\mu^-) > (7.0 \pm 0.3) \times 10^{-9}$.

The data for this study comes from an experiment conducted at the Brookhaven AGS. The diagram of Fig. 1 shows a schematic representation of the experimental apparatus. A neutral beam, produced in the forward direction by the interaction of 24 GeV protons on a copper target, passed 7.47 m through vacuum and an 8 Tesla-meter clearing field, into a 2.87 m long decay region. Gamma rays from the target were attenuated by a 2.5 cm lead beam plug. The momenta of the charged particles from K-decays were then determined by a magnetic spectrometer made up of two upstream sets of mini-drift chambers with maximum drift distance of 3 mm (labeled A and B), a magnet with a field integral of Δp_t = 220 MeV/c, and two downstream minidrift chambers (labeled C and D). The geometrical acceptance was 3.5% for $K^0_L \to e^+e^-$, 3.7% for $K^0_L \to \mu^\pm\mu^\mp$, and .024% for $K^0_L \to \pi^0 e^+e^-$.

The electrons were identified by a 3 m. long atmospheric pressure hydrogen Cerenkov counter. Pions with energies less than 8 GeV were not registered by the Cerenkov counter. The electron energies were measured in a lead glass array consisting of 244 blocks of Schott F2 glass with dimensions of 6.35 cm × 6.35 cm × 46 cm. The glass blocks were arranged in a 1 m × 1 m array with a central 12.7 cm × 38 cm hole to pass the neutral beam. The blocks were optically isolated with 50 μm. aluminized mylar. The photomultiplier bases employed a variable high voltage power supply which was connected to the photocathode and a fixed high voltage power supply which was connected to the ninth dynode of a 12 stage tube. This reduced variations in gain as a function of beam intensity. Custom built ADC modules were used to integrate the charge from the lead glass

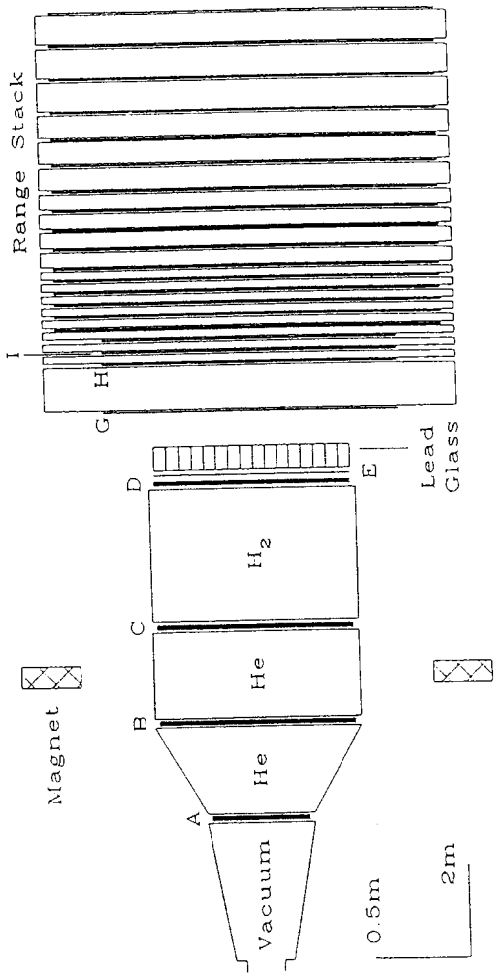

Fig. 1. Plan view of the E780 detector. Note the different horizontal and vertical scales.

counters. The signals were integrated for 120 nsec. An "in-time bit" was set if a leading edge above an effective threshold of 500 MeV occurred within ± 5 nsec. of the trigger. The pedestals were recorded at random times during the beam spill. The ADC modules subtracted the pedestals and only read out channels above a threshold of 70 MeV. We accepted typically 8×10^{11} protons per AGS pulse, which generated approximately 10^7 counts/m^2/sec. in the detector. The data was collected from February to May, 1988.

Four trigger types were collected: μe, ee, μμ, and ππ. All triggers required drift chamber hits on the left and the right of the neutral beam in the bend view drift chambers. As defined by the hardware trigger, electrons were particles that triggered the Cerenkov counter and deposited at least 1.2 GeV in the glass array; particles which penetrated a 1.05 m steel filter were defined as muons; those particles that did not activate the μ or e triggers but penetrated the glass array, but not the steel filter were classified as pions. The ππ trigger was prescaled by a factor of 128. A Fastbus processor aborted events which did not have A, B, and C drift chamber hits compatable with two tracks in the bend view which originated in the decay volume. However, no on-line cuts were made to reject three body decays. The data acquisition livetime was typically 90%.

The ee triggers largely derive from K_{e3} decays such that the pion energy is above the Cerenkov threshold while the μe triggers were generated for the most part from K_{e3} decays where the pion either punches through the steel filter or decays in flight to a muon that passes through the filter. The energy deposited in the lead glass for electrons from the K_{e3} decays was compared with the momentum determined

in the magnetic spectrometer to provide an accurate off-line calibration of the lead glass. The lead glass energy resolution was determined to be $\sigma/E = 11\%/\sqrt{E}$ (E in GeV). The resolution was measured to be $7\%/\sqrt{E}$ when the glass was purchased. We attribute the difference to radiation damage. Most of the blocks appear noticeably yellow compared to new lead glass. The lead glass position resolution was measured to be ± 6 mm. The efficiency of the Cerenkov counter was 93% for inbending electrons and 83% for outbending electrons.

Measurements of the decays $K^0_L \to \pi^0\pi^+\pi^-$ serve to determine a normalization for the $K^0_L \to \pi^0 e^+e^-$ decays as well as providing a useful measure of mass resolutions for the topologically similar $\pi^0 e^+e^-$ final states. The charged tracks were required to pass requirements on track quality and distance of closest approach at the vertex. Events were rejected if there were more than two tracks[8] pointing to the vertex. All events were required to have at least two gamma clusters in the lead glass besides the two clusters associated with the charged tracks. The gamma clusters were required to be in a fiducial region which excluded the blocks around the beam hole. Only those gamma clusters were selected such that greater than 1 GeV was deposited in the cluster and the intime bit was activated. Figure 2a shows a histogram of the measured $\gamma\gamma$ invariant mass for such events. For events with more than two gamma clusters, all $\gamma\gamma$ invariant mass combinations are shown. Only events with exactly one $\gamma\gamma$ combination within 30 MeV/c^2 of the π^0 mass were selected. If the invariant mass of the $\gamma\gamma$ set within 30 MeV/c^2 of the π^0 mass is constrained to the π^0 mass, the K-mass is determined to an

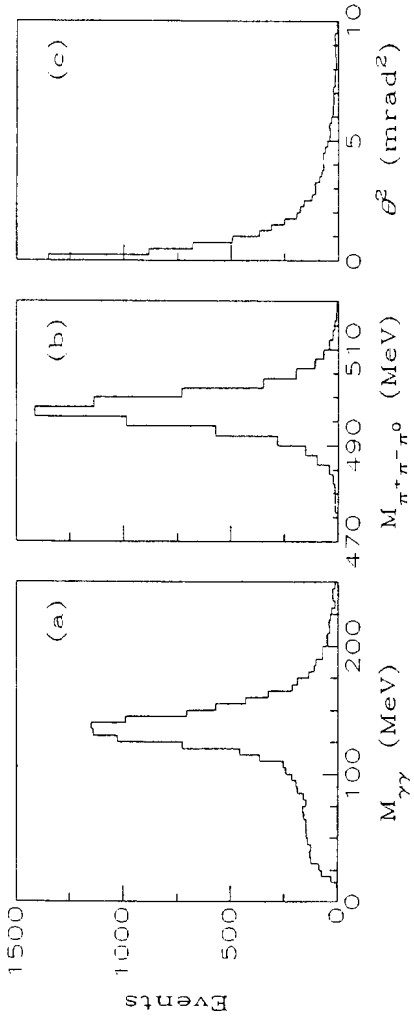

Fig. 2. Distributions of (a) $\gamma\gamma$ effective mass, (b) $\pi^+\pi^-\pi^0$ effective mass for events with $\theta^2 < 10$ mr^2, and (c) the square of the target reconstruction angle for events within 12.5 MeV/c^2 of the K mass.

uncertainty of $\sigma = 3.7$ MeV/c^2. With this result as a normalization, the mass uncertainty for the final state $\pi^0 e^+ e^-$ was calculated to be $\sigma = 4.4$ MeV/c^2.

The events are also constrained by the requirement that they point back to the target. For otherwise acceptable $\pi^0\pi^+\pi^-$ events, $\sigma(\theta) \approx 1$ mr, where θ is the angle between the line from target to the decay point and the total momentum vector. We require $\pi^+\pi^-\pi^0$ events to be within 12.5 MeV/c^2 of the K mass and have $\theta^2 < 10$ mr^2. The $\pi^+\pi^-\pi^0$ effective mass and θ^2 distributions are shown in Figs. 2b and 2c respectively. These distributions are especially clean. No corrections have been made for backgrounds under the peaks.

The resolution for e^+e^- decays is determined from the kinematically similar $K^0_L \to \pi^+\pi^-$ sample. Figure 3a shows the $\pi^+\pi^-$ effective mass for inbending events. The distribution in θ^2 is shown in Fig. 3b. The mass resolution is 2.3 MeV/c^2 for inbending events and 4.0 MeV/c^2 for outbending events. The resolution in θ is 0.33 mrad for both event samples. We require $\pi^+\pi^-$ events to be within three sigma of the K mass and have $\theta^2 < 1.5$ mr^2. However, radiative effects[9] are important for decays to $\pi^0 e^+ e^-$ and e^+e^-. For example 15% of $K^0_L \to e^+e^-$ decays will have an e^+e^- effective mass more than 20 MeV/c^2 below the K mass.

Electron identification was established off-line using the lead glass information. The momentum measured in the magnetic spectrometer was required to be close to the energy measured in the lead glass array. The distribution in E/p for K_{e3} events from μe and ee triggers is shown in Fig. 4. The tail at large E/p is due to accidental overlap at high rates and is not seen in low intensity runs. We require E/p > 0.75 for electrons. Furthermore, the electron momentum was required to be below

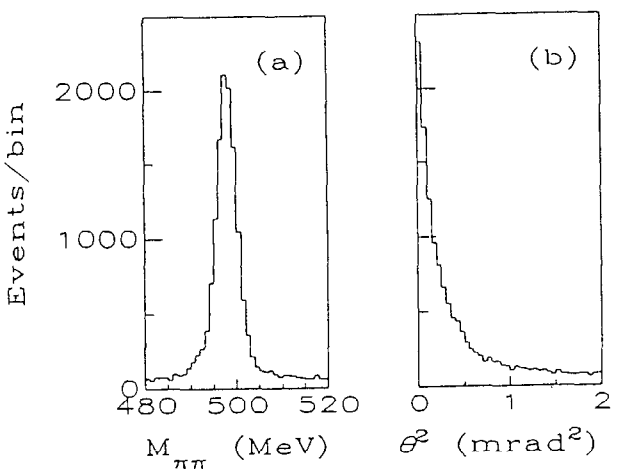

Fig. 3. Distributions of (a) the $\pi^+\pi^-$ invariant mass for inbending events with $\theta^2 < 1.5$ mrad^2 and (b) the square of the target reconstruction angle for events within three sigma of the K mass.

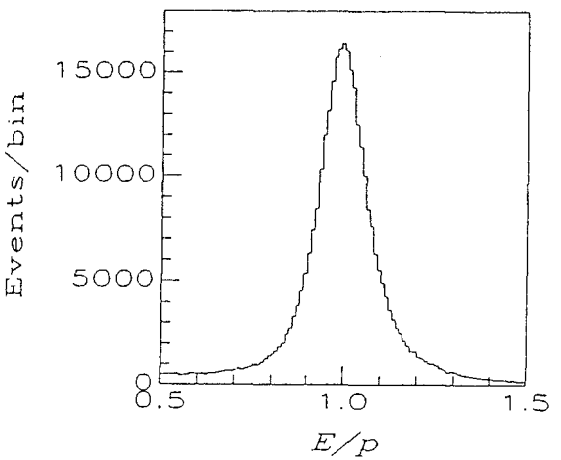

Fig. 4. Distribution of energy measured in the lead glass divided by momentum measured in the magnetic spectrometer for electrons from K_{e3} decays.

the pion Cerenkov threshold of 8 GeV/c for the $\pi^0e^+e^-$ search and the e^+e^- effective mass was required to be greater than 150 MeV/c^2 to reject π^0 Dalitz decays. The momentum asymmetry $A = (p_{max} - p_{min})/(p_{max} + p_{min})$ was required to be less than 0.6 for the e^+e^- search. From Monte Carlo calculations it was determined that > 97% of e^+e^- decays satisfy the momentum asymmetry constraint.

Figure 5 shows a plot of the e^+e^- effective mass vs. θ^2 for e^+e^- triggers which satisfy the above criteria. We find no events consistent with $K^0_L \to e^+e^-$. The nearest event with an acceptable θ^2 is 25 MeV/c^2 below the K mass. The events below the K mass are consistent with Monte Carlo calculations of K_{e3} events with the pion misidentified as an electron. The normalization for $K^0_L \to e^+e^-$ is determined by the number of observed $K^0_L \to \pi^+\pi^-$ decays. A correction of 15% was applied to account for background contributions in mass and θ^2. The background subtracted data was then fit as a function of K energy and decay position to determine the K^0_S contamination. It was determined that effectively 78% of the $\pi\pi$ decays were due to K^0_L. Then using the known $\pi\pi$ branching ratio and the ratio of ee to $\pi\pi$ acceptances as determined by Monte Carlo calculations, the single event sensitivity to $K^0_L \to e^+e^-$ was determined to be 7.2×10^{-10}. We then determine the 90% confidence level limit $BR(K^0_L \to e^+e^-) < 1.6 \times 10^{-9}$. Combining this result with our 1987 limit[7] gives a final limit $BR(K^0_L \to e^+e^-) < 1.2 \times 10^{-9}$.

A plot of $m(\pi^0e^+e^-)$ vs. θ^2 is shown in Fig. 6. There were no $\pi^0e^+e^-$ candidate events consistent with pointing back to the target. Only one of the events in the plot survives a more stringent lead glass cut of $.85 < E/p < 1.25$. The acceptance of the experiment to $\pi^0e^+e^-$ was calculated by Monte Carlo methods as a function of the e^+e^- effective mass. The

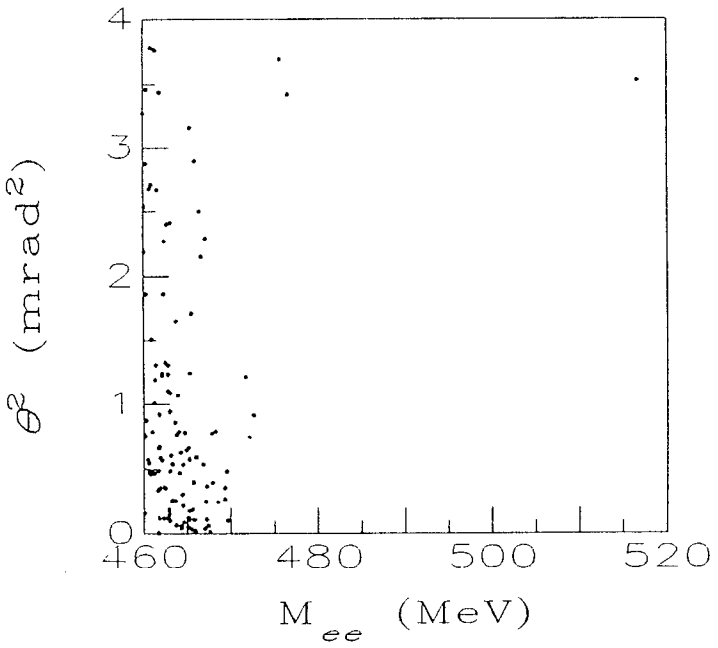

Fig. 5. Scatter plot of the e^+e^- effective mass vs. the square of the target reconstruction angle.

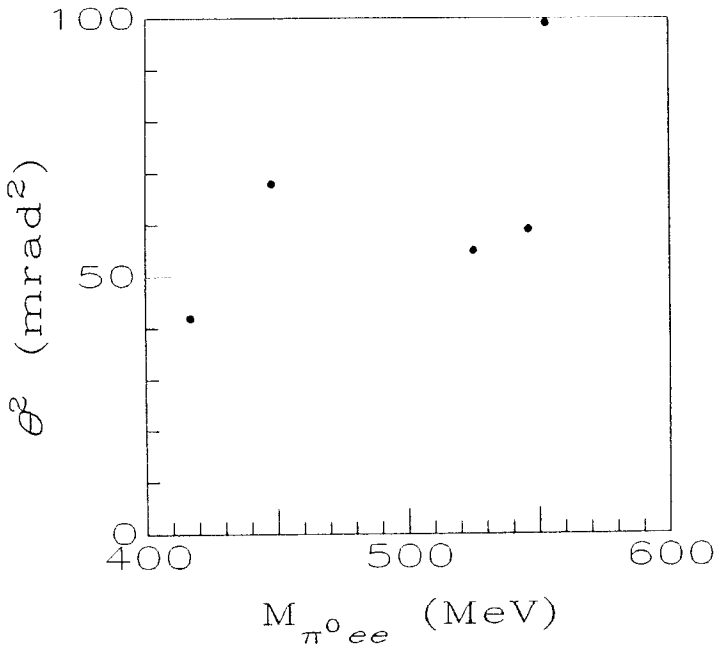

Fig. 6. Scatter plot of the $\pi^0e^+e^-$ effective mass vs. the square of the target reconstruction angle.

dileptons were generated isotropically in their rest frame. The normalization for $\pi^0e^+e^-$ was determined through an accounting of the topologically similar decay $K^0_L \to \pi^0\pi^+\pi^-$. The 90% confidence level limits on $K^0_L \to \pi^0e^+e^-$ are shown as a function of e^+e^- effective mass in Fig. 7. For a population of events distributed uniformly in the Dalitz plot, the 90% confidence limit is $BR(K^0_L \to \pi^0e^+e^-) < 3.6 \times 10^{-7}$.

During an earlier run in 1987, approximately one third of the data was taken without on-line cuts to reject three-body K decays. The ADC in-time bit was not implemented for that run. There was one event consistent with pointing back to the target ($\theta^2 = 0.7 \times 10^{-6}$). However, the $\pi^0e^+e^-$ effective mass was only 481 MeV/c^2. Furthermore, this event, which had additional hits in the first two drift chambers, was consistent with the decay $K^0_L \to \pi^0\pi^0$ with both π^0's undergoing Dalitz decay.[10] A cut was applied to the data to reject events with extra track stubs.[8] This cut rejected about 1.5% of the normalization events. After applying this cut, there were no events left in the region shown in Fig. 6. Combining the results from both runs, the 90% confidence level limit is $BR(K^0_L \to \pi^0e^+e^-) < 3.2 \times 10^{-7}$.

The constraints of kinematic reconstruction are especially important in searches for $K^0_L \to \mu^+\mu^-$ and $\mu^\pm e^\mp$ to discriminate against backgrounds from $K^0_L \to \pi\mu\nu$ and $\pi e\nu$ with the pion decaying to or being misidentified as a muon. For example, if the neutrino is produced with very little energy in the K rest frame and the muon from π decay is directed along the π trajectory, the dilepton effective mass equals 489 MeV/c^2. However, in this case the transverse momentum with respect to the target for nearly transverse K decays will be unbalanced by approximately 9 MeV/c. If the π decays so as to affect the momentum

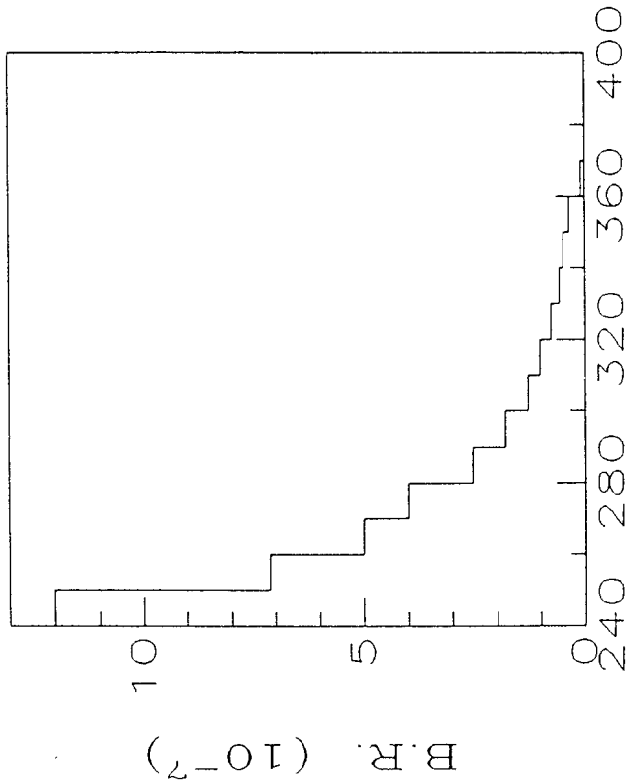

Fig. 7. Ninety percent confidence level limits on $K^0_L \to \pi^0e^+e^-$ as a function of e^+e^- effective mass.

measurement, the measured dilepton mass can even exceed the K mass. Then, however, the event will not have an acceptable θ^2. We expect similar background distributions in the $\mu^{\pm}e^{\mp}$ and $\mu^+\mu^-$ searches.

The decay $K^0_L \to \mu^+\mu^-$ served to verify our estimation of the sensitivity of the experiment. Various cuts were applied to reduce backgrounds. The momentum asymmetry $A = (p_{max} - p_{min})/(p_{max} + p_{min})$ was required to be less than 0.45; 93% of the $\pi^+\pi^-$ events pass this cut. Monte Carlo calculations show that 95% of $\mu^{\pm}e^{\mp}$ decays would pass this cut. Muons were required to penetrate at least 1.05m of steel to satisfy the trigger. Furthermore, if the muon stopped in the range stack, the energy obtained from the muon range was required to be at least 70% of the momentum as measured in the magnetic spectrometer. From our study of $K_{\mu 3}$ events, only 3% of muons fail this cut. Only inbending events were used in this analysis.

A scatter plot of $\mu^+\mu^-$ effective mass vs. θ^2 is shown in Fig. 8a. The distribution of $m(\mu^+\mu^-)$ for events which point back to the target to within 1.5 mrad^2 is shown in Fig. 8b. There is a clear peak around the K mass. All eight events are within 1.8 σ of the K mass. As stated above, we expect similar background distributions in the μe and $\mu\mu$ data. Since there are no events in the fiducial region in the μe sample (see below), we subtract no background from the number of $\mu\mu$ events in the fiducial region. The sensitivity of the experiment to the decay $K^0_L \to \mu^+\mu^-$ was determined through an accounting of the kinematically similar decay $K^0_L \to \pi^+\pi^-$. Corrections were made for the efficiency of the muon trigger counters. Using the known $\pi\pi$ branching ratio, it was determined that the single event sensitivity to $K^0_L \to \mu^+\mu^-$ was 1.3×10^{-9}. Using the single event sensitivity and the Particle Data Group world average

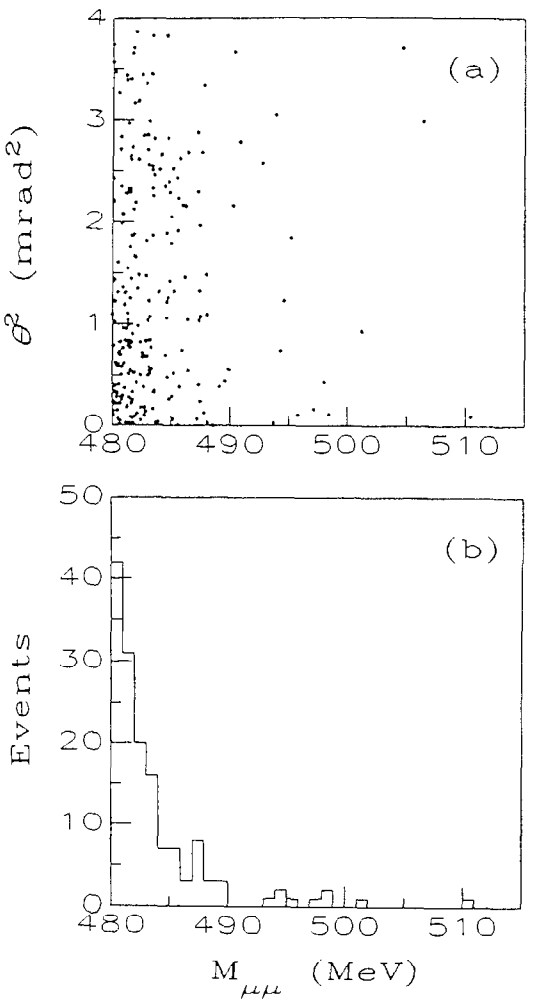

Fig. 8. a) Scatter plot of $\mu^+\mu^-$ effective mass vs. θ^2.
b) Distribution of $\mu^+\mu^-$ effective mass for events with $\theta^2 < 1.5$ mrad^2.

$BR(K^0_L \to \mu^+\mu^-) = (9.1 \pm 1.9) \times 10^{-9}$, we would expect to observe seven events, in good agreement with the eight events in the fiducial region.

The same kinematic and muon identification requirements were made on the μe triggers. Additional requirements were made on the electron track. The electron momentum was required to be less than the pion Cerenkov threshold of 8 GeV/c. Furthermore, the energy as measured in the lead glass divided by the momentum measured in the magnetic spectrometer was required to be greater than 0.75. Ninety-six percent of electrons satisfy this requirement. A scatter plot of $\mu^\pm e^\mp$ effective mass vs. θ^2 is shown in Fig. 9a. The distribution of m(μe) for events which point back to the target to within 1.5 mrad^2 is shown in Fig. 9b. There are no events close to the K mass. The closest event had an effective mass of 489.3 MeV/c^2. This is 3.7 σ below the K mass. We then find no events consistent with the decay $K^0_L \to \mu e$. The single event sensitivity to the decay $K^0_L \to \mu e$ was determined to be 1.1×10^{-9}. The 90% confidence level limit is then $BR(K^0_L \to \mu e) < 2.6 \times 10^{-9}$. Combining this result with our previous limit[7] gives a final result $BR(K^0_L \to \mu e) < 1.9 \times 10^{-9}$. This limit places constraints on models with exotic gauge bosons: assuming the boson couples to μe and sd with the universal weak coupling constant, the mass of such a boson is related to the K^0_L branching ratio by $BR(K^0_L \to \mu e) \approx 2.5 \times 10^{-3} (M_X/1\ \text{TeV})^{-4}$. Our result thus requires $M_X > 34$ TeV.

We thank the Brookhaven AGS accelerator department staff for their support. We gratefully acknowledge the timely loan of lead glass blocks from M. Kreisler and colleagues at the University of Massachusetts, Amherst, and photomultipler tubes from Brookhaven National Laboratory

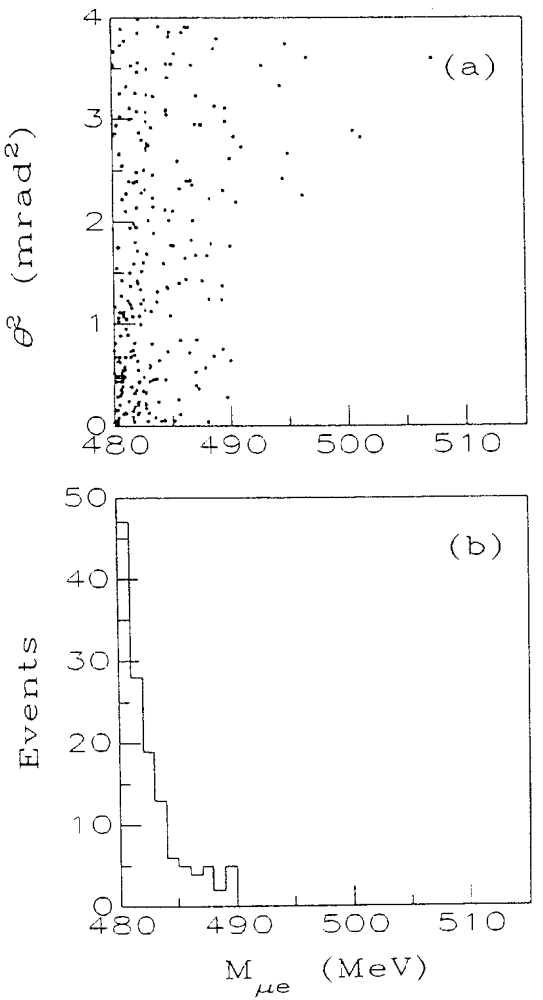

Fig. 9. a) Scatter plot of $\mu^\pm e^\mp$ effective mass vs. θ^2.
b) Distribution of $\mu^\pm e^\mp$ effective mass for events with $\theta^2 < 1.5$ mrad^2.

experiment No. 734. We gratefully acknowledge the contributions of R.K. Adair who worked on the earlier stages of the experiment. We also wish to thank Michael Lenz and Joseph Yelk who made technical contributions to the experiment. This research is supported by the U.S. Department of Energy under Contract Nos. DE-AC02-76CH00016 and DE-AC02-76ER03075.

REFERENCES

1. P. Bloch, et al., Phys. Lett. 56B, 201 (1975); N.J. Baker, et al., Phys. Rev. Lett. 59, 2832 (1987).
2. J.F. Donoghue, B.R. Holstein, and G. Valencia, Phys. Rev. D35, 2769 (1987); G. Ecker, A. Pich, and E. deRafael, Nucl. Phys. B291, 692 (1987), G. Ecker, A. Pich, and E. deRafael, Nucl. Phys. B303, 665 (1988).
3. The ratio of the K^0_L/K^+ lifetimes is 4.2. Here, K^0_L is a coherent sum of $K^0-\bar{K}$ which has the same CP as the final state π^0 + scalar; K^0_S has opposite CP.
4. L.J. Hall and L.J. Randall, Nucl. Phys. B274, 157 (1986).
5. A.S. Carroll, et al., Phys. Rev. Lett. 44, 525 (1980).
6. L.M. Sehgal, Phys. Rev. 183, 1511 (1969), M. Holder, Annals of New York Academy of Science 518, 140 (1987).
7. H.B. Greenlee, et al., Phys Rev. Lett. 60, 893 (1988).
8. An event is rejected if there is an extra space point in the A drift chamber within 6 mm of a line extrapolated from the decay vertex to an extra space point in the B drift chamber.
9. L. Bergström, Z. Phys. C20, 135 (1983).
10. M. Mannelli, et al., in Proceedings of the 23rd Recontres de Moriond, Les Arcs, France, March 6-13, 1988 (to be published).

The additional hits in the A and B drift chambers were not consistent with originating at the decay vertex within the accuracy of the drift chamber measurements. However, if their momenta were about 170 MeV/c and 200 MeV/c, the trajectories were consistent with originating at the vertex when the effects of multiple scattering in the vacuum window

and magnetic curvature in the small fringe field between the A and B chambers is taken into consideration. These particles would have curled in the spectrometer field and would not have been observed in the C and D drift chambers. The effective mass combinations are then $m(\gamma_1 e^+_1 e^-_1)$ = 125 MeV/c^2, $m(\gamma_2 e^+_2 e^-_2)$ = 145 MeV/c^2, and $m(\gamma_1\gamma_2 e^+_1 e^+_2 e^-_1 e^-_2) \approx$ 497 MeV/c^2, consistent with the π^0 and K^0 masses respectively. The lead glass E/p for the high energy positron and electron were 1.01 and 1.05 respectively. We calculate the probability of observing a $\pi^0\pi^0$ decay with both π^0's undergoing Dalitz decay such that a $\gamma\gamma e^+e^-$ effective mass combination is 480 MeV/c^2 or higher is less than 1%.

OBSERVATION OF DIRECT CP VIOLATION AND STATUS OF THE $\Phi^{00} - \Phi^{+-}$ MEASUREMENT IN THE NA-31 EXPERIMENT AT CERN

presented by G. Zech
Universität Siegen, Germany

Invited talk given at the Topical Conference of the
1988 SLAC Summer Institute

I. OUTLINE OF THE PAPER

In this talk I will present work from the NA-31 collaboration (CERN - Dortmund - Edinburgh - Dortmund - Orsay - Pisa - Siegen), [1] that recently published, [2] a three standard deviation evidence for direct CP violation in K_L decay. This measurement, based on data from 1986 is reviewed and its systematic uncertainties are described in some detail. The detector has been improved since then and new data are being collected this summer. The new detector components and first preliminary experience with them will be discussed briefly. At the end of this talk I will spend a few minutes on a measurement of the phase difference between η_{00} and η_{+-}. The data of this experiment were collected in 1987.

II. THE MEASUREMENT OF ε'/ε

Since the NA-31 beam and detector were subject of a very detailed paper, [3] I will put the main emphasis on the analysis of the data, especially on studies of the systematic uncertainties of the measurement which could not be covered in great detail in Ref. [2]. Readers interested in a more general discussion of CP violation in kaon decay, including its history and a brief description of relevant experiments, are referred to Ref. [4]. More details of the experiment and of the analysis can be found in the thesis of G. Quast, [5] Many of the results presented in this talk have been taken from there.

II.1 Definition of the Parameters Describing CP Violation in K Decay

The phenomenology of CP violation in K decay can be found in textbooks and many excellent reviews. We have collected some parameters and relations in Fig. 1. Direct CP violation manifests itself through a difference in the CP violating decay amplitudes η^{+-} of $K_L \longrightarrow \pi^+\pi^-$ and η^{00} of $K_L \longrightarrow \pi^0\pi^0$ whereas CP violation in the mass matrix has the same effect on both channels. Present experiments measure the squared ratio of these amplitudes which corresponds to the double ratio R of the partial widths of the two channels in K_L and K_S. A decomposition of the amplitudes into isospin I = 0 and I = 2 contributions leads to the parameter ε'. The value of ε'/ε is expected to be small because the I = 2 part is suppressed by the $\Delta I = 1/2$ rule. In the framework of the Kobayashi Maskawa quark mixing scheme, [6] ε'/ε can be evaluated. [7] The early estimates, [8] were rather high and triggered the present experiments. More recent calculations, [9] agree on positive values of a few parts per thousand, but have considerable theoretical uncertainties.

CP violating amplitudes in K_L decays:

$$\eta_{+-} = \frac{A(K_L \longrightarrow \pi^+\pi^-)}{A(K_S \longrightarrow \pi^+\pi^-)} \quad ; \quad \eta_{00} = \frac{A(K_L \longrightarrow \pi^0\pi^0)}{A(K_S \longrightarrow \pi^0\pi^0)}$$

Decomposition of K_L into CP eigenstates:

$$K_L \sim (\varepsilon K_1 + K_2) \; ; \qquad K_{1,2} \sim K^0 \pm \bar{K}^0 \qquad (CP = \pm 1)$$

Decomposition of decay channels into isospin I = 1 and I = 2 parts
(A_I are decay amplitudes, δ_I are $\pi\pi$ phase shifts)

$$\eta_{+-} = \varepsilon + \varepsilon' \; ; \qquad \eta_{00} = \varepsilon - 2\varepsilon' \; ; \qquad \varepsilon' \ll \varepsilon$$

$$\varepsilon' = \frac{i}{\sqrt{2}} e^{i(\delta_2 - \delta_0)} \, \mathrm{Im}(A_2/A_0) \; ;$$

$$\mathrm{phase}(\varepsilon') \approx \mathrm{phase}(\varepsilon) \qquad (\delta_2 - \delta_0 \approx \mathrm{phase}(\varepsilon))$$

$$\frac{\varepsilon'}{\varepsilon} \approx \frac{1}{6}\left(1 - |\eta_{00}|^2/|\eta_{+-}|^2\right) = \frac{1}{6}(1 - R)$$

Double Ratio:

$$R = |\eta_{00}|^2/|\eta_{+-}|^2 = \frac{\Gamma(K_L \longrightarrow \pi^0\pi^0)/\Gamma(K_S \longrightarrow \pi^0\pi^0)}{\Gamma(K_L \longrightarrow \pi^+\pi^-)/\Gamma(K_S \longrightarrow \pi^+\pi^-)}$$

Fig. 1: Definition of Parameters Describing CP Violation in Kaon Decay.

II.2 The Main Problems in Measuring R

The measurement of CP violating decays with branching ratios of the order of a permille to the precision of better than one percent is associated with considerable experimental difficulties:

i) The dominant three body decays in K_L ($K_L \longrightarrow \pi e \nu$, $\pi \mu \nu$, $\pi^+\pi^-\pi^0$, $3\pi^0$) have to be suppressed by more than a factor of 10^5. This can be achieved by identifying electrons and muons with good efficiency and by photon detection in most of the solid angle in combination with kinematic cuts. The two pion decays have to fulfill the mass constraint and the momentum vector has to point back to the production target.

ii) The relative acceptances of K_L and K_S have to be known to the precision of about 10^{-3}. The acceptance depends on the position of the decay vertex and the momentum of the kaon. Of importance are mainly the variations of the acceptance on the coordinate along the beam (z) and the momentum component parallel to the beam or equivalently to the energy (E). Therefore the acceptance cancels almost completely if the double ratio R is measured in small E and z bins and if K_L and K_S decays are measured by the same detector. However there is a secondary effect. Since the E and z distributions of K_L and K_S decays are different E and z have to be measured precisely enough to avoid differences in migration of events from bin to bin in K_L and K_S. In the NA-31 experiment the z distributions of K_L and K_S are almost identical, but the momentum spectra are very different. Consequently we need a relative precision of the neutral and the charged energy measurement of 10^{-3}.

iii) Last but not least the event rates have to be high to achieve the necessary statistical accuracy and to have enough data to study systematic uncertainties by subdividing the data sample. The experiments need high acceptances and fast data taking systems with high on-line rejection capability for the dominant three-body K_L decays.

II.3 Result and associated uncertainties

Based on about 110,000 $K_L \longrightarrow 2\pi^0$, 300,000 $K_L \longrightarrow \pi^+\pi^-$, 930,000 $K_S \longrightarrow 2\pi^0$ and 2,300,000 $K_S \longrightarrow \pi^+\pi^-$ decays we obtained for the double ratio a value of

$$R = 0.980 \pm 0.004 \pm 0.005,$$

where the statistical (0.004) and the systematic (0.005) uncertainties are about equal. The systematic errors are broken down in Table 1. The largest error (0.3 %) is due to a possible difference in the energy scales of neutral and charged decays. The background subtractions in the charged and the neutral modes have 0.2 % uncertainties each. Of similar size are effects from accidentals. The evaluation of systematic uncertainties will be discussed in sections II.7 to II.11.

Table 1: Systematic Uncertainties on the Double Ratio R (in %)

Background subtraction in $K_L \longrightarrow 2\pi^0$	0.2
Background subtraction in $K_L \longrightarrow \pi^+\pi^-$	0.2
$2\pi^0$ / $\pi^+\pi^-$ difference in energy scale	0.3
Regeneration in K_L beam	< 0.1
Scattering in the K_S beam	0.1
K_S anticounter inefficiency	< 0.1
Difference in K_L / K_S beam divergence	0.1
Calorimeter instability	< 0.1
Monte Carlo acceptance	0.1
Gains and losses by accidentals	0.2
Trigger inefficiency	0.1
Total systematic uncertainty	0.5 %

Our result for R translates into a value for ε'/ε of

$$\varepsilon'/\varepsilon = 0.0033 \pm 0.0011.$$

The double ratio R is significantly different from the prediction $R_{sw} = 1$ of the Superweak model, [10] and improves the precision of previous experiments, [11,12] considerably.

II.4 Characteristics of the NA-31 experiment

Data are taken alternatively in a K_L and a K_S beam. The detector records simultaneously both the charged and the neutral decay modes.

A large acceptance is achieved by using a 50 m long decay volume, by avoiding a magnet and a photon converter. Energies are measured by calorimeters.

The K_S target can be moved through the decay volume in steps of 1.2 m. Since the average decay length in K_S is about 5 m the z distribution of K_S can be made almost identical to that of K_L.

The two neutral beams are transported in vacuum up to the end of the detector. This vacuum reduces kaon scattering, K_S regeneration and neutron-induced kaon production to a negligible level.

The analysis is performed in bins of E and z. Within a bin the acceptances of K_L and K_S differ only by a fraction of a percent, whereas global acceptance corrections would be of the order of 10% and introduce sizable systematic uncertainties.

A schematic sketch of the experimental set-up is shown in Figure 2. For more details see Ref. [3], where the resolutions of the individual components are also given and calibration methods are described. Most components are conventional with the exception of the K_S train and the liquid argon calorimeter. The excellent performance of these two items was essential for the success of the experiment.

The observed momentum spectra of the two decay modes in the two beams are shown in Figure 3. The majority of the events in K_L are below 120 GeV. The K_S spectrum is considerably harder because low energy K_S decay inside the collimator and low energy K_L are more likely to decay than high energy K_L.

II.5 The $K \longrightarrow 2\pi^0$ Reconstruction and Background Subtraction

In the neutral decay mode $K \longrightarrow 2\pi^0 \longrightarrow 4\gamma$ (Figure 4a) the four photons are recorded in the liquid argon calorimeter (LAC) with a resolutions of $8\% / \sqrt{E}$ for the energy and of 0.75 mm for the two spatial coordinates. The center of gravity of the four energies (c.o.g.) has to be inside the kaon beam aperture. This feature can be used to reject $K \longrightarrow 3\pi^0$ events. The distance Δz of the decay vertex from the LAC can be computed from the photon energies E_i and positions x_i, y_i assuming a kaon decay according to

$$\Delta z = \frac{1}{m_K} \left\{ \sum_{i<j} E_i E_j [(x_i - x_j)^2 + (y_i - y_j)^2] \right\}^{1/2} . \qquad (1)$$

A test of the π^0 decay hypothesis is now possible by using Δz and computing the invariant masses of pairs of photons. The pairing giving invariant masses closest to those of two pions is chosen. A scatter plot of the two masses is shown in Figure 5 for K_L decays. Good $K \longrightarrow 2\pi^0$ decays cluster around the π^0 mass. The uniform background is from $3\pi^0$ events where two photons have escaped detection.

Events are selected inside the central ellipse of Figure 5. The elliptical cut was used because the two photon pair masses are correlated through the kaon mass

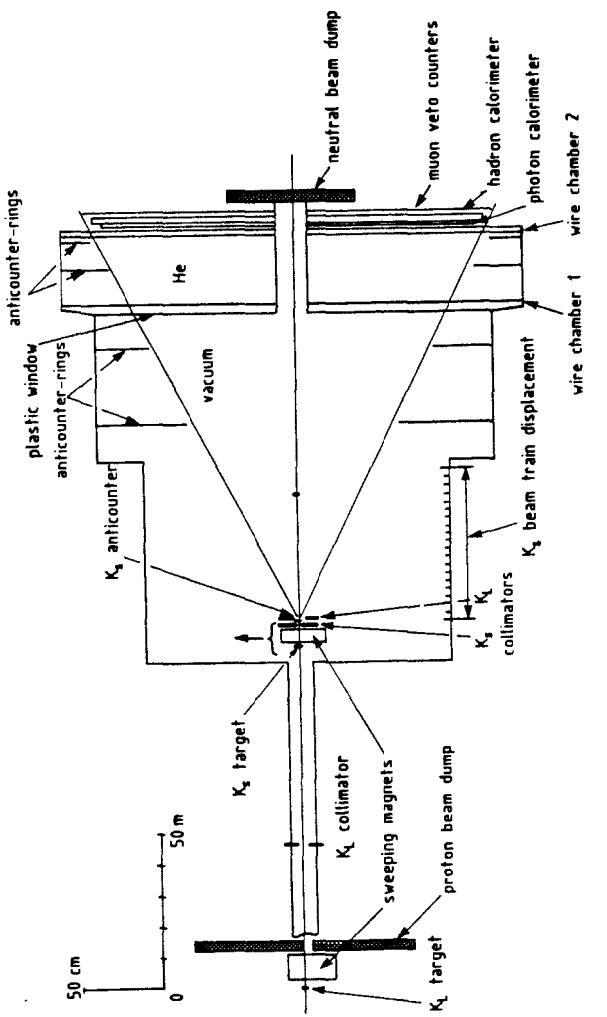

Fig. 2 Layout of the Experiment

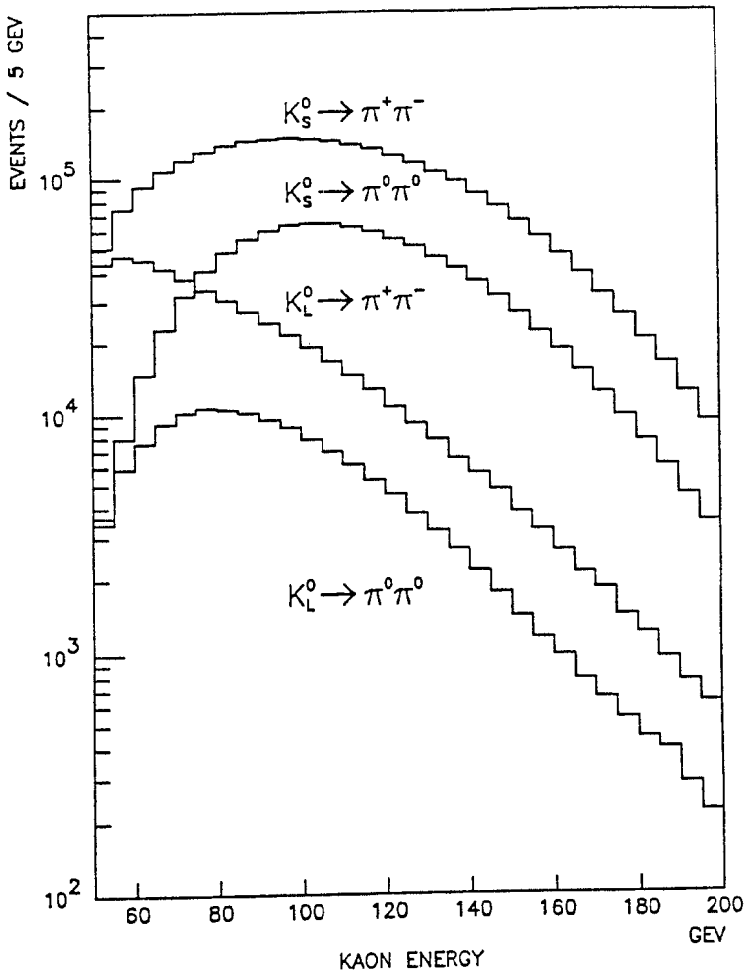

Fig. 3 Observed Kaon Energy Spectra

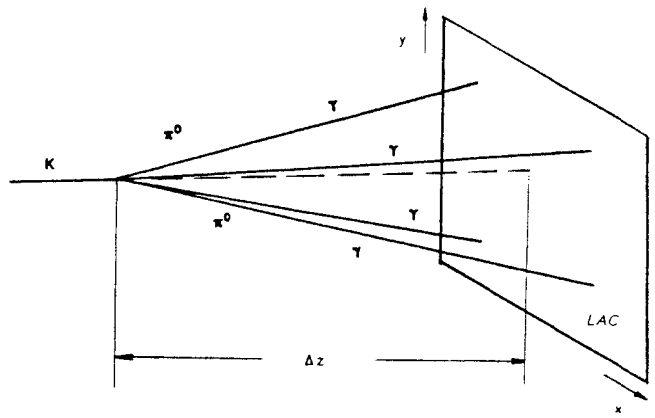

Fig. 4a Geometry of $K \longrightarrow 2\pi^0$ Events

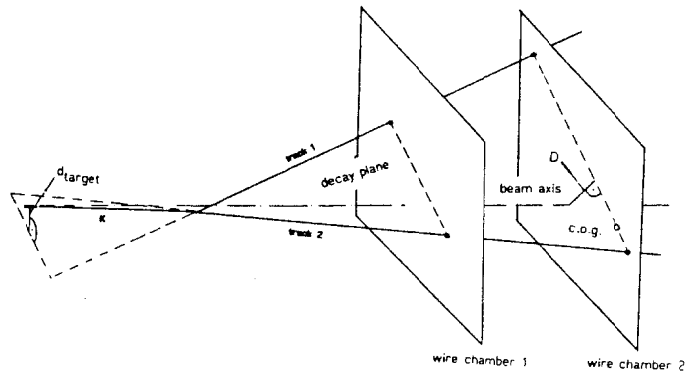

Fig. 4b Geometry of $K \longrightarrow \pi^+\pi^-$ Events

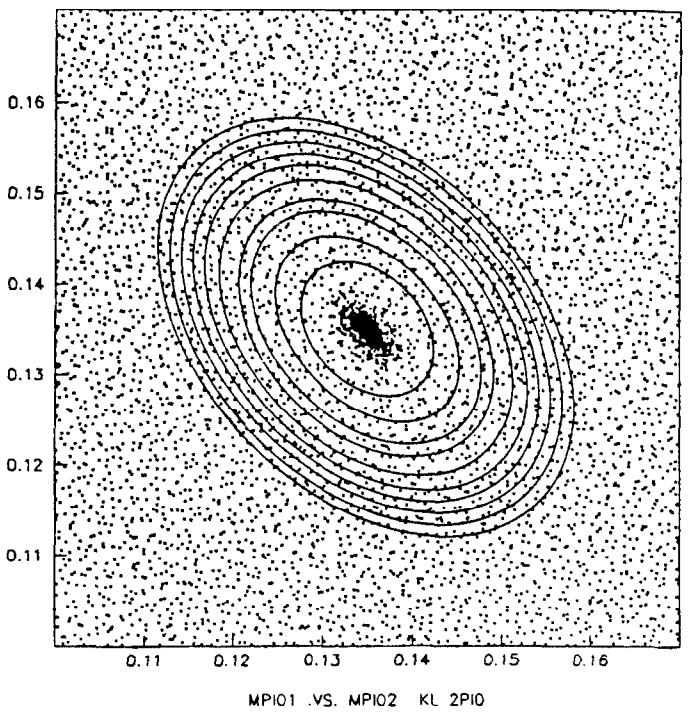

Fig. 5 Scatter Plot of $m(\gamma_1\gamma_2)$ versus $m(\gamma_3\gamma_4)$ for $K_L \longrightarrow 2\pi^0$ Events

constraint. The background is extrapolated from the outer elliptical rings which cover areas equal to that of the central ellipse. Figure 6 is the distribution of events as a function of X^2 where X^2 was assumed to be proportional to the number of the elliptical ring. A Monte Carlo simulation of the $3\pi^0$ background shows that it is flat. The loss of good events by the X^2 cut amounts to 1.5 %, the background is (4.0 +- 0.2) %. The background is almost absent in the first 20 m of the decay volume (Fig 7a) because $K_L \longrightarrow 3\pi^0$ decays with two missing photons can only acquire a reconstructed kaon mass if the opening angles of the decay are increased by moving the decay vertex towards the LAC.

The error from the background subtraction of 0.2 % quoted in Table 1 covers uncertainties in the extrapolation. A flat extrapolation is compatible with the data and was used, but a linear extrapolation would change the result only by 0.1 %. Since there is only $3\pi^0$ background which can be studied rather easily, the error is likely to decrease by further analysis work.

II.6 The $K \longrightarrow \pi^+\pi^-$ Reconstruction and Event Selection

The reconstruction of charged decays is sketched in Figure 4b. The geometry of the decay is obtained from the wire chamber coordinates. A reasonable reconstruction precision is guaranteed by a cut in the closest distance of approach (CDA) of the two tracks. This quantity is plotted in Figure 8 for K_L and K_S decays. The two distributions agree perfectly. The cut therefore has the same effect in both modes. The resolution in z is about 1 m, slightly better than in the neutral decay.

The energy of the kaon is calculated from the opening angle ϑ of the tracks and the ratio of E_1/E_2 of their energies assuming a $K \longrightarrow \pi^+\pi^-$ decay. The advantage compared to the direct measurement E_1+E_2 is twofold. The precision of about 1 % is much superior and the energy scale is independent from the energy scale of the calorimeter as long as non-linearities are small. It is mainly determined by the well measured wire chamber geometry.

The dominant background from $K \longrightarrow \pi e \nu$ is eliminated by comparing the track energies in the front part of the LAC and the hadron calorimeter (HAC). We loose 25 % of good $\pi^+\pi^-$ events by the electron cut. Another 20 % are lost by a cut in the ratios of the track energies which eliminates $\Lambda \longrightarrow p\pi^-$ decays in K_S.

Background remaining after rejection of events with observed electrons, muon or photons are mainly rejected using the $\pi^+\pi^-$ mass and the distance of the decay plane from the target (d_{target}) and further reduced by a cut in the distance of the

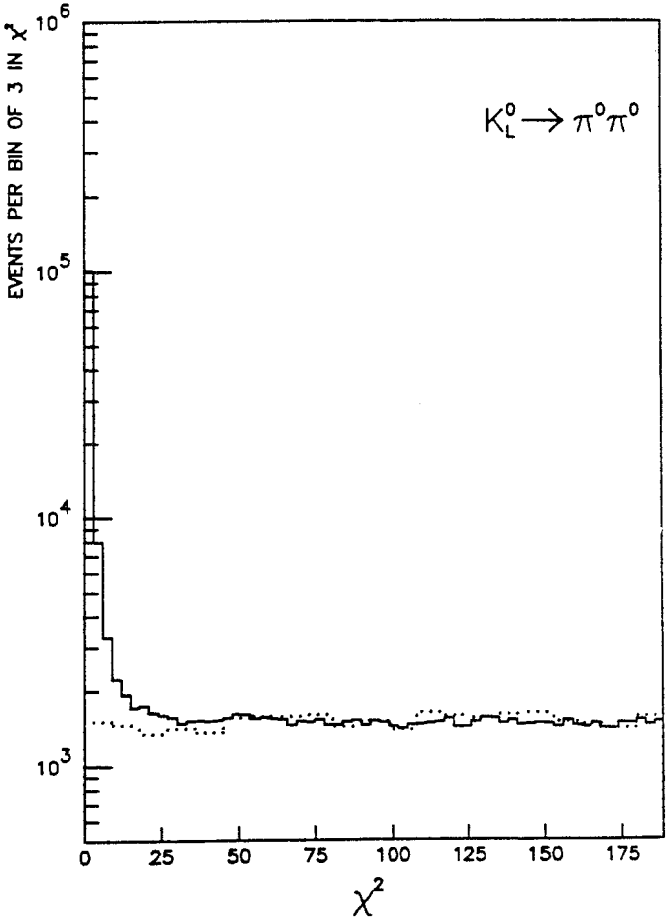

Fig. 6 Number of Events as a Function of X^2.
X^2 is computed from the ellipse numbers of Fig. 5.

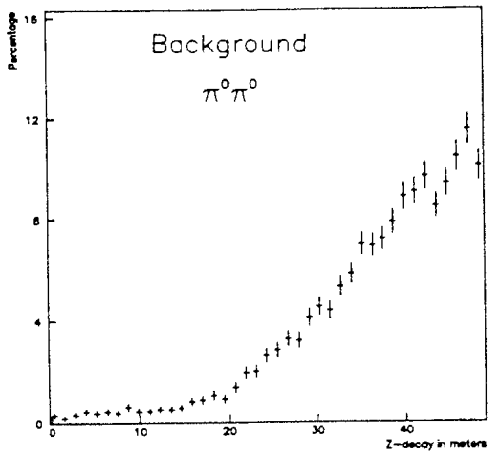

Fig. 7a Background in $K_L \longrightarrow 2\pi^0$ Events as a Function of z_{vertex}

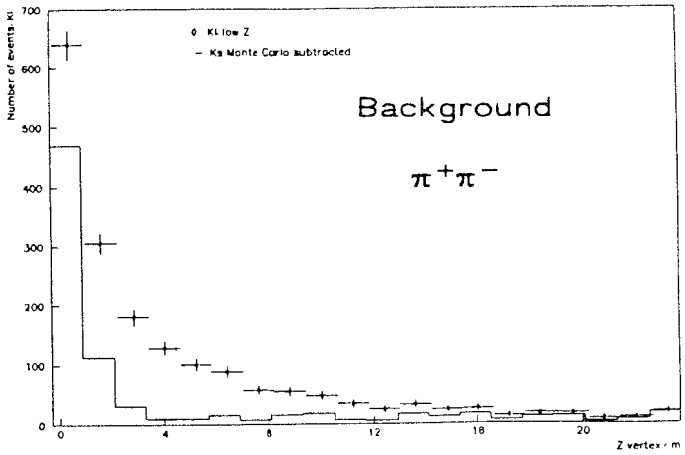

Fig. 7b Background in $K_L \longrightarrow \pi^+\pi^-$ Events as a Function of z_{vertex}

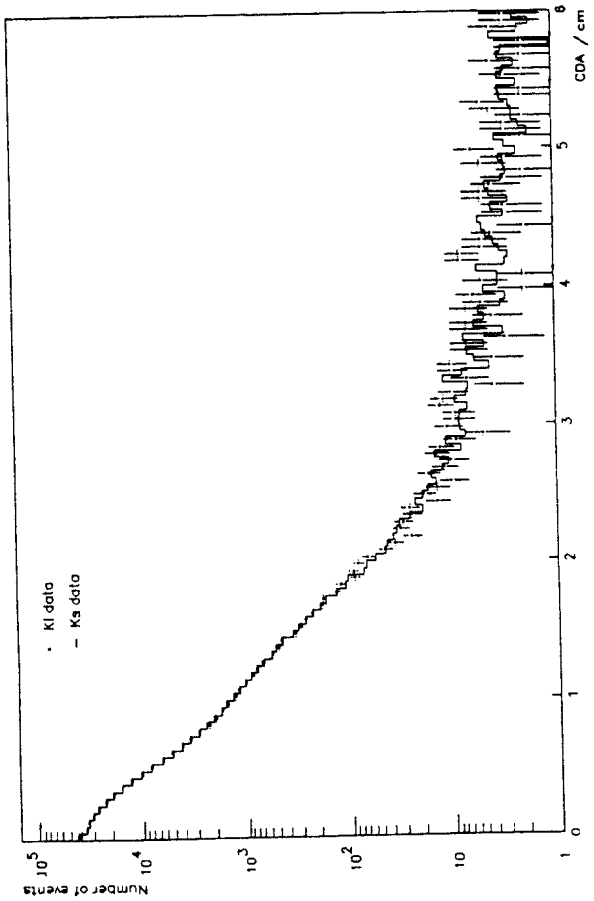

Fig. 8 Closest Distance of Approach for $K \longrightarrow \pi^+\pi^-$ Decays.
CDA_{KS} is scaled to the K_L geometry.

c.o.g. from the beam axis. The latter cut removes also events produced at the collimator. Figure 9 shows the distribution of the $\pi^+\pi^-$ mass for K_L peaking at the kaon mass with a smaller peak from $K \longrightarrow \pi^+\pi^-\pi^0$ which is well separated. A cut at 2.1 standard deviations from the kaon mass is applied. Again we have to guarantee that the K_L and K_S distributions have the same shape. The two distributions are overlayed in Figure 10a and divided through each other in Figure 10b. At the right hand-side of the peak, where background is essentially absent, the distributions agree over three orders of magnitude. The distributions of d_{target} in Figure 11 indicate the remaining background. (The quantity d_{target} has been scaled for K_S events to account for the different target positions and the correspondingly different resolutions.) The composition of the background is studied using the region of large d_{target}. The extrapolation into the accepted region below 5 cm is done using selected data samples or Monte Carlo simulations.

II.7 Treatment of Background in $K \longrightarrow \pi^+\pi^-$

The composition of the background in the signal region (d_{target} < 5 cm) and in the control region (7 cm < d_{target} < 12 cm) which is used for estimating the amount of background is given in Table 2 for the relevant background channels. The total

Table 2: Composition of Charged Background

Background	Control region	Signal region
$K_L \longrightarrow \pi e \nu$	2.8 +- 0.2	4.4 +- 0.3
$K_L \longrightarrow \pi \mu \nu$	0.5 +- 0.2	0.7 +- 0.3
$K_L \longrightarrow \pi^+\pi^-\pi^0$	0.1 +- 0.1	1.0 +- 1.0
$K_L \longrightarrow \pi^+\pi^-\pi^0$ (overlayed γ)	0.1 +- 0.0	1.2 +- 0.2
regenerated K_S	0.2 +- 0.1	0.4 +- 0.2
Total	3.7 +- 0.1	7.7 +- 2.0

background in the signal region is (0.77 +- 0.20) %. The main contribution, ≈ 60 % is K_{e3}. Background from $K \longrightarrow 3\pi$ is of two different kinds. In some cases one of the photons from the π^0 decay hits the LAC near to one of the charged pions and cannot be separated. Its energy is then added to the pion energy and thus the mass can be shifted into the accepted range. We label these events with "overlay γ". The amount of these events is not estimated from the d_{target} distribution (see

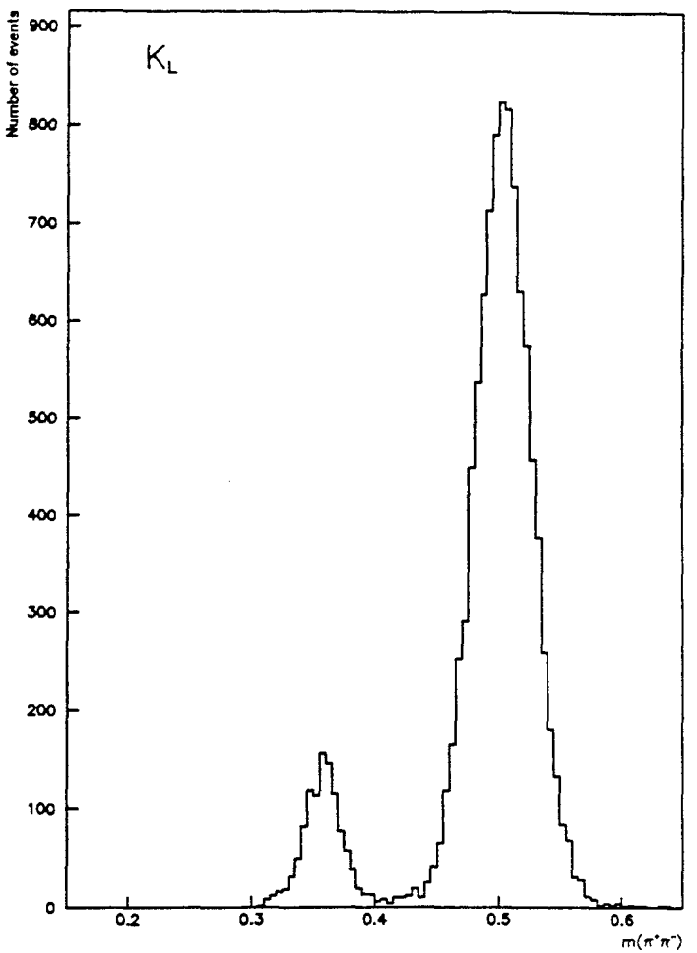

Fig. 9 Distribution of $\pi^+\pi^-$ Mass of K_L Decays.

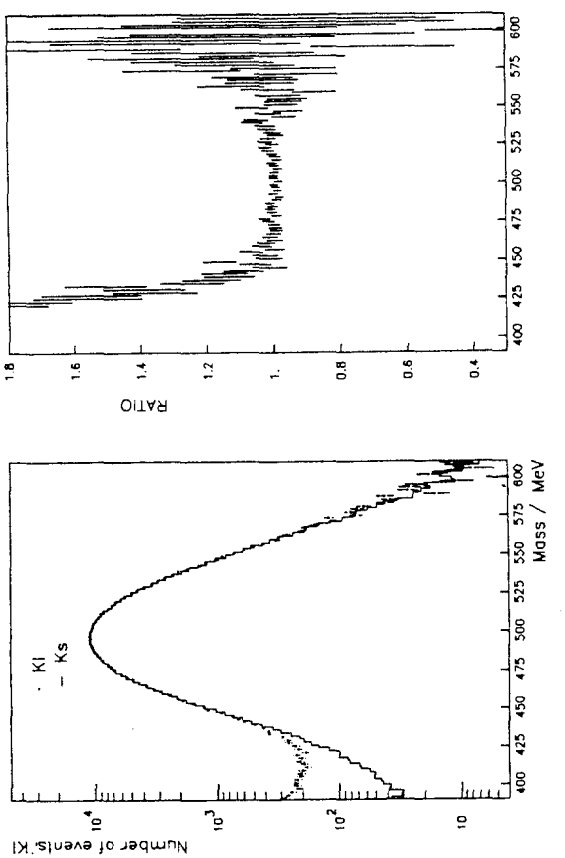

Fig. 10 Comparison of $\pi^+\pi^-$ mass distributions of K_L and K_S.
The second Fig. shows the ratio of the distributions.

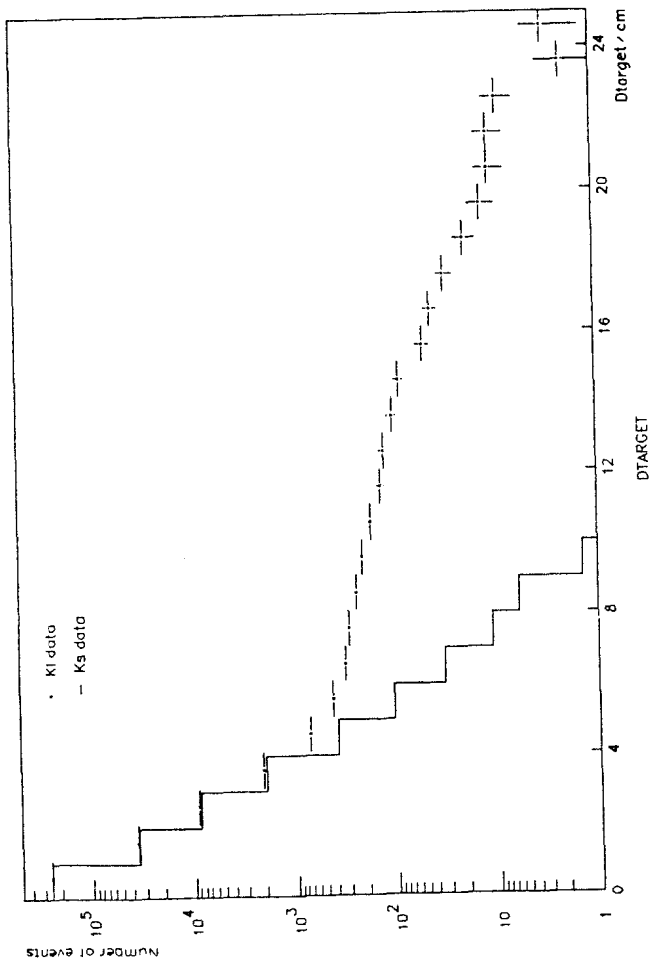

Fig. 11 Distribution of the Distance of the Decay Plane from the Target.

below). The contribution of $K \longrightarrow 3\pi$ with no overlaying photon is compatible with being zero, but cannot be excluded completely. It contributes to the uncertainty because its extrapolation factor from the control region into the signal region is large. In addition there are small contributions from $K_{\mu 3}$ and from K_S produced at the collimator edge. In the following we discuss the individual background channels in more detail.

Figure 7b shows the z distribution of events from the background region and demonstrates the presence of events produced at the final K_L collimator. The mass distribution indicates that a large fraction of those peak at the kaon mass. An estimate of the amount of K_S produced and a Monte Carlo simulation reproduces the data very well, except at the first 2.5 m. This is seen in Figure 7b where a subtraction of the simulated K_S gives a nicely flat remaining background. Nevertheless we have used only events with z greater than 10 m to reduce the contribution of K_S to a very small level. This cut unfortunately excludes in the neutral mode a very clean region where $K \longrightarrow 3\pi^0$ background is absent.

$K \longrightarrow 3\pi$ events with overlaying photon can easily be studied by looking for events where the γ is near to the charged pion but far enough to be identified in the LAC. Figure 12a is a scatter plot of the energy versus the distance to a charged pion for"photons" observed in K_L decays. Most of the dots correspond to photons faked by the reconstruction program near the hadronic shower. The number of real photons can be found by subtracting the K_S distribution where $K \longrightarrow 3\pi$ is absent. The photons are distributed uniformly around the pion. (The kinematical correlation between the γ and the charged π is very weak.) Therefore their number is equal in the regions of Figure 12a which correspond to equal areas in the LAC. That this is indeed the case is seen in Figure 12b. The flat distribution obtained after the K_S subtraction is easily extrapolated into region one which is used in the analysis.

Radiative CP=1 $K \longrightarrow \pi^+\pi^-\gamma$ decays are proportional to $K \longrightarrow \pi^+\pi^-$ in both K_S and K_L and need no special treatment. CP conserving radiative decays in K_L are negligible after cuts and are anyhow automatically subtracted together with the $K \longrightarrow \pi^+\pi^-\pi^0$ events.

The background from $K_{\mu 3}$ was unexpected. It occurs through bremsstrahlung of a hard photon in the calorimeter. The muon looses so much energy that it stops before reaching the μ veto counters. Experimentally these events have characteristic features that allow one to measure their contribution. The energy of the radiated γ is deposited in a very small spatial region, predominantly either in

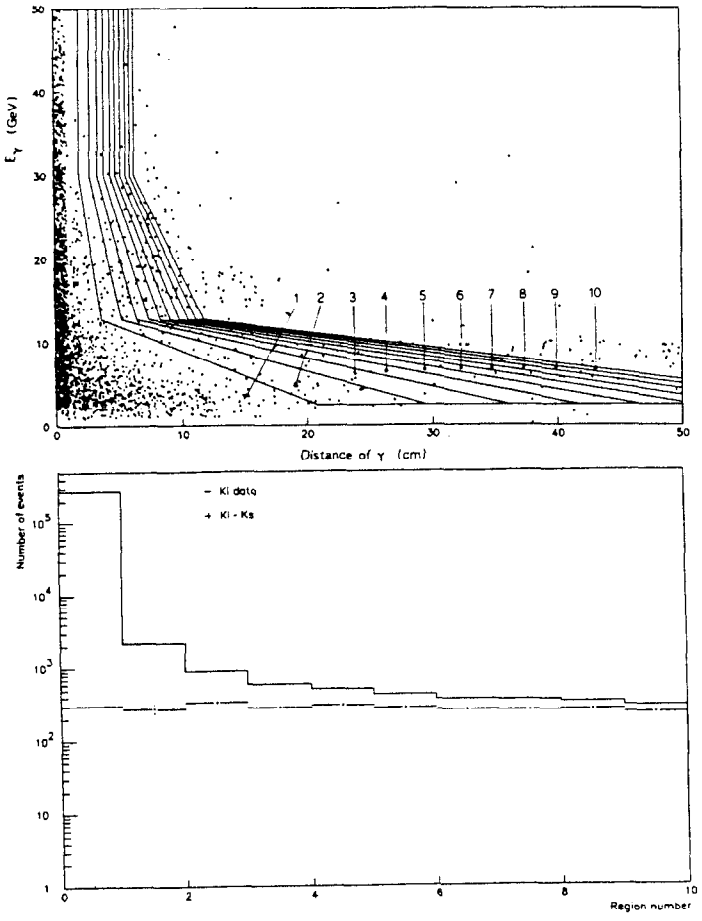

Fig. 12 Subtraction of $K \longrightarrow \pi^+\pi^-\pi^0$ Events with one Overlaying Photon.

In a) extra photons are plotted as a function of their energy and their distance to the nearest pion track.

In b) the number of photons is plotted as a function of the region number of a).

the front half or the back half of the hadron calorimeter. The front back asymmetry of the HAC energies are compared for pions from K_S and for K_L background in Figure 13b. The excess of events in K_L near 1.0 is due to muons radiating in the back part of the HAC. Furthermore the shower is normally confined to one scintillator strip. The fraction of energy deposited in the central strip associated to the track peaks near 1(Figure 13a).The relative abundance of the muon bremsstrahlung was simulated using calculations from Ref. [13]. The agreement in the distributions was very good. Figure 14 compares the mass and the d_{target} distributions.

Electrons are rejected by cutting tracks with a high ratio of the energy deposited in the front part of the LAC and the energy deposited in the HAC. Another characteristic feature is the width of the electromagnetic shower in the LAC. This variable is not used for the rejection of electrons on an event by event basis, because this would complicate the subtraction of $K \longrightarrow \pi^+\pi^-\pi^0$ with overlaying γ and the treatment of $K \longrightarrow \pi e \nu \gamma$, however it can be used to estimate the amount of K_{e3} background and to obtain a rather clean sample of these events. Reference samples have been obtained from selected K_{e3} data and from a Monte Carlo simulation. The agreement of these samples with the data is rather good as is demonstrated in Figure 15.

The various background contributions add up nicely to the total observed background. The uncertainty in these estimates leaves room for a small amount of $K \longrightarrow \pi^+\pi^-\pi^0$ with no overlaying γ. The d_{target} distribution of this possible background cannot be computed reliably but is certainly less steep than the one of $K \longrightarrow 3\pi$ with overlaying γ. This limits its maximum contribution.

The d_{target} distribution of the combined sum of all background samples is shown in Figure 16. The agreement with the data is excellent. Furthermore also the z distribution and the energy distribution of the sum of all reference samples agree very well with those of the data at high d_{target} values (Fig. 17).

II.8 Effect of Energy Scale

The difference in the energy spectra of K_L and K_S cancels in the double ratio. However, if there is a systematic shift between the neutral and the charged energie scales, the ratios $\Gamma(K_L \longrightarrow 2\pi^0)/\Gamma(K_S \longrightarrow 2\pi^0)$ and $\Gamma(K_L \longrightarrow \pi^+\pi^-)/\Gamma(K_S \longrightarrow \pi^+\pi^-)$ are measured at energies differing by ΔE and an error ΔR on R is introduced,

$$\Delta R = (f_L'/f_L - f_S'/f_S)\,\Delta E \ ,$$

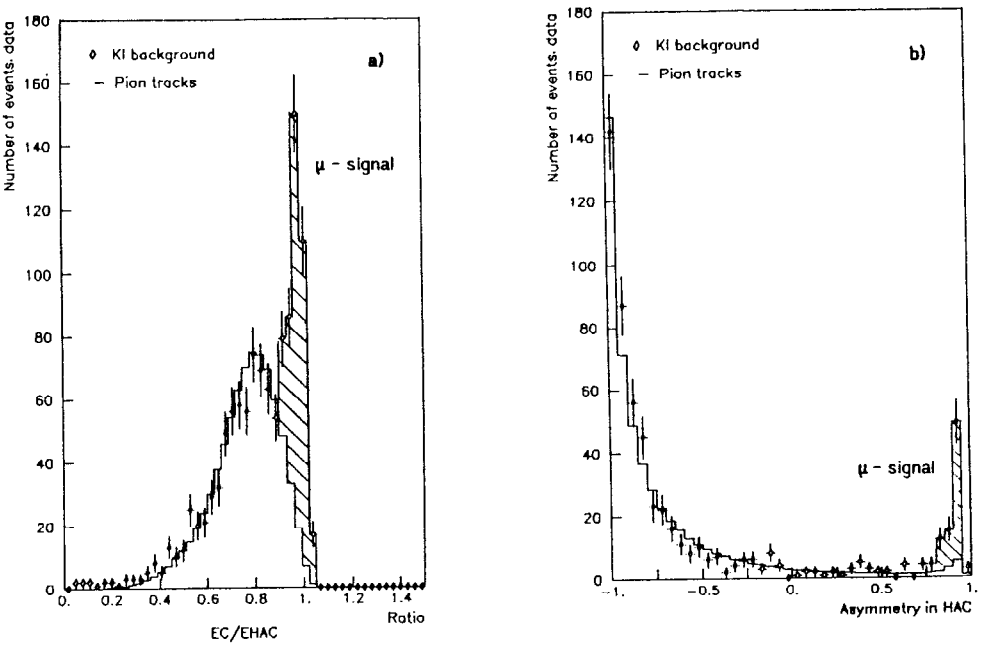

Fig. 13 $K \longrightarrow \pi \mu \nu$ Background.
Muons deposit energy mainly in one strip of the HAC (a) and either in the front or the back of the HAC (b).

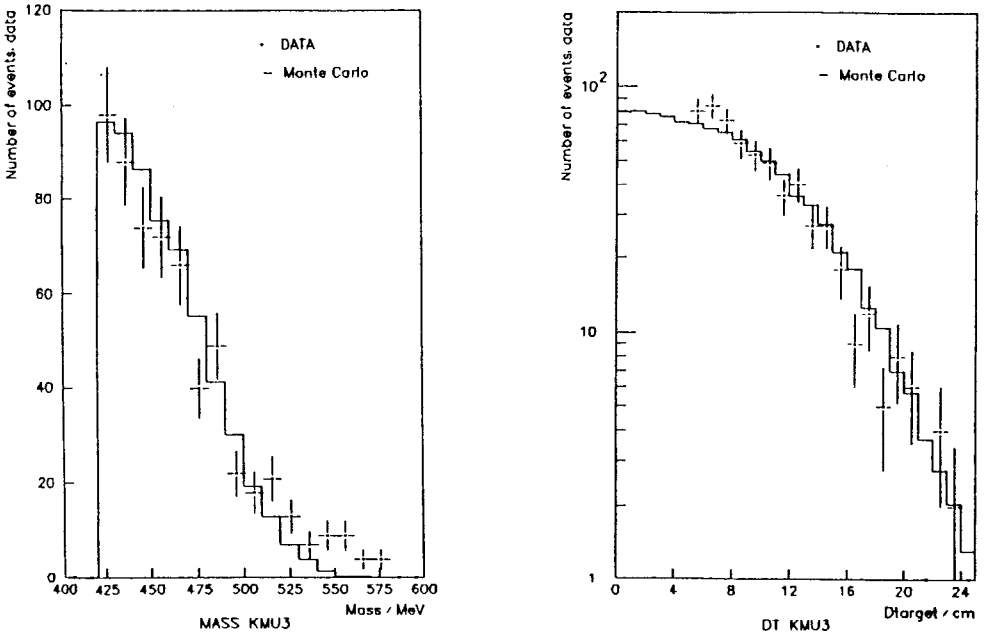

Fig. 14 Comparison of Selected Kμ3 Events with a Monte Carlo Simulation.

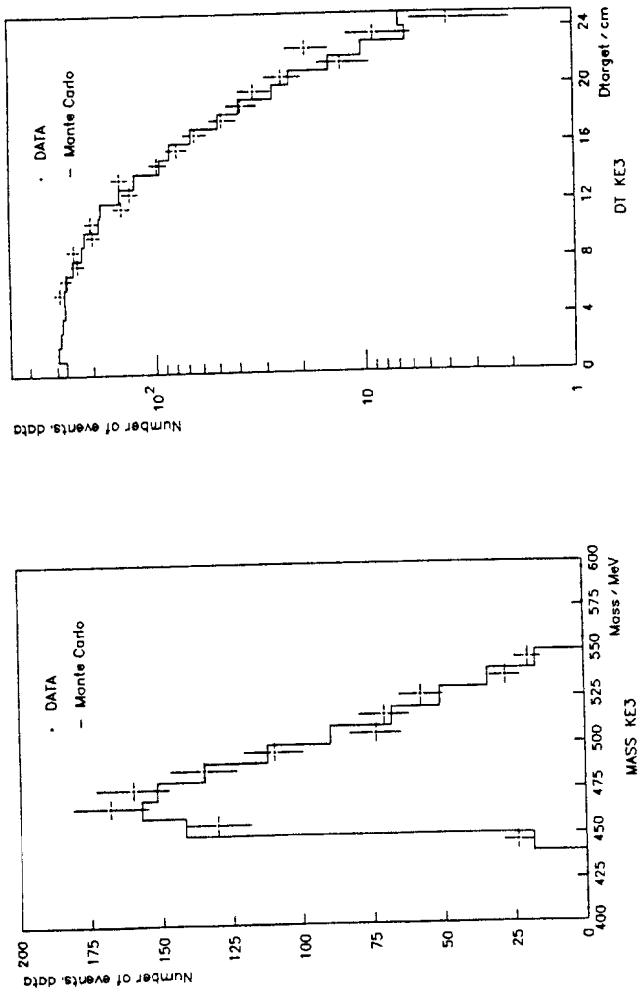

Fig. 15 Comparison of Selected Ke3 Events with a Monte Carlo Simulation.

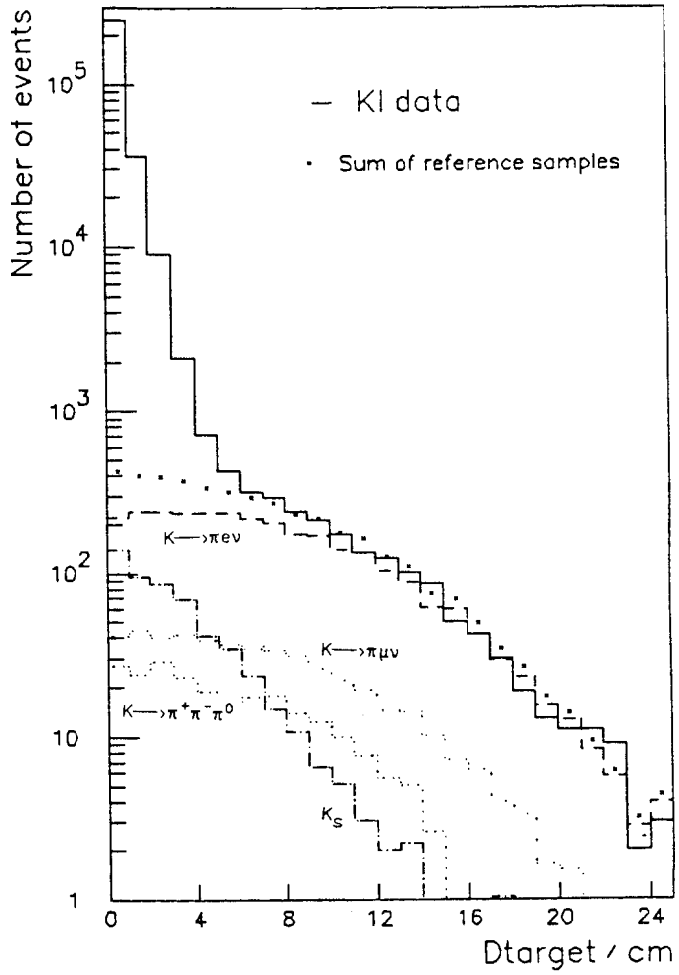

Fig. 16 Distribution of d_{target} for $K_L \longrightarrow \pi^+\pi^-$ Events.
The composition of the background and the extrapolation to small values of d_{target} are indicated.

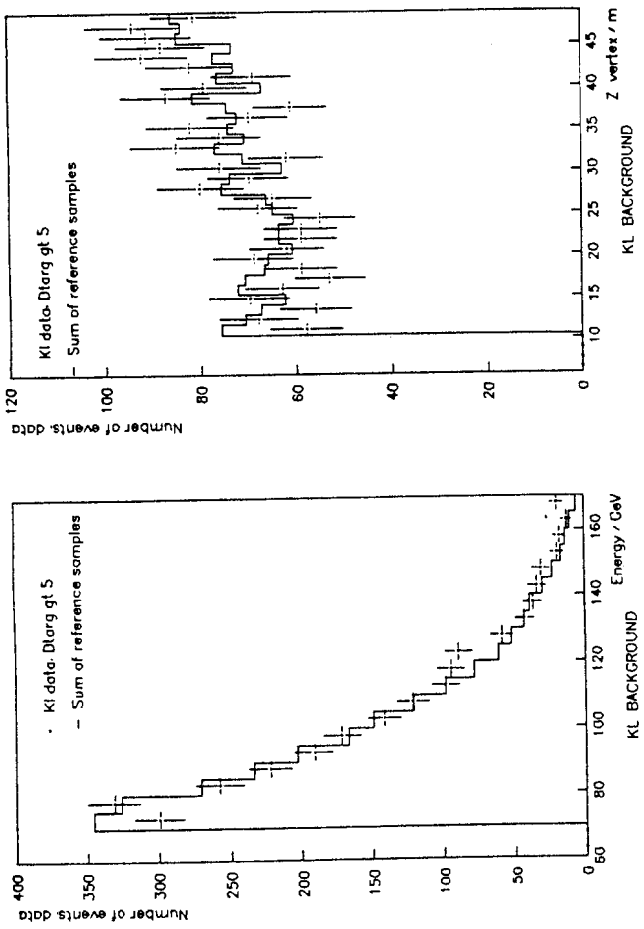

Fig. 17 Comparison of Estimated Background with Large d_{target} Data.

f and f' being the energy spectra and their derivatives, respectively. Averaged over our energy range from 70 to 170 GeV a shift of the energy by one part in thousand would result in a change of 2.5×10^{-3} in R and, correspondingly, of 0.4×10^{-3} in ε'/ε.

The neutral energy scale is fixed geometrically as is the charged. The length scale and the energy scale in $K \longrightarrow 2\pi^0$ decay are proportional as is seen easily from formula (1). The scale is adjusted such that the fitted position of the K_S anticounter agrees with the true position. The adjusted vertex distributions for neutral and for charged K_S decays is shown in Figure 18, where all K_S stations are added up. The solid line is an analytic function, where the resolution and the position are free parameters. An error of 10^{-3} in the energy scale corresponds to 10 cm shift of the anticounter. The precision of the fit is much better and the result is the same when the fit is done by comparing the data to a Monte Carlo simulation. Fitting the anti positions in 5 energy bins and 3 z bins gives a maximum deviation of 6 cm from the mean value. If this number is used as an estimate of the uncertainty we get an error on R of 1.5×10^{-3}. Non-linearities in the energy scale could affect our result, since the relation between ΔE and ΔR is energy dependent. An adjustment of the energy scale in energy and z bins changed R by 0.5×10^{-3}. Resolution effects were studied by subdividing the data in well and poorly measured events and fitting the position of the anticounter. The effect on R was 10^{-3}. The neutral energy scale is inversely proportional to the lateral length scale. The length scale in the LAC was compared to that of the wire chambers using electrons. Both agree within 0.2 mm which corresponds to an uncertainty in R of 0.5×10^{-3}.

The charged energy $E = E(m_K, \vartheta, E_1/E_2)$ is inversely proportional to the opening angle ϑ. The uncertainty of $\Delta\vartheta/\vartheta$ is about 0.4×10^{-3} leading to an uncertainty of R of 10^{-3}. That there is indeed no large error in the charged geometry is confirmed by the fit of the K_S anticounter position which was correctly reproduced without any adjustment. Non-linearities in the hadronic energy measurements influence the charged energy scale indirectly, because the ratio of the two pion energies enters in the kaon energy formula. Limits on the non-linearities of the calorimetric energy measurements of less than 1.5 % are deduced from the stability of the invariant $\pi\pi$ mass of K_S decays for different energy ratios. The corresponding uncertainty in R is 0.7×10^{-3}.

Adding up the various possible effects we conclude that the uncertainty on R from a difference in the charged and the neutral energy scales is not more than 3×10^{-3}.

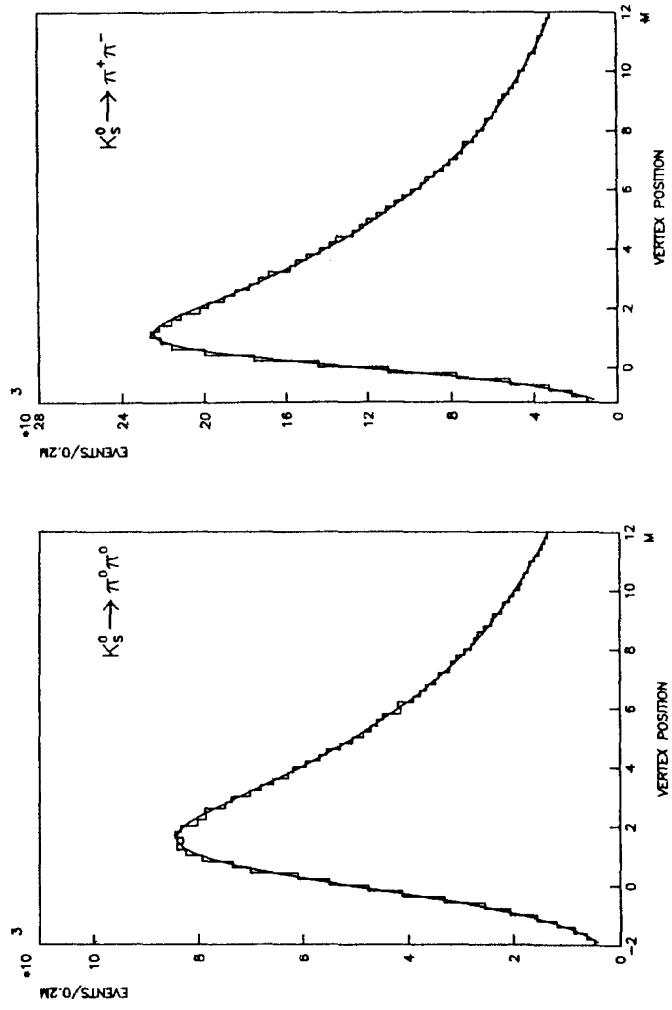

Fig. 18 Vertex Distribution of Decays Near the Anticounter.
The solid curve is a fit to the anticounter position.

We have discussed the neutral and the charged energy scale independently. In fact R depends only on the difference of the scales, or equivalently, on the difference of the ratios of the lateral and the longitudinal length scales between the neutral and the charged decays (except for non-linearities). Since in the analysis, we compare both the lateral and the longitudinal scales of the two modes directly, the independent treatment of the errors above, overestimates the errors.

II.9 Correction for Accidentals Particles

Events are rejected if additional charged tracks or photons with energies above 2.5 GeV are observed. In some rare cases an accidental particle can add enough energy to a track of an event which would otherwise be rejected by some energy cut such that it is accepted. However losses are by far more frequent than gains. The effect of accidentals was measured by overlaying random triggers, which were taken in proportion to the beam intensity, with good events. The overall correction for accidentals on R is (0.34 +- 0.20) %, where the error contains the estimated uncertainty of the overlay method. The individual corrections for the four decay channels are much larger, about 2 to 3 %. They are summarized in Table 3. The corrections on the charged and the neutral channel almost cancel, because our cuts against accidentals are symmetric for the two modes: Events are rejected in the charged mode if there is a third spacepoint in the first wire chamber or if there is one photon observed in the LAC. In the neutral mode one spacepoint in chamber one or a fifth photon in the LAC kill the event.

Table 3: Effect of Accidentals on Double Ratio

channel	ΔR (%)
$K_L \longrightarrow 2\pi^0$	- 2.6 +- 0.07
$K_L \longrightarrow \pi^+\pi^-$	+ 2.6 +- 0.05
$K_S \longrightarrow 2\pi^0$	+ 2.5 +- 0.05
$K_S \longrightarrow \pi^+\pi^-$	- 2.8 +- 0.10

II.10 Effect of the Time Stability of the Hadron Calorimeter

The cuts on the energy ratio against $\Lambda \longrightarrow p\pi^-$ decay, on the energy ratio of the front part of the LAC and the HAC against K_{e3} and on the $\pi^+\pi^-$ mass eliminate about half of our good events. We have to demonstrate that the fractional losses are the same in K_L and K_S. Differences could arise if there were variations in the

hadronic energy between the two running modes. As already mentioned above, energy variations can be determined by comparing the $\pi\pi$ mass distributions of K_L and K_S. A possible shift of the peak position is less than 0.3 MeV/c^2 (compare Figure 12). Using this number, we conclude that effects from the mass cut and the K_{e3} cut on R are below 10^{-4} and therefore completely negligible. The energy ratio cut can affect R only through a combined effect of non-linearities and a shift of the energy scale between K_L and K_S. Again no sizable effect on R is expected.

II.11 Checks of the Result

The total systematic uncertainty on R is 5×10^{-3}. The same statistical error is associated to 40,000 events. Our data samples contain considerably more events in all four event classes. Therefore we have the possibility to make statistically significant checks of the result by subdividing the data samples or by modifying the cuts. Some of the studies are summarized in Table 4. Even very drastic

Table 4: Modifications in the Analysis to Study Systematic Errors

modification	$\Delta R \times 10^3$
extrapolate $K_{\mu 3}$ as K_{e3}	- 0.2
increase $K_{\mu 3}$ by factor 2	0.2
extrapolate $K \longrightarrow \pi^+\pi^-\pi^0$ as K_{e3}	0.2
no $K \longrightarrow \pi^+\pi^-\pi^0$ without γ	- 0.5
maximum $K \longrightarrow \pi^+\pi^-\pi^0$ with maximum extrapolation factor	1.3
no regenerated K_S in K_L	0.7
e-rejection through shower width (loss of events 25% $\longrightarrow$ 8%)	0.2
extrapolate K_{e3} by Monte Carlo	- 0.2
looser mass cut (2.1 $\sigma \longrightarrow$ 2.5 σ)	- 1.0
loose centre of gravity cut (3σ)	0.10
d_{target} extrapolation from 5 to 25 cm instead of 7 to 12 cm	0.03
E_1/E_2 cut changed from 2.5 to 1.5 (50 % of good events lost)	1.8+-2.0
change # of E-z bins by factor of 4	0.1

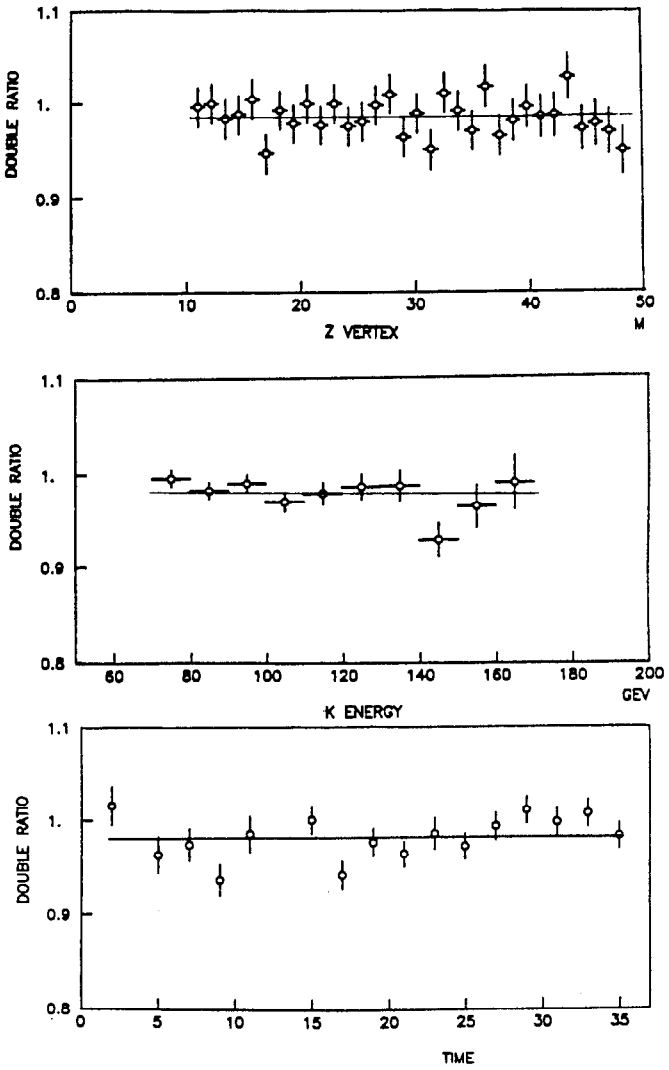

Fig. 19 Double Ratio as a Function of Vertex Position, Energy, and Time of Data Taking.

modifications of the subtraction of the charged background have little influence on the result. The three important cuts in the charged mode as discussed above can be varied without any significant effect on R.

Finally we show in Figure 19 the double ratio R as a function of the vertex position, of the kaon energy and of the time of data taking. All three functions are compatible with R being independent from z, E and time. This is not trivial, because most of the important systematic effects depend on these variables. The background $K_L \longrightarrow 2\pi^0$ strongly depends on z. The effect of a difference in the neutral and the charged energy scale is rather large at low kaon energies and changes sign at very high energies. Any time instabilities between the K_L and the K_S running would also lead to unreasonably large fluctuations of the individual measurements around the mean.

III. IMPROVEMENTS IN THE 1988 RUN

III.1 Modifications to the Experiment

The major changes were:

i) The collimation system was improved to avoid K_L or K_S scattering at the final collimator. This allows us to use the first 10 m of the decay volume which has particularly low background in the neutral decay mode.

ii) The energy of the protons hitting the K_S target was reduced and at the same time the production angle was increased. The energy spectra of K_L and K_S have become more similar thus reducing the dependence of R on the energy scales.

iii) A transition radiation detector consisting of four units with 200 polyethylene foils each was inserted in front of the LAC. This detector identifies our main background from K_{e3}.

iv) Additional γ veto counters in the beam improve $3\pi^0$ and $\pi^+\pi^-\pi^0$ rejection.

v) A third muon veto layer was added.

We have collected this summer comparable statistics as in 1986. A first look at the data shows that the new detector and beam components work satisfactorily. Figure 20 is a preliminary distribution of the pulse heights in the transition radiation detector for electrons and pions. The TRD was used to investigate the electron contribution in the tail of the d_{target} distribution and confirmed the estimate in the analysis of the 86 data.

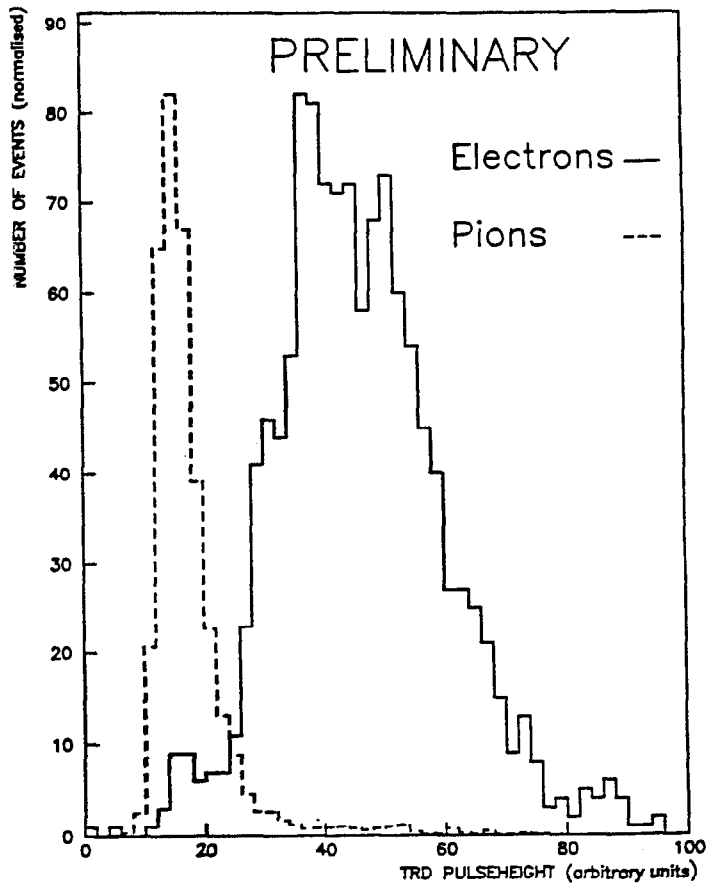

Fig. 20 Separation of Pions and Electrons by the Transition Radiation Detector.

IV. MEASUREMENT OF $\Phi_{00} - \Phi_{+-}$

IV.1 Introduction and Phenomenology

CPT conservation in the Isospin I=2 channel requires ε'/ε to be almost real (see Figure 1). Experimentally the real part is only 3×10^{-3}(see previous chapter) while the imaginary part is very large. This is seen from the Wu Yang diagram in Figure 21. If one neglects $|\varepsilon'/\varepsilon|$, η_{00} and η_{+-} should agree with the Superweak prediction ε, with phase Φ_{SW} and real part ε_L. The charged amplitude η_{+-} agrees well with this prediction but the neutral amplitude has a phase which is about two standard deviations higher than expected. This discrepancy if taken serious would require a huge CPT violation of about half a percent in the isospin I=2 channel. Such a big effect could hardly be understood, since CPT is valid to better than 10^{-18} in the kaon mass matrix. Also the agreement of the K^+ and K^- lifetimes contradicts a large CPT violation in $\Delta I=3/2$ transitions. Following Ref. [14] with some simplifications and using the new result for $|\varepsilon'/\varepsilon|$, CPT violation in neutral kaon decay is summarized in Figure 22. Some of the approximations that have been used, are only valid as long as the phase difference is large.

From these arguments it seems very likely that the observed phase difference is due to a statistical fluctuation or a measurement error. However, given the importance of the CPT theorem and the possibility to improve the old result by a new experiment with relatively small modifications of our existing set-up, we decided to re-measure the phase difference.

IV.2 Principle of the Measurement

In the NA-31 experiment the phase difference is measured from the intensity I of $K \longrightarrow \pi\pi$ decay as a function of the time after production at the target. This distribution is

$$I(t) = e^{-\Gamma_s t} + 2D|\eta|e^{-(\Gamma_s+\Gamma_L)t/2}\cos(\Delta m t - \Phi) + |\eta|^2 e^{-\Gamma_L t}, \quad (2)$$

where D is the dilution factor describing the asymmetry of $K^0$and $\bar{K}^0$production at the target. It is easy to understand that the sensitivity for a measurement of the phase per event has a maximum in the region where the first term and the the third term are about equal, that is around 12 K_S lifetimes. At short lifetimes the sensitivity per event is less, but this is almost exactly compensated by the higher number of events produced there. If the event rate that can be accepted in the accessible range of lifetimes, limits the rate of data taking, events with short lifetimes should be downscaled. This was the case in the NA-31 experiment.

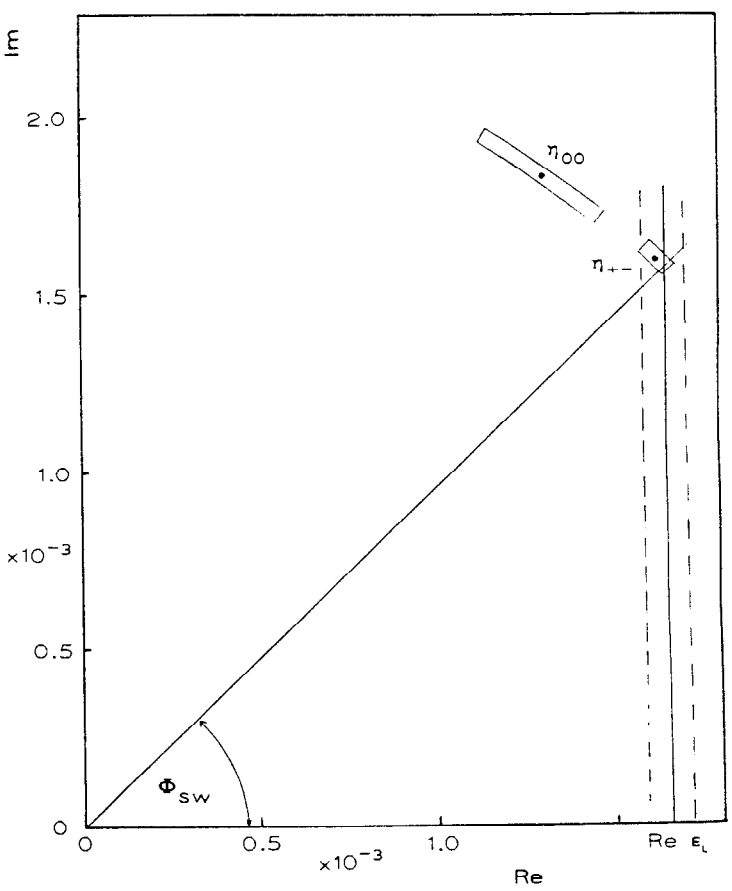

Fig. 21 Wu Yang Triangle.

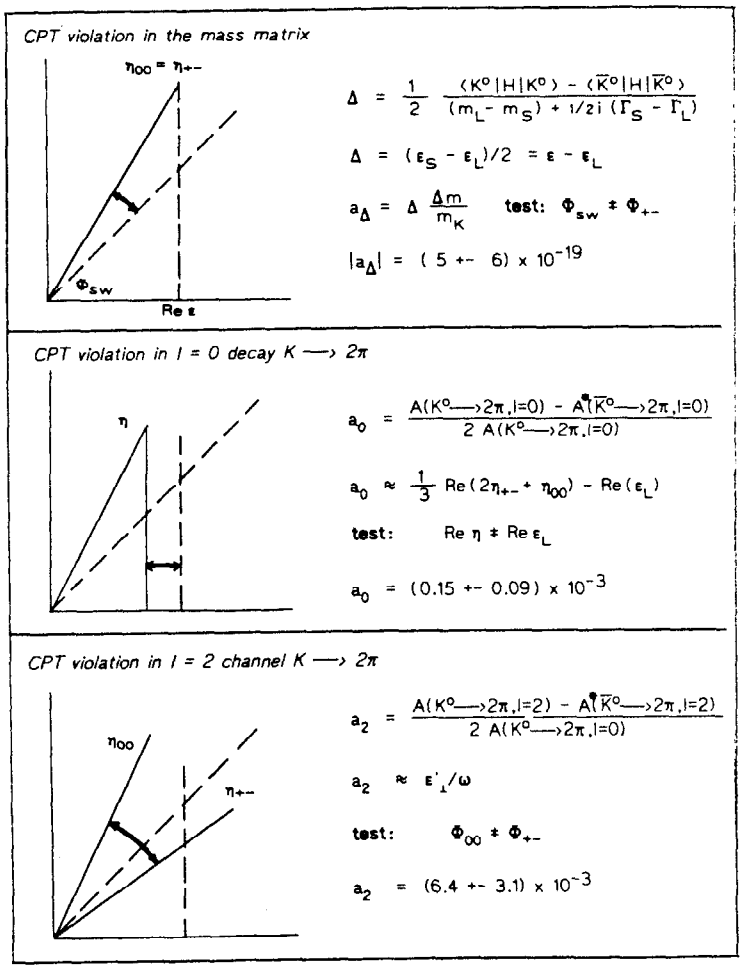

Fig. 22 Test of CPT Conservation in Neutral Kaon Decay.

A measurement of the difference of the neutral and the charged phase is very insensitive to the other parameters that appear in relation (2). However acceptance corrections are different in the two modes and have to be applied. To avoid this problem, the NA-31 experiment compares measurements from two different targets. This scheme is sketched in Figure 23. The distance of the targets corresponds for the average momentum to a phase shift of $\pi/2$. Periodically, typically once per day, we switched between the two targets. The ratio of the event distributions taken at the same position z is free from acceptance effects, but still sensitive to the phase. The double ratio, i.e. the ratio of targets for the neutral mode divided by the corresponding ratio in the charged mode is rather independent from most of the parameters except the phase difference. The expected precision of the experiment for the phase difference is about two degrees. The biggest systematic uncertainty is most likely the uncertainty of the difference in the neutral and the charged energy scale which contributes about one degree.

Figure 24 shows preliminary and partially uncorrected time distributions for the charged and the neutral decays. Especially in the $2\pi^0$ mode the progress compared to older experiments with very few events is impressive. In Figure 25 the interference term is extracted from the $\pi^+\pi^-$ time distribution. It shows nicely the oscillation with frequency Δm.

V. SUMMARY AND CONCLUSIONS

The result $\varepsilon'/\varepsilon = (3.3 \pm 1.1) \times 10^{-3}$ excludes the superweak model by three standard deviations. This is the most important conclusion of the experiment. Once more the standard model which is well compatible with this value of ε'/ε, is confirmed.

The biggest experimental uncertainty is due to a possible shift of the neutral energy scale with respect to the charged energy scale. The background subtraction in the neutral and in the charged K_L decays are well understood.

A reduction of the error can be expected from the new data. A further data taking period is scheduled for next summer. The statistics of the present analysis will be increased by a factor three with reduced systematic uncertainties.

The Fermilab experiment E731 will improve their present result with data collected last year to a similar precision as NA-31. With this measurement direct CP violation probably will be established definitely next year.

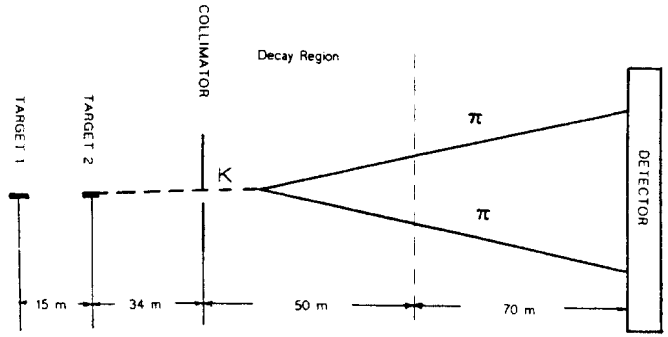

Fig. 23 Sketch of the Set-up of the ΔΦ Experiment.

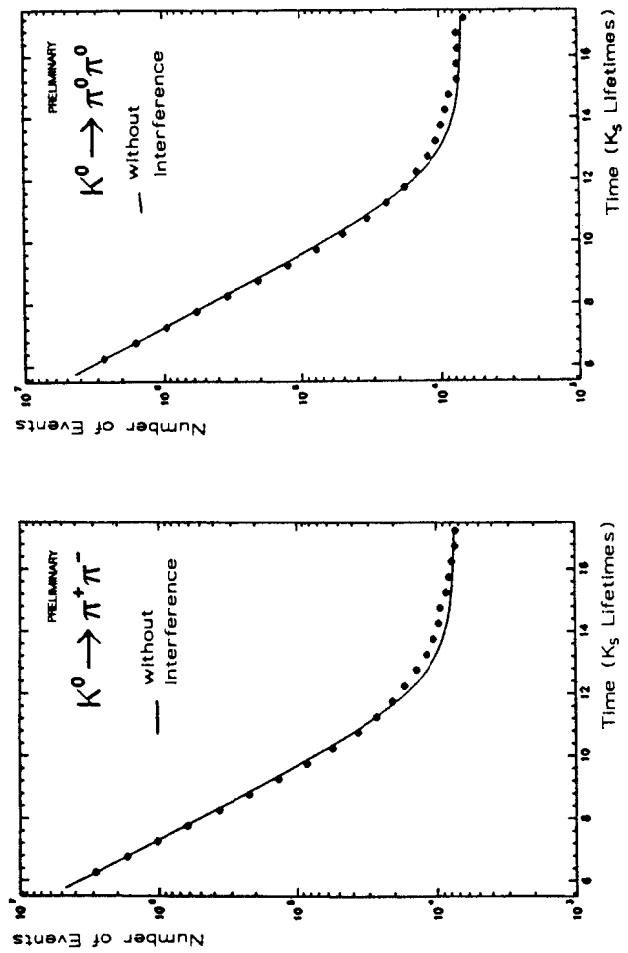

Fig. 24 Distribution of Lifetimes for $K \rightarrow 2\pi$ Decays.

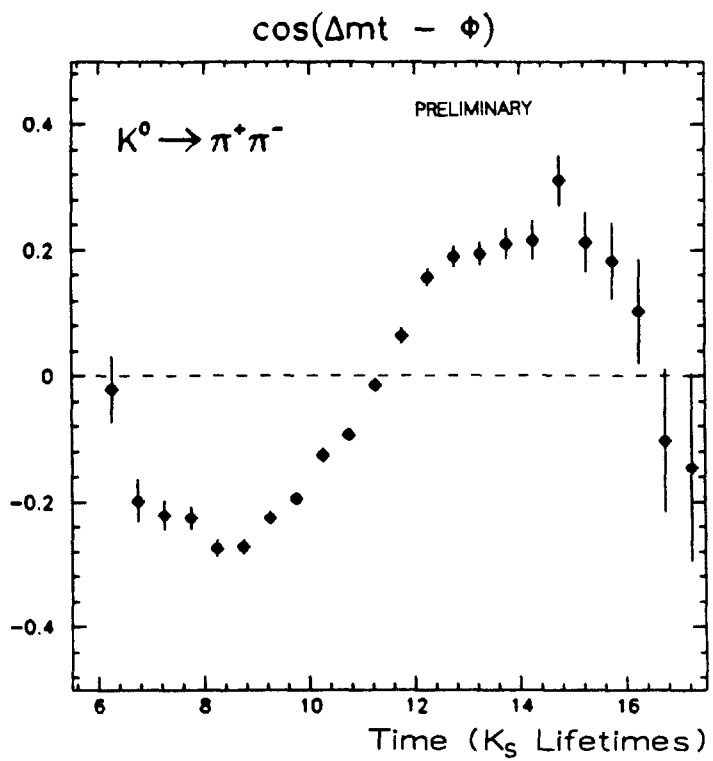

Fig. 25 Interference Term, Extracted from Curve of Fig. 24a.

The analysis of a measurement of the phase difference $\Phi_{00} - \Phi_{+-}$ is in progress. The precision of previous experiments will be improved substantially and allow us to check if the phase difference is compatible with zero, the prediction of CPT.

The neutral kaon system is still a very important field for testing fundamental symmetries in elementary particle physics and for probing the standard model. It will be complemented in the not too far future by the beauty system. B meson factories will open the possibility to get new insight into the problem of CP violation which is still far from being understood. However, results with reasonable precision cannot be expected within the next few years.

Acknowledgement

I wish to thank the directors of the SLAC Summer Institute for a pleasant and stimulating meeting. I thank my colleagues H. Burkhardt, V. Gibson and H. N. Nelson for reading the manuscript and for comments.

REFERENCES

[1] Members of the NA-31 collaboration:
G.D.Barr, P.Clarke, D.Coward, D. Cundy, N.Doble, L.H.M.H.Gatignon, V.Gibson, P.Grafström, R.Hagelberg, G.Kesseler, J. van der Lans, T.Miczaika, H.N.Nelson, P.Steffen, J.Steinberger, H.Taureg, H. Wahl, C. Youngman, (CERN); G.Dietrich, F.Eisele, W.Heinen (Univ. of Dortmund); R.K.Black, D.J.Candlin, J.Muir, K.J.Peach, B.Pijlgroms, I.P.Shipsey, W.Stephenson (Univ. of Edinburgh); H.Blümer, M.Kasemann, K.Kleinknecht, P.Mayer, B.Panzer, B.Renk, S.Röhn, H.Rohrer (Univ. of Mainz); E.Augé, R.L.Chase, M.Corti, D.Fournier, I.Harrus, P.Heusse, L.Iconomidou-Fayard, A.M.Lutz, A.C.Schaffer (Univ. of Orsay); A.Bigi, M. Calvetti, R. Carosi, R. Casali, C.Cerri, R.Fantechi, S.Galeotti, G.Gargani, I.Mannelli, E.Massa, A.Nappi, D.Passuello, G.M.Pierazzini (Univ. of Pisa); C.Becker, H.Burkhardt, D.Heyland, M.Holder, A.Kreutz, G.Quast, M.Rost, H.G. Sander, W. Weihs, G. Zech (Univ. of Siegen).

[2] H. Burkhardt et al., Phys. Lett. **206B** (1988) 163.

[3] H. Burkhardt et al., Nucl. Inst. Meth. **A268** (1988) 116.

[4] J. Steinberger CERN-EP/88-66.

[5] G. Quast, Thesis, Siegen, 1988.

[6] M. Kobayashi and K. Maskawa, Prog. Theor. Phys. **49** (1973) 652.

[7] J. Ellis, M.K. Gaillard and D.V. Nanopoulus, Nucl. Phys. **B109** (1976) 213.

[8] F.J. Gilman and M.B. Wise, Phys Lett. **83B** (1979) 83.

[9] F.J. Gilman and J.S. Hagelin, Phys. Lett. **133B** (1983) 443.
L. Wolfenstein, Ann. Rev. Nucl. and Part. Sci. **36** (1986) 137.
J.F. Donoghue et al., Int. Jour. of Mod. Phys. **2A** (1987) 319.
A.J. Buras and J.-M. Gerard, Phys. Lett. **203B** (1988) 272.

[10] L. Wolfenstein, Phys. Rev. Lett. **13** (1964) 562.

[11] M. Banner et al.,Phys. Rev. Lett. **21** (1968) 1107.
V.V. Barmin et al., Phys Lett. **33B** (1970) 377.
M. Holder et al., Phys. Lett. **40B** (1972) 141.
M. Banner et al., Phys. Rev. Lett. **28** (1972) 1597.
J.H. Christenson et al., Phys. Rev. Lett. **43** (1979) 1209.
J.K. Black et al., Phys. Rev. Lett. **54** (1985) 1628.
R.H. Bernstein et al., Phys. Rev. Lett. **54** (1985) 1631.

[12] M. Woods et al., Phys. Rev. Lett. **60** (1988) 1695.

[13] A.A. Petrukhin and V.V. Shestakov, Can. J. Phys. **46** (1968) 377.

[14] V.V. Barmin et al., Nucl. Phys. **B247** (1984) 293.

RESULTS from E731

$\frac{\epsilon'}{\epsilon}$ Measurement at FNAL

B. PEYAUD DPhPE-CEN/SACLAY
F-91191 Gif sur Yvette

ABSTRACT : The experimental result obtained in a test run (E731A at Fermilab) on the magnitude of the ratio of CP non conserving parameters ϵ'/ϵ is discussed. The same collaboration [1] took more data with an improved detector (E731B run ended in February 1988) of which 20% went through preliminary analysis. The high quality of this new run is demonstrated and it will permit to measure a non zero CP violation in the $K_2 \to 2\pi$ decay amplitude with systematics and sensitivity down to the level of 0.001 on ϵ'/ϵ.

INTRODUCTION :

It is now 24 years since the discovery of CP violation [2] and the observations of the effect are still limited to the K° - $\bar{K}^\circ$ system. When it was realized that CP violation could occur naturally through the mixing matrix of quarks and leptons with at least three generations [3] new experiments started to be performed to test the consequences of the hypothesis in the framework of the electroweak theory.

Over the last year, Fermilab has hosted the E731 collaboration to carry out a dedicated measurement of ϵ'/ϵ predicted to be non zero thus being a signal for a new source of CP violation.

PHENOMENOLOGY OF CP VIOLATION

The K° and $\bar{K}^\circ$ mesons are charge conjugate of one another with opposite strangeness and the $|K^\circ\rangle$ and $|\bar{K}^\circ\rangle$ states are appropriate to describe the strong and electromagnetic interactions of these particles. The weak decays of neutral kaons are associated with particles of definite mass and lifetimes which are linear combinations of $|K^\circ\rangle$ and $|\bar{K}^\circ\rangle$.

With a conventional choice defining CP $|K^\circ\rangle = |\bar{K}^\circ\rangle$ and CP $|\bar{K}^\circ\rangle = |K^\circ\rangle$ then $|K_1^\circ\rangle = \frac{1}{\sqrt{2}}(|K^\circ\rangle + |\bar{K}^\circ\rangle)$ and $|K_2^\circ\rangle = \frac{1}{\sqrt{2}}(|K^\circ\rangle - |\bar{K}^\circ\rangle)$ are orthogonal CP eigenstates with CP $|K_1^\circ\rangle = |K_1^\circ\rangle$ and CP $|K_2^\circ\rangle = -|K_2^\circ\rangle$. They allow then to describe the short-lived K_S° decays into the two most significant modes $\pi^+\pi^-$ and $\pi^\circ\pi^\circ$ each with CP eigenvalue of + 1, and the long-lived K_L° decays in many modes like $\pi^+\pi^-\pi^\circ$ predominantly with CP eigenvalue of -1. Making the approximation of CP invariance would then imply that $|K_S^\circ\rangle = |K_1^\circ\rangle$ and $|K_L^\circ\rangle = |K_2^\circ\rangle$.

The discovery that $K_L^\circ \to \pi^+\pi^-$ does actually occur complemented by the experimental evidence of $K_L^\circ \to \pi^\circ\pi^\circ$ decays and charge asymmetry of the semi-leptonic channels of K_L° led to rewrite the physical states in terms of a mixture of the above $|K_1^\circ\rangle$ and $|K_2^\circ\rangle$ states.

$$|K_L^\circ\rangle = \frac{1}{\sqrt{1+|\epsilon|^2}}(|K_2^\circ\rangle + \epsilon\,|K_1^\circ\rangle) \text{ mainly CP odd}$$

$$|K_S^\circ\rangle = \frac{1}{\sqrt{1+|\epsilon|^2}}(|K_1^\circ\rangle + \epsilon\,|K_2^\circ\rangle) \text{ mainly CP even}$$

where $|\epsilon| = (2.275 \pm 0.021)\ 10^{-3}$ parametrizes the mixing that originates from the off-diagonal elements of the K° - $\bar{K}^\circ$ mass matrix.

The experimental observables are the ratios of transition amplitudes for the $\pi^+\pi^-$ and $\pi^\circ\pi^\circ$ decay modes, they read :

$$\eta^{+-} = \frac{\langle \pi^+\pi^-|\,T|\,K_L\rangle}{\langle \pi^+\pi^-|\,T|\,K_S\rangle} \qquad \text{charged decays}$$

$$\eta^{\circ\circ} = \frac{\langle \pi^\circ\pi^\circ|\,T|\,K_L\rangle}{\langle \pi^\circ\pi^\circ|\,T|\,K_S\rangle} \qquad \text{neutral decays}$$

With very good accuracy these ratios are $\eta^{+-} = \epsilon + \epsilon'$ and $\eta^{\circ\circ} = \epsilon - 2\epsilon'$.

In the standard model of electroweak interaction ϵ comes from the calculation of "box" diagrams that represent $\Delta S = 2$ transitions between K° and $\bar{K}^\circ$. The new parameter ϵ' corresponds to "direct" CP violation via $K_2 \to 2\pi$ decays. The contribution to ϵ' arises mainly from "Penguin" diagrams ($\Delta S = 1$ transitions) since unlike spectator and exchange diagrams they involve three generations of quarks. Therefore if $K_2 \to 2\pi$ does not occur one has $\eta^+ = \eta^{\circ\circ} = \epsilon$, this is the superweak hypothesis.

The current predictions for ϵ'/ϵ still have large uncertainties due to calculations of hadronic matrix elements, unkown mass of the top quark and poor determination of the ratio $b \to u/b \to c$. The typical range predicted by the theory is $7 \times 10^{-3} > |\frac{\epsilon'}{\epsilon}| > 1 \times 10^{-3}$ [4]. This sets the precision of 0.001 that our experiment designed to search for direct CP violation has to reach.

THE DETECTOR AND THE EXPERIMENTAL METHOD [5]

The relative decay rates of K_L and K_S to neutral and charged pions is the double ratio $R = |\frac{\eta^{\circ\circ}}{\eta^{+-}}|^2 = 1 - 6\ \mathrm{Re}\,(\frac{\epsilon'}{\epsilon})$. This has to be measured with $\frac{\Delta R}{R} = 6 \times 10^{-3}$ to reach the statistical accuracy of 0.001 on $|\epsilon'/\epsilon|$ implying that a minimum sample of 50000 $K_L^\circ \to 2\pi^\circ$ events has to be identified and fully reconstructed in the detector. Furthermore systematic errors must be minimized and effective control of these effects is important.

The Meson Center beam line at Fermilab was used to provide high kaon flux in two parallel beams produced at 4.8 mrad by 800 GeV protons on a Be target. A four (B_4C block + Pb + scintillator) active regenerator located at 127 m from the target (Fig. 1) was moving alter-

natively between the two beams every proton spill (~ one minute) to produce coherent K_S with momentum spectrum similar to the K_L one in the range 30 - 160 GeV/c. This configuration allows simultaneous detection of K_S and K_L decays and offers total cancellation of flux ratios ans cancellation of dead time, accidental effects and innefficiency to high accuracy.

Fig. 1 : Front view of the Regenerator.

To first order, $\epsilon'/\epsilon = \frac{1}{6}(1 - R_{obs})$ where R_{obs} is given by:

$$R_{obs} = \frac{K_L \to \pi^\circ \pi^\circ}{K_S \to \pi^\circ \pi^\circ} \Big/ \frac{K_L \to \pi^+ \pi^-}{K_S \to \pi^+ \pi^-}$$

where $K_{L,S} \to \pi\pi$ are the number of observed events in each mode.

The detector (Fig. 2) measures charged particles with a drift chamber spectrometer. Position resolution of trajectories is of 110 μm per plane with 98% efficiency and mass resolution is of 3.6 MeV/c² for $K_{L,S} \to \pi^+ \pi^-$.

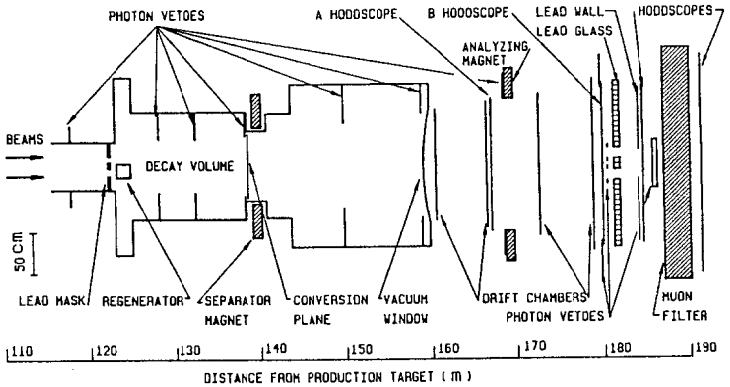

Fig. 2 : E731 Detector in the MC beam line.

The known K_e mass fixes the energy scale of the spectrometer. A circular array of 804 blocks of lead glass (Fig. 3) measures the energies and the positions of photons and electrons with resolutions respectively of $\langle \sigma_{pos} \rangle$ = 4 mm and $\sigma_E/E = 5\%/\sqrt{E} + 1.5\%$. The calibration of this electromagnetic calorimeter is known to 0.5%. A flasher system using a xenon lamp was used to monitor the stability of each block and special electron calibration runs were done during the data taking.

The decay mode $K_{L,S} \to \pi^+ \pi^-$ is observed by demanding a charged signature in the trigger plane at the end of the decay region and two tracks in the spectrometer. A semi leptonic decay (Ke_3 or $K\mu_3$) would veto this trigger.

The decay mode $K_{L,S} \to \pi^\circ \pi^\circ$ required conversion of one gamma ray in the 0.1 Xo lead converter at the trigger plane, a two track signature in the spectrometer and $>$30 GeV energy in the lead glass calorimeter.

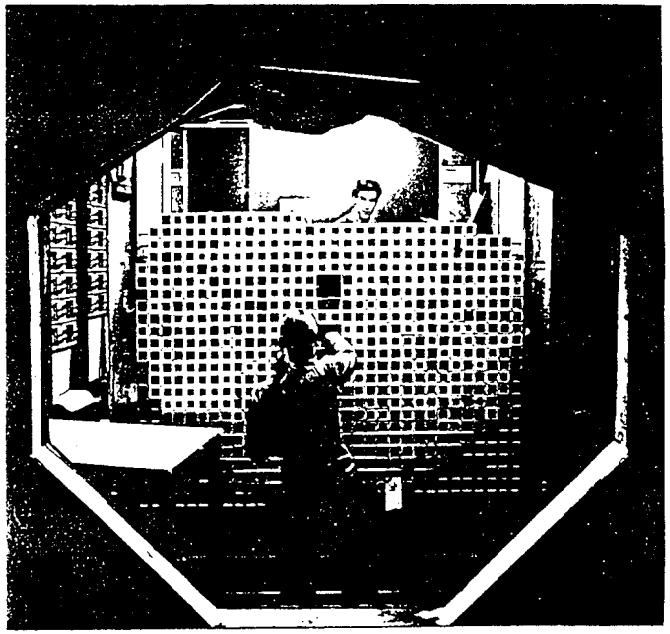

Fig. 3 : The Lead Glass array under construction.

Events having hadrons or muons were rejected by the neutral trigger and so were inelastically regenerated events (using scintillator in regenerator in veto) for both charged and neutral modes.

Different categories of reconstructed events are shown in Fig. 4, 5, 6 where it can be seen that background levels are very small. The K_S signals have residual background from incoherent regeneration : these are substracted with small uncertainty under the coherent peaks. The $K_L \rightarrow \pi^+ \pi^-$ event sample has background due to residual semileptonic decays where either a muon or an electron was misidentified as a pion. A small background coming from neutron interactions was also present at the level of 0.18% for $p_t^2 < 250$ MeV/c^2.

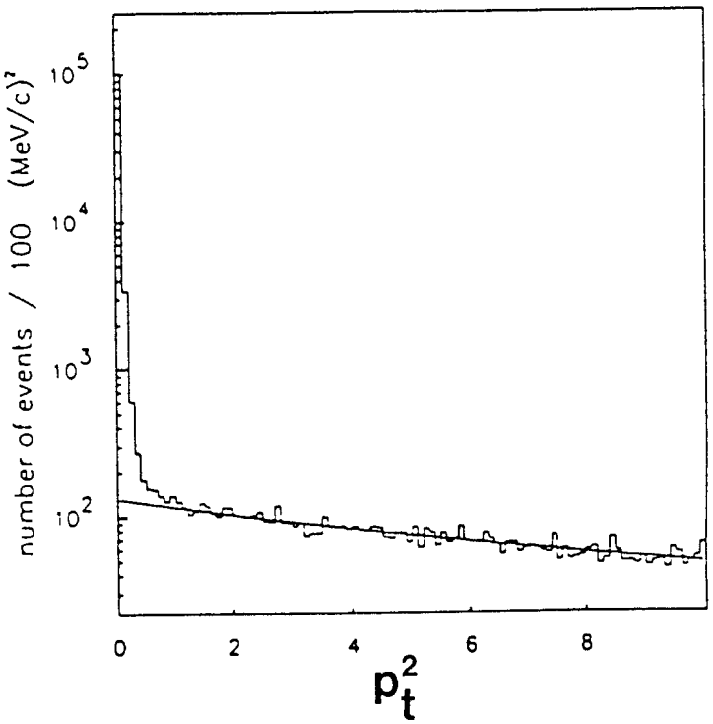

Fig. 4 : The distribution in P_t^2 for $\pi^+ \pi^-$ events in the regenerated beam (K_S).

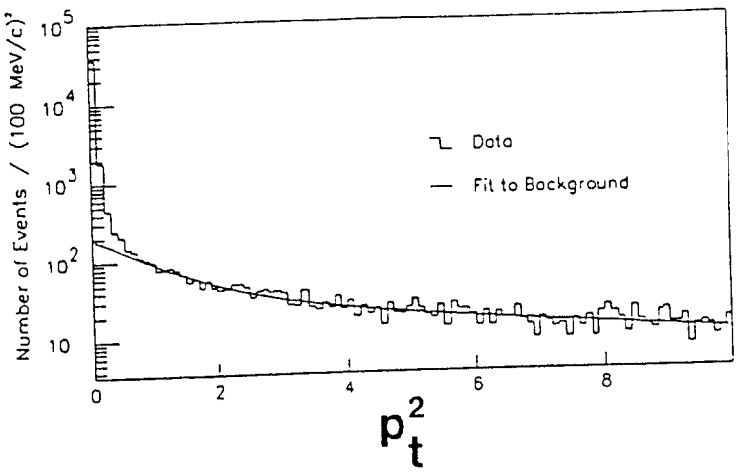

Fig. 5 : The distribution in P_t^2 for $\pi^+.\pi^-$ events in the vacuum beam (K_L).

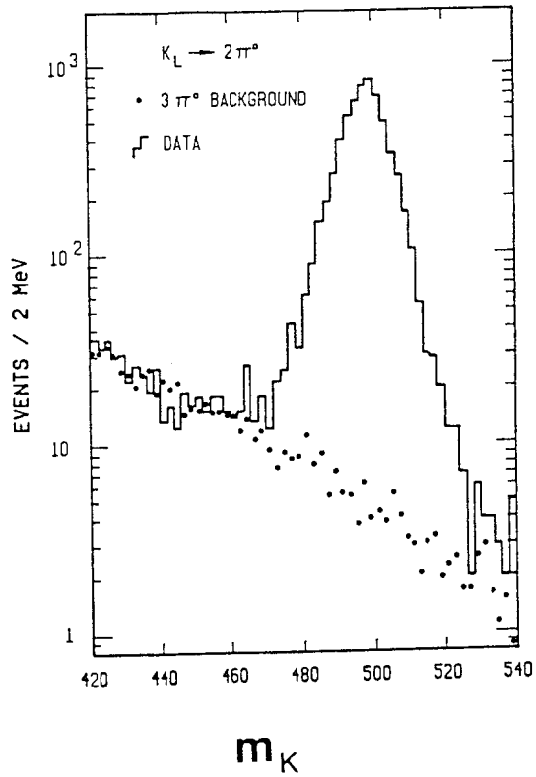

Fig. 6 : The distribution in m_K for $\pi^\circ\,\pi^\circ$ events in the vacuum beam.

The source of background in the $K_L \to 2\pi^\circ$ decay is from the dominant $K_L \to 3\pi^\circ$ decay where two photons missed the lead glass or fused in the same cluster. A detail study of these fake events was made with a high statistics Monte Carlo simulating their shape : this is in good agreement with the observed background in the mass distribution.

The final event sample for E731A is shown in the Table 1 below for each of the four decays.

	Events after bkg. subs.	Background percentage	Source of background
$K_S \to \pi^+ \pi^-$	130025	$(0.31 \pm 0.04)\%$	Incoherent + Diffractive
$K_L \to \pi^+ \pi^-$	35838	$(1.23 \pm 0.18)\%$	Semi-leptonic decays
$K_S \to \pi^\circ \pi^\circ$	21788	$(2.94 \pm 0.16)\%$	Incoherent + Diffractive
$K_L \to \pi^\circ \pi^\circ$	6747	$(1.56 \pm 0.31)\%$	$3\pi^\circ$ decays

Table 1

The ultimate accuracy on ϵ'/ϵ comes in part from the uncertainties in the background substraction that are made : this amounts to a total of 0.00066 on $|\epsilon'/\epsilon|$. The second source of systematic uncertainty comes from the acceptance corrections that have to be made to the background substracted samples. The size of the uncertainty in the charged acceptance correction was calculated to be 0.0005 on $|\epsilon'/\epsilon|$ from the known resolution smearings effects (chamber resolution + multiple scattering) and from an alternate analysis of the data in bins of momentum and vertex position for the charged data. The understanding of systematic effects in the neutral mode came mainly from the study of a large sample of $K_L \to 3\pi^\circ$ decays where the particles (photons) are the same. Various cuts were also made to the data in the vertex distribution Z (Fig. 7). We have determined a systematic error of 0.0007 on ϵ'/ϵ due to the neutral mode acceptance correction.

The determination of ϵ'/ϵ came from the fit of the corrected 2π ratio of rates and the result was :

$\epsilon'/\epsilon = 0.0032 \pm 0.0028$ (statistical) ± 0.0012 (systematic) [6].

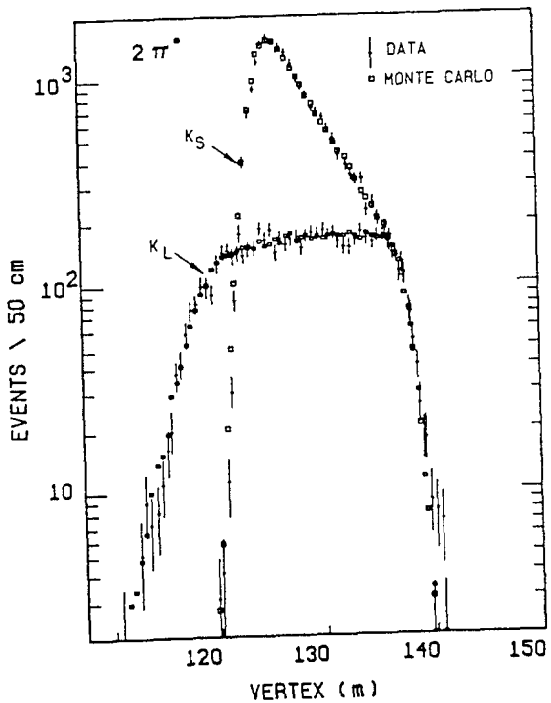

Fig. 7 : Reconstructed decay vertex for $K_{L,S} \rightarrow 2\pi^\circ$ and comparison with Monte-Carlo.

THE 1987 - 88 RUN : E731B :

A number of improvements were made to the detector and to the trigger before we took our data that amounts now to 300 10^3 events $K_L \rightarrow 2\pi^\circ$ and gives statistical accuracy of 0.0005 on ϵ'/ϵ.

The new features include for the detector :

- optimal regenerator in which diffractive K_S are reduced to minimal;
- upgrade of the photon veto system to have more powerful rejection on γ rays outside fiducial acceptance;
- upgrade of muon hodoscope to reject $K\mu_3$ more;
- conversion plane with segmentation at the end of decay region.

On the trigger side the improvements are :

- online hardware cluster finder to recognize four clusters;
- faster data acquisition with Fastbus ADC's and memories reducing the dead time per event from 6ms (E731A) to 0.7 ms (E731B);
- numerous decay channels like $3\pi^\circ$, $\pi^+\pi^-\pi^\circ$, K_{e3} are tagged to permit improved monitoring and calibration.

Neutral decays with no conversion were recorded together with the regular charged decays.

Data taking stopped in February 1988 and data reduction was made on ACP (Advanced Computer Project at FNAL) to do a preliminary analysis on 20% of the statistics.

Shall we reach the goal of having 0.0005 of systematic error on ϵ'/ϵ?

The current understanding of backgrounds with estimate on systematic errors is given in Table 2 below.

The errors will decrease when final calibrations are used (e.g. $\pi^+\pi^-\pi^\circ$ sample for energy calibration). Detail understanding of the beam shapes and spectrum is under way to have an accurate evaluation of acceptance functions.

	Level of background	Nature of background
$K_S \to \pi^+ \pi^-$	$(0.37 \pm 0.04)\%$	mostly $K \to \pi^+ \pi^-$
$K_L \to \pi^+ \pi^-$	$(0.14 \pm 0.014)\%$	Ke_3 and $K \to \pi^+ \pi^- \gamma$
$K_S \to \pi^\circ \pi^\circ$	0.02% $(3.0 \pm 0.3)\%$	$K_L \to 3\pi^\circ$ Non coherent K_S
$K_L \to \pi^\circ \pi^\circ$	$(0.3 \pm 0.08)\%$ $(4.0 \pm 0.2)\%$	$K_L \to 3\pi^\circ$ Non coherent K_S

Table 2

The quality of the data is shown in Figures 8 and 9 where 230×10^3 $K_S^\circ \to 2\pi^\circ$ and 67×10^3 $K_L^\circ \to 2\pi^\circ$ were reconstructed. Large samples of $3\pi^\circ$ events (5×10^6) and K_{e3} events (5×10^7) are invaluable to achieve systematics on acceptance at the level of few 10^{-4}.

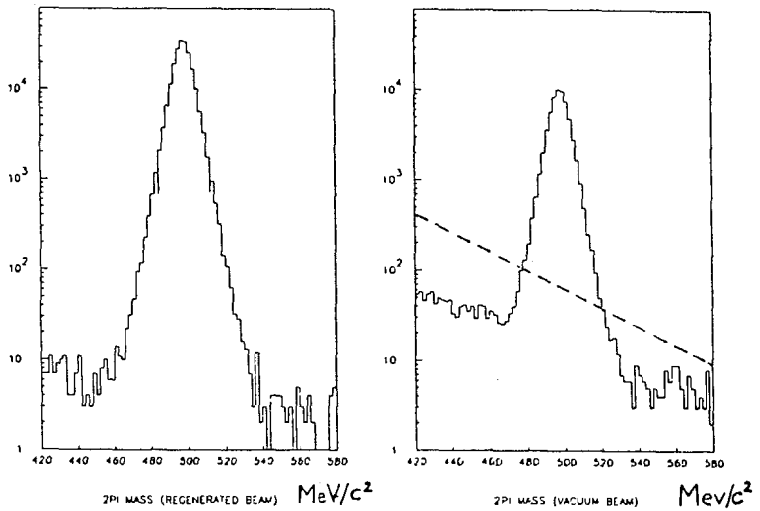

Fig. 8 : The distributions in m_K for $\pi^\circ \pi^\circ$ events for E731B. The figure on the right side shows the $K_L \to \pi^\circ \pi^\circ$ with the E731A background (dotted line).

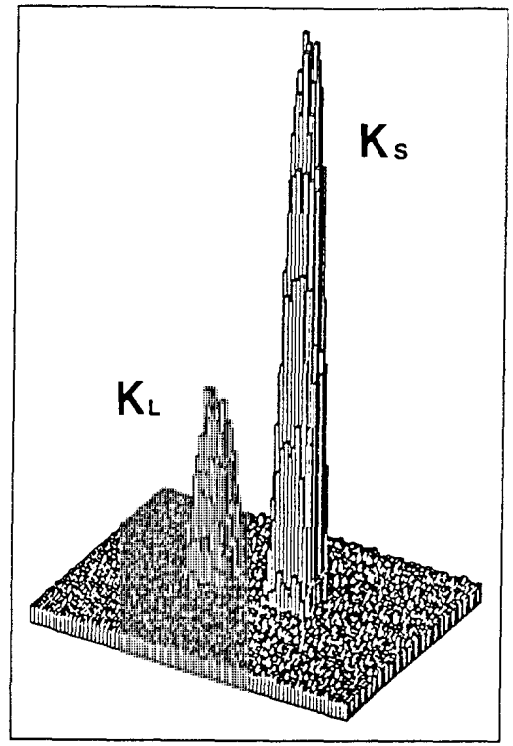

Fig. 9 : The center of energy in the Lead Glass for $K_{L,S} \to 2\pi^\circ$ in E731B. The background is non-coherent K_S decays from the regenerated beam.

Our result with total error of 0.001 on ϵ'/ϵ will become available in 1989 and comparison with the NA31 result (Ref. 7) will be of great interest.

CONCLUSIONS :

The importance of observing CP violation through direct decays of K_2 and the precise measurement of the magnitude of the effect are important to test the standard model.

This test will receive attention also from phenomena that are directly coming from heavy quark systems but it also may be feasible to have a significant improvement in the accuracy with which ϵ'/ϵ is measured in the K^0-$\bar{K}^0$ system. These two attacks are complementary rather than exclusive and they will give key numbers that the standard model will, or will not be able to correctly accommodate.

REFERENCES :

[1] FNAL experiment E731. The members of the Chicago-Elmhurst-Fermilab-Princeton-Saclay collaboration are :
L. GIBBONS, K. NISHIKAWA, V. PAPADIMITRIOU, J.R. PATTERSON, Y.W. WAH, B. WINSTEIN, R. WINSTON, M. WOODS, H. YAMAMOTO, E. SWALLOW, G.J. BOCK, R. COLEMAN, Y.B. HSIUNG, K. STANFIELD, R. STEFANSKI, T. YAMANAKA, G. BLAIR, G.D. GOLLIN, G.L. GRAZER, M. KARLSON, J.K. OKAMITSU, J.C. BRISSON, R. DAUDIN, P. DEBU, P. JARRY, B. PEYAUD, R. TURLAY, B. VALLAGE.

[2] J.H. CHRISTENSON, J.W. CRONIN, V.L. FITCH and R. TURLAY, Phys. Rev. Lett. 13, 138 (1964).

[3] M. KOBAYASHI and K. MASKAWA, Prog. Theor. Phys. 49, 652 (1973).

[4] See H. HARARI, these proceedings and also
L. WOLFENSTEIN, Ann. Rev. Nucl. Sci. 36, 137 (1986)
J.F. DONOGHUE et al., Phys. Rev. 131, 1 (1986)
A.J. BURAS and J.M. GERARD, Phys. Lett. B203, 272 (1988).

[5] A complete description of the detector and analysis is in P. JARRY, Ph.D thesis, Université de Paris-Sud, 1987 (unpublished)
M. WOODS, Ph.D thesis, University of Chicago, 1988 (unpublished).

[6] M. WOODS et al., Phys. Rev. Lett. 60, 1685 (1988).

[7] See G. ZECH, these proceedings and also
H. BURKHARDT et al., Phys. Lett. B 206, 169 (1988).

Status of the SLAC Linear Collider and Mark II*

PATRICIA R. BURCHAT

Santa Cruz Institute for Particle Physics
University of California, Santa Cruz, California, 95064

ABSTRACT

The status of the SLAC Linear Collider is discussed with emphasis on the achieved beam parameters and the diagnostic tools available near the interaction point for measuring transverse beam sizes and establishing that the two beams are colliding. Beam energy measurements from the extraction line spectrometers are also discussed. The response of the Mark II detector to beam-related backgrounds when beams are colliding is presented. With current backgrounds, Z^0 decays will be identifiable in the detector but for precise analyses the background must be reduced. A future installation of large toroid magnets in the tunnels of the final focus system is expected to reduce the backgrounds from muons by about a factor of ten. Other future installations include two vertex detectors: a three-layer silicon detector whose layers are about 3 cm from the interaction point and a high precision drift chamber. The status of these installations and the project to produce longitudinally polarized electron beams at the interaction point is discussed.

Invited talk presented at the SLAC Summer Institute on Particle Physics
Stanford, California, July 18-29, 1988

* Work supported by the U. S. Department of Energy.

1. The SLAC Linear Collider

The SLAC Linear Collider (SLC) was proposed in 1980 for two purposes:[1]

— to provide the first test of linear collider technology which will be necessary for e^+e^- physics at center-of-mass energies above about 200 GeV;

— to produce large numbers of Z^0's to provide precise tests of the standard model and an environment for searches for new particles such as quarks, leptons and the Higgs boson.

Although the SLC has not yet produced any Z^0's, much has already been learned about linear collider issues.

The overall layout of the SLC is shown in Figure 1. The same linear accelerator is used to accelerate both the electron and positron beams. Two arcs of bending magnets carry the beams to the final focus systems which focus the beams to a transverse size of a few microns. Two damping rings reduce the emittance of the beams in about five milliseconds. Positrons are produced by bombarding a target with an electron beam about two-thirds of the way down the accelerator.

On each machine cycle, the injector produces two electron bunches separated by 59 ns which enter the electron damping ring and circulate on opposite sides of the ring until the beginning of the next machine cycle. The previously stored bunches exit the damping ring and travel down the accelerator behind a positron bunch from the positron damping ring. The positron bunch and the first electron bunch are accelerated to about 50 GeV at the end of the accelerator. The second electron bunch is sent to the positron source to produce positrons for the next machine cycle. The positrons are focussed after the target and are transported back to the beginning of the accelerator and stored in the positron damping ring until the next machine cycle. After collision at the interaction point, each beam is deflected out of the final focus system into an extraction line where the beam energy is measured before the beam dump.

All parts of the SLC have now been commissioned with electron or positron beams. The luminosity at the interaction point (IP) can be written as follows:

$$\mathcal{L} = 1.5 \times 10^{27}\mathrm{cm}^{-2}\mathrm{s}^{-1}\,\frac{f}{30\,\mathrm{Hz}}\,\frac{N_-}{10^{10}}\,\frac{N_+}{10^{10}}\,\frac{4\,\mu\mathrm{m}}{\sigma_x}\,\frac{4\,\mu\mathrm{m}}{\sigma_y}$$

where f is the collision frequency, N_- and N_+ are the number of electrons and positrons per bunch at the IP, respectively, and σ_x and σ_y are the transverse beam sizes at the IP for the larger of the two beams. The achieved values for these parameters are summarized in Table 1. The first column lists the best achieved

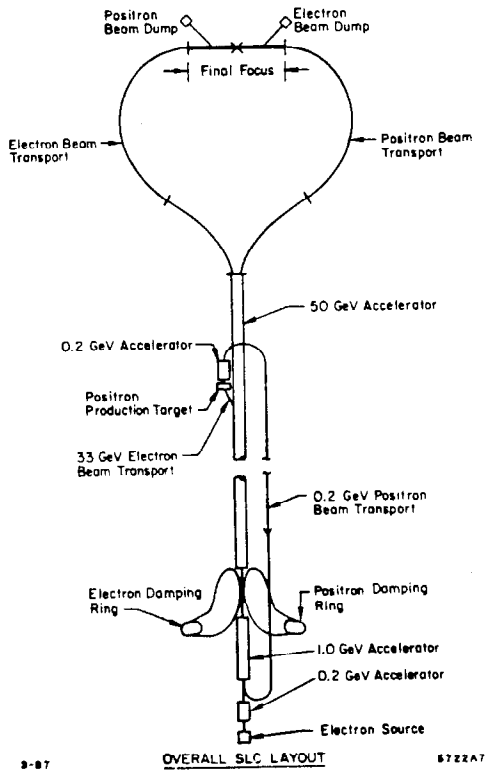

Figure 1. Layout of the SLAC Linear Collider.

Table 1. SLC parameters at the interaction point.

Parameter	Best Achieved Value	Typical Value for Current Running
f	30 Hz	30 Hz
N_-	1.5×10^{10}	0.8×10^{10}
N_+	0.7×10^{10}	0.5×10^{10}
$\sigma_x \times \sigma_y$:		
electron beam	3 μm×5 μm	6 μm×6 μm
positron beam	4 μm×4 μm	8 μm×8 μm

value and the second column lists typical values for recent colliding-beam runs. The rate for Z^0 production at the peak of the Z^0 resonance can be written in terms of the luminosity as follows:

$$Z^0 \text{ rate} \approx \frac{4}{\text{day}} \frac{\mathcal{L}}{1.5 \times 10^{27} \text{cm}^{-2}\text{s}^{-1}} \epsilon$$

where ϵ is the average efficiency for colliding beams. Each of the parameters at the IP will now be discussed and compared to the design values for the first year of running.

The entire machine is currently operating at a repetition rate of at least 30 Hz with parts of the linac running at 60 Hz in preparation for an increase to that frequency. The design frequency for first year running is 120 Hz.

The design intensity for each beam is 5×10^{10} particles per bunch. The intensity of the electron bunch is limited by bunch lengthening which occurs in the damping ring for high intensity beams because of the large effective impedance caused by irregularities in the vacuum chamber profile. The current is limited to about $(2-3) \times 10^{10}$ particles per bunch. A significant fraction of the impedance is due to corrugated copper sleeves inside the bellows. These will be replaced by smooth copper sleeves to allow an increase in current to $(3-5) \times 10^{10}$.

The positron intensity is currently limited by the efficiency for capturing the positrons after they are produced at the source and transporting them back to the beginning of the linac and into the positron damping ring. Because of the length of the bunch, the energy spread increases in the linac before the damping ring. This large energy spread leads to large beam sizes in the regions of high bending fields in the transport line from the linac to the damping ring. The aperture of this region will be increased to more efficiently transport the beam. In addition, a system to decrease the energy spread will be installed after the transport line and before the ring since the ring also has acceptance for only a limited energy spread. Eventually, the positron intensity will also be limited by the damping ring impedance and the positron damping ring will require the same improvements as the electron damping ring.

The transverse beam size at the IP is given approximately by

$$\sigma^2 = \beta\epsilon + (\eta \frac{\Delta E}{E})^2$$

where β is the value of the beta function at the IP, ϵ is the emittance, η is the dispersion at the IP, and $\frac{\Delta E}{E}$ is the fractional energy spread in the bunch. We are currently operating with an optical configuration with $\beta = 30$ mm at the IP. The design invariant emittance is $\epsilon\gamma = 3 \times 10^{-5}$ m rad. Therefore the minimum spot size at the IP is 3 μm for design emittance. If there is residual dispersion η at the IP, the energy spread of $(0.2-0.3)\%$ will also contribute to the spot size. Although the transverse beam size has been measured to be as small as 3 or 4 μm, it is often closer to 6 or 8 μm. It is not yet fully understood whether the extra contribution to the spot size is due to large effective emittance or dispersion at the IP. Residual dispersion from the arcs is routinely corrected in the the final focus system but the residual dispersion at the IP has not been thoroughly studied although the tools for doing so are available. To reach the design beam size of 2 μm, we must change the final focus optical configuration to provide $\beta = 7.5$ mm instead of 30 mm at the IP. The larger β value has the advantage of reducing beam-related backgrounds in the region of the final focussing quadrupoles (since the beam is then smaller in this region) and minimizing the relative contribution from higher order optical effects so that the lowest order contributions to the spot size can be studied.

To date, the Mark II detector has logged about 20 hours of colliding beam data. The corresponding integrated luminosity times the peak Z^0 cross section is about 0.2. The main value of this colliding beam time has been to assess beam-related backgrounds in the Mark II detector, monitor beam motion at the IP, and gain experience in tuning the beams.

2. Beam Diagnostics Near the Interaction Point

Measurements of the transverse beam size at the IP are necessary for tuning optical elements in the final focus system to minimize the spot size. In addition, diagnostics are needed to provide evidence that the two beams are colliding when they are both crossing the IP.

The transverse beam size is measured using a fine conductive wire. Initially, a wire was scanned across the beam[2] but currently the beam is scanned across a stationary carbon fiber using upstream magnets. The beam can be moved across the wire in steps as small as one micron. In each of the two transverse dimensions, there are three wires of different diameters: 4 microns, 7 microns and 28 microns.

Two signals are typically recorded for a scan: a secondary emission signal from the wire itself and a bremsstrahlung signal which is detected far from the interaction point. The secondary emission signals are different for the electron and positron beams with the positron-beam signal typically being larger. Effects which are not fully understood corrupt the secondary emission signal for electron beam intensities larger than about 6×10^9 particles per bunch. At these intensities we usually use the bremsstrahlung signal to measure the transverse beam profile. This technique will be described in more detail below. A typical electron beam profile is shown in Figure 2(a) for a step size of three microns. The vertical axis corresponds to the secondary emission signal. The beam was scanned across a seven micron diameter wire. A simple Gaussian fit to the beam profile yields a beam size (σ) of about five microns.

The wire scanner is used in automated procedures for positioning the focal point of each beam at the IP and measuring dispersion and chromaticity at the IP as well as for single beam scans. The wires are also used for initial placement of the two beams at the same point in the transverse plane to within a few microns.

For optimal luminosity, we must ensure that the two beams cross the transverse plane at the IP at the same point to within a fraction of the beam size. In principle, the wire scanner can be used for this purpose. However, scanning the beam across the wire is not compatible with running the Mark II detector with all subsystems at full voltage because of background radiation produced from the wire. A method which does not interfere with running the detector has been devised, tested and is now used routinely. This method uses the pattern of angular deflection of one beam as it is scanned across the other.[3] The angular deflection is due to the electromagnetic interaction between the two beams. In terms of the impact parameter Δ between a round target beam of transverse size

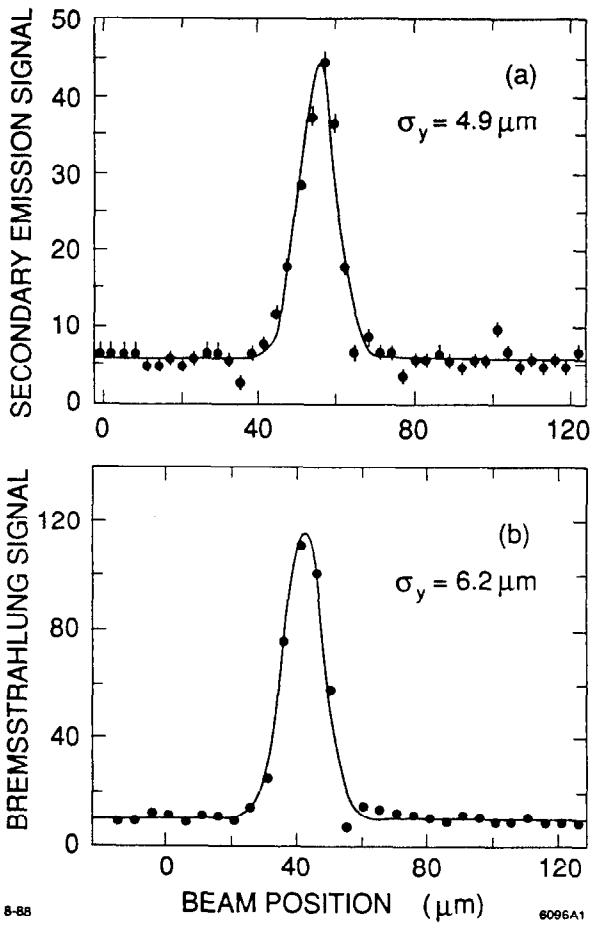

Figure 2. Typical electron beam profiles for (a) the secondary emission signal and (b) the bremsstrahlung signal.

σ and a point size probe beam, the deflection of the probe is given by

$$\theta(\Delta) = \frac{-2r_e N}{\gamma} \frac{1 - \exp(\frac{-\Delta^2}{2\sigma^2})}{\Delta}$$

where r_e is the classical radius of the electron, γ is the relativistic Lorentz factor, and N is the number of particles in the target bunch. This function is shown in Figure 3 for a target intensity of 5×10^{10} particles per bunch and for three different target sizes: two, five and ten microns. As the target beam size decreases, the maximum deflection becomes larger and occurs for smaller impact parameter leading to a more rapidly changing deflection angle as the two beams cross each other. This rate of change of deflection angle can be used for tuning on spot size as an alternative to the wire scanner. The symmetry point in the scan gives the point at which the two beams have zero impact parameter. This is used for centering the beams. Once the beams are brought into close proximity (a few to ten microns) with the wire scanner, one beam is scanned across the other in each plane. The deflection angle is fit to the above equation to determine how much one beam should be moved to center it on the other. The deflection angle is measured with three beam position monitors (BPM's) on each side of the IP. These monitors of the strip-electrode type are sensitive to each beam separately. For each beam, the BPM readings are used to fit the incoming angle, the deflection angle, and the transverse position at the IP in each plane.

A typical scan is shown in Figure 4. In this case, the positron beam was scanned across the electron beam in two micron steps in the x direction. Figure 4(a) shows the deflection angle in the $x - z$ (horizontal) plane. The beams were actually offset from each other in the y (vertical) direction by about ten microns during the scan. Hence, a deflection angle is also observed in the $y-z$ plane. This is shown in Figure 4(b). There exists an arbitrary offset in the measured deflection angle due to unknown BPM offsets. This beam deflection method is used to center the beams on each other and then to monitor how well centered the beams remain. The deflection can be measured and the beams recentered in less than 20 seconds. Hence, the beam centering can easily be monitored every 10 minutes or so. It has been found that the beams drift with respect to each other by only a small fraction of the beam width in this length of time.

Another way to establish that the two beams are centered is through the observation of beamstrahlung, the radiation emitted by one beam when it passes through the intense electromagnetic field of the other beam. Actually, beamstrahlung is also emitted when the beams are not centered but are deflecting each other. As one beam is scanned across the other, the beamstrahlung intensity is expected to grow as they get closer together and the deflection angle increases but to actually dip slightly as they become centered.

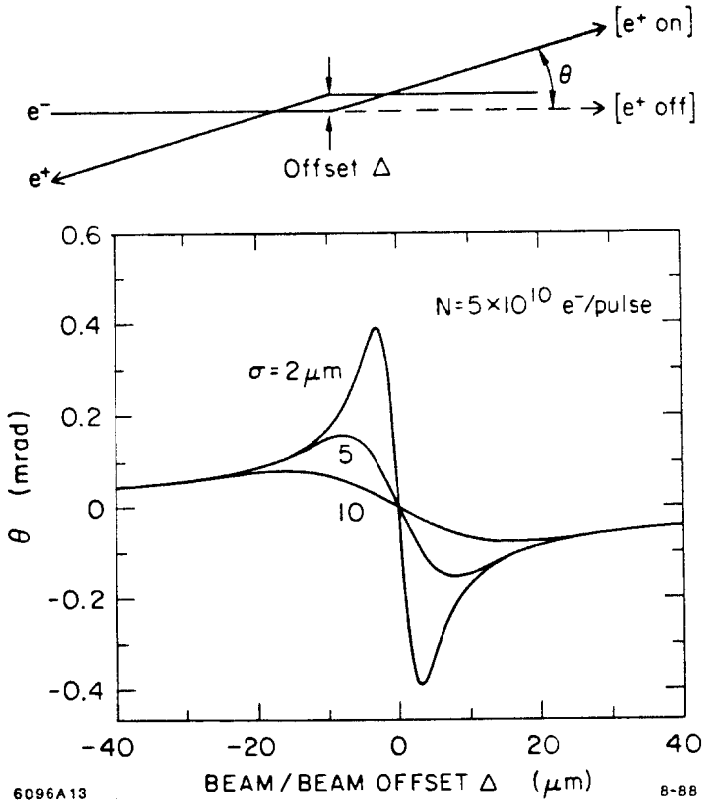

Figure 3. Theoretical deflection angle θ of a point probe as a function of impact parameter Δ between the point size probe beam and a round target beam of three sizes. The intensity of the target beam is assumed to be 5×10^{10}.

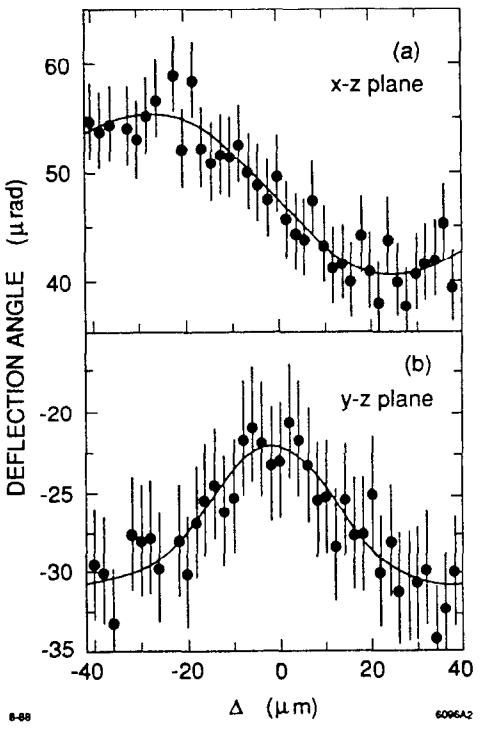

Figure 4. The deflection angle in the (a) $x-z$ plane and (b) $y-z$ plane for a positron beam scanned across an electron beam in the x direction. The beams are offset by approximately 10 μm in the y direction.

To monitor the beamstrahlung flux, Čerenkov detectors were built and installed about 40 m downstream on either side of the IP. The beamstrahlung monitor is shown schematically in Figure 5. It consists of a stainless steel plate to convert gamma rays at about 50 MeV to e^+e^- pairs. These charged particles travel through a Čerenkov detector with a threshold of about 25 MeV. A mirror and a system of light channels are used to focus the Čerenkov light onto an array of photomultiplier tubes. The whole detection system is surrounded by lead shielding for protection from beam-related backgrounds.

The beamstrahlung flux depends critically on the luminosity and the intensity and length of the target beam. At current luminosities, the beamstrahlung signal is marginal. However, the beamstrahlung monitor has been used very effectively to detect the bremsstrahlung photons emitted during a wire scan as mentioned above. Figure 2(b) shows an electron beam profile as measured by the beamstrahlung monitor. The beam was scanned across a seven micron wire in five micron steps. The profile was fit to a Gaussian function of width (σ) six microns.

3. Extraction Line Energy Spectrometer

The precise measurement of the mass of the Z^0 will provide a stringent test of the standard model. For this measurement, an accurate and precise determination of the electron and positron beam energies is necessary. This will be provided by a spectrometer system installed in each of the two extraction lines which transport the beams to their dumps.[4] The extraction line spectrometer is shown schematically in Figure 6. The spectrometer magnet is preceded and followed by smaller magnets which bend the beam in the plane perpendicular to the bend plane of the spectrometer magnet. When the beam bends in the small magnets, it produces swaths of synchrotron radiation which are detected about 15 m downstream of the spectrometer magnet.

The determination of the beam energy then depends on knowledge of the field strength of the spectrometer magnet, the distance between the spectrometer magnet and the synchrotron light monitors, and the distance between the two synchrotron stripes at the plane of the monitors. The field strength of the spectrometer magnet is about 3 T m and is known and monitored to better than 0.02%.[5] The distance to the light monitor is expected to be measured to better than 0.01%. The distance between the synchrotron stripes at the light monitors is about 26 cm and is known to better than 0.005%. These errors will combine to give a total uncertainty on the energy of each beam of less than 15 MeV. We expect an additional uncertainty in the luminosity-weighted center-of-mass

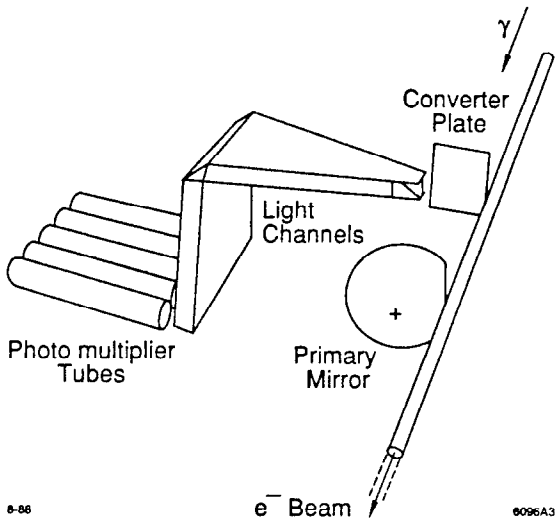

Figure 5. Schematic drawing of the beamstrahlung monitor.

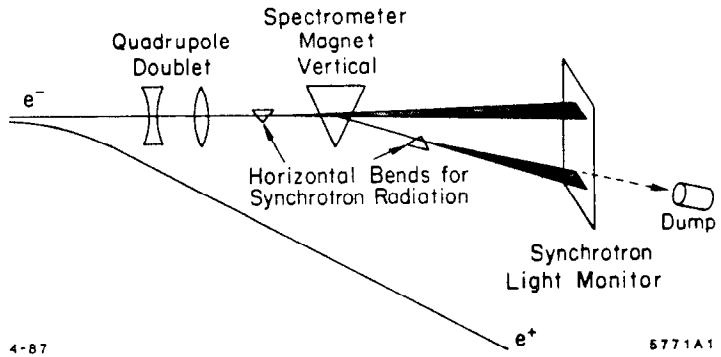

Figure 6. Schematic drawing of the extraction line spectrometer for measuring the beam energy.

energy of 15 MeV or less due to correlations in energy and transverse position for the beam at the IP. Therefore, the total systematic error on the center-of-mass energy will be about 35 MeV.

The synchrotron stripes are intercepted by phosphor screens which are monitored and digitized by a video system. The digitizations of the four stripes corresponding to the electron and positron beam, before and after the spectrometer magnet, are shown in Figure 7. Each digitization channel corresponds to 70 μm on the phosphor screen or 12 MeV in beam energy. An array of fiducial wires is located in front of each screen to provide a calibration for the exact location of the stripes. In addition to providing a measurement of the beam energy, the digitizition of the synchrotron stripes enables us to measure the energy spread within each beam by comparing the width of the stripe before and after the spectrometer magnet since we know the dispersion introduced by the magnet.

An independent method for measuring the distance between the synchrotron stripes is also being developed. This method measures the signals from an array of wires parallel to the synchrotron stripe. The signal, produced by Compton scattering, has been observed but the electronics and readout system are not yet complete.

In Figure 8, the energies of the electron and positron beams as measured by the energy spectrometer are shown for 100 consecutive triggers of the Mark II detector selected for a period of running in which the electron beam energy was quite stable.* The trigger rate was about one hertz, so this interval corresponds to a couple of minutes. It can be seen that the relative pulse-to-pulse energy resolution is very good over this short time period. The relative resolution over long time periods is under study. Based on the data accumulated so far, the design goal for the absolute resolution should be achievable without difficulty.

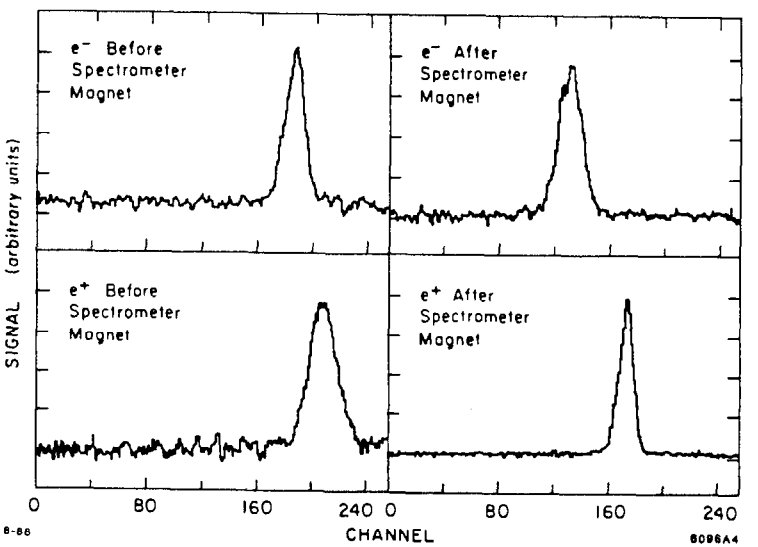

Figure 7. Digitizations of the four synchrotron stripes corresponding to the electron and positron beams, before and after the spectrometer magnet. Each digitization channel corresponds to 70 μm on the phosphor screen or 12 MeV in beam energy.

* For SLC, the two beam energies are not expected to be exactly equal.

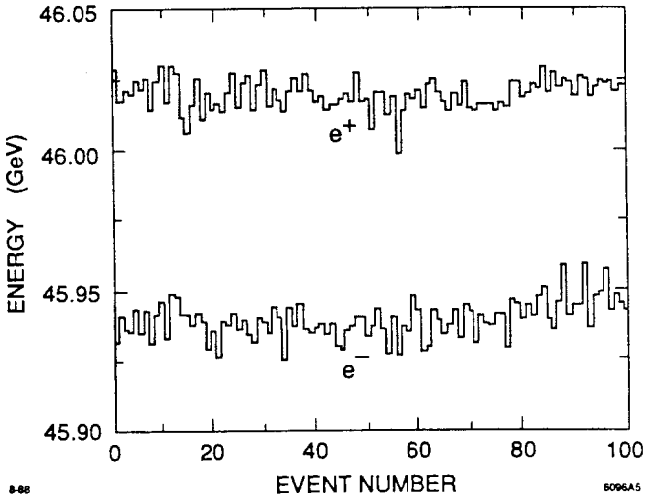

Figure 8. Energy of the electron and positron beams as measured by the extraction line energy spectrometer over a period of a couple of minutes.

4. The Response of the Mark II Detector to Beam-Related Backgrounds

An upgrade of the Mark II detector which involved replacing the drift chamber, endcaps, time-of-flight system and magnet with new systems was completed in the summer of 1985. In the winter of 1986, the upgraded detector was tested and operated at the PEP storage ring. The detector was then moved to the SLC interaction region. In the fall of 1987, the detector was moved onto the beam line. The detector has been continuously exercised on cosmic rays since its installation at SLC.

A sectional view of one quarter of the detector is shown in Figure 9. The vertex detectors have not yet been installed and will be discussed below. I will give a brief description of each detector subsystem and discuss the response of the subsystem to beam-related backgrounds in the recent colliding-beam data.

4.1 Drift Chamber

The central drift chamber consists of about 6000 readout wires arranged so that the position of a track which travels through the full radius is measured at 72 points. The chamber electronics has double-pulse capability so that tracks within about 3 mm of each other can be resolved.

The average number of drift chamber TDC hits recorded per event for random triggers in recent colliding-beam data was about 600. However, fewer than 10% of the wires had signals since many of these hits correspond to multiple hits on one wire. This background is due to both muons produced in collimators in the final focus system and electromagnetic debris produced closer to the detector.

In random triggers, about 5% of events have at least one track found by the offline track reconstruction program. However, these tracks do not originate from the interaction point, especially in the beam direction, and will therefore be easy to differentiate from tracks originating from e^+e^- annihilation.

The effect of these spurious hits on track reconstruction was studied by superimposing real background events on Monte Carlo events for Z^0 decay. It was found that approximately 3% of all tracks are lost when the background hits are added. However, these are mostly tracks with few drift chamber hits which exit through the ends of the drift chamber because they are emitted from the interaction point with a small angle with respect to the beam direction. Of the tracks which are reconstructed, approximately 90% are measured as well as they would be without the background hits. The conclusion is that 600 or fewer TDC hits per event is not a problem for offline track reconstruction.

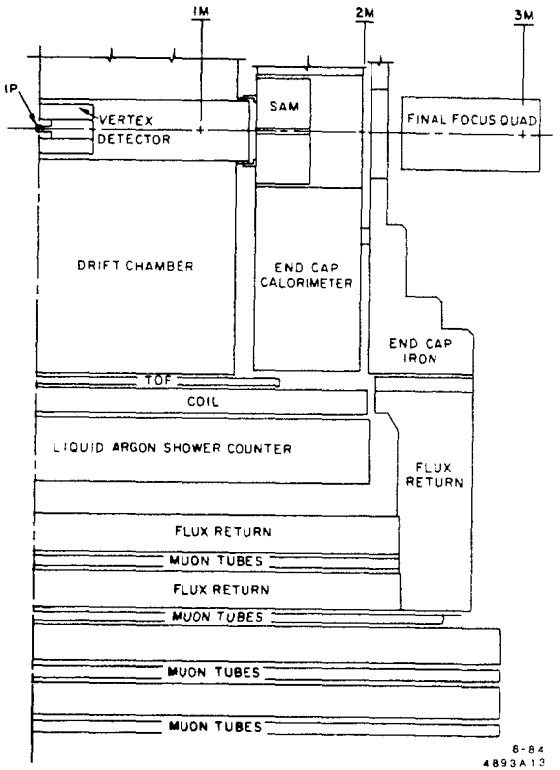

Figure 9. Sectional view of one quarter of the Mark II detector.

These spurious hits are a problem for triggering. The charged track trigger uses fairly wide swaths through the drift chamber in which to search for TDC hits. The charged track trigger is satisfied relatively easily by the background hits leading to a high trigger rate and therefore significant deadtime. This will be even more problematic when the machine repetition rate is raised from 30 Hz to 60 and then 120 Hz.

4.2 Luminosity Monitors

There are two luminosity monitors for measuring the Bhabha rate at small angles with respect to the beam direction: the small angle monitor (SAM) which subtends the region between 50 and 160 mrad and the mini-SAM which subtends the region between 15 and 25 mrad. The Bhabha rate in the SAM is about equal to the peak Z^0 rate while the Bhabha rate in the mini-SAM is about seven times greater. Both luminosity monitors are sensitive to electromagnetic radiation generated near the beam pipe.

The mini-SAM consists of about 15 radiation lengths of tungsten and scintillator read out with photomultiplier tubes. The modules are about two meters downstream of the IP and are each divided into four quadrants. During relatively quiet colliding beam runs, the equivalent electron energy deposited in a quadrant is typically a couple of GeV or less. However, occasionally much larger amounts (tens of GeV) are deposited. These large depositions usually occur in more than one quadrant and often in diagonally opposite quadrants on each side of the IP as one would expect for a Bhabha event. Fortunately, however, these large beam-related backgrounds are usually associated with only one beam and hence occur separated in time on the two sides of the IP by about 20 ns instead of simultaneously as one would expect for Bhabha events. Hence, we should be able to identify a Bhabha event in the relatively quiet colliding beam data.

The SAM consists of about 14 radiation lengths of lead and proportional tubes preceded by 9 layers of drift tubes for tracking. As for the mini-SAM, each SAM module can receive a significant amount of beam-related energy. However, the proportional tubes have enough shower position localization to easily identify a Bhabha event.

4.3 ELECTROMAGNETIC CALORIMETERS

The endcap calorimeter covers the angular region between 15° and 45° while the lead/liquid argon (LA) calorimeter covers the remainder of the large-angle region except for gaps in the azimuthal angle. The major source of beam-related backgrounds for both of these systems is muons produced in collimators in the final focus system. These muons are more problematic for the LA system than for the endcaps because in the endcaps they traverse the readout planes (proportional tubes) transversely, depositing a relatively small amount of energy, whereas in the LA system they traverse the readout layers (liquid argon) roughly parallel to the layer depositing an amount of energy through ionization equivalent to a large electromagnetic shower. The equivalent electron energy deposited by a muon traversing the LA system has a distribution which is roughly flat out to about 10 GeV or more. Some LA modules suffer from background muons more than others because of the different geometrical arrangement of shielding provided by material in the tunnels and the interaction region. For relatively quiet colliding beam data, there are typically about five to ten muons per event crossing the LA system. Not only does this make offline reconstruction of energy depositions very difficult, it also severely reduces the usefulness of the energy-based trigger.

The endcaps consist of 36 layers of lead and proportional tubes for a total of 18 radiation lengths of material. As mentioned above, muons traversing the endcaps do not have as large an impact as muons traversing the LA system. In colliding beam data, there are typically about five muons traversing each endcap. The equivalent electron energy deposited is small. Certainly the offline reconstruction of Bhabha events and energy depositions greater than about a GeV should not be a problem.

4.4 TIME-OF-FLIGHT SYSTEM

Because of the large solid angle subtended by each time-of-flight counter, this system suffers greatly from the beam-related backgrounds. With current running conditions, at least one-third of the counters typically fire per beam crossing. This makes the time-of-flight system quite ineffectual in the trigger and off-line reconstruction.

4.5 MUON SYSTEM

Currently, the muon system is relatively quiet except for the outer layers on each side. The high background levels in these layers are due to electromagnetic radiation reflecting off the walls of the collider hall and can be effectively suppressed by hanging lead shielding outside these layers. This will be done in the future.

4.6 CONCLUSIONS AND FUTURE PLANS

The current background conditions are not a problem for distinguishing Bhabhas or for offline track reconstruction. Therefore, we feel that our efficiency for reconstructing Z^0 events should be quite high. However, the backgrounds are a problem at the trigger level and may increase as the beam currents increase. During the quietest running periods, our deadtime is small but the backgrounds often fluctuate to produce unacceptably high deadtime.

One source of backgrounds is muon pairs produced in the collimators in the final focus system. These muons are usually bent out of the beampipe at the first bend magnet downstream of the collimator. Some of these muons then travel through the final focus tunnel all the way to the detector. To reduce this background, we are going to install large toroidal magnets in the final focus tunnels to bend the muons away from the detector. These toroids, some of which are modified toroids from Fermilab and others of which are newly built at SLAC, will be ready for installation in September, 1988. It is estimated that these toroids will provide a reduction of about a factor of ten in the number of muons reaching the Mark II detector. This may also provide us with the possibility of collimating more of the beam in the final focus system, increasing the muon flux but reducing the electromagnetic component of the background at the IP.

5. Vertex Detectors for the Mark II

Currently, there are no vertex detectors installed inside the central drift chamber. However, two devices are nearing completion and will be ready for installation by the end of this year: a three-layer silicon strip detector[6] and a high precision drift chamber.[7] Altogether, the tracking system will provide an impact parameter resolution of about 4 μm for high momentum tracks. The multiple scattering term contributes an extra $(32/p)$ μm where the momentum p is measured in GeV/c. The existing beam pipe and wire scanner are incompatible with the vertex detectors. A new beam pipe has been designed and is under construction. It should be ready by the end of the year. It will contain two wire

assemblies for measuring the transverse beam size about 20 cm on either side of the IP.

5.1 Silicon Strip Detector

The silicon strip detector consists of three layers at radii of 30, 34 and 38 mm. Each layer consists of 12 separate detectors as illustrated in Figure 10. Each detector consists of 512 strips giving a total of 18,000 channels which are read out by custom VLSI chips. Each 6 mm × 6 mm chip reads out 128 channels, integrating and storing the charge deposited on a strip and multiplexing the analog signal onto a serial bus. The strip pitch varies between 25 and 33 μm and the strip length varies between 75 and 94 mm. The vertex detector covers 77% of the solid angle.

Each detector is assembled into a module which consists of two readout chips wire-bonded at each end and a hybrid circuit which provides the control lines, a switchable capacitor bank for power and a differential amplifier and line driver for the analog output signals. These modules have been assembled and are ready to be installed in the mechanical support structure which is in fabrication.

Prototype tests have demonstrated that the signal-to-noise ratio is about 18, the spatial resolution per strip is 5 μm, and the double track resolution is less than 150 μm. To take advantage of the high resolution provided by the strips, their location must be known to better than a few microns. The intermodule alignment procedure will use a collimated x-ray beam. Preliminary tests of this procedure have been successful. The position of the silicon strip vertex detector with respect to the high precision drift chamber will be monitored with capacitive sensors.

5.2 Vertex Drift Chamber

The vertex drift chamber consists of ten jet cells which extend radially between 5 and 17 cm and each provide 38 measurements with an expected resolution of about 30 to 40 μm per measurement, averaged over 2 cm of drift. The chamber will operate between two and three atmospheres pressure and will use a gas with a slow drift velocity between 5 and 10 μm/ns. The double-track resolution is expected to be about 1 mm.

All hardware components are complete and the ten jet cells which are strung separately have been installed and positioned in the support structure. The detector, with the final gas system, electronics and readout system, will be operated outside the Mark II until installation at the end of this year.

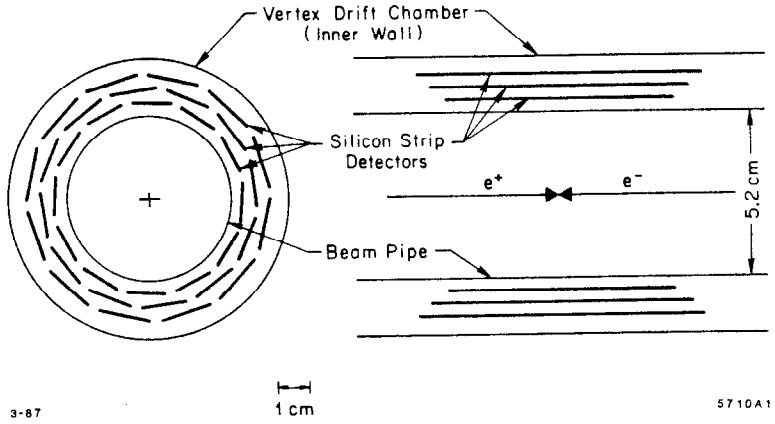

Figure 10. Schematic drawing of the silicon strip vertex detector.

6. The Polarization Project

One of the important advantages of a linear collider is the possibility of producing longitudinally polarized electrons at the IP. This allows one to measure the left-right asymmetry A_{LR} which quantifies the difference in coupling between the Z^0 and left- or right-handed electrons. A_{LR} can be related to parameters of the standard model such as $\sin^2\theta_W$ and M_Z. The forward-backward charge asymmetry A_{FB} can also be related to these parameters but has several disadvantages as a measurement compared to the left-right asymmetry. First, the left-right asymmetry is independent of the final state fermion and therefore the total Z^0 cross section contributes to this measurement. The forward-backward charge asymmetry is different for fermions of different electric charge and weak isospin. It will probably only be possible to measure A_{FB} for Z^0 decays to muons and taus (3% of the total Z^0 cross section, each) and perhaps b quarks (about 14% of the cross section). In addition, A_{FB} is changing rapidly across the Z^0 pole resulting in a measurement which is very sensitive to radiative corrections and accurate knowledge of the center-of mass energy. Also, A_{LR} changes much more slowly than A_{FB} resulting in smaller systematic errors. Finally, A_{LR} is expected to be around 0.12 (for 50% polarization) while A_{FB} is expected to be only a few percent for muon pairs.

Figure 11 summarizes the precision with which the standard model can be tested for three measurements at the SLC (M_Z, A_{FB} and A_{LR}) as a function of the number of observed Z^0 decays. The shaded regions indicate present precision and proposed sensitivity from measurements of M_W and M_Z, and ν scattering experiments. To test the standard model, we need two or more measurements of comparable precision. It can be seen from the figure that with only a few thousand observed Z^0 decays, we reach the systematic limit on the M_Z measurement corresponding to an uncertainty on $\sin^2\theta_W$ of less than 0.0005, far better than the precision of existing measurements. A measurement of A_{FB} for muon pairs requires more than 10^5 observed Z^0 decays to become competitive with existing measurements and reaches a systematic uncertainty on $\sin^2\theta_W$ of about 0.002 for more than 10^7 Z^0's. With a longitudinally polarized electron beam with polarization P_e equal to 45%, one can measure $\sin^2\theta_W$ more precisely than existing measurements with a few thousand observed Z^0 decays. The availability of this polarization is equivalent to about a factor of one hundred in luminosity for precise tests of the standard model. The systematic limit on A_{LR} depends on how well one can measure P_e. A fractional error of $\Delta P_e/P_e = 3\%$ should not be difficult and an eventual precision of 1% should be possible. A 1% precision in the measurement of P_e will result in similar systematic errors on $\sin^2\theta_W$ for the measurements of A_{LR} and M_Z.

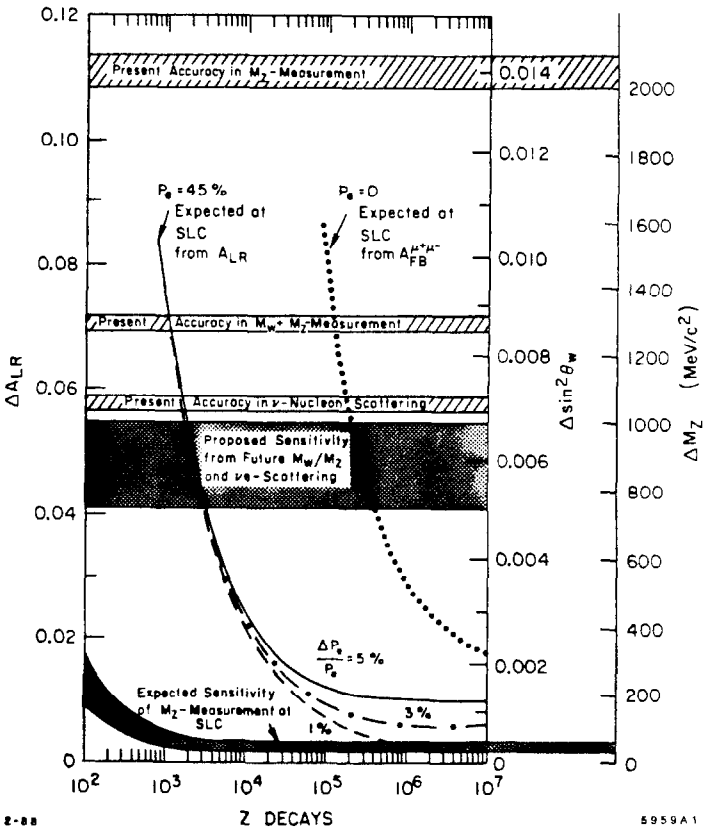

Figure 11. The uncertainties in the determination of M_Z, $\sin^2\theta_W$, or A_{LR} for various measurements which can be made at SLC as a function of the number of observed Z^0 decays. The shaded regions indicate present precision and proposed sensitivity from measurements of M_W and M_Z, and ν scattering experiments.

The layout of the SLC including special components for providing longitudinally polarized electrons at the IP[8] is shown in Figure 12. The longitudinally polarized electrons are produced by irradiating a GaAs crystal with circularly polarized light. The electron gun has been installed and the laser system is being commissioned. Three superconducting magnets are needed to rotate the spin before and after the damping ring. These magnets have been delivered to SLAC and are undergoing testing. A Møller polarimeter for measuring the polarization at the end of the linac has been installed. Another Møller polarimeter for measuring the polarization in the extraction line is ready to install. The best measurement of the polarization is expected to come from a Compton polarimeter just downstream of the IP. It should provide a measurement with 1% precision in less than a minute. A prototype detector for this system is in place for background studies. A vent shaft leading to a counting house above ground is ready for the installation of the laser and optical system.

7. Conclusions

Commissioning of the SLC is proceeding. Colliding beams have been established but the efficiency is still quite low. Although each beam parameter is within a factor of two to five of design, the luminosity achieved to date is about a factor of 400 less than design. Improvements are being implemented to increase the efficiency for colliding beams and to improve the beam parameters. New techniques have been developed for monitoring beam sizes and positions to micron precision at the interaction point.

Spectrometers for measuring the beam energy in the extraction lines have been installed. Preliminary measurements indicate that they will surpass the design goal of measuring the beam energies with a resolution better than 25 MeV.

The response of the Mark II detector under colliding beam conditions has been studied. Beam-related backgrounds fluctuate over time. In relatively quiet runs, triggering is not a problem for the charged-track trigger and the Bhabha trigger. However, low energy neutral triggers result in unacceptable deadtime or require unreasonably large thresholds. Efficient offline reconstruction of charged tracks, Bhabhas and energy clusters of a few GeV in the endcaps should be possible. However, the lead/liquid argon calorimeter and the time-of-flight system suffer from the beam-related backgrounds. A set of toroidal magnets will be installed in both final focus tunnels to attenuate the muon background by about a factor of ten.

In the near future, two high precision vertex detectors will be installed inside the central drift chamber providing excellent impact parameter resolution. Also

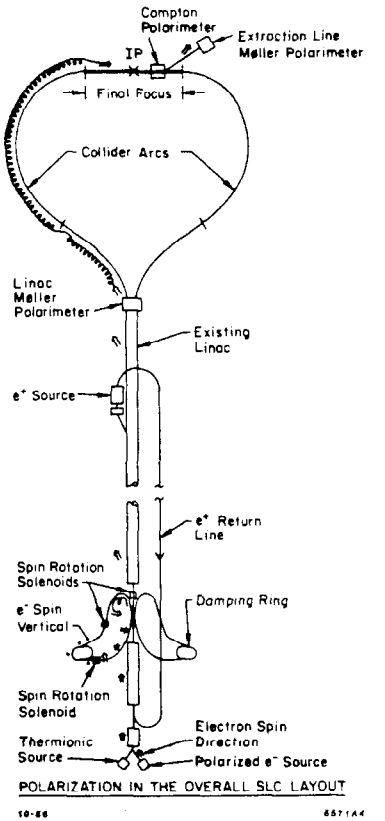

Figure 12. Layout of the SLC showing special components needed for providing longitudinally polarized electrons at the IP. The electron spin direction is shown at various points along the accelerator.

nearing completion is a project to provide longitudinally polarized electrons at the interaction point. These last two features represent significant advantages of a collider over a storage ring.

REFERENCES

1. SLAC Linear Collider Conceptual Design Report, SLAC-Report-229, 1980.
2. R. Fulton *et al.*, SLAC-PUB-4605, 1988, submitted to *Nucl. Instr. and Meth.*
3. P. Bambade, SLAC-CN-303, 1985.
4. Mark II Collaboration and SLC Final Focus Group, Extraction Line Spectrometers for SLC Energy Measurement, SLAC-SLC-PROP-2, 1986; M. Levi, Status Report on the Mark II Energy Measurement System, SLAC-REPORT-306, p. 306, 1987.
5. M. Levi, J. Nash, M. Terman and S. Watson, Precision Measurements of the SLC Spectrometer Magnets, SLAC-PUB-4654 (in preparation).
6. C. Adolphsen *et al.*, SLAC-PUB-4452, 1987.
7. J. Jaros, SLAC-PUB-4285, 1987.
8. D. Blockus *et al.*, SLAC Proposal for Polarization at the SLC, 1986.

Results from the CDF Experiment at Fermilab

The CDF Collaboration[1]

Presented by Dan Amidei
The University of Chicago

Abstract

The first CDF data run in early 1987 recorded approximately 25 nb^{-1} of proton-antiproton collisions at $\sqrt{s}$ = 1.8 TeV. Presented here are results on W boson production, inclusive jet production, jet angular distributions, jet fragmentation, inclusive charged particle rapidity density, and inclusive charged p_t distributions.

Presented at the SLAC Summer Institute on Particle Physics
Stanford, California, July 18-29, 1988

1. Introduction

The Collider Detector at Fermilab is a general purpose magnetic tracking and calorimetric device designed to study the products of proton-antiproton collisions at $\sqrt{s}$ = 1.8 TeV. I report here on results derived from an integrated luminosity of 30 nb^{-1} collected during the 1987 data run at the Fermilab Tevatron Collider. After a brief overview of the detector and the 1987 data set, I will present results on vector boson production, jet physics, and inclusive charged particle density and spectra.

2. The CDF Detector

The CDF apparatus is described in great detail in Ref. 2, and I present here only a brief overview based on Fig. 1. We use spherical coordinates with the beam line as the polar axis, θ as the polar angle and ϕ as the azimuthal coordinate. It is convenient to substitute for the polar angle the "pseudo-rapidity" η, given by $\eta=-\ln(\tan(\theta/2))$. Some convenient comparisons: $\eta \simeq 1$ for $\theta=40°$, and $\eta \simeq 4.0$ for $\theta=2°$.

The detector is built around a 1.5 Tesla superconducting solenoid coaxial with the beam. Within the magnetic volume is a cylindrical central tracking chamber (CTC), with 86 layers of sense wires distributed over a radius of 1.2 m. The resolution per wire is of order 200 μm, and the transverse momentum resolution is measured to be $\delta p_t/p_t \simeq 0.002 p_t$ for $p_t \geq 2.0$ GeV/c and $|\eta| \leq 1$. Lying between the CTC and the beryllium beam pipe are a set of 8 vertex time projection modules (VTPC) which provide R-z reconstruction of charged particles and a measurement of the event vertex position and quality.

Outside of the coil, the tracking measurement is complemented by almost 4π sampling calorimetry based on a projective tower geometry. The calorimeters are divided into three regions based on very natural geometric constraints: the central region, $|\eta|<1.0$, the plug region $1.0<|\eta|<2.2$, and the forward region, $2.2<|\eta|<4.0$. In all cases there is a mechanical segmentation into an inner electromagnetic part, with lead absorbing plates, and a larger outer hadronic part, with steel absorbers. The central region uses plastic scintillator as sampling medium, and is

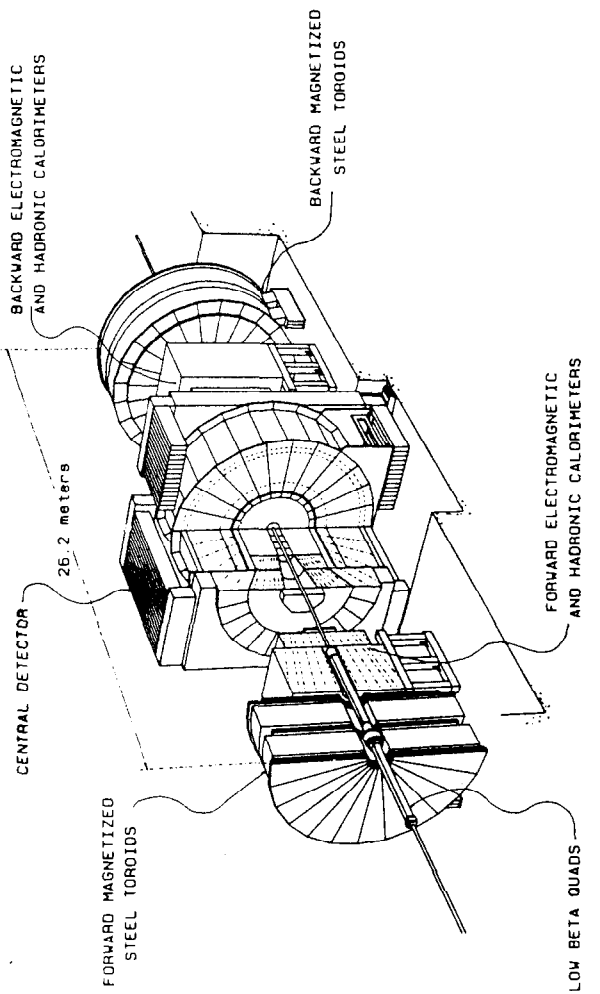

Fig. 1 The CDF Detector

segmented into towers of size $\Delta\phi$=15° and $\Delta\eta$=0.1. The central electromagnetic compartment has a depth of 20 radiation lengths and a resolution $\sigma_E/E = 14\%/\sqrt{E}$; the central hadronic compartment is 5 absorption lengths deep and has $\sigma_E/E = 70\%/\sqrt{E}$. The plug and forward regions use gas proportional sampling with a tower size of $\Delta\phi$=5° and $\Delta\eta$=0.1.

Muon coverage in the central region consists of 4 layers of drift chambers behind the hadron calorimeters in the region $|\eta|<0.7$. The system is essentially 100% efficient for muons over 3 GeV/c. In the forward regions on both sides are muon spectrometers consisting of large magnetized toroids with drift chamber planes and triggering scintillation counters.

Two sets of scintillation counters are mounted on the front of the forward electromagnetic calorimeters in the region $3.2\leq|\eta|<5.9$. These "beam-beam" counters (BBC) are used for luminosity measurement and triggering.

3. The 1987 Data Set

The Fermilab Tevatron Collider supplied colliding beams of protons and antiprotons in the period from February to May 1987. Average instantaneous luminosities of order 10^{29} $cm^{-1}s^{-1}$ were achieved. CDF logged several kinds of data sets, depending on triggers and beam energies. The "Level 1 Buffet" data set contains high transverse momentum physics selected by the following calorimetric and tracking triggers:

Jet:	ΣE_t >20-45 GeV in towers with 1.0 GeV or more.
Electron:	1 tower in EM calorimeter with E_t >(7.0-12.0) GeV.
CMU:	Central muon stub matched to a trigger track.
FMU:	Track candidate in forward muon road.

Valid Level 1 triggers consisted of any of the above conditions in combination with the presence of hits on both sides of the beam-beam counters during a 15 nsec window centered on the beam crossing. The E_t thresholds were roughly adjusted with luminosity to maintain a constant data acquisition rate. Approximately 30 nb^{-1} of the 70 nb^{-1} delivered were written to tape.

Another low bias or "minimum bias" data set was collected with a trigger requiring only coincidence of hits in the beam-beam counters in time with the beam crossing. Approximately 56,000 events were recorded at 1.8 TeV. In addition, a smaller sample of 9,400 events was recorded at $\sqrt{s}$ = 0.63 TeV.

4. Vector Boson Production

Intermediate W bosons are produced in $p\bar{p}$ collisions via the Drell-Yan process and then identified by their decays into charged leptons and neutrinos.[3] The W bosons were studied at CDF in two parallel analyses, one based on the missing transverse energy associated with the unreconstructed neutrino, and the other on the identification of isolated electrons. Both paths start from a common data set of 25.3 nb^{-1} culled from runs that are free of gross detector malfunctions. The two approaches have very different systematics, but converge on the same sample, providing a powerful cross-check on detector performance and efficiencies.

The missing E_t analysis is outlined in Fig. 2. We defined E_t^{miss} as the magnitude of the vector sum of the transverse energy over all calorimeter towers in the region $|\eta|$ less than 3.6 and required events to have E_t^{miss} greater than 25.0 GeV. A jet clustering algorithm was applied to the calorimeter tower array, and events are required to have a jet cluster with E_t greater than 15.0 GeV in the region $|\eta|$ less than 1.0.[7] A total of 1614 events passed these cuts.

We next selected on the quality of the E_t^{miss} signal. Cosmic rays and main ring splashes are suppressed by requiring that less than 3.0 GeV of the central hadronic energy deposition occur outside of a 20 nsec window centered at the beam crossing. Mismeasured QCD dijets were suppressed by requiring the absence of any jet with E_t greater than 5.0 GeV in the ϕ cone of 180°±30° opposite the leading cluster. Finally, we evaluate the significance of E_t^{miss} by comparing it to the size of the overall random

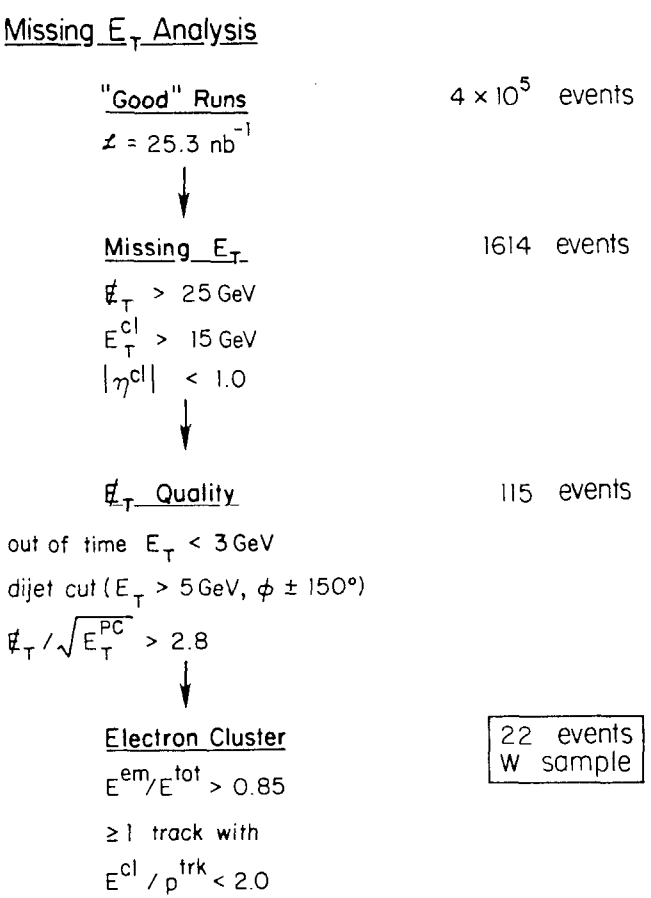

Fig. 2 The W boson analysis based on missing E_t.

error from calorimeter fluctuations. This is well measured in minimum bias events, where the distribution of E_t^{miss} is found to be Gaussian with width 1.0 $\sqrt{E_t^{PC}}$ where E_t^{PC} is the scalar sum of the transverse energy in the central and plug calorimeters. Events were required to have a significance of $E_t^{miss}/\sqrt{E_t^{PC}}>2.8$.

After these E_t^{miss} quality cuts, 115 events remained. These were searched for electron-like clusters according to the rather loose requirements of $E^{em}/E^{tot}>0.85$ along with a matched track of momentum p such that $E^{tot}/p<2.0$. Twenty-two events contained such electron signatures. A typical such event is shown in Fig. 3, where the R-ϕ projection of the CTC is at the top of the page, and the LEGO representation of the calorimeter is beneath. In the CTC, we see one stiff track with p_t = 28.3 GeV pointing to a tower of the electromagnetic calorimeter recording 39.0 GeV. (The rectangle is a cursor in the interactive display program.) In the LEGO plot, we see that the tower actually has E_t^{em}=27.2 GeV in an otherwise unoccupied event.

The distribution of E_t^{miss} vs. E_t^{miss} significance for the electron and non-electron events is displayed in Figs. 4a and 4b, and shows a clear separation between samples. Most of the events in the non-electron sample were found to be the kinds of missing E_t backgrounds described above. One of the two events at large E_t^{miss} in Fig. 4b is a mismeasured tri-jet, which passes the dijet cut; the other contains a narrow hadronic jet and is consistent with the signature for $W \to \tau\nu$ followed by hadronic tau decay.

The W analysis based on electrons, outlined in Fig. 5, begins with the selection of events containing an isolated electromagnetic cluster in the central region $|\eta|<1.0$ with cluster $E_t>15$ GeV. An "electromagnetic" cluster has the ratio E^{had}/E^{em} less than 0.05, a value determined from calorimeter test beam data. If we let E_t^{cone} be the total transverse energy in a cone of radius $R = [\Delta\eta^2+\Delta\phi^2]^{1/2}=0.4$, centered on the electromagnetic cluster, the "isolation" is defined to be:

$$I \equiv \frac{E_t^{cone} - E_t^{clus}}{E_t^{clus}}$$

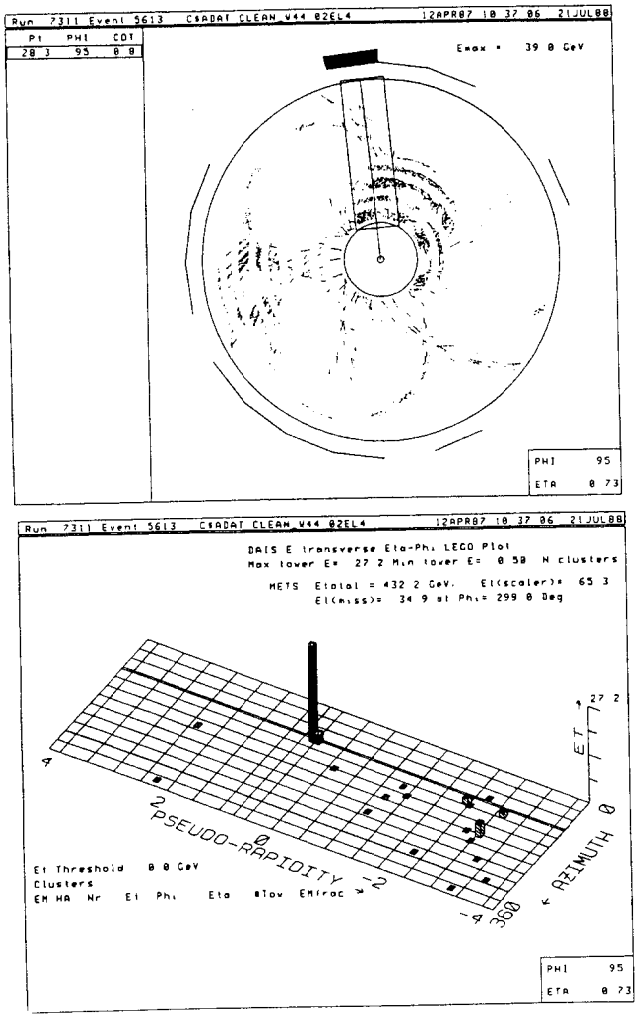

Fig. 3 A generic $W \to e\nu$ event.

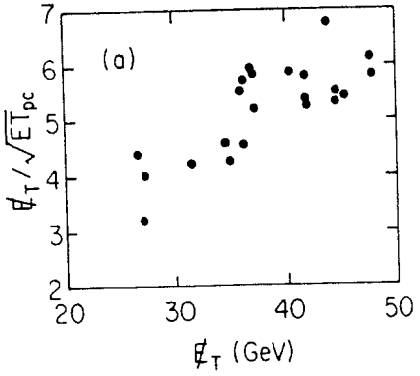

Fig. 4a E_t^{miss} significance vs. E_t^{miss} for the electron sample.

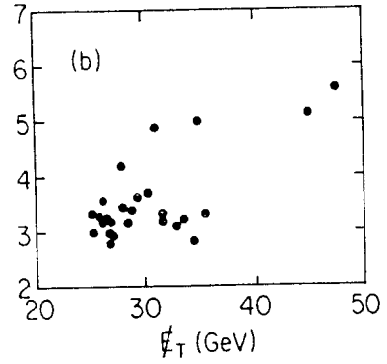

Fig. 4b E_t^{miss} significance vs. E_t^{miss} for the NON electron sample.

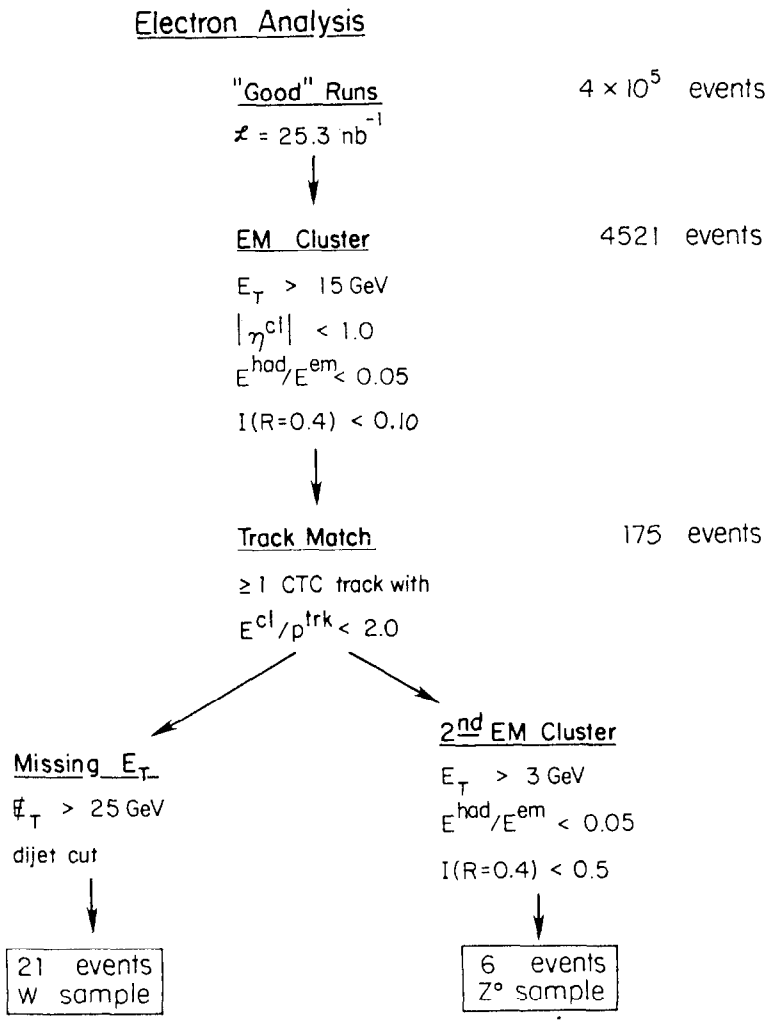

Fig. 5 The W boson analysis based on isolated electrons.

We required I less than 0.10 and found 4521 events which pass both cuts. In these events, we further demanded that a charged track of momentum p extrapolate to the electromagnetic cluster, and that E^{clus}/p be less than 2.0. Of the 175 passing events, 6 were found to have a second electromagnetic cluster and a large mass for the cluster pair; these were removed to a separate Z^0 study. One such event is depicted in Fig. 6.

In the remaining 169 events we then demanded the relatively loose missing E_t signature of $E_t^{miss}>25.0$ GeV and the anti-dijet cut as described above. Twenty-one candidates were found. The distributions of the electron variables in these events are presented in Figs. 7a,b,c and show rather clean electron characteristics, with distributions apparently unbiased by the selection requirements. And most happily, ALL of these events were in the sample identified via the missing E_t analysis.

We take the 22 events from the E_t^{miss} analysis as our final W sample. The distribution of electron p_t has the anticipated Jacobian form, as seen in Fig. 8. The distribution of transverse mass

$$M_t = [2E^e_t E^\nu_t (1 - \cos\Delta\phi_{e\nu})]^{1/2}$$

is shown in Fig. 9a; the smooth curve is the ISAJET result for M_W=83.0 GeV/c^2.[4]

The cross section for this process is derived from the measured luminosity in the beam-beam counters and various corrections for efficiency, acceptance, and backgrounds. The effect of the rapidity cuts, calorimeter cracks, and thresholds were studied via Monte Carlo; all other efficiencies were derived from the data. The net efficiency is estimated to be about 30%. Backgrounds from jets were estimated from jet data and the background from the sequential decay $W \to \tau \to \nu$ was estimated from Monte Carlo; The total background contribution is less than 1 event. We find for the cross section:

$$\sigma \cdot B = 2.6 \pm 0.6 \pm 0.4 \text{ nb}$$

where the first error is statistical and the second is systematic. Our result is displayed along with previous results in Fig. 9b, and shows good agreement with the theoretically calculated increase of W production for $\sqrt{s}$ = 1.8 TeV.[5,6]

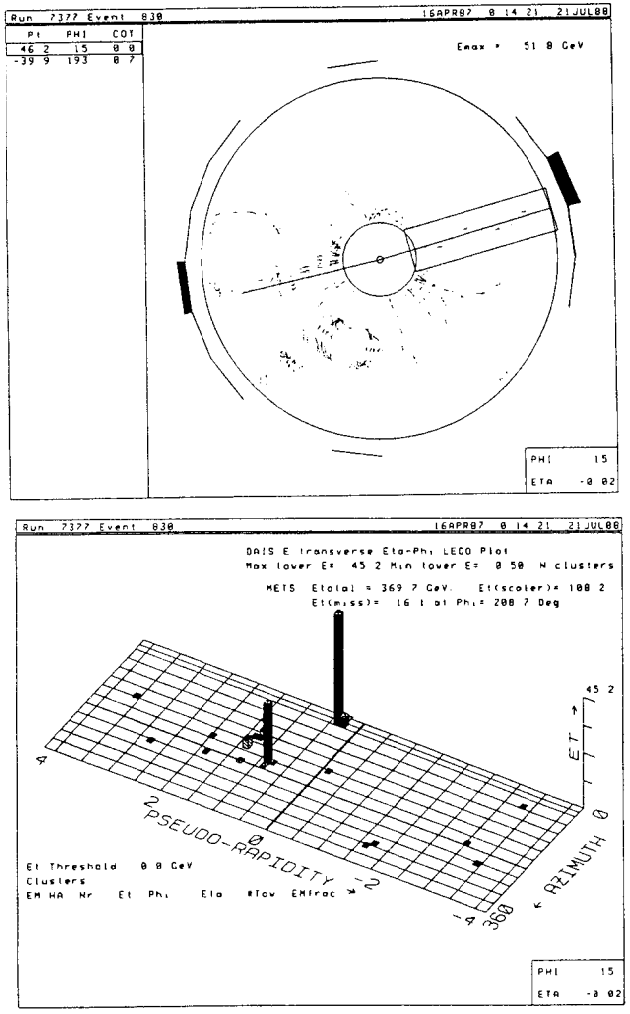

Fig. 6 A generic $Z^0 \rightarrow e^+e^-$ decay.

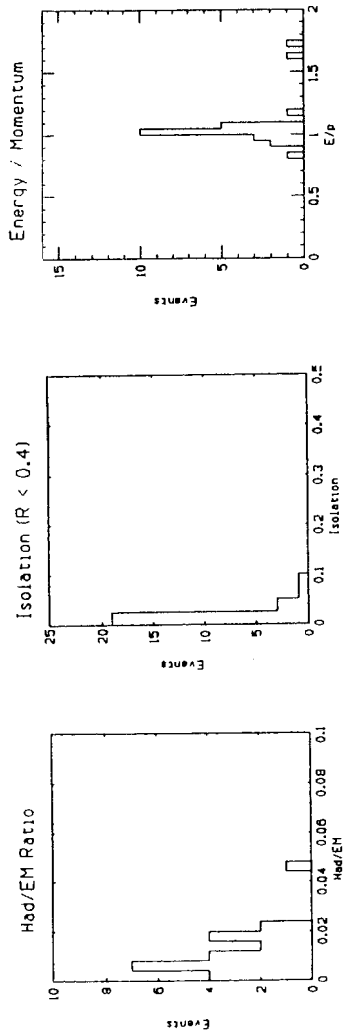

Fig. 7a. E^{had}/E^{em}

Fig. 7b. Isolation

Fig. 7c. E^{clus}/p^{trk}

Fig. 7 Electron quantities in the W sample.

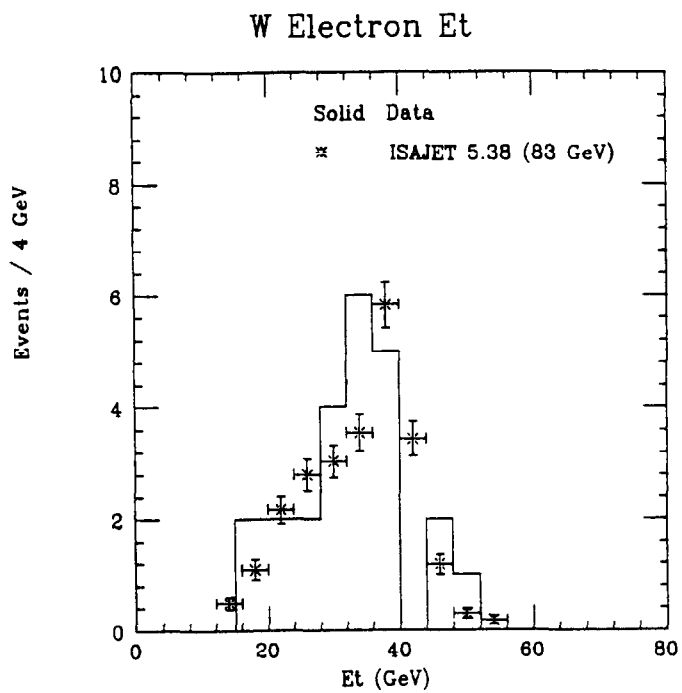

Fig. 8 Electron p_t in the W sample.

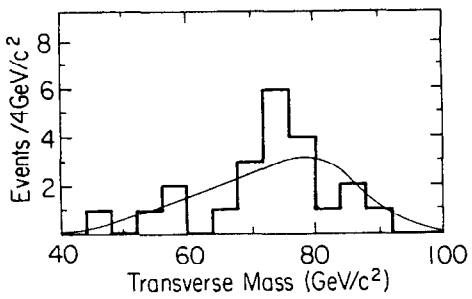

Fig. 9a Transverse mass distribution for W sample.

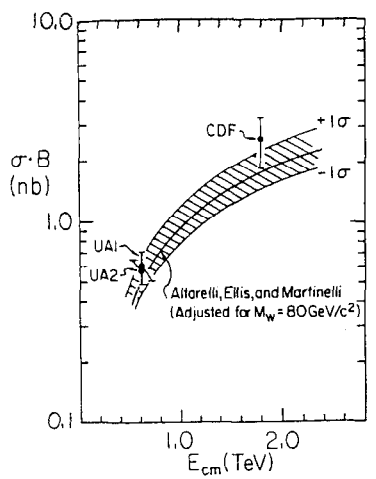

Fig. 9b W production cross section.

5. Jet Production

At $\sqrt{s}$ = 1.8 TeV, we expect the final states from our high ΣE_t triggers to be dominated by hadronic jets resulting from hard parton-parton scatterings and associated gluon bremsstrahlung. A typical two-jet event is shown in Fig. 10.

a. Jet Reconstruction

The jet kinematics are reconstructed by applying to the calorimeter array an algorithm which associates locally deposited energy into clusters: the jet direction is measured by the cluster centroid, and the jet energy by the total cluster energy.[7]

The validation of the jet energy scale has been pursued with great industry. The central calorimeter has been calibrated in test beams of 50 GeV pions and electrons. The calibration is tracked forward through movable internal Cs^{137} sources and a variety of flashers and lasers, and has an anticipated absolute accuracy of about 2%. We have studied various unavoidable effects which contribute to errors in the measured energy. The nonlinearity of calorimeter response at low energies was measured using isolated tracks reconstructed in the CTC. Charged tracking and Monte Carlo were used to study the effect of fragmentation fluctuations; Monte Carlo was also used to study the effect of leakage and cracks. The net correction due to these effects varies from 33% to 20% of the cluster energy as that energy goes from 40 GeV to the highest measured jets of about 250 GeV. The error on this correction varies from 12% to 4% over the same interval.

After all corrections are applied, we measure the intrinsic jet E_t resolution via the momentum balance in two-jet events.[8] For a jet E_t=50 GeV, we find the distribution of opposite jet momenta has a Gaussian distribution with σ=9.0 GeV.

b. Inclusive Jet Cross Section

The apparent differential cross section, $d\sigma/dE_t$, can be computed from the measured luminosities and the number of jets at each E_t. The true cross section was derived by deconvoluting the jet E_t resolution from the apparent cross section, a procedure whose uncertainty is estimated to vary

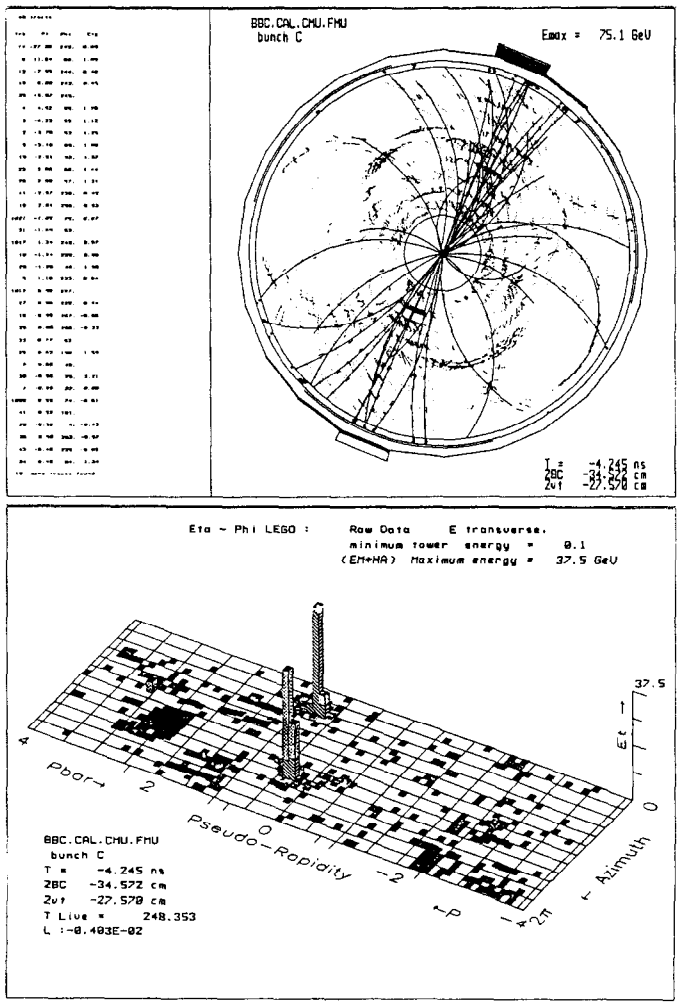

Fig. 10 A generic two-jet event.

from 25% to 5% over the jet E_t interval 40 GeV to 250 GeV . In Fig. 11 we show this corrected differential cross section averaged over the fiducial central eta interval $0.1 < |\eta| < 0.7$. Events used in this analysis have a good vertex located within 60 cm of the detector center, and have good timing in the sense described in the missing E_t analysis. To insure a well understood acceptance, we also required a central jet with E_t greater than the $\not{E}_t$ threshold. The errors in each bin include the statistical error as well as systematic contributions from uncertainties in the luminosity and the corrections discussed above. The full systematic error ranges from 70% to 34% of the cross section over the 40 GeV to 250 GeV interval.

Also shown in Fig. 11 is a range of predictions from the lowest order QCD calculation. This calculation uses 2 → 2 tree graphs, evolved structure functions and running α_s. The family of curves arises from the choice of structure function and the α_s momentum transfer scale.[9] The normalization is absolute. Within errors all calculations show good agreement with the data.

The CDF result is compared with experiments at other energies in Fig. 12.[10] The increased sensitivity to large E_t as a result of increased $\sqrt{s}$ is apparent. At the highest jet E_t, this distribution is a probe of possible quark substructure. The well known parameterization of quark constituent scattering as a 4-fermion contact interaction predicts an enhancement in cross section as the jet E_t approaches the compositeness scale Λ^*.[11] The best current limit is from the UA experiments, which find that Λ^* is greater than about 400 GeV, based on about 600 nb^{-1}.[10] In Fig. 13 we show that this is obviously confirmed by the CDF data; analysis in progress will move this limit out to about 700 GeV, based only on 30 nb^{-1} of data.[12] In this case, the advantage of higher energy is seen to far outweigh the advantage of a factor of 20 in integrated luminosity.

c. Jet Angular Distributions

The distribution of the jet center of mass scattering angle has been measured in both two and three-jet events. In the two-jet case, the predominant t-channel subprocesses of quark-quark and gluon-gluon scattering are expected to occur with the characteristic Rutherford form:

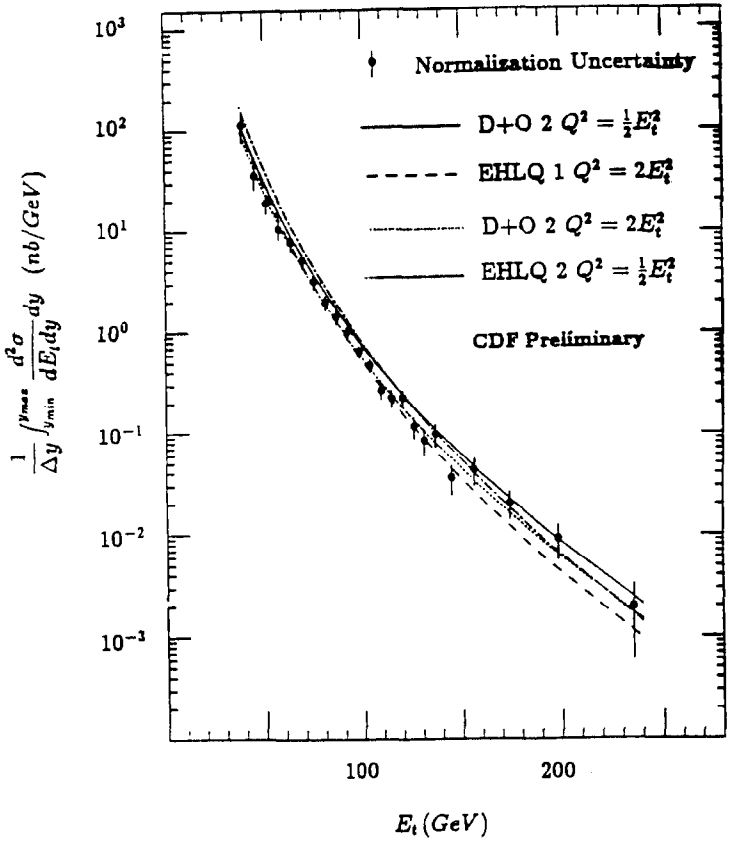

Fig. 11 The inclusive jet cross section.

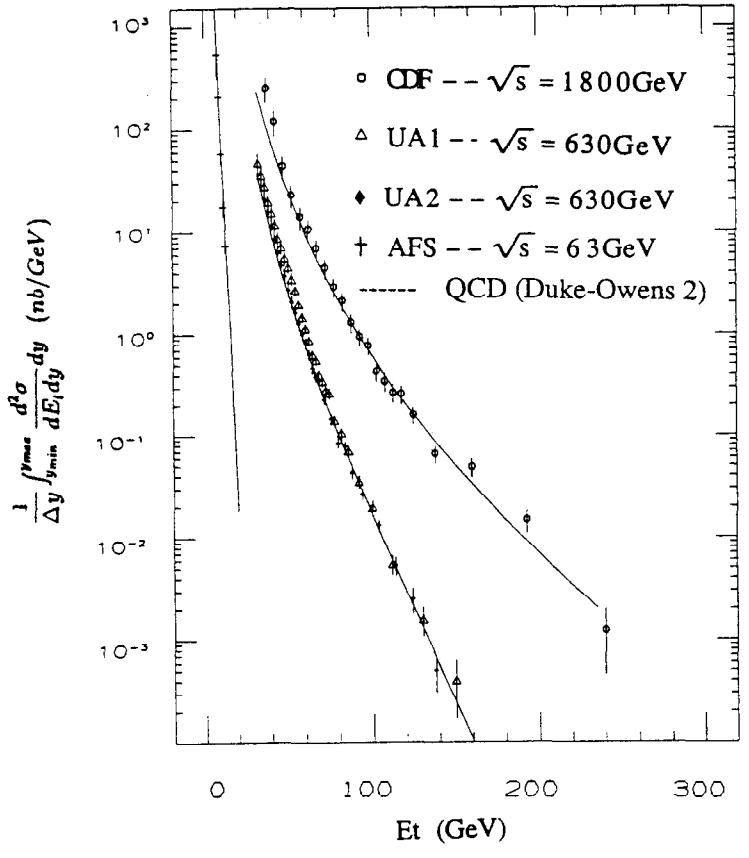

Fig. 12 Jet spectra in colliding hadron experiments.

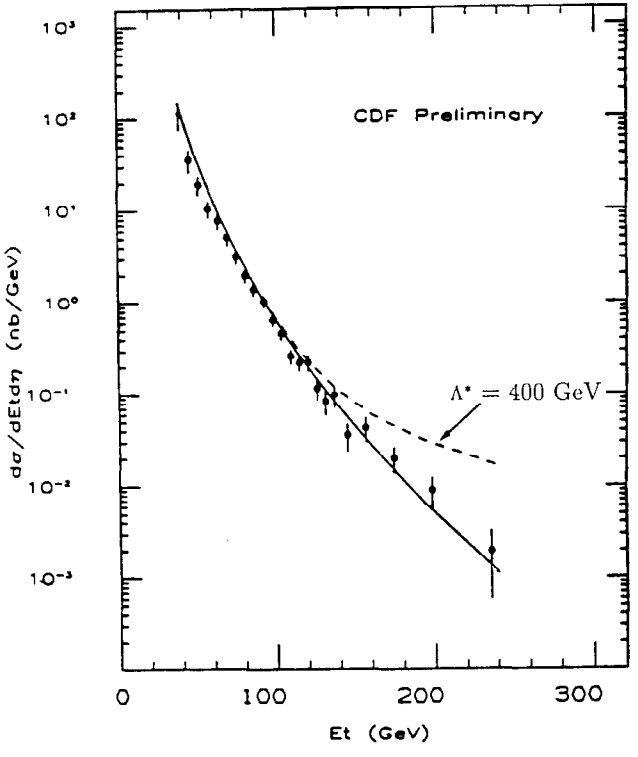

Fig. 13 Inclusive jet cross section with modification for quark compositeness at scale $\Lambda^* = 400$ GeV.

$$\frac{d\hat{\sigma}}{d\cos\theta^*} \propto \frac{\alpha_s^2(Q^2)}{\hat{s}} \frac{1}{(1-\cos^2\theta^*)^2}$$

where θ^* is the center-of-mass scattering angle and $\hat{s}$ is the subprocess momentum transfer. In the three-jet case, since the third jet is usually the result of gluon bremsstrahlung, θ^* of the leading jet is expected to again have the Rutherford form.

We studied jet angular distributions using a sample which satisfied the quality cuts of the inclusive jet analysis and the additional requirement of a second jet with $E_t \geq 10$ GeV in the azimuthal interval of $180^\circ \pm 30^\circ$ opposite the leading jet. The passing events were boosted into the longitudinal center-of-mass frame, and θ^* was taken to be the angle of the jets with respect to the beam axis.

We controlled the effect of limited detector acceptance by cutting on the interval $y^* = 0.5|y_1 - y_2|$, where y_1 and y_2 are the jet rapidities. To study the effect of this cut, we examined the three requirements $|y^*| \leq 0.7, 1.0, 1.2$. The acceptance corrections were determined via Monte Carlo, and are small for the first cut and of order 20% for the third cut.

The angle θ^* is obtained from the relation $\cos\theta^* = \tanh(y^*)$. The distribution $dN/d\cos\theta^*$ for the three in the two-jet data sets is displayed in Fig. 14a, along with the curve from a first order QCD calculation. Note that the combination of the finite angular acceptance with our E_t trigger thresholds produces effective two-jet invariant mass thresholds of 114, 140, and 164 GeV respectively. All three data sets show good agreement with the QCD prediction, in spite of different acceptances.

A similar analysis has been done for three-jet events. See Ref. 13 for a discussion of the additional care required regarding uniform detector acceptance in this case. In Fig. 14b we show the distribution $dN/d\cos\theta^*$ for the leading jet, and the QCD calculation from the previous plot. There is, again, good agreement between theory and data, indicating that most three-jet events can be described as the result of a $2 \rightarrow 2$ subprocess supplemented with initial or final state gluon bremsstrahlung.

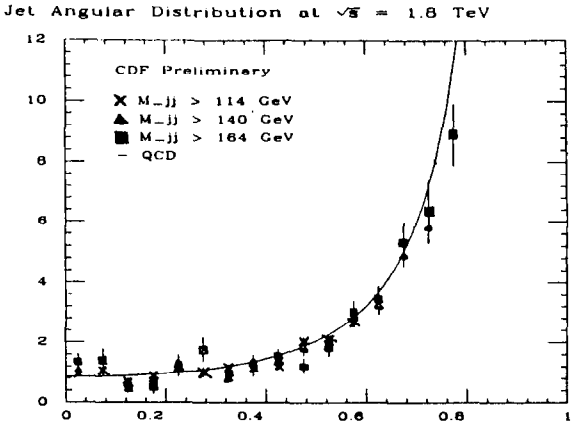

Fig. 14a $dN/d\cos\theta^*$ for QCD di-jets.

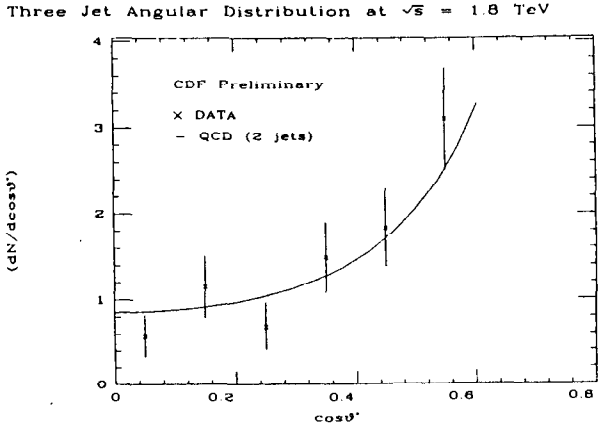

Fig. 14b $dN/d\cos\theta^*$ for QCD tri-jets.

d. Jet Fragmentation

The excellent track finding efficiency and resolution afforded by the CDF central tracking chamber allows study of the charged particle fragmentation in hadronically produced jets. Track quality requirements for this study are similar to those discussed briefly in the section on inclusive charged p_t spectra in Sec. 6. Studies in which real track measurements were overlayed with Monte Carlo events provided an estimated average tracking efficiency of 90% in jet events, and 85% in the dense jet core.[14]

We measured the rapidity y of the jet tracks with respect to the jet axis inferred from the calorimeter cluster centroid. Figure 15a shows the efficiency corrected distribution dN/dy for a large jet sample, binned according to three sets of dijet invariant masses. Note the suggestion of "rapidity plateau" that broadens with increasing jet energy. We used the number of tracks having $y \geq 2$ with respect to the jet axis as a measure of the jet core charged multiplicity. The rapidity cut eliminates a small bias due to the p_t cutoff in the tracking (400 MeV/c) and the effect of the underlying event. The jet multiplicity as a function of di-jet mass is shown in Fig. 15b, along with results from other experiments.[15] Hadronically produced jets at very high energies are seen to have a mean core multiplicity which is consistent with a smooth extrapolation from e^+e^- results at much lower energies.

6. Minimum Bias Physics

One of the most familiar results from high energy hadron collisions is the rapidity plateau in charged particle production. The rapidity is defined as

$$y = 0.5 \ln \left[\frac{E + p_{\parallel}}{E - p_{\parallel}} \right].$$

For light particles this is approximately a function of polar angle alone, which we define as the "pseudo-rapidity":

$$y \simeq \eta = -\ln(\tan(\theta/2)).$$

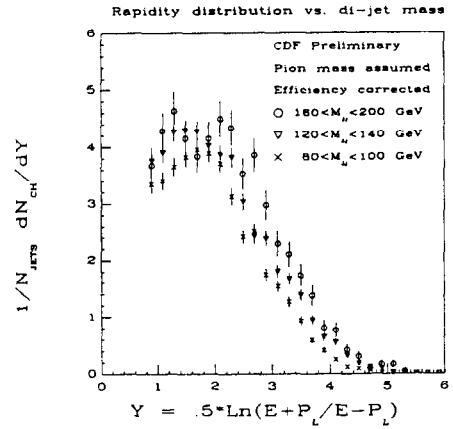

Fig. 15a dN/dy for charged particles in jets. Rapidity y is measured with respect to the jet axis.

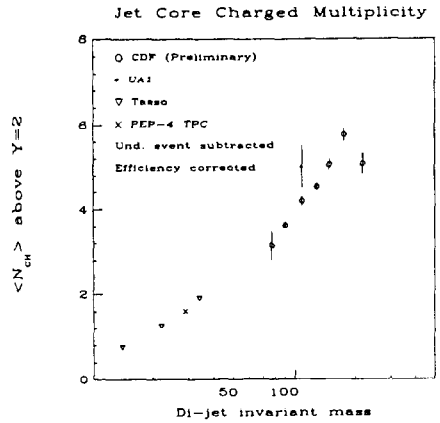

Fig. 15b Jet total charged "multiplicity" with $y \geq 2$ with respect to the jet axis.

At CDF, the VTPC chambers measure the polar angle distribution of charged particles with good efficiencies between rapidities of ±3.0. The uncorrected distribution of $dN/d\eta$ vs. η for the minimum bias data sample is shown in Fig. 16, along with results from UA5.[16] The CDF data shows a plateau out to the limits of our acceptance at $\eta = 2.8$. The effects of reconstruction efficiency, decays, conversions, and secondary interactions are under study; preliminary results indicate that the total correction will be less than 10%. The slight dip at small η can be understood in terms of the difference between y and η; the distribution of dN/dy is flat. The central densities are measured to be:

$$dN/d\eta)_{\eta=0} = 2.95 \pm 0.3 \text{ at } 630 \text{ GeV}$$
$$dN/d\eta)_{\eta=0} = 3.98 \pm 0.4 \text{ at } 1800 \text{ GeV}$$

The 630 GeV result is in good agreement with results from UA5, but the 1800 GeV result lies above the best ln(s) fit to the lower energy data.[17]

The inclusive charged transverse momentum distribution in the minimum bias samples was measured in the central tracking system. Tracks with momenta down to 400 MeV/c were included if they passed certain quality requirements, including the traversal of all CTC layers ($|\eta|$ less than 1.0), and an extrapolation to within 5.0σ of the event vertex in R-ϕ and to within 5 cm in z. The track finding efficiency in this sample was estimated via several methods to be approximately 99%.[18]

The observed p_t spectrum was corrected for decay in flight, neutral decays, and conversions, with no correction larger than 5%. The uncertainty due to misreconstruction and the distortion due to finite momentum resolution were found to be negligible. The invariant cross section follows from the p_t spectrum and the measured luminosities. All particles are assumed to be pions.

Our result is shown in Fig. 17 for the two center-of-mass energies 0.63 TeV and 1.8 TeV. The smooth curves are a fit to the parameterization:

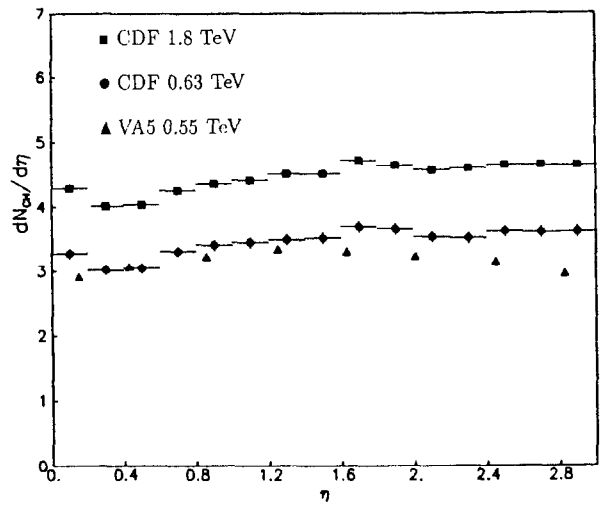

Fig. 16 $dN/d\eta$ for the CDF minimum bias samples and other experiments.

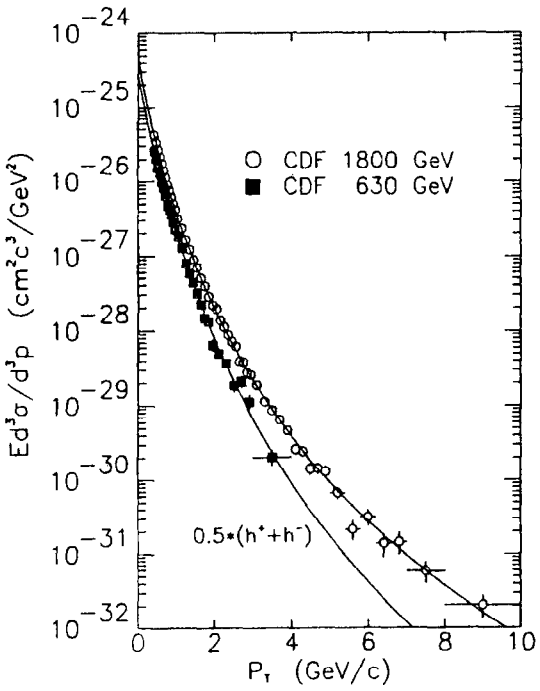

Fig. 17 The inclusive charged transverse momentum spectrum for the minimum bias samples.

$$E\frac{d^3\sigma}{d^3p} = \frac{Ap_o^{\,n}}{(p_t+p_o)}\,.$$

Our results, and a comparison to UA1 are as follows:

	1.8 TeV	0.63 TeV	0.55 TeV (UA1)
p_o	1.3 GeV/c	1.3 GeV/c	1.3 GeV/c
n	8.28±.02	8.89±.06	9.14±.02
A	0.45±.01	0.33±.01	0.46±.01

We find that p_0 and n are highly correlated, and simply fix p_o value above. The fit result was found to be independent of the lower p_t cut-off. Our result at 0.63 TeV is in reasonable agreement with the UA1 result;[19] our result at 1.8 TeV shows that the p_t distribution continues to flatten with increasing c.m. energy as observed in other experiments.[20]

7. Conclusion

Analysis of a small preliminary data set has produced significant results on W boson, jet, and inclusive particle production, as well as establishing the power of the CDF detector for reconstructing physics at $\sqrt{s}$=1.8 TeV. Realistic expectations for the next Tevatron Collider run in the Fall and Winter of 1988/1989 foresee an integrated luminosity of more than one inverse picobarn, and CDF stands poised for the opportunity to go right to the Top.

This work would not have been possible without the dedication, skill, and hard work of the Accelerator Division of Fermilab. We thank the staffs of our institutions for their many contributions to the construction of the detector. This work was supported by the U.S. Department of Energy, the National Science Foundation, Istituto Nazionale di Fisica Nucleare of Italy, the Ministry of Science, Culture and Education of Japan, and the Alfred P. Sloan Foundation.

References

1. Argonne National Laboratory; Brandeis University; University of Chicago; Fermi National Accelerator Laboratory; INFN, Laboratori Nazionali di Frascati, Italy; Harvard University; University of Illinois; KEK, Japan; Lawrence Berkeley Laboratory; University of Pennsylvania; INFN, University and Scuola Normale Superiore of Pisa, Italy; Purdue University; Rockefeller University; Rutgers University; Texas A&M University; University of Tsukuba, Japan; University of Wisconsin.

2. F. Abe et al., Nucl. Instrum. Methods 271A, 387 (1988).

3. S. D. Drell, T-M. Yan, Phys. Rev. Lett. 25, 316 (1970).

4. The ISAJET Monte Carlo Program is described in F. Paige and S. D. Protopopescu, BNL 38034 (1986).

5. C. Albajar et al., Phys. Lett. 198B, 271 (1987); G. Arnison et al., Phys. Lett. 122B, 103 (1983); M. Banner et al., Phys. Lett. 122B, 476 (1983).

6. G. Altarelli, K. Ellis, M. Greco, G. Martinelli, Nucl. Phys. B246, 12 (1984); G. Altarelli, K. Ellis, G. Martinelli, Z. Phys. C27, 617 (1985).

7. The cluster algorithm is described in a talk by S. Kim, Proc. Physics in Collision 7, Tsukuba (1987).

8. We have used the technique described in P. Bagnaia et al., Phys. Lett. 144B, 283 (1984).

9. E. Eichten et al., Rev. Mod. Phys. 56, 579 (1984); D. Duke and J. Owens, Phys. Rev. D30, 49 (1984).

10. J. Appel et al., Phys. Lett. 160B, 349 (1985); G. Arnison et al., Phys. Lett. 172B, 461 (1986).

11. E. Eichten, K. Lane, M. Peskin, Phys. Rev. Lett. 50, 811 (1983).

12. F. Abe et al., submitted to Phy. Rev. Lett.

13. J. Patrick, talk at 7th Topical Workshop on Proton-Antiproton Collider Physics, Fermi National Accelerator Laboratory (1988).

14. B. Hubbard, talk at 7th Topical Workshop on Proton-Antiproton Collider Physics, Fermi National Accelerator Laboratory (1988).

15. K. Althoff et al., Z. Phys. C22, 307 (1984); G. Arnison et al., Nucl. Phys. B276, 253 (1986).

16. G. Alner et al., Phys. Rep. 154, 247 (1987).

17. G. Ekspong, Nucl. Phys. A461, 145 (1987).

18. F. Abe et al., Phys. Rev. Lett. 61, p. 1819 (1988).

19. G. Arnison et al., Phys. Lett. 118B, 167 (1982).

20. D. Antreasyan et al., Phys. Rev. D19, 764 (1979); B. Alper et al., Nucl. Phys. B87, 19 (1975); M. Banner et al., Phys. Lett. 122B, 322 (1983).

1988 SLAC SUMMER INSTITUTE LIST OF PARTICIPANTS

Iris Abt
SLAC
Mail Bin 96
P.O. Box 4349
Stanford, CA 94309
Bitnet: ABT@SLACVM

Gerard D. Agnew
Brunel University
Rm. F67, GEC Mirst Research
East Lane, Wembley
Middx., HA9 7PP, England
Bitnet: GAGNEW@VZ.RL.AC.UK

Changrim Ahn
SLAC
Mail Bin 81
P.O. Box 4349
Stanford, CA 94309
Bitnet: AHN@SLACVM

Roy Aleksan
SLAC
Mail Bin 78
P.O. Box 4349
Stanford, CA 94309
Bitnet: ROY@SLACVM

James Alexander
SLAC
Mail Bin 61
P.O. Box 4349
Stanford, CA 94309
Bitnet: JIMA@SLACVM

Max J. Allen
University of Victoria
Dept. of Physics
P.O. Box 1700
Victoria, BC, Canada V8W 2Y2
Bitnet: MAX@SLACVM

Dante Amidei
University of Chicago
Enrico Fermi Institute
5640 Ellis Avenue
Chicago, IL 60637
Bitnet: DAN@FNAL

Farhang Amiri
Weber State College
Physics Dept.
Ogden, UT 84408

Carlos G. Arroyo
Columbia University
Dept. of Physics
New York, NY 10027
Bitnet: ARROYO@SLACVM

David Aston
SLAC
Mail Bin 62
P.O. Box 4349
Stanford, CA 94309
Bitnet: DYAEB@SLACVM

William B. Atwood
SLAC
Mail Bin 96
P.O. Box 4349
Stanford, CA 94309
Bitnet: ATWOOD@SLACVM

Doris A. Averill
Indiana University
Dept. of Physics
Bloomington, IN 47405
Bitnet: DORIS@SLACVM

Mark D. Baker
M.I.T.
Dept. of Physics
Cambridge, MA 02139
Bitnet: MBAKER@FNAL

Joseph Ballam
SLAC
Mail Bin 78
P.O. Box 4349
Stanford, CA 94309
Bitnet: JBALLAM@SLACVM

Giuseppe Ballocchi
University of Rochester
Dept. of Physics & Astronomy
Rochester, NY 14627
Bitnet: BEAR@FNAL

Timothy L. Barklow
SLAC
Mail Bin 61
P.O. Box 4349
Stanford, CA 94309
Bitnet: TIMB@SLACVM

John E. Bartelt
SLAC
Mail Bin 78
P.O. Box 4349
Stanford, CA 94309
Bitnet: BARTELT@SLACVM

Gabriel Bassompierre
Lab de Phys. des Particules
Ch. de Bellevue, B.P. 909
F-74019 Annecy-le-Vieux
CEDEX, France

Roberto Battiston
Perugia University
Dipartimento di Fisica
Via Pascoli
I-06100 Perugia, Italy
Bitnet: RBN@SLACVM

Andrew Bazarko
Columbia University
Pupin Hall
New York, NY 10027
Bitnet: BAZARKO@SLACVM

Alice L. Bean
University of California
Dept. of Physics
Santa Barbara, CA 93106
Bitnet: BEAN@UCSB

Andrew T. Belk
Imperial Coll. Sci. Tech.
Blackett Lab
Prince Consort Road
London, SW7 2AZ, England
Bitnet: BELK@CERNVM

Richard S. Benson
University of Minnesota
School of Physics & Astronomy
Minneapolis, MN 55455
Bitnet: BENSON@FNAL

Karl Berkelman
Cornell University
Newman Lab
Ithaca, NY 14853
Bitnet: KB@CRNLNS

Timothy L. Bienz
SLAC
Mail Bin 62
P.O. Box 4349
Stanford, CA 94309
Bitnet: BIENZ@SLACVM

Ikaros Bigi
SLAC
Mail Bin 81
P.O. Box 4349
Stanford, CA 94309
Bitnet: BIGI@UNDHEP

Gian Mario Bilei
Perugia University
Dipartimento di Fisica
Via Paccoli
I-06100 Perugia, Italy
Bitnet: GMB@SLACVM

Uwe Binder
CERN- EP Division
CH-1211 Geneva 23
Switzerland
Bitnet: BINDER@CERNVM

P. Fred Bird
SLAC
Mail Bin 62
P.O. Box 4349
Stanford, CA 94309
Bitnet: BIRD@SLACVM

Richard Blankenbecler
SLAC
Mail Bin 81
P.O. Box 4349
Stanford, CA 94309
Bitnet: RZBTH@SLACVM

Elliott Bloom
SLAC
Mail Bin 98
P.O. Box 4349
Stanford, CA 94309
Bitnet: ELLIOTT@SLACVM

Gerard R. Bonneaud
LPNHE Ecole Polytechnique
Route de Saclay
F-91128, Palaiseau, France
Bitnet: BONNEAUD@CERNVM

Giovanni Bonvicini
University of Michigan
Dept. of Physics
Ann Arbor, MI 48109
Bitnet: GIOVANNI@SLACVM

Harald P. Borner
Oxford University
Nuclear Physics Lab
1 Keble Road
Oxford OX1 3RH, England

Fabio Bossi
Laboratori Naz. Di Frascati
INFN
P.O. Box 13
I-00044 Frascati, Italy
Bitnet: BOSSI@VAXLNF

Stephen E. Bougerolle
University of Victoria
Dept. of Physics
P.O. Box 1700
Victoria, BC, Canada V8W 2Y2
Bitnet: STEVEB@SLACSLD

Gary R. Bower
SLAC
Mail Bin 96
P.O. Box 4349
Stanford, CA 94309
Bitnet: GRB@SLACVM

Bennet B. Brabson
Indiana University
Dept. of Physics
Bloomington, IN 47405
Bitnet: BBRABSON@SLACVM

Alan M. Breakstone
University of Hawaii
Dept. of Physics
Honolulu, HI 96822
Bitnet: ALANB@SLACVM

Jean-Claude Brient
SLAC
Mail Bin 65
P.O. Box 4349
Stanford, CA 94309
Bitnet: JCBRIENT@SLACVM

Dave I. Britton
TRIUMF
4004, Wesbrook Mall
Vancouver, BC, Canada
V6T 2A3
Bitnet: BRITPIENU@TRIUMFCL

Roger K. Brooks
SLAC
Mail Bin 81
P.O. Box 4349
Stanford, CA 94309
Bitnet: RBROOKS@SLACVM

Charles Brown
Fermilab
MS 122
P.O. Box 500
Batavia, IL 60510

Kirk O. Bunnell
SLAC
Mail Bin 65
P.O. Box 4349
Stanford, CA 94309
Bitnet: KIRK@SLACVM

Patricia Burchat
SLAC
Mail Bin 95
P.O. Box 4349
Stanford, CA 94309
Bitnet: PAT@SLACVM

David L. Burke
SLAC
Mail Bin 61
P.O. Box 4349
Stanford, CA 94309
Bitnet: DAVEB@SLACVM

Thompson H. Burnett
University of Washington
Dept. of Physics, FM-15
Seattle, WA 98195
Bitnet: THB@SLACVM

Jerome K. Busenitz
University of Notre Dame
Dept. of Physics
Notre Dame, IN 46556
Bitnet: BUSENITZ@FNAL

Blas Cabrera
Stanford University
Dept. of Physics
Stanford, CA 94305

Shen-Ou D. Cai
Northwestern University
Dept. of Physics
Evanston, IL 60208

Alessandro Calcaterra
Lab. Nazionali di Frascati
Via E. Fermi, 40
C.P. 13
I-00044, Frascati, Italy
Bitnet: ACAL@SLACVM

Barbara Camanzi
Istituto Naz. Fiz. Nucleare
via Paradiso 12
I-44100 Ferrara, Italy

Massimo Carpinelli
INFN-Pisa
Via Livornese 582/A
I-56010 San Piero a Grado
Italy
Bitnet: CARPINELL@IPIVAXIN

Andrea Castro
Istituto Naz. Fiz. Nucleare
via Marzolo 8
I-35100 Padova, Italy
Bitnet: CASTRO@VAXFPD.INFNET

George B. Chadwick
SLAC
Mail Bin 94
P.O. Box 4349
Stanford, CA 94309
Bitnet: GBC@SLACVM

Swati Chakravarty
Carleton University
Dept. of Physics
Ottawa, ON, Canada K1S 5B6
Bitnet: SWATI@NRCHEP

Vladimir Chaloupka
University of Washington
Dept. of Physics, FM-15
Seattle, WA 98195
Bitnet: CHALOUPK@UWAPHAST

Lee Chang
Tsinghua University
Dept. of Physics
Beijing 100084
People's Republic of China

Maurice P. Chapellier
Comm. a l'Energie Atomique
B.P. No. 511
F-75 Paris 15, France
Bitnet: CHAP@FRSOL11

Harry W.K. Cheung
University of Colorado
Physics Department
Campus Box 390
Boulder, CO. 80309
Bitnet: H CHEUNG@COLOPHYS

Mokhtar Chmeissani
University of Michigan
Dept. of Physics
Ann Arbor, MI 48109
Bitnet: CHMEISSANI@UMIPHYS

Hing T. Cho
University of Oklahoma
Dept. of Physics & Astronomy
440 West Brooks, Room 131
Norman, OK 73019

Jong Bum Choi
SLAC
Mail Bin 81
P.O. Box 4349
Stanford, CA 94309
Bitnet: CHOI@SLACVM

Sergio Conetti
McGill University
Physics Dept.
3600 University Ave.
Montreal, PQ, Canada H3A 2T8
Bitnet: SERGIO@FNAL

Adrian R. Cooper
SLAC
Mail Bin 81
P.O. Box 4349
Stanford, CA 94309
Bitnet: ADRIAN@SLACVM

Dieter Cords
SLAC
Mail Bin 78
P.O. Box 4349
Stanford, CA 94309
Bitnet: CORDS@SLACVM

Correa, Alberto DosReis
Fermilab
MS 122
P. O. Box 500
Batavia, IL 60510

David P. Coupal
SLAC
Mail Bin 95
P.O. Box 4349
Stanford, CA 94309
Bitnet: DPC@SLACVM

David H. Coward
SLAC
Mail Bin 65
P.O. Box 4349
Stanford, CA 94309
Bitnet: DHC@SLACVM

Paschal A. Coyle
University of California
SCIPP
Santa Cruz, CA 95064
Bitnet: PASCHAL@SLACVM

Qiang Dai
SLAC
Mail Bin 78
P.O. Box 4349
Stanford, CA 94309
Bitnet: DAI@SLACVM

Mourad Daoudi
University of California
Physics Dept.
Riverside, CA 92521
Bitnet: DAOUDI@SLACVM

Sridhara Dasu
SLAC
Mail Bin 62
P.O. Box 4349
Stanford, CA 94309
Bitnet: DASU@SLACVM

Michel Davier
University Paris Sud
Lab de l'Accelerateur Lineaire
Batiment 200
F-91405 Orsay, CEDEX, France
Bitnet: DAVIER@FRLAL51

Andrew J. Davies
University of Melbourne
School of Physics
Parkville, Vict. 3052
Australia

Wim deBoer
SLAC
Mail Bin 61
P.O. Box 4349
Stanford, CA 94309
Bitnet: WDB@SLACVM

Pascal Debu
DPhPE - CEA Cen Saclay
B.P. no. 2
F-91191 Gif-sur-Yvette
France
Bitnet: DEBU@FRSAC12

Bernd Dehning
Max Planck Inst. fur Phys.
Fohringer Weg 2
Postfach 40 12 12
D-8000 Munich 40, West Germany
Bitnet: DEHNING@CERNVM

Stefano Dell'Uomo
Ist. Naz. di Fis. Nucleare, Rome
P.le A. Moro 2
I-00185 Rome, Italy
Bitnet: DELLUOMO@VAXROM.INFNET

Patrizia DeSimone
Lab. Nazionale di Frascati
Via Enrico Fermi 8
I-00044 Frascati, Roma
Italy
Bitnet: PATRIZIA@SLACVM

Claudio O. Dib
SLAC
Mail Bin 81
P.O. Box 4349
Stanford, CA 94309
Bitnet: DIB@SLACVM

Robert DiRosario
University of Illinois
Dept. of Physics
1110 West Green Street
Urbana, IL 61801
Bitnet: ROBERT@SLACVM

Lance Dixon
SLAC
Mail Bin 81
P.O. Box 4349
Stanford, CA 94309
Bitnet: STUBBINS@SLACVM

Brian L. Dougherty
Lawrence Berkeley Lab
Bldg. 50A, Room 6141
University of California
Berkeley, CA. 94720

Marvin H. Douglas
U.C. San Diego
Dept. of Physics
B-019
La Jolla, CA 92093
Bitnet: MHDMAS@SDPH1.BITNET

Sidney Drell
SLAC
Mail Bin 80
P.O. Box 4349
Stanford, CA 94309
Bitnet: DRELL@SLACVM

Richard J. Dubois
TRIUMF, University of Victoria
Dept. of Physics
P.O. Box 1700
Victoria, BC, Canada V8W 2Y2
Bitnet: RICHARD@SLACVM

Jean E. Duboscq
University of California
Dept. of Physics
Santa Barbara, CA 93106
Bitnet: DUBOSCQ@SBHEP

Isard Dunietz
SLAC
Mail Bin 81
P.O. Box 4349
Stanford, CA 94309
Bitnet: ISI@SLACVM

William Dunwoodie
SLAC
Mail Bin 62
P.O. Box 4349
Stanford, CA 94309
Bitnet: WMD@SLACVM

James Eastman
Lawrence Berkeley Lab
MS 50-137
Berkeley, CA 94720
Bitnet: EASTMAN@LBL.GOV

Frederik C. Erne
NIKHEF - H
P. O. Box 41882
1009 DB Amsterdam
The Netherlands
Bitnet: U00042@HASARAS

Rahim Esmailzadeh
SLAC
Mail Bin 81
P.O. Box 4349
Stanford, CA 94309
Bitnet: RAHIM@SLACVM

Gary Feldman
SLAC
Mail Bin 78
P.O. Box 4349
Stanford, CA 94309
Bitnet: GARY@SLACVM

David N. Fernandes
SLAC
Mail Bin 61
P.O. Box 4349
Stanford, CA 94309
Bitnet: DAVEF@SLACVM

Michael J. Fero
M.I.T.
Dept. of Physics
Cambridge, MA 02139
Bitnet: MFERO@SLACVM

R. Clive Field
SLAC
Mail Bin 78
P.O. Box 4349
Stanford, CA 94309
Bitnet: SARGON@SLACVM

Carlos E. Figueroa
University of California
SCIPP
Santa Cruz, CA 95064
Bitnet: CARLOS@SLACSLD

Giuseppe Finocchiaro
SLAC
Mail Bin 43
P.O. Box 4349
Stanford, CA 94309
Bitnet: SLD::FINOCCHIARO,
VAXRON::FINOCCHIARO

Fausto Fiorani
University di Parma
Dipartimento di Fisica
Viale delle Scienze
I-43100 Parma, Italy
Bitnet: FIORANI@VAXPR.INFNET

Luca Fiorani
SLAC
Mail Bin 96
P.O. Box 4349
Stanford, CA. 94309

Carrie S. Fordham
SLAC
Mail Bin 95
P.O. Box 4349
Stanford, CA 94309
Bitnet: CARRIE@SLACVM

Raymond E. Frey
University of Michigan
Dept. of Physics
Ann Arbor, MI 48109
Bitnet: RAYFREY@SLACVM

Dieter Freytag
SLAC
Mail Bin 57
P.O. Box 4349
Stanford, CA. 94309
DRF@SLACVM

Alfred Fridman
SLAC, Bin 98
P.O. Box 4349
Stanford, CA 94309
Bitnet: FRIDMAN@SLACVM

Joshua Frieman
SLAC
Mail Bin 81
P.O. Box 4349
Stanford, CA 94309

John R. Fry
University of Liverpool
Dept. of Physics
P.O. Box 147
Liverpool L69 3BX, England
Bitnet: JRF@CERNVM

David Fryberger
SLAC
Mail Bin 20
P.O. Box 4349
Stanford, CA 94309
Bitnet: DAFRA@SLACVM

Michele Gallinaro
Lab. Nazionali, Frascati
via E. Fermi, 8
C.P. 13
1-00044 Frascati, Rome
Italy
Bitnet: MICHGALL@IRMLNF

Kock-Kiam Gan
SLAC
Mail Bin 61
P.O. Box 4349
Stanford, CA 94309
Bitnet: KKG@SLACVM

Arthur F. Garfinkel
Purdue University
Dept. of Physics
Lafayette, IN 47907
Bitnet: GARFINKEL@FNAL

Earl Gero
University of Michigan
Dept. of Physics
Ann Arbor, MI 48109
Bitnet: GERO@SLACVM

Duncan B. Gibaut
Carnegie Mellon University
Dept. of Physics
Pittsburgh, PA 15213
Bitnet: GIBAUT@FNAL

Valerie Gibson
CERN - EP Division
CH-1211 Geneva 23
Switzerland
Bitnet: GIBSON@CERNVM

Fred J. Gilman
SLAC
Mail Bin 81
P.O. Box 4349
Stanford, CA 94309
Bitnet: GILMAN@SLACVM

Gary Gladding
University of Illinois
Dept. of Physics
1110 W. Green St.
Urbana, IL 61801
Bitnet: GLADDING@SLACVM

Thomas Glanzman
SLAC
Mail Bin 78
P.O. Box 4349
Stanford, CA 94309
Bitnet: DRAGON@SLACVM

Gary L. Godfrey
SLAC
Mail Bin 98
P.O. Box 4349
Stanford, CA 94309
Bitnet: GLGCB@SLACVM

Paolo Gomes
University of California
SCIPP
Physics Board of Study
Santa Cruz, CA. 95064

Xin L. Gong
University of Hawaii
Dept. of Physics
Honolulu, HI 96822
Bitnet: XIN@SLACVM

Christoph Grab
SLAC
Mail Bin 65
P.O. Box 4349
Stanford, CA 94309
Bitnet: GRAB@SLACVM

Giorgio Gratta
University of California
Nat. Sci. II
SCIPP
Santa Cruz, CA 95064
Bitnet: GRATTA@SLACVM

Paul Griffin
SLAC
Mail Bin 81
P.O. Box 4349
Stanford, CA 94309
Bitnet: PAG@SLACVM

Paul Grosse-Wiesmann
SLAC
Mail Bin 95
P.O. Box 4349
Stanford, CA 94309
Bitnet: PGW@SLACVM

Francoise Guerin
SLAC
Mail Bin 81
P.O. Box 4349
Stanford, CA 94309

David J. Hadden
SLAC
Bin 81
P.O. Box 4349
Stanford, CA. 94709

Lawrence J. Hall
University of California
Dept. of Physics
Berkeley, CA 94720
Bitnet: HALL LJ@LBL

Gail G. Hanson
SLAC
Mail Bin 78
P.O. Box 4349
Stanford, CA 94309
Bitnet: GAIL@SLACVM

Haim Harari
Weizmann Inst. of Science
Dept. of Nuclear Physics
P.O. Box 26
76100 Rehovoth, Israel
Bitnet: FHHARARI@WEIZMANN

Robert F. Harr
Lawrence Berkeley Lab
Bldg. 50, Rm. 2160
Berkeley, CA 94720
Bitnet: HARR@SLACVM

Frederik A. Harris
University of Hawaii
Dept. of Physics \& Astronomy
Honolulu, HI 96822
Bitnet: HARRIS@UHHEPG

Paul F. Harrison
Liverpool University
Dept. of Physics
P.O. Box 147
Liverpool L69 3BX, England
Bitnet: PFH@CERNVM

Keith W. Hartman
Pennsylvania State University
Dept. of Physics
104 Davey Lab.
University Park, PA 16802
Bitnet: HARTMAN@FNAL

Despina Hatzifotiadou
CERN- EP Division
CH-1211 Geneva 23
Switzerland
Bitnet: DESPINA@CERNVM

Christopher Hawkins
SLAC
Mail Bin 61
P.O. Box 4349
Stanford, CA 94309
Bitnet: HAWKINS@SLACVM

John L. Hearns
Glasgow University
Dept. of Physics & Astronomy
Glasgow G12 8QQ
Scotland
Bitnet: AL03@GWIA

Christopher Hearty
Lawrence Berkeley Lab
University of California
Berkeley, CA 94720
Bitnet: HEARTY@SLACVM

Thomas M. Himel
SLAC
Mail Bin 95
P.O. Box 4349
Stanford, CA 94309
Bitnet: TMH@SLACVM

Chili Ho
University of California
Physics Dept.
Riverside, CA 92521

Sven Olof Holmgren
Stockholm University
Inst. of Physics
Vanadisvagen 9
S-11346 Stockholm, Sweden
Bitnet: HOLMGREN@SLACVM

Paul Hong
Northwestern University
Dept. of Physics
Evanston, IL 60208
Bitnet: c/o CHANG@FNAL

Seong J. Hong
University of Michigan
Dept. of Physics
Ann Arbor, MI 48109
Bitnet: HONG@SLACVM

Alan K. Honma
University of Victoria
Dept. of Physics
P.O. Box 1700
Victoria, BC, Canada V8W 2Y2
Bitnet: HONMA@SLACVM

Kent Hornbostel
SLAC
Mail Bin 81
P.O. Box 4349
Stanford, CA 94309
Bitnet: KENT@SLACVM

David P. Hutchinson
SLAC
Mail Bin 61
P.O. Box 4349
Stanford, CA 94309
Bitnet: DPH@SLACVM

Eric Roy Hyatt
Columbia University
Nevis Labs
P.O. Box 137
Irvington, NY 10533
Bitnet: HYATT@NEVIS

James E. Hylen
Johns Hopkins University
Dept. of Physics
Baltimore, MD 21218
Bitnet: JZH@SLACVM

Carl J. Im
SLAC
Mail Bin 81
P.O. Box 4349
Stanford, CA 94309
Bitnet: JUNG@SLACVM

Walter Innes
SLAC
Mail Bin 61
P.O. Box 4349
Stanford, CA 94309
Bitnet: WALT@SLACVM

George Irwin
Stanford University
Dept. of Physics
Stanford, CA 94309
Bitnet: GMIEG@SLACVM

Bob Jacobsen
SLAC
Mail Bin 95
P.O. Box 4349
Stanford, CA 94309
Bitnet: JACOBSEN@SLACVM

John A. Jaros
SLAC
Mail Bin 61
P.O. Box 4349
Stanford, CA 94309
Bitnet: JOHN@SLACVM

Anthony Johnson
Boston University
Dept. of Physics
590 Commonwealth Ave.
Boston, MA 02215
Bitnet: TONYJ@SLACVM

Matthew Jones
University of Victoria
Dept. of Physics
P.O. Box 1700
Victoria, BC, Canada V8W 2Y2
Bitnet: MJONES@SLACVM

Chang-Kee Jung
SLAC
Mail Bin 95
P.O. Box 4349
Stanford, CA 94309
Bitnet: ALPINIST@SLACVM

Tina M. Kaarsberg
State University of New York
Dept. of Physics
Stony Brook, NY 11794
Bitnet: TINA@CRNLNS

Marek Karliner
SLAC
Mail Bin 81
P.O. Box 4349
Stanford, CA 94309
Bitnet: MAREK@SLACVM

Nobu Katayama
State University of New York
Dept. of Physics
Albany, NY 12222
Bitnet: NK@CRNLNS

Mituaki Katuya
University of Shizuoka
Lab. Comp. Science
Yada 395, Shizuoka 422
Japan

Russel Kauffman
SLAC
Mail Bin 81
P.O. Box 4349
Stanford, CA 94309
Bitnet: KAUFFMAN@SLACVM

Hideaki Kawahara
SLAC
Mail Bin 62
P.O. Box 4349
Stanford, CA 94309
Bitnet: KAWAHARA@SLACVM

Lewis P. Keller
SLAC
Mail Bin 20
P.O. Box 4349
Stanford, CA 94309
Bitnet: LXKRA@SLACVM

Stephane A. Keller
Iowa State University
171-H University Village
Ames, IO 50010
Bitnet: KELLER@ALISUVAX

Peter Chong-Ho Kim
SLAC
Mail Bin 65
P.O. Box 4349
Stanford, CA 94309
Bitnet: PKIM@SLACVM

Mary King
University of California
SCIPP
Physics Board of Study
Santa Cruz, CA. 95064
Bitnet: MARYK@SLACVM

William T. Kirk
SLAC
Mail Bin 80
P.O. Box 4349
Stanford, CA 94309
Bitnet: BILLKIRK@SLACVM

Igor Klebanov
SLAC
Mail Bin 81
P.O. Box 4349
Stanford, CA 94309
Bitnet: IGOR@SLACVM

Spencer Klein
SLAC
Mail Bin 95
P.O. Box 4349
Stanford, CA 94309
Bitnet: SPENCER@SLACVM

Dale S. Koetke
SLAC
Mail Bin 61
P.O. Box 4349
Stanford, CA 94309
Bitnet: DALEK@SLACVM

Sachio Komamiya
SLAC
Mail Bin 95
P.O. Box 4349
Stanford, CA 94309
Bitnet: SACHIO@SLACVM

Jacobo Konigsberg
University Of California
Dept. of Physics
Knudsen Hall 4-140
Los Angeles, CA 90024
Bitnet: KONIGSBE@BNLVMA

Masatoshi Koshiba
CERN - EP Division
CH-1211 Geneva 23
Switzerland

Wayne Koska
University of Michigan
Dept. of Physics
Ann Arbor, MI 48109
Bitnet: KOSKA@SLACVM

Lee Anne Kowalski
SLAC
Mail Bin 61
P.O. Box 4349
Stanford, CA 94309
Bitnet: ANNE@SLACVM

Witold Kozanecki
SLAC
Mail Bin 95
P.O. Box 4349
Stanford, CA 94309
Bitnet: WITOLD@SLACVM

Frederic J. Kral
Lawrence Berkeley Lab
MS 50A-2160
University of California
Berkeley, CA. 94720
Bitnet: KRAL@SLACVM

Juergen Krueger
DESY
Notkestrasse 85
D-2000 Hamburg 52
West Germany
Bitnet: F35KRU@DHHDESY3

Michael P. Kuhlen
California Inst. Tech.
Dept. of Physics
Mail 356-48
Pasadena, CA 91125
Bitnet: KUHLEN@SLACVM

Paul F. Kunz
SLAC
Mail Bin 62
P.O. Box 4349
Stanford, CA 94309
Bitnet: PFKEB@SLACVM

Masahiro Kuze
University of Tokyo
Dept. of Physics
7-3-1 Hongo, Bunkyo-ku
Tokyo 113, Japan
Bitnet: KUZE@JPNKEKVX

Jonathan Labs
SLAC
Mail Bin 65
P.O. Box 4349
Stanford, CA 94309
Bitnet: JONLABS@SLACVM

Armando Lanaro
University of Rochester
Dept. of Physics & Astronomy
Rochester, NY 14627
Bitnet: LANARO@FNAL

Andrew Lankford
SLAC
Bin 95
P.O. Box 4349
Stanford, CA 94309
Bitnet: LANKFORD@SLACVM

Jan A. Lauber
University of Colorado
Dept. of Physics & Astrophysics
P.O. Box 390
Boulder, CO 80309
Bitnet: LAUBER@COLOPHYS

Lap Y. Lee
California Inst. Tech.
Lauritsen Lab 356-48
Pasadena, CA 91125
Bitnet: LYL@CITHEX.Bitnet

David W.G.S. Leith
SLAC
Mail Bin 62
P.O. Box 4349
Stanford, CA 94309
Bitnet: LEITH@SLACVM

David C. Lewellen
SLAC
Mail Bin 81
P.O. Box 4349
Stanford, CA 94309
Bitnet: DCL@SLACVM

Steven C. Lin
Columbia University
Dept. of Physics
New York, NY 10027
Bitnet: LIN@SLACVM

Willis T. Lin
University of California
Physics Dept.
Riverside, CA 92521
Bitnet: WXLP09@SLACPHYS

Christopher B. Lirakis
Northeastern University
Dept. of Physics
Boston, MA 02115
Bitnet: LIRAKIS@FNAL"

William S. Lockman
University of California
SCIPP
Santa Cruz, CA 95064
Bitnet: BILLY@SLACVM

Kenneth R. Long
Rutherford and Appleton Labs
Chilton
Didcot, Oxon. OX2 7NR, England
Bitnet: LONG@UKACRL

John LoSecco
University of Notre Dame
Dept. of Physics
Notre Dame, IN 46556
LOSECCO@UNDHEP

Xing-Min Lu
Columbia University
Pupin Hall, Box 105
New York, NY 10027
Bitnet: XLU@SLACVM

Vera G. Luth
SLAC
Mail Bin 95
P.O. Box 4349
Stanford, CA 94309
Bitnet: VGL@SLACVM

David B. MacFarlane
McGill University
Physics Dept.
3600 University Ave.
Montreal PQ
Canada H3A 2T8
Bitnet:
DBMACF@PHYSICS.MCGILL.CDN

Leon Madansky
Johns Hopkins University
Dept. of Physics
34th and Charles St.
Baltimore, MD 21218

Walid Majid
University of Illinois
Dept. of Physics
1110 W. Green St.
Urbana, IL 61801
Bitnet: WALID@SLACVM

Eric J. Mannel
University of Notre Dame
Dept. of Physics
Notre Dame, IN 46556
Bitnet: MANNEL@FNAL

Giancarlo Mantovani
University of Perugia
Dipartimento di Fisica
I-06100 Perugia
Italy
Bitnet: GIANCARL@IPGUNIV

Thomas Markiewicz
SLAC
Mail Bin 96
P.O. Box 4349
Stanford, CA 94309
Bitnet: TWMARK@SLACVM

Jose L. Martinez
University of Cincinnati
Dept. of Physics
Cincinnati, OH 45221
Bitnet: JLM@SLACVM

Hiroaki Masuda
SLAC
Mail Bin 96
P.O. Box 4349
Stanford, CA 94309
Bitnet: MASUDA@SLACVM

Lisa Mathis
Lawrence Berkeley Lab
University of California
Berkeley, CA 94720
Bitnet: LGMP04@LBL.GOV

Laurent Mathys
SLAC
Mail Bin 62
P.O. Box 4349
Stanford, CA 94309
Bitnet: MATHYS@SLACVM

John A.J. Matthews
Johns Hopkins University
Physics Dept.
Baltimore, MD 21218
Bitnet: JYM@SLACVM

Tom Mattison
SLAC
Mail Bin 95
P.O. Box 4349
Stanford, CA 94309
Bitnet: MATTISON@SLACVM

John McGowan
University of Illinois
Dept. of Physics
1110 W. Green St.
Urbana, IL 61801
Bitnet: JFM@SLACVM

Brian T. Meadows
University of Cincinnati
Dept. of Physics
Cincinnati, OH 45221
Bitnet: BRIAN@SLACVM

Joao R.T. de Mello-Neto
Fermilab
M.S. 122, E769
P.O. Box 500
Batavia, IL 60510
Bitnet: J MELLO@FNAL

David J. Mellor
University of Illinois
Dept. of Physics
1110 W. Green St.
Urbana, IL 61801
Bitnet: DJM@SLACVM

Robert Lee Messner
SLAC
Bin 94
P.O. Box 4349
Stanford, CA. 94309
Bitnet: ROM@SLACVM

Douglas G. Michael
Harvard University
Dept. of Physics
Cambridge, MA 02138
Bitnet: MICHAEL@FNAL

E. Cas Milner
Los Alamos National Lab
MS H846, P.O. Box 1663
Los Alamos, NM 87545
Bitnet: MILNER@LAMPF

Jussara M. de Miranda
Fermilab
MS 122
P.O. Box 500
Batavia, IL 60510
Bitnet: J MIRANDA@FNAL

Michiko Miyamoto
Kobe College
11-2, 1-chome
Yamate, Nakasuji
Takarazuka City
Hyogo Prefecture
Japan 665

Kenneth C. Moffeit
SLAC
Mail Bin 78
P.O. Box 4349
Stanford, CA 94309
Bitnet: MOFFEIT@SLACVM

Rollin Morrison
University of California
Dept. of Physics
Santa Barbara, CA 93106

William M. Morse
Brookhaven National Lab
Physics Dept., Bldg. 510A
Upton, L.I., NY 11973-5000
Bitnet: JNET%"MORSE@BNLCLI"

Benoit Mours
Lab de Phys. des Particules
Ch. de Bellevue, B.P. 909
F-74019 Annecy-le-Vieux
CEDEX, France
Bitnet: MOURS@CERNVM

Steve Mrenna
Johns Hopkins University
Dept. of Physics & Astronomy
Homewood Campus
Baltimore, MD 21218
Bitnet: INS CSM@JUHVMS

George Mundy
SLAC
Mail Bin 96
P.O. Box 4349
Stanford, CA 94309
Bitnet: MUNDY@SLACVM

Charles T. Munger
SLAC
Mail Bin 61
P.O. Box 4349
Stanford, CA 94309
Bitnet: CHARLES@SLACVM

William Murray
Indiana University
Dept. of Physics
Bloomington, IN 47405
Bitnet: MURRAY@SLACVM

Tadashi Nagamine
Kyoto University
Dept. of Physics
Yoshida-honmachi, sakyo-ku
Kyoto-shi 606, Japan
Bitnet: NAGAMINE@FNAL

Jordan A. Nash
SLAC
Mail Bin 95
P.O. Box 4349
Stanford, CA 94309
Bitnet: JAN@SLACVM

Eric Michael Nelson
SLAC
Mail Bin 26
P.O. Box 4349
Stanford, CA 94309
Bitnet: ENELSON@SLACVM

Ai G. Nguyen
Michigan State University
Dept. of Physics
East Lansing, MI 48824
Bitnet: AINGUYEN@FNAL

H. Pierre Noyes
SLAC
Mail Bin 81
P.O. Box 4349
Stanford, CA 94309
Bitnet: NOYES@SLACVM

Mirko M. Nussbaum
University of Cincinnati
Dept. of Physics
Cincinnati, OH 45221
Bitnet: MMN@SLACVM

Kathryn O'Shaughnessy
SLAC
Mail Bin 78
P.O. Box 4349
Stanford, CA 94309
Bitnet: KATHYO@SLACVM

Harold O. Ogren
Indiana University
Dept. of Physics
Bloomington, IN 47405
Bitnet: OGREN@SLACVM

Heungmin Oh
University of California
Physics Dept.
Riverside, CA 92521
Bitnet: OH@SLACTWGM

Tsunehiko Omori
Nat. Lab. for High Energy Physics
KEK
Oho, Tsukuba-shi
Ibaraki-ken 305, Japan
Bitnet: OMORI@JPNKEKVM

Jeffrey S. Orszak
Boston University
Dept. of Physics
590 Commonwealth Ave.
Boston, MA 02215
Bitnet: JEFFO@SLACVM

Wolfgang K.H. Panofsky
SLAC
Mail Bin 76
P.O. Box 4349
Stanford, CA 94309

Sherwood Parker
University of Hawaii
Dept. of Physics
Honolulu, HI 96822
Bitnet: SHER@SLACVM

Larry Parrish
University of Washington
Dept. of Physics
Seattle, WA 98195

Michele Pauluzzi
Perugia University
Dipartimento di Fisica
Via Pascoli
I-06100 Perugia, Italy
Bitnet: PAULUZZI@SLACVM

Martin L. Perl
SLAC
Mail Bin 61
P.O. Box 4349
Stanford, CA 94309
Bitnet: MARTIN@SLACVM

Ida M. Peruzzi
Laboratori Naz. di Frascati
via E. Fermi, 40
C.P. 13
I-00046 Frascati (Rome)
Italy
Bitnet: IMP@SLACVM

Michael Peskin
SLAC
Mail Bin 81
P.O. Box 4349
Stanford, CA 94309
Bitnet: MPESKIN@SLACVM

Bernard Peyaud
DPhPE - CEA Cen Saclay
B.P. no. 2
F-91191 Gif-sur-Yvette, France

Marcello Piccolo
Laboratori Nazionali, Frascati
via E. Fermi, 40
C.P. 13
I-00044 Frascati, Rome, Italy
Bitnet: MXP@SLACVM

Livio Piemontese
Istituto Naz. Fiz. Nucleare
via Paradiso 12
I-44100 Ferrara, Italy
Bitnet: LIVIO@SLACVM

Dale Pitman
SLAC
Mail Bin 65
P.O. Box 4349
Stanford, CA 94309
Bitnet: PITMAN@SLACVM

Rainer Pitthan
SLAC
Mail Bin 96
P.O. Box 4349
Stanford, CA 94309
Bitnet: RAINER@SLACVM

Eric J. Prebys
University of Rochester
Dept. of Physics & Astronomy
Rochester, NY 14627
Bitnet: PREBYS@FNAL

Charles Prescott
SLAC
Mail Bin 80
P.O. Box 4349
Stanford, CA 94309
Bitnet: PRESCOTT@SLACVM

Nading Qi
Academia Sinica
Inst. of High Energy Physics
P. O. Box 918
Beijing
The People's Republic of China

Helen Quinn
SLAC
Mail Bin 81
P.O. Box 4349
Stanford, CA 94309
Bitnet: QUINN@SLACVM

Patricia Rankin
SLAC
Mail Bin 78
P.O. Box 4349
Stanford, CA 94309
Bitnet: TRICIA@SLACVM

Blair N. Ratcliff
SLAC
Mail Bin 62
P.O. Box 4349
Stanford, CA 94309
Bitnet: BLAIR@SLACVM

Paul Rensing
SLAC
Mail Bin 62
P.O. Box 4349
Stanford, CA 94309
Bitnet: RENSING@SLACVM

Patrick G. Reutens
SLAC
Mail Bin 96
P.O. Box 4349
Stanford, CA 94309
Bitnet: REUTENS@SLACVM

Jeffrey D. Richman
University of California
Dept. of Physics
Santa Barbara, CA 93106
Bitnet: RICHMAN@SLACVM

Burton Richter
SLAC
Mail Bin 80
P.O. Box 4349
Stanford, CA 94309
Bitnet: KATHY@SLACVM

John Keith Riles
SLAC
Mail Bin 95
P.O. Box 4349
Stanford, CA 94309
Bitnet: KEITHR@SLACVM

E. Michael Riordan
SLAC
Mail Bin 80
P.O. Box 4349
Stanford, CA 94309
Bitnet: EMR@SLACVM

Jack L. Ritchie
SLAC
Mail Bin 63
P.O. Box 4349
Stanford, CA 94309
Bitnet: RITCHIE@SLACVM

Leon S. Rochester
SLAC
Mail Bin 96
P.O. Box 4349
Stanford, CA 94309
Bitnet: LSREA@SLACVM

Maria P. Roco
University of Iowa
Dept. of Physics & Astronomy
Iowa City, IA 52242
Bitnet: ROCO@SLACVM

Natalie A. Roe
SLAC
Mail Bin 61
P.O. Box 4349
Stanford, CA 94309
Bitnet: NATALIE@SLACVM

Matt Sands
University of California
SCIPP
Santa Cruz, CA 94064
Bitnet: SANDS@SLACVM

Jack Sandweiss
Yale University
Dept. of Physics
P.O. Box 6666
New Haven, CT 06511

Attilio Santocchia
Perugia University
Dipartimento di Fisica
Via Pascoli
I-06100 Perugia, Italy
Bitnet: SANTOCCH@SLACVM

Markus W. Schaad
Lawrence Berkeley Lab
University of California
Berkeley, CA 94720
Bitnet: SCHAAD@SLACVM

Heidi M. Schellman
University of Chicago
Dept. of Physics
Chicago, IL 60637
Bitnet: SCHELLMA@FNAL

Rafe H. Schindler
SLAC
Mail Bin 65
P.O. Box 4349
Stanford, CA 94309
Bitnet: RAFE@SLACVM

Daniel V. Schroeder
SLAC
Mail Bin 81
P.O. Box 4349
Stanford, CA 94309
Bitnet: DVS@SLACVM

David C. Schultz
SLAC
Mail Bin 62
P.O. Box 4349
Stanford, CA 94309
Bitnet: DCS@SLACVM

Alan J. Schwartz
Stanford University
High Energy Physics Lab
Stanford, CA 94305-4080
Bitnet: SCHWARTZ@HARVHEP

Felix Sefkow
DESY
Notkestrasse 85
D-2000 Hamburg 52
West Germany
Bitnet: F15SEF@DHHDESY3

Stephen L. Shapiro
SLAC
Mail Bin 62
P.O. Box 4349
Stanford, CA 94309
Bitnet: SHAPIRO@SLACVM

Vivek A. Sharma
Syracuse University
Dept. of Physics
Syracuse, NY 13244
Bitnet: VS@CRNLNS

Stephen Sharpe
SLAC
Mail Bin 81
P.O. Box 4349
Stanford, CA 94309
Bitnet: SHARPE@SLACVM

Junpei Shirai
Nat. Lab. for High Energy Physics
KEK
Oho, Tsukuba-shi
Ibaraki-ken 305, Japan
Bitnet: SHIRAI@JPNKEKVM

Ian M. Silvester
Oxford University
Nuclear Physics Lab
Keble Road
Oxford OX1 3RH, England
Bitnet: IS@UK.AC.RL

Armand Simon
Max Planck Inst. fur Kernphysik
Postfach 103 980
D-6900 Heidelberg, West Germany
Bitnet: ASO@CERNVM

Constantine Simopoulos
SLAC
Mail Bin 62
P.O. Box 4349
Stanford, CA 94309
Bitnet: CONSIM@SLACVM

Robert L. Singleton
SLAC
Mail Bin 81
P.O. Box 4349
Stanford, CA. 94309
Bitnet: BOBS@SLACVM

Stewart A.J. Smith
Princeton University
Dept. of Physics
P.O. Box 708
Princeton, NJ 08544
Bitnet: SMITH@PUPHEP

Arthur E. Snyder
Indiana University
Dept. of Physics
Bloomington, IN 47405

Randy J. Sobie
University of British Columbia
Physics Dept.
Vancouver, BC, V6T 2A3
Canada
Bitnet: SOBIE@SLACVM

Jacob Sonnenschein
SLAC
Mail Bin 81
P.O. Box 4349
Stanford, CA 94309
Bitnet: COBI@SLACVM

Kevin Sparks
University of California
Dept. of Physics
Davis, CA 95616
Bitnet: SPARKS@UCDHEP

Thomas Steele
SLAC
Mail Bin 95
P.O. Box 4349
Stanford, CA 94309
Bitnet: TOMIS@SLACVM

Ian E. Stockdale
University of Illinois
Dept. of Physics
1110 W. Green St.
Urbana, IL 61801
Bitnet: IES@SLACVM

Calvin Stubbins
SLAC
Mail Bin 81
P.O. Box 4349
Stanford, CA 94309
Bitnet: STUBBINS@SLACVM

Fumihiko Suekane
Nat. Lab. for High Energy Physics
KEK
Oho, Tsukuba-shi
Ibaraki-ken 305, Japan

Morris Swartz
SLAC
Mail Bin 78
P.O. Box 4349
Stanford, CA 94309
Bitnet: MORRIS@SLACVM

Anthony Szumilo
University of Washington
Dept. of Physics
Seattle, WA 98195
Bitnet: SZUMILO@SLACSLD

Lucas Taylor
Imperial Coll. Sci. Tech.
Blackett Lab
Prince Consort Road
London, SW7 2AZ, England
Bitnet: TAYLORL@CERNVM

Richard E. Taylor
SLAC, Bin 96
P.O. Box 4349
Stanford, CA 94309
Bitnet: RETAYLOR@SLACVM

Nobukazu Toge
SLAC
Mail Bin 62
P.O. Box 4349
Stanford, CA 94309
Bitnet: TOGE@SLACVM

Walter H. Toki
SLAC
Mail Bin 65
P.O. Box 4349
Stanford, CA 94309
Bitnet: TOKI@SLACVM

Yung-Su (Paul) Tsai
SLAC
Mail Bin 81
P.O. Box 4349
Stanford, CA 94309
Bitnet: YSTTH@SLACVM

Andre S. Turcot
University of Victoria
Dept. of Physics
P.O. Box 1700
Victoria, BC, Canada V8W 2Y2
Bitnet: TURCOT@UVVM

Marc Turcotte
TRIUMF
University of British Columbia
Dept. of Physics
Vancouver, BC, Canada V6T 1W5
Bitnet: MARC@SLACVM

Georg Tysarczyk
University of Heidelberg
Physikalisches Inst.
Philosophenweg 12
D-6900 Heidelberg, West Germany
Bitnet: GEORG@DHDIHEP1

Tracy Usher
University of California
Dept. of Physics
Irvine, CA 92717
Bitnet: TUSHER@UCIVMSA

Chukwuma Kenneth Uzo
SLAC
Mail Bin 98
P.O. Box 4349
Stanford, CA 94309
Bitnet: KENUZO@SLACVM

Jaroslav Va'Vra
SLAC
Mail Bin 62
P.O. Box 4349
Stanford, CA 94309
Bitnet: JJV@SLACVM

Richard J. VanKooten
SLAC
Mail Bin 95
P.O. Box 4349
Stanford, CA 94309
Bitnet: RICKV@SLACVM

Cristina Vannini
INFN-Pisa
Via Livornese 582/A
I-56010 San Piero a Grado
Italy
Bitnet: CVN@SLACVM
VANNINI@IPIINFN

Geert J. VanOldenborgh
NIKHEF
P. O. Box 41882
1009 DB Amsterdam
The Netherlands
Bitnet: T19@NIKHEFH.HEP.NL

Piero Giorgio Verdini
INFN-Pisa
Via Livornese 582/A
I-56010 San Piero a Grado
Italy
Bitnet: PGV@SLACVM
VERDINI@IPIINFN

Purushotham Voruganti
SLAC
Mail Bin 78
P.O. Box 4349
Stanford, CA 94309
Bitnet: PURU@SLACVM

Michael F. Wade
Durham University
Dept. of Physics
South Road
Durham DH1 3LE, England
Bitnet: MFW@UK.AC.DUR.HEP

Tony Waite
University of Victoria
Dept. of Physics
P.O. Box 1700
Victoria, BC, Canada V8W 2Y2
Bitnet: APW@SLACVM

Mark Walton
SLAC
Mail Bin 81
P.O. Box 4349
Stanford, CA 94309
Bitnet: WALTON@SLACVM

Ning Wang
University of California
Dept. of Physics
Berkeley, CA 94720

Zi Wang
Utah State University
Dept. of Physics
Logan, UT 84322

Bennie F.L. Ward
University of Tennessee
Dept. of Physics
401 Nielsen Physics Bldg.
Knoxville, TN 37996-1200
Bitnet: BFLW@SLACVM

Steven R. Wasserbaech
SLAC
Mail Bin 65
P.O. Box 4349
Stanford, CA 94309
Bitnet: SRW@SLACVM

Achim W. Weidemann
University of Tennessee
Dept. of Physics
Knoxville, TN 37996
Bitnet: ACHIM@SLACVM

Andreas Weigend
SLAC
Mail Bin 95
P.O. Box 4349
Stanford, CA 94309
Bitnet: WEIGEND@SLACVM

Alan Weinstein
SLAC
Mail Bin 65
P.O. Box 4349
Stanford, CA 94309
Bitnet: AJW@SLACVM

Marvin Weinstein
SLAC
Mail Bin 81
P.O. Box 4349
Stanford, CA 94309
Bitnet: NIV@SLACVM

Christopher Wendt
SLAC
Mail Bin 81
P.O. Box 4349
Stanford, CA 94309
Bitnet: WENDT@SLACVM

Norbert Wermes
CERN
CH-1211 Geneva 23
Switzerland
Bitnet: NNW@CERNVM

Judd O'Hara Wilcox
University of California
Dept. of Physics
Davis, CA 95616
Bitnet: WILCOX@UCDHEP

Raymond Willey
University of Pittsburgh
Dept. of Physics
Pittsburgh, PA 15260
Bitnet: WILLEY@PITTVMS

David A. Williams
University of California
SCIPP
Santa Cruz, CA 95064
Bitnet: WILLIAMS@SLACTBF

Michael S. Witherell
University of California
Dept. of Physics
Santa Barbara, CA 93106
Bitnet: WITHERELL@SBHEP

Lincoln Wolfenstein
Carnegie Mellon University
Dept. of Physics
Pittsburgh, PA 15213

John W. Womersley
University of Florida
Dept. of Physics
Gainesville, FL 32611
Bitnet: WOMERSLEY@FNAL

Gwo-Guang Wong
University of California
Physics Dept.
Riverside, CA 92521

Michael Woods
SLAC, Bin 78
P.O. Box 4349
Stanford, CA 94309
Bitnet: MWOODS@SLACVM

Guy Wormser
SLAC
Mail Bin 95
P.O. Box 4349
Stanford, CA 94309
Bitnet: WORMSER@SLACVM

Jeffery L. Wyss
Ist. Naz. Fiz. Nucleare
via Marzolo 8
I-35100 Padua, Italy
Bitnet: WYSS@VAXFPD.INFNET

Chiaki Yanagisawa
State University of New York
Dept. of Physics
Stony Brook, NY 11794
Bitnet: CHIAKI@CUSB

George P. Yost
University of California
Dept. of Physics
Berkeley, CA 94720
Bitnet: GPY@SLACVM

Charles C. Young
SLAC
Mail Bin 96
P.O. Box 4349
Stanford, CA 94309
Bitnet: YOUNG@SLACVM

Michael Vincent Yurko
Indiana University
Dept. of Physics
Bloomington, IN 47405
Bitnet: MYURKO@SLACVM

Carla Zaccardelli
University of California
SCIPP
Nat. Sci. II
Santa Cruz, CA 95064
Bitnet: ZACCCARDE@SLACVM

Geordie H. Zapalac
SLAC
Mail Bin 98
P.O. Box 4349
Stanford, CA 94309
Bitnet: GEORDIE@SLACVM

Richard W. Zdarko
SLAC
Mail Bin 36
P.O. Box 4349
Stanford, CA 94309
Bitnet: RWZP06@SLACMAC

Guenter Zech
University of Siegen
Fachbereich fur Physik
Postfach 101240
D-5900 Siegen, West Germany

Tianchi Zhao
University of Washington
Dept. of Physics
Seattle, WA 98195
Bitnet: TCZ@FNAL

THE SLAC SUMMER INSTITUTES ON PARTICLE PHYSICS

1973 - 1987

1973 DEEP INELASTIC ELECTROPRODUCTION

"Hadron Production in Deep Inelastic Processes"	J. D. Bjorken
"Hadron Production in the Collision of Virtual Photons with Nucleons – an Experimental Review"	M. Perl
"Phenomenological Analysis"	F. J. Gilman
"Asymptotic Behavior and Short Distance Singularities"	Y. Frishman

WEAK CURRENTS AND INTERACTIONS

"Raw Notes of Lectures on Current Algebra and PCAC"	S. Drell
"Experimental Phenomenology"	M. Schwartz S. Wojcicki
"Gauge-Theories of Weak and Electromagnetic Interaction"	T. Appelquist
"How to Transform Current Quarks to Constituent Quarks and Try to Predict Hadron Decays"	J. Primack M. Kugler

1974 THE STRONG INTERACTIONS

"Diffractive Processes"	D.W.G.S. Leith
"Amplitude Structure in Two- and Quasi-Two-Body Processes"	M. Davier
"Resonances: Experimental Review"	R.J. Cashmore
"Resonances: A Quark View of Hadron Spectroscopy and Transitions"	F. J. Gilman
"Lectures on Inclusive Hadronic Processes"	D. Sivers
"Large Momentum Transfer Processes"	R. Blankenbecler
"Hadron Dynamics"	H.D.I. Abarbanel

1975 DEEP HADRONIC STRUCTURE AND THE NEW PARTICLES

"Leptons as a Probe of Hadronic Structure"	F. J. Gilman
"Lepton Scattering as a Probe of Hadron Structure"	E. D. Bloom
"High $p_\perp$ Dynamics"	J. D. Bjorken
"Hadronic Collision and Hadronic Structure (An Experimental Review)"	M. Davier
"The New Spectroscopy"	H. Harari
"The New Spectroscopy (An Experimental Review)"	G. H. Trilling

1976 WEAK INTERACTIONS AT HIGH ENERGY AND THE PRODUCTION OF NEW PARTICLES

"Weak Interaction Theory and Neutral Currents"	J. D. Bjorken
"Weak Interactions at High Energy"	S. G. Wojcicki
"ψ Spectroscopy"	G. J. Feldman
"A New Lepton?"	G. J. Feldman
"Lectures on the New Particles"	J. D. Jackson
"New Particle Production"	D. Hitlin

1977 QUARK SPECTROSCOPY AND HADRON DYNAMICS

"Quarks and Leptons"	H. Harari
"Quark Confinement"	S. D. Drell
"Hadron Spectroscopy"	F. J. Gilman
"Lectures on the Quark Model, Ordinary Mesons, Charmed Mesons, and Heavy Leptons"	M. L. Perl
"Quarks and Particle Production"	K. C. Moffeit

1978 WEAK INTERACTIONS – PRESENT AND FUTURE

"Accelerator Neutrino Experiments"	D. H. Perkins
"Weak Interactions at High Energies"	J. Ellis
"Gauge Theories of the Weak Interactions"	H. Quinn
"Weak Decays"	S. Wojcicki

1979 QUANTUM CHROMODYNAMICS

"Lepton Nucleon Scattering"	W. G. Atwood
"Massive Lepton Pair Production"	R. Stroynowski
"QCD Phenomenology of the Large P_T Processes"	R. Stroynowski
"Perturbative Quantum Chromodynamics"	S. J. Brodsky
"Elements of Quantum Chromodynamics"	J. D. Bjorken

1980 **THE WEAK INTERACTIONS**

"Gauge Theories of Weak Interactions"	M. J. Veltman
"Neutrinos and Neutrino Interactions"	F. J. Sciulli
"Weak Decays of Strange and Heavy Quarks"	D. Hitlin
"From the Standard Model to Composite Quarks and *Leptons*"	H. Harari
"Physics of Particle Detectors"	D. M. Ritson J. Jaros J. Marx H. A. Gordon R. S. Gilmore W. B. Atwood

1981 **THE STRONG INTERACTIONS**

"Quark-Antiquark Bound State Spectroscopy and QCD"	E. D. Bloom
"Meson Spectroscopy: Quark States and Glueballs"	M. S. Chanowitz
"Quantum Chromodynamics and Hadronic Interactions at Short Distances"	S. J. Brodsky
"*Untangling Jets from* Hadronic Final States"	G. Fox
"Heavy Flavor Production from Photons and Hadrons"	C. A. Heusch
"Design Constraints and Limitations in e^+e^- Storage Rings"	J. LeDuff
"Linear Colliders: A Preview"	H. Wiedemann

1982 **PHYSICS AT VERY HIGH ENERGIES**

"Expectations for Old and New Physics at High Energy Colliders"	R. N. Cahn
"Beyond the Standard Model in Lepton Scattering and Beta Decay"	M. Strovink
"Grand Unification, Proton Decay, and *Neutrino Oscillations*"	H. H. Williams
"e^+e^- Interactions at Very High Energy: Searching Beyond the Standard Model"	J. Dorfan
"The Gauge Hierachy Problem, Technicolor, Supersymmetry, and All That"	L. Susskind
"Composite Models for Quarks and Leptons"	H. Harari
"Electron-Proton Colliding Beams: *The Physics Programme and the Machine*"	B. H. Wiik

1983 **DYNAMICS AND SPECTROSCOPY AT HIGH ENERGY**

"Jets in QCD: A Theorist's Perspective"	S. Ellis
"Jets in e^+e^- Annihilation"	R. Hollebeek
"Jet Production in High Energy Hadron Collisions"	R. F. Schwitters
"Aspects of the Dynamics of Heavy-Quark Systems"	M. E. Peskin
"Heavy Particle Spectroscopy and Dynamics B's to Z's"	M. G. D. Gilchriese
"... And for Our Next Spectroscopy?"	J. Ellis
"Review of the Physics and Technology of Charged Particle Detectors"	A. H. Walenta
"A Review of the Physics and Technology of High-Energy Calorimeter Devices"	P. M. Mockett

1984 **THE SIXTH QUARK**

"The Last Hurrah for Quarkonium Physics: The Top System"	E. Eichten
"Developments in Solid State Vertex Detectors"	C. J. S. Damerell
"Experimental Methods of Heavy Quark Detection"	T. Himel
"Production and Uses of Heavy Quarks"	G. L. Kane
"Weak Interactions of Quarks and Leptons: Experimental Status"	S. Wojcicki
"The Experimental Method of Ring-Imaging Cherenkov (RICH) Counters"	T. Ekelöf
"Weak Interactions of Quarks and Leptons (Theory)"	H. Harari

PIEF-FEST

"Pief"	S. Drell
"Accelerator Physics"	R. R. Wilson
"High Energy Theory"	T. D. Lee
"Science and Technology Policies for the 1980s"	F. Press
"*Inclusive Lepton-Hadron Experiments*"	J. Steinberger
"Forty-Five Years of e^+e^- Annihilation Physics: 1956 to 2001"	B. Richter
"We Need More Piefs"	J. Wiesner

1985 **SUPERSYMMETRY**

"Introduction to Supersymmetry"	J. Polchinski
"Signatures of Supersymmetry in e^+e^- Collisions"	D. Burke
"Properties of Supersymmetric Particles & Processes"	R. M. Barnett
"Supersymmetry: Experimental Signatures at Hadron Colliders"	P. Darriulat
"Superworld/Hyperworlds"	M. E. Peskin
"Very High Energy Colliders"	B. Richter
"Some Issues Involved in Designing a 1 TeV (c.m.) $e^{\pm}$ Linear Collider Using Conventional Technology"	G. A. Loew
"Wake Field Accelerators"	P. B. Wilson
"Plasma Accelerators"	R. D. Ruth & P. Chen
"Collider Scaling and Cost Estimation"	R. B. Palmer

1986 **PROBING THE STANDARD MODEL**

"Electroweak Interactions —Standard and Beyond"	H. Harari
"CP and Other Experimental Probes of Electroweak Phenomena"	B. Winstein
"Pertubative QCD: K-Factors"	R. Field
"Experimental Tests of Quantum Chromodynamics"	J. Dorfan
"Phenomenology of Heavy Quark Systems"	F. Gilman
"Heavy Quark Spectroscopy and Decay"	R. Schindler
"Some Aspects of Computing in High Energy Physics"	P. Kunz
"Data Acquisition for High Energy Physics Experiments"	M. Breidenbach

1987 **LOOKING BEYOND THE Z**

"Theory of e^+e^- Collisions at Very High Energy"	M. E. Peskin
"Prospects for Physics at e^+e^- Linear Colliders"	G. J. Feldman
"Physics with Polarized Electron Beams"	M. L. Swartz
"Electron-Proton Physics at HERA"	G. Wolf
"Hadron Colliders Beyond the Z^0"	C. Quigg
"Physics at Hadron Colliders (Experimental View)"	J. L. Siegrist
"The Dialogue Between Particle Physics and Cosmology"	B. Sadoulet

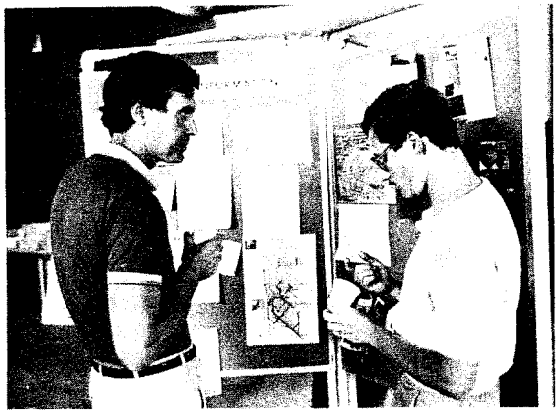

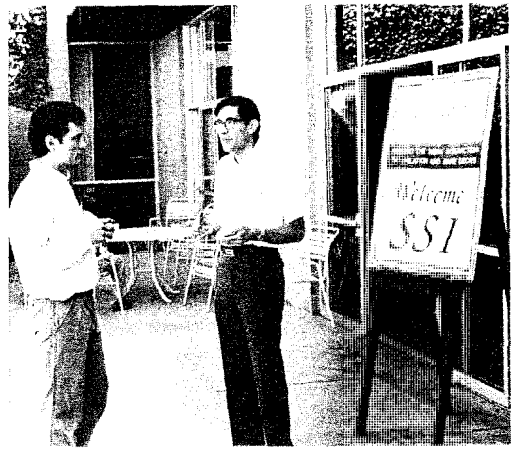
Welcome
SSI